UC Riverside

UC Riverside Electronic Theses and Dissertations

Title

Electron-Deficient Photosensitizers for Initiating Hole Transfer in Bioinspired Molecular Electrets

Permalink

https://escholarship.org/uc/item/8mj8w5g8

Author

Espinoza, Eli Misael

Publication Date

2019

Peer reviewed|Thesis/dissertation

eScholarship.org Powered by the California Digital Library
University of California

UNIVERSITY OF CALIFORNIA
RIVERSIDE

Electron-Deficient Photosensitizers for Initiating Hole Transfer in Bioinspired Molecular Electrets

A Dissertation submitted in partial satisfaction
of the requirements for the degree of

Doctor of Philosophy

in

Chemistry

by

Eli Espinoza

March 2019

Dissertation Committee:
Dr. Valentine I. Vullev, Chairperson
Dr. Yinsheng Wang
Dr. Gregory Beran

Copyright by
Eli Espinoza
2019

The Dissertation Eli Espinoza is approved:

_____

_____

_____

Committee Chairperson

University of California, Riverside

Acknowledgements:

I'm very grateful to my mentor, Dr. Valentine Vullev, for the time and dedication he's given which was pivotal to realize my potential as a physical organic chemist. His unique style of mentoring and his immense knowledge of science was indispensable to my academic career. много Благодаря!!!

I'm thankful to my committee members: Dr. Yinsheng Wan and Dr. Gregory Beran for their help throughout my graduate experience. I'm thankful for Dr. Beran for his guidance with computational chemistry. I would also like to extend my gratitude to the Department of Chemistry for ensuring Teaching Assistantships throughout my graduate studies.

I'm appreciative for Dr. Daniel Gryko and very thankful for Dr. Frank Quina. The time I spent in Poland and Brazil not only transformed me as a chemist but it also gave me the opportunity to broaden my horizon.

I am very thankful for my good friend Esteban Rodriguez. His artistic skills afforded us a front cover for a journal. Thank you for helping me out despite your busy schedule.

I am also very thankful for my former lab partner and good friend Narek Darabedian for helping me with several of my projects. Thank you for being available to aide me in my research and for your contribution to the papers we published together.

I am extremely grateful for my lab partners, present and past. They are nothing short of amazing in my eyes. I would like to thank Dr. Vicente Nunez for being the stepping stone for me joining the Vullev group. I am thankful to Dr. Jillian Larsen-Clinton for being an amazing lab partner and for her companionship through the greater part of my graduate studies. I would also like to thank John A. Clark and James B. Derr for working with me during the latter part of my graduate work. The late nights and early mornings with them will be cherished memories. I am thankful for Jesse Tamayo and Max Mayther for their companionship and scientific discussions. I am grateful to have worked with amazing undergraduates: Michelle Wurch, Marianne Morales and Joey Soliman. Thank you Dr. Vullev for being an amazing P.I and the Vullev group for being amazing friends and coworkers.

Lastly, I would like to thank my family. My two brothers: Fernando and Israel Espinoza and my sister Rebecca Calderon, whom never stopped believing in me and especially for my mom and dad, Matilde Espinoza and Rafael Espinoza, whom have shown me unconditional love and support throughout my education. Muchas gracias por el sacrificio y esfuerzo que hicieron para proveer por nosotros!!!

ABSTRACT OF THE DISSERTATION

Electron-Deficient Photosensitizers for Initiating Hole Transfer in Bioinspired Molecular Electrets

by

Eli Espinoza

Doctor of Philosophy, Graduate Program in Chemistry
University of California, Riverside, March 2019
Dr. Valentine I. Vullev, Chairperson

Molecular-level control of charge transfer is essential for organic electronics and solar energy conversion, as well as for comprehending a wide range of biological processes. Photoconversion efficiency is mainly hindered by interfacial charge recombination. In nature, charge recombination is suppressed by incorporating molecular electrets, systems with ordered electric dipoles. Local electric fields originating from molecular dipoles can thus aid in overcoming charge recombination while promoting the desired forward charge transfer. Protein alpha helices present the best example for natural molecular electrets, that is, they have intrinsic dipoles originating from the ordered amide and hydrogen bonds.

A principal challenge of polypeptide charge transfer systems composed of native amino acids is the inherent distance limitation for efficient transduction of electrons and holes. Along their backbones and hydrogen bonds, protein α-helices mediate electron transfer via tunneling, the rate constants of which, k_{et}, fall off exponentially with an

increase in the length of the electron-transfer pathways, r_{et}, i.e. $k_{et} \propto \exp(-\beta r_{et})$. Specifically, for protein α-helices, β is about 1.3 $Å^{-1}$. The inherent presence of competing nanosecond processes, such as fluorescence, internal conversion and intersystem crossing, therefore, places a practical limit of about 2 nm for attaining photoinduced charge transfer with acceptable efficiency in such bimolecular structures.

Because of the importance of long-ranger charge transfer via hole hopping, we focus on the development of suitable electron deficient sensitizer for initiation hole transfer. Hence, the photosensitizer must absorb away from the electron donor in the visible region of the spectrum, and have a carboxylic acid (or amine) functionality for covalent attachment to molecular electrets that are polypeptides themselves.

Therefore, my initial studies focused on characterization of non-native aromatic beta-amino acid residues, derived from anthranilic acid, as building blocks of hole-transfer molecular electrets. The aromatic moieties provide the means for attaining long-range hole transfer. Chemical modification of the distal position of the anthranilamides allows for adjusting the reduction potentials of oxidation over a range of one volt. My major contribution to this work was discovering what makes oxidized *N*-Acylanthranilamides stable. By correlating the electrochemical data with the spin-density distribution of the radical cation, I determined that for radical cations of the anthranilamide to be stable 1) their reduction potential must be at about 1.5 V or below vs. S.C.E., and 2) the electron spin density should not extend over the C-terminal amide. Indeed, this proved valuable for increasing our library of building blocks for molecular electrets that have practical

feasibility.

A significant part of my studies encompass various aspects of synthesis of electron deficient photosensitizers for initiating the hole transfer in the anthranilamides, focusing on pyrene, nitropyrene and diketopyrollopyrolle chromophores. From my pyrene work I was able to shed light on the effect of the orientation of amide bonds on the electronic properties of polycyclic aromatic molecules. Incorporating an electron deficient diketopyrollopyrollo chromophore as an electron acceptor in donor-acceptor conjugates, where we use anthranilamides as donors, allowed us to determine the two important requirements for enhancing dipole effects on charge transfer and how to harness them. 1) The electric dipole has to be as close as possible to the charge-transfer systems. Indeed, incorporating the dipoles in the components of the charge-transfer systems presents the ideal case. 2) The media polarity should be lowered. While non-polar media impedes charge-separation processes, it also enhances the permiation of the dipole-generated electric fields. We demonstrated that the later of those two opposing effects can prevail. Changing the solvent from acetonitrile to toluene leads to a six-fold increase in charge separation rates when the electron transfers along the dipole. The same change in the solvent polarity completely shuts down the charge transfer when the electron is pushed to move against the dipole. These findings show rectification of photoinduced charge separation that is practically infinity and have important implications about the utility of dipole effects for electronic and energy materials and devices.

The most significant contributions from my doctoral research include: (1) the determination of the effects of location and strength of electron donating substituents on

the stability of the radical cations of the non-native amino acids for building molecular electrets; (2) demonstrating that amide bonds are not just linker but they can significantly affect the properties of the moieties they are attached to; and (3) developing of electron-deficient and conjugating them with anthtanilamides, which showed us to demonstrate dramatic dipole effects on charge transfer.

Table of Contents

List of Figures

Chapter 1

Chapter 2

Chapter 3

Chapter 4

Chapter 5

Chapter 6

Chapter 7

Chapter 8

List of Schemes

List of Tables

Chapter 7

Chapter 8

List of Charts

Chapter 3

Chapter 4

Chapter 6

Chapter 8

List of Abbreviations

Aa: Anthranilamide

$CHCl_3$: Chloroform

C_{el}: Electrolyte Concentration

CT: Charge Transfer

CV: Cyclic VOltammetry

D: Debye

DCM: Dichloromethane

DFNBA: 4,5-difluoro-2-nitrobenzoic acid

DFT: Density Functional Theory

DNA: Deoxyribonucleic acid

E_{00}: zero-to-zero energies

$E^{(0)}$: Electrode Potential

$E^{(1/2)}$: Half-wave Potential

E_a: Anodic Peak

E_c: Cathodic Peak

E_{CO}: Cutoff Reduction Potential

ET: Electron Transfer

eV: Electron Volt

EDG: Electron Donating Group

ε : Dielectric Constant

^{19}F NMR: Fluorine Nuclear Magnetic Resonance

Fmoc: Fluorenylmethyloxycarbonyl

h+: Hole

HOMO: Highest Molecular Orbital

LE: Locally Excited

LUMO: Lowest Molecular Orbital

MeCN: Acetonitrile

M: Molarity

NOESY: Nuclear Overhauser Effect Spectroscopy (2D NMR)

NMR: Nuclear Magnetic Resonance

NPy: Nitropyrene

PC: Propylene Carbonate

PhCN: Benzonitrile

Pip: Piperidine

PNA: Peptide Nucleic Acid

Py: Pyrene

SCE: Standard Calomel electrode

SDD: Spin-Density Distribution

tBoc: *tert*-butyloxycarbonyl

UV: Ultraviolet

V: Volt

Chapter 1

Introduction

Bioinspired Approach Toward Molecular Electrets: Synthetic Proteome for Materials

Need for alternative energy

With the rise of the world energy consumption and with the threat of climate change, the need for carbon neutral energy technologies is dire. The abundant and practically unlimited energy from the sun is a promising solution for meeting the constantly increasing global energy needs [1, 2]. Worldwide, the average energy consumption rate approaches 20 TW [3, 4]. Conversely, sunlight brings energy to the Earth's surface at a rate of 1.76×10^5 TW. Considering the global albedo of about 30 %, the solar energy bombards the surface of the planet with a rate of 1.2×10^5 TW, of which about 600 TW are practically utilizable.

Viable solar-energy technologies ought to comprise light harvesting, energy conversion, and energy storage. Charge-transfer (CT) processes, occurring at the nanometer scales, are key for efficient transformations of light radiation to electrical, chemical and other forms of energy. Therefore, the ability to control CT at a molecular level is key for energy science and engineering.

For more than two billion years solar energy has sustained life on earth after the Great Oxygenation Event (GOE) following the emergence of photosynthesis [5, 6]. Nature, thus, provides us with some of the best examples for harvesting solar light and storing it in the form of chemical energy; that is, in the form of high- energy chemical bonds. Therefore, understanding how natural processes work and utilizing this knowledge is required for efficient light-harvesting and energy-conversion tools.

Biomimicry, biomimesis and bioinspiration

Biomimicry, involving sheer imitation of biological systems, encompasses the first steps toward understanding how living systems work [7]. *Biomimesis* aims not only at structural resemblances, but also at functionalities similar to these of the natural systems [7]. *Bioinspiration*, however, takes features from biology and employs them in manners atypical for living systems, paving roads to functionalities that are beyond what Nature can offer [7].

Photinduced charge transfer process

Photoexcitation of electron donor-acceptor (DA) conjugates leads to the formation of electron-hole pairs. This photoinduced charge separation (CS) is representative of light harvesting and energy conversion of the absorbed radiation energy to CT states. Once the CS forms, the photogenerated holes and electrons have to move away from each other in order to utilize the harvested energy. Charge recombination (CR), however, bringing the DA systems to their ground states, is frequently the likely outcome. Local-field effects originating from ordered electric dipoles can provide a means for steering electrons and holes away from each other and controlling the different CT processes. Therefore, electrets, which are systems with co-directionally ordered electric dipoles and electrostatic analogs of magnets, offer unexplored potentials for energy science and engineering.

Dipole Effects on Charge Transfer

Local electric fields, originating from molecular dipoles, have profound effects on

the electronic properties of the microenvironment. As a result, local electric fields from molecular dipoles and ions affect ET [8–13], providing a promising means for increasing the efficiency of the desired CT processes while suppressing the undesired ones. Small dipolar moieties modify the electron affinity and the ionization energy of materials [14–18]. Because of their rectifying capabilities, dipolar π-conjugated molecules have been a focus for molecular and organic electronics [19–21]. At metal-semiconductor interfaces, monolayers of organic molecules containing polar functional groups alter the rectification characteristics of such Schottky junctions [22–24]. Push-pull conjugates within CT organic structures on semiconductor surfaces introduce molecular dipoles that not only affect the electronic properties of the material but also modify the kinetics of interfacial ET [25]. Similarly, at a molecular level, dipole-generated fields shift the energy levels of the frontier orbitals of the electron donors and acceptors [26].

In the search for achieving control over CT using local electric fields, molecular electrets, such as protein helices, present one of the best choices because of their large permanent electric dipoles. With intrinsic dipoles of about 5 Debyes (D) per residue that points from the C- to the N-terminus [26-30, 31, 32, 33–36], protein α-helices generate in their vicinity fields in the order of GV/m. (The direction of electric dipoles is from their negative to positive poles [37]).

In the late 1990s, Galoppini and Fox demonstrated for the first time the effect dipoles have on photoinduced CT [38–40]. They employed 14-residue-long polypeptides that show high propensity for assuming helical secondary structures. Synthetic α-L-amino

acids, containing donor and acceptor moieties attached to their side chains, are placed six-residues apart in the middle of the polypeptide sequences. Upon photoexcitation of the acceptor, an electron moves from the HOMO of the donor to fill the newly generated vacancy in the acceptor "HOMO." (Strictly speaking, after photoexcitation, the HOMO becomes a singly occupied MO; and because the transfer is along the HOMOs of the CT species following the excitation of the acceptor [41–45], it can be viewed as hole transfer rather than electron transfer). The rates of CT are up to about 30 times larger when the acceptor is positioned close to the N-terminus than to the C-terminus of the helices [46]. That is, the rates are faster for electrons moving toward the positive poles of the dipole than toward the negative ones, which encompasses the most important discovery described in these first reports.

This effect of macromolecular dipoles on CT kinetics is ascribed to field-induced changes in the CT driving force, $-\Delta G_{CT}^{(0)}$ [26, 47]. The CS state is polarized and generates a dipole that points from the radical anion of the reduced acceptor to the radical cation of the oxidized donor. Opposing orientation between the CS dipole and the permanent electric dipole of the helix stabilizes the CS state and increases the CT driving force (if the system operates in the Marcus Normal region). Conversely, co-directional orientation of the CS and helix dipoles leads to a decrease in the CT rates. This dipole-induced Franck-Condon effect on the CT kinetics is especially prevalent for small $-\Delta G_{CT}^{(0)}$, and for systems with an identical electronic coupling between the donor and the acceptor for the CS states oriented along and against the permanent macromolecular dipole. When the structures with opposing dipole direction are not completely symmetrical, the differences in the electronic

coupling can prevail over the dipole-induced effect for relatively large $-\Delta G_{CT}^{(0)}$ [48].

Since the beginning of the 21st century, studies of dipole effects on CT have focused on systems comprising polypeptide helices [26, 9, 13, 49–62]. Donor-bridge-acceptor (DBA) constructs, where the bridge is a helix, allow for testing dipole-induced charge-transfer rectification, i.e. the difference between the rates of ET along the dipole vs. ET against the dipole [58]. Self-assembled monolayers (SAMs) of polypeptide helices on gold surfaces show similar dipole-induced rectification of interfacial CT [9], i.e. of CT across a junction between liquid and a solid conductor. A junction between solid conductors interfaced with assemblies of polypeptide helices extends the studies of such dipole effects onto charge-transport currents [50–52]. The use of polypeptides composed of residues with chargeable side chains such as lysine, however, raises question about the effect of the counterions in the SAMs on the measured rectification, which may depend on the state of protonation of the polypeptides. Furthermore, while the use of gold interfaces provides important fabrication advantages, it also poses a potential for forming conducting pillar-like nanostructures within the bioorganic SAMs due to the mobility of gold atoms under the large field gradients inherent for such junctions. Such artifacts would interfere with analysis of the measured results. Nevertheless, the facile interfacing of gold with organic conjugates has made it possible to realize molecular junction and advance the fields not only of interfacial charge transfer, but also of molecular charge transport.

A principal challenge of polypeptide CT systems composed of native amino acids is the inherent distance limitation for efficient CT. Along their backbones and hydrogen

bonds, protein α-helices mediate ET via tunneling, the rate constants of which, k_{et}, fall off exponentially with an increase in the length of the ET pathways, r_{et}, i.e. $k_{et} \propto \exp(-\beta r_{et})$. Specifically, for protein α-helices, β is about 1.3 $Å^{-1}$ [63, 64–66]. The inherent presence of competing nanosecond processes, such as fluorescence, internal conversion and intersystem crossing, therefore, places a practical limit of about 2 nm for attaining photoinduced CT with acceptable efficiency in such bimolecular structures. Conversely, the inability of polypeptides, composed solely of native amino acids, to accept electrons or holes without undergoing reductive or oxidative degradation, prevents alternative mechanisms for achieving long-range CT. Another characteristic that limits the utility of bio- molecules for materials applications is their conformational instability when placed outside of their native environment. Overall, the challenge for preserving the protein secondary structure, and thus the expected functionality, places additional constraints on the design and engineering of systems comprising biological and biomimetic macromolecular components.

Nevertheless, nature still provides some of the best examples for mediating efficient CT in low-dielectric-constant media, i.e. in proteins and across lipid bilayers. Proteins can mediate long-range CT via electron-hopping or hole-hopping along cofactors or redox-active residues (e.g. tyrosine and tryptophan [67]). Photosynthetic reaction centers and mitochondrial respiratory complex are some of the best examples for such electron-transfer chains [68].

Poly- and oligonucleotides present another example for mediating efficiently long-range CT at distances exceeding 2 nm [69, 70]. Short tunneling steps between the HOMOs of electron-rich bases in deoxyribonucleic acid (DNA) double strands lead to hole hopping that can be efficient at distances of several nanometers but limited by the dynamics (and the persistence length) of the macromolecule. Peptide nucleic acids (PNA) present a key alternative for achieving long-range hole hopping. As a result of their small helical twist, the PNA structure provides a better electronic coupling between neighboring bases in comparison with DNA [70]. Furthermore, the backbone of PNA contains secondary and tertiary amides. That is, unlike native polynucleotides, PNA strands do not have ionic charges along their backbones, which proves beneficial for examining dipole-generated local-field effects on CT kinetics, e.g. along single-strand PNA oligomers [41]. For observing dipole effects on long range CT mediated by such double-stranded biomolecules, however, the two biopolymers in the double helices have to be oriented in the same, rather than in opposite, direction. This structural requirement can place constraints on the utility of PNA as molecular electrets.

Electrets in nature

Protein helices present a perfect example of macromolecules with large intrinsic dipoles [27-30, 71, 72], i.e. they are molecular electrets [73]. Much like magnets, the intrinsic electric dipole moments in these protein structures originate from the ordered orientation of amide and hydrogen bonds [31, 32, 74, 75]. Therefore, protein and polypeptide helices are dipole-polarization electrets.

Polypeptides composed of α-amino acids mediate electron transfer (ET) via tunneling, which has unfeasibly low efficiency for ET distances exceeding 2 nm [76, 63, 77–80]. An array of electronically coupled cofactors, or redox active side chains of amino acids (such as the indole in tryptophan) can provide path- ways for efficient long-range ET or hole transfer (HT) [67, 68, 81]. Indeed, arrays of redox species that are not electronically coupled with one another prove ineffective for long-range CT, demonstrating the importance for the precise three-dimensional (3D) spatial arrangements of the moieties comprising ET and HT pathways.

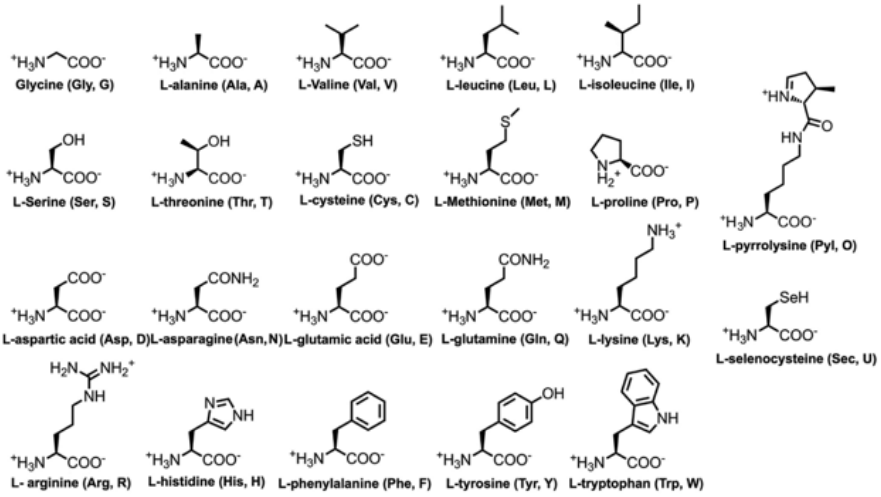

Fig. 1-1: The 22 proteogenic native amino acids. The state of protonation is depicted for physiological pH.

Our Approach

In nature, the 22 proteogenic native amino acids are the key building blocks for proteomes that reflect the amazing diversity of life on Earth [81-93]. Proteogenic residues are α-L-amino acids, differing only by a single side chain connected to their α-carbons, that can be genetically coded and expressed in a cell proteome (Fig. 1-1).

Using the bioinspiration approach we thus utilize molecular dipoles for optimizing CT systems. This approach thus provides the foundation for describing the bioinspired rationale for the design of molecular electrets that combines the intrinsic dipolar features of protein helices, with pathways for long-range CT, observed in other biological systems [69, 70]. Molecular electrets are polypeptides of non-native amino acids, based on anthranilamide (Aa) structures (Fig. 1-2). These constructs of non-native residues possess

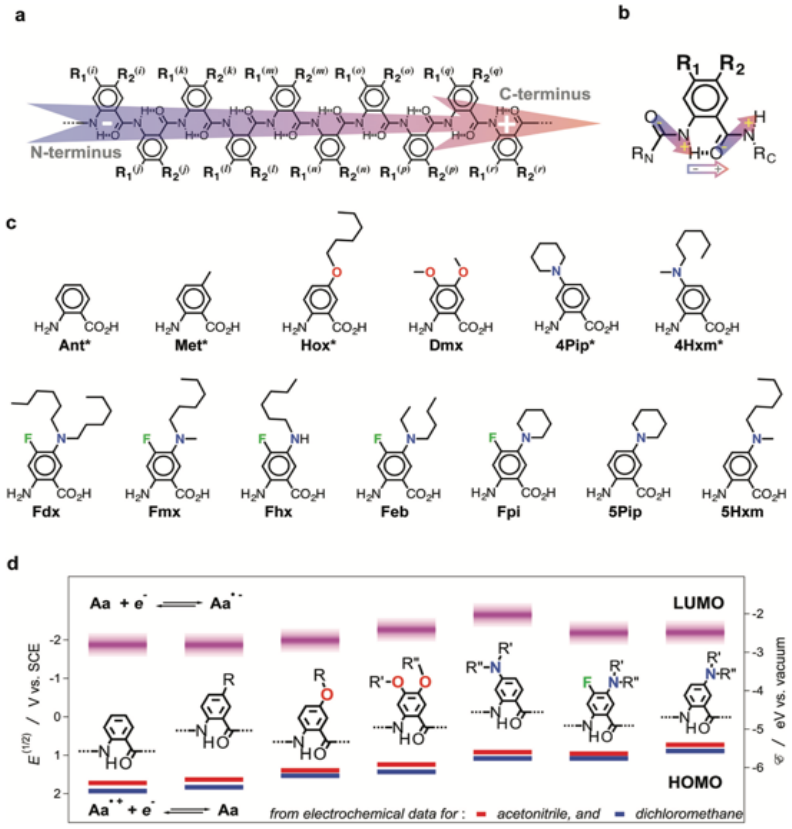

Fig. 1-2: Bioinspired molecular electrets based on anthranilamide (Aa) structures. (a) Structure of Aa oligomer with indication of its permanent ground-state electric dipole moment. (b) Origin of the permanent dipole from the amide bonds (filled arrows). The dipole is enhanced by the change in polarization upon hydrogen bond formation (hollow arrow). (c) Non-native amino acids, synthetic derivatives of anthranilic acid, for hole-transfer molecular electrets (*manifest irreversible oxidation, as determined from electrochemical studies on residues with N- and C-termini capped as alkylamides) [94-96, 8]. (d) Reduction potentials and energy levels of the frontier orbitals of Aa residues with different types of electron-donating groups and C- and N-termini capped as alkylamides [94, 95, 9]. The reduction potentials of the residue oxidation are for neat solvents that were obtained from extrapolation of cyclic voltammetry results to zero electrolyte concentration [36–39]. The energy levels of the LUMOs were esti- mated from the reduction potentials for oxidation and the optical HOMO-LUMO gap, E_{00} [96]. The LUMO levels show the average between the results from the measurements for dichloromethane and for acetonitrile.

large permanent electric dipole moments originating from the ordered amide and hydrogen bonds (Fig. 1-2a,b). Unlike proteins, however, they have a backbone of directly linked aromatic moieties that can provide pathways for long-range charge transfer. The two distal positions of each of the Aa residue are key sites for tuning the electronic properties by attaching different substituents. We focus on electron-donating substituents (Fig. 1-2c,d) producing residues for HT molecular electrets [94–96]. One of the distal sites, R_2 (Fig. 1-1a,b), of th e N-terminal residue proves immensely beneficial for initiating hole transfer along Aa oligomers, i.e. for initiating a sequence of ET steps along the highest occupied molecular orbitals (HOMOs) of the aromatic residues. Therefore, the side chains of the non-native Aa residues can not only serve as handles for tuning their electronic and photonic properties, but also provide pathways for initiating efficient CT.

The bioinspired molecular electrets are polypeptides composed of non-native β-amino acids. Each of the electret residues has two side chains, R_1 and R_2, on the distal positions 4 and 5, respectively. In similarity with the native biomolecular structures, a set of a dozen or a couple of dozen non-native Aa amino acids (Fig. 1-2c) can provide countless CT functionalities when combined in different primary sequences. Indeed, the partial π-conjugation through the amide bonds, connecting the aromatic moieties, provides a strong electronic coupling needed for the short electron-hopping steps between the neighboring residues. The amide mediated electronic coupling, however, is not strong enough to generate the formation of CT bands that can be detected in absorption or emission spectra, and the frontier orbitals tend to be relatively localized over individual residues [73, 97]. Therefore, characterizing the electronic and the photonic properties of

individual Aa residues has a considerable predictive power of their characteristics when incorporate into Aa oligomers. The rational control of the primary sequence of the Aa oligomers provides a means for the design of CT pathways. Adding or removing charge traps and adding or removing potential barriers are some of the unexplored possibilities for the Aa electrets.

Much like amino acids, varying the two side chains opens up possibilities for making a diverse set of non- native amino acids for a "synthetic proteome" of molecular electrets with wide range of electronic properties and CT capabilities. Using three types of electron-donating substituents (alkyl, alkoxyl and amines), and placing them at the two distal positions, we vary the reduction potential for the oxidation of these residues over the range of one volt (Fig. 1-2d). It corresponds to adjusting the energies of the HOMOs of these residues between about −6.5 and −5.5 eV vs. the vacuum level (Fig. 1-1d), which give us an attractive range for hole- conducting materials. Another interesting finding involves a fine-tuning of the reduction potentials of the Aa residues by changing the positions of their side chains. It is important not only the type of a side chain (e.g. alkyl, alkoxyl and amine), but also where the side chain is located (i.e. position 4 vs. position 5). For example, shifting an amine substituent from position 4 to position 5 causes about a 200 mV negative shift in the reduction potential of oxidation.

When designing hole-transfer systems, it is key to utilize components that can hold positive charges (i.e. holes) without undergoing irreversible transformations. Therefore, using electrochemical and computational analysis, we discovered two requirements for an

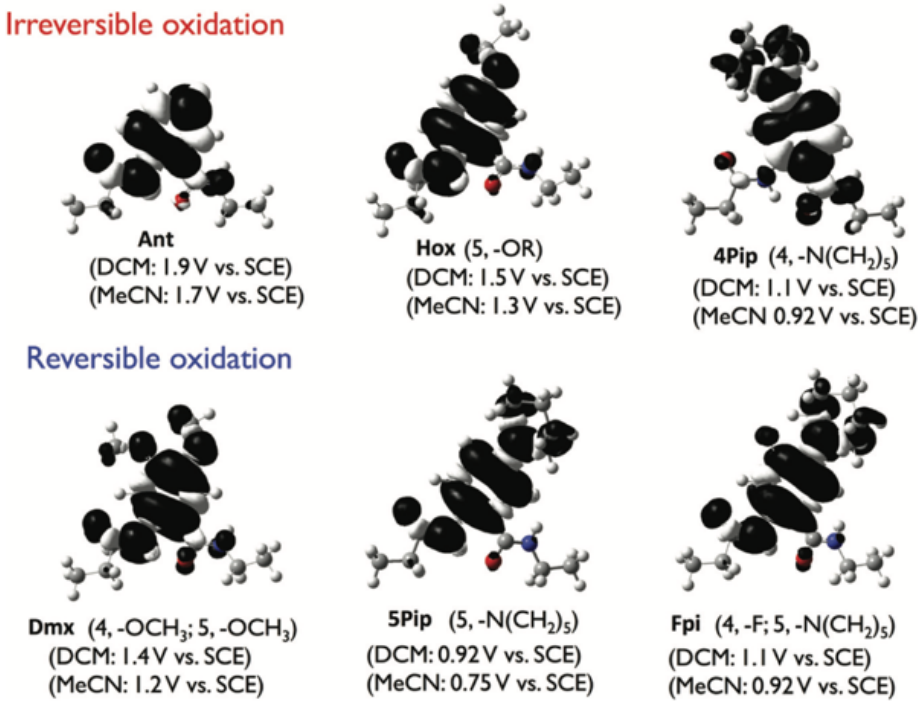

Fig. 1-3: Examples of spin-density distributions of the radical cations of Aa residues (Fig. 1c), with N- and C-termini capped as alkylamides (black – excess spin up, i.e. radical cation; and white, excess spin down) [95, 96, 9]. The residues are grouped according to the reversibility of their electrochemical oxidation. The reduction potentials for the oxidized Aa residues for the neat dichloromethane (DCM) and acetonitrile (MeCN) are obtained from extrapolation to zero electrolyte concentration [10–13].

Aa residue to maintain its chemical stability under hole-transfer conditions: (1) the reduction potential for oxidizing it cannot be more positive than a cutoff potential of about 1.2 or 1.5 V vs. SCE for acetonitrile and dichloromethane media, respectively, and (2) the strongest electron-donating side chain of the residue should be attached at position 5, i.e. at the para position to the N-terminal amide, in order to prevent the spin density distribution of the radical cation from extending over the C-terminal amide (Fig. 1-3).

The development of the electret "synthetic proteome" aims at diversity of electronic properties and charge-transfer functionalities. The position of the side chain of the Aa residues has a compounded effect on these key features: it affects their total electric dipoles, reduction potentials and stability against oxidative degradation. Indeed, multifaceted

analyses of structure-function relationships and holistic design approaches are essential for the development of the Aa bioinspired molecular electrets. This complexity offers unexplored possibilities for the search of emerging properties essential for electronic materials and energy-conversion systems.

Marcus Transition-State Theory for Analysis of Electron Transfer

Marcus transition-state theory provides an excellent approach for describing the dependence of rates of non-adiabatic electron transfer on the thermodynamic driving force, $-\Delta G°$. In the potential-energy curves, represented by parabolic functions that show the initial state (*i*) and the final state (*f*) of an electron transfer process, best illustrate the Marcus theory (figure 1-4). A Gaussian function allows for expressing the classical Marcus rates of electron transfer in terms of unimolecular rate constants, k_{et}:

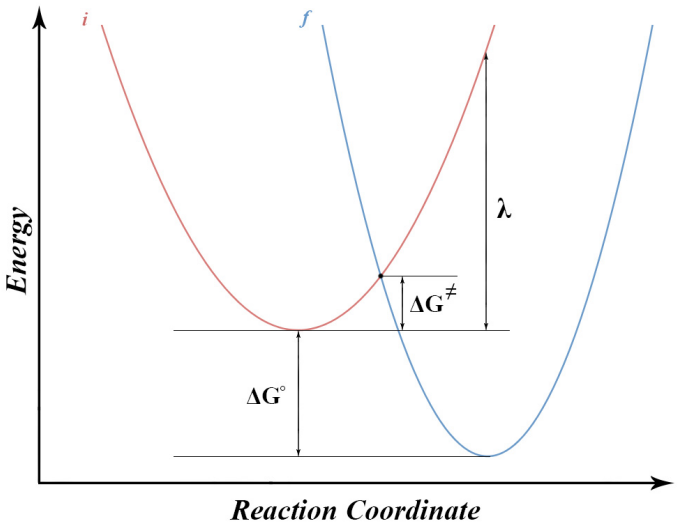

Figure 1-4. State diagram showing non-adiabatic electron transfer reaction: *i* and *f* are the initial and final states of the system. $\Delta G°$ is the energy difference between the relaxed initial and final states. The crossing point between the i and f states is the transition state and $\Delta G^{\neq}$ is the energy difference between the transition state and the relaxed initial state, i.e., it is the free activation energy which is the energy required to go over the barrier for reaching the final state. λ is the reorganization energy, which is the energy required to reorganize the nuclei of the reacting system and the solvent environment.

$$k_{et} = \frac{2\pi}{\hbar}|H_{if}|^2 \frac{1}{\sqrt{4\pi\lambda k_B T}} \exp\left(-\frac{(\lambda + \Delta G^\circ)^2}{4\lambda k_B T}\right) \quad (1)$$

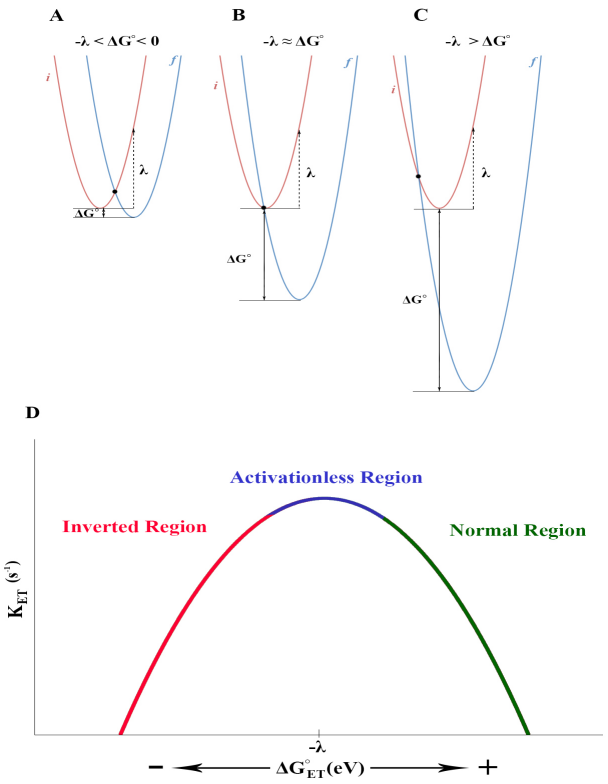

Figure 1-5. Transition between the Marcus normal and inverted regions by changing the driving force. (A-C) State diagrams showing (A) Marcus normal region in which the rate of electron transfer increases with an increase in driving force, $-\Delta G^\circ$, because $\Delta G^{\neq}$ decreases as ΔG° becomes more negative. (B) Activationless region where $-\lambda \approx \Delta G^\circ$, and the potential energy surface of *f* crosses the bottom of the well of *i*. Hence, the free activation energy is equal to 0. (C) Marcus inverted region where the potential well of *f* crosses *i* at its distal side, i.e., the transition state is the furthest from the bottom of the potential energy surface of the final state. Thus, an increase in the driving force, $-\Delta G^\circ$, increases $\Delta G^{\neq}$, and decreases the rate of the reaction. (D) Summary of the Marcus theory showing the relationship between the rate constant and the driving force of the reaction, i.e., the rate of electron transfer increases with an increase in the driving force, to reach $-\lambda \approx \Delta G^\circ$, which corresponds to the activationless region. After this tip of the Marcus curve, as the driving force increases, the rates of electron transfer decreases, illustrating the inverted region.

where λ is the reorganization energy (inner and outer), ΔG° is the standard free energy change of the reaction, T is temperature and k_B is the Boltzmann constant. The transition-state energy, $\Delta G^{\neq}$, for non-adiabatic processes (i.e., the free activation energy) involves a quadratic relationship:

$$\Delta G^{\neq} = ((\lambda + \Delta G^\circ)^2)/4\lambda \quad (2)$$

This quadratic relationship defines two distinct regions of dependence of the electron-transfer kinetics on the thermodynamic characteristics of the system. When $-\lambda \approx \Delta G^\circ$, electron transfer is is in an activationless regime of operation, placing the system at the tip of the Marcus curve (Figure 1-5a). The Marcus normal region where ΔG° is less negative

than $-\lambda$, i.e., $-\lambda < \Delta G° < 0$, and k_{et} increases with an increasing driving force $-\Delta G°$, which appears quite intuitive (Figure 1-5b). The Marcus inverted region is where $-\lambda$ is less negative than $\Delta G°$, i.e., $-\lambda > \Delta G°$, the electron transfer is a strongly exergonic process, and k_{et} decreases with an increasing driving force, $-\Delta G°$, which appears somewhat counterintuitive (Figure 1-5c).

Marcus-Hush formalism (eq. 1) aids the understanding of inner sphere electron transfer. This formalism accounts for the solvation effect of charge transfer as introduced by the outter-sphere (or medium) reorganization energy, λ_{outer}. The total reorganization energy, λ, therefore can thus be expressed as the sum of the inner (i.e., molecular reorganization) and the outer (i.e., solvent reorientation) nuclear modes:

$$\lambda = \lambda_{inner} + \lambda_{outer} \quad (3)$$

This theory focusses on non-adiabatic processes, where the nuclei at the transition state do not move during the electron transfer, illustrating systems with weak donor-acceptor electronic coupling. For strong donor-acceptor electronic couplings, i.e., adiabatic electron transfer, the nuclear motion is coupled to the electron motion, and the "traditional" Marcus theory cannot account for such kinetics.

Furthermore, Marcus-Hush formalism assumes a normal distribution of density of vibrational states at the transition state, as reflected by the Gaussian function (eq. 1). Inclusion of specific frequencies (or an average of frequencies) of vibrational modes that contribute considerably to the electron transfer, as proposed by J. Jortner, leads to the Marcus-Levich-Jortner formalism (see the Supplemental Information at the end of chapter 8 for equation).

Considering photoinduced electron transfer (PET), the Rehm-Weller equation expresses the electron-transfer driving force in terms of excitation energy, reduction potentials, $E^{(0)}$, and other quantitates that are easily measurable:

$$\Delta G_{\mathrm{ET}}^{(0)} = F\left(E_{D^{x+1}|D^{x}}^{(0)} - E_{A^{y}|A^{y-1}}^{(0)}\right) - E_{00} + \Delta G_{\mathrm{S}} + W \tag{4}$$

where E_{00} is the zero-to-zero energy, i.e., the excitation energy, of the donor or the acceptor; ΔG_{S} is the Born solvation term that accounts for the variations in the solvation energy of the oxidized and reduced forms of the donor and the acceptor due to differences in the media for which the reduction potentials and E_{00} are estimated; and W represents the changes in the donor-acceptor Coulomb interaction before and after PET.

In biological and non-biological systems, many ET processes occur on a regular basis. Marcus theory has been of great importance for understanding such processes. Protein helices, being the best examples of natural molecular electrets, affect the reduction potentials during CT transfer (due to the electric fields generated by the intrinsic dipole moment originating from the ordered amide and hydrogen bonds). In turn, this dipole-induced modulation of $\Delta G_{\mathrm{ET}}^{(0)}$ affects $\Delta G^{\neq}$ and the electron-transfer kinetics. Therefore, it is of great importance to understand the dipole effect on CT process that has a huge impact on energy science and engineering.

In summary, the most important contributions from my doctoral work are: (1) the determination of the effects of the location and strength of the electron donating moieties on the stability of the radical cations of the anthranilamides for making molecular electrets (2) demonstrating that amide "linkers" are more than a "linker" and can affect the electronic

properties depending on the position of the amide and (3) developing a suitable electron-deficient chromophore and conjugating them with anthranilamides to demonstrate dramatic dipole effects on charge transfer.

References

[1] N. S. Lewis. *Science* **351**, 353 (2016).

[2] K. W. J. Barnham, M. Mazzer, B. Clive. *Nat. Mater.* **5**, 161 (2006).

[3] J. Conti, P. Holtberg, J. Diefenderfer, A. LaRose, J. T. Turnure, L. Westfall. Report: U.S. Energy Information Administration, O ce of Energy Analysis, U.S. Department of Energy (2016).

[4] Y. Chang, J. Lee, H. Yoon. *Energ. Policy* **50**, 154 (2012).

[5] J. W. Schopf. *Biochemistry (Moscow)* **79**, 165 (2014).

[6] A. L. Sessions, D. M. Doughty, P. V. Welander, R. E. Summons, D. K. Newman. *Curr. Biol.* **19**, R567 (2009).

[7] V. I. Vullev. *J. Phys. Chem. Lett.* **2**, 503 (2011).

[8] S. M. Kapetanaki, M. Ramsey, Y. M. Gindt, J. P. M. Schelvis. *J. Am. Chem. Soc.* **126**, 6214 (2004).

[9] S. Yasutomi, T. Morita, Y. Imanishi, S. Kimura. *Science* **304**, 1944 (2004).

[10] N. Gergel-Hackett, I. Aguilar, C. A. Richter. *J. Phys. Chem. C* **114**, 21708 (2010).

[11] J. Albero, E. Martinez-Ferrero, D. Iacopino, A. Vidal-Ferran, E. Palomares. *Phys. Chem. Chem. Phys.* **12**, 13047 (2010).

[12] Y. F. Wang, Y. Li, Z. J. Zhou, Z. R. Li, D. Wu, J. G. Huang, F. L. Gu. *ChemPhysChem* **13**, 756 (2012).

[13] J. A. Gao, P. Muller, M. Wang, S. Eckhardt, M. Lauz, K. M. Fromm, B. Giese. *Angew. Chem. Int. Edit.* **50**, 1926 (2011).

[14] P. K. Santra, A. F. Palmstrom, J. T. Tanskanen, N. Yang, S. F. Bent. *J. Phys. Chem. C* **119**, 2996 (2015).

[15] A. M. Munro, B. Zacher, A. Graham, N. R. Armstrong. *ACS Appl. Mater. Interfac.* **2**, 863 (2010).

[16] P. R. Brown, D. Kim, R. R. Lunt, N. Zhao, M. G. Bawendi, J. C. Grossman, V. Bulovic. *ACS Nano* **8**, 5863 (2014).

[17] H. J. Lee, A. C. Jamison, T. R. Lee. *Acc. Chem. Res.* **48**, 3007 (2015).

[18] R. Hunger, W. Jaegermann, A. Merson, Y. Shapira, C. Pettenkofer, J. Rappich. *J. Phys. Chem. B* **110**, 15432 (2006).

[19] R. M. Metzger. *Chem. Rev.* **115**, 5056 (2015).

[20] R. M. Metzger. *Chem. Rev.* **103**, 3803 (2003).

[21] R. M. Metzger, B. Chen, U. Hopfner, M. V. Lakshmikantham, D. Vuillaume, T. Kawai, X. L. Wu, H. Tachibana, T. V. Hughes, H. Sakurai, J. W. Baldwin, C. Hosch, M. P. Cava, L. Brehmer, G. J. Ashwell. *J. Am. Chem. Soc.* **119**, 10455 (1997).

[22] A. Vilan, A. Shanzer, D. Cahen. *Nature* **404**, 166 (2000).

[23] D. G. Wu, J. Ghabboun, J. M. L. Martin, D. Cahen. *J. Phys. Chem. B* **105**, 12011 (2001).

[24] G. Ashkenasy, D. Cahen, R. Cohen, A. Shanzer, A. Vilan. *Acc. Chem. Res.* **35**, 121 (2002).

[25] J. Nieto-Pescador, B. Abraham, J. J. Li, A. Batarseh, R. A. Bartynski, E. Galoppini, L. Gundlach. *J. Phys. Chem. C* **120**, 48 (2016).

[26] Y.-G. K. Shin, M. D. Newton, S. S. Isied. *J. Am. Chem. Soc.* **125**, 3722 (2003).

[27] A. Wada. *J. Chem. Phys.* **29**, 674 (1958).

[28] W. G. J. Hol, P. T. Van Duijnen, H. J. C. Berendsen. *Nature* **273**, 443 (1978).

[29] W. G. J. Hol. *Adv. Biophys.* **19**, 133 (1985).

[30] H. Nakamura, A. Wada. *J. Phys. Soc. Jap.* **54**, 4047 (1985).

[31] A. Wada. *Adv. Biophys.* **9**, 1 (1976).

[32] W. G. J. Hol. *Progr. Biophys. Mol. Biol.* **45**, 149 (1985).

[33] A. Wada. *J. Chem. Phys.* **31**, 495 (1959).

[34] A. Wada. *J. Chem. Phys.* **30**, 328 (1959).

[35] W. G. J. Hol, M. C. H. De Maeyer. *Biopolymers* **23**, 809 (1984).

[36] W. G. J. Hol, R. K. Wierenga. "The α-helix dipole and the binding of phosphate groups of coenzymes and substrates by proteins," in *X-ray Crystallography and Drug Action: the Ninth Course of the International School of Crystallography*, A. S. Horn and C. J. de Ranter (Eds.), pp. 151–168, Oxford University Press, Oxford, UK (1984).

[37] J. W. Hovick, J. C. Poler. *J. Chem. Educ.* **82**, 889 (2005).

[38] E. Galoppini, M. A. Fox. *J. Am. Chem. Soc.* **118**, 2299 (1996).

[39] M. A. Fox, E. Galoppini. *J. Am. Chem. Soc.* **119**, 5277 (1997).

[40] A. Knorr, E. Galoppini, M. A. Fox. *J. Phys. Org. Chem.* **10**, 484 (1997). G.

[41] G. Jones II, V. Vullev, E. H. Braswell, D. Zhu. *J. Am. Chem. Soc.* **122**, 388 (2000).

[42] G. Jones II, V. I. Vullev. *Org. Lett.* **4**, 4001 (2002).

[43] G. Jones II, L. N. Lu, V. Vullev, D. Gosztola, S. Greenfield, M. Wasielewski. *Bioorg. Medi. Chem. Lett.* **5**, 2385 (1995).

[44] G. Jones II, X. Zhou, V. I. Vullev. *Photochem. Photobiol. Sci.* **2**, 1080 (2003).

[45] G. Jones II, D. Yan, J. Hu, J. Wan, B. Xia, V. I. Vullev. *J. Phys. Chem. B* **111**, 6921 (2007).

[46] K. J. Kise, B. E. Bowler. *Inorg. Chem.* **42**, 3891 (2003).

[47] A. Fedorova, A. Chaudhari, M. Y. Ogawa. *J. Am. Chem. Soc.* **125**, 357 (2003).

[48] D. Bao, S. Upadhyayula, J. M. Larsen, B. Xia, B. Georgieva, V. Nunez, E. M. Espinoza, J. D. Hartman, M. Wurch, A. Chang, C.-K. Lin, J. Larkin, K. Vasquez, G. J. O. Beran, V. I. Vullev. *J. Am. Chem. Soc.* **136**, 12966 (2014).

[49] T. Morita, S. Kimura, S. Kobayashi, Y. Imanishi. *J. Am. Chem. Soc.* **122**, 2850 (2000).

[50] C. Shlizerman, A. Atanassov, I. Berkovich, G. Ashkenasy, N. Ashkenasy. *J. Am. Chem. Soc.* **132**, 5070 (2010).

[51] S. Sek, K. Swiatek, A. Misicka. *J. Phys. Chem. B* **109**, 23121 (2005).

[52] S. Sek, A. Misicka, K. Swiatek, E. Maicka. *J. Phys. Chem. B* **110**, 19671 (2006).

[53] H. S. Mandal, H. B. Kraatz. *Chem. Phys.* **326**, 246 (2006).

[54] B. Giese, M. Wang, J. Gao, M. Stoltz, P. Muller, M. Graber. *J. Org. Chem.* **74**, 3621 (2009).

[55] B. R. Chaudhry, J. D. E. T. Wilton-Ely, A. B. Tabor, D. J. Caruana. *Phys. Chem. Chem. Phys.* **12**, 9996 (2010).

[56] E. Gatto, M. Caruso, A. Porchetta, C. Toniolo, F. Formaggio, M. Crisma, M. Venanzi. *J. Peptide Sci.* **17**, 124 (2011).

[57] C. L. Moss, T. W. Chung, J. A. Wyer, S. B. Nielsen, P. Hvelplund, F. Turecek. *J. Am. Soc. Mass Spectrom.* **22**, 731 (2011).

[58] L. Garbuio, S. Antonello, I. Guryanov, Y. Li, M. Ruzzi, N. J. Turro, F. Maran. *J. Am. Chem. Soc.* **134**, 10628 (2012).

[59] M. Lauz, S. Eckhardt, K. M. Fromm, B. Giese. *Phys. Chem. Chem. Phys.* **14**, 13785 (2012).

[60] I. Swierszcz, P. Skurski, J. Simons. *J. Phys. Chem. A* **116**, 1828 (2012).

[61] O. Cramariuc, P. J. Aittala, T. I. Hukka. *J. Mol. Model.* **19**, 697 (2013).

[62] I. Anusiewicz, P. Skurski, J. Simons. *J. Phys. Chem. B* **118**, 7892 (2014).

[63] H. B. Gray, J. R. Winkler. *Q. Rev. Biophys.* **36**, 341 (2003).

[64] C. Narth, N. Gillet, F. Cailliez, B. Levy, A. de la Lande. *Acc. Chem. Res.* **48**, 1090 (2015).

[65] H. B. Gray, J. R. Winkler. *Annu. Rev. Biochem.* **65**, 537 (1996).

[66] M. A. Wolak, A. Balae , S. Gutmann, H. J. Helmrich, R. Vosloo, M. M. Beerbom, E. Wierzbinski, D. H. Waldeck, S. Bezer, C. Achim, D. N. Beratan, R. Schlaf. *J. Phys. Chem. C* **115**, 17123 (2011).

[67] C. Shih, A. K. Museth, M. Abrahamsson, A. M. Blanco-Rodriguez, A. J. Di Bilio, J. Sudhamsu, B. R. Crane, K. L. Ronayne, M. Towrie, A. Vlcek, Jr., J. H. Richards, J. R. Winkler, H. B. Gray. *Science* **320**, 1760 (2008).

[68] J. J. Warren, J. R. Winkler, H. B. Gray. *Coord. Chem. Rev.* **257**, 165 (2013).

[69] F. D. Lewis. *Israel J. Chem.* **53**, 350 (2013).

[70] R. Venkatramani, S. Keinan, A. Balae , D. N. Beratan. *Coord. Chem. Rev.* **255**, 635 (2011).

[71] K. R. Shoemaker, P. S. Kim, E. J. York, J. M. Stewart, R. L. Baldwin. *Nature* **326**, 563 (1987).

[72] D. J. Lockhart, P. S. Kim. *Science* **260**, 198 (1993).

[73] M. K. Ashraf, R. R. Pandey, R. K. Lake, B. Millare, A. A. Gerasimenko, D. Bao, V. I. Vullev. *Biotechnol. Progr.* **25**, 915 (2009).

[74] S. Yamabe, K. Morokuma. *J. Am. Chem. Soc.* **97**, 4458 (1975).

[75] T. R. Dyke, J. S. Muenter. *J. Chem. Phys.* **60**, 2929 (1974).

[76] J. R. Winkler, H. B. Gray. *Chem. Rev.* **92**, 369 (1992).

[77] J. E. Miller, A. J. Di Bilio, W. A. Wehbi, M. T. Green, A. K. Museth, J. R. Richards, J. R. Winkler, H. B. Gray. *Biochim. Biophys. Acta, Bioenerg.* **1655**, 59 (2004).

[78] H. B. Gray, J. R. Winkler. *Proc. Natnl. Acad. Sci. USA* **102**, 3534 (2005).

[79] J. R. Winkler, H. B. Gray, T. R. Prytkova, I. V. Kurnikov, D. N. Beratan. "Electron transfer through proteins," in *Bioelectronics: From Theory to Applications*, I. Willner and E. Katz (Eds.), pp. 15–33, Wiley-VCH Verlag GmbH & Co. KGaA, Weinheim, FRG (2005). doi: 10.1002/352760376X.ch2.

[80] J. R. Winkler, A. R. Dunn, C. R. Hess, H. B. Gray. "Electron tunneling through iron and copper proteins," in *Bioinpro- ganic Electrochemistry*, O. Hammerich and J. Ulstrup (Eds.), pp. 1–23, Springer, Dordrecht, The Netherlands (2008). DOI:10.1007/978-1-

4020-6500-2_1.

[81] A. Operamolla, R. Ragni, F. Milano, R. R. Tangorra, A. Antonucci, A. Agostiano, M. Trotta, G. Farinola. *J. Mater. Chem. C* **3**, 6471 (2015).

[82] A. Moura, M. A. Savageau, R. Alves. *PLoS One* **8**, e77319 (2013).

[83] A. Ambrogelly, S. Palioura, D. Soll. *Nat. Chem. Biol.* **3**, 29 (2007).

[84] A. Bock, K. Forchhammer, J. Heider, W. Leinfelder, G. Sawers, B. Veprek, F. Zinoni. *Mol. Microbiol.* **5**, 515 (1991).

[85] C. Ling, E. D. Wang. *Prog. Biochem. Biophys.* **32**, 490 (2005).

[86] A. A. Turanov, X. M. Xu, B. A. Carlson, M. H. Yoo, V. N. Gladyshev, D. L. Hatfield. *Adv. Nutr.* **2**, 122 (2011).

[87] M. A. Gaston, L. W. Zhang, K. B. Green-Church, J. A. Krzycki. *Nature* **471**, 647-U131 (2011).

[88] S. Castellano, A. M. Andres, E. Bosch, M. Bayes, R. Guigo, A. G. Clark. *Mol. Biol. Evol.* **26**, 2031 (2009).

[89] R. Longtin. *J. Natl. Cancer I* **96**, 504 (2004).

[90] J. F. Atkins, R. Gesteland. *Science* **296**, 1409 (2002).

[91] C. Hertweck. *Angew. Chem. Int. Edit.* **50**, 9540 (2011).

[92] Z. H. Ming, L. R. Zhong. *Prog. Biochem. Biophys.* **29**, 831 (2002).

[93] F. Quitterer, A. List, P. Beck, A. Bacher, M. Groll. *J. Mol. Biol.* **424**, 270 (2012).

[94] J. M. Larsen, E. M. Espinoza, J. D. Hartman, C.-K. Lin, M. Wurch, P. Maheshwari, R. K. Kaushal, M. J. Marsella, G. J. O. Beran, V. I. Vullev. *Pure Appl. Chem.* **87**, 779 (2015).

[95] E. M. Espinoza, J. M. Larsen, V. I. Vullev. *J. Phys. Chem. Lett.* **7**, 758 (2016).

[96] J. M. Larsen-Clinton, E. M. Espinoza, M. F. Mayther, J. Clark, C. Tao, D. Bao, C. M. Larino, M. Wurch, S. Lara, V. I. Vullev. *Phys. Chem.y Chem. Phys.* **19**, 7871 (2017).

[97] B. Xia, D. Bao, S. Upadhyayula, G. Jones, V. I. Vullev. *J. Org. Chem.* **78**, 1994 (2013).

Chapter 2

Building Blocks for Bioinspired Electrets: Molecular-Level Approach to Materials for Energy and Electronics

Abstract

In biology, an immense diversity of protein structural and functional motifs originates from only 20 native amino acids arranged in various sequences. Is it possible to attain the same diversity in electronic materials based on organic macromolecules composed of non-native residues with different characteristics? This publication describes the design, preparation and characterization of non-native aromatic β-amino acid residues, i.e., derivatives of anthranilic acid, for polyamides that can efficiently mediate hole transfer. Chemical derivatization with three types of substituents at two positions of the aromatic ring allows for adjusting the energy levels of the frontier orbitals of the anthranilamide residues over a range of about one electron volt. Most importantly, the anthranilamide residues possess permanent electric dipoles, adding to the electronic properties of the bioinspired conjugates they compose, making them molecular electrets.

Introduction

Charge transfer (CT) drives almost any phenomenon known to us from a molecular to macroscopic scale. At a cellular level, CT is responsible for a range of chemical and biochemical transformations, and is essential for life on Earth to exist [1-5]. In addition to its vital role in living systems, CT resides at the heart of energy conversion, transduction and storage [6-13], and provides signal transduction for devices integral to our modern lifestyles [14, 15]. For more than a century, the key importance of CT has sustained the ever-growing scientific interest in it.

Among the four fundamental forces in the universe, electromagnetic interactions are the second strongest, weaker only than the nuclear strong force [16]. Unlike nuclear forces, however, electromagnetism prompts long-range interactions making it deterministic for condensed matter [17]. Even minute displacement of charges can result in macroscopically observable phenomena [18-28]. Similarly, with the development of metamaterials, controlling nanometer-scale CT allows for an emergence of unprecedented properties.

The value of the capability to control CT at molecular and nanometer scales cannot be overstated. The utility of local electric fields, generated from molecular and macromolecular dipoles, for ion transport and electron transfer is paramount for living systems [29-31]. Hence, molecular electrets present an important paradigm for guiding CT. (Dipole-polarization electrets are the electrostatic analogues of magnets, i.e., they possess co-directionally ordered electric dipole moments.).

Protein helices represent one of the best examples for molecular electrets, and their electronic properties are essential for various processes in biology [29, 30]. Biomimetic systems, based on polypeptide helices comprising native α-amino acids, rectify the directionality of CT [32-36]. These protein structures, however, possess drawbacks that are inherent to electret materials. Electrets are dielectrics and they may not contain free charge carriers. Free-moving charges in the electret or in the surrounding media would screen the dipole-generated fields eliminating the dipole effect. Hence, electron tunneling is representative of the prevalent mechanism of CT mediated by biological and biomimetic polypeptide structures [37-43]. Tunneling, however, limits the distance of efficient CT to about 2 nm [37, 38]. Sites where charges can temporarily reside (such as redox active cofactors, nucleotides, or amino-acid side chains) can greatly extend the CT distance beyond the 2-nm tunneling limit [5, 44]. Good electronic coupling between a sequence of redox moieties ensures pathways for efficient multiple electron tunneling short steps allowing long-range CT to occur, i.e., long-range electron or hole hopping [5, 44].

To address some of the challenges with polypeptide biological and biomimetic structures, we have undertaken a bioinspired approach to designing molecular electrets in the search of properties that are beyond what natural systems can offer [45-48]. Composed of anthranilamide (**Aa**) residues, the bioinspired electrets possess ordered amide and hydrogen bonds that, similar to the ordered peptide bonds in protein helices, generate an axial electric dipole (Figure 2-1). In addition to determining that these oligomers of aromatic *ortho*-amino acids are indeed molecular electrets [46], we also demonstrated that the **Aa** dipole rectifies charge transfer [45]. Furthermore, derivatizing an anthranilamide

with a secondary amine as R_2 at the 5th position (Figure 2-1), yields a residue that not only is a good electron donor, but also can host a positive charge for seconds as evident from the reversible electrochemical oxidation [45]. The ability to accommodate positive charges is a promising feature for mediating CT via hole (h^+) hopping.

Chemical derivatization provides a means to widely diversify the electronic properties of the **Aa** residues. With all trans amide bonds, the **Aa** oligomers assume an extended conformation, which also is key for their intrinsic dipole. To maintain this extended conformation, it is essential to prevent steric hindrance between residues proximal within an oligomer sequence. Therefore, only the distal sites, i.e., the 4th and 5th position in the aromatic rings of the residues (corresponding to R_1 and R_2, respectively, on Figure 2-1), are available for chemical derivatization.

Each of the 20 native amino acids differs from the rest by only a single side chain. The side chains of these α-L-amino acid residues govern the conformational folds, and overall the protein structural and functional features. Conversely, the non-native anthranilic residues have two side chains (R_1 and R_2, Figure 2-1) that can be used for adjusting their electronic properties. To explore the potential of these bioinspired molecular electrets as CT-controlling materials it is paramount to design a set of non-native **Aa** residues with diverse electronic characteristics.

Aromatic *poly*- and *oligo*-amides, such as Huc's foldamers [49-51], provide incomparable venues for exploring biological types of structural motifs, the diversity of which expands beyond what the natural systems can offer [52-56]. Indeed, the rich π-conjugation of such foldamers governs their immensely promising CT characteristics [57].

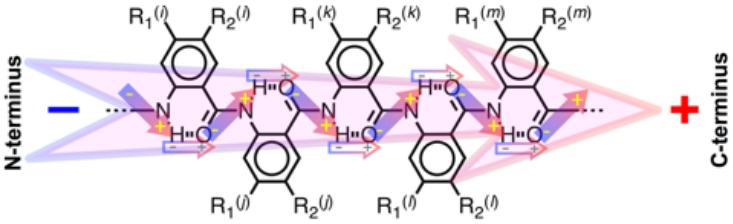

Figure 2-1. Bioinspired molecular electret composed of anthranilamide residues (---**Aa**$^{(i)}$- **Aa**$^{(j)}$- **Aa**$^{(k)}$- **Aa**$^{(l)}$- **Aa**$^{(m)}$---) and the origin of its electric dipole from the ordered orientation of the amide linkers and the polarization of the hydrogen bonds.

Our focus, conversely, is on extended aromatic structures, such as **Aa** oligomers (Figure 1) [46, 48, 58], which are not truly foldamers. While the common theme as electrets with extended conformations and large intrinsic dipoles is conserved in the **Aa** structures, alterations of the side chains (R_1 and R_2, Figure 2-1) provides venues for achieving diversity in the electronic properties of such aromatic *poly* and *oligo*-amides.

Herein, we demonstrate the preparation and characterization of eight non-native Aa residues with their N- and C-termini capped as alkyl amides (Figure 2-2). In addition to the basic anthranilamide residue (Ant) where $R_1 = R_2 = H$, we investigate Aa derivatives with three types of electron-donating substituents for R_1 and R_2: alkyl (i.e., methyl), alkyoxyls (i.e., methoxy and hexyloxy groups) and amines (i.e., piperidinyl and hexylmethylamine). Electrochemical and spectroscopy studies allowed for estimating the energy levels of the frontier orbitals of these Aa residues. Density functional theory (DFT) calculations yielded information about the intrinsic electric dipoles of the Aa derivatives and provided visualization of their highest occupied and lowest unoccupied molecular orbitals (HOMO and LUMO,

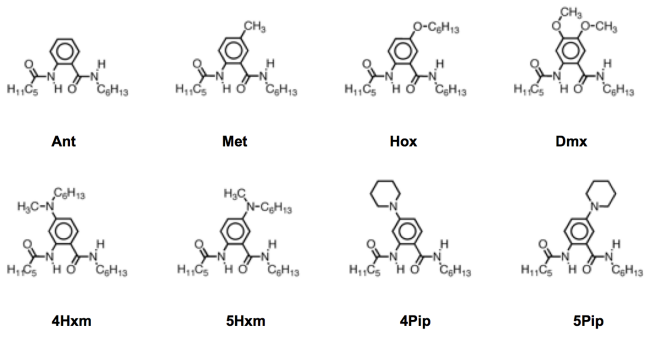

Figure 2-2. Anthranilamide residues.

respectively).

In agreement with the contribution from the amide and hydrogen bonds [48], the magnitudes of the dipole moments of the Aa residues exceed 4 D. The chemical derivatization with the three listed electron-donating groups at the two positions of the Aa aromatic ring (i.e., the 4^{th} and 5^{th}) allow for adjusting the reduction potentials of the Aa oxidation over the range of about 1 V. This range is quite significant: adjusting the HOMO energy levels over 1 eV provides an incomparable means for modulating the hole-transfer pathways along sequences composed of such Aa residues.

In addition, the results demonstrate that the electronic properties of Aa depend on both the type of substituted groups used and the exact position of these groups. That is, an electron-donating group (EDG) as a substituent at the 4^{th} and 5^{th} positions can yield three distinct Aa residues with different electronic properties. A residue with R_1 = EDG and R_2 = H has different properties from a residue with R_1 = H and R_2 = EDG that also differs from a residue with R_1 = EDG and R_2 = EDG. This feature demonstrates diversity in electronic characteristics that can be achieved via permutations within a single Aa residue, something that native amino acids with single side chains cannot offer. It illustrates some of the advantages of bioinspired over biomimetic approaches [47].

RESULTS

Preparation of the anthranilamide residues

As polypeptide conjugates of aromatic non-native β-amino acids, we build the **Aa** oligomers from their C- to their N-termini [46]. Each **Aa** residue is added to the sequence as a 2-nitrobenzoic acid derivative [45, 46]. A selective reduction of the nitro group to

amine prepares the thus added N-terminal residue for the next amide-coupling step [46]. The use of "traditional" synthetic protocols, where each residue is introduced as an N_β-Fmoc or N_β-tBoc anthranilic acid derivative, renders negligible to no yields. The electron-withdrawing nitro group at *ortho* position ensures the electrophilicity of the carbonyl carbon of the activated carboxylate that is needed for coupling it with the N-terminal amine. The N-terminal anthranilic amines are weak nucleophiles due to the neighboring electron-withdrawing carbonyls.

To attain a diversity of **Aa** residues, we focus on the preparation of a variety of 4- and 5- derivatives of the 2-nitrobenzoic acid as precursors for non-native **Aa** residues. Three types of substituents at R_1 and R_2 positions (Figure 2-1) allow for producing electron-rich **Aa** residues with a wide distribution of the energy levels of their frontier orbitals: (1) strong electron-donating groups, dialkylamines; (2) moderately strong electron-donating groups, alkoxyls; and (3) a weak electron-donating group, methyl. Starting with fluoro-derivatives, nucleophilic aromatic substitution allow for introducing amines as substituents at the 4^{th} and 5^{th} positions of the 2-nitrobenzoic acid. In the 5-fluoro-2-nitrobenzoic acid, the C-F bond at the *para* position in relevance to the nitro group is quite polarized, making that carbon susceptible to the attack from an amine nucleophile. Using a cyclic secondary amine, i.e., piperidine, requires relatively short reaction times under conventional heating to produce in quantitative yields the nitrobenzoic precursor for the 5Pip residue (Scheme 2-1a) [45]. In the 4-fluoro-2-nitrobenzoic acid, the C-F bond is not as polarized due to the *meta* (rather than *para*) position of the nitro group. For the precursor for the 4Pip residue, therefore, the same nucleophilic aromatic substitution with

the 4-fluoro-2-nitrobenzoic acid requires longer reaction times for attaining similar yields (Scheme 2-1b).

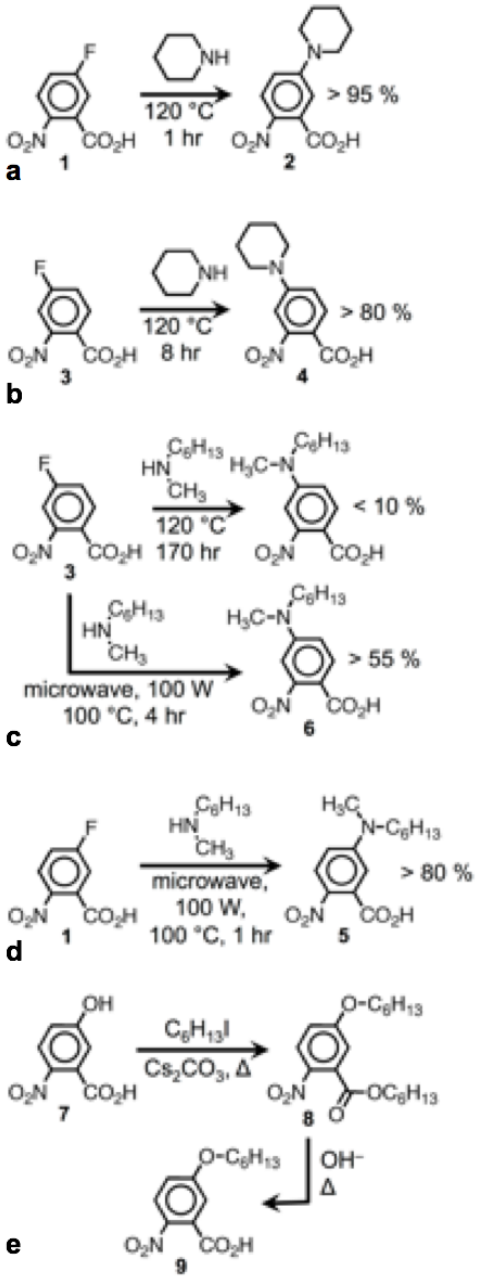

Scheme 2-1. Syntheses of the 2-nitrobenzoic acid precursors for (a) 5Pip, (b) 4Pip, (c) 5Hxm, (d) 4Hxm, and (e) Hox.

A synthetic challenge arises when the nucleophiles are non-cyclic secondary amines. Entropic restrictions decrease the nucleophilic reactivity of dialkylamines as the length of their chains increases [59]. Under conventional heating, the substitution of fluorine in 4-fluoro-2-nitrobenzoic acid with hexylmethylamine leads to negligible yields even when the reaction proceeds for unreasonably long periods of time (Scheme 2-1c).

Utilizing microwave radiation as a heat source allows for addressing this challenge. Although still debated, microwave heating may enhance reaction rates via the entropy components of their activation energies [60, 61], making it appropriate for overcoming the limitations imposed by amine nucleophiles with long alkyl chains. Employing microwave heating, indeed, allows us to develop procedures that lead to

completion of the syntheses of the hexylmethylamino precursors for 4Hxm and 5Hxm (Figure 2-2) within reasonable time durations (Scheme 2-1c,d).

The starting material for the Hox precursor is 5-hydroxy-2-nitrobenzoic acid, the carboxylate and the phenolate of which are indiscriminately strong nucleophiles readily producing the dialkyl derivatives. An extra hydrolysis step leads to the Hox nitrobenzoic precursor (Scheme 2-1e). Coupling of the 2-nitrobenzoic acids with 1-hexylamine, followed by selective reduction of the nitro group to amine and another amide coupling produces the eight **Aa** residues [45].

Reduction potentials

Electrochemical studies allow for quantifying the propensity of the **Aa** residues to serve as electron donors and to potentially mediate hole transfer. The reduction potentials of the oxidation of the **Aa** residues (i.e., $E^{(0)}_{\mathbf{Aa}^{\bullet+}/\mathbf{Aa}}$: $\mathbf{Aa}^{\bullet+} + e^- \rightarrow \mathbf{Aa}$) provide a means for quantifying their electron-donating capabilities [62], and for estimating the energy levels of their HOMOs [63].

To elucidate the media effects on the electronic properties, we focus on the dependence of the **Aa** electrochemical potentials on the solvent polarity [64-68]. Our selection includes five aprotic solvents with different polarity that have electrochemical windows extending over the expected potentials needed for the oxidation of the **Aa** residues: chloroform ($CHCl_3$), dichloromethane (DCM), benzonitrile (PhCN), acetonitrile (MeCN), and propylene carbonate (PC).

As a representation of the standard electrode potentials, $E^{(0)}$, the half-wave potentials, $E^{(1/2)}$, are readily obtained from cyclic voltammetry (CV). For reversible

electrochemical oxidation, $E^{(1/2)}$ represents the average between the peak potentials of the anodic and the cathodic waves. If the lifetimes of the radical cations, $\mathbf{Aa}^{\bullet+}$, generated on the surface of the working electrode do not extend over milliseconds and seconds (the time scales of CV), the cathodic wave becomes undetectable. For such electrochemically irreversible oxidation, the potential at the inflection point of the rise of the anodic wave provides an estimate for $E^{(1/2)}$ (see Supplementary Material). 5Hxm, 5Pip, and Dmx manifest electrochemically reversible oxidation indicating that these residues produce radical cations with pronounced stability.

While electrochemical measurements require media with high electrolyte concentrations, it is the information for $E^{(0)}$ in neat solvents that is directly relevant to spectroscopy and computational data [65]. From the dependence of the measured $E^{(1/2)}_{Aa^{\bullet+}/Aa}$ on the electrolyte concentration, C_{el}, therefore, we extrapolate the values of the reduction potentials of the residues for zero electrolyte concentration, i.e., the **Aa** $E^{(C_{el}=0)}_{Aa^{\bullet+}/Aa}$ potentials for neat solvents, (Figure 2-3a) [65].

Based on the Born solvation energy [69], a linear correlation $E^{(C_{el}=0)}_{Aa^{\bullet+}/Aa}$ between and the inverse dielectric constant of the neat solvents, ε^{-1}, reveals the effects of the media polarity on the electrochemical properties of each **Aa** residue (Figure 2-3b,c). As expected, an increase in the solvent polarity (i.e., a decrease in ε^{-1}) shifts the potentials to less positive values, elevating the energy levels of the HOMOs, and improving the capabilities of the residues as electron donors (Figure 2-3b,c). The stabilization of the radical cations, $\mathbf{Aa}^{\bullet+}$, by polar media accounts for this negative shifts of the measured potentials.

For each solvent, an increase in the electron-donating strength of the substituents, from methyl to amines, causes negative shifts in the reduction potentials. The potential of the best electron donor, 5Hxm, is about 1 V more negative than that of Ant (Figure 2-3b, Table 2-1). This finding is consistent with our theoretical predictions that placing dialkylamine at the 5th position of anthranilamides elevates the energy levels of their

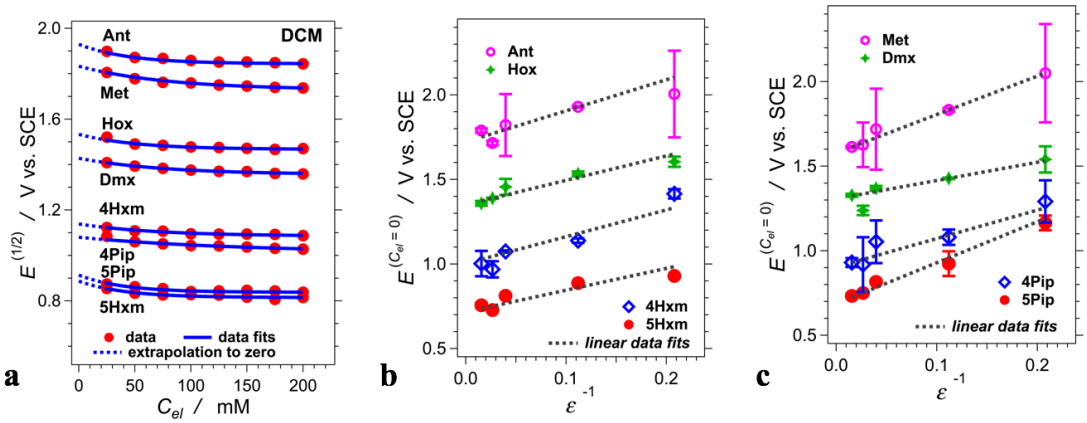

Figure 2-3. Solvent dependence of the electrochemical potentials of the anthranilamide residues. (a) Dependence of the half-wave potentials of the **Aa** residues on the electrolyte concentration, C_{el} (for DCM in the presence of $(C_4H_9)_4NPF_6$ as electrolyte). Extrapolation to zero electrolyte concentration from exponential data fits provides the estimates for the reduction potentials of the residues in neat solvents. (b,c) Dependence of the extrapolated potentials for neat solvents on the media dielectric characteristics obtained from measurements for five different solvents: propylene carbonate, PC (ε^{-1} = 0.016); acetonitrile, MeCN (ε^{-1} = 0.027); benzonitrile, PhCN (ε^{-1} = 0.040); dichloromethane, DCM (ε^{-1} = 0.11); and chloroform (ε^{-1} = 0.21).

HOMOs with about 1 eV [48].

While the amine-derivatized **Aa** residues are the best electron donors, moving the amine substituents from the 4th to the 5th position causes another negative shift (of about 0.2 – 0.4 V) in the potentials (Figure 2-3b,c). The alkylamines in 5Pip and 5Hxm are *para*-oriented to the electron-donating N-terminal amide and *meta*-oriented to the electron-withdrawing C-terminal amide. This *para*-orientation between the two electron-donating groups in 5Pip and 5Hxm can account for the more negative values of their potentials in

comparison with 4Pip and 4Hxm.

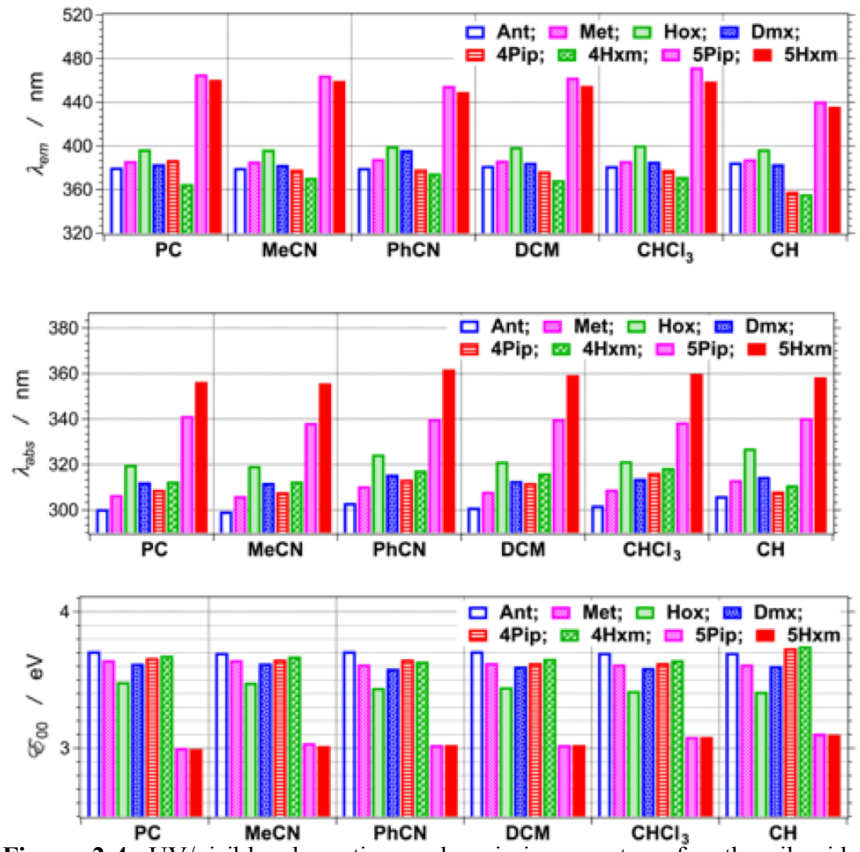

Figure 2-4. UV/visible absorption and emission spectra of anthranilamide residues for various solvent media: propylene carbonate (PC), acetonitrile (MeCN), benzonitrile (PhCN), dichloromethane (DCM), chloroform ($CHCl_3$), and cyclohexane (CH). (a) Absorption spectra of the eight residues for MeCN. (b) Fluorescence spectra of the residues recorded for MeCN and DCM ($\lambda_{ex} = 310$ nm; each fluorescence spectrum was normalized by $\times\ (1 - 10^{-A(\lambda ex)})^{-1}$). (c) Absorption and fluorescence spectra for Hox in the different solvents ($\lambda_{ex} =$ 310 nm; each fluorescence spectrum was normalized to the height of the red-most band of the corresponding absorption spectrum; except for PC, the baselines of the spectra are elevated from 0 for improved visualization; the arrows point to wavelength, λ_{00}, of crossing point between the two spectra that is used for calculating the zero-to-zero energy, $\mathscr{E}_{00} = h\ c\ /\ \lambda_{00}$).

This "reinforcement" from two electron-donating groups *para*-positioned to each other can account for stabilizing the radical cations, $\mathbf{Aa}^{\bullet+}$, and the reversible electrochemical oxidation of 5Pip and 5Hxm. This argument should hold also for the other electron-donating groups at the 5th position.

While Dmx manifests reversible oxidation, however, the cyclic voltammograms of Hox and Met exhibit irreversible behavior. Despite the stabilization that 5-methyl and 5-hexyloxy groups might provide to the racial cations of Met and Hox, respectively, their

reduction potentials appear positive enough to irreversibly cleave the amide bonds attached to the aromatic rings [70].

Photophysical properties

While electrochemical analysis provides information about the capabilities of the **Aa** residues to serve as electron donors and hole transducers, optical spectroscopy reveals complementary features about the energetics of the **Aa** frontier orbitals. In particular, UV/visible absorption and fluorescence spectroscopy provide a means for estimating the zero-to-zero energies, $\mathscr{E}_{00}$. $\mathscr{E}_{00}$ represents optical HOMO-LUMO gaps, which in molecular photophysics can be viewed as the optical band gaps of these **Aa** building blocks for organic materials.

The eight **Aa** residues absorb in the UV spectral region and fluoresce with substantial quantum yields, ranging between about 0.1 and 0.3 (Figure 2-4) The wavelength where the intensity-normalized absorption and emission spectra cross provides a means for estimating $\mathscr{E}_{00}$ (Figure 2-4c)

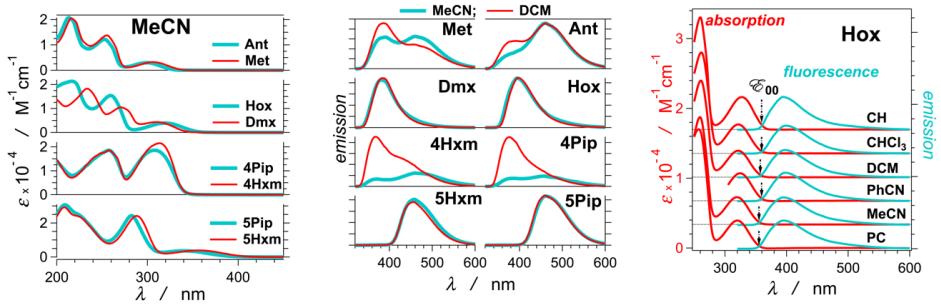

Figure 2-5. Absorption and emission properties of the anthranilamide residues. (a) Wavelengths of the maxima of the most red-shifted bands of the absorption spectra of the eight residues for different solvents: propylene carbonate (PC), acetonitrile (MeCN), benzonitrile (PhCN), dichloromethane (DCM), chloroform ($CHCl_3$), and cyclohexane (CH). (b) Wavelengths of the maxima of the fluorescence spectra of the eight residues in different solvents (λ_{ex} = 310 nm). For each residue that, due to aggregation, exhibits two fluorescence bands, the wavelength of the blue-shifted maximum is reported. (c) Zero-to-zero energy values of the anthranilamide residues, extracted from wavelength where the normalized absorption and emission spectra cross (Figure 2-4).

[71-74]. For the **Aa** residues, $\mathscr{E}_{00}$ ranged from about 3 to 3.7 eV (Figure 2-5c). The capability of the alkyloxy and the dialkylamine substituents to extend the π-conjugation of the aromatic rings leads to a decrease in $\mathscr{E}_{00}$ that is consistent with narrowing the HOMO-LUMO gaps of the residues. This effect, however, was pronounced only for strong electron-donating substituents placed at the *para* position to the N-terminal amides (5Pip and 5Hxm vs. 4Pip and 4Hxm, Figure 2-5).

Similar comparison for the alkyloxy-derivatized residues reveals that the spectral features of Hox are red-shifted compared to these of Dmx (Figure 2-5). This red spectral shifts for Hox vs. Dmx, are most likely due to the methoxy group at the 4th position of Dmx. An electron-donating group at the 4th position appears to cause blue spectral shifts. Even strong electron-donating groups, such as amines, placed at the 4th position, i.e., 4Hxm and 4Pip, result in **Aa** residues with spectral features similar to those of Met and Ant (Figure 2-5).

While $\mathscr{E}_{00}$ depends on the R_1 and R_2 substituents, the solvent polarity has insignificant to no effect on the spectral properties of the **Aa** residues (Figure 2-4, 2-5). This lack of substantial solvatochromism is consistent with our previous experimental observations and theoretical findings for Ant and 5Pip derivatives [45, 46]. The anthranilamides are, indeed, polar molecules. The observed lack of significant solvatochromism, therefore, suggests that photoexcitation of the **Aa** residues does not substantially alter their polarity. That is, the permanent ground-state dipoles have dominating effect on the ground- and excited-state polarity of the **Aa** conjugates.

Another feature revealed by the emission spectra of the **Aa** residues is their

propensity to aggregate. As expected from our previous studies [46], two of the residues, Ant and Met, exhibit fluorescence bands with two peaks (Figure 2-4b), the ratios between which are concentration dependent. We ascribe the red-shifted peak, the intensity of which increases with an increase in concentration, to aggregates that form at the excited and/or the ground state [46, 75-80]. The trends from this assignment of the fluorescence spectra indicate that the chlorinated hydrocarbons, such as DCM, tend to suppress aggregation (Figure 2-4b).

In addition, 4Pip and 4Hxm also aggregate at μM concentrations when dissolved in some of the tested organic solvents (Figure 2-4b). This finding was somewhat surprising because the residues with identical alkyl chains attached to them, 5Pip and 5Hxm, did not manifest detectable aggregation even at concentrations reaching 1 mM. These findings show that the position of substituents with alkyl chains (i.e., R_1 vs R_2) pronouncedly affects the aggregation propensity of the **Aa** derivatives. To confirm this trend, other two residues, Hox and Dmx, that also contain alkyl chains at the 5^{th}, also show a single fluorescence peak, indicating that they do not manifest detectable aggregation in the tested organic solvents (Figure 2-4b).

Comparison between 4Pip and 4Hxm reveals an important trend about the dependence of the aggregation propensity on the structure of the substituents. Both residues aggregate when dissolved in most organic solvents at μM concentrations. In chlorinated solvents, however, while 4Pip exists as a monomer, 4Hxm manifests some propensity for aggregation (Figure 2-4b). Both residues contain secondary amines at the 4^{th} positions of their aromatic rings. Both substituents contain more than five carbons in their alkyl chains

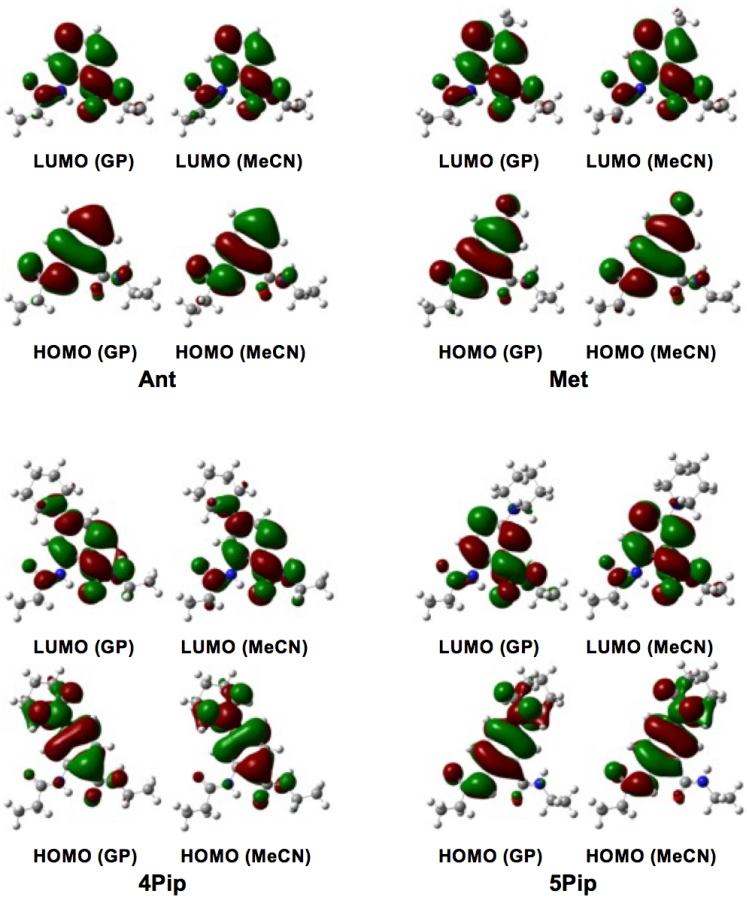

Figure 2-6. HOMOs and LUMOs of Ant, Met, 4Pip and 5Pip for the gas phase (GP) and for acetonitrile (MeCN), obtained from DFT calculations. For the computational studies, the alkyl chains at the C- and N-termini were truncated to C_2H_5. The residues are displayed with their N-termini oriented to the left and the C-termini – to the right. (See the Supplementary Material for the HOMOs and LUMOs of all eight residues.)

(piperidinyl for 4Pip, and hexyl and methyl for 4Hxm, Figure 2-2). In fact, 4Hxm has a longer chain than 4Pip. Contrarily to correlating improved solubility with increased length of alkyl substituents, however, 4Hxm has a larger propensity for aggregation than 4Pip. In the piperidinyl substituents more carbons are located closer to the aromatic ring than in hexylmethylamine. This increase in the volume of the solvation cavity immediately next to the aromatic moieties (that may drive aggregation) appears to have dominant effect on improving the residue solubility. This trend indicates that long linear chains, such as hexyls, do not improve the solubility in organic solvents to the extent that branched substituents, such as piperidinyl, do.

Permanent electric dipoles and distribution of the frontier orbitals

Ab initio computational studies provide further key information about the electronic properties of the **Aa** residues and the dependence of these properties on the media polarity. Ground-state DFT calculations at the B3LYP/6-311+G(d,p) level [81-83] performed using Gaussian 09 [84] revealed that the HOMOs and LUMOs of all eight **Aa** residues are predominantly localized on their aromatic rings (Figure 2-6). For the residues with no substituents or with relatively weak electron-donating R_1 and R_2 groups, i.e., for Ant, Met, Hox and Dmx, the HOMOs extend over the N-terminal amide bond, while the LUMOs tend to delocalize over both amides (Figure 2-6). Placing a strong electron-donating group on the 5^{th} position (i.e., R_2 = dialkylamine) amplifies these orbital-delocalization trends (see 5Pip on Figure 2-6, and 5Hxm in the Supplementary Material). Conversely, placing the same strong electron-donating groups on the 4^{th} position shifts the delocalization of the HOMOs to the C-terminal amides (see 4Pip Figure 2-6, and 4Hxm in the Supplementary Material).

To account for the solvent effects on the electronic properties of the **Aa** residues, we introduced DCM and MeCN to the calculations using a polarizable continuum model [85-87]. Inclusion of the solvents had no visible effect on the distribution of frontier orbitals (Figure 2-6). Most importantly, the optimized structures of the eight **Aa** residues remain practically identical when varying the solvent media (see Supplementary Material). While the anthranilamides are polar molecules, principally because of the amide dipoles, these computational findings suggest that the preferential **Aa** conformation, with *trans* amides, is not affected by changes in the solvent polarity.

The permanent electric dipoles are the most important feature of the **Aa** residues, making them promising building blocks for electrets. The predicted dipole moment of Ant is about 4.7 D (Table 2-1), which is consistent with the contributions of 1.9 D from each of the two amides and of 0.9 D from the polarization due to the hydrogen bonding (Figure 2-1) [48]. Adding methyl to the 5th position, such as in Met, slightly enhances the dipole (Table 2-1), which is consistent with the 5-methyl-induced polarization of the aromatic

Table 2-1. Electronic characteristics of the anthranilamide residues.[a]

	R_1	R_2	μ [b] / D			E [c] / V vs. SCE		$\mathcal{E}_{00}$ [d] / eV	
			vacuum	DCM	MeCN	DCM	MeCN	DCM	MeCN
Ant	H	H	4.71	6.38	6.68	1.93	1.72	3.7	3.7
Met	H	CH_3	4.96	6.79	7.12	1.83	1.63	3.6	3.6
Hox	H	OC_6H_{13}	6.42	8.56	8.96	1.53	1.39	3.4	3.5
Dmx	OCH_3	OCH_3	4.53	6.37	6.72	1.43	1.24	3.6	3.6
4Pip	$N(CH_2)_5$	H	4.46	6.26	6.62	1.08	0.919	3.6	3.7
5Pip	H	$N(CH_2)_5$	5.52	7.61	8.00	0.923	0.750	3.0	3.0
4Hxm	$N(CH_3)C_6H_{13}$	H	4.42	6.31	6.69	1.14	0.968	3.7	3.7
5Hxm	H	$N(CH_3)C_6H_{13}$	6.59	8.85	9.24	0.887	0.727	3.0	3.0

[a] From experimental and theoretical studies of the eight residues where R_1 and R_2 correspond to the 4th and 5th positions, respectively, in the aromatic rings (Figure 1, 2). [b] Dipole moments are obtained from DFT calculations for gas phase (vacuum) and for structures where the solvents, DCM and MeCN, are implemented as dielectric continua. The orientation of the molecular dipoles is from the N to the C-termini of the anthranilamide residues. [c] Reduction potentials for the residue oxidation, i.e., $\mathbf{Aa}^{\bullet+} + e^- \rightarrow \mathbf{Aa}$, for neat solvents obtained from extrapolation of half-wave potentials to zero electrolyte concentration (Figure 3a). [d] The zero to zero energy from the crossing point of the normalized absorption and fluorescence spectra (Figure 4).

ring co-directionally with the total dipole from the amide and hydrogen bonds. This enhancement effect on the **Aa** dipole is even more pronounced for Hox, 5Hxm and 5Pip, where R_2 electron-donating groups have mesomeric, rather than inductive, effects on the aromatic ring (Table 2-1). Conversely, when an electron-donating group is at the 4th

position, such as in 4Hxm and 4Pip, the substituent-induced polarization of the aromatic ring has a diminishing effect on the total residue dipole (Table 2-1).

Solvent polarity further enhances the magnitude of the **Aa** dipoles (Table 2-1). Because the electronic and structural properties of the **Aa** residues have a negligible dependence on the media, this polarity-driven enhancement can be attributed to the effect of the **Aa** dipoles on the solvent itself. As we have shown for simple aliphatic amides, such dipole enhancement results from the Onsager fields inside the solvation cavities of the solutes [66, 88]. The **Aa** dipoles polarize the solvent media in the proximity to the solvation cavities. This polarization increases the displacements between the centers of the positive and negative charges of the solvated **Aa** molecules, increasing the magnitudes of their total dipole moments.

DISCUSSION

The solvent effect on the permanent molecular dipoles has important implications on the CT properties of the anthranilamides. Others and we have shown that an increase in solvent polarity diminishes the dipole effects on CT [32, 33, 45], which is attributed to the screening of the dipole-generated electric field by the surrounding polar media. Concurrently, the media polarity enhances the dipole-generated field inside a solvated molecule [66]. Conversely, for the reported solvent effects on dipole-mediated CT, the electron donor and acceptor are linked in a manner that places both or either of them outside the solvation cavity containing the groups generating the dipole fields. That is, the sources of the permanent dipoles are frequently polypeptide helices, and the redox moieties involved in the CT are located at certain distance from the helix backbones, linked to side

chains of residues composing the polypeptide. Thus, while the electron-tunneling pathways may transverse through cavities with solvent-induced enhancement of dipolar fields, the solvation of the acceptor and/or of the donor, outside these cavities, principally affects the CT kinetics.

As an alternative to protein-derived structures, anthranilamide molecular electrets have the structural and electronic features for exploration of solvation dependence of dipole-mediated CT. The aromatic moieties, providing sites for charge hopping, are directly linked via amides that are responsible for the permanent dipole moments. Hence, the intertwining of the charge-hopping sites and the dipolar groups generating the fields situates them within the same solvation cavity.

While the dipole-generated fields of such electrets can guide the CT processes, the ability to tune energetics along the CT pathways should not be undermined. The electron-donating substituents stabilize positive charges, h^+, injected in the aromatic residues, as evident from the negative shifts in the reduction potentials of **Aa** oxidation when R_1 and R_2 are changed from hydrogen to alkyloxyls and to amines (Table 2-1). The ability to adjust the **Aa** reduction potentials over a range of 1 V shows a key advantage of anthranilamide CT electrets illustrating their promising potential and utility.

Frequently, potential wells with depth in the order of a few hundred millielectronvolts are responsible for undesired charge-trapping and charge-recombination, decreasing performance efficiencies of materials and devices [89-93]. For **Aa** residues, only a single change in the position of an amine from R_2 to R_1 lowers their HOMO energy with about 0.3 eV, which exceeds the thermal energy, k_BT, by more than an order of

magnitude. Overall, the magnitude of the substituent effects on the electronic properties of the **Aa** residues is comparable with the energetics that governs CT processes responsible for the performance of electronic materials and devices.

Considering such applications, three of the residues, Dmx, 5Hxm and 5Pip, appear to have the most desirable characteristics. First, they all exhibit reversible electrochemical oxidation making them excellent sites for h^+ hopping. Indeed, the potentials of Hox, Met and Ant are positive enough to cause oxidative cleavage of the amide bonds [70] that sustain the structural integrity of the macromolecules these residues may compose. Therefore, their use may be limited to introducing them as tunneling barriers on the CT pathways. Conversely, 4Hxm and 4Pip present a curious case. Their reduction potentials do not appear positive enough to induce amide oxidation. Can 4Hxm and 4Pip, then, mediate h^+ hopping without oxidative cleavage? The cyclic voltammetry results indicate that $4Hxm^{\bullet+}$ and $4Pip^{\bullet+}$ have lifetimes much shorter than hundreds of milliseconds, making the cathodic waves undetectable. If the life of these radical cations, however, is longer than a few nanoseconds, 4Pip and 4Hxm still can be viable sites for h^+ hopping that does not cause irreversible damage of the molecular structures.

Second, 5Hxm, 5Pip and Dmx do not aggregate at hundreds of μM concentrations. This feature is important not only for solution phase studies, but also for processing materials composed of these residues. In addition to these three residues, the lack of aggregation propensities of Hox can also prove beneficial for macromolecular designs. While electronically Hox residues may be used solely for adding tunneling barriers along

CT pathways, introducing Hox to anthranilamide macromolecules will improve their solubility in organic media. Again, 4Hxm and 4Pip appear to have an outlier-like behavior. The six-carbon alkyl chains of their R_1 substituents do not eliminated their propensity for aggregation. Polarizable chlorinated solvents appear to at least partially suppress the aggregation of the 4-amino residues. 4Hxm and 4Pip, however, tend to aggregate when dissolved in other organic solvents.

Overall, 5Hxm, 5Pip, Dmx and Hox appear as most viable building blocks for molecular electrets that can readily mediate efficient long-range CT. Indeed, this analysis is based on conjugates composed of single **Aa** residues. Although the electronic properties of anthranilamide oligomers have negligible dependence on the number of residues [46], the single-residue findings should be viewed as important guidelines, rather than strict rules. Therefore, we cannot rule out the potential utility of 4Hxm and 4Pip. The irreversible electrochemical oxidation and the aggregation propensity of 4Hxm and 4Pip are not truly desirable features. Before these two residues are tested as building blocks of **Aa** oligomers, it will be premature to decide how adverse these features may prove. Conversely, the energy levels of their HOMOs of the 4-amino **Aa** residues are located between of the HOMOs of Dmx and 5Pip, making 4Hxm and 4Pip still attractive candidates for the exploration of the diversity of the CT molecular electrets.

In living organisms, each of the 20 native amino acids has quite a difference relative abundance in the known proteins they compose [94]. Similarly, in the design of CT molecular electrets, not all the **Aa** residues need to be equally present. Some residues, such as 5Hxm and Hox, may play principal role in determining the structural and electronic

characteristics of the molecular electrets. Other residues, such as Ant and Met, may be used scarcely as “dopants.”

Conclusions

Their permanent dipole moments make anthranilamides attractive candidates for charge-transfer systems. Combinations of three types of electron-donating substituents at two possible positions yield a set of non-native **Aa** residues with diverse electronic properties. In proteomics, permutations using 20 native amino acids lead to countless structure-function relationships. We believe that, in a similar manner, the herein described non-native **Aa** residues are key building blocks for countless macromolecular systems with a wide range of unexplored electronic features.

References

1. D. N. Beratan, C. Liu, A. Migliore, N. F. Polizzi, S. S. Skourtis, P. Zhang, Y. Zhang. *Acc. Chem. Res.* **48**, 474-481 (2015).

2. U. Brandt. *BIOspektrum* **20**, 267-270 (2014).

3. F. Sun, Q. Zhou, X. Pang, Y. Xu, Z. Rao. *Curr. Op. Struct. Biol.* **23**, 526-538 (2013).

4. P. Venditti, L. Di Stefano, S. Di Meo. *Mitochondrion* **13**, 71-82 (2013).

5. J. J. Warren, J. R. Winkler, H. B. Gray. *Coordinat. Chem. Rev.* **257**, 165-170 (2013).

6. J. Barber, P. D. Tran. *J. Royal Soc., Interface* **10**, 20120984/20120981-20120984/20120916 (2013).

7. G. Centi, S. Perathoner. *Chemical Energy Storage*, 379-400 (2013).

8. K. S. Joya, Y. F. Joya, K. Ocakoglu, R. van de Krol. *Angew. Chem. Int. Edit.* **52**, 10426-10437 (2013).

9. D. G. Nocera. *Acc. Chem. Res.* **45**, 767-776 (2012).

10. J. Michl. *Nat. Chem.* **3**, 268-269 (2011).

11. S. Kirner, M. Sekita, D. M. Guldi. *Adv. Mater.* **26**, 1482-1493 (2014).

12. D. Gust, T. A. Moore, A. L. Moore. *Acc. Chem. Res.* **42**, 1890-1898 (2009).

13. D. L. DuBois. *Inorg. Chem.* **53**, 3935-3960 (2014).

14. C. Zhang, Y. Yan, Y. S. Zhao, J. Yao. *Acc. Chem. Res.* **47**, 3448-3458 (2014).

15. T. W. Ng, M. F. Lo, M. K. Fung, W. J. Zhang, C. S. Lee. *Adv. Mater.* **26**, 5569-5574 (2014).

16. T. Shears. *Phil. Trans. Royal Soc. A* **370**, 805-817 (2012).

17. N. Nagaosa, Y. Tokura. *Physica Scripta, T* **T146**, 014020/014021-014020/014015 (2012).

18. B. M. Savoie, N. E. Jackson, L. X. Chen, T. J. Marks, M. A. Ratner. *Acc. Chem. Res.* **47**, 3385-3394 (2014).

19. J. N. Israelachvili, K. Kristiansen, M. A. Gebbie, D. W. Lee, S. H. Donaldson, S. Das, M. V. Rapp, X. Banquy, M. Valtiner, J. Yu. *J. Phys. Chem. B* **117**, 16369-16387 (2013).

20. M. W. Williams. *AIP Advances* **2**, 010701, 010710 pp (2012).

21. S. Upadhyayula, T. Quinata, S. Bishop, S. Gupta, N. R. Johnson, B. Bahmani, K. Bozhilov, J. Stubbs, P. Jreij, P. Nallagatla, V. I. Vullev. *Langmuir* **28**, 5059-5069 (2012).

22. K. Chau, B. Millare, A. Lin, S. Upadhyayula, V. Nuñez, H. Xu, V. I. Vullev. *Microfluid. Nanofluid.* **10**, 907-917 (2011).

23. B. Millare, M. Thomas, A. Ferreira, H. Xu, M. Holesinger, V. I. Vullev. *Langmuir* **24**, 13218-13224 (2008).

24. V. Nuñez, S. Upadhyayula, B. Millare, J. M. Larsen, A. Hadian, S. Shin, P. Vandrangi, S. Gupta, H. Xu, A. P. Lin, G. Y. Georgiev, V. I. Vullev. *Anal. Chem.* **85**, 4567-4577 (2013).

25. C. Hong, D. Bao, M. S. Thomas, J. M. Clift, V. I. Vullev. *Langmuir* **24**, 8439-8442 (2008).

26. V. I. Vullev, J. Wan, V. Heinrich, P. Landsman, P. E. Bower, B. Xia, B. Millare, G. Jones, II. *J. Am. Chem. Soc.* **128**, 16062-16072 (2006).

27. G. Jones, II, V. I. Vullev. *J. Phys. Chem. A* **106**, 8213-8222 (2002).

28. G. Jones, II, V. I. Vullev. *Photochem. Photobiol. Sci.* **1**, 925-933 (2002).

29. D. A. Doyle, J. M. Cabral, R. A. Pfuetzner, A. L. Kuo, J. M. Gulbis, S. L. Cohen, B. T. Chait, R. MacKinnon. *Science* **280**, 69-77 (1998).

30. R. Dutzler, E. B. Campbell, M. Cadene, B. T. Chait, R. MacKinnon. *Nature* **415**, 287-294 (2002).

31. S. Tanaka, R. A. Marcus. *J. Phys. Chem. B* **101**, 5031-5045 (1997).

32. E. Galoppini, M. A. Fox. *J. Am. Chem. Soc.* **118**, 2299-2300 (1996).

33. M. A. Fox, E. Galoppini. *J. Am. Chem. Soc.* **119**, 5277-5285 (1997).

34. S. Yasutomi, T. Morita, Y. Imanishi, S. Kimura. *Science* **304**, 1944-1947 (2004).

35. Y.-G. K. Shin, M. D. Newton, S. S. Isied. *J. Am. Chem. Soc.* **125**, 3722-3732 (2003).

36. B. Giese, M. Graber, M. Cordes. *Curr. Op. Chem. Biol.* **12**, 755-759 (2008).

37. H. B. Gray, J. R. Winkler. *Q. Rev. Biophy.* **36**, 341-372 (2003).

38. H. B. Gray, J. R. Winkler. *Proc. Natnl. Acad. Sci. U.S.A.* **102**, 3534-3539 (2005).

39. V. I. Vullev, G. Jones, II. *Res. Chem. Intermed.* **28**, 795-815 (2002).

40. G. Jones, II, V. I. Vullev. *Org. Lett.* **4**, 4001-4004 (2002).

41. G. Jones, II, V. Vullev, E. H. Braswell, D. Zhu. *J. Am. Chem. Soc.* **122**, 388-389 (2000).

42. G. Jones, II, L. N. Lu, V. Vullev, D. Gosztola, S. Greenfield, M. Wasielewski. *Bioorg. Med. Chem. Lett.* **5**, 2385-2390 (1995).

43. G. Jones, II, X. Zhou, V. I. Vullev. *Photochem. Photobiol. Sci.* **2**, 1080-1087 (2003).

44. S. L. Mayo, W. R. Ellis, Jr., R. J. Crutchley, H. B. Gray. *Science* **233**, 948-952 (1986).

45. D. Bao, S. Upadhyayula, J. M. Larsen, B. Xia, B. Georgieva, V. Nunez, E. M. Espinoza, J. D. Hartman, M. Wurch, A. Chang, C.-K. Lin, J. Larkin, K. Vasquez, G. J. O. Beran, V. I. Vullev. *J. Am. Chem. Soc.* **136**, 12966-12973 (2014).

46. B. Xia, D. Bao, S. Upadhyayula, G. Jones, V. I. Vullev. *J. Org. Chem.* **78**, 1994-2004 (2013).

47. V. I. Vullev. *J. Phys. Chem. Lett.* **2**, 503–508 (2011).

48. M. K. Ashraf, R. R. Pandey, R. K. Lake, B. Millare, A. A. Gerasimenko, D. Bao, V. I. Vullev. *Biotechnol. Progr.* **25**, 915-922 (2009).

49. I. Huc. *Eur. J. Org. Chem.*, 17-29 (2004).

50. L. Sebaoun, V. Maurizot, T. Granier, B. Kauffmann, I. Huc. *J. Am. Chem. Soc.* **136**, 2168-2174 (2014).

51. R. Orlowski, O. Vakuliuk, M. P. Gullo, O. Danylyuk, B. Ventura, B. Koszarna, A. Tarnowska, N. Jaworska, A. Barbieri, D. T. Gryko. *Chem. Commun.* **51**, 8284-8287 (2015).

52. N. Chandramouli, Y. Ferrand, G. Lautrette, B. Kauffmann, C. D. Mackereth, M. Laguerre, D. Dubreuil, I. Huc. *Nat. Chem.* **7**, 334-341 (2015).

53. Q. A. Gan, Y. Ferrand, C. Y. Bao, B. Kauffmann, A. Grelard, H. Jiang, I. Huc. *Science* **331**, 1172-1175 (2011).

54. A. S. Voisin-Chiret, S. Rault. *Pure Appl. Chem.* **84**, 2467-2478 (2012).

55. D. W. Zhang, X. Zhao, Z. T. Li. *Acc. Chem. Res.* **47**, 1961-1970 (2014).

56. P. Prabhakaran, G. Priya, G. J. Sanjayan. *Angew. Chem. Int. Edit.* **51**, 4006-4008 (2012).

57. M. Wolffs, N. Delsuc, D. Veldman, N. Van Anh, R. M. Williams, S. C. J. Meskers, R. A. J. Janssen, I. Huc, A. P. H. J. Schenning. *J. Am. Chem. Soc.* **131**, 4819-4829 (2009).

58. Y. Hamuro, S. J. Geib, A. D. Hamilton. *J. Am. Chem. Soc.* **118**, 7529-7541 (1996).

59. G. Mansour, W. Creedon, P. C. Dorrestein, J. Maxka, J. C. MacDonald, R. Helburn. *J. Org. Chem.* **66**, 4050-4054 (2001).

60. C. O. Kappe, B. Pieber, D. Dallinger. *Angew. Chem. Int. Edit.* **52**, 1088-1094 (2013).

61. A. de la Hoz, A. Diaz-Ortiz, A. Moreno. *Chem. Soc. Rev.* **34**, 164-178 (2005).

62. D. Rehm, A. Weller. *Israel. J. Chem.* **8**, 259-271 (1970).

63. S. Trasatti. *Pure Appl. Chem.* **58**, 955-966 (1986).

64. D. Bao, S. Ramu, A. Contreras, S. Upadhyayula, J. M. Vasquez, G. Beran, V. I. Vullev. *J. Phys. Chem. B* **114**, 14467-14479 (2010).

65. D. Bao, B. Millare, W. Xia, B. G. Steyer, A. A. Gerasimenko, A. Ferreira, A. Contreras, V. I. Vullev. *J. Phys. Chem. A* **113**, 1259-1267 (2009).

66. S. Upadhyayula, D. Bao, B. Millare, S. S. Sylvia, K. M. M. Habib, K. Ashraf, A. Ferreira, S. Bishop, R. Bonderer, S. Baqai, X. Jing, M. Penchev, M. Ozkan, C. S.

Ozkan, R. K. Lake, V. I. Vullev. *J. Phys. Chem. B* **115**, 9473-9490 (2011).

67. J. Hu, B. Xia, D. Bao, A. Ferreira, J. Wan, G. Jones, V. I. Vullev. *J. Phys. Chem. A* **113**, 3096-3107 (2009).

68. J. Wan, A. Ferreira, W. Xia, C. H. Chow, K. Takechi, P. V. Kamat, G. Jones, V. I. Vullev. *J. Photochem. Photobiol. A* **197**, 364-374 (2008).

69. M. Born. *Z. Phys.* **1**, 45-48 (1920).

70. J. F. Odonnell, C. K. Mann. *J. Electroanal. Chem.* **13**, 157–162 (1967).

71. S. Guo, D. Bao, S. Upadhyayula, W. Wang, A. B. Guvenc, J. R. Kyle, H. Hosseinibay, K. N. Bozhilov, V. I. Vullev, C. S. Ozkan, M. Ozkan. *Adv. Funct. Mater.* **23**, 5199-5211 (2013).

72. V. I. Vullev, G. Jones. *Tetrahedr. Lett.* **43**, 8611-8615 (2002).

73. G. Jones, II, D. Yan, J. Hu, J. Wan, B. Xia, V. I. Vullev. *J. Phys. Chem. B* **111**, 6921-6929 (2007).

74. H. Lu, D. Bao, M. Penchev, M. Ghazinejad, V. I. Vullev, C. S. Ozkan, M. Ozkan. *Adv. Sci. Lett.* **3**, 101-109 (2010).

75. G. Jones, II, V. I. Vullev. *J. Phys. Chem. A* **105**, 6402-6406 (2001).

76. G. Jones, II, V. I. Vullev. *Org. Lett.* **3**, 2457-2460 (2001).

77. J. M. Vasquez, A. Vu, J. S. Schultz, V. I. Vullev. *Biotechnol. Progr.* **25**, 906-914 (2009).

78. W. Wang, S. Guo, M. Penchev, J. Zhong, J. Lin, D. Bao, V. Vullev, M. Ozkan, C. S. Ozkan. *J. Nanosci. Nanotechnol.* **12**, 6913-6920 (2012).

79. M. Ghazinejad, J. R. Kyle, S. Guo, D. Pleskot, D. Bao, V. I. Vullev, M. Ozkan, C. S. Ozkan. *Adv. Funct. Mater.* **22**, 4519-4525 (2012).

80. V. I. Vullev, H. Jiang, G. Jones, II. *Topics in Fluorescence Spectroscopy* **10**, 211-239 (2005).

81. A. D. Becke. *J. Chem. Phys.* **98**, 5648-5652 (1993).

82. C. T. Lee, W. T. Yang, R. G. Parr. *Phys. Rev. B* **37**, 785-789 (1988).

83. R. Krishnan, J. S. Binkley, R. Seeger, J. A. Pople. *J. Chem. Phys.* **72**, 650-654 (1980).

84. M. J. Frisch. (2009).

85. E. Cances, B. Mennucci. *J. Math. Chem.* **23**, 309-326 (1998).

86. B. Mennucci, E. Cances, J. Tomasi. *J. Phys. Chem. B* **101**, 10506-10517 (1997).

87. E. Cances, B. Mennucci, J. Tomasi. *J. Chem. Phys.* **107**, 3032-3041 (1997).

88. L. Onsager. *J. Am. Chem. Soc.* **58**, 1486-1493 (1936).

89. X. Y. Zhu, Q. Yang, M. Muntwiler. *Acc. Chem. Res.* **42**, 1779-1787 (2009).

90. R. D. Pensack, J. B. Asbury. *J. Phys. Chem. Lett.* **1**, 2255-2263 (2010).

91. J. Guo, H. Ohkita, H. Benten, S. Ito. *J. Am. Chem. Soc.* **132**, 6154-6164 (2010).

92. M. Muntwiler, Q. Yang, W. A. Tisdale, X. Y. Zhu. *Phys. Rev. Lett.* **101**, 196403/196401-196403/196404 (2008).

93. H. Scher, S. Rackovsky. *J. Chem. Phys.* **81**, 1994-2009 (1984).

94. A. Moura, M. A. Savageau, R. Alves. *PLoS One* **8**, e77319 (2013).

Experimental

Materials

5-fluoro-2-nitrobenzoic acid (1), 4-fluoro-2-nitrobenzoic acid (3), 5-hydroxy-2-nitrobenzoic acid (7), 4,5-dimethoxy-2-nitrobenzoic acid (16), 5-methyl-2-nitrobenzoic acid (18), and 2-nitrobenzoic acid (20), and hexanoic anhydride were purchased from TCI America. Tin (II) chloride dihydrate ($SnCl_2 \cdot 2\ H_2O$), *N,N'*-Diisopropylcarbodiimide (DIC, 99%), *N*-hydroxysuccinimide (NHS, 98%), *N,N*-dimethylacetamide (anhydrous), cesium carbonate (Cs_2CO_3, 99.995%), *N,N*-diisopropylethylamine (DIPEA, 99.5%), 4-(dimethylamino)pyridine (DMAP, 99%), zinc (purum, powder), ammonium formate, triethylamine (Et_3N), tetrabutylammonium hexafluorophosphate, *N*-hexylmethylamine, and *n*-hexylamine were purchased from Sigma-Aldrich. All other reagents (including HPLC grade, spectroscopic grade and anhydrous solvents) were purchased from Fisher Scientific. 2-nitro-5-(piperidin-*N*-yl)benzoic acid (2), *N*-hexyl-2-nitro-5-(piperidin-*N*-yl)benzamide (10), and 2-hexanamido-*N*-hexyl-5-(piperidin-*N*-yl)benzamide (5Pip) were prepared following protocols that we have previously described [S1].

General synthesis information

Proton (^1H) NMR spectra were recorded at 400 MHz at ambient temperature using degassed $CDCl_3$ as solvent. ^{13}C NMR spectra were recorded at 100 MHz at ambient temperature with $CDCl_3$ as solvent. Chemical shifts are reported in parts per million relative to $CDCl_3$ (^1H, δ = 7.241; ^{13}C, δ = 77.233). Data for ^1H NMR are reported as follows: chemical shift, integration, multiplicity (s = singlet, d = doublet, t = triplet, q = quartet, p = pentaplet/quintet, m = multiplet), integration and coupling constants. All ^{13}C

NMR spectra were recorded with complete proton decoupling. The microwave-mediated reactions were carried out in 5-ml microwave reaction vials at atmospheric pressure in a microwave reactor, Discover CEM (CEM Corporation, Matthews, NC, USA), at a constant temperature with a preset upper limit of the radiation power. High-resolution mass-spectra were obtained on a Q-TOF mass spectrometer. Analytical thin layer chromatography (TLC) was performed using 0.25 mm silica gel 60-F plates. Flash chromatography was performed using 60 Å, 32−63 μm silica gel. Yields refer to chromatographically pure materials, unless otherwise stated.

2-nitro-4-(piperidin-N-yl)benzoic acid (4) (Scheme 2S-3b)

4-fluoro-2-nitrobenzoic acid (3) (740 mg, 4 mmol) and piperidine (2 ml, 20 mmol) were mixed in a 50 ml flask equipped with a water-cooled condenser and immersed in a temperature-controlled oil bath. The mixture was refluxed at 105 °C for 10 h. After cooling to room temperature, the reaction solution was diluted with 100 ml DCM, and washed with 1M HCl (100 ml × 3) and with brine (100 ml × 3). The organic layer was collected, dried over Na_2SO_4, and concentrated *in vacuo* to produce yellow powder (976 mg, 3.9 mmol, 97%) of 2-nitro-4-(piperidin-1-yl)benzoic acid (4): ^{1}H-NMR (400 MHz, $CDCl_3$) δ/ppm: 7.84 (1 H, d, J = 9.2 Hz), 6.87 (2 H, m), 3.38 (4 H, m), 1.67 (6 H, s); ^{13}C-NMR (400 MHz, $CDCl_3$) δ/ppm: 168.94, 154.18, 153.38, 133.58, 114.46, 107.88, 48.61, 25.35, 24.28; HRMS m/z calculated for $C_{12}H_{18}N_3O_4^+$ $(M + NH_4)^+$ 268.1292, found 268.1304 $(M + NH_4)^+$.

5-(hexyl(methyl)amino)-2-nitrobenzoic acid (5) (Scheme 2S-3d)

5-fluro-2-nitrobenzoic acid (1) (185mg, 1 mmol) and *N*-hexylmethylamine (384 µl, 2.5 mmol) were mixed and heated in a microwave reactor at 100 °C (power ≤ 100 W) for 1 hr. After cooling, the reaction mixture was diluted with 50 ml DCM and sequentially washed with 5% HCl, brine, and MilliQ. The organic phase was dried over anhydrous Na_2SO_4 and concentrated *in vacuo.* Purification using flash chromatography (stationary phase: silica gel; eluent gradient from 100% hexanes to 30% DCM in hexanes with 1% acetic acid added to all eluent solvents) to produce yellow powder (275 mg, 0.98 mmol, 98%) of 5-(hexyl(methyl)amino)-2-nitrobenzoic acid (5): ^{1}H-NMR (400 MHz, $CDCl_3$) δ/ppm: 11.08 (1 H, s), 8.00 (1 H, d, J = 9.4 Hz), 6.69 (1 H, d, J = 2.8), 6.61 (1 H, dd, J_1 = 9.4 Hz, J_2 = 2.8 Hz), 3.41 (2 H, t, J = 7.6 Hz), 3.07 (3 H, s), 1.60 (2 H, p, J = 6.5 Hz), 1.3 (6 H, m), 0.87 (3 H, t, J = 6.9 Hz); ^{13}C-NMR (400 MHz, $CDCl_3$) δ/ppm: 173.43, 152.78, 133.79, 131.64, 127.44, 111.43, 110.10, 52.99, 39.09, 31.75, 27.01, 26.80, 22.77, 14.18; HRMS m/z calculated for $C_{14}H_{21}N_2O_4^+$ $(M + H)^+$ 281.1496, found 281.1499 $(M + H)^+$.

4-(hexyl(methyl)amino)-2-nitrobenzoic acid (6) (Scheme 2S-3c)

Starting with 4-fluro-2-nitrobenzoic acid (3) (555 mg, 3 mmol) and *N*-hexylmethylamine (910 µl, 6 mmol) the procedure was similar to that for 5, but the microwave heating time was increased to 4 h. Purification following the procedure for 5 produced yellow powder (480 mg, 1.7 mmol, 57%) of 4-(hexyl(methyl)amino)-2-nitrobenzoic acid (6): ^{1}H-NMR (400 MHz, $CDCl_3$) δ/ppm: 7.84 (1 H, d, J = 8.8 Hz), 6.66 (1 H, dd, J_1 = 8.9 Hz, J_2 = 2.6 Hz), 6.64 (1 H, d, J = 2.5), 3.36 (2 H, t, J = 7.6 Hz), 3.02 (3 H, s), 1.57 (2 H, p, J = 7.2 Hz), 1.3 (6 H, m), 0.87 (3 H, t, J = 6.9 Hz); ^{13}C-NMR (400 MHz, $CDCl_3$) δ/ppm: 169.33, 153.57, 153.79, 133.58, 112.14, 107.59, 105.51, 52.86, 38.86, 31.76, 26.88, 26.80, 22.79, 14.19;

HRMS m/z calculated for $C_{14}H_{20}N_2NaO_4^+$ $(M + Na)^+$ 303.1315, found 303.1324 $(M + Na)^+$.

Hexyl 5-(hexyloxy)-2-nitrobenzoate (8) (Scheme 2S-3e)

5-hydroxy-2-nitrobenzoic acid (7) (915 mg, 5 mmol), (3.26 g, 10 mmol) cesium carbonate and 1-iodohexane (1.62 ml, 11 mmol) were dissolved in 100 ml anhydrous *N,N*-dimethylacetamide and flushed with nitrogen. The reaction immediately turned yellow and the mixture was kept at 150 °C for 3 h. Upon cooling, the reaction mixture was suspended in DCM, washed with acidic and basic aqueous solutions, and dried over anhydrous Na_2SO_4 to produce slightly yellow oil. Purification using flash chromatography (stationary phase: silica gel and a 10% sodium carbonate; eluent gradient: from 100% hexanes to 30% DCM in hexanes) afforded 934 mg (2.66 mmol, 97% yield) of hexyl 5-(hexyloxy)-2-nitrobenzoate (8): ^{1}H-NMR (400 MHz, $CDCl_3$) δ/ppm: 7.93 (1 H, d, J = 9.0 Hz), 6.97 (1 H, d, J = 2.6 Hz), 6.86 (1 H, dd, J_1 = 9.0 Hz, J_2 = 2.7 Hz), 4.27 (2 H, t, J = 6.8 Hz), 3.99 (2 H, t, J = 6.5 Hz), 1.75 (2 H, p, J = 7.0 Hz), 1.66 (2 H, p, J = 7.3 Hz), 1.40 (2 H, m), 1.3 (10 H, m), 0.83 (6 H, tt, J = 7.0 Hz); ^{13}C-NMR (400 MHz, $CDCl_3$) δ/ppm: 166.27, 163.10, 139.79, 131.63, 126.66, 115.84, 114.69, 69.28, 66.72, 31.51, 31.45, 28.91, 28.31, 25.60, 25.56, 22.61, 22.58, 14.03; HRMS m/z calculated for $C_{19}H_{30}NO_5^+$ $(M + H)^+$ 352.2118, found 352.2118 $(M + H)^+$.

5-(hexyloxy)-2-nitrobenzoic acid (9) (Scheme 2S-3e)

8 (934 mg, 2.66 mmol) was dissolved in 2 ml ethanol and while stirring, 1 ml of 3 M KOH in ethanol was added drop-wise. The basified solution was heated to 60 °C. The progress of the reaction was monitored with TLC. After the complete consumption of the starting

material, the reaction solution was allowed to cool to room temperature and quenched by slowly adding it to a mixture od DCM and 5% aqueous HCl. The organic phase was collected, washed with MilliQ water, dried over anhydrous Na_2SO_4, and concentrated *in vacuo* to produce white solid (640 g, 2.4 mmol, 92%) of 5-(hexyloxy)-2-nitrobenzoic acid (9): ^{1}H-NMR (400 MHz, $CDCl_3$) δ/ppm: 8.01 (1 H, d, J = 9.1 Hz), 7.13 (1 H, d, J = 2.7 Hz), 7.02 (1 H, dd, J_1 = 9.1 Hz, J_2 = 2.7 Hz), 4.05 (2 H, t, J = 6.5 Hz), 1.81 (2 H, p, J = 7.1 Hz), 1.45 (2 H, p, J = 7.1 Hz), 1.32 (4 H, m), 0.89 (3 H, t, J = 6.9 Hz); ^{13}C-NMR (400 MHz, $CDCl_3$) δ/ppm: 170.89, 163.12, 140.09, 130.38, 126.81, 116.74, 114.92, 69.49, 31.60, 29.00, 25.69, 22.71, 14.15; HRMS m/z calculated for $C_{13}H_{18}NO_5^+$ $(M + H)^+$ 268.1179, found 268.1192 $(M + H)^+$.

N-hexyl-2-nitro-4-(piperidin-N-yl)benzamide (11) (Scheme 2S-1a)

DIC (467 µl, mmol) was added to 10 ml ice-chilled DMF solution of 4 (250 mg, 1 mmol) and NHS (230 mg, 2 mmol). After stirring the mixture for 2 h at 0 °C, *n*-hexylamine (400 µl, 3 mmol) was added drop-wise. The solution was stirred at 0 °C for additional 0.5 h, allowed to warm up to room temperature, and stirred for an additional hour. The thus obtained viscous reaction mixture was diluted with DCM, washed with 5% HCl and MilliQ water, and dried over anhydrous N_2SO_4. The DCM was removed under reduced pressure to produce yellow solid. Purification using flash chromatography (stationary phase: silica gel; eluent gradient: from 100 % hexanes to 50 % ethyl acetate in hexanes) afforded 250 mg yellow powder (0.75 mmol, 75%) of *N*-hexyl-2-nitro-4-(piperidin-*N*-yl)benzamide (11): ^{1}H-NMR (400 MHz, $CDCl_3$) δ/ppm: 7.17 (2 H, m), 6.85 (1 H, dd, J_1 = 8.6 Hz, J_2 = 2.6 Hz), 5.46 (1 H, t, J = 5.5 Hz), 3.20 (6 H, m), 1.59 (6 H, m), 1.46 (2 H, p, J = 6.6 Hz),

1.22 (6 H, m), 0.81 (3 H, t, J = 6.9 Hz); ^{13}C-NMR (400 MHz, $CDCl_3$) δ/ppm: 166.62, 152.28, 148.61, 129.51, 120.85, 117.79, 109.56, 48.96, 40.14, 31.54, 29.26, 26.62, 25.22, 24.08, 22.59, 14.06; HRMS m/z calculated for $C_{18}H_{28}N_3O_3^+$ $(M + H)^+$ 334.2125, found 334.2139 $(M + H)^+$.

N-hexyl-5-(hexyl(methyl)amino)-2-nitrobenzamide (12) (Scheme 2S-1a)

Applying the procedure for 11 to a crude 5 (210 mg, 0.75 mmol) plus an additional hexane wash of the final solid product afforded 242 mg of yellow solid (0.66 mmol, 89%) of 12: ^{1}H-NMR (400 MHz, $CDCl_3$) δ/ppm: 8.00 (1 H, d, J = 9.4 Hz), 6.54 (1 H, dd, J_1 = 9.4 Hz, J_2 = 2.9 Hz), 6.47 (1 H, d, J = 2.9 Hz), 5.73 (1 H, t, J = 5.6 Hz), 3.38 (4 H, m), 3.03 (3 H, s), 1.58 (4 H, m), 1.3 (12 H, m), 0.86 (6 H, tt); ^{13}C-NMR (400 MHz, $CDCl_3$) δ/ppm: 166.42, 152.94, 136.55, 133.27, 127.69, 110.76, 110.11, 52.87, 40.47, 38.97, 31.75, 31.67, 29.34, 27.00, 26.82, 26.79, 22.76, 14.22, 14.18; HRMS m/z calculated for $C_{20}H_{33}N_3NaO_3^+$ $(M + Na)^+$ 386.2414, found 386.2421 $(M + Na)^+$.

N-hexyl-4-(hexyl(methyl)amino)-2-nitrobenzamide (13) (Scheme 2S-1a)

Applying the procedure for 11 to a crude 6 (210 mg, 0.75 mmol), using EDC instead of DIC, and adding a washing step of the final solid product with hexanes afforded 94 mg yellow powder (0.26 mmol, 13%) of 13: ^{1}H-NMR (400 MHz, $CDCl_3$) δ/ppm: 7.27 (1 H, d, J = 8.7 Hz), 7.01 (1 H, d, J = 2.6 Hz), 6.70 (1 H, dd, J_1 = 8.7 Hz, J_2 = 2.6 Hz), 5.95 (1 H, t, J = 5.4 Hz), 3.32 (4 H, m), 2.95 (3 H, s), 1.53 (4 H, m), 1.27 (12 H, m), 0.85 (6 H, tt); ^{13}C-NMR (400 MHz, $CDCl_3$) δ/ppm: 166.84, 150.35, 149.19, 129.72, 118.66, 114.53, 106.45, 52.64, 40.33, 38.63, 31.75, 31.65, 29.50, 26.78, 26.66, 22.73, 14.18, 14.15; HRMS m/z calculated for $C_{20}H_{34}N_3O_3^+$ $(M + H)^+$ 364.2595, found 364.2613 $(M + H)^+$.

N-hexyl-5-hexyloxy-2-nitrobenzamide (14) (Scheme 2S-1a)

Applying the procedure for 11 to 9 (534 mg, 2 mmol) afforded 423 mg of white solid (1.2 mmol, 60%) of 14: ^{1}H-NMR (400 MHz, $CDCl_3$) δ/ppm: 7.98 (1 H, d, J = 9.1 Hz), 6.86 (1 H, dd, J_1 = 9.1 Hz, J_2 = 2.7 Hz), 6.80 (1 H, d, J = 2.7 Hz), 6.09 (1 H, t, J = 5.6 Hz), 3.99 (2 H, t, J = 6.5 Hz), 3.32 (2 H, q, J = 6.8 Hz), 1.76 (2 H, p, J = 7.0 Hz), 1.55 (2 H, p, J = 7.3 Hz), 1.41 (2 H, m), 1.3 (10 H, m), 0.86 (6 H, tt); ^{13}C-NMR (400 MHz, $CDCl_3$) δ/ppm: 166.90, 163.51, 138.57, 135.98, 127.17, 115.22, 114.32, 69.32, 40.42, 31.62, 31.59, 29.26, 29.01, 26.75, 25.68, 22.70, 14.17, 14.15; HRMS m/z calculated for $C_{19}H_{31}N_2O_4^+$ $(M + H)^+$ 351.2278, found 351.2281 $(M + H)^+$.

N-hexyl-4,5-dimethoxy-2-nitrobenzamide (16) (Scheme 2S-1a)

A mixture of 4,5-dimethoxy-2-nitrobenzoic acid (15) (454 mg, 2 mmol) and 2ml thionyl chloride was refluxed at 70 °C for 2 hours. The thionyl chloride was evaporated out and a solution of 490 mg DMAP, 10 ml *n*-hexylamine and 15 ml of 1,2-dimethoxyethane was added and refluxed at 85 °C for 3 hours. The reaction was slowly poured in 200 mL of 5% HCl and allowed stay overnight. The formed precipitate was collected by vacuum filtration to afford 492 mg of white solid (1.6 mmol, 80%) of 16: ^{1}H-NMR (400 MHz, $CDCl_3$) δ/ppm: 7.57 (1 H, s), 6.85 (1 H, s), 6.76 (1 H, t, J = 5.3 Hz), 3.95 (3 H, s), 3.94 (3 H, s), 3.34 (2 H, q, J = 7.2 Hz), 2.33 (2 H, t, J = 7.6 Hz), 1.60 (2 H, p, J = 7.3 Hz), 1.55 (2 H, p, J = 7.3 Hz), 1.3 (6 H, m), 0.87 (3 H, t, J = 6.9 Hz); ^{13}C-NMR (400 MHz, $CDCl_3$) δ/ppm: 166.92, 153.68, 149.49, 138.76, 127.90, 110.45, 107.39, 56.85, 56.73, 40.65, 31.67, 29.34, 26.82, 22.76, 14.23; HRMS m/z calculated for $C_{15}H_{23}N_2O_5^+$ $(M + H)^+$ 311.1601, found 311.1611 $(M + H)^+$.

N-hexyl-5-methyl-2-nitrobenzamide (18) (Scheme 2S-1a)

Applying the procedure for 11 to 5-methyl-2-nitrobenzoic acid (17) (181 mg, 1 mmol), and using EDC (430 mg, 2.24 mmol) and DIC (470 µl, 3 mmol) instead of only DIC, afforded 56 mg of white solid (0.21 mmol, 21%) of 18: ^{1}H-NMR (400 MHz, $CDCl_3$) δ/ppm: 7.89 (1 H, d, J = 8.4 Hz), 7.27 (1 H, dd, J_1 = 8.4 Hz, J_2 = 1.5 Hz), 7.21 (1 H, d, J = 1.5 Hz), 6.02 (1 H, s), 3.35 (2 H, q, J = 7.1 Hz), 2.40 (3 H, s), 1.56 (2 H, p, J = 7.2 Hz), 1.3 (6 H, m), 0.86 (3 H, t, J = 6.8 Hz); ^{13}C-NMR (400 MHz, $CDCl_3$) δ/ppm: 166.96, 145.45, 144.08, 133.52, 130.73, 129.46, 124.72, 40.44, 31.64, 29.36, 26.76, 22.73, 21.54, 14.19; HRMS m/z calculated for $C_{14}H_{21}N_2O_3^+$ $(M + H)^+$ 265.1547, found 265.1556 $(M + H)^+$.

N-hexyl-2-nitrobenzamide (20) (Scheme 2S-1a)

Applying the procedure for 11 to 2-nitrobenzoic acid (19) (501 mg, 3 mmol) afforded 548 g of white solid (2.19 mmol, 73%) of 20: ^{1}H-NMR (400 MHz, $CDCl_3$) δ/ppm: 7.90 (1 H, dd, J_1 = 8.1 Hz, J_2 = 1.1 Hz), 7.55 (1 H, td, J_1 = 7.5 Hz, J_2 = 1.2 Hz), 7.46 (1 H, td, J_1 = 7.8 Hz, J_2 = 1.4 Hz), 7.37 (1 H, dd, J_1 = 7.5 Hz, J_2 = 1.4 Hz), 6.40 (1 H, t, J = 6.0 Hz), 3.28 (2 H, td, J_1 = 7.1 Hz, J_2 = 6.1 Hz), 1.51 (2 H, p, J = 7.2 Hz), 1.26 (6 H, m), 0.84 (3 H, t, J = 6.9 Hz); ^{13}C-NMR (400 MHz, $CDCl_3$) δ/ppm: 166.61, 146.49, 133.69, 133.24, 130.30, 128.84, 124.44, 40.36, 31.58, 29.22, 26.67, 22.67, 14.14; HRMS m/z calculated for $C_{13}H_{19}N_2O_3^+$ $(M + H)^+$ 251.1396, found 251.1393 $(M + H)^+$.

2-hexanamido-N-hexyl-4-(piperidin-N-yl)benzamide or hexyl N-hexanoyl-4-(piperidin-N-yl)anthranilamide (4Pip) (Scheme 2S-1b,c)

In a 50-ml flask equipped with a water-cooled condenser, 11 (400 mg, 1.2 mmol) and $SnCl_2{\cdot}2H_2O$ (4-to-5 fold molar excess) were suspended in 3 ml EtOH and purged with

nitrogen [S2]. The mixture was refluxed at 80 °C and the progress of the reaction was monitored with TLC. After complete reduction of the nitro group (usually about 3 h), the ethanol was removed under reduced pressure and 3 ml DMF was added to the reaction solid under nitrogen. Upon suspending the solid, 0.4 ml hexanioc anhydride was added drop-wise. After stirring for 15 min, 0.25 ml Et_3N was added drop-wise and the mixture was allowed to stir for 4 h. The reaction mixture was dissolved in 50 ml DCM, washed with a saturated aqueous solution of Na_2CO_3 and dried over anhydrous Na_2SO_4. Purification using flash chromatography (stationary phase: silica gel; eluent gradient: from 100 % hexanes to 50 % ethyl acetate in hexanes) to afford 103 mg of a white solid (0.26 mmol, 21%) of 4Pip: ^{1}H-NMR (400 MHz, $CDCl_3$) δ/ppm: 11.73 (1 H, s), 8.28 (1 H, d, J = 2.6 Hz), 7.29 (1 H, d, J = 9.0 Hz), 6.39 (2 H, m), 3.31 (2 H, q, J = 6.7 Hz), 3.22 (4 H, m), 2.33 (2 H, t, J = 7.6 Hz), 1.66 (2 H, p, J = 7.5 Hz), 1.55 (8 H, m), 1.27 (10 H, m), 0.83 (6 H, tt, J_1 = 7.0, J_2 = 6.4 Hz); ^{13}C-NMR (400 MHz, $CDCl_3$) δ/ppm: 172.58, 169.20, 154.20, 142.05, 127.82, 108.41, 108.30, 105.81, 48.78, 39.94, 38.79, 31.62, 31.46, 29.72, 26.81, 25.50, 25.30, 24.46, 22.67, 22.53, 14.11, 14.03; HRMS m/z calculated for $C_{24}H_{39}N_3O_2^+$ $(M)^+$ 401.3037, found 401.3021 $(M)^+$.

2-hexanamido-N-hexyl-5-(hexyl(methyl)amino)benzamide or hexyl N-hexanoyl-5-(hexyl(methyl)amino)anthranilamide (5Hxm) (Scheme 2S-1b,c)

Applying the procedure for 4Pip to crude 12 (203 mg; 0.550 mmol), and using 1,2-dimethoxy ethane instead of EtOH for the $SnCl_2$ reduction step, afforded 69 mg white solid (0.159 mmol, 29%) of 5Hxm: ^{1}H-NMR (400 MHz, $CDCl_3$) δ/ppm: 10.16 (1 H, s), 8.23 (1 H, d, J =9.0 Hz), 6.79 (1 H, dd, J_1 =9.0 Hz, J_2 = 2.7 Hz), 6.67 (1 H, d, J = 2.7 Hz), 6.30 (1

H, s), 3.38 (2 H, q, J = 6.7 Hz), 3.24 (2 H, t, J = 7.5 Hz), 2.87 (3 H, s), 2.32 (2 H, t, J = 6.9 Hz), 1.67 (2 H, p, J = 7.1 Hz), 1.60 (2 H, p, J = 7.4 Hz), 1.51 (2 H, p, J = 6.5 Hz), 1.3 (16 H, m), 0.87 (9 H, m); ^{13}C-NMR (400 MHz, $CDCl_3$) δ/ppm: 172.02, 169.74, 145.40, 128.57, 123.83, 123.75, 116.54, 110.21, 53.48, 40.23, 38.39, 31.89, 31.68, 31.62, 29.67, 27.00, 26.86, 26.60, 25.66, 22.84, 22.78, 22.62, 14.21, 14.16, 14.09; HRMS m/z calculated for $C_{26}H_{44}N_3O_2^+$ $(M - H)^+$ 430.3428, found 430.3429 $(M - H)^+$.

2-hexanamido-N-hexyl-4-(hexyl(methyl)amino)benzamide or hexyl N-hexanoyl-4-(hexyl(methyl)amino)anthranilamide (4Hxm) (Scheme 2S-1b,c)

Applying the procedure for 5Hxm to 13 (60 mg; 0.164 mmol) produced 20 mg of 4Hxm (0.046 mmol; 28%): ^{1}H-NMR (400 MHz, $CDCl_3$) δ/ppm: 11.76 (1 H, s), 8.14 (1 H, d, J = 1.7 Hz), 7.26 (1 H, d, J = 8.9 Hz), 6.27 (1 H, dd, J_1 = 9.0 Hz, J_2 = 2.0 Hz), 6.02 (1 H, s), 3.34 (4 H, m), 2.97 (3 H, s), 2.38 (2 H, t, J = 7.7 Hz), 1.71 (2 H, p, J = 7.6 Hz), 1.57 (4 H, p, J = 7.1 Hz), 1.3 (16 H, m), 0.85 (9 H, m); ^{13}C-NMR (400 MHz, $CDCl_3$) δ/ppm: 172.75, 169.44, 152.27, 142.36, 127.84, 105.56, 103.15, 52.63, 40.01, 39.01, 31.89, 31.74, 31.62, 29.92, 29.87, 27.09, 26.94, 26.92, 25.48, 22.84, 22.80, 22.65, 14.24, 14.17; HRMS m/z calculated for $C_{26}H_{46}N_3O_2^+$ $(M + H)^+$ 432.3585, found 432.3626 $(M + H)^+$.

2-hexanamido-N-hexyl-5-hexyloxybenzamide or hexyl N-hexanoyl-5-hexyloxyanthranilamide (Hox) (Scheme 2S-1b,c)

Under nitrogen, 14 (424 mg, 1.2 mmol), ammonium formate (760 mg, 12 mmol) and zinc dust (434 mg, 6.7 mmol) were suspended in 2 ml 1,2-dimethoxyethane and stirred for 6 hours [S3]. The reaction mixture was filtered and the filtrate was diluted with DCM, washed 1% HCl and MilliQ water. The DCM was removed *in vacuo* and 2 mL of DMF

was added under nitrogen. Sequentially, hexanoic anhydride (0.23 ml, 1 mmol) and Et_3N (0.14 ml, 1 mmol) were added drop-wise and the mixture was stirred at room temperature for 2 hours. The reaction mixture was diluted with 50 ml ethylacetate, washed with 5% HCl and MilliQ water, and dried over Na_2SO_4, and concentrated *in vacuo*. Purification using flash chromatography (stationary phase: silica gel; eluent gradient: from 100 % hexanes to 50 % ethyl acetate in hexanes) afforded 205 mg white solid (0.49 mmol, 40%) of Hox: ^{1}H-NMR (400 MHz, $CDCl_3$) δ/ppm: 10.56 (1 H, s), 8.28 (1 H, d, J = 9.1 Hz), 6.91 (1 H, d, J = 2.8 Hz), 6.86 (1 H, dd, J_1 = 9.1 Hz, J_2 = 2.8 Hz), 6.79 (1 H, t, J = 5.2 Hz), 3.84 (2 H, t, J = 6.6 Hz), 3.32 (2 H, q, J = 6.7 Hz), 2.28 (2 H, t, J = 7.7 Hz), 1.65 (4 H, m), 1.55 (2 H, p, J = 7.3 Hz), 1.3 (16 H, m), 0.84 (9 H, t, J = 6.5 Hz); ^{13}C-NMR (400 MHz, $CDCl_3$) δ/ppm: 172.15, 168.88, 154.44, 132.19, 123.13, 122.86, 117.11, 113.52, 68.57, 40.21, 38.35, 31.70, 31.63, 31.53, 29.53, 29.35, 26.83, 25.80, 25.48, 22.70, 22.52, 14.13, 14.05; HRMS m/z calculated for $C_{25}H_{42}N_2NaO_3^+$ $(M + Na)^+$ 441.3088, found 441.3109 $(M + Na)^+$.

2-hexanamido-N-hexyl-4,5-dimethoxybenzamide or hexyl N-hexanoyl-4,5-dimethoxyanthranilamide (Dmx) (Scheme 2S-1b,c)

Applying the procedure for 5Hxm to 16 (156 mg, 0.5 mmol) produced 20 mg of Dmx (0.053 mmol; 11%): ^{1}H-NMR (400 MHz, $CDCl_3$) δ/ppm: 11.32 (1 H, s), 8.35 (1 H, s), 6.88 (1 H, s), 6.40 (1 H, t, J = 5.3 Hz), 3.85 (3 H, s), 3.82 (3 H, s), 3.34 (2 H, q, J = 6.8 Hz), 2.33 (2 H, t, J = 7.6 Hz), 1.67 (2 H, p, J = 7.5 Hz), 1.55 (2 H, p, J = 7.4 Hz), 1.3 (10 H, m), 0.85 (3 H, t, J = 6.5 Hz), 0.84 (3 H, t, J = 6.7 Hz); ^{13}C-NMR (400 MHz, $CDCl_3$) δ/ppm: 172.41, 168.91, 152.36, 144.00, 135.71, 111.70, 109.76, 104.84, 56.64, 56.11, 40.23,

38.64, 31.63, 31.51, 29.70, 26.84, 25.36, 22.70, 22.55, 14.14, 14.07; HRMS m/z calculated for $C_{21}H_{34}N_2NaO_4^+$ $(M + Na)^+$ 401.2411, found 401.2426 $(M + Na)^+$.

2-hexanamido-N-hexylbenzamide or hexyl N-hexanoylanthranilamide (Ant) (Scheme 2S-1b,c)

Applying the procedure for 5Hxm to 20 (250 mg, 1 mmol) produced 28 mg of Ant (0.09 mmol, 9% yield): ^{1}H-NMR (400 MHz, $CDCl_3$) δ/ppm: 11.00 (1 H, s), 8.56 (1 H, d, J = 8.8 Hz), 7.42 (2 H, m), 7.01 (1 H, s), 6.31 (1 H, s), 3.40 (2 H, q, J = 6.7 Hz), 2.36 (2 H, t, J = 7.6 Hz), 1.70 (2 H, p, J = 7.5 Hz), 1.60 (2 H, p, J = 7.5 Hz), 1.3 (10 H, m), 0.88 (6 H, t, J = 7.0 Hz); ^{13}C-NMR (400 MHz, $CDCl_3$) δ/ppm: 172.46, 169.21, 139.75, 132.58, 126.51, 122.72, 121.72, 120.83, 40.27, 38.69, 31.68, 31.59, 29.86, 26.87, 25.48, 22.78, 22.61, 14.22, 14.15; HRMS m/z calculated for $C_{19}H_{30}N_2NaO_2^+$ $(M + Na)^+$ 341.2199, found 341.2196 $(M + Na)^+$.

2-hexanamido-N-hexyl-5-methylbenzamide or hexyl N-hexanoyl-5-methylanthranilamide (Met) (Scheme 2S-1b,c)

Applying the procedure for 5Hxm to 18 (264 mg, 1 mmol) produced 86 mg of the final Met (0.26 mmol; 25%): ^{1}H-NMR (400 MHz, $CDCl_3$) δ/ppm: 10.85 (1 H, s), 8.44 (1 H, dd, J_1 = 8.5 Hz, J_2 = 2.8 Hz), 7.23 (1 H, d, J = 8.6 Hz), 7.18 (1 H, d, J = 1.9 Hz), 6.24 (1 H, s), 3.39 (2 H, q, J = 7.2 Hz), 2.35 (2 H, t, J = 7.6 Hz), 2.29 (3 H, s), 1.70 (2 H, p, J = 7.5 Hz), 1.60 (2 H, p, J = 7.4 Hz), 1.3 (10 H, m), 0.88 (3 H, t, J = 6.5 Hz), 0.87 (3 H, t, J = 6.7 Hz); ^{13}C-NMR (400 MHz, $CDCl_3$) δ/ppm: 172.44, 169.29, 137.03, 133.07, 132.35, 126.95, 121.80, 121.09, 40.25, 38.56, 34.28, 31.67, 31.56, 29.64, 26.86, 25.50, 22.74, 22.57, 14.19,

14.11; HRMS m/z calculated for $C_{20}H_{32}N_2NaO_2^+$ $(M + Na)^+$ 355.2356, found 355.2371 $(M + Na)^+$.

Methods

UV/visible absorption and emission spectroscopy

Steady-state absorption spectra were recorded in a transmission mode using a JASCO V-670 spectrophotometer (Tokyo, Japan); and steady-state emission spectra were measured, also in a transmission mode, with a FluoroLog-3 spectrofluorometer (Horiba-Jobin-Yvon, Edison, NJ, USA) as previously reported [S4, S5].

Electrochemical measurements

Cyclic voltammetry was conducted using Reference 600^{TM} Potentiostat/Galvanostat/ZRA (Gamry Instruments, PA, U.S.A.), equipped with a three-electrode cell, as previously described [S6]. The half-wave potentials, $E^{(1/2)}$, were determined form the midpoints between the cathodic and anodic peak potentials for reversible oxidation; and from the inflection points of the anodic waves for irreversible oxidation (Figure S1). Specifically, the anodic and cathodic peak potentials, E_a and E_c, respectively, were determined from the zero points of the first derivatives of the voltammograms, i.e., the potentials where $\partial I/\partial E = 0$ at $\partial E/\partial t = constant$ (Figure 2S-1). For reversible oxidation $E^{(1/2)} = (E_a + E_c) / 2$. For irreversible oxidation, $E^{(1/2)}$ was estimated from the inflection point of the rise of the anodic wave, i.e., from the zero point of the second derivative, $\partial^2 I/\partial E^2 = 0$ at $\partial E/\partial t = constant$ (Figure 2S-1). The second derivatives of reversible voltammograms show that the inflection-point potentials are quite close to the mid-points between E_a and E_c, ensuring the reliability for the estimates of $E^{(1/2)}$ from the

inflection points of irreversible voltammograms. The voltammograms showing reversible oxidation were recorded at a scan rate of 200 mV/s. When the oxidation was irreversible, the voltammograms were recorded at scan rate between 20 and 50 mV/s. From the dependence of $E^{(1/2)}$ on the electrolyte concentration, the potentials for neat solvents were estimated from extrapolations to zero (Figure 2-1a) [S6, S7].

Computational methods

Geometries were optimized using Gaussian 09 both in the gas phase and with implicit polarizable continuum solvent models for dichloromethane (DCM) and acetonitrile (MeCN). All optimizations where performed using B3LYP with a 6-311+G(d,p) basis and a pruned (99, 590) "ultrafine" integration grid. The inclusion of a solvent has minimal impact on the final optimized geometries, as shown in Figure 2S-2, which superimposes the gas phase optimized geometries with the structures optimized in DCM and MeCN for each of the Aa residues. Likewise, the inclusion of solvent effects has no qualitative impact on the HOMO charge distribution, as shown in Figures S3 and S4. We therefore only report results for the gas phase and MeCN calculations for the HOMO/LUMO figures.

Figures 2-4, S3 and S4 illustrate the charge distribution in the HOMO and LUMO for each of the residues in both the gas phase and in MeCN. These figures clearly indicate a pronounced shift in the electron density of the HOMO for both the 4Hxm and 4Pip species relative to the other anthranilamides. Table 1 provides the magnitude of the dipole moments for each residue computed from the optimized structures for the gas phase, DCM and DCM.

Supplementary Figures

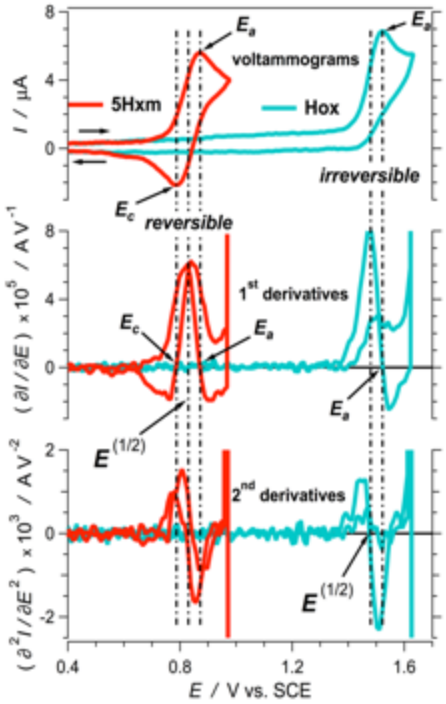

Figure 2S-1. Cyclic voltammograms and their 1st and 2nd derivatives used for extracting half-wave reduction potentials, $E^{(1/2)}$, of the residues exhibiting reversible (e.g., 5Hxm) and irreversible (e.g., Hox) electrochemical oxidation (100 mM NBu_4PF_6 in DCM).

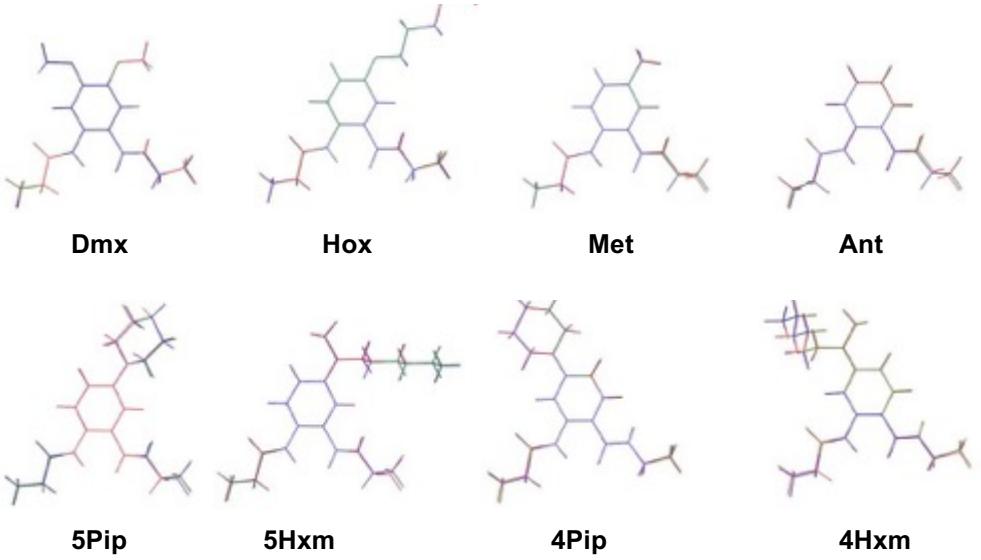

Figure 2S-2. Overlays of relaxed ground-state structures of the eight Aa residues in the gas phase, in DCM, and in MeCN, obtained from DFT calculations. For each residue, the three structures in the different media show a good overlap, suggesting for negligible solvent effect on the anthranilamide conformations. For online viewing, red is for the structures in the gas phase, green is for the structures in DCM, and blue s for the structures in MeCN. For the computational studies, the alkyl chains at the C- and N-termini were truncated to C_2H_5.

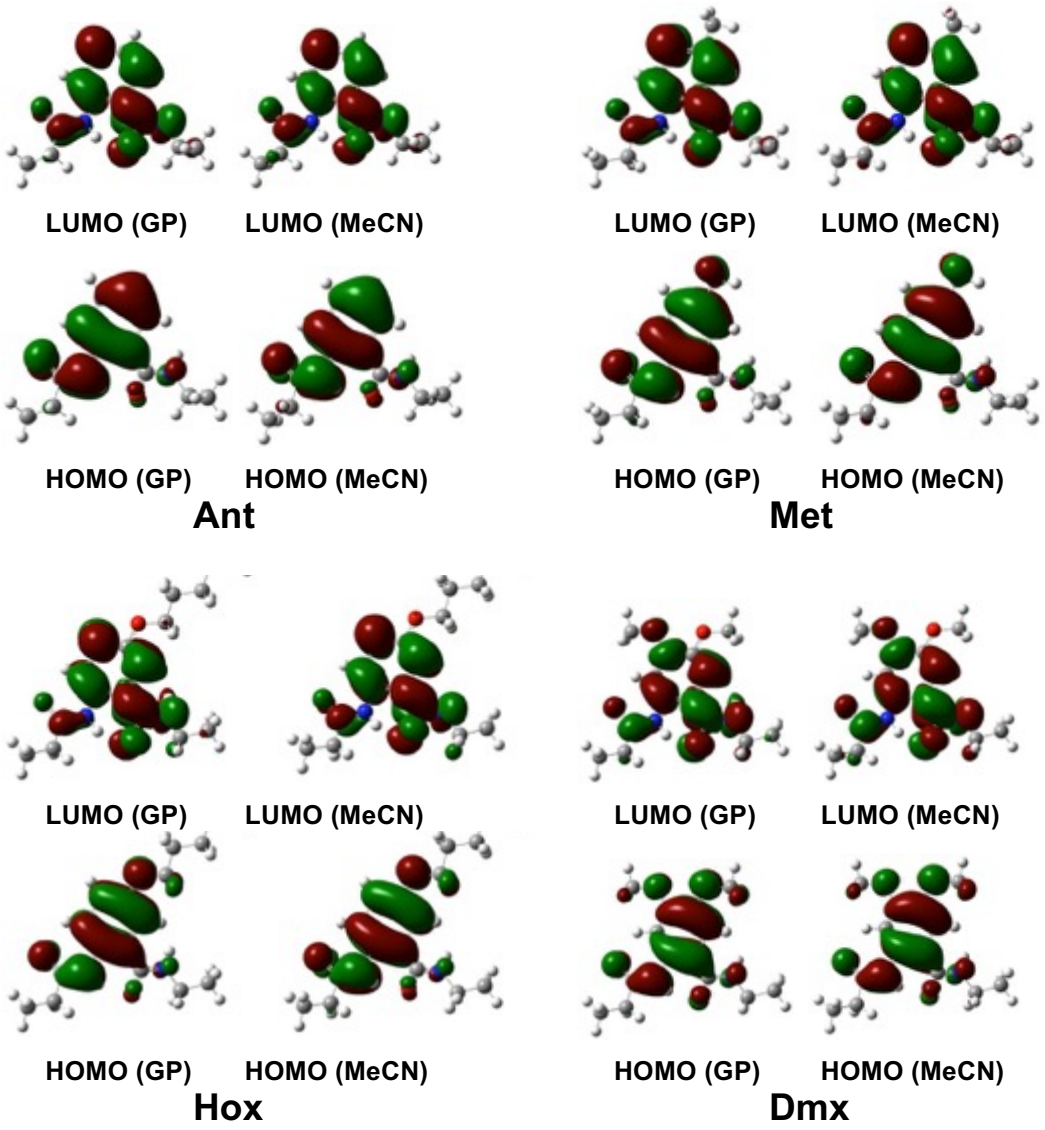

Figure 2S-3. HOMOs and LUMOs of Ant, Met, Hox and Dmx for the gas phase (GP) and for acetonitrile (MeCN), obtained from DFT calculations. For the computational studies, the alkyl chains at the C- and N-termini were truncated to C_2H_5. The residues are displayed with their N-termini oriented to the left and the C-termini – to the right.

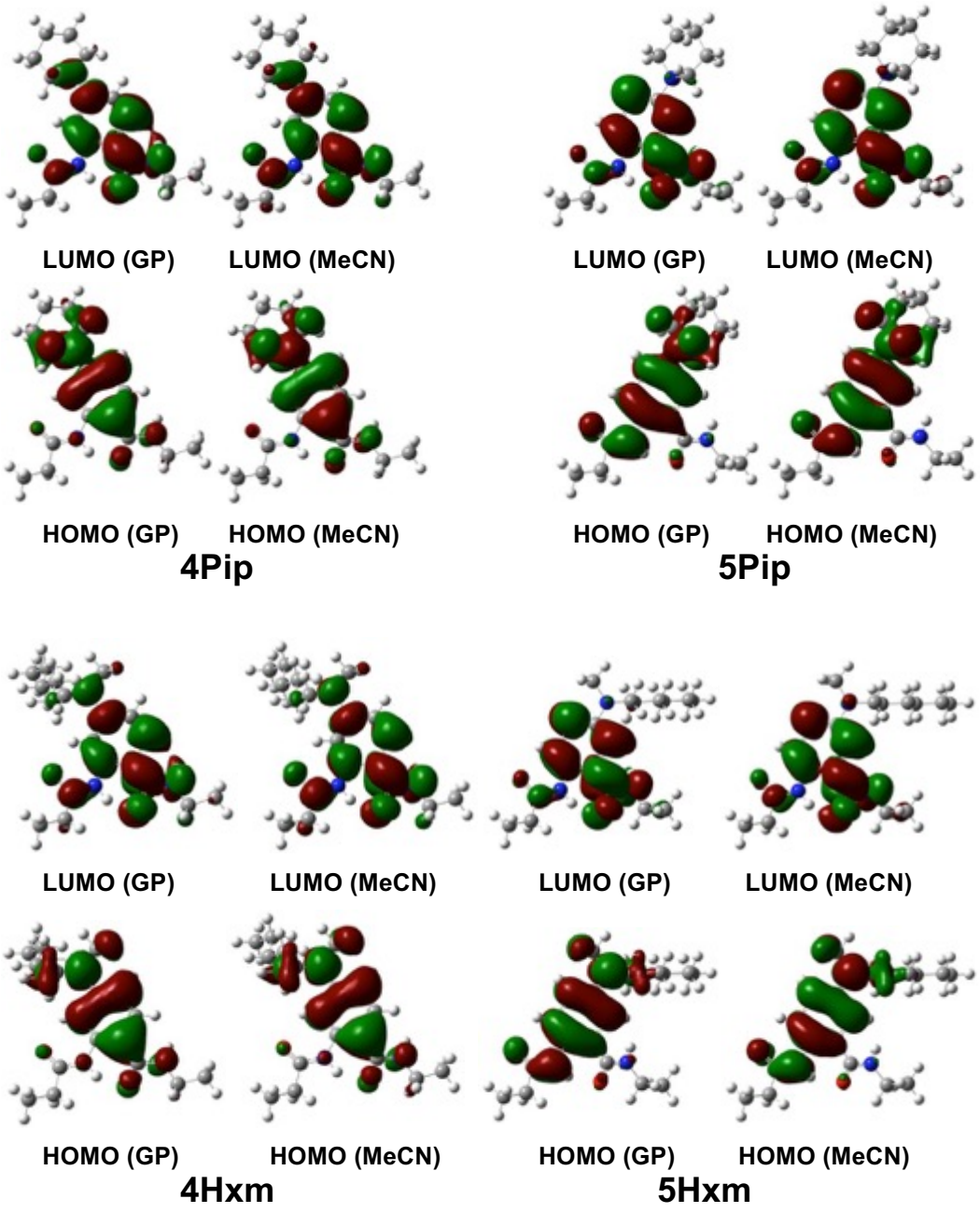

Figure 2S-4. HOMOs and LUMOs of the amine-reprivatized residues for the gas phase (GP) and for acetonitrile (MeCN), obtained from DFT calculations. For the computational studies, the alkyl chains at the C- and N-termini were truncated to C_2H_5. The residues are displayed with their N-termini oriented to the left and the C-termini – to the right.

Supplementary Schemes

Scheme 2S-1. Synthesis of the anthranilamides from the corresponding 2-nitrobenzoic acids.

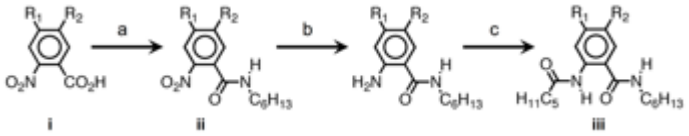

-R_1	-R_2	i	ii	iii
-H	-$N(CH_2)_5$	2	10	5Pip
-$N(CH_2)_5$	-H	4	11	4Pip
-H	-$N(CH_3)C_6H_{13}$	5	12	5Hxm
-$N(CH_3)C_6H_{13}$	-H	6	13	4Hxm

-R_1	-R_2	i	ii	iii
-H	-OC_6H_{13}	9	14	Hox
-OCH_3	-OCH_3	15	16	Dmx
-H	-CH_3	17	18	Met
-H	-H	19	20	Ant

(a) DIC, HNS, $C_6H_{13}NH_2$, DMF, r.t.; (b) $SnCl_2$, $H_3CO(CH_2)_2OCH_3$, reflux; or Zn, $NH_4(HCO_2)$, MeOH, r.t. (the produced amines were detected with TLC and HRMS, but not isolated); (c) $(C_5H_{11}CO)_2O$, Et_3N, DMF, r.t.

Supplemental References

S1. D. Bao, S. Upadhyayula, J. M. Larsen, B. Xia, B. Georgieva, V. Nunez, E. M. Espinoza, J. D. Hartman, M. Wurch, A. Chang, C.-K. Lin, J. Larkin, K. Vasquez, G. J. O. Beran, V. I. Vullev. *Journal of the American Chemical Society* **136**, 12966-12973 (2014).

S2. F. D. Bellamy, K. Ou. *Tetrahedron Letters* **25**, 839-842 (1984).

S3. D. C. Gowda, B. Mahesh, S. Gowda. *Indian Journal of Chemistry, Section B: Organic Chemistry Including Medicinal Chemistry* **40B**, 75-77 (2001).

S4. J. Wan, A. Ferreira, W. Xia, C. H. Chow, K. Takechi, P. V. Kamat, G. Jones, V. I. Vullev. *Journal of Photochemistry and Photobiology, A: Chemistry* **197**, 364-374 (2008).

S5. J. Hu, B. Xia, D. Bao, A. Ferreira, J. Wan, G. Jones, V. I. Vullev. *Journal of Physical Chemistry A* **113**, 3096-3107 (2009).

S6. D. Bao, B. Millare, W. Xia, B. G. Steyer, A. A. Gerasimenko, A. Ferreira, A. Contreras, V. I. Vullev. *Journal of Physical Chemistry A* **113**, 1259-1267 (2009).

S7. D. Bao, S. Ramu, A. Contreras, S. Upadhyayula, J. M. Vasquez, G. Beran, V. I. Vullev. *Journal of Physical Chemistry B* **114**, 14467-14479 (2010).

Chapter 3

What Makes Oxidized *N*-Acylanthranilamides Stable?

ABSTRACT

Oligoamides composed of anthranilic acid derivatives present a promising choice for mediating long-range charge transfer and controlling its directionality. Hole hopping, modulated by the anthranilamide (Aa) permanent dipoles, provides a plausible means for such rectified long-range charge transduction. All aliphatic and most aromatic amides, however, decompose upon oxidation, rendering them unacceptable for hole-hopping pathways. We, therefore, employ electrochemical and computational analysis to examine how to suppress oxidative degradation and stabilize the radical cations of *N*-acylated Aa derivatives. Our findings reveal two requirements for attaining long-lived radical cations of these aromatic amides: (1) keeping the reduction potentials for oxidizing the Aa residues under about 1.4 V vs. SCE; and (2) adding an electron-donating group para to the N-terminal amide of the aromatic ring, which prevents the electron spin density of the radical cation from extending over the C-terminal amide. These findings provide essential information for the design of hole-transfer amides.

Introduction

As the electrostatic analogues of magnets, dipole-polarization electrets contain polar groups with their electric dipole moments arranged in a co-directional manner.[1-6] The electric fields originating from such ordered dipoles can pronouncedly affect charge-transfer processes.[7-9] However, because mobile charge carriers can readily redistribute and screen the fields from permanent dipoles, all electrets are dielectrics, unable to efficiently mediate long-range electron transduction.

Protein helices are some of the best known macromolecular electrets with permanent dipoles of about 2 to 5 D per residue originating from ordered amide and hydrogen bonds.[10-13] As a result, the electric fields in the vicinity of these macromolecular structures can amount to MV/m and GV/m, capable of rectifying electron transfer[14-16] and facilitating ion transport.[17,18] Along their backbones, however, proteins mediate electron transfer via tunneling, which cannot be efficient at distances exceeding about 2 nm.[19-24] Conversely, multiple short tunneling steps along arrays of cofactors can provide a means for efficient long-range electron transfer (i.e., via electron hopping), as observed for photosynthesis and respiration protein assemblies.[25-28] Similarly, DNA and PNA strands, comprising arrays of nucleotides with relatively low reduction potentials, provide pathways for efficient long-range hole hopping at distances considerably exceeding 2 nm.[29,30]

Combining favorable electret and charge-transfer features of biological and biomimetic systems, oligomers of anthranilic acid derivatives possess large permanent dipole moments and have the potential to mediate charge hopping.[2-4,9,31] These bioinspired molecular electrets are polypeptides composed of non-native aromatic β-amino acids with

Chart 3-1. Bioinspired Molecular Electrets and Their Anthranilic Residues.[a]

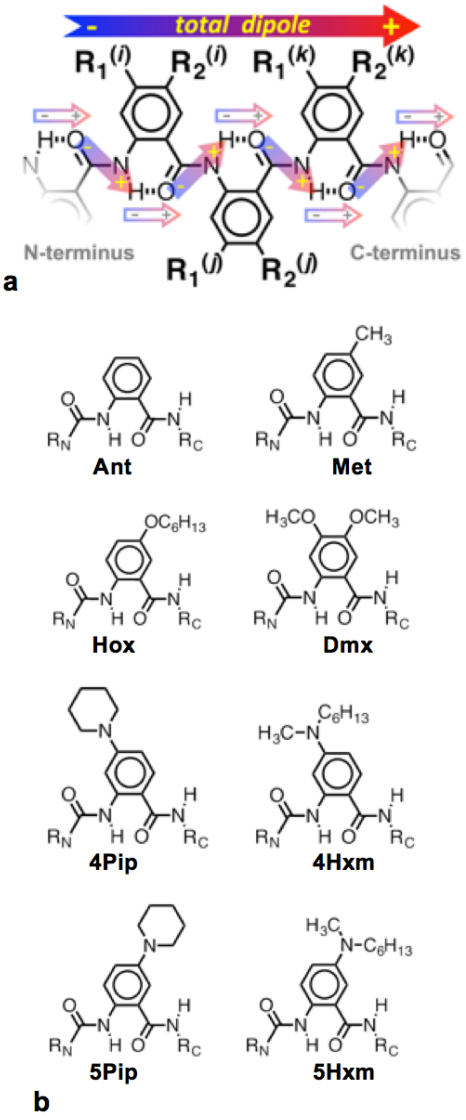

[a] (a) Molecular electrets composed of anthranilic acid residues and the origin of their permanent electric dipole from ordered amide bonds and a co-directional shift in the electron density (from O to H) upon hydrogen bonding. (b) *N*-acylated anthranilamide residues with electron-donating substituents as side chains, R_1 and R_2, and *n*-alkyl chains at their N- and C-termini ($R_N = C_5H_{11}$; $R_C = C_6H_{13}$).

dipoles originating from ordered amide and hydrogen bonds (Chart 3-1a).[3,4] The aromatic residues, directly linked with amide bonds, provide π-conjugation extending over the anthranilamide (Aa) backbones, which can serve as pathways for efficient long-range electron or hole transfer. Even a single *N*-acylated Aa residue pronouncedly rectifies charge transfer: accelerating photoinduced charge separation, while impeding charge recombination.[9] These properties make the anthranilic molecular electrets promising candidates for electronics and energy applications.[32-36]

A key feature of the anthranilic acid residues is their two side chains, R_1 and R_2 (Chart 3-1a), which provide an important means for tuning their electronic properties. In analogy with the structural and functional diversity of proteins attained by the side chains of the native amino acids combined in different sequences, the

two side chains of the anthranilic residues are a key means for pursuing a wide variety of electronic functionalities for these bioinspired molecular electrets.

Focusing on Aa residues for hole transfer, we select three types electron-donating substituents as side chains: alkyl, alkyloxy and amine groups (Chart 3-1b). In order to be feasible for mediating hole hopping, Aa residues should be able to sustain positive charges without undergoing oxidative degradation. We use the reversibility of electrochemical oxidation, estimated from cyclic voltammetry (CV), to examine if the radical cations of the different Aa residues are sufficiently stable. The CV results for the Aa residues reveal a cutoff reduction potential, E_{co}, that varies slightly for different solvent media: i.e., all the tested amides undergoing oxidation at potentials more positive than E_{co} manifest irreversibility. Conversely, not all Aa residues with reduction potentials more negative than E_{co} undergo reversible oxidation. Spin-density distribution of the radical cations, obtained from DFT calculations, correlates the extension of the positive charge over the C-terminal amide with the irreversibility of the oxidation behavior, which can prove to be an important predictive tool for the design of aromatic amides for hole-transfer organic materials.

Results

Varying the electron-donating substituents allows us to adjust the reduction potentials of the oxidation of the Aa residues over a range of about 1 V (Table 3-1). As expected, an increase in the solvent polarity causes a negative shift in the reduction potentials, i.e., making the oxidation more favorable (Table 3-1).[37-43] Furthermore, it is important not only what the substituent is, but also what its position is in the aromatic ring. Comparing 4Hxm and 5Hxm, for example, reveals that moving the amine from position 4 to position 5 (i.e., from R_1 to R_2) lowers the reduction potential with more than 200 mV

Table 3-1. Half-wave reduction potentials of the oxidation of *N*-acyl Aa residues, $Aa^{\bullet+} + e^- \rightleftharpoons Aa$.

			$E^{(1/2)}$ / V vs. SCE [a]		
	$-R_1$	$-R_2$	$CHCl_3$ [b] (• = 4.8)	DCM [b] (• = 8.9)	MeCN [b] (• = 37)
Ant	-H	-H	2.01 ± 0.26	1.93 ± 0.06	1.72 ± 0.02
Met	-H	$-CH_3$	2.05 ± 0.29	1.83 ± 0.01	1.63 ± 0.13
Hox	-H	$-OC_6H_{13}$	1.60 ± 0.03	1.53 ± 0.01	1.39 ± 0.01
Dmx	$-OCH_3$	$-OCH_3$	1.54 ± 0.08	1.43 ± 0.01	1.24 ± 0.03
4Pip	$-N(CH_2)_5$	-H	1.29 ± 0.12	1.08 ± 0.05	0.92 ± 0.16
5Pip	-H	$-N(CH_2)_5$	1.16 ± 0.04	0.92 ± 0.07	0.75 ± 0.01
4Hxm	$-N(CH_3)C_6H_{13}$	-H	1.42 ± 0.03	1.14 ± 0.01	0.97 ± 0.05
5Hxm	-H	$-N(CH_3)C_6H_{13}$	0.93 ± 0.01	0.89 ± 0.01	0.72 ± 0.01

[a] For Dmx, 5Pip and 5Hxm, $E^{(1/2)}$ are estimated as the average of the anodic and the cathodic potentials, i.e., $E^{(1/2)} = (E_a + E_c) / 2$ (Figure 1). For Ant, Met, Hox, 4Pip and 4Hxm, $E^{(1/2)}$ is obtained from the inflexion points of the anodic waves (Figure 1). [b] From the dependence of $E^{(1/2)}$ on C_{el} for each solvent, the values of $E^{(1/2)}$, reported in this table, are from extrapolations to zero electrolyte concentration.[37-39] (• – static dielectric constant, i.e., relative permittivity at zero frequency, of each solvent; $CHCl_3$ – chloroform; DCM – dichloromethane; and MeCN – acetonitrile).

(Table 3-1). The other two amine-derivatized residues, 4Pip and 5Pip, exhibit the same trend.

While the wide tunability of the electronic properties of the Aa residue is their most attractive property, most of them exhibit irreversible electrochemical oxidation, suggesting for the formation of radical cations with relatively short lifetimes even when in aprotic solvents (Figure 1a). Indeed, all aliphatic and many aromatic amides exhibit such chemical

irreversibility due to electrochemical oxidative degradation.[44,45] As expected, increasing the electron-donating strength of the substituents causes a substantial negative shift in the Aa reduction potentials (Figure 3-1, Table 3-1). As this negative shift becomes significant enough, the Aa voltammograms start to exhibit reversibility (Figure 3-1a,b). While the residue with a single alkyloxy group (Hox) exhibits irreversible oxidation, an addition of a second alkyloxyl (as in Dmx) results in 100-mV negative shift and reversible voltammograms (Figure 3-1a). Similarly, replacing the alkyloxyl in Hxm with an amine (as in 5Hxm and 5Pip) results not only in half-a-volt negative shift in the reduction potential, but also in reversible oxidation behavior (Figure 3-1a,b).

These findings suggest for a cutoff potential, E_{co}, of the chemical reversibility of Aa electrochemical oxidation that is lower than the reduction potential of Hox and higher than that of Dmx. If the formation of the radical cations requires potentials more positive than E_{co}, the conditions are oxidative enough to cause degradation, most likely a cleavage of the amide bonds, which is a common outcome from electrochemical oxidation of such aromatic conjugates.[45] Therefore, to attain chemical reversibility, and sufficient stability of radical cations, such as of Dmx, 5Pip and 5Hxm, the oxidation should be at reduction potentials more negative than E_{co}.

Strictly speaking, Dmx, 5Pip and 5Hxm exhibit quasi-reversible oxidation. While the peaks of the anodic and cathodic currents on their voltammograms are practically the same, the separation between the anodic and the cathodic peak potentials ranges between 70 and 100 mV when recorded at 0.1 V s^{-1} . This separation between the peak potentials increases with increasing the scan rate. This observation indicates that the interfacial

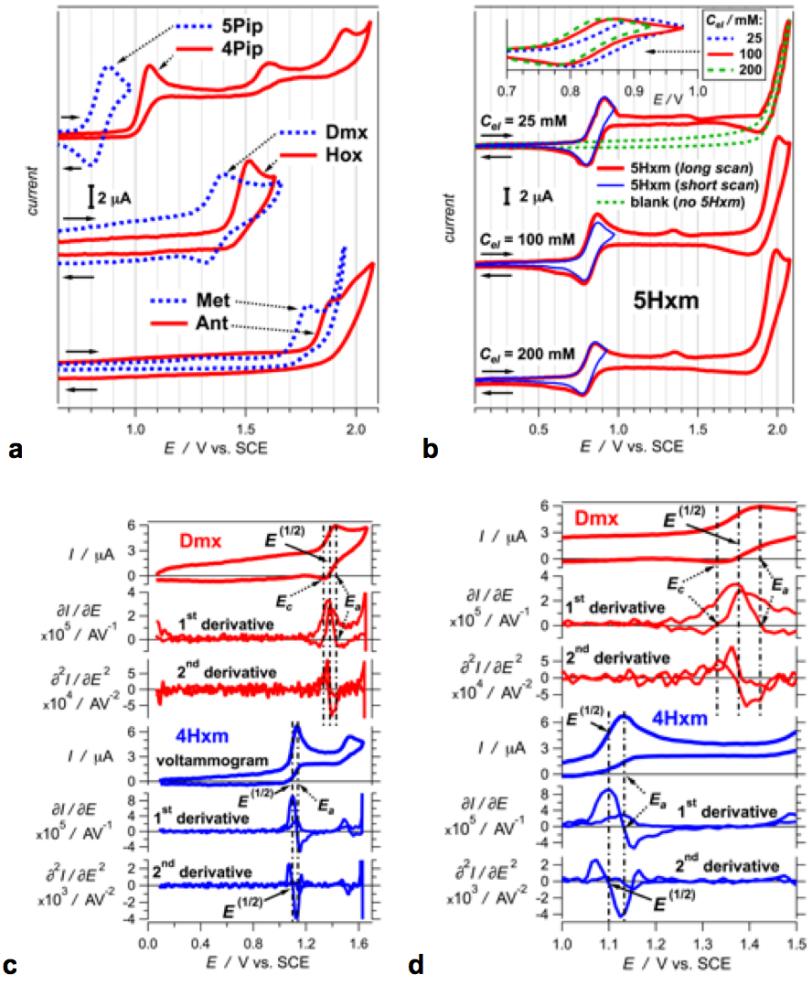

Figure 3-1. Cyclic voltammograms of Aa residues with electron-donating side chains (Chart 1), for dichloromethane (DCM) with NBu_4PF_6 as a supporting electrolyte at different concentration, C_{el}. (a) Voltammograms of six Aa residues with manifesting oxidation at different potentials (DCM; C_{el} = 200 mM). (b) Voltammograms of 5Hxm for DCM in the presence of different electrolyte concentrations. (inset: the first oxidation waves recorded at different C_{el}.) (c,d) Extracting half-wave potentials, $E^{(1/2)}$, from voltammograms with Faradaic currents comparable to the Ohmic and capacitance currents (DCM; C_{el} = 200 mM). For Dmx, when the anodic and cathodic peaks are apparent, $E^{(1/2)} = (E_a + E_c) / 2$, where E_a and E_c are the anodic and cathodic peak potentials, respectively, determined from the zero points of the first derivative, i.e., at E where $\partial I/\partial E = 0$. For 4Hxm, when only the cathodic peak is not present, $E^{(1/2)}$ is extracted from the first inflection point of the anodic wave, i.e., at E where $\partial^2 I/\partial E^2 = 0$. Scan rates: 0.02 V s^{-1} for the irreversible voltammograms (4Pip, 4Hxm, Hox, Met, and Ant); and 0.05 V s^{-1} for the quasi-reversible ones (5Pip, 5Hxm, and Dmx).

charge-transfer rates are slower than the mass transport rates of Aa and $Aa^{\bullet+}$ toward and away from the electrode surface. That is the oxidation is electrochemically irreversible and chemically reversible. Therefore, we report the reduction potentials as half-wave potentials, $E^{(1/2)}$. Nevertheless, even such quasi-reversible behavior is indicative for relatively stable long-lived radical cations of Dmx, 5Pip and 5Hxm.

For reversible and quasi-reversible cyclic voltammograms, the midpoint between the anodic and cathodic peak potentials (E_a and E_c, respectively) provides an estimate for $E^{(1/2)}$ (Figure 3-1c,d). Conversely, for irreversible behavior, where the cathodic peak is not apparent and E_c cannot be determined, the first inflection point of the anodic wave provides an acceptable estimate for $E^{(1/2)}$. In fact, the potentials at the inflection points of reversible waves, determined from the second derivatives of the voltammograms (i.e., E where $\partial^2 I/\partial E^2 = 0$), are quite close to $E^{(1/2)}$ obtained from $(E_a + E_c) / 2$ (Figure 3-1c,d). This observation justifies the use of the inflection points for estimating half-wave potentials from irreversible cyclic voltammograms.

The electrochemical reduction potentials of the Aa residues manifest dependence on the concentration of the supporting electrolyte, C_{el}. Decreasing C_{el} causes a positive shift in $E^{(1/2)}$ (Figure 3-1b). This concentration dependence of the reduction potentials allows for extrapolation of $E^{(1/2)}$ to $C_{el} = 0$, i.e., obtaining $E^{(1/2)}$ for neat solvents (Table 3-1),[37,38] which have significant relevance to charge-transfer studies.[9,37]

Keeping $E^{(1/2)} < E_{co}$ to attain reversible or quasi-reversible oxidation proves successful for Dmx, 5Pip and 5Hxm. Placing a strong electron-donating group on the 4th rather than the 5th position of the Aa aromatic ring (as in 4Hxm and 4Pip) results in $E^{(1/2)} < E_{co}$ but does not provide reversibility of the oxidation (Figure 1a). $E^{(1/2)}$ of 4Hxm and 4Pip is about 100 to 400 mV more negative than $E^{(1/2)}$ of Dmx (Table 3-1), and yet unlike Dmx, 4Hxm and 4Pip undergo irreversible oxidation. What is the reason for this discrepancy and what compromises the stability of the radical cations of the 4-amino Aa derivatives?

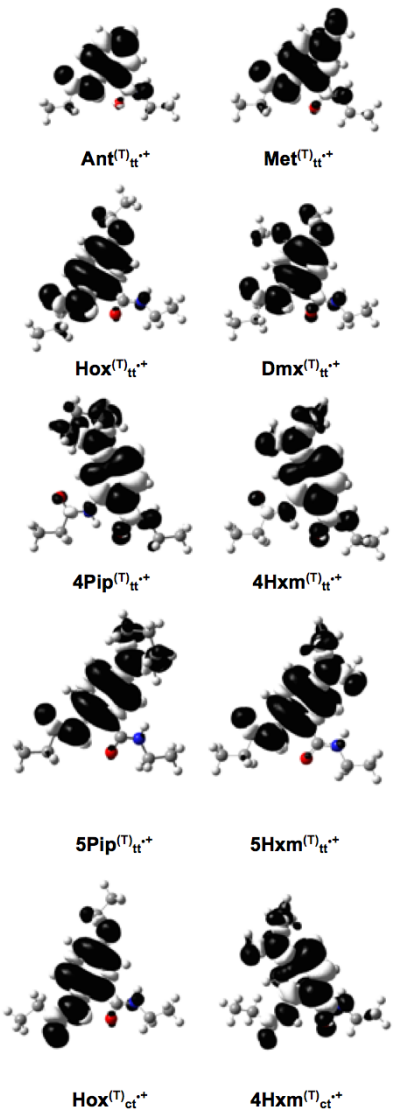

Figure 3-2. Electron spin density of the radical cations of the Aa residues (black – excess spin up, i.e., radical cation; and white, excess spin down). For each of the computations, the long alkyl chains of the structures are truncated (T) to ethyls. Truncation and conformational changes of the alkyl chains do not alter the spin-density distribution. Even switching an amide from *trans* to *cis* does not cause noticeable changes on the distribution over the reset of the structure (compare the two bottom *cis-trans*, $Aa^{(T)}{}_{ct}{}^{\bullet+}$, structures with the corresponding *trans-trans*, $Aa^{(T)}{}_{tt}{}^{\bullet+}$, ones

To elucidate the reason for this discrepancy with the irreversible oxidation of 4Pip and 4Hxm, we resort to computational analysis utilizing density functional theory (DFT) calculations, and focusing on the distribution of the electron spin density of the radial cations of the Aa residues. The positive charge of the radical cation of the residue without any substituents, $Ant^{\bullet+}$, spreads over the aromatic ring, extending mostly over the N-terminal amide and to a lesser extent over to the nitrogen of the C-terminal amide (Figure 3-2). Electron-donating groups at the 5th position enhance this electron spin-density distribution extending over the N-terminal and receding from the C-terminal amide. It is an especially pronounced effect for the strong electron-donating groups of the 5-amino $Aa^{\bullet+}$ derivatives, $5Hxm^{\bullet+}$ and $5Pip^{\bullet+}$ (Figure 3-2). Conversely, placing the same strong electron-donating groups on the 4th position, as in $4Pip^{\bullet+}$ and $4Hxm^{\bullet+}$, drastically changes the distribution of the positive charge, as apparent from the comparisons of $4Pip^{\bullet+}$ vs. $5Pip^{\bullet+}$, and $4Hxm^{\bullet+}$ vs. $5Hxm^{\bullet+}$ (Figure 3-2).

In the radical cations of 4Hxm and 4Pip, the electron spin-density extends predominantly over the C-terminal amide, rather than the N-terminal one (Figure 3-2).

Discussion

Cleavage of the amide bonds (C-C(O)NHC, CC(O)-NHC, or CC(O)NH-C) is the most likely outcome from the oxidative decomposition of aromatic amides.[45] Concurrently, the principal difference between the radical cations of the 4-amino derivatives and the rest of the $Aa^{\bullet+}$ is the distribution of the positive charge over the C-termianl amides (Figure 3-2). Therefore, it appears that while the N-terminal Aa amide requires $E > E_{co}$ for irreversible cleavage, the C-terminal Aa amide is susceptible to milder oxidizing conditions at $E < E_{co}$.

Extending the positive charge over the C-terminal amide can lead to its deprotonation, providing a plausible route for the observed decomposition of the oxidized 4-amino Aa residues. To examine the importance of the C-amide deprotonation, we prepared a derivative of 4Pip with a tertiary C-amide, i.e., $4Pip_{C\text{-}Pip}$ (Figure 3-3a). The spin-density distribution of $4Pip^{(T)}{}_{C\text{-}Pip}$ (Figure 3-3b) is practically the same as the one for $4Pip^{(T)}$ (Figure 3-2), indicating that adding the piperidine ring to the C-terminus does not noticeably alter the electronic structure of the radical cation. Conversely, the cyclic voltammograms of $4Pip_{C\text{-}Pip}$ for DCM (a relatively non-polar solvent with pronounced polarizability) manifest a small cathodic peak when the sweep is reversed (Figure 3-3c). In comparison, the cyclic voltammograms for 4Pip and 4Hxm do not show detectable cathodic peaks (Figure 3-1). This feature indicates that while $4Pip_{C\text{-}Pip}$, which lacks a C-terminal amide hydrogen, still shows chemical irreversibility, the irreversibility is partially

suppressed. Thus, we can conclude that most plausibly the deprotonation of the C-terminal amide represents only one of the routes responsible for the oxidative degradation of the 4-amino Aa residues.

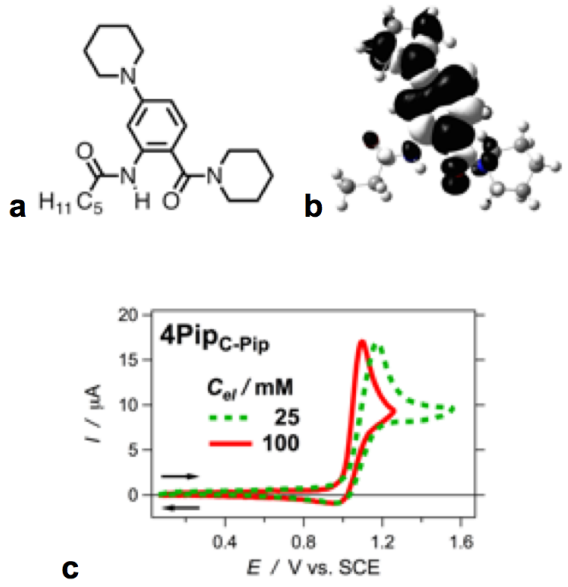

Figure 3-3. 4-piperidinyl Aa residue with a piperidine-capped C-terminus, $4Pip_{C\text{-}Pip}$. (a) Structure of $4Pip_{C\text{-}Pip}$. (b) Electron spin density of $4Pip_{C\text{-}Pip}^{\bullet+}$. (c) Cyclic voltammograms of $4Pip_{C\text{-}Pip}$ for DCM with NBu_4PF_6 as a supporting electrolyte at different concentration, C_{el} (scan rate: 0.05 V s^{-1}). The value of $E^{(1/2)}$ extrapolated to zero electrolyte concentration, i.e., for neat DCM,[37-39,46,47] is 1.09 ± 0.02 V vs. SCE.

To attain reversible or quasi-reversible electrochemical oxidation of *N*-acylated anthranilamides and stabilize their radical cations, it is essential to lower their reduction potentials by adding electron-donating substituents. Meanwhile, to prevent steric hindrance between the residues in the Aa oligomers, we focus on substituents at the 4th and the 5th distal position of the Aa aromatic ring, corresponding to the R_1 and R_2 side chains, respectively (Chart 3-1a). Making the aromatic ring sufficiently electron rich by adding electron-donating groups, however, is a necessary but not a sufficient condition for stabilizing the Aa radical cations. Placing electron-donating groups on the 5th position (as R_2 side chains) is another requirement for ensuring chemical reversibility of the electrochemical oxidation and long-lived $Aa^{\bullet+}$. While these findings are key specifically for the anthranilic molecular electrets (Chart 3-1a), they underline important considerations for the design of aromatic amides for electronic and energy applications where hole transfer is crucial.

EXPERIMENTAL METHODS

The eight residues, N_C-hexyl N_2-hexanoyl(*xyz*)anthranilamide (where for Ant, (*xyz*) is blank; for Met, (*xyz*) = -5-methyl; for Hox, (*xyz*) = -5-hexyloxy; for Dmx, (*xyz*) = -4,5-dimethoxy; for 4Hxm, (*xyz*) = -4-(hexyl(methyl)amino); for 5Hxm, (*xyz*) = -5-(hexyl(methyl)amino); for 4Pip, (*xyz*) = -4-(piperidin-*N*-yl); and for 5Pip, (*xyz*) = -5-(piperidin-*N*-yl)) are prepared as previously described.[9,39] Adopting the same procedures, we prepared $4Pip_{C\text{-}Pip}$ in five synthetic steps from commercially available starting materials: 4-fluoro-2-nitrobensoic acid, piperidine, and hexanoic anhydride.

(2-nitro-4-(piperidin-N-yl)-benzoyl)piperidine (precursor for $4Pip_{C\text{-}Pip}$). 2-nitro-4-(piperidin-*N*-yl)-benzoic acid (125 mg , 0.5 mmol), prepared as previously described,[31,39] was placed in a 100-ml Schlenk tube equipped with a magnetic stir bar. While purging with argon, 5 ml dry DCM and 3 drops of DMF were added, and the reaction vessel was immersed in a dry-ice/acetone bath. Oxalyl chloride (130 µl, 1.5 mmol) was slowly added and the reaction mixture was allowed to gradually warm up to room temperature. The progress of the reaction was monitored using TLC of the reaction mixture treated with methanol and within 30 min the conversion was quantitative. The liquid, including the left over oxalyl chloride, was removed *in vacuo*, followed by several addition and removal of small portions (5 ml) of DCM. The thus dried reaction mixture was dissolved in dry 5 ml DCM, and piperidine (150 µL, 1.5 mmol) was slowly added to it while purged with argon. The Schlenk tube was immersed in a dry-ice/acetone bath and pyridine (60 µl, 0.75 mmol) was slowly added to it. The reaction mixture was allowed to warm up to room temperature and was stirred for an additional hour. The solution was diluted with 25 ml of DCM, and

washed with 5% HCL (100 ml × 2) and with brine (100 ml). The organic layer was collected, dried over Na_2SO_4, and concentrated *in vacuo*. The product was purified using flash chromatography (column, 1" internal diameter, was packed with silica gel in hexanes, 6" to 8" height of the packed stationary phase). Isocratic elution at 70% ethyl acetate and 30% hexanes produced the fraction of interest (as monitored with TLC) to afford, after drying, yellow solid (75 mg, 0.24 mmol, 48%) of (2-nitro-4-(piperidin-*N*-yl)-benzoyl)piperidine: ^{1}H-NMR (400 MHz, $CDCl_3$) □/ppm: 7.56 (1 H, d, J = 2.4 Hz), 7.15 (1 H, d, J = 8.5 Hz), 7.08 (1 H, dd, J_1 = 8.6 Hz, J_2 = 2.4 Hz), 3.71 (2 H, s), 3.27 (4 H, t, J = 5.1 Hz), 3.17 (2 H, t, J = 5.5 Hz), 1.66 (10 H, m), 1.45 (2 H, s); ^{13}C-NMR (400 MHz, $CDCl_3$) □/ppm: 167.22, 152.22, 146.75, 128.81, 122.14, 120.25, 110.19, 49.46, 48.19, 42.98, 26.17, 25.45, 25.42, 24.77, 24.28; HRMS m/z calculated $C_{17}H_{23}N_3O_3^+$ $(M + H)^+$ 318.1818, found 318.1827 $(M + H)^+$.

(N-hexanoyl-2-amino-4-(piperidin-N-yl)-benzoyl)piperidine (4Pip$_{C\text{-}Pip}$). (2-nitro-4-(piperidin-*N*-yl)-benzoyl)piperidine (75 mg, 0.24 mmol) and $Co_2(CO)_8$ (149 mg, 0.47 mmol) were added to a 100-ml pressure tube.[48] While purging with argon, 5 ml of 1,2-dimethoxyethane and 2 drops of DI water were added. While mixing, the pressure tube was immersed in a temperature-controlled oil bath. The mixture was heated to 90 °C and stirred for an hour. The reaction mixture was filtered; the filtrate was collected, diluted with 25 ml DCM, and washed with water (100 ml). The organic layer was collected, dried over Na_2SO_4, and concentrated *in vacuo*. While purging with argon, the resulting solid was transferred into a Schlenk tube using 5 ml dry DCM; hexanoic anhydride (163 μL, 0.708 mmol) was added, and the solution was cooled on a dry-ice/acetone bath. After adding

pyridine (38 μl, 0.47 mmol), the solution was allowed to warm up to room temperature and stirred for additional 1.5 h. The reaction solution was diluted with 25 ml DCM, and washed with an aqueous solution of Na_2CO_3 (100 ml × 2) and with brine (100 mL). The organic layer was collected, dried over Na_2SO_4, concentrated *in vacuo*, and purified using flash chromatography (column, 1" internal diameter, was packed with silica gel in hexanes, 6" to 8" height of the packed stationary phase). Isocratic elution at 70% ethyl acetate and 30% hexanes produced the fraction of interest. After further wash with Na_2CO_3 solution and drying, the solvent was removed *in vacuo* to produce white solid (37 mg, 0.096 mmol, 40%) of $4Pip_{C\text{-}Pip}$: ^{1}H-NMR (400 MHz, $CDCl_3$) □/ppm: 9.56 (1 H, s), 8.00 (1 H, d, J = 2.4 Hz), 7.04 (1 H, d, J = 8.7 Hz), 6.50 (1 H, dd, J_1 = 8.7 Hz, J_2 = 2.3 Hz), 3.53 (4 H, s), 3.24 (4 H, t, J = 5.1 Hz), 2.32 (2 H, t, J = 7.5 Hz), 1.68 (8 H, m), 1.56 (6 H, m), 1.32 (4 H, m), 0.87 (3 H, t, J = 6.8 Hz); ^{13}C-NMR (400 MHz, $CDCl_3$) □/ppm: 172.11, 170.52, 153.45, 139.60, 129.19, 112.27, 108.92, 108.06, 49.35, 38.42, 31.52, 26.44. 25.73, 25.39, 24.84, 24.56, 14.14; HRMS m/z calculated $C_{23}H_{35}N_3O_2^+$ $(M + H)^+$ 386.2807, found 386.2821 $(M + H)^+$.

Cyclic voltammetry is conducted using Reference 600™ Potentiostat/Galvanostat/ZRA (Gamry Instruments, PA, U.S.A.), connected to a three-electrode cell, at scan rates of 20 to 500 mV s^{-1}, as previously described.[37,38] Anhydrous aprotic solvents with different polarity, chloroform ($CHCl_3$), dichloromethane (DCM), and acetonitrile (MeCN), are employed with different concentrations of tetrabutylammonium hexafluorophosphate (NBu_4PF_6) as supporting electrolyte. Prior to recording each

voltammogram, the sample was extensively purged with argon while maintaining its volume of 5 ml by adding more of the anhydrous solvent.

For each Aa residue and each solvent, a set of voltammograms is recorded where the electrolyte concentration is increased from 25 mM to 200 mM in steps of 25 mM. The half-wave potentials, $E^{(1/2)}$, are determined form the midpoints between the cathodic and anodic peak potentials for reversible or quasi-reversible oxidation; and from the inflection points of the anodic waves for irreversible oxidation (Figure 3-1c,d). The anodic and cathodic peak potentials, E_a and E_c, respectively, are determined from the zero points of the first derivatives of the voltammograms, i.e., the potentials where $\partial I/\partial E = 0$ at $\partial E/\partial t =$ constant (Figure 3-1c,d). The inflection points are determined from the zero point of the second derivatives of the voltammograms, $\partial^2 I/\partial E^2 = 0$ at $\partial E/\partial t =$ constant (Figure 3-1c,d).

The second derivatives of reversible and quasi-reversible voltammograms show that the inflection-point potentials are quite close to the mid-points between E_a and E_c, ensuring the reliability for the estimates of $E^{(1/2)}$ from the inflection points of irreversible voltammograms. To correct for potential drifts in the reference electrode (which is SCE, connected with the cell via a salt bridge) ferrocene was used as a standard ($E^{(1/2)} = 0.45 \pm 0.01$ V vs. SCE for MeCN, 100 mM NBu_4BF_4).[37] Voltammograms of the standard are recorded before and after each set of measurements. From the dependence of $E^{(1/2)}$ on the electrolyte concentration, the potentials for each neat solvents are estimated from extrapolations to zero (Table 3-1).[37,38]

The *N*-acylated Aa residues (Chart 3-1b) are modeled using density functional theory (DFT). For simplicity, the aliphatic chains are truncated to two carbons. The DFT

calculations are performed at the B3LYP/6-311+G(d,p) level[9,39,46,49-51] for the gas phase using Gaussian 09.[52] Spin-unrestricted calculations are used for radical-cation (doublet state) modeling.

REFERENCES

(1) Sessler, G. M. Electrets: Recent Developments. *J. Electrostatics* **2001**, *51*, 137-145.

(2) Vullev, V. I. From Biomimesis to Bioinspiration: What's the Benefit for Solar Energy Conversion Applications? *J. Phys. Chem. Lett.* **2011**, *2*, 503–508.

(3) Xia, B.; Bao, D.; Upadhyayula, S.; Jones, G.; Vullev, V. I. Anthranilamides as Bioinspired Molecular Electrets: Experimental Evidence for a Permanent Ground-State Electric Dipole Moment. *J. Org. Chem.* **2013**, *78*, 1994-2004.

(4) Ashraf, M. K.; Pandey, R. R.; Lake, R. K.; Millare, B.; Gerasimenko, A. A.; Bao, D.; Vullev, V. I. Theoretical Design of Bioinspired Macromolecular Electrets Based on Anthranilamide Derivatives. *Biotechnol. Prog.* **2009**, *25*, 915-922.

(5) Jasper, W. J.; Mohan, A.; Hinestroza, J.; Barker, R. Degradation Processes in Corona-Charged Electret Filter-Media with Exposure to Ethyl Benzene. *J. Eng. Fiber. Fabr.* **2007**, *2*, 19-24.

(6) Upadhyayula, S.; Bao, D.; Millare, B.; Sylvia, S. S.; Habib, K. M. M.; Ashraf, K.; Ferreira, A.; Bishop, S.; Bonderer, R.; Baqai, S.; et al. Permanent Electric Dipole Moments of Carboxyamides in Condensed Media: What Are the Limitations of Theory and Experiment? *J. Phys. Chem. B* **2011**, *115*, 9473-9490.

(7) Galoppini, E.; Fox, M. A. Effect of the Electric Field Generated by the Helix Dipole on Photoinduced Intramolecular Electron Transfer in Dichromophoric 〈-Helical Peptides. *J. Am. Chem. Soc.* **1996**, *118*, 2299-2300.

(8) Yasutomi, S.; Morita, T.; Imanishi, Y.; Kimura, S. A Molecular Photodiode System That Can Switch Photocurrent Direction. *Science* **2004**, *304*, 1944-1947.

(9) Bao, D.; Upadhyayula, S.; Larsen, J. M.; Xia, B.; Georgieva, B.; Nunez, V.; Espinoza, E. M.; Hartman, J. D.; Wurch, M.; Chang, A.; et al. Dipole-Mediated Rectification of Intramolecular Photoinduced Charge Separation and Charge Recombination. *J. Am. Chem. Soc.* **2014**, *136*, 12966-12973.

(10) Hol, W. G. J. Effects of the Alpha-Helix Dipole upon the Functioning and Structure of Proteins and Peptides. *Adv. Biophys.* **1985**, *19*, 133-165.

(11) Hol, W. G. J.; Van Duijnen, P. T.; Berendsen, H. J. C. The Alpha-Helix Dipole and the Properties of Proteins. *Nature* **1978**, *273*, 443-446.

(12) Wada, A. Dielectric properties of polypeptide solutions. II. Relation Between the Electric Dipole Moment and the Molecular Weight of the Alpha-Helix. *J. Chem. Phys.* **1959**, *30*, 328-329.

(13) Shin, Y.-G. K.; Newton, M. D.; Isied, S. S. Distance Dependence of Electron Transfer Across Peptides with Different Secondary Structures: The Role of Peptide Energetics and Electronic Coupling. *J. Am. Chem. Soc.* **2003**, *125*, 3722-3732.

(14) Fox, M. A.; Galoppini, E. Electric Field Effects on Electron Transfer Rates in Dichromophoric Peptides: The Effect of Helix Unfolding. *J. Am. Chem. Soc.* **1997**, *119*, 5277-5285.

(15) Garbuio, L.; Antonello, S.; Guryanov, I.; Li, Y.; Ruzzi, M.; Turro, N. J.; Maran, F. Effect of Orientation of the Peptide-Bridge Dipole Moment on the Properties of Fullerene-Peptide-Radical Systems. *J. Am. Chem. Soc.* **2012**, *134*, 10628-10637.

(16) Shlizerman, C.; Atanassov, A.; Berkovich, I.; Ashkenasy, G.; Ashkenasy, N. *De Novo* Designed Coiled-Coil Proteins with Variable Conformations as Components of Molecular Electronic Devices. *J. Am. Chem. Soc.* **2010**, *132*, 5070-5076.

(17) Doyle, D. A.; Cabral, J. M.; Pfuetzner, R. A.; Kuo, A. L.; Gulbis, J. M.; Cohen, S. L.; Chait, B. T.; MacKinnon, R. The Structure of the Potassium Channel: Molecular Basis of K^+ Conduction and Selectivity. *Science* **1998**, *280*, 69-77.

(18) Dutzler, R.; Campbell, E. B.; Cadene, M.; Chait, B. T.; MacKinnon, R. X-ray Structure of a CIC Chloride Channel at 3.0 Angstrom Reveals the Molecular Basis of Anion Selectivity. *Nature* **2002**, *415*, 287-294.

(19) Gray, H. B.; Winkler, J. R. Long-Range Electron Transfer. *Proc. Natl. Acad. Sci. U. S. A.* **2005**, *102*, 3534-3539.

(20) Gray, H. B.; Winkler, J. R. Electron Transfer in Proteins. *Annu. Rev. Biochem.* **1996**, *65*, 537-561.

(21) Vullev, V. I.; Jones, G., II Photoinduced Charge Transfer in Helical Polypeptides. *Res. Chem. Intermed.* **2002**, *28*, 795-815.

(22) Jones, G., II; Lu, L. N.; Vullev, V.; Gosztola, D.; Greenfield, S.; Wasielewski, M. Photoactive Peptides. 6. Photoinduced Electron Transfer for Pyrenesulfonamide Conjugates of Tryptophan-Containing Peptides. Mitigation of Fluoroprobe Behavior in N-Terminal Labeling Experiments. *Bioorg. Med. Chem. Lett.* **1995**, *5*, 2385-2390.

(23) Jones, G., II; Vullev, V.; Braswell, E. H.; Zhu, D. Multistep Photoinduced Electron Transfer in a *de Novo* Helix Bundle: Multimer Self-Assembly of Peptide Chains Including a Chromophore Special Pair. *J. Am. Chem. Soc.* **2000**, *122*, 388-389.

(24) Jones, G., II; Vullev, V. I. Photoinduced Electron Transfer between Non-Native Donor-Acceptor Moieties Incorporated in Synthetic Polypeptide Aggregates. *Org. Lett.* **2002**, *4*, 4001-4004.

(25) Warren, J. J.; Winkler, J. R.; Gray, H. B. Hopping Maps for Photosynthetic Reaction Centers. *Coord. Chem. Rev.* **2013**, *257*, 165-170.

(26) Wittekindt, C.; Schwarz, M.; Friedrich, T.; Koslowski, T. Aromatic Amino Acids as Stepping Stones in Charge Transfer in Respiratory Complex I: An Unusual Mechanism Deduced from Atomistic Theory and Bioinformatics. *J. Am. Chem. Soc.* **2009**, *131*, 8134-8140.

(27) Capaldi, R. A. The Complexity of a Respiratory Complex. *Nat. Struct. Biol.* **1996**, *3*, 570-574.

(28) Eberhard, S.; Finazzi, G.; Wollman, F. A. The Dynamics of Photosynthesis. *Annu. Rev. Genet.* **2008**, *42*, 463-515.

(29) Lewis, F. D. Distance-Dependent Electronic Interactions Across DNA Base Pairs: Charge Transport, Exciton Coupling, and Energy Transfer. *Isr. J. Chem.* **2013**, *53*, 350-365.

(30) Venkatramani, R.; Keinan, S.; Balaeff, A.; Beratan, D. N. Nucleic Acid Charge Transfer: Black, White and Gray. *Coord. Chem. Rev.* **2011**, *255*, 635-648.

(31) Larsen, J. M.; Espinoza, E. M.; Vullev, V. I. Bioinspired Molecular Electrets: Bottom-up Approach to Energy Materials and Applications. *J. Photon. Energy.* **2015**, *5*, 055598.

(32) Guo, S.; Bao, D.; Upadhyayula, S.; Wang, W.; Guvenc, A. B.; Kyle, J. R.; Hosseinibay, H.; Bozhilov, K. N.; Vullev, V. I.; Ozkan, C. S.; et al. Photoinduced Electron Transfer Between Pyridine Coated Cadmium Selenide Quantum Dots and Single Sheet Graphene. *Adv. Funct. Mater.* **2013**, *23*, 5199-5211.

(33) Wang, W.; Guo, S.; Penchev, M.; Zhong, J.; Lin, J.; Bao, D.; Vullev, V.; Ozkan, M.; Ozkan, C. S. Hybrid Low Resistance Ultracapacitor Electrodes Based on 1-Pyrene Butyric acid Functionalized Centimeter-Scale Graphene Sheets. *J. Nanosci. Nanotechnol.* **2012**, *12*, 6913-6920.

(34) Lin, J.; Zhong, J.; Bao, D.; Reiber-Kyle, J.; Wang, W.; Vullev, V.; Ozkan, M.; Ozkan, C. S. Supercapacitors Based on Pillared Graphene Nanostructures. *J. Nanosci. Nanotechnol.* **2012**, *12*, 1770-1775.

(35) Ghazinejad, M.; Kyle, J. R.; Guo, S.; Pleskot, D.; Bao, D.; Vullev, V. I.; Ozkan, M.; Ozkan, C. S. Non-Invasive High-Throughput Metrology of Functionalized Graphene Sheets. *Adv. Funct. Mater.* **2012**, *22*, 4519-4525.

(36) Lu, H.; Bao, D.; Penchev, M.; Ghazinejad, M.; Vullev, V. I.; Ozkan, C. S.; Ozkan, M. Pyridine-Coated Lead Sulfide Quantum Dots for Polymer Hybrid Photovoltaic Devices. *Adv. Sci. Lett.* **2010**, *3*, 101-109.

(37) Bao, D.; Millare, B.; Xia, W.; Steyer, B. G.; Gerasimenko, A. A.; Ferreira, A.; Contreras, A.; Vullev, V. I. Electrochemical Oxidation of Ferrocene: A Strong Dependence on the Concentration of the Supporting Electrolyte for Nonpolar Solvents. *J. Phys. Chem. A* **2009**, *113*, 1259-1267.

(38) Bao, D.; Ramu, S.; Contreras, A.; Upadhyayula, S.; Vasquez, J. M.; Beran, G.; Vullev, V. I. Electrochemical Reduction of Quinones: Interfacing Experiment and Theory for Defining Effective Radii of Redox Moieties. *J. Phys. Chem. B* **2010**, *114*, 14467-14479.

(39) Larsen, J. M.; Espinoza, E. M.; Hartman, J. D.; Lin, C.-K.; Wurch, M.; Maheshwari, P.; Kaushal, R. K.; Marsella, M. J.; Beran, G. J. O.; Vullev, V. I. Building Blocks for Bioinspired Electrets: Molecular-Level Approach to Materials for Energy and Electronics. *Pure Appl. Chem.* **2015**, *87*, 779-792.

(40) Jones, G., II; Yan, D.; Hu, J.; Wan, J.; Xia, B.; Vullev, V. I. Photoinduced Electron Transfer in Arylacridinium Conjugates in a Solid Glass Matrix. *J. Phys. Chem. B* **2007**, *111*, 6921-6929.

(41) Hu, J.; Xia, B.; Bao, D.; Ferreira, A.; Wan, J.; Jones, G.; Vullev, V. I. Long-Lived Photogenerated States of α-Oligothiophene-Acridinium Dyads Have Triplet Character. *J. Phys. Chem. A* **2009**, *113*, 3096-3107.

(42) Vullev, V. I.; Jones, G. Photoinduced Electron Transfer in Alkanoylpyrene Aggregates in Conjugated Polypeptides. *Tetrahedron Lett.* **2002**, *43*, 8611-8615.

(43) Wan, J.; Ferreira, A.; Xia, W.; Chow, C. H.; Takechi, K.; Kamat, P. V.; Jones, G.; Vullev, V. I. Solvent Dependence of the Charge-Transfer Properties of a Quaterthiophene-Anthraquinone Dyad. *J. Photochem. Photobiol., A* **2008**, *197*, 364-374.

(44) Odonnell, J. F.; Mann, C. K. Controlled-Potential Oxidation of Aliphatic Amides. *J. Electroanal. Chem.* **1967**, *13*, 157–162.

(45) Golub, T.; Becker, J. Y. Electrochemical Oxidation of Amides of Type $Ph_2CHCONHAr$. *Org. Biomol. Chem.* **2012**, *10*, 3906-3912.

(46) Espinoza, E. M.; Larsen, J. M.; Vullev, V. I. Electrochemical Properties of Residues for Bioinspired Molecular Electrets. *ECS Transactions* **2015**, *66*, 1-9.

(47) Espinoza, E. M.; Xia, B.; Darabedian, N.; Larsen, J. M.; Nunez, V.; Bao, D.; Mac, J. T.; Botero, F.; Wurch, M.; Zhou, F.; Vullev, V. I. Nitropyrene Photoprobes: Making Them, and What Are They Good for? *Eur. J. Org. Chem.* **2016**, *2016*, 343-356.

(48) Lee, H.-Y.; An, M. Selective Reduction of the Nitro-Group Using $Co_2(CO)_8$-H2O. *Bull. Korean Chem. Soc.* **2004**, *25*, 1717-1719.

(49) Lee, C. T.; Yang, W. T.; Parr, R. G. Development of the Colle-Salvetti Correlation-Energy Formula into a Functional of the Electron-Density. *Phys. Rev. B* **1988**, *37*, 785-789.

(50) Krishnan, R.; Binkley, J. S.; Seeger, R.; Pople, J. A. Self-Consistent Molecular Orbital Methods. XX. A Basis Set for Correlated Wave Functions. *J. Chem. Phys.* **1980**, *72*, 650-654.

(51) Becke, A. D. Density-Functional Thermochemistry. III. The Role of Exact Exchange. *J. Chem. Phys.* **1993**, *98*, 5648-5652.

(52) Frisch, M. J.; Trucks, G. W.; Schlegel, H. B.; Scuseria, G. E.; Robb, M. A.; Cheeseman, J. R.; Scalmani, G.; Barone, V.; Mennucci, B.; Petersson, G. A., et al. *Gaussian 09*, Revision A.1; Gaussian, Inc.: Wallingford, CT, 200

Supplemental Figures

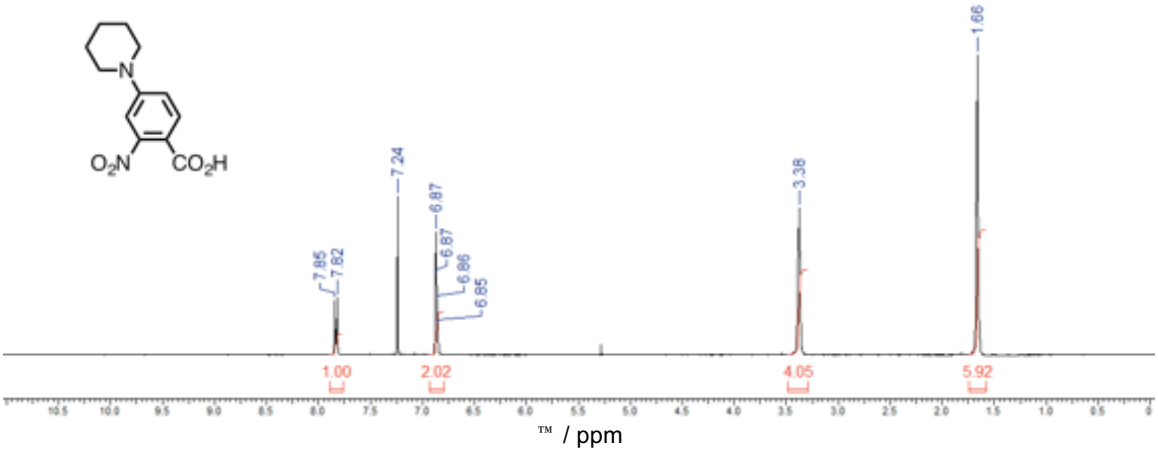

Figure 3S-1. [1]H 1D NMR spectrum of 2-nitro-5-(piperidin-*N*-yl) benzoic acid (CDCl3).

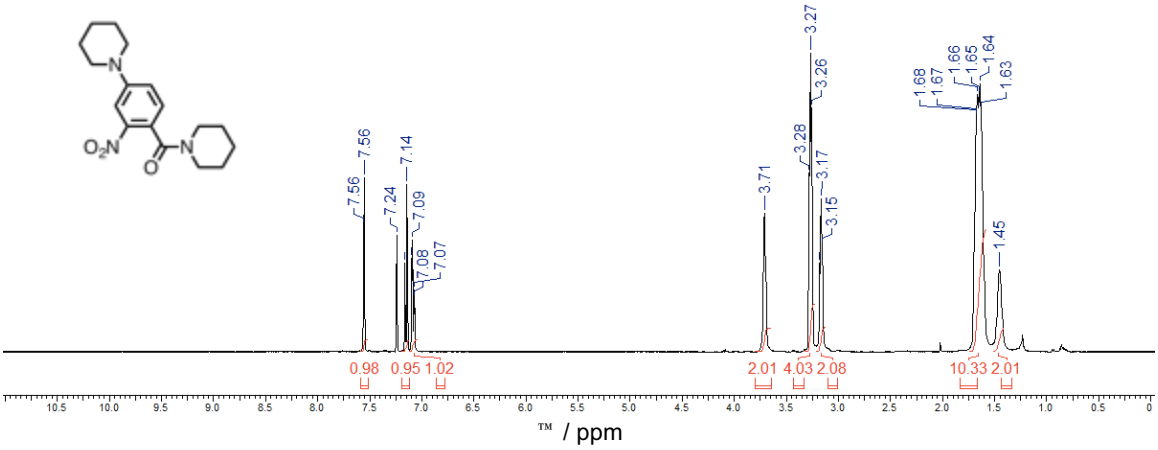

a

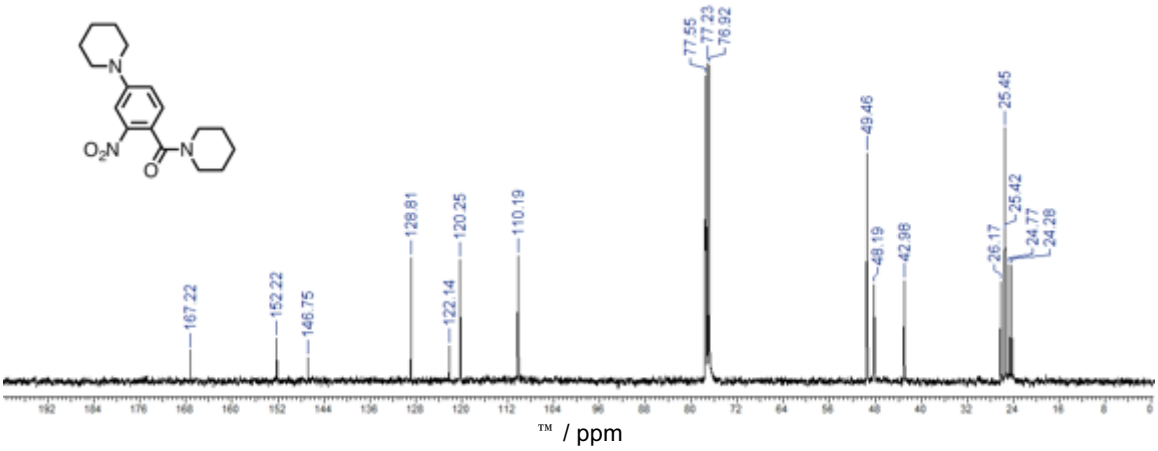

b

Figure 3S-2. 1D NMR spectra, (a) ^{1}H and (b) ^{13}C, of (2-nitro-4-(piperidin-*N*-yl)-benzoyl) piperidine (CDCl3).

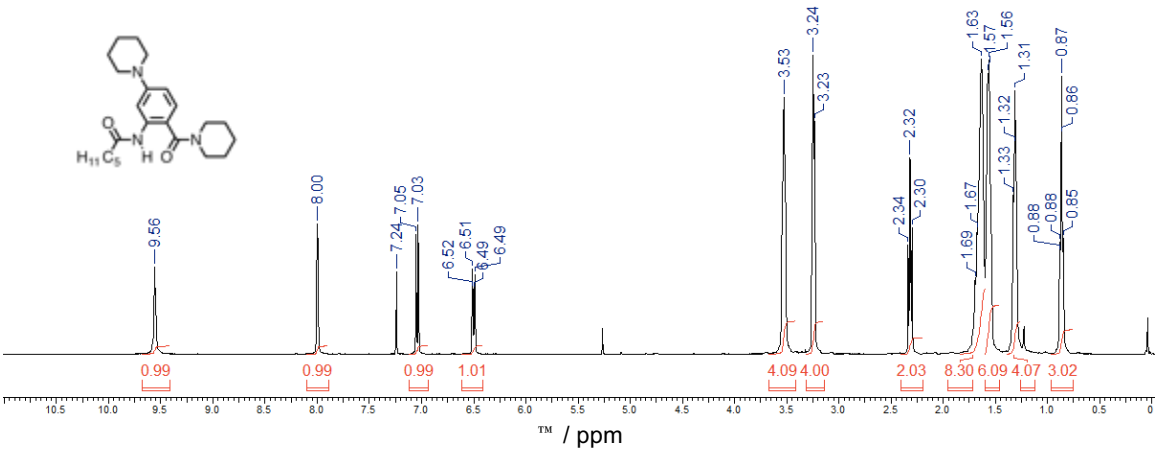

a

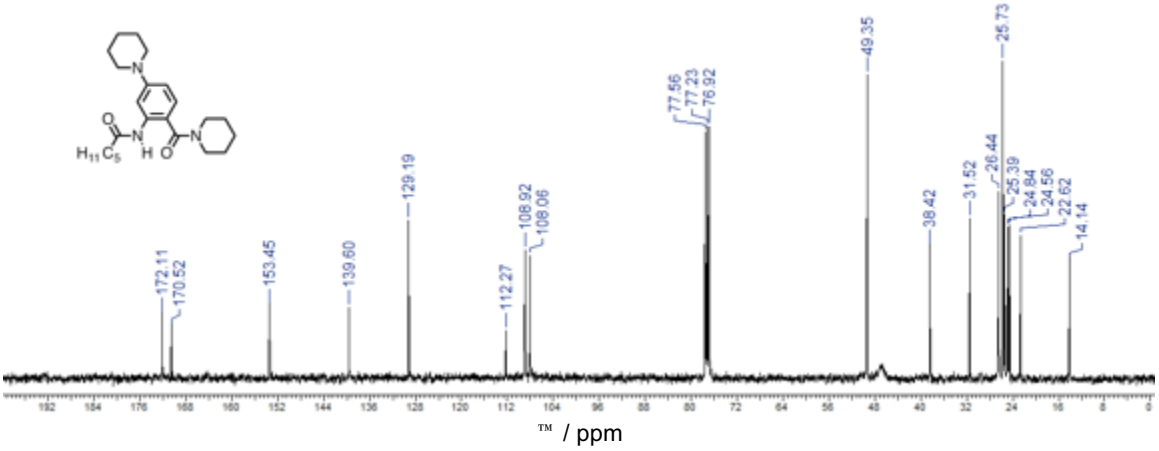

b

Figure 3S-3. 1D NMR spectra, (a) ^{1}H and (b) ^{13}C, of 4PipC-Pip (CDCl3).

Supplemental Schemes

Scheme 3S-1. Synthesis of 4PipC-Pip.

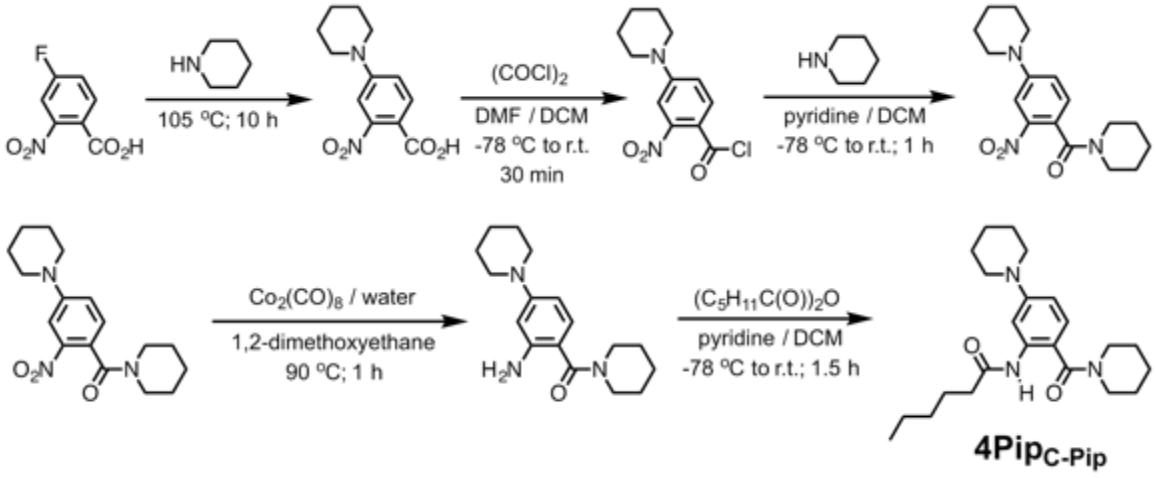

Chapter 4

Practical Aspects of Cyclic Voltammetry: How to Estimate Reduction Potentials when Irreversibility Prevails

Abstract

What is the best approach for estimating standard electrochemical potentials, $E^{(0)}$, from voltammograms that exhibit chemical irreversibility? The lifetimes of the oxidized or reduced forms of the majority of known redox species are considerably shorter than the voltammetry acquisition times, resulting in irreversibility and making the answer to this question of outmost importance. Half-wave potentials, $E^{(1/2)}$, provide the best experimentally obtainable representation of $E^{(0)}$. Due to irreversible oxidation or reduction, however, the lack of cathodic or anodic peaks in cyclic voltammograms renders $E^{(1/2)}$ unattainable. Therefore, we evaluate how closely alternative potentials, readily obtainable from irreversible voltammograms, estimate $E^{(0)}$. Our analysis reveals that, when $E^{(1/2)}$ is not available, inflection-point potentials provide the best characterization of redox couples. While peak potentials are the most extensively used descriptor for irreversible systems, they deviate significantly from $E^{(0)}$, especially at high scan rates. Even for partially irreversible systems, when the cathodic peak is not as pronounced as the anodic one, the half-wave potentials still provide the best estimates for $E^{(0)}$. The importance of these findings extends beyond the realm of electrochemistry and impacts fields, such as materials engineering, photonics, cell biology, solar energy engineering and neuroscience, where cyclic voltammetry is a key tool.

Introduction

Cyclic voltammetry (CV) is the hallmark of electrochemical analysis and it impacts on countless fields outside of chemistry, such as materials science, photonics, cell biology, neuroscience, electrical engineering and condensed-phase physics.[1-7] Voltammograms provide a wealth of information about the charge-transfer and mass-transport processes at the surfaces of the working electrodes.[8-11] The evolving voltammetry theories, based on Butler-Volmer and Marcus-Hush formalisms, reveal key mechanistic insights about these interfacial phenomena.[12-16]

Estimating standard electrochemical potentials ($E^{(0)}$) of oxidation and reduction encompasses one of the most widely spread uses of CV, which makes this technique popular. The strong correlation of $E^{(0)}$ with the energy levels of frontier orbitals and band edges defines the invaluable importance of the electrochemical potentials for characterization of electronic properties of molecular species and materials. Combining the Butler-Volmer equation with Fick's second law results in an expression of the Faradaic current (i_F) in terms of the applied potential (E), where $E^{(0)}$ is one of the parameters. This expression of i_F as a function of E, however, is an integral equation and its solution remain in the realm of numerical analysis, rendering it impractical for routine estimations of $E^{(0)}$ from voltammograms. Therefore, half-wave potentials ($E^{(1/2)}$) have become the preferred representation of $E^{(0)}$, i.e., $E^{(1/2)} \approx E^{(0)}$ for reversible oxidation and reduction. The average between the anodic (E_a) and the cathodic (E_c) potentials define $E^{(1/2)}$, which are facile to extract from cyclic voltammograms manifesting reversibility (Figure 4-1a).[8] This definition of $E^{(1/2)}$ also extends to quasireversible cases (i.e., chemically reversible and

electrochemically irreversible) when the rates of interfacial electron transfer are slower that the rates of mass transport to and away from the electrode and $|E_a - E_c|$ increases with an increase in the scan rate.[8,17]

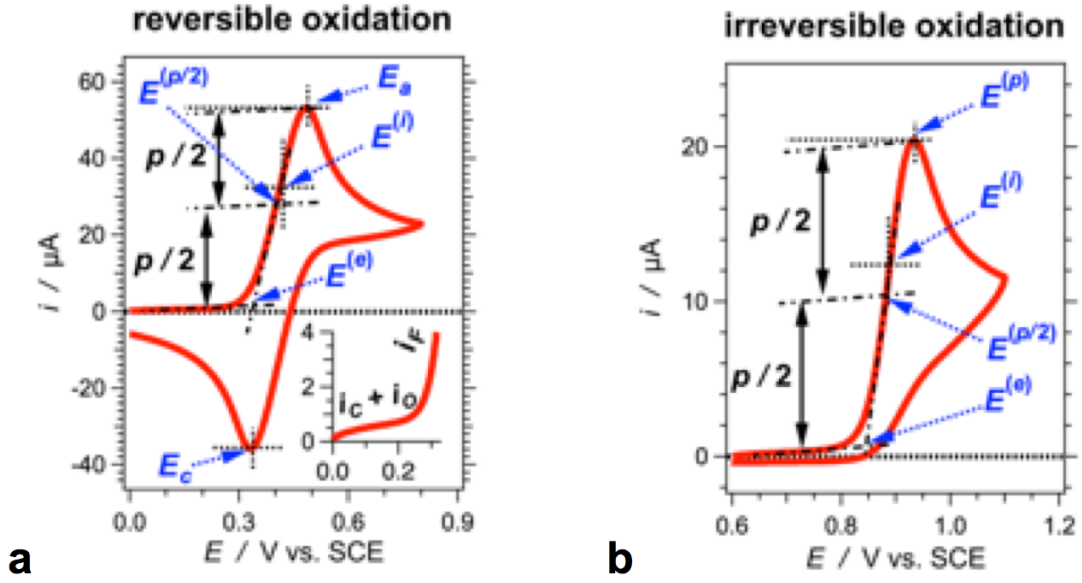

Figure 4-1. Examples of cyclic voltammograms showing chemically reversible and irreversible oxidation with designated potentials: E_a = anodic potential, E_c = cathodic potential, $E^{(i)}$ = inflection-point potential, $E^{(p/2)}$ = half-peak potential, $E^{(e)}$ = edge potential. (a) 1 mM ferrocene. Inset: the initiation of the scan showing the rise of the Faradaic current, i_F, on the background of the capacitance current, i_C, and the Ohmic current, i_O. (b) 1 mM 4Pip. (For both voltammograms: 200 mM $N(C_4H_9)_4PF_6$ in MeCN, and v = 100 mV s^{-1}.)

The conundrum is how to estimate $E^{(0)}$ from voltammograms showing chemically irreversible oxidation and reduction (Figure 4-1b). Another question is how well $E^{(1/2)}$ estimates $E^{(0)}$ in the cases of partial chemical reversibility. For the rest of this discussion, we refer to "chemical reversibility" as "reversibility."

Chemical conversion, such as decomposition or dimerization, of the species produced on the electrode surface upon oxidation or reduction is the source of the observed chemical irreversibility. Two principal approaches allow for gaining reversibility: (1) increasing the scan rates so that the acquisition of the voltammograms is much faster than the lifetime of the formed oxidized or reduced species; and (2) lowering the temperature in

order to slow down the undesired chemical conversions. The former approach produces voltammograms suffering from enormous capacitance currents (i_C) that are inherent for large scan rates. At scan rates of kV/s and MV/s, Faradaic signals can be orders of magnitude smaller than the background, and decreasing the area of the working electrode, in order to decrease i_C, decreases the signal-to-noise ratios. Conversely, lowering the temperature sufficiently enough to attain reversibility limits the number of usable solvents with acceptable electrochemical windows due to their freezing points. Indeed, both of these approaches are quite involved, and they have not gained popularity as routine methods for electrochemical analysis.

When cyclic voltammograms show irreversible behavior, the most common practice involves reporting the peak potentials ($E^{(p)}$), i.e., anodic potentials (E_a) for oxidation or cathodic potentials (E_c) for reduction (Figure 4-1a). Voltammograms of reversible processes, however, elucidate that the values of the peak potentials deviate quite a bit from $E^{(1/2)}$, especially for large scan rates.

Another option involves the use of the edge potentials ($E^{(e)}$) of the anodic or cathodic waves as estimates of $E^{(0)}$ of irreversible processes (Figure 4-1). At the edges of the voltammogram waves, $E^{(e)}$ represents the potentials of the first detectable Faradaic currents. Thus, $E^{(e)}$ underestimates $E^{(0)}$ of oxidation and overestimates $E^{(0)}$ of reduction by a few k_BT/F (k_BT is the thermal energy and F is the Faraday constant).

Conversely, we determined that the potentials, $E^{(i)}$ (Figure 4-1), at the inflection points of the anodic and cathodic waves are quite close to $E^{(1/2)}$ for reversible processes.[18] Therefore, we employ $E^{(i)}$ for estimating $E^{(0)}$ of irreversible oxidation and reduction.[19-23]

Recently, Nicewicz et al. proposed the use of the half-peak potentials ($E^{(p/2)}$) for estimating $E^{(0)}$ of cyclic voltammograms showing irreversibility (Figure 4-1).[24] For symmetrical sigmoid curves progressing along the ordinate, the inflection points are at their half-heights, but the voltammogram waves do not necessary have such a shape leading to the peaks.

Herein, we review $E^{(1/2)}$, $E^{(i)}$, $E^{(p/2)}$, $E^{(p)}$, and $E^{(e)}$ extracted from cyclic voltammograms for reversible, irreversible and partially reversible electrochemical oxidation. ANOVA analysis provides statistical quantification of how close the values of $E^{(i)}$, $E^{(p/2)}$, $E^{(p)}$, and $E^{(e)}$ are to those of $E^{(1/2)}$ for different scan rates. The values of $E^{(i)}$ are the closest to those of $E^{(1/2)}$, but $E^{(p/2)}$ fairs almost as well as $E^{(i)}$ in the statistical analysis. A straightforward differential analysis, i.e., the first and second derivatives of the cyclic voltammograms, provides convenient ways for determining peak potentials and inflection points. In addition, this differential approach proves immensely beneficial for estimating the reversibility of the electrochemical processes. Regression analysis reveals that even for partially reversible system, $E^{(1/2)}$ still provides a good estimate for $E^{(0)}$.

Experimental

Materials and general synthetic considerations.

All reagents and solvents were purchased from TCI America, Sigma-Aldrich and Alfa Aesar and used as received. The reaction progress was monitored by the means of thin layer chromatography (TLC), which was performed with aluminium foil plates, covered with silica gel 60 F254 (Merck). The products were purified using column chromatography packed with Kieselgel 60 (Merck). All reported ^{1}H-NMR and ^{13}C-NMR spectra were

recorded on a 600 MHz spectrometer. Chemical shifts (δ / ppm) were determined using the solvent peaks as internal references. High-resolution mass spectra were obtained using electrospray MS (ESI-MS).

2-nitro-N-(tert-pentyl)-4-(piperidin-1-yl)benzamide (1).

2-Nitro-4-(piperidin-N-yl)-benzoic acid (1.0 g, 4 mmol), prepared as previously described,[25] was placed in a 100 mL Schlenk tube equipped with a magnetic stir bar. While purging with argon, chloro-*N*,*N*,*N*′,*N*′- tetramethylformamidinium hexafluorophosphate (2.0 g, 6 mmol) and 5 mL of dry DCM were added. The Schlenk tube was immersed in a dry ice/acetone bath and 2-methylbutan-2-amine (940 μL, 8 mmol) was slowly added to it followed by the addition of *N*-methylmorpholine (1.5 mL, 14 mmol). The reaction mixture was allowed to warm up to room temperature and was stirred overnight. The solution was diluted with 25 mL of DCM, and washed with 5% HCL (2 × 100 mL) and with a brine solution (100 mL). The organic layer was collected, dried over Na_2SO_4, and concentrated *in vacuo*. The product was purified using flash chromatography (column: 1" internal diameter, packed with silica gel in hexanes, 6" to 8" height of the packed stationary phase). Purification using flash chromatography (stationary phase: silica gel; eluent gradient: from 100% hexanes to 100% ethyl acetate) afforded 1.01 g (3.17 mmol, 79% yield) of a yellow solid of 2-nitro-*N*-(*tert*-pentyl)-4-(piperidin-1-yl)benzamide. ^{1}H NMR (600 MHz, $CDCl_3$) δ/ppm: 7.34 (1 H, d, *J*=2.56 Hz), 7.30 (1 H, d, *J*=8.70 Hz), 7.00 (1 H, d, *J*=7.68 Hz), 5.43 (1 H, s), 3.27 (4 H, m), 1.79 (2 H, q, *J*=7.68 Hz), 1.67 (4 H, m), 1.62 (2H, m), 1.37 (s, 1 H), 0.91 (3 H, t, *J*=7.42 Hz). ^{13}C NMR (600 MHz, $CDCl_3$) δ/ppm: 165.87, 152.15, 148.25, 129.42, 122.43, 118.32, 109.84, 54.61, 49.22, 32.87, 26.19, 25.09, 24.00, 8.34. HRMS

(*m/z*, ESI-TOF): calcd. for $C_{17}H_{26}N_3O_3^+$: 320.1974 $[M + H]^+$; found, 320.1956.

N-(tert-pentyl)-4-(piperidin-1-yl)-2-(2-propylpentanamido)benzamide (4Pip).

1 (510 mg, 1.6 mmol) and dicobalt octacarbonyl (1.1 g, 3.2 mmol) were placed in a 100 mL Schlenk tube equipped with a magnetic stir bar. While purging with argon, 5 mL of 1,2-dimethoxyethane and 2 drops of DI water were added. While stirring, the pressure tube was immersed in a temperature-controlled oil bath. The mixture was heated to 90 °C and stirred for an hour. The reaction mixture was filtered; the filtrate was collected, diluted with 25 mL DCM, and washed with water (100 mL). The organic layer was collected, dried over Na_2SO_4, and concentrated *in vacuo*. The formed amine was used for the next step without further purification. While purging with argon, the resulting organic solid was transferred into a Schlenk tube using 5 mL dry DCM. The Schlenk tube was immersed in a dry ice/acetone bath, allowed to cool down, followed by addition of pivaloyl chloride (500 μL, 4 mmol) and *N*-methylmorpholine (750 μL, 6.8 mmol). The reaction mixture was allowed to warm up to room temperature and was stirred overnight. The solution was diluted with 25 mL of DCM, and washed with 5% HCL (2 ×100 mL) and with a brine solution (100 mL). The organic layer was collected, dried over Na_2SO_4, and concentrated *in vacuo*. The product was purified using flash chromatography (column: 1" internal diameter, was packed with silica gel in hexanes, 6" to 8" height of the packed stationary phase). Purification using flash chromatography (stationary phase: silica gel: eluent gradient: from 100% hexanes to 100% ethyl acetate) afforded 435 mg, (1.2 mmol, 73% yield) of 4Pip. ^{1}H NMR (600 MHz, $CDCl_3$) *δ*/ppm: 11.51 (1 H, s), 8.29 (1 H, s), 7.21 (1 H, m), 6.47 (1 H, s), 5.68 (1 H, s), 3.27 (4 H, s), 1.80 (2 H, q, *J*=7.17 Hz), 1.63 (4 H, s), 1.58

(2 H, s), 1.36 (6 H, s), 1.29 (10 H, s), 0.86 (3 H, t, J=7.42 Hz). ^{13}C NMR (600 MHz, $CDCl_3$) δ/ppm: 178.04, 168.99, 153.96, 141.31, 127.35, 111.18, 108.33, 106.54, 54.38, 48.94, 40.18, 32.72, 27.59, 26.52, 25.38, 24.30, 8.39. HRMS (*m/z*, ESI-TOF): calcd. for $C_{22}H_{36}N_3O_3^+$: 390.2757 $[M + H]^+$; found, 374.2814.

Methods.

CV measurements were conducted using Reference 600^{TM} Potentiostat / Galvanostat / ZRA (Gamry Instruments, PA, U.S.A.), connected to a three-electrode cell equipped with a glassy carbon working electrode, an SCE reference electrode (connected to the cell via a salt bridge), and a platinum counter electrode, as previously described.[26,27] The salt bridge was filled with a saturated KCl solution. Anhydrous acetonitrile (MeCN) was employed with different concentrations of a supporting electrolyte, $N(C_4H_9)_4PF_6$, $N(C_4H_9)_4BF_4$ and $LiClO_4$. Prior to recording each voltammogram the sample is extensively purged with argon while maintaining its volume constant by adding more of the anhydrous solvent. For each sample, a set of voltammograms is recorded where the electrolyte concentration is increased from 25 mM to 200 mM in increments of 25 mM, at scan rates, ν = 10, 20, 50, 100, 200 and 500 mV s^{-1}. For each sample and at each of the conditions and the scan settings, a triplicate of triplicates was measured, and the reported error bars represent plus-minus one standard deviation. That is, the same sample was measured three times in three different days, and at each measurement three voltammograms were recorded.

Analysis of the voltammograms and the obtained electrochemical potentials was carried out using Igor Pro, v. 7.02 (WaveMetrics, Inc., Lake Oswego, Oregon, U.S.A.).

The half-wave potentials, $E^{(1/2)}$, are determined from the midpoints between the cathodic and anodic peak potentials, E_a and E_c, respectively. E_a and E_c are determined from the zero points of the first derivatives of the voltammograms, i.e., the potentials where $\partial i/\partial E = 0$ at $\partial E/\partial t$ = constant. The inflection point potentials, $E^{(i)}$, are determined from the zero points of the second derivatives at the rising spans of the anodic waves of the voltammograms, i.e., the potentials where $\partial^2 i/\partial E^2 = 0$ at $\partial E/\partial t$ = constant. When the signal-to-noise ratios of the second derivatives are not high enough, they are smoothed using 4th order Savitzky-Golay algorithm. Linear fits of the voltammogram sections after the initial capacitance rise and before the Faradaic wave provide the estimates for the baselines. Similar linear fits of the anodic waves after the beginning of the initial Faradaic rise and before the curvature leading to the peak yields the anodic asymptotic lines. The edge potentials, $E^{(e)}$, are estimates from the points where these asymptotes cross the baselines. The peak heights, p, is determined from the current difference between the anodic peak and inclined baseline at the peak potential. The potentials at the points on the rising anodic wave that corresponds to p/2 provide the estimates for $E^{(p/2)}$. Functions, built in Igor Pro, were used for the statistical tests that produced the p-values.

Results and Discussion

General considerations.

Conducting CV measurements is relatively easy, which makes this technique as popular as it is. Setting up the reference electrode, however, can be a potential source for errors. While, for example, "pseudo reference" electrodes, such as silver wires, have their role in broadening the field, they inherently have a range of shortcomings that are beyond

the scope of this discussion. Conversely, we employ saturated calomel electrode (SCE) that, when not in use, we store in saturated aqueous solution of KCl. To prevent cross-contamination with the sample, we use a salt bridge for connecting the SCE electrode with the cell. Ideally, the salt bridge should contain the same solution with which the reference electrode is filled. It ensures that the electrolyte composition inside the electrode remains unchanged, and hence, prevents drifts of its potential during extended use.

When the reference electrode is water-based, however, such aqueous salt bridges present two practical issues for organic electrochemical analysis: (1) huge junction potentials between the bridge and the electrolyte solutions of the cell when using low-polarity solvents, such as $CHCl_3$ and CH_2Cl_2; and (2) water leakage from the bridge into the cell, which may present challenges when the dryness of the organic solution is important for the analysis. The use of a salt bridge that contains electrolyte solution in a moderately polar water-miscible organic solvent, such as acetonitrile and DMF, present a means for addressing both of those issues. Such a setup splits the huge junction potential into two moderate ones: at the bridge-electrode and the bridge-cell interfaces. Also, leaking an aprotic organic solvent with a wide electrochemical window into the sample solution is a better alternative to leaking water. This setup, however, is not ideal, either. Although it is slow, the diffusion of the component of the organic solution in such bridges across the frit of the reference electrode can cause drifts in the potential during extended use. Therefore, regular monitoring of the performance of the reference electrode, using samples with well-known potentials, is paramount for electrochemical analysis.

For analysis of reversible oxidation, we focus on ferrocene (Chart 4-1), which is one of the most broadly studied compounds in analytical electrochemistry and its voltammograms manifest pronounced reversibility.[28-31] In voltammetry, therefore, ferrocene has gained popularity as a convenient internal standard and frequently potentials are reported vs. its oxidation.[32-34] As robust as the ferrocene-ferrocenium redox couple is, its use for a reference should be approached with caution. The reduction potential of ferrocenium strongly depends on the solvent polarity and the electrolyte concentration.[26] (According to the accepted convention, $E^{(0)}$ represents the reduction potentials of the oxidized components of redox couples, regardless whether the voltammograms examine the reduction or oxidation propensity of the analyte.[35,36])

To illustrate CV analysis of irreversible and partially reversible oxidation, we focus on electron rich anthranilamide residues that we developed as building blocks for hole-transfer bioinspired molecular electrets.[37-40] Placing an amine on position 5, such as in 5Pip (Chart 4-1), stabilizes the radical cation and leads to reversible electrochemical behavior.[18,21] Moving the amine to position 4, however, e.g., 4Pip (Chart 4-1), causes a positive shift of the anodic wave along with irreversible behavior.[18,21] We demonstrated that eliminating the proton on the C-terminal amide of 4Pip and replacing it with an alkyl group stabilizes the radical cation, $4Pip^{\bullet+}$, leading to voltammograms showing partial reversibility and showing that the amide proton is involved in the oxidative degradation of 4Pip.[18] In this study, we test if the α-protons on the aliphatic chains attached to the two amides are responsible for the decomposition of $4Pip^{\bullet+}$. Therefore, we use a derivative of 4Pip capped with tertiary alkyl substituents (Chart 4-1).

Chart 4-1. Analytes used for this study.

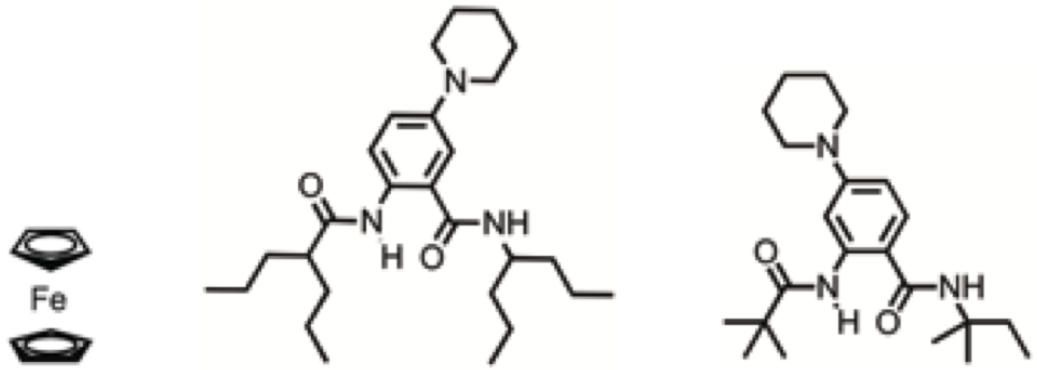

ferrocene **5Pip** **4Pip**

For a solvent, we employ dry acetonitrile (MeCN) because its moderately high polarity minimizes the dependence of the measured potentials on the electrolyte concentration, C_{el}.[26,27] Nevertheless, we still extrapolate the measured potentials to $C_{el} = 0$ (Figure 4-2), estimating their values for the neat solvent.[26,27] The extrapolated values of $E^{(1/2)}$ for electrolyte-free media relate the electrochemical findings with results from optical studies,[22,26,41] which prove especially invaluable for analyzing systems mediating photoinduced charge transfer.[19,42,43]

The best way to validate the extrapolation of potential values to $C_{el} = 0$ is to test the same analyte with different electrolytes in the same solvent. Furthermore, the extrapolated potentials should be invariant to the sample concentration. For three different supporting electrolytes and ferrocene concentration between 1 and 20 mM, the extrapolation to $C_{el} = 0$ yields values for $E^{(1/2)}$ that are the same within experimental uncertainty (Figure 4-2). This finding validates the extrapolation approach for estimating $E^{(1/2)}$ for neat solvents.

Conversely, the trends of $E^{(1/2)}$ vs. C_{el} reveal two features that are important for CV experimental designs. First, an increase in ferrocene concentration increases the standard deviations of the extrapolated potentials (Figure 4-2b). That is, increasing the analyte concentration increases the uncertainty of estimating the potentials for neat solvents, which appears to originate from deviations of the $E^{(1/2)}$ values for small C_{el}. This finding strongly suggests that the concentration of the supporting electrolyte should exceed the concentration of the analyte by at least a factor of 5 or 10.

Second, while lowering the electrolyte concentration converges $E^{(1/2)}$ to the same value, there is a significant difference between the potentials for perchlorate and the other two electrolytes (Figure 4-2a). Also, the values of $E^{(1/2)}$ for $LiClO_4$ show stronger dependence on C_{el} than those for the PF_6 and BF_4 salts. While increasing the concentration of the supporting electrolyte improves the conductance of electrochemical cells and decreases the Ohmic current (i_O), it also changes the dielectric constant of the solvent (ε). About ten years ago, we demonstrated that this variation in the dielectric properties of the media is responsible for the dependence of $E^{(1/2)}$ on C_{el} for electrolytes with bulky polarizable ions, such as $N(C_4H_9)_4PF_6$ and $N(C_4H_9)_4BF_4$.[26] The results for $LiClO_4$ appear to suggest that this salt drastically changes the properties of acetonitrile. Indeed, as a hard Lewis acid, Li^+ can affect the structure of solvents such as acetonitrile.[44] Still, it is unlikely for the lithium ions of the electrolyte to increase the dielectric constant of the solution to a large enough extent to induce 100-mV negative shifts of $E^{(1/2)}$ (Figure 4-2a). Considering the Born solvation energy, $E^{(1/2)}$ is proportional to $(1 - \varepsilon^{-1})$.[26,45] For polar media, therefore, variations in ε will have quite smaller effect on ε^{-1} (and on the reduction potentials) than

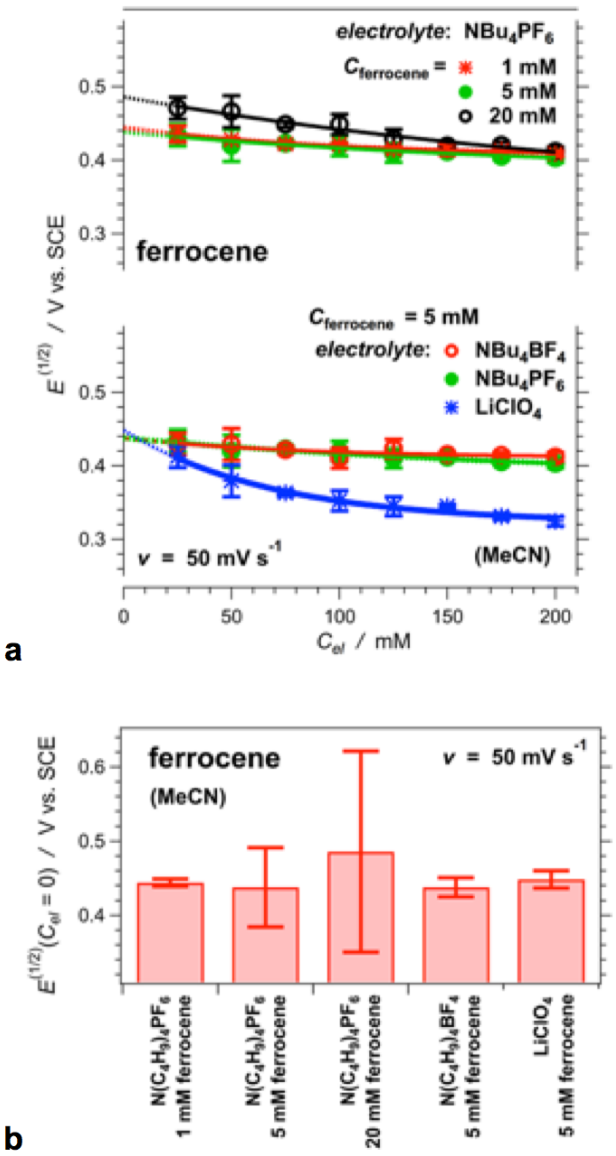

Figure 4-2. Extrapolation of the half-wave potentials of ferrocene to zero electrolyte concentration using different electrolytes and different ferrocene concentrations recorded at 50 mV s^{-1}. (a) Dependence of the half-wave potentials on the electrolyte concentration. The solid lines represent the data fits and the dotted lines – extrapolation to zero. (b) Comparison between the half-wave potentials obtained from the extrapolation to zero electrolyte concentration.

for non-polar solvents.[26,27] Hence, differences in the interactions between the electrolyte ions and the solvent cannot singlehandedly provide an explanation for the observed trends (Figure 4-2a).

Recently, Miller *et al.* demonstrated the drastic effects that pairing with the ions of the supporting electrolyte can have on electrochemical potentials.[46] The anions of the three electrolytes, PF_6^-, BF_4^- and ClO_4^-, have similar radii and comparable electronic properties.[47] Conversely, $N(C_4H_9)_4^+$ and Li^+ are distinctly different. Unlike $N(C_4H_9)_4^+$, small alkaline ions, such as Li^+ and Na^+, have a strong propensity for coordination with oxygen-containing ligands, such as water. In organic solvents, which cannot provide such ligation, these cations are often prone to

aggregation with the analyte. As an electron-rich compound, ferrocene has nucleophilic properties[48-50] and a propensity for binding alkaline ions,[51] especially Li^+.[52-54]

Binding lithium ions adds positive charges to the complexes with ferrocene and should impede the extraction of electrons. Hence, $LiClO_4$ should cause a positive shift in the reduction potential, which is contrary to what we observe (Figure 4-2a).

While electrochemical potentials correlate with the energy levels of the frontier orbitals of the analyte,[55-62] $FE^{(0)}$ and $FE^{(1/2)}$ of the oxidation and reduction do not measure the energies, respectively, of the highest occupied molecular orbitals (HOMOs) and the lowest unoccupied molecular orbitals (LUMOs). That is, the negative $E^{(1/2)}$ shifts,

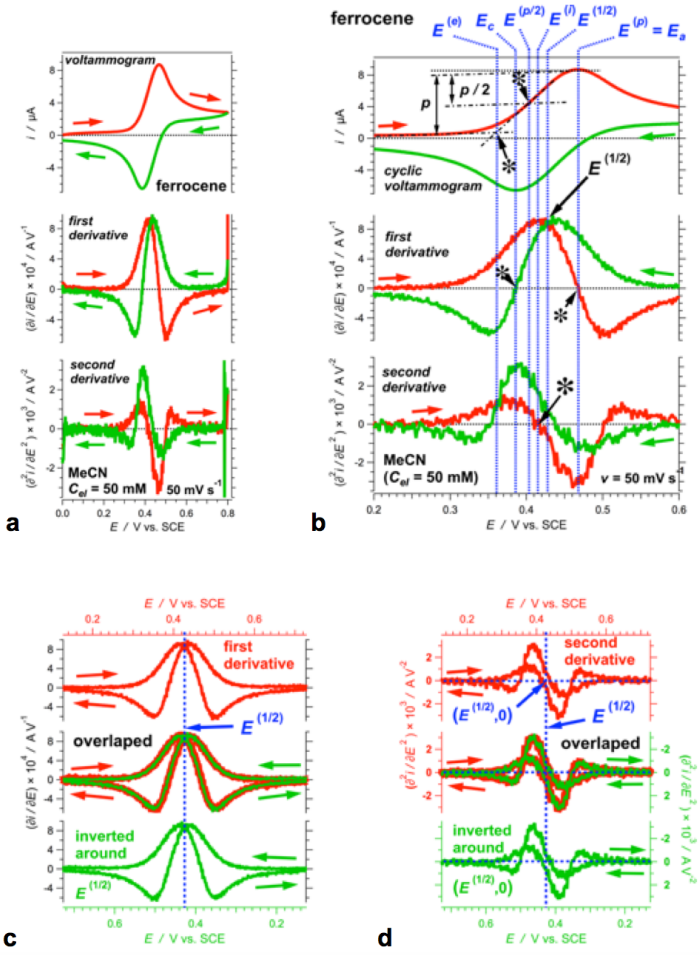

Figure 4-3. Cyclic voltammogram and its derivatives of ferrocene (1 mM), recorded in the presence of 50 mM $N(C_4H_9)_4PF_6$ as a supporting electrolyte at 50 mV s^{-1}. (a) The voltammograms and its first and second derivatives where different colors represent the forward and the back scans as designated by the arrows. (b) Representation of the voltammogram and its derivatives, zoomed on the anodic and the cathodic waves, with designation of the different potentials of interest. (c) Demonstration of the axial symmetry of the first derivative. The derivative (upper curve) and its representation inverted around $E = E^{(1/2)}$ (lower curve) overlap perfectly (middle curves). (d) Demonstration of the centrosymmetric shape the second derivative. The derivative (upper curve) and its representation inverted around $E = E^{(1/2)}$ and around $i = 0$ (lower curve) overlap perfectly (middle curves).

induced by $LiClO_4$ (Figure 4-2a), do not indicate that the electrolyte raises the HOMO energy of ferrocene. Rather, $FE^{(1/2)}$ measures energy differences between the oxidized and the reduced forms of the analyte. Differences between the solvation energies of these two forms further modulate $E^{(1/2)}$. The change in the analyte charge during oxidation or reduction is the principal contribution to these solvation-energy differences.

Therefore, a loss of a lithium ion during the oxidation of Li^+-ferrocene complexes can account for the observed trends (Figure 4-2a). In addition to an entropic gain, oxidizing a Li^+-ferrocene complex to a ferrocenium ion conserves the positive charge on the analyte and minimizes the changes in the solvation energy, assuming that the excess number of ClO_4^- counterions can readily "assimilate" the released Li^+ ions. In this manner, Li^+ interaction with ferrocene can improve the ease of its oxidation and lower the reduction potential (Figure 4-2a).

Overall, the supporting electrolyte is not necessarily a passive component of the samples. For the rest of the study, we employ $N(C_4H_9)_4PF_6$, and limit the analyte concentration to 1 mM to ensure reliable extrapolation to $C_{el} = 0$.

Reversible oxidation.

The first and the second derivatives of cyclic voltammograms are immensely instrumental for determining some of the key potentials of the analyte (Figure 4-3a,b). The zero values of the first derivatives, $\partial i/\partial E = 0$, yield the peak potentials, E_a and E_c, essential for calculating $E^{(1/2)}$, i.e., $E^{(1/2)} = (E_a + E_c) / 2$ (Figure 3b). Also, for oxidation, the peak potentials of interest correspond to the anodic peaks, i.e., $E^{(p)} = E_a$. The potentials at which

the second derivatives assume zero, $\partial^2 i/\partial E^2 = 0$, represent the inflection points of the voltammograms and provide a straightforward way for determining $E^{(i)}$ (Figure 4-3b).

The derivatives also reveal a range of subtle details that are not truly apparent in the voltammogram. After all, differentiation eliminates the offset induced by i_C and yields in a constant value for the small linear rise due to i_R (Figure 4-1, 4-3). Visual inspection of the derivatives allows for facile examination of the reversibility. If a process is reversible, the first derivatives of its cyclic voltammograms have axial symmetry across $E = E^{(1/2)}$ with the forward and back sweep crossing at $E^{(1/2)}$ (Figure 4-3c). In addition, reversibility yields second derivatives that are centrosymmetric around the point on the ordinate corresponding to the half-wave potential, i.e., ($E^{(1/2)}$,0) (Figure 4-3d). As revealed by their derivatives, all voltammograms of ferrocene manifest reversibility.

The cyclic voltammograms of irreversible oxidation does not show cathodic peaks and cannot provide a means for estimating $E^{(1/2)}$ from E_a and E_c. Therefore, using the characteristic of the anodic waves of reversibly oxidizable ferrocene provides the ideal means for examining which of the potentials have values close to those of $E^{(1/2)}$. In addition to $E^{(i)}$ and $E^{(p)}$, which we estimate from the derivatives of the voltammograms, we also examined $E^{(p/2)}$ and $E^{(e)}$. The half-height peak potential, $E^{(p/2)}$, corresponds to the potential of the rising anodic wave that is in the middle between the peak and the baseline (Figure 4-1, 4-3b). The crossing of the asymptotic lines of the baseline and the rising anodic wave provides the estimates for the edge potentials $E^{(e)}$ (Figure 4-1, 4-3b).

Because $E^{(0)}$ is a fundamental characteristic, it is invariant to experimental parameters, such as scan rate (v). To examine the invariance of the different potentials on

Table 4-1. *p*-values from linear regression tests of the dependence of the different potentials on the scan rate.[a]

potential		ferrocene		5Pip
	C_{el} =	100 mM	0 mM [b]	0 mM [b]
$E^{(1/2)}$		0.14	0.27	0.054
$E^{(i)}$		5.1×10^{-6}	0.014	4.2×10^{-4}
$E^{(p/2)}$		2.5×10^{-9}	6.8×10^{-3}	5.6×10^{-4}
$E^{(p)}$		1.7×10^{-7}	3.3×10^{-3}	3.7×10^{-5}
$E^{(e)}$		0.023	0.11	0.20

[a] H_0: The relation E vs. v has a slope 0. Small p-values permit rejection of H_0 and suggest that E depends on v. [b] From extrapolation to zero electrolyte concentration.

the scan rates (Figure 4-4), we resort to a linear regression analysis with a null hypothesis (H_0) that the linear relationship E vs. v has a slope 0. The calculated p-values represent the probability to obtain the measured potentials if H_0 is correct. While such analysis does not validate H_0, it can readily allow rejecting H_0 when p is a small number, i.e., when $p < \alpha$, and $\alpha = 0.01$, 0.05 or 0.1 depending on the selected confidence interval. The immensely small p-values for $E^{(p)}$, $E^{(i)}$ and $E^{(p/2)}$, extracted from voltammograms of samples with different electrolyte concentrations (Table 4-1), clearly show that we can readily reject the H_0 for these potentials. We can also reject H_0 for $E^{(e)}$ for $\alpha = 0.05$ or larger. That is, $E^{(p)}$, $E^{(i)}$, $E^{(e)}$ and $E^{(p/2)}$ show dependence on v with 95% confidence (Figure 4a). Examining the scan-rate dependence of the extrapolated potentials for neat solvent reveal the same trends (Figure 4b). While the extrapolation increases the uncertainty and the p-values, we can still reject the H_0 for $E^{(p)}$, $E^{(i)}$ and $E^{(p/2)}$ with the same confidence of 95% (Table 4-1).

The edge potential, $E^{(e)}$, appears to show some invariance to v (Figure 4-4). Despite the relatively small uncertainty (small standard deviations) of its estimates, its p-values are not too small, i.e., $p > 0.01$ for $C_{el} = 100$ mM and $p > 0.1$ for a neat solvent. This finding indicates that the inception of the Faradaic signal does not have a strong dependence on

the scan rate, which is consistent with large electron-transfer rates and with a relatively large amount of analyte adsorbed on the surface of the working electrode.

Because of the lack of invariance with v for most of the potentials, we test how close $E^{(p)}$, $E^{(i)}$, $E^{(p/2)}$ and $E^{(e)}$ are to $E^{(1/2)}$ for each scan rates. We employ a Welch's analysis of variance (ANOVA) where H_0 states that the means of the compared potentials are the same, and the p-values represent the probability of obtaining the observed values when H_0 is correct. While small p-values, i.e., $p < \alpha$, permit rejection of H_0, ANOVA does not provide the basis for accepting H_0 when $p > \alpha$.

For data directly obtained from the measured voltammograms, e.g., for C_{el} = 100 mM, we can clearly reject H_0 for $E^{(e)}$ and $E^{(p)}$ with 95% confidence (Table 4-2). That is, the peak potentials and the edge potentials are not a good representation of $E^{(1/2)}$, and of $E^{(0)}$ for that matter. For $E^{(p/2)}$, only v = 200 and 500 mV s^{-1} yield p larger than about 0.05 and we can reject H_0 with 95% confidence for most of the examined scan rates (Table 4-2). Hence, $E^{(p/2)}$ is not a good representation of $E^{(1/2)}$ and of $E^{(0)}$ for small scan rates.

The ANOVA tests for the inflection potential, $E^{(i)}$, appear most encouraging. If we adopt a less conservative 90% confidence, we can perhaps reject H_0 only for 10 and 20 mV s^{-1}. With 95% confidence, however, we cannot truly reject H_0 for any of the scan rates for $E^{(i)}$. While ANOVA does not validate the acceptance of H_0, these findings imply that the inflection potentials provide the best estimates for $E^{(0)}$, when $E^{(1/2)}$ cannot be calculated due to irreversibility, for example.

The extrapolation of the different potentials to C_{el} = 0 adds uncertainty in their estimates, which affects the outcome of the ANOVA tests. While the trends appear the

same, the *p*-values for the extrapolated potentials are larger than the *p*-values for those obtained directly from the voltammograms, e.g., for C_{el} = 100 mM (Table 4-2). With 95% confidence we can still reject H_0 for the edge potentials even at $C_{el} = 0$, confirming that $E^{(e)}$ does not provide a good estimate for $E^{(0)}$. We cannot reject H_0 for any of the other cases for $C_{el} = 0$, except perhaps for $E^{(p)}$ at 500 mV s^{-1}, assuming 90% confidence (Table 4-2).

Overall for oxidation of ferrocene, the inflection potentials, $E^{(i)}$, provides the best estimates for $E^{(0)}$ (Table 4-2). The half-peak potentials, $E^{(p/2)}$, also appear promising for representing $E^{(0)}$, especially for larger scan rates. The peak potentials, $E^{(p)}$, are positively shifted from $E^{(1/2)}$ by 30 to 100 mV (Figure 4-4). With this level of uncertainty, however, the peak potentials, $E^{(p)}$, could be representative of $E^{(1/2)}$ but only for small scan rates. In contrast, for all cases the edge potentials, $E^{(e)}$, underestimate $E^{(1/2)}$ by about 70 – 80 mV for all scan rates (Figure 4-4), and should not be used for representing $E^{(0)}$.

While $E^{(1/2)}$ and $E^{(e)}$ are invariant to *v*, an increase in the scan rate causes positive shifts of $E^{(p)}$, $E^{(p/2)}$ and $E^{(i)}$ (Figure 4-4). These shifts bring the values of $E^{(p)}$ away from $E^{(1/2)}$ and the values of $E^{(i)}$ and $E^{(p/2)}$ closer to $E^{(1/2)}$. While at truly small scan rates, peak potentials can represent $E^{(0)}$ with some uncertainty, the values of $E^{(p)}$ can never overlap with those of $E^{(1/2)}$. Conversely, an increase in the scan rates makes $E^{(i)}$ closely overlap with $E^{(1/2)}$ for *v* of 100 mV s^{-1} and larger (Figure 4-4). The values of $E^{(p/2)}$ show a similar trend and an overlap with $E^{(1/2)}$ at 500 mV s^{-1}. For the examined scan rates, however, the

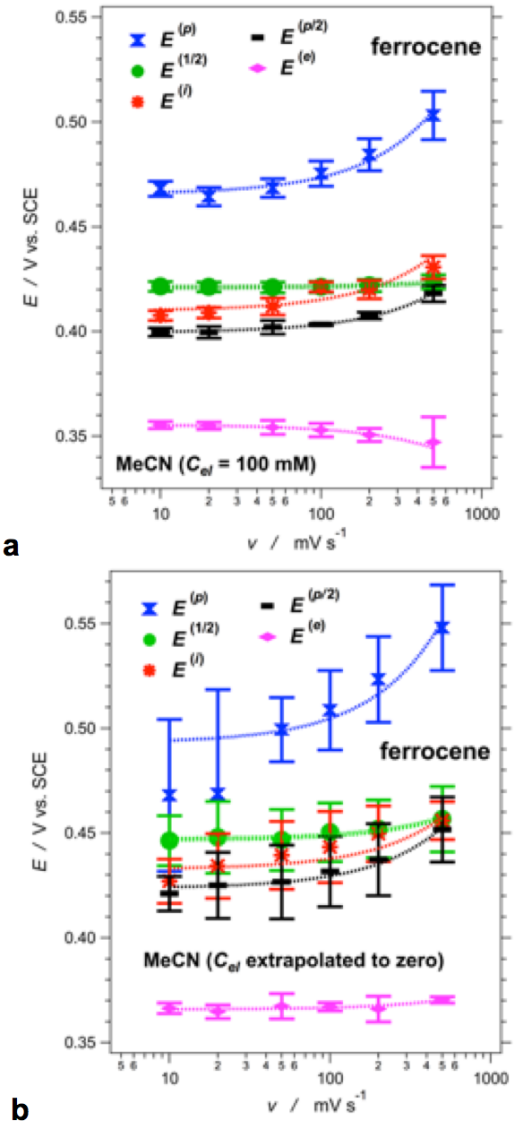

Figure 4-4. Dependence of the different potentials of ferrocene (1 mM) on the scan rate. (a) The potentials are obtained from voltammograms recorded for samples containing 100 mM $N(C_4H_9)_4PF_6$ as a supporting electrolyte. (b) The potentials are obtained from extrapolation to zero electrolyte concentration.

half-peak potentials show larger underestimates of $E^{(1/2)}$ than $E^{(i)}$, making the inflection potentials the preferred representation of $E^{(0)}$ when $E^{(1/2)}$ is inaccessible.

When partial irreversibility is not obvious.

Ferrocene-ferrocenium is an extensively studied well-behave redox couple and serves as an excellent model for testing concepts and ideas. To further validate and expand the findings from the ferrocene studies, we focus on an electron-rich amidated non-native amino acid, 5Pip (Chart 4-1), the dipole of which can induce significant rectification of charge transfer.[42]

The cyclic voltammograms of 5Pip show excellent reversibility in anhydrous media, especially for polarizable solvents, such as CH_2Cl_2.[18,21] We observe similar behavior of 5Pip for this setup with aqueous salt bridge, but only at high scan rates (Figure

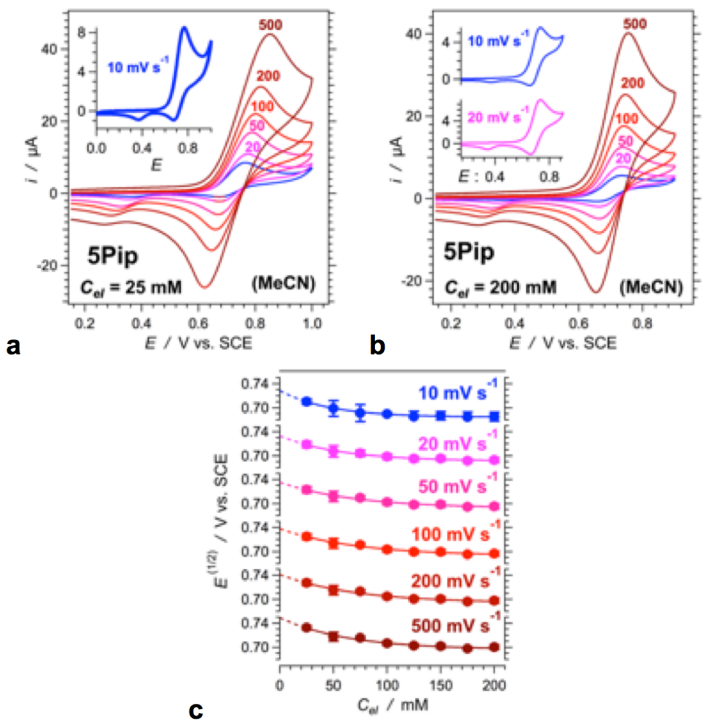

Figure 4-5. Cyclic voltammograms of 5Pip (1 mM) recorded at different scan rates in the presence of different concentrations of $N(C_4H_9)_4PF_6$ as a supporting electrolyte. (a,b) Voltammograms of samples containing 25 and 200 mM electrolyte. (c) Dependence of the half-wave potentials on the electrolyte concentration for the different scan rates. The solid lines represent the data fits and the dotted lines – the extrapolation to zero electrolyte concentration.

4-5a,b). At scan rates of 10 and 20 mV s^{-1}, however, the cathodic wave appears smaller than the anodic peak; and an additional small cathodic peak at about 0

.3 V vs. SCE becomes apparent (insets of Figure 4-5a,b).

The first derivatives of the cyclic voltammograms of 5Pip clearly show a lack of symmetry for small scan rates, which is consistent with deviation from reversibility (Figure 4-6). As the scan rates increase, the first derivatives gradually gain symmetry and the additional cathodic peak at 0.3 V vs. SCE becomes less apparent. At 500 mV s^{-1}, the oxidation is practically reversible, i.e., the first derivative exhibits axial symmetry across $E^{(1/2)}$, and the area of the second cathodic peak drops to less than 5% of the area under the anodic wave.

These findings are consistent with degradation of the oxidized analyte, $5Pip^{\bullet+}$, within the timescales of acquisition at small scan rates. The timespans between the beginning of the anodic and the completion of the cathodic waves range from about 2 s, for 500 mV s^{-1}, to about 70 s, for 10 mV s^{-1} (Figure 4-6c). Hence, the observed partial

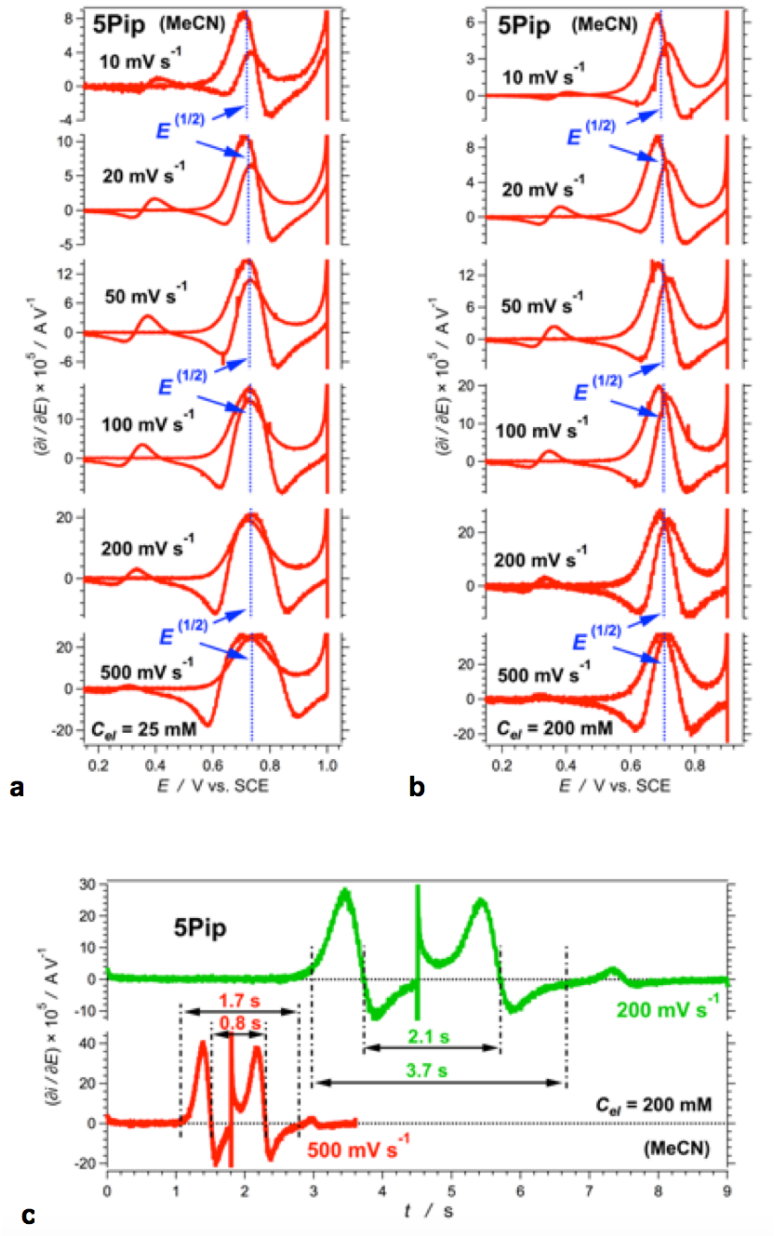

Figure 4-6. First derivatives of cyclic voltammograms of 5Pip (1 mM) recorded at different scan rates in the presence of 25 and 200 mM of $N(C_4H_9)_4PF_6$ as a supporting electrolyte. (a,b) the first derivatives. The obtained half-wave potentials are shown. (c) Dependence of the first derivatives on the scanning time showing the durations of data acquisition for different scan rates.

reversibility is consistent with a lifetime of $5Pip^{\bullet+}$ that is in the order of 100 s under the conditions of the measurements.

Regardless the partial irreversibility, the presence of anodic and cathodic peaks allows for estimating the half-wave potentials of 5Pip for different scan rates and electrolyte concentrations. Extrapolation to C_{el} = 0 yields similar values of $E^{(1/2)}$ for the different scan rates (Figure 4-5c). Increasing v from 10 to 500 mV s^{-1} increases $E^{(1/2)}(C_{el} = 0)$ from about 0.73 to 0.75 V vs. SCE (Figure 4-7). The results for $E^{(1/2)}$ at 500 mV s^{-1} are the best estimates for $E^{(0)}$ because of the reversibility at

this scan rate. Despite the induced irreversibility, decreasing the scan rates by a factor of 50 changes $FE^{(1/2)}$ by less than k_BT. This finding has important implications, demonstrating that even for partially reversible behavior, $E^{(1/2)}$ still provides the best estimates for $E^{(0)}$.

The extrapolated potentials for a neat solvents show that $E^{(1/2)}$, $E^{(i)}$ and $E^{(p/2)}$ of 5Pip practically overlap (Figure 4-7), and the ANOVA tests yield large *p*-values when comparing $E^{(1/2)}$ with $E^{(i)}$ and $E^{(p/2)}$ (Table 4-2). The values of $E^{(p)}$ and $E^{(e)}$ are distinctly separated from $E^{(1/2)}$ (Figure 7), and except for 10 mV s^{-1}, all *p*-values from the ANOVA test comparing $E^{(e)}$ with $E^{(1/2)}$ are smaller than 0.05 (Table 4-2). While the differences between $E^{(p)}$ with $E^{(1/2)}$ are similar to those between $E^{(e)}$ with $E^{(1/2)}$, the ANOVA *p*-values for $E^{(p)}$ vs. $E^{(1/2)}$ are quite large due to uncertainty of estimating the peak potentials, which is similar to what we observe for ferrocene (Table 4-2). While the statistical analysis does not allow the rejection of H_0, as an indication that $E^{(p)}$ vs. $E^{(1/2)}$ are significantly different, the large

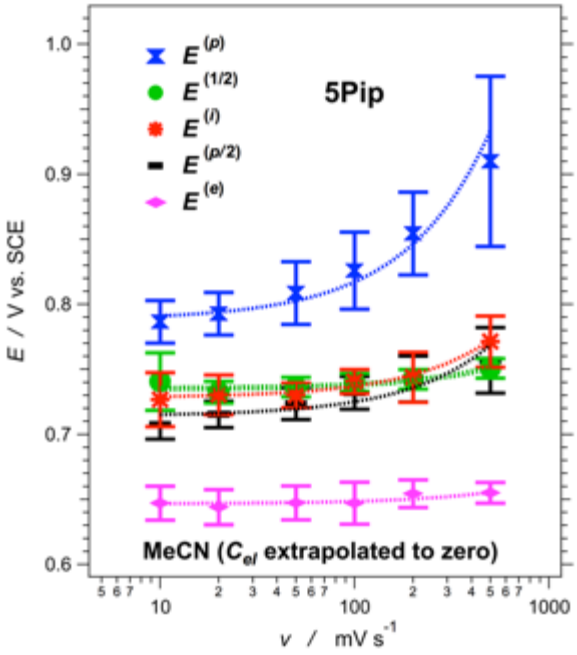

Figure 4-7. Dependence of the different potentials of 5Pip (1 mM) on the scan rate. The potentials are obtained from extrapolation to zero concentration of $N(C_4H_9)_4PF_6$ (Figure 5c).

variations in the estimates $E^{(p)}$ (Figure 4-4b, 4-7) renders the peak potentials unattractive for quantification of molecular electronic characteristics.

Irreversible behavior.

For systems undergoing irreversible oxidation or reduction, $E^{(p)}$ (i.e., E_a or E_c, respectively) is the most frequent choice for representing their electrochemical potentials. This practice has a lot of shortcomings since the peak potentials are immensely sensitive

Table 4-2. *p*-values from Welch's ANOVA tests comparing $E^{(1/2)}$ the other potentials.[a]

sample	C_{el} / mM	v / mV s^{-1}	($E^{(1/2)}$, $E^{(i)}$)	($E^{(1/2)}$, $E^{(p/2)}$)	($E^{(1/2)}$, $E^{(p)}$)	($E^{(1/2)}$, $E^{(e)}$)
ferrocene	100	10	0.050	0.019	8.2×10^{-3}	1.8×10^{-3}
		20	0.070	0.027	0.013	1.9×10^{-3}
		50	0.19	0.043	0.011	3.9×10^{-3}
		100	0.42	0.022	0.015	3.8×10^{-3}
		200	0.75	0.049	0.017	3.6×10^{-3}
		500	0.40	0.39	0.022	0.022
	0 [b]	10	0.35	0.22	0.72	0.022
		20	0.61	0.43	0.73	0.041
		50	0.77	0.47	0.13	0.038
		100	0.78	0.48	0.13	0.028
		200	0.91	0.57	0.10	0.029
		500	0.97	0.84	0.071	0.032
5Pip	0 [b]	10	0.68	0.31	0.23	0.067
		20	0.91	0.33	0.081	0.031
		50	0.65	0.47	0.10	0.027
		100	0.96	0.63	0.11	0.034
		200	0.94	0.99	0.076	0.021
		500	0.42	0.83	0.14	0.013

[a] H_0: $E^{(1/2)}$ and $E^{(x)}$ have the same means, where $x = i, p/2, p$ and e. Small p-values permit rejection of H_0 and suggest that $E^{(1/2)}$ and $E^{(x)}$ have different values. [b] From extrapolation to zero electrolyte concentration.

to experimental settings (e.g., scan rate, sample concentration, and electrolyte concentration), and the inherent properties of the redox couples (e.g., rates of interfacial electron transfer and diffusion). The studies with ferrocene and 5Pip show that inflection and half-peak potentials provide good estimates of $E^{(0)}$, better than the peak potentials. To illustrate how they compare for irreversible oxidation, we choose another electron-rich non-native amino acid derivative, 4Pip (Chart 4-1), forming a radical cation that is unstable under the CV conditions.[18,21]

In anthranilamide (Aa) residues, moving the amine from 5th to 4th position (i.e., 5Pip vs. 4Pip) makes the oxidation of these derivatives completely irreversible due to a significant change in the spin-density distribution in their radical cations.[18] Extending the positive charge of $Aa^{\bullet+}$ moieties over their C-terminal amides leads to decomposition. A loss of an amide proton is a possible path for this oxidative degradation. As we showed, derivatizing 4Pip with a tertiary C-terminal amide, i.e., -C(O)N(R_2)-, induces partial reversibility.[18] It confirms that the C-terminal amide proton contributes to the instability of $4Pip^{\bullet+}$ but is not solely responsible for the oxidative degradation.

Another possibility involves the alkyl α-protons next to the amides. In all Aa derivatives, these α-protons are deshielded, with chemical shifts downfield from those of the rest of the alkyl protons, which may make them labile enough under oxidative conditions. To test it, in this study we capped 4Pip amides with tertiary alkyl chains (Chart 4-1). For all scan rates and electrolyte concentrations, the cyclic voltammograms of the *t*-alkyl capped 4Pip show complete irreversibility, with no detectable cathodic peaks. Hence,

removal of the α-protons next to the amides does not stabilize the radical cation of 4Pip for the timescales of the CV data acquisition.

The first and second derivatives of the cyclic voltammograms of the irreversible oxidation of 4Pip do not show symmetric features (Figure 4-8a). The derivatives of the anodic wave of 4Pip appear the same as those of ferrocene and 5Pip. It is, however, the derivatives of the cathodic waves that discern irreversible from reversible oxidation (Figure 4-3, 4-6, 4-8a).

Because the anodic waves of the voltammograms and their derivatives are quite similar for analytes undergoing reversible and irreversible oxidation, we can reliably use them for estimating $E^{(i)}$, $E^{(p/2)}$ and $E^{(e)}$, in addition to $E^{(p)}$ (Figure 4-8a), and extrapolate them to zero electrolyte concentration. Similar to 5Pip, the scan-rate dependence of the extrapolated potentials of 4Pip show clustering of the values for $E^{(i)}$ and $E^{(p/2)}$. Conversely, $E^{(e)}$ and $E^{(p)}$ are well separated from $E^{(i)}$ and $E^{(p/2)}$ (Figure 4-8b).

As the scan rates vary from 10 to 500 mV s^{-1}, $E^{(p)}$ of 4Pip increases with 150 mV, while $E^{(i)}$ and $E^{(p/2)}$ increase with about 80 mV (Figure 4-8b). For 4Pip, this increase in the potentials is predominantly at the small scan rates. Hence, between 100 and 500 mV s^{-1}, $E^{(i)}$ and $E^{(p/2)}$ of 4Pip vary within about 40 mV (i.e., less than $2k_BT$), while the $E^{(p)}$ of 4Pip varies over 100 mV (Figure 4-8b). Considering that reversible oxidation results in the best overlap of $E^{(1/2)}$ with $E^{(i)}$ and $E^{(p/2)}$ at scan rates between 100 and 500 mV s^{-1} (Figure 4-4, 4-7), which is the range where $E^{(i)}$ and $E^{(p/2)}$ of 4Pip show the smallest dependence on v, makes the inflection and half-peak potentials the best estimate for $E^{(0)}$ of the irreversibly behaving systems, 4Pip.

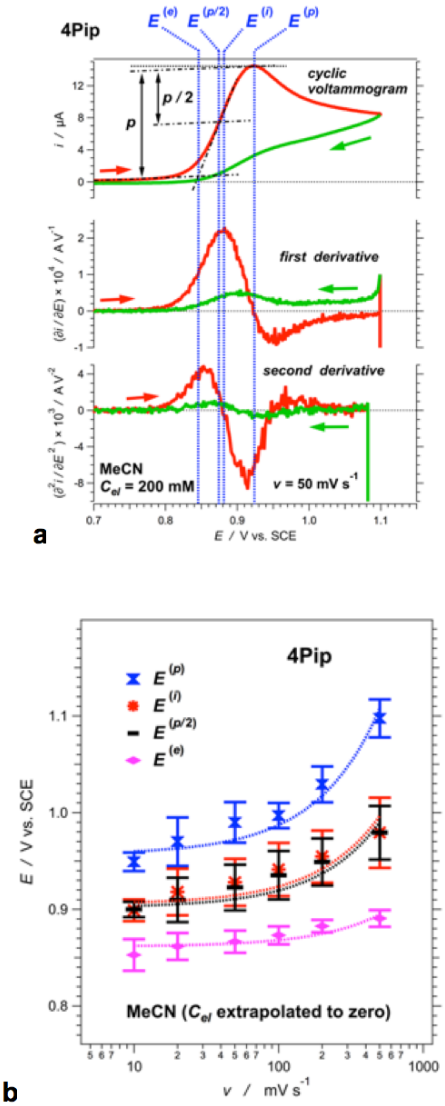

Figure 4-8. Electrochemical properties of 4Pip. (a) Cyclic voltammogram, along with its first and second derivative, of 4Pip (1 mM) recorded at 50 mV s^{-1} in the presence of 200 mM $N(C_4H_9)_4PF_6$. The different potentials obtainable from the anodic wave are designated. (b) Dependence of the different potentials of 4Pip on the scan rate. The potentials are obtained from extrapolation to zero concentration of $N(C_4H_9)_4PF_6$.

Conclusion

The half-wave potential, which are readily obtainable from cyclic voltammograms, are by far the best representation for $E^{(0)}$ even in cases manifesting partial irreversibility due to slow decomposition of the produced species. Conversely, all evidence suggest that when $E^{(1/2)}$ is not attainable due to complete chemical irreversibility, the inflection potentials and the half-peak potentials provide the best estimates for $E^{(0)}$, for moderate scan rates, e.g., 100 – 500 mV s^{-1}. While in many cases $E^{(i)}$ and $E^{(p/2)}$ perform almost the same, the values of $E^{(i)}$ tend to be inherently closer to $E^{(1/2)}$ than those of $E^{(p/2)}$. This report provides an important foundation and key evidence for transforming widely accepted practices of analyzing electrochemical findings in order to improve and broaden their utility.

References

1. C. Costentin, J.-M. Saveant and C. Tard, *ACS Energy Lett.*, **3**, 695 (2018).

2. N. Arshad and S. I. Farooqi, *Appl. Biochem. Biotechnol.*, **186**, 1090 (2018).

3. N. T. Rodeberg, S. G. Sandberg, J. A. Johnson, P. E. M. Phillips and R. M. Wightman, *ACS Chem. Neurosci.*, **8**, 221 (2017).

4. F. Harnisch and S. Freguia, *Chem. Asian J.*, **7**, 466 (2012).

5. I. Hwang and K. Yong, *ChemElectroChem*, **2**, 634 (2015).

6. C. E. Nebel, B. Rezek, D. Shin and H. Watanabe, *Physica Status Solidi A*, **203**, 3273 (2006).

7. N. Armaroli, G. Accorsi, F. Song, A. Palkar, L. Echegoyen, D. Bonifazi and F. Diederich, *ChemPhysChem*, **6**, 732 (2005).

8. D. A. C. Brownson *et al.*, in *The Handbook of Graphene Electrochemistry*, D. A. C. Brownson and C. E. Banks Editors, p. 23, Springer-Verlag London Ltd. (2014).

9. B. J. Adesokan, X. Quan, A. Evgrafov, A. Heiskanen, A. Boisen and M. P. Soerensen, *J. Electroanal. Chem.*, **763**, 141 (2016).

10. N. Elgrishi, K. J. Rountree, B. D. McCarthy, E. S. Rountree, T. T. Eisenhart and J. L. Dempsey, *J. Chem. Educ.*, **95**, 197 (2018).

11. N. V. Rees and R. G. Compton, *Chem. Commun.*, **46**, 4238 (2010).

12. J. A. V. Butler, *Trans. Faraday Soc.*, **19**, 734 (1924).

13. T. Erdey-Gruz and M. Volmer, *Z. physik. Chem.*, **150**, 203 (1930).

14. R. A. Marcus, *Angew. Chem. Int. Ed. Engl.*, **32**, 1111 (1993).

15. C. Batchelor-McAuley, E. Kaetelhoen, E. O. Barnes, R. G. Compton, E. Laborda and A. Molina, *ChemistryOpen*, **4**, 224 (2015).

16. E. Laborda, M. C. Henstridge, C. Batchelor-McAuley and R. G. Compton, *Chem. Soc. Rev.*, **42**, 4894 (2013).

17. R. M. Wightman, M. R. Deakin, P. M. Kovach, W. G. Kuhr and K. J. Stutts, *J. Electrochem. Soc.*, **131**, 1578 (1984).

18. E. M. Espinoza, J. M. Larsen and V. I. Vullev, *J. Phys. Chem. Lett.*, **7**, 758 (2016).

19. A. Purc, E. M. Espinoza, R. Nazir, J. J. Romero, K. Skonieczny, A. Jeżewski, J. M. Larsen, D. T. Gryko and V. I. Vullev, *J. Am. Chem. Soc.*, **138**, 12826 (2016).

20. E. M. Espinoza, J. M. Larsen-Clinton, M. Krzeszewski, N. Darabedian, G. D. T. and V. I. Vullev, *Pure Appl. Chem.*, **89**, 1777 (2017).

21. J. M. Larsen-Clinton, E. M. Espinoza, M. F. Mayther, J. Clark, C. Tao, D. Bao, C. M. Larino, M. Wurch, S. Lara and V. I. Vullev, *Phys. Chem. Chem. Phys.*, **19**, 7871 (2017).

22. E. M. Espinoza, J. A. Clark, J. B. Derr, D. Bao, B. Georgieva, F. H. Quina and V. I. Vullev, *ACS Omega*, **3**, 12857 (2018).

23. H. G. Ryu, M. F. Mayther, J. Tamayo, C. Azarias, E. M. Espinoza, M. Banasiewicz, L. G. Lukasiewicz, Y. M. Poronik, A. Jezewski, J. Clark, J. B. Derr, K. H. Ahn, D. T. Gryko, D. Jacquemin and V. I. Vullev, *J. Phys. Chem. C*, Ahead of Print (2018).

24. H. G. Roth, N. A. Romero and D. A. Nicewicz, *Synlett*, **27**, 714 (2016).

25. J. M. Larsen, E. M. Espinoza, J. D. Hartman, C.-K. Lin, M. Wurch, P. Maheshwari, R. K. Kaushal, M. J. Marsella, G. J. O. Beran and V. I. Vullev, *Pure Appl. Chem.*, **87**, 779 (2015).

26. D. Bao, B. Millare, W. Xia, B. G. Steyer, A. A. Gerasimenko, A. Ferreira, A. Contreras and V. I. Vullev, *J. Phys. Chem. A*, **113**, 1259 (2009).

27. D. Bao, S. Ramu, A. Contreras, S. Upadhyayula, J. M. Vasquez, G. Beran and V. I. Vullev, *J. Phys. Chem. B*, **114**, 14467 (2010).

28. E. Halls Jonathan, A. Hernan-Gomez, D. Burrows Andrew and F. Marken, *Dalton Transactions*, **41**, 1475 (2012).

29. Zheng, Evans and Nelsen, *J. Org. Chem.*, **65**, 1793 (2000).

30. B. Bry and B. Tremillon, *J. Electroanal. Chem. Interfac. Electrochem.*, **46**, 71 (1973).

31. S. P. Gubin, S. A. Smirnova, L. I. Denisovich and A. A. Lubovich, *J. Organometallic Chem.*, **30**, 243 (1971).

32. A. M. Bond, K. B. Oldham and G. A. Snook, *Anal. Chem.*, **72**, 3492 (2000).

33. A. M. Bond, E. A. McLennan, R. S. Stojanovic and F. G. Thomas, *Anal. Chem.*, **59**, 2853 (1987).

34. R. R. Gagne, C. A. Koval and G. C. Lisensky, *Inorg. Chem.*, **19**, 2854 (1980).

35. S. Trasatti, *Pure Appl. Chem.*, **58**, 955 (1986).

36. W. M. Latimer, *J. Am. Chem. Soc.*, **76**, 1200 (1954).

37. J. M. Larsen, E. M. Espinoza and V. I. Vullev, *J. Photon. Energy.* , **5**, 055598 (pp. 1 (2015).

38. M. K. Ashraf, R. R. Pandey, R. K. Lake, B. Millare, A. A. Gerasimenko, D. Bao and V. I. Vullev, *Biotechnol. Progr.*, **25**, 915 (2009).

39. V. I. Vullev, *J. Phys. Chem. Lett.*, **2**, 503 (2011).

40. B. Xia, D. Bao, S. Upadhyayula, G. Jones and V. I. Vullev, *J. Org. Chem.*, **78**, 1994 (2013).

41. E. M. Espinoza, B. Xia, N. Darabedian, J. M. Larsen, V. Nunez, D. Bao, J. T. Mac, F. Botero, M. Wurch, F. Zhou and V. I. Vullev, *Eur. J. Org. Chem.*, **2016**, 343 (2016).

42. D. Bao, S. Upadhyayula, J. M. Larsen, B. Xia, B. Georgieva, V. Nunez, E. M. Espinoza, J. D. Hartman, M. Wurch, A. Chang, C.-K. Lin, J. Larkin, K. Vasquez, G. J. O. Beran and V. I. Vullev, *J. Am. Chem. Soc.*, **136**, 12966 (2014).

43. M. Krzeszewski, E. M. Espinoza, C. Cervinka, J. B. Derr, J. A. Clark, D. Borchardt, G. J. O. Beran, D. T. Gryko and V. I. Vullev, *Angew. Chem., Int. Ed.*, **57**, 12365 (2018).

44. O. Borodin, S.-D. Han, J. S. Daubert, D. M. Seo, S.-H. Yun and W. A. Henderson, *J. Electrochem. Soc.*, **162**, A501 (2015).

45. M. Born, *Zeitschrift fuer Physik*, **1**, 45 (1920).

46. M. J. Bird, T. Iyoda, N. Bonura, J. Bakalis, A. J. Ledbetter and J. R. Miller, *J. Electroanal. Chem.*, **804**, 107 (2017).

47. T. Kakiuchi, J. Noguchi and M. Senda, *J. Electroanal. Chem.*, **327**, 63 (1992).

48. M. Rosenblum, J. O. Santer and W. G. Howells, *J. Am. Chem. Soc.*, **85**, 1450 (1963).

49. A. F. Cunningham, Jr., *J. Am. Chem. Soc.*, **113**, 4864 (1991).

50. M. J. Mayor-Lopez, J. Weber, B. Mannfors and A. F. Cunningham, Jr., *Organometallics*, **17**, 4983 (1998).

51. A. H. Ilkhechi, J. M. Mercero, I. Silanes, M. Bolte, M. Scheibitz, H.-W. Lerner, J. M. Ugalde and M. Wagner, *J. Am. Chem. Soc.*, **127**, 10656 (2005).

52. J. Rodríguez-Otero, E. M. Cabaleiro-Lago, Á. Peña-Gallego and M. Merced Montero-Campillo, *Tetrahedron*, **65**, 2368 (2009).

53. A. Irigoras, J. M. Mercero, I. Silanes and J. M. Ugalde, *J. Am. Chem. Soc.*, **123**, 5040 (2001).

54. M. Scheibitz, R. F. Winter, M. Bolte, H.-W. Lerner and M. Wagner, *Angew. Chem. Int. Ed.*, **42**, 924 (2003).

55. N. Grover, M. Sankar, Y. Song and K. M. Kadish, *Inorganic Chemistry*, **55**, 584 (2016).

56. M. Boulkroune, L. Ignatovich, V. Muravenko, J. Spura, A. Chibani and V. Jouikov, *Chem. Heterocyclic Compounds*, **49**, 1579 (2014).

57. S. Zhu, Q. Song, S. Zhang and Y. Ding, *J. Mol. Struct.*, **1035**, 224 (2013).

58. T. Fujimoto, M. M. Matsushita and K. Awaga, *J. Phys. Chem. C*, **117**, 5552 (2013).

59. M. Schmittel, Q. Shu and M. E. Cinar, *Dalton Transactions*, **41**, 6064 (2012).

60. K. R. Edelman and B. J. Holliday, *Inorg. Chem.*, **49**, 6787 (2010).

61. A. A. Popov, I. E. Kareev, N. B. Shustova, E. B. Stukalin, S. F. Lebedkin, K. Seppelt, S. H. Strauss, O. V. Boltalina and L. Dunsch, *J. Am. Chem. Soc.*, **129**, 11551 (2007).

62. G. V. Loukova and V. V. Strelets, *Russ. Chem. Bull.*, **49**, 1037 (2000).

Chapter 5

Nitropyrene Photoprobes: Making Them, And What Are They Good for?

Abstract

Pyrene derivatives are among the most widely used organic fluorescent photoprobes. Many of them are photosensi- tizers for hole injection. Pyrenes, however, are mostly UV absorbers, limiting their utility for photonic applications. Nitration of pyrene shifts its absorption to the visible region. Conversely, nitration of pyrene that is already derivatized for covalent labeling, produces mixtures of isomers that are challenging to separate. We present a robust procedure for attaining isomerically pure nitropyrenes. NMR analysis provides unequivocal assignments of the regioisomers and of the structures of the disubstituted nitropyrenes. The added substituents negligibly affect the electronic properties of the nitropyrenes. Photoexcited nitropyrenes undergo efficient triplet formation, making them an attractive choice for triplet sensitizers and photooxidants. Hence, facile and reliable preparation of disubstituted nitropyrenes provides venues for exploring their electronic and photonic utility.

Introduction

This publication describes a robust procedure for preparation of nitropyrene-carboxyl derivatives that can be functionalized as aliphatic amines or carboxylates (Figure 5-1, Scheme 5-1). The principal challenge that we address is reproducible isolation of regioisomers of disubstituted nitropyrenes. Electrochemical and photophysical studies reveal that such functionalization causes minimal perturbation of the electronic properties of 1-nitropyrene (NPy).

Pyrene is one of the most broadly used and best-studied lipophilic photoprobes.[1] Referred to as nanographene,[2] pyr- ene is a polyaromatic hydrocarbon (PAH), comprising almost equal number of quaternary and tertiary carbons, i.e., about 40 % of its carbons are quaternary. At the edges, the tertiary carbons provide the chemical reactivity of this PAH. The π-conjugation, distributed over all carbons, governs its electronic and optical properties.

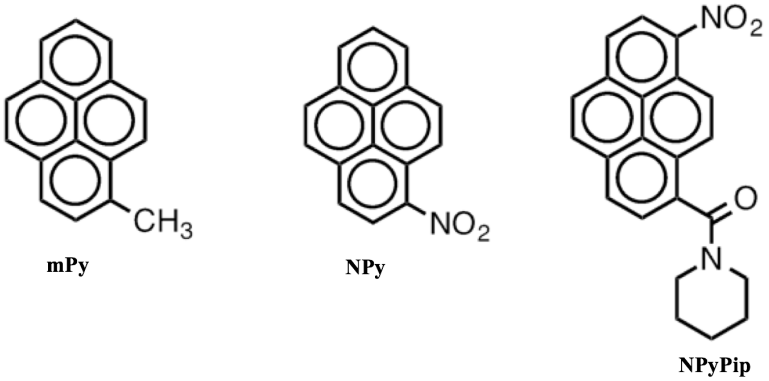

mPy NPy NPyPip

Figure 5-1. Structures of 1-methylpyrene (mPy), 1-nitropyrene (NPy) and (8- nitropyren-1-yl)(piperidin-1-yl)methanone (NPyPip).

Similar to graphene sheets that form graphite, driven by π– π interactions, pyrenes self-assemble into supramolecular and nanometer-size structures with emerging photonic and electronic properties.[3] This propensity for aggregation proves beneficial for forming quaternary structures of synthetic bio- molecules.[4] Along with manifesting large

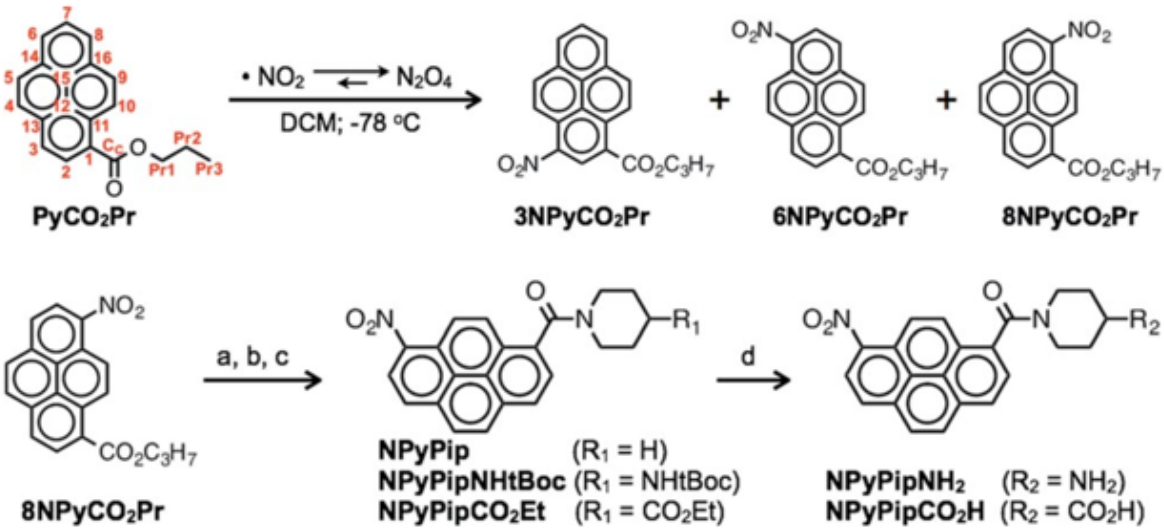

Scheme 5-1. Synthesis of disubstituted nitropyrenes. (a) KOH/C_2H_5OH, 60 °C; (b) $SOCl_2$, 80 °C; (c) $HN(CH_2CH_2)_2CH\text{-}R^1$; (d) F_3CCO_2H, room temp., if $R^1 = NHtBoc$; or KOH/C_2H_5OH, 60 °C, if $R^1 = CO_2Et$.

fluorescence quantum yields and unusually long singlet-excited state lifetimes, the aggregation propensity of alkylpyrenes makes them unique photoprobes for monitoring interactions in lipophilic environment.[5] Changes in the color of the fluorescence of pyrene- labeled macromolecule from blue to green are an easily detect- able indication for aggregation.[6]

Pyrene, however, absorbs in the near UV spectral region (300–350 nm), limiting its utility as a photoprobe to cases where selective UV photoexcitation is possible.[4a,7] Functionalizing pyrene with electron-donating and -withdrawing groups shifts its absorption toward the visible spectral region.[8] For example, electron-withdrawing (EW) groups, such as ketones or aldehydes, bring the pyrene absorption close to the edge be- tween the UV and visible spectral regions.[7a,9] Nitropyrenes, containing an especially strong EW substituent, are yellow com- pounds with absorption that extends in the visible region of the spectrum, i.e., to wavelengths longer than 410 nm.[10] The mutagenicity and

carcinogenicity of nitropyrenes have made them objects for biomedical and environmental research.[11]

Upon photoexcitation, nitropyrenes undergo efficient inter- system crossing (ISC) making these PAH derivatives excellent triplet photosensitizers.[10b] In parallel, the strong EW capabilities of the nitro group make nitropyrenes good electron accept- ors.[10d] Alkyl substituents have negligible effect on the reduction potential of pyrene.[7a,7c] Replacing alkyl with alkanoyl substituents causes a 0.6-V positive shift in the reduction potential.[7a,9b] Conversely, replacing an alkyl substituent with a nitro group causes a positive shift exceeding 1 V.[11f,12]

These electronic characteristics make nitropyrenes unique photosensitizers. To utilize nitropyrenes as photoprobes and as building blocks for polymers and electronic materials, it is vital to provide a means for covalent conjugation without perturbing the effect of the EW nitro group. Substituted nitropyrenes present the simplest scenario for pursuing such venues of exploration, i.e., the nitro group governs the electronic properties of the PAH and the other functional group offers a means for covalent linking. Although it is the "simplest scenario," access to disubstituted nitropyrenes with sufficient regioisomeric purity is still limited.

Reduction to 4,5,9,10-tetrahydropyrene allows for adding functional groups at positions 2 and 7 with pronounced regioselectivity, which followed by re-oxidation, yields 2,7-disubstituted pyrenes.[13] The preparation of sufficiently pure 4,5,9,10-tetrahydropyrene, however, is challenging.[13a,14] Also, substituents at positions 2 and 7 do

not have a strong electronic coup- ling with the pyrene π-conjugation[15] due to the nodal plane in the frontier orbitals.[16]

Pyrene has four sites for preferential aromatic substitution: positions 1, 3, 6, and 8 of this PAH (see $PyCO_2Pr$ on Scheme 5-1).[1a] Although this regioselectivity considerably simplifies the synthetic goals, nitration of 1-substituted pyrenes still yields mixtures of mainly three isomers (Scheme 5-1) that have relatively close chromatographic retention times. While nitration is well understood, doubly nitrated products or substitutions at positions 4, 5, 9, and 10, even under mild conditions, present further complications in the isolation of the targeted compounds.

Herein we present a facile procedure for preparing amino and carboxyl derivatives of nitropyrene with pronounced isomeric purity (Scheme 5-1). While normal-phase HPLC allows for efficient isolation of the various regioisomers, we employ solely "regular" column flash chromatography in the steps leading to the targeted compounds. Optimizing the procedures based on readily available techniques and establishing their reproducibility are important characteristics for the utility of the developed synthetic routes. We demonstrate unequivocal assignment of the exact positions of the nitro groups in the isolated isomers using a range of two-dimensional NMR techniques. Steady-state and time-resolved spectroscopy show that the carboxylamide linker does not significantly change the photophysical properties of the nitropyrene. Cyclic voltammetry reveal that the additional carboxylamide causes only a small positive shift (ca. 30-mV) in the reduction potential of nitropyrene.

Results

Synthetic Routes

Carboxylates present a good choice for conjugating the targeted pyrene derivatives to macromolecules and other structures. While, 1-pyrenecarboxylic acid ($PyCO_2H$) is commercially available, it can also be readily prepared from pyrene via Friedel–Crafts acylation, followed by a haloform reaction.[17] Furthermore, the EW carbonyl of $PyCO_2H$ decreases the susceptibility of the pyrene ring to oxidation during the nitration step, resulting in a relatively clean mixture of products. $PyCO_2H$, how- ever, has limited solubility in most organic solvents. Therefore, we protect the carboxyl as an ester, $PyCO_2R$, prior to nitration allowing it to proceed under relatively mild condition, e.g., –78 °C. In fact, limited solubility renders the utility of alternative routes, such as nitration of 1-acetylpyrene followed by haloform reaction, unfeasible.

Radical nitration of PAHs has received a great deal of attention because it allows for adopting mild reaction conditions and yields solely mononitrated products.[18] While cooling the reaction mixture decreases the solubility of pyrene conjugates, low temperature is favorable for these chemical transformations. The nitration mixture contains N_2O_4 and NO_2 that are in equilibrium. NO_2 is a reactive radical that can cause a range of undesired processes. Lowering the temperature shifts the equilibrium toward its dimer, N_2O_4 (Scheme 5-1), and allows for its "slow" release as it gets consumed by the desired nitration processes. Solutions of N_2O_4 in chlorinated media have blue color. An increase in the relative concentration of NO_2 (which is a brown gas) changes the color of such solutions

to green. This feature is important for monitoring the reaction conditions. At room temperature the nitration mixture (NO_2 and N_2O_4 dis- solved in dichloromethane) is green. It has to be cooled until it turns blue before adding it to the solution of the PAH starting material, which also should be maintained at the same low temperature. In addition to this thermodynamic effect, the low temperature ensures the kinetic preference for the formation of mostly the isomers with a nitro group at position 3, 6 or 8.

Even when we implement low temperatures, the radical nitration of $PyCO_2R$ with N_2O_4/NO_2 proceeds to completion in relatively short times, resulting in quantitative yields of solely mononitrated isomers with the nitro group mainly at positions 3, 6, and 8 (Scheme 5-1, Figure 5-2, a, b). A detailed analysis, using Soxhlet-assisted extraction, reveals the formation of other mononitrated isomers (< 10%) when the N_2O_4 solution is added fast, or the reaction mixture is not completely cooled down to the temperature of dry-ice/acetone bath (Figure 5-2, b).

Facile isolation of a pure regioisomer is most important for the utility of this synthetic route. Therefore, the alkyl group, R, of the ester plays a crucial role in the design of the synthetic procedure. A short chain, e.g., R = CH_3 or C_2H_5, ensures that the exact position of the nitro group has a dominating effect on the chromatographic retention times of the isomers. The nitrated methyl and ethyl esters of the pyrenecarboxylic acid, however, have relatively low solubility in common organic sol- vents, leading to widened chromatographic peaks and bands (Figure 5-2, a), and limiting the amount of material that can be introduced in a column for separation. This limitation presents challenges to

attempts for scaling up the preparation. Conversely, long flexible alkyl chains, R, immensely improve the solubility of the nitrated pyrene esters in organic solvents. This improved solubility and affinity for the eluent media, however, overwhelms the chromatographic discernibility between the regioisomers. That is, small ester substituents provide improved resolution but limit the amount of material that can be purified at each

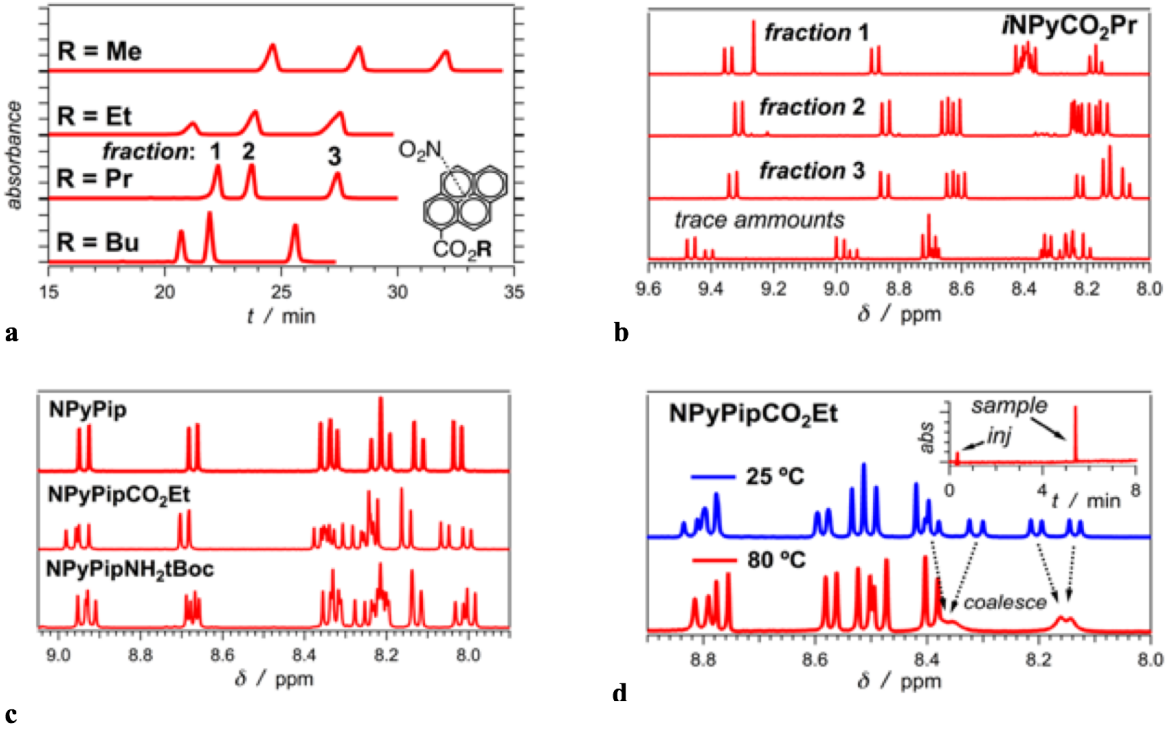

Figure 5-2. Analysis of the products at various stages of the preparation of the nitropyrene derivatives. (a) Chromatograms, monitored at 400 nm, from normal-phase HPLC tests of the nitration products of different esters of 1- pyrenecarboxylic acid, Me = methyl, Et = ethyl, Pr = *n*-propyl, and Bu = *n*- butyl (hexanes/ethyl acetate gradient, injection: 25 µL sample with 1 mg/mL concentration). (b) Aromatic region of ^{1}H-NMR spectra ($CDCl_3$) of the samples isolated from the three HPLC fractions of the nitrated propyl ester of 1-pyrenecarboxylic acid. The lowest spectrum is for the solid residue (< 5 %) remaining after extensive wash with hexanes (using Soxhlet apparatus) of i$NPyCO_2Pr$ mixture obtained from nitration when the N_2O_2 solution was not added slowly. (c) Aromatic region of ^{1}H-NMR spectra ($CDCl_3$) of NPyPip, and two derivatives, $NPyPipCO_2Et$ and $NPyPipNH_2tBoc$, that have a diasterogenic carbon. (d) Temperature dependence of ^{1}H-NMR spectra ([D_6]DMSO) of $NPyPipCO_2$ Et, showing coalescence of some of the peaks. Inset: chromatogram, monitored at 400 nm, from LCMS analysis of $NPyPipCO_2Et$ showing, in addition to the injection (*inj*) signal, only a single sample peak (*m/z* = 431.1599, ascribed to $[M + H]^+$).

run. Large substituents allow for introducing large quantities of material in the chromatographic columns, at the cost of losing the resolution between some of the elution

bands of the regioisomers.

Considering these opposing effects, we determined that substituents with intermediate size, such as *n*Pr and *n*Bu esters, provide an excellent compromise (Figure 5-2, a). Conversely, the aqueous wash after the alkaline hydrolysis of the purified isomers (Scheme 5-1) poses additional consideration for the procedure. The decrease in the molecular weight of aliphatic alcohols improves their water solubility, making the *n*-propyl ester, $PyCO_2Pr$ (Scheme 5-1), the preferred compromise for accommodating the opposing effects and requirements.

One of the three major regioisomers of the nitrated *n*-propyl ester (with the longest retention time) is well resolved chromatographically (Figure 5-2, a). In fact, using only flash chromatography allows for reproducible isolation of this well separated isomer in a single run. It is propyl 8-nitropyrene-1-carboxylate ($8NPyCO_2Pr$), as we assign using NMR analysis. Because of the relative ease of isolation of this particular disubstituted isomer, we base the rest of the procedures on it (Scheme 5-1). Hydrolysis of $8NPyCO_2Pr$ yields 8-nitropyrene-1-carboxylic acid, $NPyCO_2H$, which we conjugate with piperidine derivatives as potential linkers for photolabeling (Scheme 5-1). The piperidine derivative of the 8-nitropyrenecarboxyl, NPyPip, is a model for the chromophore in the prepared conjugates and we focus the electrochemical and photophysical studies on it.

Restricted bond rotation due to π-conjugation, results in diastereogenicity that causes splits in some of the chemical shifts. The pyperidinyl ^{1}H and ^{13}C NMR chemical

shifts of NPyPip are consistent with "locked" conformers, i.e., NPyPip has five ^{13}C and six ^{1}H signals (with integration 1:1:2:2:2:2 protons) in the aliphatic NMR regions, instead of the expected three carbon and three proton signals (with integration 4:4:2 protons) for the symmetric pyperidine ring. This finding is not surprising for compounds containing amides or other bonds that are partially π-conjugated and the rotation around them is slower than the NMR spectroscopic data acquisition times. The observed number of NMR peaks, however, is smaller than what it would be expected for the two π-conjugated slow rotating bonds inducing this effect; i.e., (1) the bond between the pyrene C^1 carbon and the carbonyl carbon, C^C (Scheme 5-1); and (2) the amide bond. Indeed, extension of the π-conjugation along these two bonds stabilizes the planar structures. Rotation around the C^1– C^C bond leads to two planar (or close-to planar) conformers, i.e., *Z* and *E* (Scheme 5-2). The steric hindrance between the piperidinyl substituent with C^{10}–H^{10} of the pyrene rings makes the *E* conformer less favorable than the *Z* one (Scheme 5-2). While the *Z* conformer also has some overlap between the piperidinyl and the pyrene H^2 (Scheme 5-2), the steric hindrance is considerably more prohibitive for the *E* structure, suggesting that these conjugates exist predominantly in their *Z* configurations.

A functional group on the piperidinyl (Pip) ring, i.e., NPyPipR where R = NH_2, CO_2H, NHtBoc or CO_2Et (Scheme 5-1), causes additional splitting in the chemical shifts of the piperidine protons and carbons. Furthermore, in NPyPipR some of the pyrene ^{1}H and ^{13}C signals are split in comparison with those in NPyPip (Figure 5-2, c). The ^{1}H NMR spectra of the NPyPipR conjugates show up to 20-Hz splits in the signals of some of the

Scheme 5-2. Conformational transitions of NPyPipR. Green balls: overlaps between hydrogen atoms; red balls: overlaps between carbon–hydrogen bonds.

aromatic protons (Figure 5-2, c, d). Concurrently, signals in the ^{13}C NMR spectra of the same compounds, recorded under ^{1}H-^{13}C decoupling, appear as doublets with up to 10-Hz splits. Elevating the temperature leads to coalescence of these split NMR peaks (Figure 5-2, d), which is consistent with accelerating the rotational modes around the partially π-conjugated bonds responsible for the observed patterns of the NMR signals. Because of the relative complexity of the NMR spectra, we employ liquid chromatography-mass spectrometry (LCMS) to further confirm the purity and the identity of the NPyPipR conjugates (see Supporting Information). Because the conformational dynamics, involving the restricted modes of bond rotation, is faster than the chromatographic timescales, all conjugates elute as single peaks, showing the corresponding *m*/*z* ratios (Figure 5-2, d, inset).

Because of the symmetry of the piperidine ring, a substituent on the carbon at the 4th position should not generate an enantiomeric center. Considering the whole structure, however, reveals that substituents on the 4th piperidinyl carbon induce ax- ial chirality (Scheme 5-2) if the rotation around the amide bond is slow enough for the different conformers to appear as distinct species in the NMR spectra. While NMR spectroscopy cannot discern enantiomers, twists in the molecular structures (which are close to planar but not planar) induce additional asymmetries that make the substituents on the 4th

piperidinyl carbon diastereogenic, affecting not only the aliphatic but also the aromatic ^{1}H and ^{13}C NMR signals.

Assigning the Nitro-Group Positions in the Regioisomers

The chromatographic fractions of the mixture of the nitrated propyl esters correspond to different regioisomers. The protons of each regioisomer exhibit distinctly different chemical shifts, making NMR spectroscopy a preferred tool for assigning the position of the nitro group. Indeed, for the sake of utility of the synthetic route, we are mainly interested in the isomer with longest retention time that is chromatographically well re- solved. For completeness, however, we employ HPLC to isolate the three abundant isomers of the mononitrated propyl ester, and assign the positions of their nitro groups.

The patterns of coupling between the pyrene protons pro- vide basic information for identifying the isomers of the mono- nitrated $PyCO_2Pr$. If the nitration is at position 6 or 8, the pyrene protons appear as eight doublets in the aromatic region of the ^{1}H NMR spectra. For a 7-nitro isomer, the aromatic protons also form eight doublets. The weak *meta*-coupling between H^6 and H^8 (J about 1 to 2 Hz), however, may make these two doublets appear as singlets in a case of peak broadening. Mononitration at the other position (i.e., 2, 3, 4, 5, 9, and 10) results in patterns comprising six doublets, a triplet (H^7), and a singlet (the proton next to the nitro group).

The isomer with the shortest retention time, i.e., from frac- tion 1 (Figure 5-2, a), exhibits a singlet at δ = 9.26 ppm and a triplet at δ = 8.17 ppm (Figure 2, b). As HMBC reveal, the three- bond coupling, ^{3}J, between the 9.26-ppm ^{1}H singlet and the carbonyl

carbon of the ester (C^C) suggests that this isomer is the 3-nitro derivative, $3NPyCO_2Pr$ (see Supporting Information). While H^7 corresponds to the 8.17-ppm triplet, the proton next to the nitro group exhibits a singlet. Furthermore, the only possible $^2J_{C,H}$ or $^3J_{C,H}$ coupling of C^C with a pyrene proton is with H^2 (Scheme 5-1), validating the assignment of this isomer to $3NPyCO_2Pr$.

The other two isomers exhibit patterns of eight doublets in their aromatic regions (Figure 5-2, b), indicating that they are the 6- and 8-nitro derivatives. To assign the exact position of the nitro groups in these two isomers, we resort to two-dimensional (2D) NMR studies.[19] Correlation spectroscopy (COSY) reveals which protons are attached to neighboring carbons. ^{13}C- ^1H HSQC spectroscopy shows to which carbon each proton is bonded, i.e., revealing single-bond coupling, $^1J_{C,H}$, patterns. ^{13}C- ^1H HMBC spectroscopy relates chemical shifts of protons and carbons that are two- and three-bonds apart, i.e., $^2J_{C,H}$ and $^3J_{C,H}$ coupling, respectively.[19] For the aliphatic region, $^2J_{C,H}$ and $^3J_{C,H}$ coupling produce strong HMBC signals. For the pyrene (aromatic) region, the strong signals are only from $^3J_{C,H}$, while $^2J_{C,H}$ coupling yields weak or undetectable HMBC signals.

From the three major isomers, the one with the longest retention time, i.e., from fraction 3 (Figure 5-2, a), shows seven doublets in the aromatic region, one of which (at ca. 8.15 ppm) integrates to two protons (Figure 5-2, b). HMBC analysis con- firmed that the most deshielded carbon, δ ca. 167 ppm, is the carbonyl one, C^C, which can exhibit $^3J_{C,H}$ only with H^{Pr1} and H^2 and cannot have any $^2J_{C,H}$ correlations (Scheme 5-1, Figure 5-3, c,

d). These structural features allow for assigning the doublet at 8.7 ppm to H^2. From the chemical shift of H^2, COSY and HSQC allow for straightforward assignments of H^3, C^2, and C^3 (Figure 5-3, a, b).

Based on the structure (Scheme 5-1), H^3 should exhibit $^3J_{C,H}$ correlation with C^1, C^4 and C^{12}, of which C^1 and C^{12} are quaternary, i.e., they do not show HSQC $^1J_{C,H}$ signals. Furthermore, C^4 should manifest three-bond heteronuclear coupling only with one proton, H^3. If detectable, additional two HMBC signals for H^3 can originate from two-bond coupling with C^2 and C^{13}. From all five carbons that can exhibit $^2J_{C,H}$ or $^3J_{C,H}$ coupling with H^3, only C^2 and C^4 have protons directly attached to them, i.e., only C^2 and C^4 can show HSQC $^1J_{C,H}$ signals. HMBC experiments re- veal that H^3 has strong correlation signals with three carbons (Figure 5-3, d–h). Of these three, only the carbon with δ ca. 130.5 ppm shows $^1J_{C,H}$ HSQC signal, and it is not the already assigned C^2 (Figure 5-3, b). Therefore, C^4 is the only possibility for the carbon with δ ca. 130.5 ppm and, as HSQC signals show, one of the protons with the overlapping doublets at ca. 8.15 ppm is H^4 (Figure 5-3, b). The remaining two H^3-correlated carbons (with δ ca. 124 and 126 ppm) can be assigned to C^1 and C^{12}. Indeed, C^{13} can show a weak $^2J_{C,H}$ correlation with H^3, but it also has to have a strong $^3J_{C,H}$ HMBC signals with H^2. Neither the 124-ppm, nor the 126-ppm carbon shows HMBC correlation with H^2. Hence, neither of them is C^{13}. Both, C^1 and C^{12}, are three bonds away from H^{10} (Scheme 5-1). In addition to H^3, only the most deshielded proton shows HMBC correlation with both, the 124-ppm and 126-ppm carbons (Figure 3, e, f), allowing for assigning H^{10}, H^9, C^9, and C^{10} (Figure 5-3, a, b).

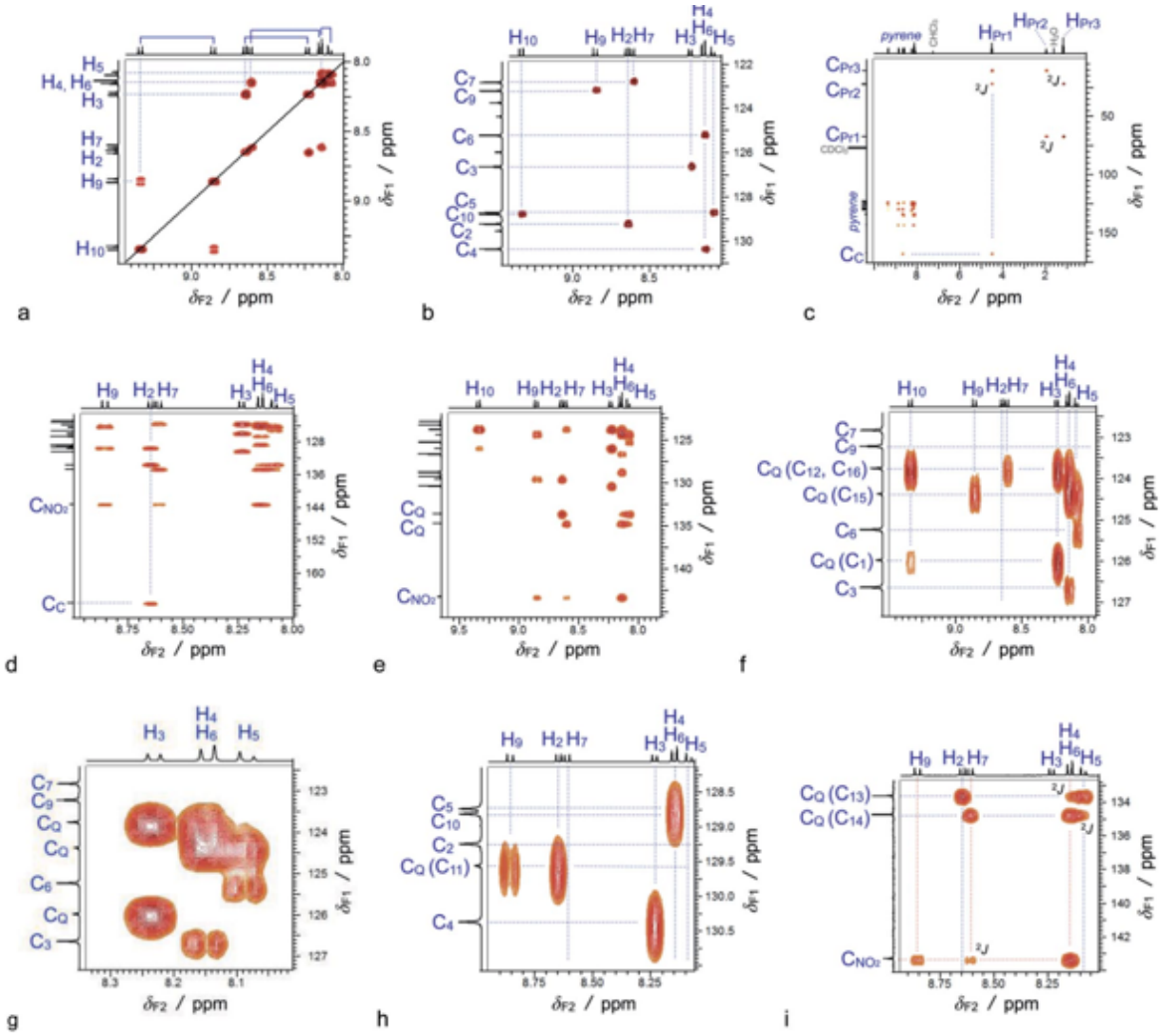

Figure 5-3. 2D NMR spectra of the third major chromatographic fraction (normal phase) of the nitrated propyl ester of the 1-pyrenecarboxylic acid. The spectra reveal that the nitro group is at the eighth position, allowing the assignment of this isomer as propyl 8-nitropyrene-1-carboxylate. Spectra of (a) COSY, showing $^{3}J_{H,H}$ coupling correlations, and (b) HSQC, showing $^{1}J_{C,H}$ coupling correlations, zoomed in the aromatic region with the assignments of the pyrene protons and tertiary carbons (Scheme 5-1). (c) HMBC spectrum showing the $^{3}J_{C,H}$ correlation between the propyl proton, H^{Pr1}, and carbonyl carbon, C^{C}. The four two-bond carbon-proton correlations in the aliphatic region (C^{Pr2}-H^{Pr1}, C^{Pr3}-H^{Pr2}, C^{Pr1}-H^{Pr2}, and C^{Pr2}-H^{Pr3}) are indicated with ^{2}J. (d–i) HMBC spectra zoomed in various aromatic regions, showing mostly $^{3}J_{C,H}$ correlations between the pyrene protons and: (1) the eight tertiary carbons, C^{2}–C^{7}, C^{9}, and C^{9}, (2) the seven quaternary carbons, C^{Q}: C^{1}, and C^{11}–C^{16}, (3) the carbonyl carbon, C^{C}, and (4) the carbon to which the nitrogroup is attached, C_{NO2}. (i) The relatively weak two-bond correlation observed for C^{13}, C^{14} and C_{NO2} are indicated with ^{2}J.

The only possibility for $^{3}J_{C,H}$ coupling of C^{9} is with H^{8} (Scheme 5-1). C^{9}, however, does not exhibit any detectable HMBC signals (Figure 5-3, f), suggesting that H^{8} does not

exist in this isomer, i.e., the nitro group is connected to C^8. Indeed, HMBC experiments did not show the two-bond coupling between C^9 and H^{10} (Figure 5-3, f), which we attribute to the weak or undetectable nature of $^2J_{C,H}$ signals for the pyrene region in these HMBC experiments. Conversely, heteronuclear two-bond correlation (H2BC) spectroscopy,[20] which is optimized for $^2J_{C,H}$ coupling, shows strong correlation signals between C^9 and H^{10}, confirming the assignments (see Supporting Information). Thus, the lack of correlation between C^9 and H^8 is not a result of a weak or undetectable signal; instead, it suggests that no proton is attached to C^8. Furthermore, H^9 is three-bonds away from three carbons, C^8, C^{11} and C^{15}, of which only C^{11} and C^{15} are quaternary (Scheme 5-1). None of the three carbons, with which H^9 shows HMBC signals (Figure 5-3, e, f, h, i), however, show $^1J_{C,H}$ coupling in HSQC (Figure 5-3, b), confirming that there is no pro- ton attached directly to C^8, and the only possibility for the nitro group is to be at the eighth position, i.e., $C^8 = C_{NO2}$.

Following this train of thought, we assign all ^{13}C and ^1H chemical shifts (Figure 5-3). To test the robustness of this analysis, we examine alternative assignments where we assume that the nitro group is at the sixth position, i.e., $C^6 = C_{NO2}$. Such an assumption cannot account for a number of the correlations that are present in the NMR spectroscopic data. Concurrently, a similar NMR analysis allows for independent assignment of the isomer from fraction 2 to 6NPyCO$_2$Pr (see Supporting Information). Thus, the isomer from fraction 3, which we use for preparing the NPyPipR conjugates, is the 8-nitro derivative, 8NPyCO$_2$Pr (Scheme 5-1).

Because we use normal phase chromatography, it is reason- able to assume that this isomer, 8NPyCO$_2$Pr, is more polar than 3NPyCO$_2$Pr and 6NPyCO$_2$Pr. The nodal plane in the frontier orbitals is along the major H^3–C^3–C^{15}–C^{16}–C^7–H^7 axis,[16a,16b] split- ting the pyrene π-conjugated system in two, where C^1 and C^8 are on one side and C^3 and C^6 – on the other. In 8NPyCO$_2$Pr both electron-withdrawing groups are on the same side, i.e., at positions one and eight, polarizing the pyrene rings and making this isomer the most polar of the three.

Electrochemical Reduction of Nitropyrenes

The reduction potentials of the nitropyrenes, as determined using cyclic voltammetery (CV), provide a means for evaluating their capability of these conjugates to act as electron acceptors. We focus on the CV behaviour of NPy and NPyPip (Figure 5-1), which allows for estimating the effect of the secondary amide on the reduction potential of this nitrated PAH.

For both nitropyrenes the cyclic voltammograms show cathodic waves at about –1 V vs. saturated calomel electrode (SCE) and second waves, twice larger than the first ones, at about –1.5 V vs. SCE (Figure 5-4, a, b). Reversing the sweeps right after the first cathodic waves yields anodic waves with comparable magnitude, which is indicative of reversible electrochemical reduction of the nitropyrenes (for aprotic media) if they are not over-reduced, e.g., if only a single electron is added to the LUMOs of these PAH conjugates.

The reversible waves, at about –1 V, show dependence on the concentration of the supporting electrolyte, C_{el}. An increase in C_{el} causes positive shifts in the potentials of the

cathodic peaks (Figure 5-4, b), which is consistent with stabilization of the formed charged species, i.e., the nitropyrene radical anions, in media with an increased ionic strength.

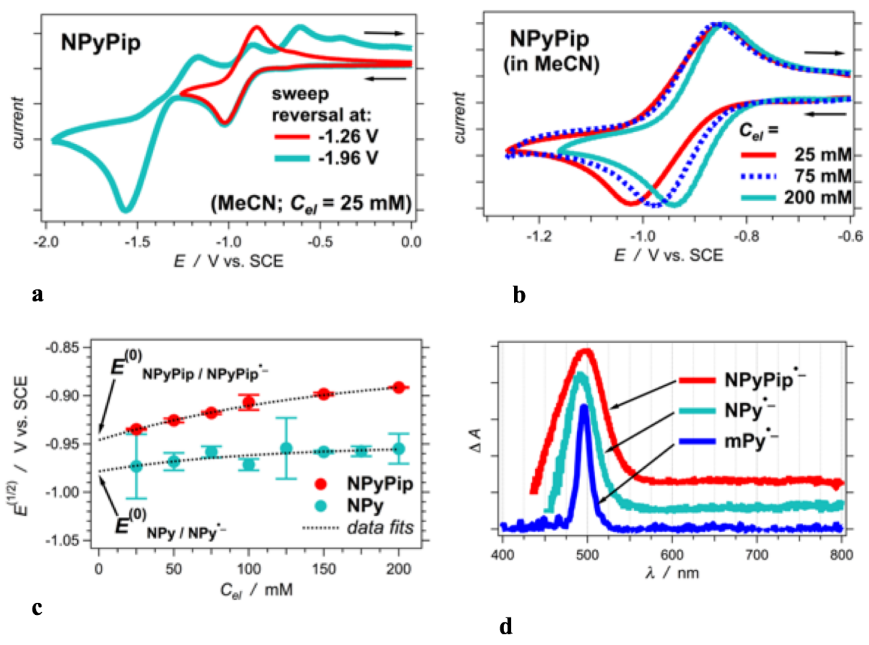

Figure 5-4. Electrochemical reduction of nitropyrenes in acetonitrile (MeCN) containing different amounts of supporting electrolyte, tetrabutylammonium hexafluorophosphate. (a) Cyclic voltammograms of NPyPip where the sweeps are reversed after the first cathodic wave (at about –1.2 V vs. SCE) and after the second wave (at about –2.0 V vs. SCE). (b) Cyclic voltammograms of NPy- Pip, reversed after the first cathodic waves, and recorded at different electro- lyte concentrations, C_{el}. (a,b) for NPy see Supporting Information. (c) Dependence of the half-wave potentials, $E^{(1/2)}$, obtained from the first reduction waves of NPy and NPyPip, on the electrolyte concentration. Extrapolation to zero electrolyte concentration, $C_{el} = 0$, allows for estimating the reduction potentials, $E^{(0)}$, for neat solvent, MeCN.[21] (d) Differential absorption spectra recorded at the first cathodic waves of NPy, NPyPip and 1-methylpyrene (mPy, Figure 5-1) for MeCN, C_{el} = 100 mM.

Extrapolation to zero electrolyte concentration from the de- pendence of the half- wave potentials, $E^{(1/2)}$, on C_{el} provides estimates of the reduction potentials of the nitropyrenes for neat solvent, MeCN (Figure 5-4, c). The reduction potential of NPyPip is about 30 mV more positive than that of NPy. Hence, conjugating the nitrated pyrene with a carboxamide only slightly affects its electron-accepting properties.

Spectroelectrochemistry shows that the first reduction step of NPyPip and NPy leads to transients with similar absorption bands at about 500 nm (Figure 5-4, d).

Coincidentally, the radical anion of alkylpyrenes, such as 1-methylpyrene (mPy), shows sharp absorption at about 500 nm.[7c] Furthermore, the radical anion of alkenoylpyrenes absorbs in the same region, showing a broad ΔA band at about 480 nm.[9b] This finding indicates that while π-conjugating substituents broaden the ΔA bands of pyrene radical anions, they do not alter the energy difference between the doublet states involved in the $D_1 \rightarrow D_{1+n}$ transition responsible for the observed transient absorption. These trends also suggest that the radical anion (spin density) of NPyPip is mainly localized on the pyrene polyaromatic ring system.

Photophysics of Nitropyrenes

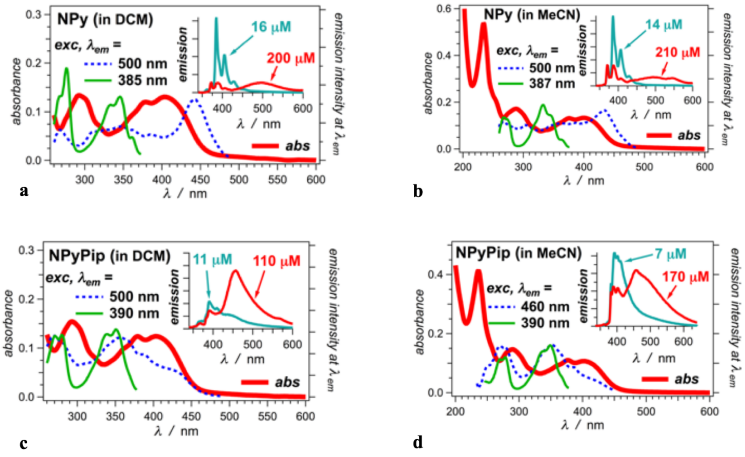

Figure 5-5. Absorption (*abs*), emission, and excitation (*exc*) spectra of NPy and NPyPip recorded for dichloromethane (DCM) and acetonitrile (MeCN) media. For the absorption spectra, the sample concentration is 10 μM. For the emis- sion spectra (displayed in the insets, λ_{ex} = 325 nm) the sample concentration is designated. Excitation spectra are recorded while the emission intensity is monitored at different wavelengths, λ_{em}.

The nitropyrenes, i.e., NPy and NPyPip, manifest absorption at the blue edge of the visible spectrum that extends to about 450 nm (Figure 5-5). A few recent reports demonstrate that NPy exhibits weak fluorescence with emission quantum yields in the order of 10^{-4}, and picosecond lifetimes.[10b,22] We examine this lead, and as attractive as the idea for fluorescent pyrene photoprobes susceptible to excitation with visible light is, our findings

suggest that the observed emission does not originate from the nitropyrenes.

Indeed, when excited at about 400 nm, NPy and NPyPip manifest broad emission bands centered around 500 nm. The emission quantum yields (in the order of 10^{-4} and 10^{-3}), how- ever, show dependence on sample concentration and on excitation wavelength, λ_{ex}. Moving λ_{ex} to the mid UV region, e.g., λ_{ex} = 325 nm, results in emission from the nitropyrene samples that has the spectral features of pyrene undergoing ground- or excited-state aggregation: i.e., sharp fluorescence with distinct vibronic features at about 400 nm, and a broad featureless band at about 500 nm (insets on Figure 5-5). For each sample, the ratio between the intensities of these 400-nm and 500-nm fluorescence bands is concentration dependent, which is evidence that the broad red-shifted emission is due to aggregation.[1b,4,23] The polarity dependence of the broad aggregate emission band is consistent with the formation of exciplexes or ground-state charge-transfer aggregates.[24]

The 400-nm fluorescence bands completely overlap with the absorption spectra of the samples. The emission at 400 nm, recorded for nitropyrenes, manifests biexponential decays with lifetimes of about 20 ns and 100 ns (see Supporting Information). Such singlet-excited-state lifetimes are typical for strongly fluorescent pyrene derivatives with quantum yields, φ_f, larger than about 0.1.[4c,9b,25] As evident from the transient absorption studies, presented below, NPy and NPyPip undergo efficient triplet formation in the picosecond time domain, with ISC rate constants that are orders of magnitude faster than the measured emission decay rates. Hence, unless emission originates from long-lived upper excited states that do not feed into the lowest signet excited state (which is absurdly unlikely), the

observed 400-nm fluoresce cannot be from the nitropyrenes.

Excitation spectra further confirm this conclusion. Neither of them resembles the absorption of NPy or NPyPip regardless weather the emission, λ_{em}, is monitored at the red or the blue edges of the fluorescence spectra (Figure 5-5).

What is the origin of the observed fluorescence? Nitro- pyrenes are good electron acceptors that can undergo irreversible reduction (Figure 5-4, a). Hence, even the slightest reducing tendencies of the organic media that solubilizes the nitro- pyrenes may produce minute traces of fluorescent imputes. Strongly fluorescent impurities even at levels not exceeding 0.1 % can still account for φ_f in the order of 10^{-4} to 10^{-3}. All samples for these studies are, indeed, recrystallized and some are doubly recrystallized. The propensity of pyrene compounds for π–π stacking, however, may ensure that such impurities form ground-state charge-transfer aggregates with the abundant nitropyrenes in the samples, resulting in the red-shifted broad fluorescence bands that manifest solvatochromism.[26] The aggregation of the impurities would prevent their complete separation (using chromatography or recrystallization) from the principal nitropyrene components of the samples. At μM and nM sample concentrations, used for spectroscopic studies, the fluorescent trace compounds dissociated from the nitropyrenes exhibit the observed long-lived emission bands at 400 nm.

Upon photoexcitation, NPyPip and NPy form transients that have distinct overlapping absorption bands at about 440 and 500 nm (Figure 5-6, a, b). In addition, the NPyPip exhibits a weak broad band at about 600–700 nm, which is especially apparent for aprotic solvent media (Figure 5-6, a–c). Because this broad band at the red region of the

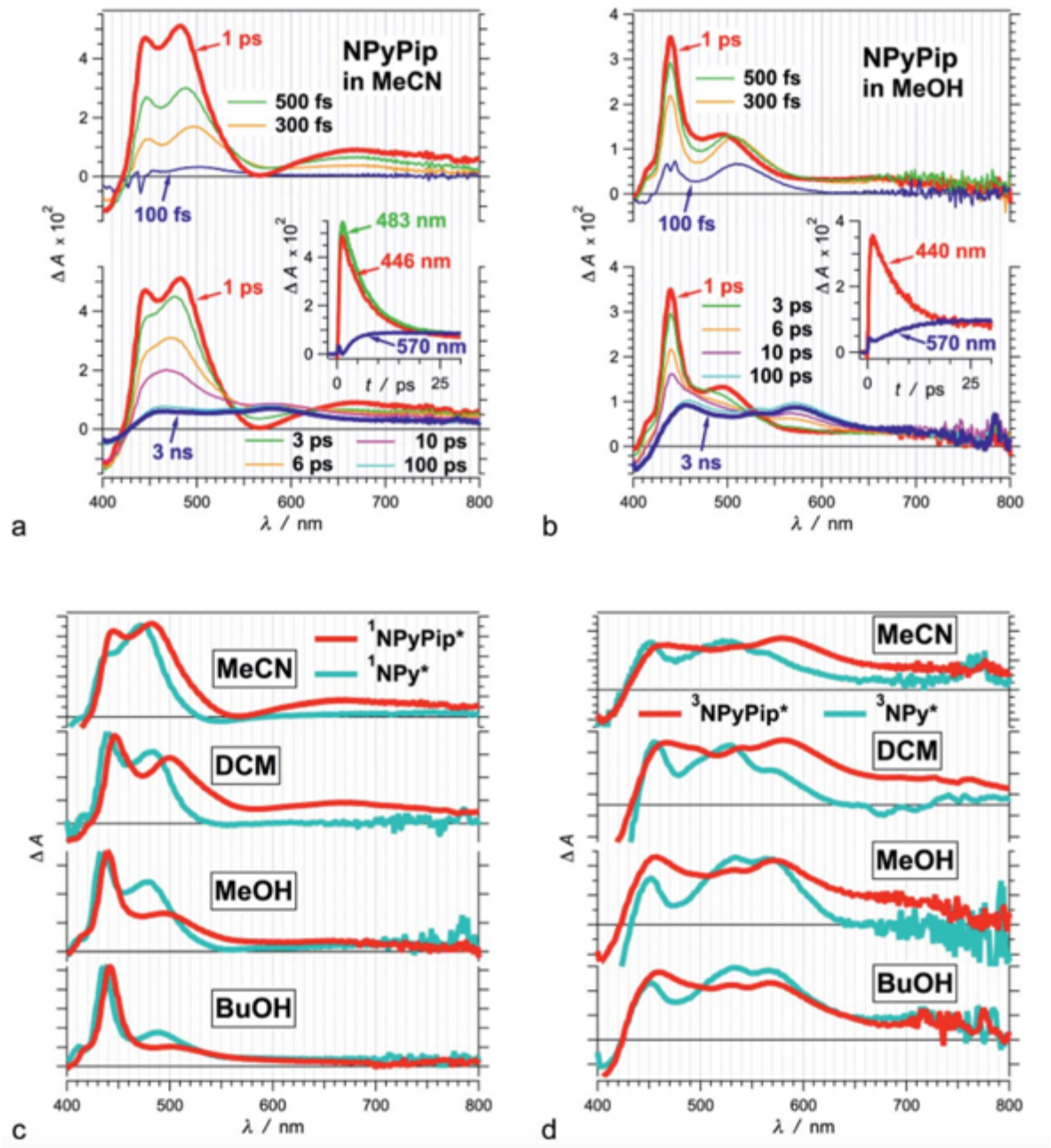

Figure 5-6. Transient absorption spectra of NPy and NPyPip for different solvents. (a,b) Spectra recorded at different times showing the growth and decay of the singlet-excited-state transient and the growth of the triplet transient of NPyPip for (a) acetonitrile (MeCN) and (b) methanol (MeOH). (c) Spectra of the singlet-excited-state transients of NPy and NPyPip, recorded 1 ps after the pump (excitation) pulse, for MeCN, dichloromethane (DCM), MeOH, and 1-butanol (BuOH).[27] (d) Spectra of the singlet-excited transients of NPy and NPyPip, recorded 0.1 to 3 ns after the pump pulse, for different solvents. (λ_{ex} = 390 nm; 50 fs pulse width at 800 nm, 4 μJ per pulse[27b, 28]).

spectrum is not detectable for NPy, its appearance in this wavelength range is attributed to

the amide of the NPyPip. Overall, the addition of the amide to the NPy causes slight red shifts in the transient absorption bands, consistent with extending the π-conjugation bringing closer the energy levels of the excited states responsible for the observed transitions (the spectra of NPy vs. NPyPip, Figure 5-6, c, d). These three transient-absorption bands (at about 440, 500 and 650 nm), ascribed to the singlet-excited state, form in the sub-picosecond time domain and have picosecond lifetimes.

For all samples, the 440-nm band is relatively narrow and its maximum remains stationary with time, suggesting that the energy gap between the states involved in the transition responsible for this absorption is conserved. Conversely, the band around 500 nm is relatively broad and manifests more than 20- nm blue shift as it grows and decays (Figure 5-6, a, b). Further- more, the 500-nm band shows a strong dependence on the proticity, rather than on the polarity, of the media. For aprotic media, the band at about 500 nm dominates the transient spectra at the early femto- and picosecond time scales (Figure 5-6, a, c). The presence of protic solvents, however, weakens its relative intensity (Figure 5-6, b, c). A previous report ascribes the long- wavelength band (500 nm) to a conformer in which the nitro group is twisted and the short-wavelength band (440 nm) to a planar structure.[10c] The solvents we use, however, appears to prevent a clear a transition from the twisted to the planar excited-state conformer as it would have been expected for NPy.

The picosecond decay of the singlet-excited state transient absorption is concurrent with a growth of a broad feature with maxima at about 460, 530 and 570 nm (Figure 5-6, a, b). We ascribe this long-lived transient, with broad absorption bands, to the triplet state of the nitropyrenes (Figure 5-6, d).[10b,10c,22c]

For protic solvents, the decay rates of the S_1 440-nm band match the rise rates of the triplets (Figure 5-6, b, inset), hence, they are readily ascribed to the rates of intersystem crossing (ISC). For the aprotic solvents, however, where the 500-nm S_1 band is prevailing, the growth rates of the triplet transients do not appear to have an obvious match with the rates of the singlet decays (Figure 6, a, inset), therefore, we resort to multi- exponential global fits (see Supporting Information). For the aprotic solvents, the global fits allow for quantification of the ISC rates (Table 5-1). For the protic solvents, the rate constants of ISC are in agreement with the rates obtained from local fits, i.e., where each decay and rise curve are fitted individually (Table 5-1). For NPy, the global fits reveal some relatively slow rise components in the kinetics of triplet growth that do not necessarily match any of the decays of the 440-nm and 500-nm principal transient absorption bands of ^{1}NPy* (Table 5-1). These findings suggest for multiple ISC pathways that seem to be eliminated by the amide substituent in NPyPip.

The nitropyrenes undergo efficient triplet formation with time constants ranging between about 3 and 10 ps. The solvent polarity does not have as apparent effect on the ISC kinetics as the proticity of the solvent media. Protic media appear to slow down the ISC. It is consistent with interfering with pathways involving states with n→π* character that become eliminated from the singlet-triplet transitions upon hydrogen bonding with the alcohols. This phenomenon is characteristic for certain carbonyl derivatives of pyrene, where hydrogen bonding shifts the energy of n→π* states suppressing triplet formation to allow fluorescence with adequate quantum yields.[9a] In the case of nitro- pyrenes, however,

hydrogen bonding may impede, rather than eliminate, the ISC processes.

Table 5-1. Rates of decay of the singlet-excited states and of growth of the triplet states of NPy and NPyPip representing the kinetics of ISC.

	Solvent[a]	$^1k_d \times 10^{-10}$ / s^{-1} [b]	$^3k_r \times 10^{-10}$ / s^{-1} [c]	$^3k_r^{(GF)} \times 10^{-10}$ / s^{-1} [d]
NPy	MeCN	–	–	39.7 ± 1.3
	DCM	–	–	7.43 ± 5.4[e]
	MeOH	16.7 ± 0.4	16.2 ± 0.6	18.0 ± 0.3
				1.67 ± 0.13[e]
	BuOH	17.4 ± 1.9	18.6 ± 0.7	16.9 ± 0.2
				0.761 ± 0.086[e]
NPyPip	MeCN	–	–	28.5 ± 0.5
	DCM	–	–	19.6 ± 0.4
	MeOH	14.3 ± 0.1	13.8 ± 0.3	13.9 ± 0.1
	BuOH	12.4 ± 0.1	15.0 ± 0.4	13.0 ± 0.2

[a] Two aprotic solvents: acetonitrile (MeCN) and dichloromethane (DCM); and two protic solvents: methanol (MeOH) and 1-butanol (BuOH). MeCN and MeOH are relatively polar and with low viscosity, DCM and BuOH are rela- tively non-polar. BuOH has higher viscosity than the other three solvents. [b] Obtained from exponential fits of the ΔA decay of the peak situated between about 435 and 445 nm, ascribed to the singlet-excited state transient. [c] Obtained from exponential fits of the ΔA rise of the transient ascribed to the triplet excited state; recorded at 570 nm where the triplet absorption is significant and the singlet absorption is minimal. [d] Obtained from multiex- ponential global fits. The rate constants correspond to the rise components of the triplet transients, and they match principal decay compounds of the 440-nm transient-absorption bands. [e] For the protic solvents, 3NPy* shows also slow rise compounds that do not match any of decays the major 1NPy* bands between 430 and 550 nm; instead, the slow components match a decay at wavelength shorter than about 420 nm. Furthermore, the rate con- stant of the 3NPy* rise for DCM matches a decay component that is more prevalent in the 410-nm region than for the 440-nm and 500-nm bands (see Supporting Information).

The spectral and electrochemical properties of nitropyrenes make them desirable photoprobes for triplet sensitization and for inducing a hole transfer by extracting an electron from neighboring electron donors. The latter feature is most likely the reason for the presence of traces of fluorescent impurities from the irreversible reduction of the nitropyrenes. Indeed, such minute amounts of fluorescent impurities appear to be inherent

for any nitropyrene. Their presence, however, does not detectably affect the photodynamics of nitropyrenes as monitored with transient absorption spectroscopy (Figure 5-6), ensuring the utility of these nitrated PAHs as photonic agents for triplet formation and for initiation of charge transfer.

The excitation energy of nitropyrenes at the red edge of their absorption, corresponding to their "optical" HOMO–LUMO gap, is about 2.8 eV. The lowest triplet state, T_1, of NPy is about 1.6 eV above the ground state, S_0. While these energetics are about 200-meV shy from meeting a principal requirement for singlet fission, i.e., $E(S_1) \geq 2\,E(T_1)$,[29] further substituent tuning that may lower the energy of T_1 more than that of S_1, will lead to promising exploration of this class of chromophores in the quest for overcoming the Shockley and Queisser limit. In terms of considerations for singlet fission, nitropyrenes readily form crystalline solids and their excited states have a strong charge-transfer character.

Conclusion

The most crucial step in the synthetic route is the separation of the three regioisomers produced from the nitration (Scheme 5-1). The presented strategies focus on the preparing nitropyrenes with an aliphatic carboxyl or amine groups because of the pronounced utility of these two functionalities.[4a,7c,9b,30] We intentionally anchor the amine and carboxyl via a saturated linker to prevent their interference with the electronic properties of the nitropyrene chromophore. Indeed, carboxyls and amines are some of the most widely used groups for covalent photolabeling of biomolecules and polymers. Amine

and carboxyl groups also provide a means for anchoring to inorganic chalcogenide and oxide surfaces, important for photonic and electronic hybrid materials.[28a,31] The electronic properties of nitropyrens make them attractive candidates for photonic application where photo-oxidation or transitions between singlet and triplet manifolds is important.

Experimental Section

General Synthesis Information

The NMR spectra were recorded at 400 MHz at ambient temperature (unless otherwise stated) using deuterated solvents, $CDCl_3$, [D_6]DMSO, [D_7]DMF, and CD_3OD. Chemi- cal shifts are reported in parts per million relative to: $CDCl_3$ (^1H, δ = 7.241 ppm; ^{13}C, δ = 77.233 ppm), [D_6]DMSO (^1H, δ = 2.505 ppm; ^{13}C, δ = 39.517 ppm), [D_7]DMF (^1H, δ = 8.031 ppm; ^{13}C, δ = 163.153 ppm), and CD_3OD (^1H, δ = 3.315 ppm; ^{13}C, δ = 49.157 ppm). Data for ^1H NMR are reported as follows: chemical shift, integration, multiplicity (s = singlet, d = doublet, t = triplet, q = quartet, p = pentet/quintet, h = hextet/sextet, m = multiplet), and coupling con- stants. All ^{13}C NMR spectra were recorded with complete proton decoupling. High-resolution mass spectra (HRMS) were obtained us- ing an Agilent LCTOF (6200) mass spectrometer (Agilent Technolo- gies, Santa Clara, CA) and Exactive™ mass spectrometer (Thermo Fisher Scientific, Inc., San Jose, CA). Analytical thin layer chromatog- raphy (TLC) was performed using 0.25 mm silica gel 60-F plates. Flash chromatography was performed using 60 Å, 32–63 μm silica gel, yields refer to chromatographically pure materials, unless other- wise stated.

1-Propyl Pyrene-1-carboxylate ($PyCO_2Pr$): 1-Pyrenecarboxylic acid (500 mg, 2.0 mmol) and $SOCl_2$ (5 mL, 69 mmol) were mixed in a 50 mL round-bottomed flask, equipped to a water-cooled con- denser, and immersed in a temperature controlled oil bath. The mixture was refluxed at 110 °C for 1 h. After cooling to room temperature, the liquid was evaporated from the solution until dry. DMAP (273 mg, 2.2 mmol) in propanol (3 mL, 40 mmol) was added to the chlorinated product. The mixture was refluxed at 110 °C and the progress of the reaction was monitored with TLC. Usually after an hour, no starting material was detected and a single green-fluorescent spot represented the major TLC-detectable component of the mixture. After cooling to room temperature, the clear solution was added dropwise in 100 mL of 1 % hydrochloric acid. White precipitate formed immediately. The precipitate was allowed to set- tle overnight and collected via filtration to yield (574 mg, 1.9 mmol, 98 %) of propyl $PyCO_2Pr$: ^1H NMR (400 MHz, $CDCl_3$): δ = 9.25 (d, J = 9.5Hz,1H), 8.62 (d, J = 8.1Hz,1H), 8.24 (m,3H), 8.17 (m,2H), 8.06 (m,2H), 4.46 (t, J = 6.7Hz,2H), 1.92 (h, J = 7.1Hz,2H), 1.12 (t, J = 7.4 Hz, 3 H) ppm. ^{13}C NMR ($CDCl_3$): δ = 168.31, 134.51, 134.48, 131.28, 130.84, 129.77, 129.59, 128.57, 127.41, 126.51, 126.48, 128.35, 125.16, 125.09, 124.47, 124.34, 61.44, 14.72 ppm. HRMS: m/z calculated $C_{20}H_{16}O_2$ M^+ 288.1138, found 289.1145 M^+.

Methyl Pyrene-1-carboxylate ($PyCO_2Me$): Following the proce- dure for $PyCO_2Pr$, while starting with 201 mg (0.82 mmol) 1-pyrene- carboxylic acid and treating the acyl chloride with methanol instead of propanol, produced 203 mg (0.78 mmol, 95 % yield) of $PyCO_2Me$: ^{1}HNMR(400MHz,$CDCl_3$):δ=9.24(d,J=9.4Hz,1H),8.61(d,J= 8.2 Hz, 1 H), 8.22

(m, 3 H), 8.14 (d, *J* = 9.0 Hz, 1 H), 8.13 (d, *J* = 8.0Hz,1H),8.04(m,2H),4.09(s,3H)ppm.^{13}CNMR($CDCl_3$):δ= 168.69, 134.53, 131.32, 131.20, 130.58, 129.81, 128.64, 128.61, 127.35, 126.49, 126.37, 126.10, 125.03, 124.39, 124.31, 123.67, 52.51 ppm. HRMS: *m*/*z* calculated $C_{18}H_{12}O_2$ $[M + H]^+$ 261.0912, found 261.091 $[M + H]^+$.

Ethyl Pyrene-1-carboxylate ($PyCO_2Et$): Following the procedure for $PyCO_2Pr$, while starting with 202 mg (0.82 mmol) 1-pyrene- carboxylic acid and treating the acyl chloride with ethanol instead of propanol, produced 203 mg (0.74 mmol, 90 % yield) of $PyCO_2Et$: ^{1}HNMR(400MHz,$CDCl_3$):δ=9.25(d,*J*=9.5Hz,1H),8.62(d, *J* = 8.1Hz, 1H), 8.24 (m,3H), 8.17 (m,2H), 8.06 (m,2H), 4.56 (q, *J* = 7.1Hz, 2H), 1.52 (t, *J* = 7.1Hz, 3H) ppm.^{13}CNMR($CDCl_3$):δ= 168.31, 134.46, 131.26, 130.64, 129.77, 129.59, 128.57, 127.41, 126.51, 126.46, 126.35, 125.16, 125.09, 124.47, 124.34, 61.44, 14.72 ppm. HRMS: *m*/*z* calculated $C_{19}H_{14}O_2$ $[M + H]^+$ 275.1078, found 275.1067 $[M + H]^+$.

1-Butyl Pyrene-1-carboxylate ($PyCO_2Bu$): Following the procedure for $PyCO_2Pr$, while starting with 106 mg (0.43 mmol) 1-pyrene- carboxylic acid, produced 53 mg (0.17 mmol, 40% yield) of $PyCO_2Bu$: ^{1}H NMR (400 MHz, $CDCl_3$): δ = 9.22 (d, *J* = 9.5 Hz, 1 H), 8.59 (d, *J* = 8.1 Hz, 1 H), 8.23 (m, 3 H), 8.14 (m, 2 H), 8.03 (m, 2 H), 4.48 (t, *J* = 6.6 Hz, 2 H), 1.85 (p, *J* = 7.4 Hz, 2 H), 1.56 (h, *J* = 7.6 Hz, 2 H), 1.01 (t, *J* = 7.4 Hz, 3 H) ppm. ^{13}C NMR ($CDCl_3$): δ = 168.42, 134.43, 131.23, 130.60, 129.72, 129.53, 128.51, 127.35, 126.47, 126.42, 126.30, 125.10, 125.05, 124.42, 124.29, 124.15, 65.35, 31.10, 19.63, 14.00 ppm.

HRMS: *m/z* calculated $C_{21}H_{19}O_2$ $[M + H]^+$ 303.1380, found 303.1375 $[M + H]^+$.

Propyl Nitropyrene-1-carboxylates (iNPyCO$_2$Pr, *i* = 3, 6, 8): Dry dichloromethane (DCM) was chilled in a bath of dry ice and ace- tone. Nitrogen dioxide (NO_2) gas was produced from the oxidation of copper filings with concentrated nitric acid. To ensure that no traces of NO are present, the NO_2 stream was mixed with an excess of dry air and passed through the chilled DCM. The DCM solution turned blue due to the formation of N_2O_4. If the solution is warmed up, its color changes to green, due to the thermally induced shift in the equilibrium to NO_2 (i.e., to the decomposition N_2O_4). 12 mL of the cold N_2O_4 solution were added in small portions slowly, drop- wise, to 10 mL of DCM solution containing PyCO$_2$Pr (450 mg, 1.6 mmol), which was also pre-chilled in a bath of dry ice and ace- tone. The progress of the reaction was monitored with TLC, until the bright green fluorescent spot disappeared and two distinct yel- low spots formed. (The yellow spots may or may not show very weak fluorescence.) The reaction mixture was added to a 100 mL of aqueous solution, saturated with $NaHCO_3$, and extracted with 50 mL of DCM. (***Caution:*** *Add the nitration reaction mixture slowly to the hydrogen carbonate solution, and carefully stir, to prevent splashing from violent formation of gaseous* CO_2.) The collected DCM solution was further washed with saturated solution of $NaHCO_3$ (2 × 50 mL), dried with anhydrous Na_2SO_4, and concentrated in vacuo to produce a yellow powder of a mixture of propyl nitropyrenecarboxyl isomers (423 mg, 1.3 mmol, 81 % crude yield). The mixture of the nitrited propyl pyrenecarboxylates (98 mg, 0.29 mmol) was purified using flash chromatography (stationary phase: silica gel; eluent gradient: from 100 % hexanes to 50 %

ethyl acetate in hexanes) to afford 92 mg (93 % column yield) of bright yellow powder. NMR analysis showed that the yellow powder con- tained equal amounts 3NPyCO$_2$Pr, 6NPyCO$_2$Pr, and 8NPyCO$_2$Pr, indi- cating that the nitration has equal selectivity for the positions 3, 6, and 8 of PyCO$_2$Pr: HRMS: *m*/*z* calculated $C_{20}H_{15}NO_4$ M^- 333.1001, found 333.0930 M^-.

1-Propyl 8-Nitropyrene-1-carboxylate (8NPyCO$_2$Pr): 102 mg of the crude nitration product, containing the *i*NPyCO$_2$Pr regioisomers, was subjected to flash chromatography (column, with 1″ internal diameter, was packed with silica gel in hexanes; 6″ to 8″ height of the packed stationary phase). Slow hexane/ethyl acetate gradient allowed separation of two principal yellow bands. The second eluted band was collected, tested with TLC to show a single yellow spot, and dried in vacuo to afford 21.5 mg (21 % column yield) of 8NPyCO$_2$Pr: ^{1}H NMR (400 MHz, $CDCl_3$): δ = 9.33 (d, *J* = 10.0 Hz, 1 H), 8.85 (d, *J* = 10.0 Hz, 1 H), 8.64 (d, *J* = 8.1 Hz, 1 H), 8.60 (d, *J* = 8.4 Hz, 1 H), 8.22 (d, *J* = 8.1 Hz, 1 H), 8.14 (d, *J* = 8.7 Hz, 2 H), 8.08 (d,*J*=8.9Hz,1H), 4.48(t,*J*=6.7Hz,2H),1.94 (h, *J* = 7.1Hz,2H), 1.14 (t, *J* = 7.4 Hz, 3 H) ppm. ^{13}C NMR ($CDCl_3$): δ = 167.63, 143.54, 134.95, 133.84, 130.59, 129.78, 129.47, 129.03, 128.96, 126.87, 126.20, 125.46, 124.60, 123.97, 123.43, 123.04, 67.51, 22.43, 10.97 ppm. HRMS: *m*/*z* calculated $C_{20}H_{15}NO_4$ $[M + H]^+$ 334.1074, found 334.1080 $[M + H]^+$.

Propyl 3-Nitropyrene-1-carboxylate (3NPyCO$_2$Pr): 40 mg of the nitration product, containing the *i*NPyCO$_2$Pr regioisomers, which was purified with flash chromatography,

were dissolved in 1 mL of DCM, was loaded and injected (in several runs) in an HPLC equipped with a normal-phase semipreperative column. Hexanes/ ethyl acetate gradient (0.33 %/min, starting with 99.5 % hexanes, at flow rate of 10 mil/min) was applied. The first yellow fraction was collected and dried in vacuo to produce 12 mg (30 % HPLC column yield) of 3NPyCO$_2$Pr: ^{1}H NMR (400 MHz, $CDCl_3$): δ = 9.35 (d, J = 9.4 Hz, 1 H), 9.26 (s, 1 H), 8.88 (d, J = 9.4 Hz, 1 H), 8.40 (m, 4 H), 8.17 (t, J = 7.6 Hz, 1 H), 4.49 (t, J = 6.7 Hz, 2 H), 1.94 (h, J = 7.2 Hz, 2 H), 1.12 (t, J = 7.4 Hz, 3 H) ppm. ^{13}C NMR ($CDCl_3$): δ = 166.53, 142.23, 1134.78, 133.63, 132.77, 130.44,130.27, 129.04, 128.69, 127.74, 127.32, 125.76, 125.34, 124.77, 123.60, 123.40, 121.61, 67.75, 22.39, 10.91 ppm.

1-Propyl 6-Nitropyrene-1-carboxylate (6NPyCO$_2$Pr): Following the procedure for 3NPyCO$_2$Pr, and collecting the second HPLC yel- low fraction, resulted in in 11 mg (28 % HPLC column yield) of 6NPyCO$_2$Pr: ^{1}H NMR (400 MHz, $CDCl_3$): δ = 9.31 (d, J = 9.4 Hz, 1 H), 8.84 (d,J=9.4Hz,1H), 8.65 (d,J=8.1Hz,1H), 8.62 (d,J=8.4Hz, 1H), 8.24 (d,J=8.1Hz,1H), 8.23 (d,J=9.5Hz,1H), 8.18(d,J= 8.5Hz,1H), 8.15 (d,J=9.4Hz,1H), 4.48 (t,J=6.7Hz,2H), 1.93 (h, J=7.1Hz,2H), 1.13 (t,J=7.4Hz,3H)ppm.^{13}CNMR($CDCl_3$): δ = 167.72, 143.84, 134.20, 132.97, 131.26, 130.80, 129.43, 128.78, 128.32, 126.72, 126.39, 125.45, 124.71, 124.54, 123.69, 123.05, 67.49, 22.42, 10.96 ppm.

Methyl Nitropyrene-1-carboxylate (iNPyCO$_2$Me, regio isomers): Following the procedure for *i*NPyCO$_2$Pr, while starting with 25.8 mg PyCO$_2$Me (0.094 mmol), after flash-chromatography column, re- sulted in 18 mg (0.059 mmol) of yellow powder (63 % yield) of a mixture of *i*NPyCO$_2$Me regioisomers: HRMS: m/z calculated $C_{18}H_{12}NO_4$ [M +

H]$^+$ 306.0761, found 306.0700 [M + H]$^+$.

Ethyl Nitropyrene-1-carboxylate (iNPyCO$_2$Et, regio isomers): Following the procedure for *i*NPyCO$_2$Pr, while starting with 24.5 mg PyCO$_2$Et (0.089 mmol), after flash-chromatography column, resulted in 24 mg (0.075 mmol) of yellow powder (85 % yield) of a mixture of *i*NPyCO$_2$Et regioisomers: HRMS: *m*/*z* calculated $C_{19}H_{14}NO_4$ [M + H]$^+$ 320.0917, found 320.0900 [M + H]$^+$.

Butyl Nitropyrene-1-carboxylate (iNPyCO$_2$Bu, regio isomers): Following the procedure for *i*NPyCO$_2$Pr, while starting with 130 mg PyCO$_2$Bu (0.43 mmol), after flash-chromatography column, resulted in 142 mg (0.408 mmol) of yellow powder (95 % yield) of a mixture of *i*NPyCO$_2$Bu regioisomers: HRMS: *m*/*z* calculated $C_{21}H_{18}NO_4$ [M + H]$^+$ 348.1230, found 348.1200 [M + H]$^+$.

8-Nitropyrene-1-carboxylic Acid (NPyCO$_2$ H): Potassium hydrox- ide (400 mg) was dissolved in 3.6 mL of ethanol and added to a round-bottomed flask containing 8NPyCO$_2$Pr (300 mg, 0.90 mmol) already dissolved in 3.6 mL of ethanol. The solution was heated to 75 °C and the progress of the hydrolysis was monitored with TLC. After the reaction was completed (after about 30 min of heating) the ethanol was evaporated in vacuo. The remaining solid was sus- pended in small mount of ethanol and added drop wise to 100 mL of 5 % HCl. The formed yellow precipitate was allowed to settle overnight and collected via filtration to produce 250 mg orange solid (0.86 mmol, 95 % yield) of NPyCO$_2$H: ^{1}H NMR (400 MHz, [D$_6$]DMSO):δ=9.40 (d,*J*=9.1Hz,1H), 8.77 (d,*J*=9.9Hz,1H), 8.76 (d, *J* =

8.4 Hz, 1 H), 8.69 (d, J = 8.0 Hz, 1 H), 8.54 (d, J = 8.6 Hz, 1 H), 8.52 (d, J = 8.6 Hz, 1 H), 8.47 (d, J = 8.9 Hz, 1 H), 8.42 (d, J = 8.9 Hz, 1 H) ppm. ^{13}C NMR ([D_6]DMSO): δ = 168.24, 143.12, 134.55, 133.23, 130.81, 129.37, 128.91, 128.68, 128.66, 127.34, 126.81, 128.11, 123.59, 123.07, 123.02, 122.75, 122.54 ppm. HRMS: m/z calculated $C_{17}H_9N_1O_4$ M^- 291.0549, found 291.0537 M^-.

(8-Nitropyren-1-yl)(piperidin-1-yl)methanone (NPyPip): NPy- CO_2H (55 mg, 0.15 mmol) was dissolved in $SOCl_2$ (0.5 mL, 6.9 mmol) in a 50 mL round-bottomed flask equipped to a water-cooled con- denser and immersed in a temperature controlled oil bath. The mix- ture was heated at 80 °C for 3 h. After cooling to room temperature, $SOCl_2$ was evaporated from the solution until dryness. The acyl hal- ide was dissolved in dry DCM and chilled in a water ice bath. Piper- dine (51 μL, 0.42 mmol) in dry DCM was added to the acyl halide solution and heated overnight at 45 °C under nitrogen gas. After acid wash, the organic phase was collected and the product was purified using flash chromatography (stationary phase: 90 % silica gel and 10 % potassium carbonate; eluent gradient: from 100 % DCM to 75 % methanol in DCM). The sample was then recrystallized twice from ethanol to afford 27 mg of yellow crystalline material (0.076 mmol, 49 % yield) of NPyPip: ^{1}H NMR (400 MHz, $CDCl_3$): δ = 8.94 (d,J=9.7Hz,1H), 8.67 (d,J=8.5Hz,1H), 8.33 (m,2H), 8.22 (m,2H), 8.12 (d,J=8.9Hz,1H), 8.02 (d,J=7.8Hz,1H), 4.02 (p, J=6.0Hz,1H), 3.92 (p,J=6.1Hz,1H), 3.12(t,J=5.6Hz,2H), 1.81 (t,J=5.5Hz,2H), 1.70 (dq,J=10.8,5.3Hz,2H), 1.41(p,J= 5.7 Hz, 2 H) ppm. ^{13}C NMR ($CDCl_3$): δ = 168.89, 143.43, 135.40, 134.25, 131.43, 130.81, 128.47, 127.77, 127.70, 126.72, 125.13, 125.05, 124.79, 124.04, 123.25,

123.11, 48.74, 43.25, 26.91, 26.11, 24.74 ppm. HRMS: *m*/*z* calculated $C_{22}H_{18}N_2O_3$ $[M - H]^-$ 357.1248, found 357.1234 $[M - H]^-$.

***tert*-Butyl-[1-(8-nitropyrene-1-carbonyl)piperidin-4-yl] Carbam- ate (NPyPipNHtBoc):** Following the procedure for NPyPip, using 53.3 mg of $NPyCO_2H$ (0.183 mmol), 4-(*tert*-butoxycarbonyl- amino)piperidin (0.3 mmol) and DMAP (45 mg, 0.369 mmol), instead of piperdine, afforded 66.2 mg (0.153 mmol, 83.6 % yield after re-crystallization) of MPyPipNHtBoc (LCMS reveals a single chromato- graphic peak): ^{1}H NMR (400 MHz, $CDCl_3$): δ = 8.93 (dd, *J* = 9.6, 7.8 Hz, 1 H), 8.67 (dd, *J* = 8.5, 4.0 Hz, 1 H), 8.33 (m, 1.5 H), 8.27 (d, *J* = 9.7 Hz, 0.5 H), 8.22 (ddd, *J* = 8.4, 5.7, 2.4 Hz, 2 H), 8.13 (m, 1 H), 8.01 (m, 1 H), 4.91 (t, *J* = 15 Hz, 1 H), 4.53 (m, 1 H), 3.72 (s, 1 H), 3.31 (m, 1 H), 3.09 (m, 2 H), 2.18 (m, 1 H), 1.66 (m, 3 H), 1.41 (d, *J* = 4.7 Hz, 9 H) ppm. ^{13}C NMR ($CDCl_3$): δ = 168.99, 155.25, 155.22, 143.48, 143.42, 135.40, 135.36, 133.57, 133.47, 131.64, 131.56, 130.83, 130.74, 128.16, 128.11, 127.96, 127.93, 127.74, 127.67, 126.74, 126.69, 125.30, 125.06, 124.89, 124.70, 124.06, 123.99, 123.39, 123.34, 123.26, 48.08, 46.65, 46.38, 41.24, 41.13, 33.67, 32.78, 32.56, 28.58 ppm. HRMS: *m*/*z* calculated $C_{27}H_{27}N_3O_5$ $[M + H]^+$ 474.2024, found 474.2023 $[M + H]^+$.

(4-Aminopiperidin-1-yl)(8-nitropyren-1-yl)methanone (NPy- PipNH$_2$): NPyPipNHtBoc (30 mg, 0.063 mmol) was dissolved in 1 mL of trifluoroaceticacid (TFA) and stirred for 1 h. TFA was evaporated to afford 22 mg (0.060 mmol, 94 % yield) of $NPyPipNH_2$ (LCMS re- veals a single chromatographic peak): ^{1}H NMR (400 MHz, CD_3OD): δ = 8.86 (dd, *J* = 15, 9.6 Hz, 1 H), 8.68 (dd, *J* = 8.4, 6.0 Hz, 1 H), 8.50 (d, *J* =

7.8 Hz, 1 H), 8.37 (m, 2.5 H), 8.27 (m, 1.5 H), 8.12 (dd, J = 14, 7.8 Hz, 1 H), 5.05 (t, J = 11 Hz, 1 H), 3.45 (m, 2 H), 3.23 (m, 2 H), 2.28 (m, 1 H), 1.84 (m, 2 H), 1.54 (m, 1 H) ppm. ^{13}C NMR (CD_3OD): δ = 171.17, 145.02, 136.58, 133.75, 133.34, 131.82, 131.75, 129.34, 129.02, 128.97, 128.66, 127.86, 126.94, 126.90, 126.26, 126.10, 125.91, 125.24, 124.28, 124.18, 54.95, 47.07, 46.77, 41.49, 41.39, 31.97, 31.59, 31.21, 31.03 ppm. HRMS: m/z calculated $C_{22}H_{19}N_3O_3$ $[M + H]^+$ 374.1426, found 374.1435 $[M + H]^+$.

Ethyl 1-(8-Nitropyrene-1-carbonyl)piperidine-4-carboxylate ($NPyPipCO_2Et$): Applying the procedure for NPyPip, using 57 mg of $NPyCO_2H$ (0.196 mmol) and ethyl 4-piperidinecarboxylate instead of piperdine afforded 66 mg (0.15 mmol, 78 % yield) of NPyPip- CO_2Et (LCMS reveals a single chromatographic peak): ^{1}H NMR (400MHz,$CDCl_3$):δ=8.95(dd,J=13,9.7Hz,1H),8.69(d,J= 8.4 Hz, 1 H), 8.34 (m, 2 H), 8.24 (m, 2 H), 8.15 (d, J = 8.8 Hz, 1 H), 8.03 (dd, J = 22, 7.8 Hz, 1 H), 4.79 (m, 1 H), 4.15 (q, J = 7.1 Hz, 2 H), 3.36 (m, 1 H), 3.26 (m, 1 H), 3.04 (m, 1 H), 2.59 (m, 1 H), 2.17 (dt, J = 8.9, 4.5 Hz, 1 H), 1.94 (m, 1 H), 1.70 (m, 1 H), 1.61 (m, 1 H), 1.25 (td, J = 7.1, 2.7 Hz, 3 H) ppm. ^{13}C NMR (CD_3OD): δ = 174.25, 174.08, 169.04, 135.39, 133.61, 131.61, 131.57, 130.81, 130.76, 128.23, 128.19, 127.93, 127.76, 127.63, 126.81, 126.67, 125.26, 125.09, 125.02, 124.71, 124.06, 124.00, 123.37, 123.31, 61.00, 47.03, 46.81, 41.52, 41.14, 41.12, 29.06, 28.73, 28.33, 14.42 ppm. HRMS: m/z calculated $C_{25}H_{22}N_2O_5$ $[M + H]^+$ 431.1613, found 431.1601 $[M + H]^+$.

1-(8-Nitropyrene-1-carbonyl)piperidine-4-carboxylic Acid [5c, ($NPyPipCO_2H$)]:

NPyPipCO_2Et (10.8 mg, 0.025 mmol) was dissolved in 4.5 mL of 1 M solution of KOH in ethanol in a round-bottomed flask equipped to a water-cooled condenser and immersed in a temperature controlled oil bath. The mixture was heated to 75 °C for one hour. The solution was added to 50 mL of 5 % hydrochloric acid and the formed precipitate was collected using filtration, to yield 7.7 mg (0.019 mmol, 76 % yield) of NPyPipCO_2H (LCMS reveals a single chromatographic peak): ^{1}H NMR (400 MHz, [D_7]DMF): δ = 12.62 (br.s,1H), 8.95 (dd, *J* = 15,9.6Hz,1H), 8.84(d, *J* =8.6Hz,1 H), 8.65 (dd, *J* = 7.8, 3.1 Hz, 1 H), 8.58 (m, 2.5 H), 8.45 (m, 1.5 H), 8.25 (dd, *J* = 34.7, 7.8 Hz, 1 H), 4.75 (m, 1 H), 3.37 (m, 1.5 H), 3.21 (m, 1.5 H), 2.70 (m, 1 H), 2.17 (dd, *J* = 13.3, 2.7 Hz, 1 H), 1.95 (m, 0.5 H), 1.79 (m,1.5H), 1.65 (q,*J*=9.4Hz,0.5H), 1.53 (q,*J*=9.4Hz,0.5 H) ppm. ^{13}C NMR ([D_7]DMF): δ = 176.67, 168.92, 144.37, 138.40, 135.64, 132.35, 131.97, 129.83, 129.55, 129.13, 129.04, 128.84, 127.47, 126.74, 126.44, 126.31, 125.54, 124.99, 124.52, 124.45, 124.23, 123.43, 105.66, 47.71, 47.45, 41.98, 41.84, 41.63, 29.77, 29.26, 29.21 ppm. HRMS: *m*/*z* calculated $C_{23}H_{18}N_2O_5$ $[M + H]^+$ 403.1216, found 403.1296 $[M + H]^+$.

High Performance Liquid Chromatography (HPLC): Normal phase analysis was performed using HPLC System Gold from Beck- man, equipped with analytical (4.6 mm × 250 mm) and semiprepar- ative (11 mm × 250 mm) columns, packed with silica (5 μm). For the analytical settings (Figure 5-2, a), hexanes/ethyl acetate gradient (1 %/mL) was applied with flow rate of 1 mL/min. For the LCMS analysis (Figure 5-2, d, inset), reverse-phase HPLC was employed, us- ing a Kinetex C18 column (1.7 μm, 2.0 mm × 50 mm, 100 Å) from Phenomenex (Torrance, CA) with a flow rate of 0.5 mL/min at 40 °C. The mobile

phase contained water and acetonitrile with 0.1 % for- mic acid (V/V). The gradient was ramped from 5 % to 95 % acetonitrile over 7 min, returned from 95 % to 5 % over 0.5 min, and main- tained at 5 % acetonitrile for 2.5 min prior to next injection.

Electrochemical Measurements: Cyclic voltammetry (CV) was con- ducted using Reference 600^{TM} Potentiostat/Galvanostat/ZRA (Gamry Instruments, PA, U.S.A.), equipped with a three-electrode cell. The half-wave reduction potentials, $E^{(1/2)}$, of the nitropyrenes were obtained from cyclic voltammograms recorded for samples of the analytes (1 to 5 mM) dissolved in dry acetonitrile containing different concentrations, C_{el}, of supporting electrolyte, tetrabutyl- ammonium hexafluorophosphate. Prior each measurements, the surfaces of the glassy carbon working electrode was cleaned and dried, and the solution was purged with high-purity argon. During the measurements, the stream of argon was allowed to blanket the solutions without stirring them. From the dependence of $E^{(1/2)}$ on C_{el}, extrapolations to zero electrolyte concentration provided esti- mates of the reduction potentials, $E^{(0)}$, for acetonitrile (Figure 5-4, c). The SCE reference electrode was connected to the cell via salt bridges, and CV of ferrocene samples (before and after each series of measurements) provided a means for correcting for potential drifts (usually, less than 50 mV), due to diffusion of water miscible organic solvents into the reference electrode. The SCE electrode is stored in freshly prepared saturated KCl solution in MilliQ water.

For spectroelectrochemical measurements, a three-electrode cell was assembled in a 10-mm×10-mm quartz cuvette, the bottom 5 mm of which narrowed to 2-mm×10-mm.

UV/Vis light source and a CCD spectrometer were connected with the cuvette holder via optical fibers. The working electrode, platinum mesh, was placed in the 2-mm×10-mm confined section at the bottom of the cuvette and the light beam was aligned to pass through the mesh. Platinum and silver wires were used for a counter and pseudoreference electrodes, respectively. The latter was calibrated with ferrocene samples. The intensities, $I(E)$, of the light passing through the sample and the working electrode were recorded at different potentials, E, while sweeping the voltage. The change in the absorbance, ΔA, for each potential, corresponding to the spectra of the electrochemically reduced species, i.e., radical anions of the nitropyrenes, was calculated in respect with the intensity at 0 V vs. the reference, $\Delta A(E) = \log [I(0)/I(E)]$.

UV/Vis absorption and Emission Spectroscopy: Steady-state absorption spectra were recorded in a transmission mode using a JASCO V-670 spectrophotometer (Tokyo, Japan); and steady-state emission and excitation spectra were measured, also in a transmission mode, with a FluoroLog-3 spectrofluorometer (Horiba–Jobin– Yvon, Edison, NJ, USA).

Time correlated single photon counting (TCSPC) measurements were also carried out using the FluoroLog-3 instrument, which was equipped with a UV diode (278 nm) as a pulsed excitation source, run at 250 kHz frequency. Decays were recorded at different emission wavelengths, λ , corresponding to the monomer (λ ca. $_{em}$ 400 nm) and aggregate (λ_{em} ca. 500 nm) fluorescence as revealed on the steady-state spectra. The emission lifetimes were obtained from biexponential data fits.

Transient Absorption Spectroscopy: The transient-absorption data (Figure 5-6) were recorded in transmission mode with 2-mm quartz cuvettes using a Helios pump-probe spectrometer (Ultrafast Systems, LLC, Florida, USA) equipped with a delay stage allowing maximum probe delays of 3.2 ns at 7 fs temporal step resolution. Immediately prior the measurements, all samples were purged with argon. The laser source for the Helios was a SpitFire Pro 35F regenerative amplifier (Spectra Physics, Newport, CA, USA) generating 800-nm pulses (pulse width between 35 and 50 fs, 4.0 mJ per pulse, at 1 kHz). The amplifier was pumped with of an Empower 30 Q- switched laser operated at 20 W (the second harmonic). A MaiTai SP oscillator provided the seed beam (55 nm bandwidth). The wave- length of the pump was tuned using an optical parametric ampli- fier, OPA-800CU (Newport Corporation, Newport, CA, USA), equipped with a second and fourth harmonic signal generators. For optimal OPA performance, the pulse duration from the amplifier was tuned to 50 fs. The signal was tuned to 1,560 nm and the power of the signal and the idler prior the second harmonic generator was stabilized at about 150 to 200 mW. The pulse after the fourth har- monic generator was fine-tuned to 390 nm, and the power was stabilized at 5 to 7 μJ per pulse.

References

1. a) T. M. Figueira-Duarte, K. Müllen, *Chem. Rev.* **2011**, *111*, 7260–7314; b) V. I. Vullev, H. Jiang, G. Jones II, *Topics in Fluorescence Spectroscopy* **2005**, vol. 10, p. 211–239; c) F. Fages, S. Leroy, T. Soujanya, J.-E. Sohna Sohna, *Pure Appl. Chem.* **2001**, *73*, 411–414; d) M. E. Ostergaard, P. J. Hrdlicka, *Chem. Soc. Rev.* **2011**, *40*, 5771–5788; e) C. Wang, C. Wu, Y. Chen, Y. Song, W. Tan, C. J. Yang, *Curr. Org. Chem.* **2011**, *15*, 465–476; f) C. Bohne, M. Barra, R. Boch, E. B. Abuin, J. C. Scaiano, *J. Photochem. Photobiol. A* **1992**, *65*, 249–265.

2. a) S. Perumal, B. Minaev, H. Aagren, *J. Chem. Phys.* **2012**, *136*, 104702/ 104701–104702/104716; b) E. San-Fabiin, F. Moscardo, *Int. J. Quantum Chem.* **2013**, *113*, 815–819.

3. a) S. S. Babu, V. K. Praveen, A. Ajayaghosh, *Chem. Rev.* **2014**, *114*, 1973– 2129; b) J. Duhamel, *Langmuir* **2012**, *28*, 6527–6538; c) S. Karuppannan, J.-C. Chambron, *Chem. Asian J.* **2011**, *6*, 964–984; d) E. Manandhar, K. J. Wallace, *Inorg. Chim. Acta* **2012**, *381*, 15–43; e) D. W. Johnson, K. N. Ray- mond, *Inorg. Chem.* **2001**, *40*, 5157–5161; f) M. I. Souza, Y. M. Jaques, G. P. de Andrade, A. O. Ribeiro, E. R. da Silva, E. E. Fileti, E. d. S. Avilla, M. V. B. Pinheiro, K. Krambrock, W. A. Alves, *J. Phys. Chem. B* **2013**, *117*, 2605–2614; g) W. Wang, S. Guo, M. Penchev, J. Zhong, J. Lin, D. Bao, V. Vullev, M. Ozkan, C. S. Ozkan, *J. Nanosci. Nanotechnol.* **2012**, *12*, 6913– 6920.

4. a) G. Jones II, V. Vullev, E. H. Braswell, D. Zhu, *J. Am. Chem. Soc.* **2000**, *122*, 388–389; b) G. Jones II, V. I. Vullev, *Org. Lett.* **2001**, *3*, 2457–2460; c) G. Jones II, V. I. Vullev, *J. Phys. Chem. A* **2001**, *105*, 6402–6406.

5. a) G. Bains, A. B. Patel, V. Narayanaswami, *Molecules* **2011**, *16*, 7909–7935; b) J. Duhamel, *Polymers* **2012**, *4*, 211–239; c) N. Adamek, M. A. Geeves, *Experientia Suppl.* **2014**, *105*, 87–104.

6. a) J. Martins, D. Arrais, M. Manuel, *Chem. Phys. Lipids* **2012**, *165*, 866–869; b) P. Somerharju, *Chem. Phys. Lipids* **2002**, *116*, 57–74; c) R. Saxena, S. Shrivastava, A. Chattopadhyay, *J. Phys. Chem. B* **2008**, *112*, 12134–12138; d) L. Le Guyader,

C. Le Roux, S. Mazeres, H. Gaspard-Iloughmane, H. Gornitzka, C. Millot, C. Mingotaud, A. Lopez, *Biophys. J.* **2007**, *93*, 4462– 4473; e) N. B. Karmen, N. P. Milyutina, A. A. Orlov, *Bull. Exp. Biol. Med.* **2005**, *139*, 562–564; f) M. Hashimoto, S. Hossain, S. Masumura, *Exp. Ger- ontol.* **1999**, *34*, 687–698; g) E. H. W. Pap, A. Hanicak, A. van Hoek, K. W. A. Wirtz, A. J. W. G. Visser, *Biochemistry* **1995**, *34*, 9118–9125.

7. a) V. I. Vullev, G. Jones, *Tetrahedron Lett.* **2002**, *43*, 8611–8615; b) G. Jones II, X. Zhou, V. I. Vullev, *Photochem. Photobiol. Sci.* **2003**, *2*, 1080– 1087; c) D. Bao, S. Upadhyayula, J. M. Larsen, B. Xia, B. Georgieva, V. Nunez, E. M. Espinoza, J. D. Hartman, M. Wurch, A. Chang, C.-K. Lin, J. Larkin, K. Vasquez, G. J. O. Beran, V. I. Vullev, *J. Am. Chem. Soc.* **2014**, *136*, 12966–12973.

8. a) Y. Niko, S. Sasaki, S. Kawauchi, K. Tokumaru, G.-i. Konishi, *Chem. Asian J.* **2014**, *9*, 1797–1807; b) Y. Niko, Y. Cho, S. Kawauchi, G.-i. Konishi, *RSC Adv.* **2014**, *4*, 36480–36484; c) Y. Li, D. Wang, L. Wang, Z. Li, Q. Cui, H. Zhang, H. Yang, *J. Lumin.* **2012**, *132*, 1010–1014; d) Y. Niko, S. Kawauchi, G.-i. Konishi, *Chem. Eur. J.* **2013**, *19*, 9760–9765; e) R. Flamholc, D. Plazuk, J. Zakrzewski, R. Metivier, K. Nakatani, A. Makal, K. Wozniak, *RSC Adv.* **2014**, *4*, 31594–31601.

9. a) C. Armbruster, M. Knapp, K. Rechthaler, R. Schamschule, A. B. J. Parusel, G. Kohler, W. Wehrmann, *J. Photochem. Photobiol. A* **1999**, *125*, 29–38; b) G. Jones II, V. I. Vullev, *Org. Lett.* **2002**, *4*, 4001–4004.

10. a) Z. I. Garcia-Berrios, R. Arce, *J. Phys. Chem. A* **2012**, *116*, 3652–3664; b) R. Arce, E. F. Pino, C. Valle, J. Agreda, *J. Phys. Chem. A* **2008**, *112*, 10294– 10304; c) C. E. Crespo-Hernandez, G. Burdzinski, R. Arce, *J. Phys. Chem. A* **2008**, *112*, 6313–6319; d) G. Jones II, L. N. Lu, V. Vullev, D. Gosztola, S. Greenfield, M. Wasielewski, *Bioorg. Med. Chem. Lett.* **1995**, *5*, 2385–2390.

11. a) J. Singh, S. Singh, B. Shaik, O. Deeb, N. Sohani, V. K. Agrawal, P. V. Khadikar, *Chem. Biol. Drug Des.* **2008**, *71*, 230–243; b) T. Kameda, A. Aki- yama, M. Yoshita, C. Tachikawa, A. Toriba, N. Tang, K. Hayakawa, *J. Health Sci.* **2011**, *57*, 372–377; c) Y.-W. Sun, F. P. Guengerich, A. K. Sharma, T. Boyiri, S. Amin, K. El-Bayoumy, *Chem. Res. Toxicol.* **2004**, *17*, 1077–1085; d) A. Toriba, H. Kitaoka,

R. L. Dills, S. Mizukami, K. Tanabe, N. Takeuchi, M. Ueno, T. Kameda, N. Tang, K. Hayakawa, C. D. Simpson, *Chem. Res. Toxicol.* **2007**, *20*, 999–1007; e) K. N. Kirouac, A. K. Basu, H. Ling, *Nucleic Acids Res.* **2013**, *41*, 2060–2071; f) H. Jung, A. U. Shaikh, R. H. Heflich, P. P. Fu, *Environ. Mol. Mutagen.* **1991**, *17*, 169–180; g) A. Mayati, E. Le Fer- rec, J. A. Holme, O. Fardel, D. Lagadic-Gossmann, J. Oevrevik, *Toxicol. In vitro* **2014**, *28*, 1153–1157.

12. a) W. A. Lopes, P. A. d. P. Pereira, H. Viertler, J. B. de Andrade, *J. Braz. Chem. Soc.* **2005**, *16*, 1099–1103; b) B. Lu, J. Xu, C. Fan, F. Jiang, H. Miao, *Electrochim. Acta* **2008**, *54*, 334–340; c) R. Zahradnik, K. Bocek, *Collect. Czech. Chem. Commun.* **1961**, *26*, 1733–1748; d) J. Barek, J. Zima, J. C. Moreira, A. Muck, *Collect. Czech. Chem. Commun.* **2000**, *65*, 1888–1896.

13. a) A. Musa, B. Sridharan, H. Lee, D. L. Mattern, *J. Org. Chem.* **1996**, *61*, 5481–5484; b) X. Zheng, M. E. Mulcahy, D. Horinek, F. Galeotti, T. F. Mag- nera, J. Michl, *J. Am. Chem. Soc.* **2004**, *126*, 4540–4542; c) T. Iwamoto, E. Kayahara, N. Yasuda, T. Suzuki, S. Yamago, *Angew. Chem. Int. Ed.* **2014**, *53*, 6430–6434; *Angew. Chem.* **2014**, *126*, 6548; d) T. Umemoto, S. Satani, Y. Sakata, S. Misumi, *Tetrahedron Lett.* **1975**, 3159–3162; e) R. G. Harvey, M. Konieczny, J. Pataki, *J. Org. Chem.* **1983**, *48*, 2930–2932; f) D. Rausch, C. Lambert, *Org. Lett.* **2006**, *8*, 5037–5040; g) H. Lee, R. G. Harvey, *J. Org. Chem.* **1986**, *51*, 2847–2848.

14. a) T. Yamato, S. Ide, K. Tokuhisa, M. Tashiro, *J. Org. Chem.* **1992**, *57*, 271– 275; b) D. M. Connor, S. D. Allen, D. M. Collard, C. L. Liotta, D. A. Schiraldi, *J. Org. Chem.* **1999**, *64*, 6888–6890; c) M. Tashiro, T. Yamato, K. Kobayashi, T. Arimura, *J. Org. Chem.* **1987**, *52*, 3196–3199.

15. S.-S. Li, K.-J. Jiang, C.-C. Yu, J.-H. Huang, L.-M. Yang, Y.-L. Song, *New J. Chem.* **2014**, *38*, 4404–4408.

16. a) A. G. Crawford, A. D. Dwyer, Z. Liu, A. Steffen, A. Beeby, L.-O. Palsson, D. J. Tozer, T. B. Marder, *J. Am. Chem. Soc.* **2011**, *133*, 13349–13362; b) S. Thekku Veedu, D. Raiser, R. Kia, M. Scholz, S. Techert, *J. Phys. Chem. B* **2014**, *118*, 3291–3297; c) K. Muellen, *Helv. Chim. Acta* **1978**, *61*, 2307– 2317.

17. a) P. Babu, N. M. Sangeetha, P. Vijaykumar, U. Maitra, K. Rissanen, A. R. Raju, *Chem. Eur. J.* **2003**, *9*, 1922–1932; b) M. Barfield, M. J. Collins, J. E. Gready, S. Sternhell, C. W. Tansey, *J. Am. Chem. Soc.* **1989**, *111*, 4285– 4290.

18. a) D. S. Ross, G. P. Hum, R. J. Schmitt, *Adv. Chem., Ser.* **1988**, *217*, 155– 168; b) L. Eberson, F. Radner, *Acta Chem. Scand., Ser. B* **1985**, *B39*, 343– 356; c) F. Radner, *Acta Chem. Scand., Ser. B* **1983**, *B37*, 65–67.

19. E. Kupce, *Top. Curr. Chem.* **2013**, *335*, 71–96.

20. a) O. Petersen Bent, E. Vinogradov, W. Kay, P. Wurtz, T. Nyberg Nils, O. Duus, J. W. Sorensen Ole, *Carbohydr. Res.* **2006**, *341*, 550–556; b) N. T. Nyberg, J. O. Duus, O. W. Sorensen, *J. Am. Chem. Soc.* **2005**, *127*, 6154– 6155.

21. a) D. Bao, B. Millare, W. Xia, B. G. Steyer, A. A. Gerasimenko, A. Ferreira, A. Contreras, V. I. Vullev, *J. Phys. Chem. A* **2009**, *113*, 1259–1267; b) D. Bao, S. Ramu, A. Contreras, S. Upadhyayula, J. M. Vasquez, G. Beran, V. I. Vullev, *J. Phys. Chem. B* **2010**, *114*, 14467–14479.

22. a) A. K. Mora, S. Murudkar, P. K. Singh, N. S. K. Gowthaman, T. Mukherjee, S. Nath, *J. Photochem. Photobiol. A* **2013**, *271*, 24–30; b) S. Murudkar, A. K. Mora, P. K. Singh, S. Nath, *J. Phys. Chem. A* **2011**, *115*, 10762–10766; c) R. Arce, E. F. Pino, C. Valle, I. Negron-Encarnacion, M. Morel, *J. Phys. Chem. A* **2011**, *115*, 152–160.

23. a) B. Xia, D. Bao, S. Upadhyayula, G. Jones, V. I. Vullev, *J. Org. Chem.* **2013**, *78*, 1994–2004; b) J. M. Larsen, E. M. Espinoza, V. I. Vullev, *J. Photon. Energy* **2015**, *5*, 055598; c) J. M. Larsen, E. M. Espinoza, J. D. Hartman, C.- K. Lin, M. Wurch, P. Maheshwari, R. K. Kaushal, M. J. Marsella, G. J. O. Beran, V. I. Vullev, *Pure Appl. Chem.* **2015**, published online ahead of print.

24. a) F. Garo, R. Haener, *Angew. Chem. Int. Ed.* **2012**, *51*, 916–S916/911-S916/ 923,

919; *Angew. Chem.* **2012**, *124*, 940; b) K. Sen, S. Bandyopadhyay, D. Bhattacharya, S. Basu, *J. Phys. Chem. A* **2001**, *105*, 9077–9084; c) H. Ino- mata, H. Hamatani, N. Wada, Y. Yagi, S. Saito, *J. Phys. Chem.* **1993**, *97*, 6332–6333; d) A. Y. Sosorev, D. Y. Paraschuk, *Isr. J. Chem.* **2014**, *54*, 650– 673; e) S. A. Zapunidy, D. S. Martyanov, E. M. Nechvolodova, M. V. Tsika- lova, Y. N. Novikov, D. Y. Paraschuk, *Pure Appl. Chem.* **2008**, *80*, 2151– 2161; f) A. A. Bakulin, S. A. Zapunidy, M. S. Pshenichnikov, P. H. M. van Loosdrecht, D. Y. Paraschuk, *Phys. Chem. Chem. Phys.* **2009**, *11*, 7324– 7330; g) S. Laricchia, E. Fabiano, F. Della Sala, *J. Chem. Phys.* **2013**, *138*, 124112/124111–124112/124112; h) T.-W. Ng, M.-F. Lo, M.-K. Fung, W.-J. Zhang, C.-S. Lee, *Adv. Mater.* **2014**, *26*, 5569–5574.

25. O. Taratula, J. Rochford, P. Piotrowiak, E. Galoppini, R. A. Carlisle, G. J. Meyer, *J. Phys. Chem. B* **2006**, *110*, 15734–15741.

26. a) J. Guasch, L. Grisanti, M. Souto, V. Lloveras, J. Vidal-Gancedo, I. Ratera, A. Painelli, C. Rovira, J. Veciana, *J. Am. Chem. Soc.* **2013**, *135*, 6958–6967; b) X. Y. Shen, W. Z. Yuan, Y. Liu, Q. Zhao, P. Lu, Y. Ma, I. D. Williams, A. Qin, J. Z. Sun, B. Z. Tang, *J. Phys. Chem. C* **2012**, *116*, 10541–10547; c) Q. Zhang, H. Kuwabara, W. J. Potscavage, S. Huang, Y. Hatae, T. Shibata, C. Adachi, *J. Am. Chem. Soc.* **2014**, *136*, 18070–18081; d) G. Jones II, D. Yan, J. Hu, J. Wan, B. Xia, V. I. Vullev, *J. Phys. Chem. B* **2007**, *111*, 6921–6929; e) J. Wan, A. Ferreira, W. Xia, C. H. Chow, K. Takechi, P. V. Kamat, G. Jones, V. I. Vullev, *J. Photochem. Photobiol. A* **2008**, *197*, 364–374; f) J. Hu, B. Xia, D. Bao, A. Ferreira, J. Wan, G. Jones, V. I. Vullev, *J. Phys. Chem. A* **2009**, *113*, 3096–3107; g) J. P. Palmans, M. Van der Auweraer, A. Swinnen, F. C. De Schryver, *J. Am. Chem. Soc.* **1984**, *106*, 7721–7728.

27. a) J. M. Vasquez, A. Vu, J. S. Schultz, V. I. Vullev, *Biotechnol. Prog.* **2009**, *25*, 906–914; b) S. Upadhyayula, V. Nunez, E. M. Espinoza, J. M. Larsen, D. Bao, D. Shi, J. T. Mac, B. Anvari, V. I. Vullev, *Chem. Sci.* **2015**, *6*, 2237– 2251.

28. a) S. Guo, D. Bao, S. Upadhyayula, W. Wang, A. B. Guvenc, J. R. Kyle, H. Hosseinibay, K. N. Bozhilov, V. I. Vullev, C. S. Ozkan, M. Ozkan, *Adv. Funct. Mater.* **2013**, *23*, 5199–5211; b) V. Nuñez, S. Upadhyayula, B. Millare, J. M. Larsen, A. Hadian, S. Shin, P. Vandrangi, S. Gupta, H. Xu, A. P. Lin, G. Y. Georgiev, V. I. Vullev, *Anal. Chem.* **2013**, *85*, 4567–4577.

29. a) M. B. Smith, J. Michl, *Chem. Rev.* **2010**, *110*, 6891–6936; b) V. M. Nichols, M. T. Rodriguez, G. B. Piland, F. Tham, V. N. Nesterov, W. J. Youngblood, C. J. Bardeen, *J. Phys. Chem. C* **2013**, *117*, 16802–16810.

30. a) V. I. Vullev, *J. Phys. Chem. Lett.* **2011**, *2*, 503–508; b) B. Bahmani, S. Gupta, S. Upadhyayula, V. I. Vullev, B. Anvari, *J. Biomed. Opt.* **2011**, *16*, 051303/051301–051303/051310; c) S. Upadhyayula, D. Bao, B. Millare, S. S. Sylvia, K. M. M. Habib, K. Ashraf, A. Ferreira, S. Bishop, R. Bonderer, S. Baqai, X. Jing, M. Penchev, M. Ozkan, C. S. Ozkan, R. K. Lake, V. I. Vullev, *J. Phys. Chem. B* **2011**, *115*, 9473–9490; d) S. Upadhyayula, T. Quinata, S. Bishop, S. Gupta, N. R. Johnson, B. Bahmani, K. Bozhilov, J. Stubbs, P. Jreij, P. Nallagatla, V. I. Vullev, *Langmuir* **2012**, *28*, 5059–5069; e) B. Bahmani, C. Y. Lytle, A. M. Walker, S. Gupta, V. I. Vullev, B. Anvari, *Int. J. Nanomed.* **2013**, *8*, 1609–1620.

31. a) A. Vallee, V. Humblot, C.-M. Pradier, *Acc. Chem. Res.* **2010**, *43*, 1297– 1306; b) H. Lu, D. Bao, M. Penchev, M. Ghazinejad, V. I. Vullev, C. S. Ozkan, M. Ozkan, *Adv. Sci. Lett.* **2010**, *3*, 101–109; c) U. K. Gautam, M. Ghosh, M. Rajamathi, R. Seshadri, *Pure Appl. Chem.* **2002**, *74*, 1643–1649; d) Y. Zhang, E. Galoppini, *ChemSusChem* **2010**, *3*, 410–428; e) M. Garcia- Iglesias, J.-J. Cid, J.-H. Yum, A. Forneli, P. Vazquez, M. K. Nazeeruddin, E. Palomares, M. Gratzel, T. Torres, *Energy Environ. Sci.* **2011**, *4*, 189–194.

Supplemental Figures

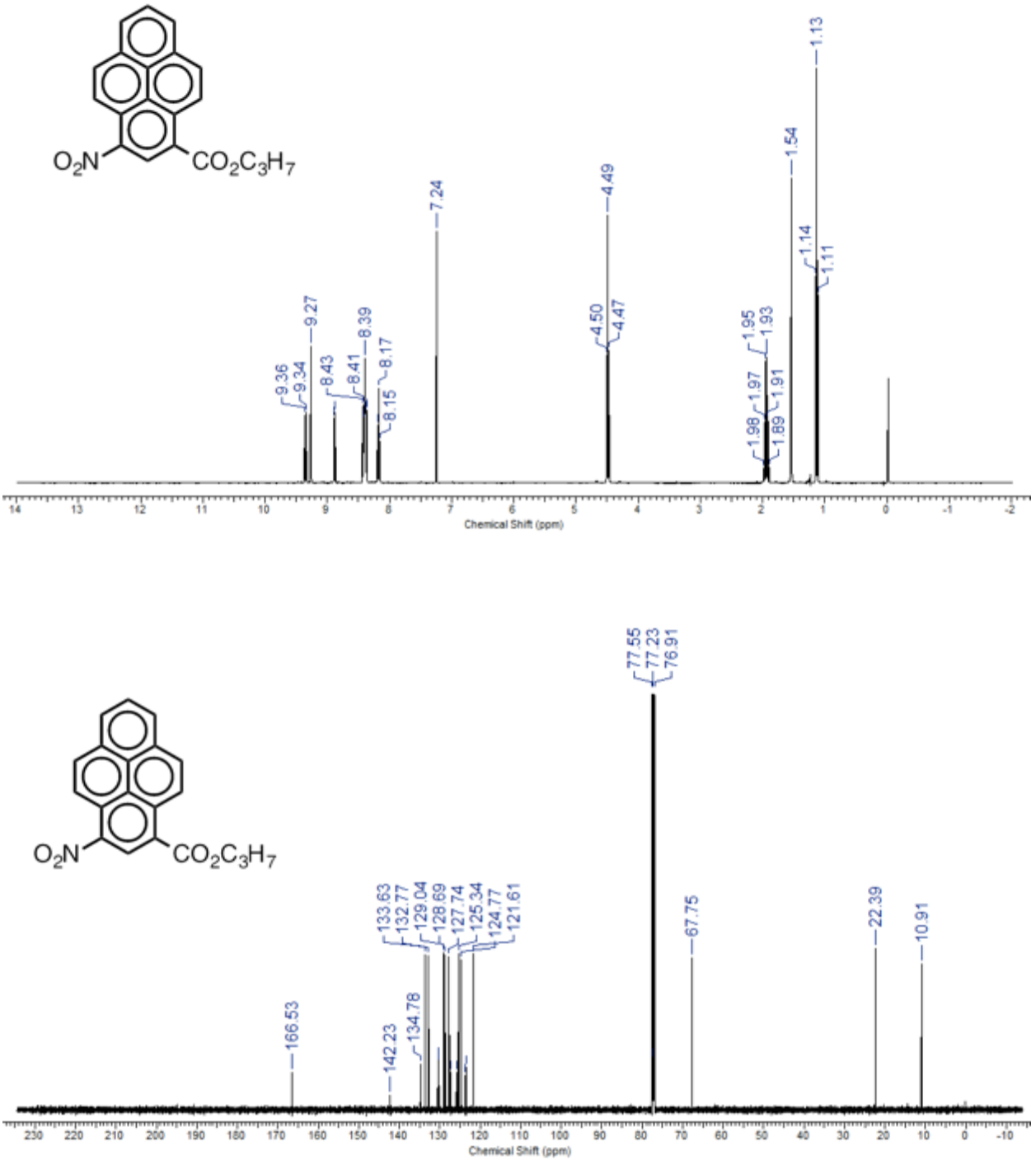

Figure 5S-1. One-dimensional (1D) NMR spectra of 3NPyCO$_2$Pr.

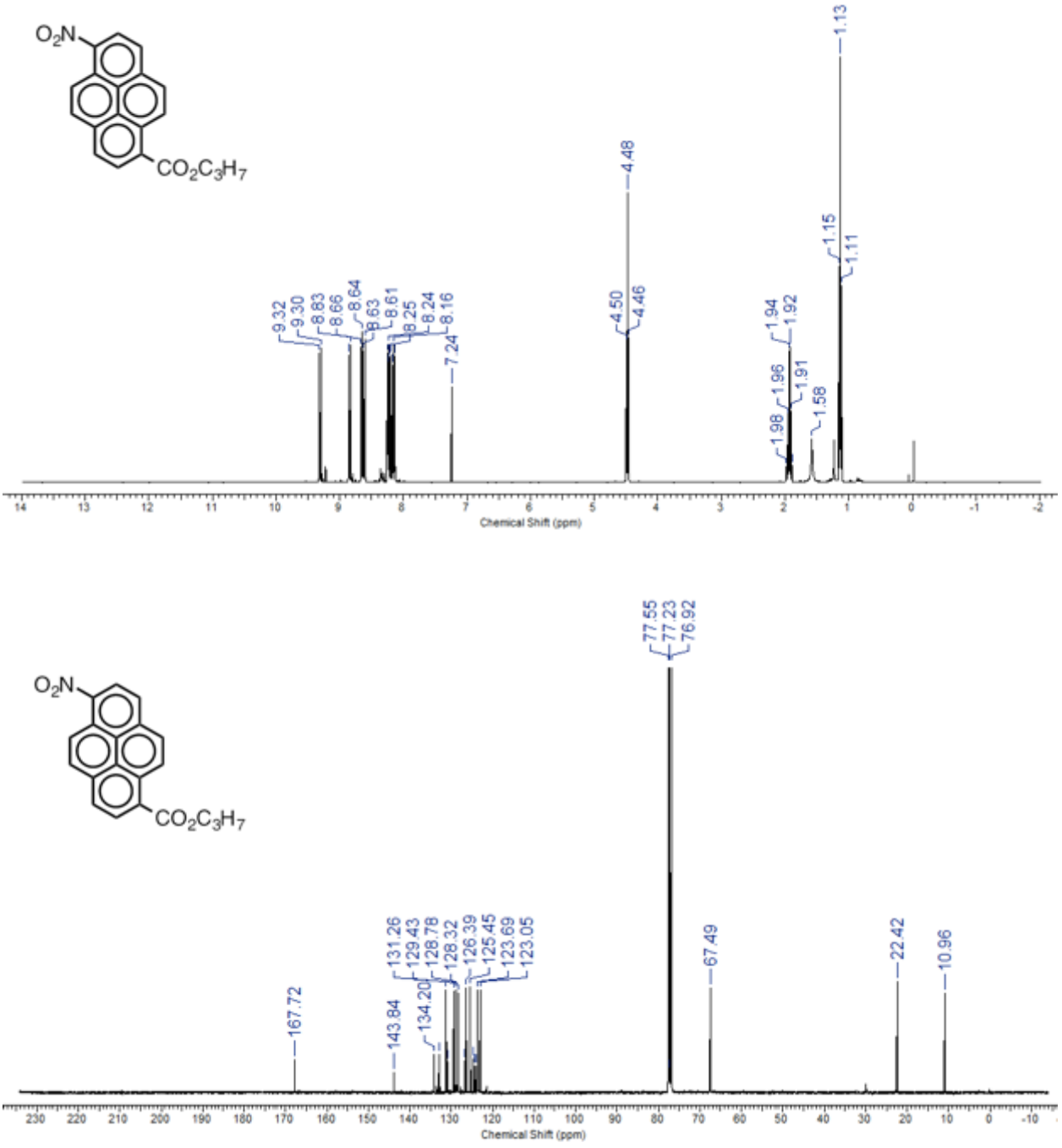

Figure 5S-2. One-dimensional (1D) NMR spectra of 6NPyCO2Pr.

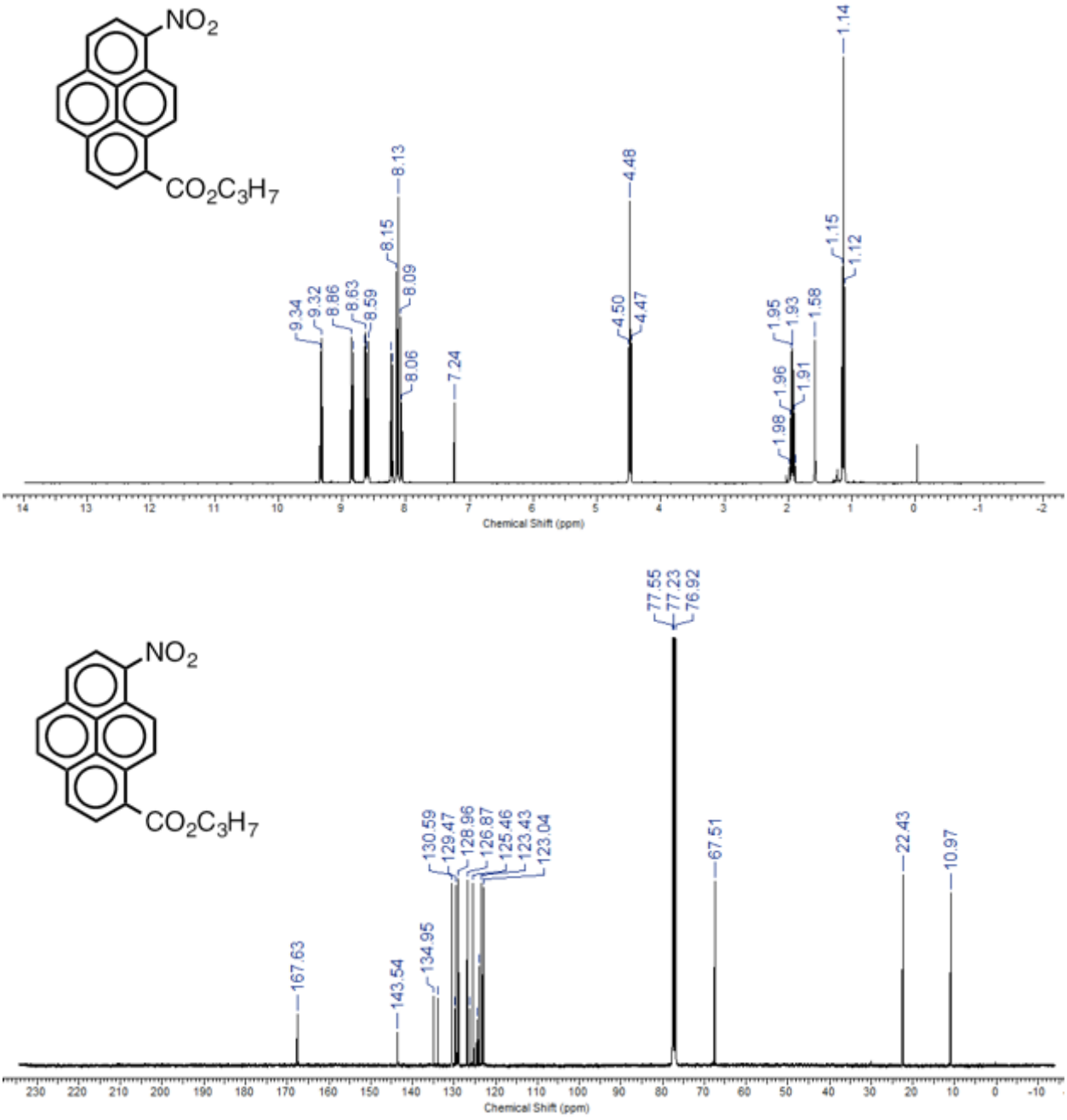

Figure 5S-3. One-dimensional (1D) NMR spectra of 8NPyCO2Pr.

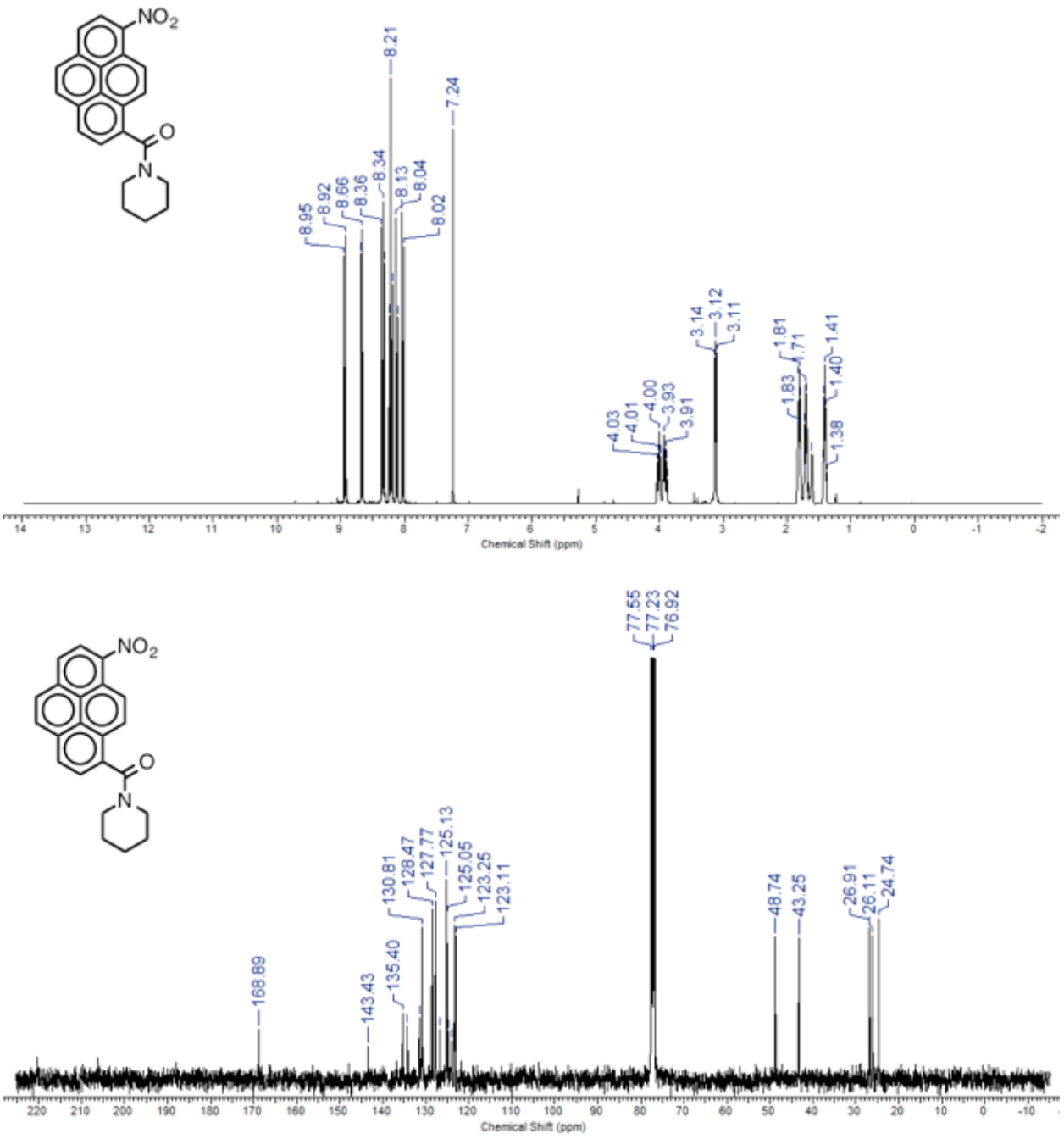

Figure 5S-4. One-dimensional (1D) NMR spectra of NPyPip.

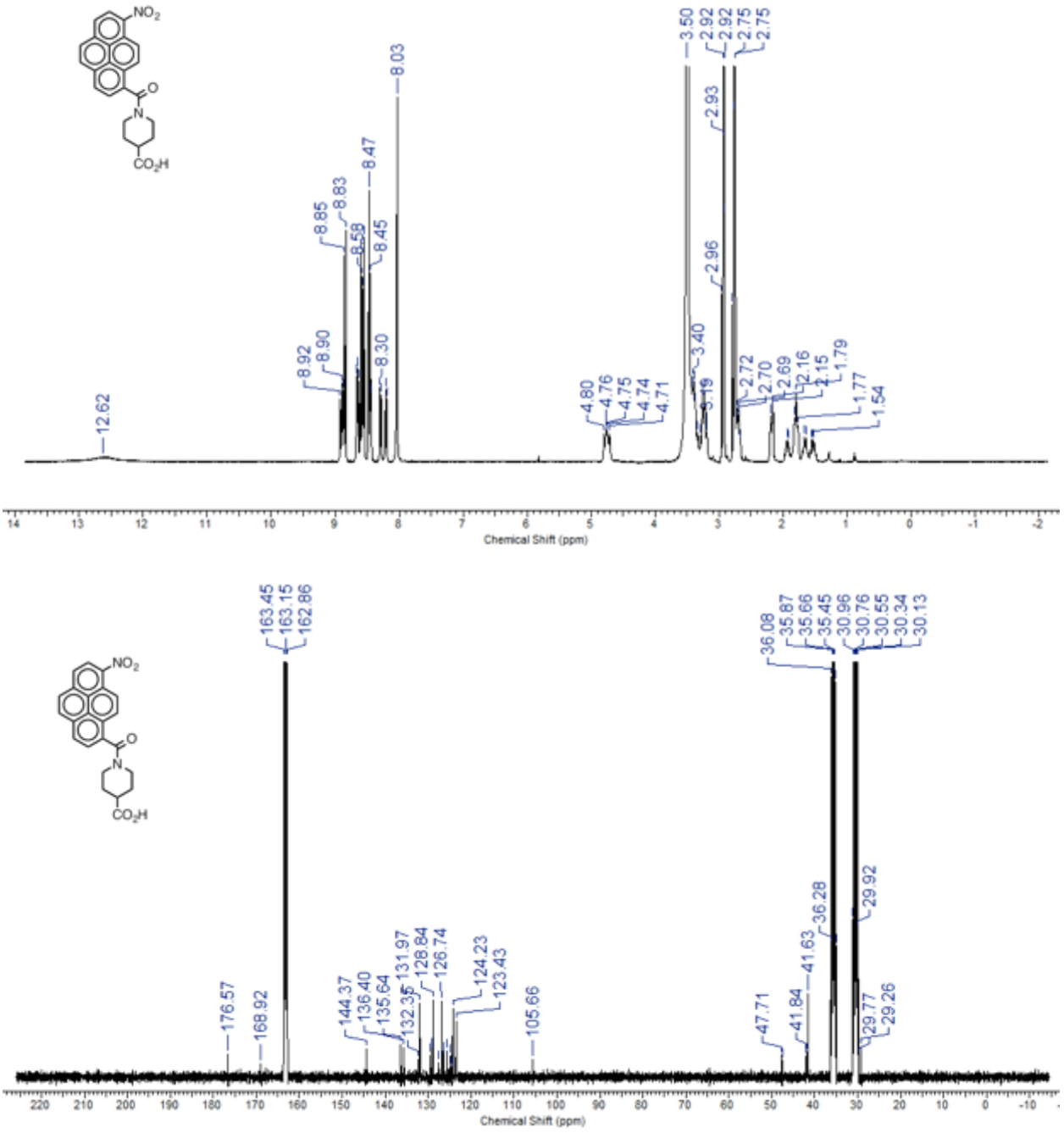

Figure 5S-5. One-dimensional (1D) NMR spectra of NPyPipCO2H.

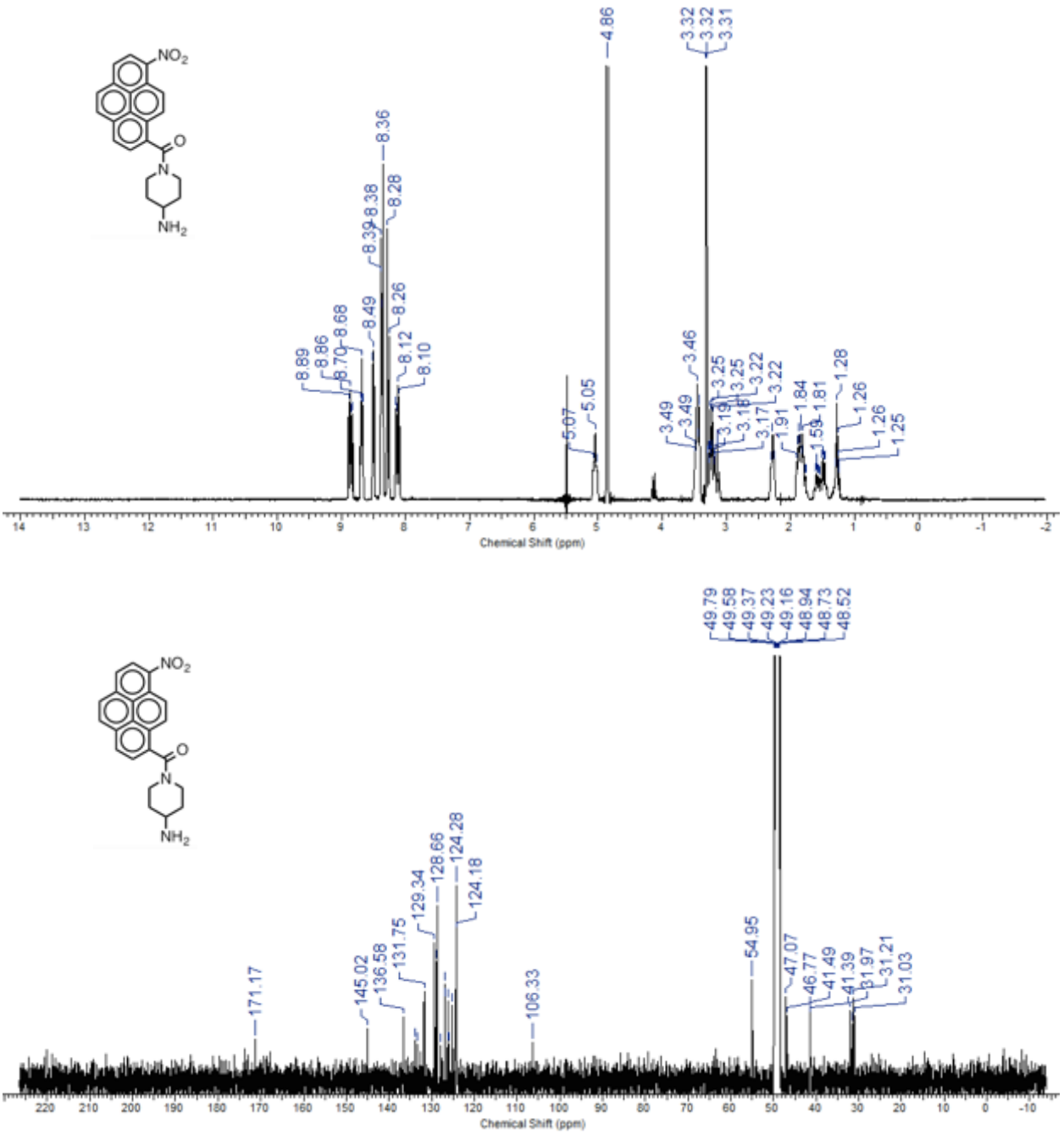

Figure 5S-6. One-dimensional (1D) NMR spectra of $NPyPipNH_2$.

LCMS of the NPyPipR products and intermediates (R = CO_2Et, NH-tBoc, CO_2H and NH_2)

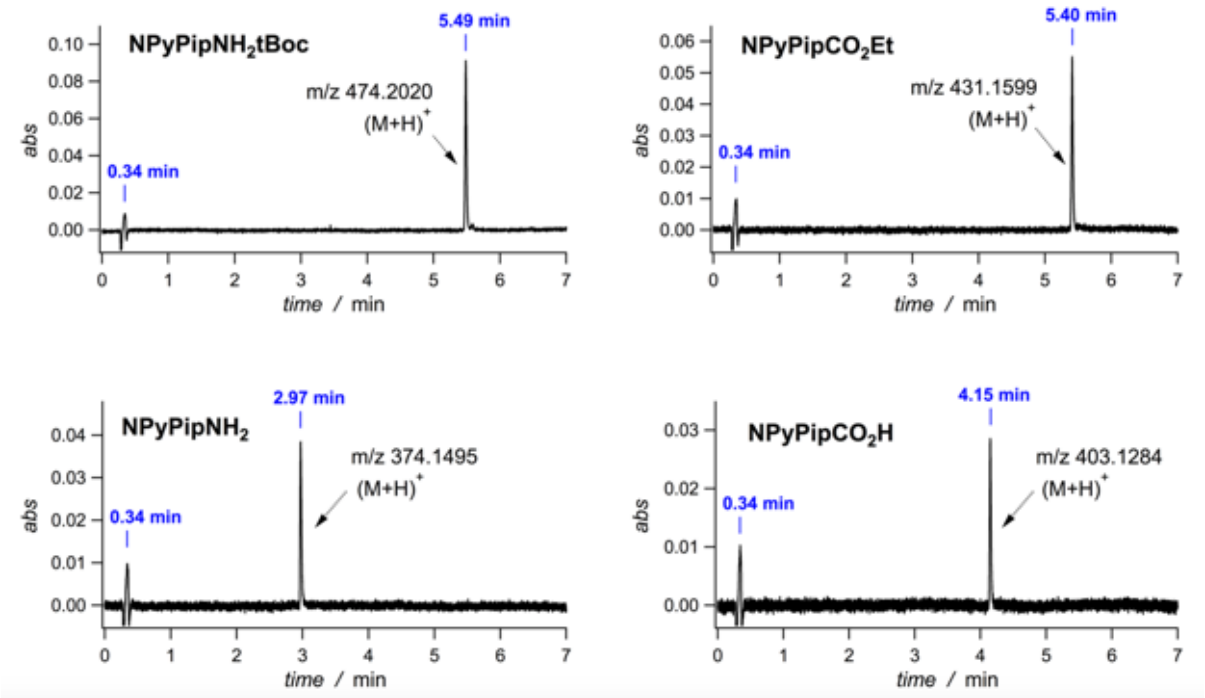

Figure 5S-7. Chromatograms from the LCMS analysis of the NPyPipR conjugates (absorption @ 400 nm). Reverse phase HPLC (C18 stationary phase); mobile phase contained water and acetonitrile with 0.1% formic acid (V/V) and flown at 0.5 ml/min. The gradient was ramped from 5% to 95% acetonitrile over 7 min.

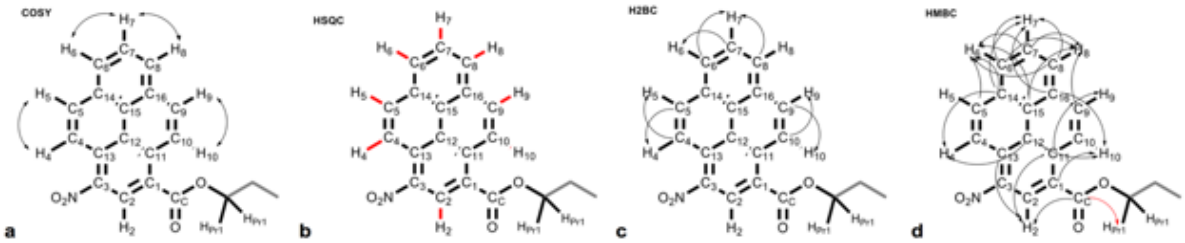

Figure 5S-8. Key cross-correlations obtained from 2D NMR spectroscopy of fraction 1 (Table 5S-1, Figure 2a): (a) COSY; (b) HSQC, the observed ^{13}C-^{1}H ^{1}J correlations are highlighted in red; (c) H2BC; and (d) HMBC, the red arrow depicts the observed correlation between the carbonyl carbon (C_C) and the 1-propyl proton (H_{Pr1}), which is not listed in Table S1 depicting only the chemical shifts from the aromatic region.

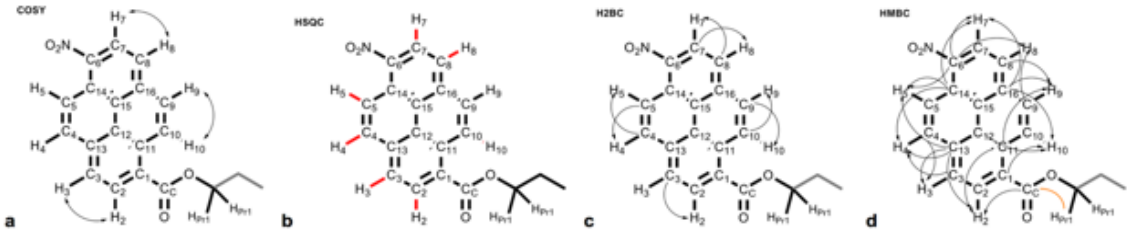

Figure 5S-9. Key cross-correlations obtained from 2D NMR spectroscopy of fraction 2 (Table S2, Figure 2a): (a) COSY; (b) HSQC, the observed ^{13}C-^{1}H ^{1}J correlations are highlighted in red; (c) H2BC; and (d) HMBC.

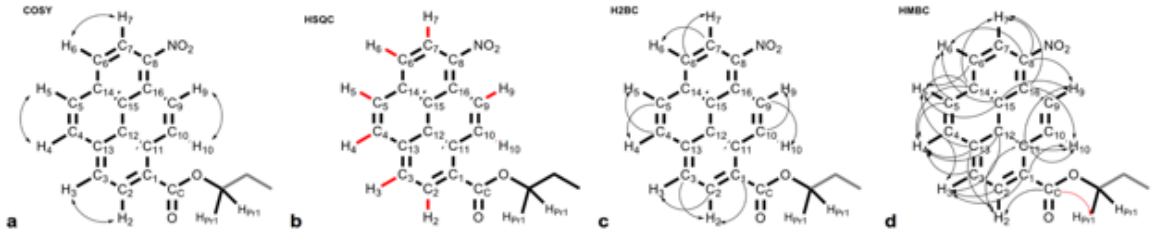

Figure 5S-10. Key cross-correlations obtained from 2D NMR spectroscopy of fraction 3 (Table S3, Figure 2a, Figure 3): (a) COSY; (b) HSQC, the observed ^{13}C-^{1}H ^{1}J correlations are highlighted in red; (c) H2BC; and (d) HMBC, the red arrow depicts the observed correlation between the carbonyl carbon (C_C) and the 1-propyl proton (H_{Pr1}), which is not listed in Table S3 depicting only the chemical shifts from the aromatic region.

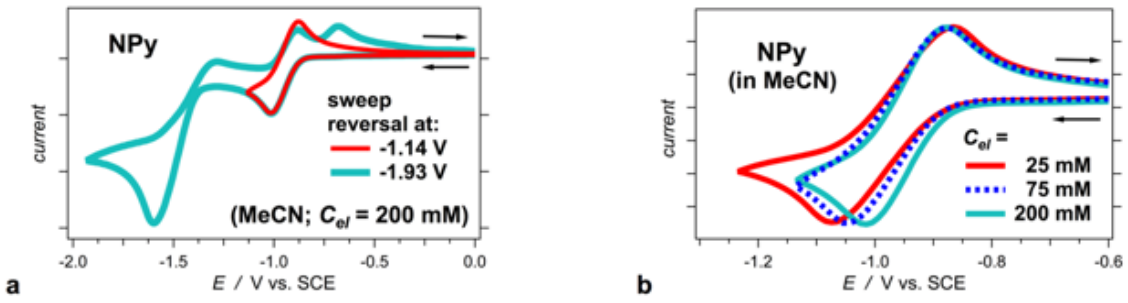

Figure 5S-11. Electrochemical reduction of 1-nitropyrene, NPy, in acetonitrile (MeCN) containing different amounts of supporting electrolyte, tetrabutylammonium hexafluorophosphate. (a) Cyclic voltammograms of NPy where the sweeps are reversed after the first cathodic wave (at about –1.2 V vs. SCE) and after the second wave (at about –2.0 V vs. SCE). (b) Cyclic voltammograms of NPy, reversed after the first cathodic waves, and recorded at different electrolyte concentrations, C_{el}.

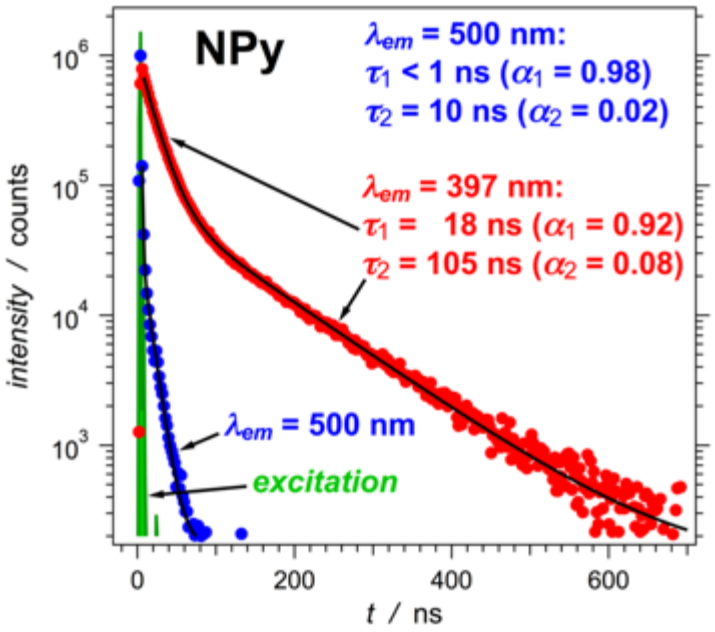

Figure 5S-12. Emission decays of NPy sample (10 ⌈M in MeCN) obtained from TCSPC measurements. (λ_{ex} = 278 nm, half-height pulse width = 1 ns). The coloured dots/circles represent the data points. The black solid lines represent the fits of the fluorescence intensity, $F(t)$, with a biexponentialfunction:$F(t) = F(0) + A_1 \exp(-t/\tau_1) + A_2 \exp(-t/\tau_1)$;where $\alpha_1 = A_1/(A_1 + A_2)$, and $\alpha_2 = A_2/(A_1 + A_2)$.

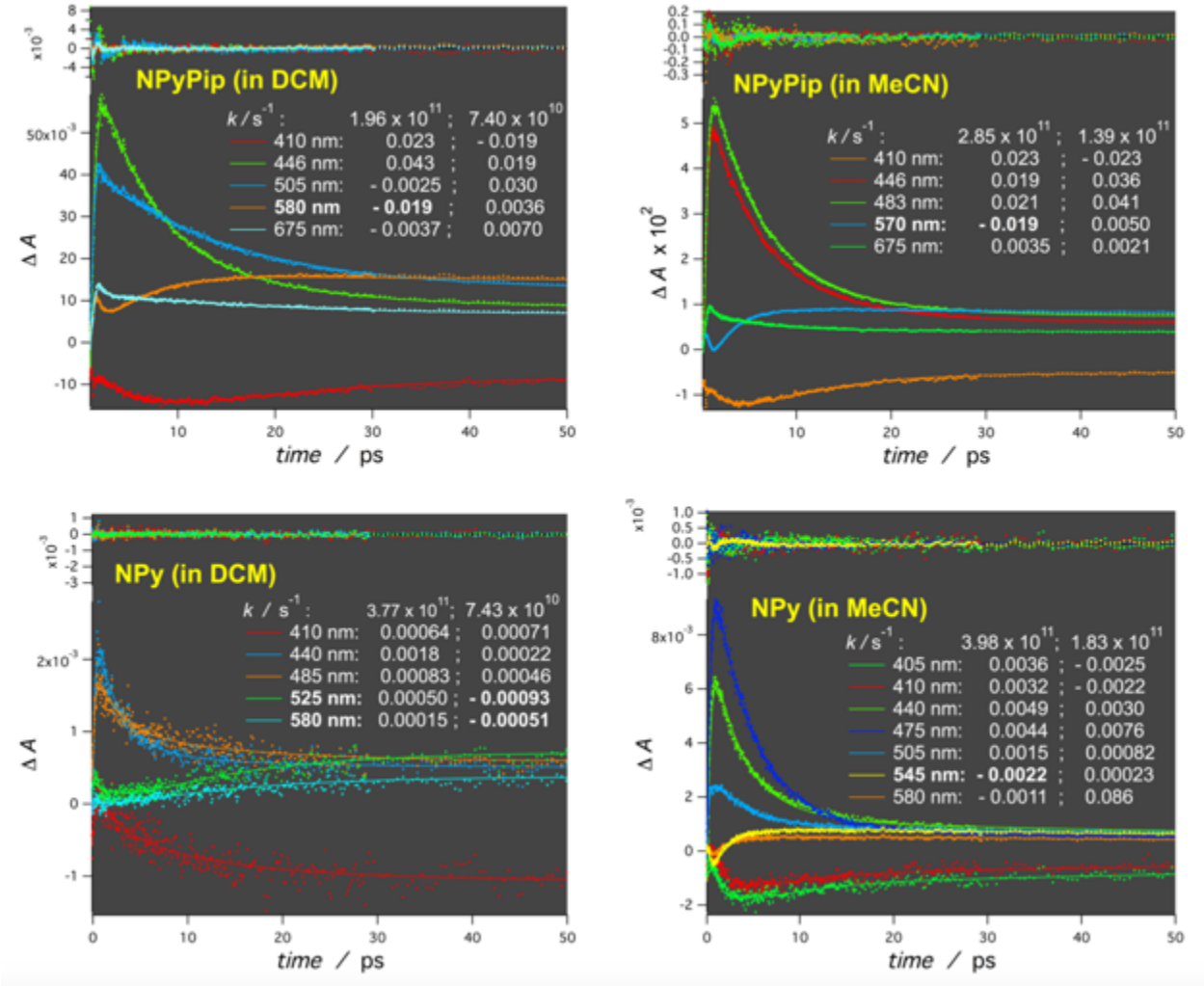

Figure 5S-13. Summaries of multi-exponential global fits of transient-absorption kinetics of NPy and NPyPip for aprotic solvents. The numbers under each of the rate constants represent the values of the preexponential parameter for the corresponding wavelength. The dots represent the data, the solid lines – the fitting curves, and the fitting residuals are displayed on the top of each graph. (λ_{ex} = 390 nm; 50 fs pulse width at 800 nm, 4 (J per pulse).

Tables

Table 5S-1. 2D NMR correlations of the aromatic ^{1}H with ^{13}C (HSQC, H2BC, and HMBC) and with other ^{1}H (COSY) for fraction 1, assigned to 3NPyCO2Pr.[a]

Atom #	$\delta(^{13}C)$	$\delta(^{1}H)$	COSY, $\delta(^{1}H)$ / ppm	HSQC, $\delta(^{1}H)$ / ppm	H2BC, $\delta(^{1}H)$ / ppm	HMBC, $\delta(^{1}H)$ / ppm
1	123.4 ppm					9.35 (H_{10})
2	125.3 ppm	9.26 ppm		9.26 (H_2)		
3 (NO_2)	142.2 ppm					9.26 (H_2)
4	121.6 ppm	8.88 ppm	8.42 (H_5)	8.88 (H_4)	8.42 (H_5)	
5	133.6 ppm	8.42 ppm	8.88 (H_4)	8.42 (H_5)	8.88 (H_4)	8.38 (H_6)
6	128.7 ppm	8.38 ppm	8.17 (H_7)	8.38 (H_6)	8.17 (H_7)	8.40 (H_8); 8.17 (H_7)
7	127.7 ppm	8.17 ppm	8.39 (H_6, H_8)	8.17 (H_7)	8.39 (H_6, H_8)	8.38 (H_6); 8.40 (H_8)
8	129.0 ppm	8.40 ppm	8.17 (H_7)	8.40 (H_8)	8.17 (H_7)	8.38 (H_6); 8.17 (H_7)
9	132.8 ppm	8.37 ppm	9.35 (H_{10})	8.37 (H_9)	9.35 (H_{10})	8.40 (H_8)
10	124.8 ppm	9.35 ppm	8.37 (H_9)	9.35 (H_{10})	8.37 (H_9)	
11	134.8 ppm					9.26 (H_2); 8.37 (H_9)
12	125.8 ppm					9.35 (H_{10}); 8.88 (H_4)
13	127.3 ppm					9.26 (H_2)
14	130.2 ppm					8.88 (H_4); 8.38 (H_6); 8.17 (H_7)
15	123.6 ppm					8.38 (H_6); 8.40 (H_8)
16	130.4 ppm					9.35 (H_{10}); 8.17 (H_7)
Carbonyl	166.5 ppm					9.26 (H_2)

[a] The numbering of the atoms (Scheme 5-1) and the cross-correlations are depicted on Figure 5S-1. The 2D NMR measurements were carried out with HPLC-pure sample, isolated from fraction 1 (Figure 5-2a) and dissolved in CDCl3.

Table 5S-2. 2D NMR correlations of the aromatic ^{1}H with ^{13}C (HSQC, H2BC, and HMBC) and with other ^{1}H (COSY) for fraction 2, assigned to 6NPyCO2Pr.[a]

Atom #	$\delta(^{13}C)$	$\delta(^{1}H)$	COSY, $\delta(^{1}H)$ / ppm	HSQC, $\delta(^{1}H)$ / ppm	H2BC, $\delta(^{1}H)$ / ppm	HMBC, $\delta(^{1}H)$ / ppm
1	126.7 ppm					9.31 (H_{10})
2	129.4 ppm	8.65 ppm	8.24 (H_3)	8.65 (H_2)		
3	126.4 ppm	8.24 ppm	8.65 (H_2)	8.24 (H_3)	8.65(H_2)	8.23 (H_4)
4	131.3 ppm	8.23 ppm	8.84 (H_5)	8.23 (H_4)	8.84(H_5)	8.24 (H_3)
5	123.7 ppm	8.84 ppm	8.23 (H_4)	8.84 (H_5)	8.23(H_4)	
6 (NO_2)	143.8 ppm					8.84 (H_5); 8.62 (H_7); 8.18 (H_8)
7	123.0 ppm	8.62 ppm	8.18 (H_8)	8.62 (H_7)	8.18 (H_8)	
8	125.5 ppm	8.18 ppm	8.62 (H_7)	8.18 (H_8)	8.62 (H_7)	8.15 (H_9)
9	128.8 ppm	8.15 ppm	9.31 (H_{10})	8.15 (H_9)	9.31(H_{10})	8.18 (H_8)
10	128.3 ppm	9.31 ppm	8.15 (H_9)	9.31 (H_{10})	8.15 (H_9)	
11	130.8 ppm					8.65 (H_2); 8.15 (H_9)
12	124.0 ppm					9.31 (H_{10})
13	132.9 ppm					8.84(H_5); 8.65 (H_2); 8.24(H_3); 8.23 (H_4)
14	124.7 ppm					8.84 (H5); 8.62 (H7); 8.23 (H4)
15	124.5 ppm					
16	134.2 ppm					9.31 (H_{10}); 8.62 (H_7); 8.15 (H_9)
Carbonyl	167.7 ppm					8.65 (H_2)

[a] The numbering of the atoms (Scheme 5-1) and the cross-correlation are depicted on Figure 5S-2. The 2D NMR measurements were carried out with HPLC-pure sample, isolated from fraction 2 (Figure 5-2a) and dissolved in CDCl3.

Table 5S-3. 2D NMR correlations of the aromatic ^{1}H with ^{13}C (HSQC, H2BC, and HMBC) and with other ^{1}H (COSY) for fraction 3, assigned to 8NPyCO2Pr.[a]

Atom #	δ (^{13}C)	δ (^{1}H)	COSY, δ (^{1}H) / ppm	HSQC, δ (^{1}H) / ppm	H2BC, δ (^{1}H) / ppm	HMBC, δ (^{1}H) / ppm
1	126.2 ppm				8.64 (H_2)	8.22 (H_3); 9.33 (H_{10})
2	129.5 ppm	8.64 ppm	8.22 (H_3)	8.64 (H_2)	8.22 (H_3)	8.22 (H_3)
3	126.9 ppm	8.22 ppm	8.64 (H_2)	8.22 (H_3)	8.64 (H_2)	8.14 (H_4)
4	130.6 ppm	8.14 ppm	8.08 (H_5)	8.14 (H_4)		8.22 (H_3)
5	128.9 ppm	8.08 ppm	8.14 (H_4)	8.08 (H_5)	8.14 (H_4)	8.14 (H_6); 8.14 (H_4)
6	125.5 ppm	8.14 ppm	8.60 (H_7)	8.14 (H_6)	8.60 (H_7)	8.08 (H_5)
7	123.0 ppm	8.60 ppm	8.14 (H_6)	8.60 (H_7)	8.14 (H_6)	
8 (NO_2)	143.5 ppm					8.85 (H_9); 8.60 (H_7); 8.14 (H_6)
9	123.4 ppm	8.85 ppm	9.33 (H_{10})	8.85 (H_9)	9.33 (H_{10})	
10	129.0 ppm	9.33 ppm	8.85 (H_9)	9.33 (H_{10})	8.85 (H_9)	
11	129.8 ppm					9.33 (H_{10}); 8.85 (H_9); 8.64 (H_2)
12	124.0 ppm					8.22 (H_3); 9.33 (H_{10}); 8.14 (H_4)
13	133.8 ppm					8.64 (H_2); 8.14 (H_4); 8.08 (H_5)
14	134.9 ppm					8.60 (H_7); 8.14 (H_6); 8.14 (H_4)
15	124.6 ppm					8.14 (H_6); 8.08 (H_5); 8.85 (H_9)
16	124.0 ppm					9.33 (H_{10}); 8.60 (H_7)
Carbonyl	167.6 ppm					8.64 (H_2)

[a] The numbering of the atoms (scheme 5-1) and the cross-correlations are depicted on Figure 5S-3. The 2D NMR measurements (Figure S3, solvent: CDCl3) were carried out with chromatographically pure sample, isolated from the second major yellow fraction from normal-phase flash chromatography and confirmed with HPLC to be fraction 3 (Figure 5-2a).

Chapter 6

How Do Amides Affect the Electronic Properties of Pyrene?

Abstract

The electronic properties of amide linkers, which are intricate components of biomolecules, offer a wealth of unexplored possibilities. Herein, we demonstrate how the different modes of attaching an amide to a pyrene chromophore affect the electrochemical and optical properties of the chromophore. Thus, although they cause minimal spectral shifts, amide substituents can improve either the electron-accepting or electron-donating capabilities of pyrene. Specifically, inversion of the amide orientation shifts the reduction potentials by 200 mV. These trends indicate that, although amides affect to a similar extent the energies of the ground and singlet excited states of pyrene, the effects on the doublet states of its radical ions are distinctly different. This behavior reflects the unusually strong orientation dependence of the resonance effects of amide substituents, which should extend to amide substituents on other types of chromophores in general. These results represent an example where the Hammett sigma constants fail to predict substituent effects on electrochemical properties. On the other hand, Swain−Lupton parameters are found to be in good agreement with the observed trends. Examination of the frontier orbitals of the pyrene derivatives and their components reveals the underlying reason for the observed amide effects on the electronic properties of this polycyclic aromatic hydrocarbon and points to key molecular-design strategies for electronic and energy-conversion systems.

Introduction

The importance of amides as building blocks in living systems cannot be overstated. Peptide bonds hold proteins together, and the amide propensity for hydrogen bonding defines the secondary structures des have been at the forefront of materials science and engineering.[5–9] Due to their extendeand the functionality of these biopolymers.[1–3] Since the invention of nylon,[4] synthetic polyamid π-conjugation, amide bonds are rigid and assume planer conformations.[10–14]

In addition to functioning as bonding elements and hydrogen-bonding cross-linkers, amides also have interesting electronic properties. The amide dipoles, ranging between 3 and 5 D,[15] render many vital enzymatic and cellular processes possible.[16–18] Ordered amide and hydrogen bonds give rise to the enormous macrodipoles of protein helices,[18–20] providing guidelines for bioinspired designs.[21–31] In addition to making ion channels functional,[17,32] such dipolar amide conjugates prove invaluable for rectifying the directionality of electron transfer and transport.[20,33–38] Aliphatic amides oxidize at about 1.5 V versus saturated calomel electrode (SCE)[39] and have optical gaps of 5.6 eV between their highest occupied molecular orbitals (HOMOs) and lowest unoccupied molecular orbitals (LUMOs), corresponding to an n–π* transition around 222 nm,[11] making them electron-rich π-conjugated UV absorbers.

Except for a few reports on how the orientation of amide bonds affects molecular properties, such as enantioselectivity, catalytic activity, and the biological uptake of

nanoconstructs,[40–42] the understanding of the effects of this important substituent on the characteristics of organic chromophores remains in the realm of empirical deductions. Even the classical Hammett constants predict that, regardless of their orientation, amides should be electron-withdrawing groups.[43] However, the Swain–Lupton resonance parameters, accounting for the mesomeric effects of functional groups,[44] do suggest that there should be a difference between the effects of amides attached via their nitrogens or via their carbonyl carbons.[43,44]

Substituent effects on electronically excited states correlate roughly with ground-state descriptors such as Hammett constants. However, because it is the difference between the ground and excited states that defines the optical properties of a molecule, if a substituent affects the energies of both the ground and excited states in the same manner, the shifts in the optical spectra will be negligible, regardless of how strong these effects are. Furthermore, despite all advances in physical organic chemistry during the 20th century, the search for reliable descriptors of substituent effects on excited-state properties is still in its infancy.[45] Thus, systematic studies on how amides and other substituents affect transitions between different electronic states are important for filling key voids in physical organic chemistry and other pertinent fields.

The question of interest here is, aside from serving as linkers, hydrogen-bonding sites, and dipole sources, how do amide functionalities impact the electronic properties of π-conjugated moieties to which they are attached?

To test this capability of amides, we focus on pyrene as the π-conjugated moiety. Pyrene and its derivatives are among the most widely used chromophores due to their good fluorescence quantum yields (ϕ_f) and the unusually long lifetime (τ) of the singlet excited states.[46–49] The potentials at which they oxidize and reduce make pyrenes a popular choice as electron donors and acceptors.[50–56] Along with their attractive optical and electrochemical properties, the strong propensity for self-assembly via π-stacking, which pyrene and its derivatives exhibit,[57–59] allows them to serve as building blocks for electronic and photonic materials and interfaces.[60–70]

To examine how amides affect the electronic properties of pyrene, we attach them in opposite orientations directly to the aromatic ring ($Py_{N\text{-}C}$ and $Py_{C\text{-}N}$, Chart 6-1). Insertion of a methylene linker ($Py_{mN\text{-}C}$ and $Py_{mC\text{-}N}$, Chart 6-1) breaks the π- conjugation between the amide and the pyrene moiety, permitting an evaluation of the amide effects in the absence of strong electronic coupling with the polycyclic aromatic hydrocarbons (PAHs). Unlike other π-conjugating substituents, such as nitro, nitroso, and alkanoyl groups,[53,71] amides, even when directly attached to pyrene, cause small shifts in the UV/visible absorption and fluorescence spectra. The most profound effect of the amides is on the reduction potentials of oxidation and reduction of pyrene. Thus, although amides affect to a similar extent the energies of the ground and singlet excited states of pyrene, their effects on the doublet states of their radical ions are quite different.

Results

Molecular Design Considerations

Chart 6-1. Structures of Pyrene Derivatives with Differently Oriented Secondary Amides Attached Directly ($Py_{N\text{-}C}$ and $Py_{C\text{-}N}$) and via a Methylene Linker ($Py_{mN\text{-}C}$ and $Py_{mC\text{-}N}$).

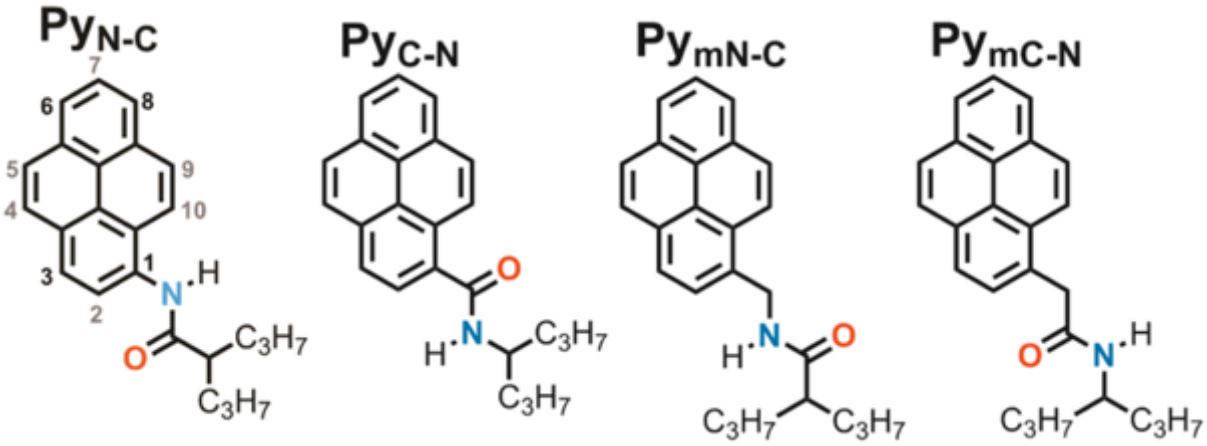

Amide coupling between the corresponding amine and carboxylic-acid derivatives yields the pyrene−amide conjugates in good yields after chromatographic purification and recrystallization steps (Chart 6-1). The positions 1, 3, 6, and 8 ($Py_{N\text{-}C}$ on Chart 6-1) are the most susceptible to electrophilic and radical substitutions.[71−73] Therefore, this study focuses on pyren-1-yl amides (Chart 6-1).

Amide Effects on Optical Properties of Pyrene

The optical spectra of the four pyrene−amide derivatives (Chart 6-1) investigated here show features characteristic of pyrene. In addition to the transitions to upper excited states, the substituents perturb the symmetry of pyrene, enhancing the intensity of the symmetry-forbidden $S_0 \rightarrow S_1$ electronic absorption at 375 nm (Figure 6-1a). Although the perturbation of the symmetry is stronger for $Py_{N\text{-}C}$ and $Py_{C\text{-}N}$ than for the methylene-linked

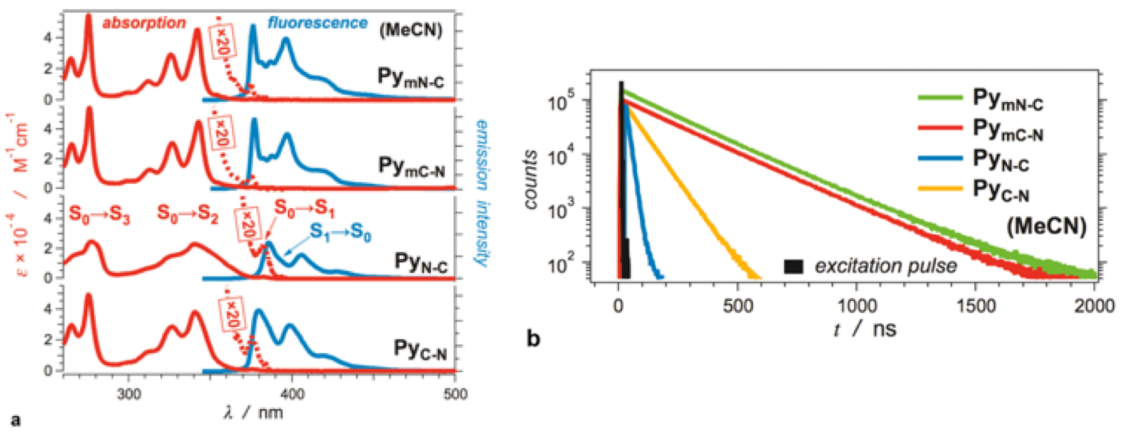

Figure 6-1. Optical properties of the pyrene–amide derivatives in acetonitrile (MeCN), purged with argon. (a) Absorption and fluorescence spectra (λ_{ex} = 335 nm) with the various transitions designated. The dotted lines represent the absorption spectra amplified by a factor of 20 for visualization of the $S_0 \rightarrow S_1$ forbidden transitions. (b) Time-correlated single-photon counting (TCSPC) emission-decay curves recorded at the fluorescence maxima (λ_{ex} = 278 nm; excitation-pulse width = 0.9 ns).

derivatives, the amide substituents do not cause large spectral shifts (Figure 6-1a). The spectra of Py_{mN-C} and Py_{mC-N} resemble those of alkyl-substituted pyrenes,[57,74] indicating that methylene linkers do indeed effectively reduce the interaction between the amide and the pyrene π- conjugated system. Direct attachment of the amide via its carbon, Py_{C-N}, broadens the absorption and emission bands (Figure 1a) and decreases the zero-to-zero transition energy (ε_{00}) by less than k_BT (Table 6-1). Attaching the amide moiety via its nitrogen, Py_{N-C}, enhances the spectral broadening and decrease ε_{00} a bit further.

The emission-decay kinetics shows the same trends (Figure 6-1b). Py_{mN-C} and Py_{mC-N} exhibit large values of τ (Table 1), which are comparable to those of alkyl-substituted pyrenes.[57,59,74] Attaching the amide directly via its carbonyl carbon, Py_{C-N}, shortens τ, reflecting the enhancement of the intensity of the symmetry-forbidden $S_1 \rightarrow S_0$ transition. Attaching the amide group via its nitrogen, Py_{N-C}, shortens τ even further (Figure 6-1b and

Table 6-1).

Table 6-1. Photophysical Properties of the Pyrene–Amide Derivatives for Various Solvents

					$h\Delta\nu$ (eV)[b]	
	solvent	φ_f	τ (ns)	$\mathcal{E}_{00}$ (eV)[a]	S_2[c]	S_1[d]
$Py_{mN\text{-}C}$	MeCN	0.41	217	3.30	0.34	0.013
	DCM	0.38	150	3.30	0.31	0.011
	$CHCl_3$	0.38	99.6	3.31	0.31	0.009
$Py_{mC\text{-}N}$	MeCN	0.44	216	3.30	0.34	0.018
	DCM	0.39	139	3.29	0.31	0.020
	$CHCl_3$	0.29	111	3.29	0.31	0.015
$Py_{N\text{-}C}$	MeCN	0.23	13.7	3.23	0.42	0.029
	DCM	0.26	13.7	3.22	0.40	0.025
	$CHCl_3$	0.19	12.2	3.23	0.39	0.026
$Py_{C\text{-}N}$	MeCN	0.44	69.3	3.28	0.37	0.039
	DCM	0.42	36.6	3.27	0.37	0.041
	$CHCl_3$	0.42	29.2	3.26	0.37	0.050

[a]From the crossover point of the normalized $S_0 \rightarrow S_1$ absorption and the fluorescence bands. [b]Stoke's shifts: $\Delta\nu$ is the difference between the frequencies of the absorption and fluorescence maxima, and h is the Planck constant. [c]Using the $S_0 \rightarrow S_1$ absorption maximum for $\Delta\nu$. [d]Using the $S_0 \rightarrow S_1$ absorption maximum.

Stoke's shifts ($\Delta\nu$), estimated from the absorption and emission maxima at about 340 and 380 nm, respectively, encompass $S_2 \rightarrow S_1$ internal conversion as well as relaxation of S_1. The latter is small, since the $\Delta\nu$ values using the $S_0 \rightarrow S_1$ absorption are minute and are comparable to those of quantum dots and solid-state materials (Table 6-1).[75–77] This finding indicates that solvation effects following photoexcitation do not appreciably perturb the geometry of these pyrene derivatives.

The photophysical trends (Figure 6-1 and Table 6-1) reflect the consequences of π-conjugation of the amide with the PAH. The effects are, indeed, more pronounced when the amide is directly attached via its nitrogen than its carbonyl carbon. Also, the close resemblance between the properties of $Py_{mN\text{-}C}$ and $Py_{mC\text{-}N}$ indicates that the amide electric dipoles, which generate large fields even across methylene linkers,[38] are not responsible for the observed effects. The lack of a significant solvent dependence of ε_{00} and $\Delta\nu$ (Table 1) further confirms that amide dipoles do not contribute to the differences between the photophysics of the four derivatives. The decrease in ϕ_f and τ in chlorinated solvents (Table 6-1), which was also reported for pyrene itself,[49] may be a polarity effect. Photoinduced charge-transfer interactions with the solvent, however, might account for it as well.[78]

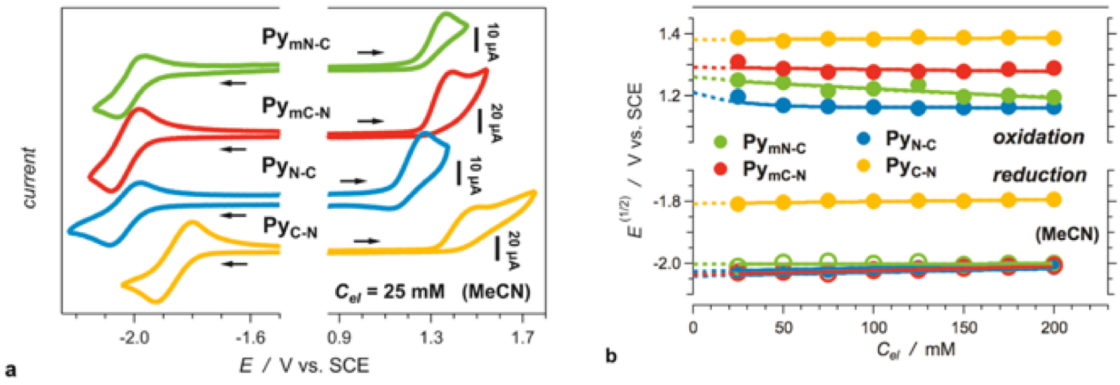

Figure 6-2. Electrochemical properties of the pyrene–amide derivatives in acetonitrile purged with argon in the presence of different concentrations, C_{el}, of supporting electrolyte, $(n\text{-}C_4H_9)_4NPF_6$. (a) Cyclic voltammograms for C_{el} = 25 mM (scan rate = 100 mV s^{-1}). For reversible reduction, the half-wave potentials, $E^{(1/2)}$, are determined from the average between the anodic and cathodic peak potentials. For irreversible oxidation, $E^{(1/2)}$ is estimated from the inflection-point potentials of the anodic waves.[81] (b) Dependence of $E^{(1/2)}$ on C_{el}. The solid lines represent the data fits, and the dotted lines show extrapolations of the potentials to $C_{el} = 0$, to yield $E^{(1/2)}$ for neat solvent.[80,82]

Amide Effects on Reduction and Oxidation Properties of Pyrene

Cyclic voltammetry of the pyrenea- mides, dissolved in MeCN, shows that all derivatives except $Py_{C\text{-}N}$ have reduction potentials ($E_{Py|Py^{\bullet-}}$) around −2 V versus SCE (Figure 2 and Table 6-2). For Py_{C_N}, $E_{Py|Py^{\bullet-}} = -1.8$ V versus SCE. The potentials at which pyrenes oxidize, expressed as reduction potentials of the radical cations ($E_{Py^{\bullet+}|Py}$), range from 1.2 V versus SCE for $Py_{N\text{-}C}$ to 1.4 V versus SCE for $Py_{C\text{-}N}$ (Table 6-2). The electrochemical HOMO–LUMO gaps, i.e., $E_{Py^{\bullet+}|Py} - E_{Py|Py^{\bullet-}}$, match the optical $_{00}$ quite well (Tables 6-1 and figure 6-2). This finding suggests a negligible difference between the energies of the solvated ions and the photoexcited species.[79]

Overall, attaching the amide group to pyrene via the carbonyl carbon lowers the energy of the HOMO and LUMO, enhancing the propensity of the pyrene chromophore to act as an electron acceptor. Conversely, attaching the amide group via the nitrogen elevates the energy of the pyrene HOMO without affecting the energy of the LUMO. This narrowing of the HOMO–LUMO gap, reflected in the value of ε_{00}, makes $Py_{N\text{-}C}$ a better electron donor than the other three derivatives.

For dichloromethane (DCM), the potentials at which the pyrenes oxidize, expressed as reduction potentials of the radical cations, show the same trends but are shifted to more positive values by about 100–200 mV in comparison with those for MeCN (Table 6-2). Thus, a decrease in the polarity of the medium destabilizes the radical cations that are formed upon oxidation and increases the corresponding reduction potentials of the oxidized

pyreneamides, $E_{Py^{\bullet+}|Py}$. Unfortunately, the reduction potentials of the pyrene derivatives,

Table 6-2. Reduction and Oxidation Properties of the Four Pyrene–Amide Derivatives

		$E^{(1/2)}$ (C_{el} = 0) (V vs SCE)[a]			
	solvent	$E_{Py^{\bullet+}|Py}$[c]	$E_{Py|Py^{\bullet-}}$[d]	IE (eV)[b]	EA (eV)[b]
$Py_{mN\text{-}C}$	MeCN	1.30 ± 0.17	−2.01 ± 0.01	5.58	2.35
	DCM	1.44 ± 0.05		5.74	2.17
	$CHCl_3$			5.82	2.00
$Py_{mC\text{-}N}$	MeCN	1.29 ± 0.01	−2.04 ± 0.08	5.55	2.32
	DCM	1.44 ± 0.02		5.65	2.18
	$CHCl_3$			5.81	2.00
$Py_{N\text{-}C}$	MeCN	1.21 ± 0.38	−2.04 ± 0.01	5.36	2.33
	DCM	1.33 ± 0.13		5.48	2.17
	$CHCl_3$			5.62	1.98
$Py_{C\text{-}N}$	MeCN	1.38 ± 0.01	−1.81 ± 0.01	5.63	2.49
	DCM	1.60 ± 0.03		5.75	2.34
	$CHCl_3$			5.89	2.17

[a]Half-wave reduction potentials for neat solvents obtained from extrapolation to C_{el} = 0 (Figure 6-2b).[80] [b]Ionization energy (IE) from the difference between the density functional theory (DFT)-calculated energies of the ground state and the radical cation and electron affinity (EA) from the difference between the energies of the ground state and the radical anion, as implemented by Koopman's theorem. For the calculations, the B3LYP density functional and the 6-311+G(d,p) basis set were used together with implementation of the polarizable continuum model (PCM). [c]Potentials at which oxidation occurs, expressed as the reduction potentials of the radical cations, $Py^{\bullet+} + e^- \rightarrow Py$. [d]Reduction potential of the pyrene derivatives, i.e., $Py + e^- \rightarrow Py^{\bullet-}$.

$E_{Py|Py^{\bullet-}}$, are outside the electrochemical window of DCM and the potentials at which both the oxidation and reduction occur are both outside the electrochemical window of $CHCl_3$.

To address the lack of electrochemical information for these cases, we resort to density functional theory (DFT) calculations of the ionization energies (IE) and electron

affinities (EA) of the pyrene derivatives. The values of IE and EA show the same trends as those of the reduction potentials and provide information on the reduction and oxidation properties that are electrochemically inaccessible for some of the solvents. For each of the pyrene derivatives, IE increases and EA decreases with a decrease in the solvent polarity (Table 6-2), which is consistent with destabilization of both doublet states, i.e., of the radical cation and the radical anion. Thus, a decrease in medium polarity increases the electrochemical HOMO–LUMO gap, i.e., $E_{Py^{\bullet+}|Py} - E_{Py|Py^{\bullet-}} \approx IE - EA$, while ε_{00} is invariant with the solvent. For low-polarity solvents, therefore, the stabilization due to Coulombic interactions between the photogenerated hole and the unpaired electron in the singlet excited state becomes particularly important.

In contrast to the amide effects on the optical properties of the pyrene derivatives, which appear to be subtle, the effects on their electrochemical behavior are substantial when the amide is directly attached to the chromophore. Inverting the orientation of the amide causes a 200 mV shift in the reduction potentials, which can represent a huge difference in the design of molecules for electronics and optoelectronics.

Attaching an amide via its carbonyl carbon causes positive shifts in both reduction potentials, $E_{Py^{\bullet+}|Py}$ and $E_{Py|Py^{\bullet-}}$ (Table 6-2), and some broadening of the absorption and emission bands (Figure 6-1a) but does not lead to dramatic bathochromic shifts or to a decrease in ε_{00} (Figure 6-1a and Table 6-1). In contrast, attaching the amide via its nitrogen results in much more evident changes in the optical properties of pyrene, broadening the absorption and emission spectra and decreasing ε_{00}, φ_f, and τ (Figure 6-1 and Table 6-1).

In addition, $Py_{N\text{-}C}$ exhibits a negative shift of $E_{Py^{\bullet+}|Py}$ and no shift of $E_{Py|Py^{\bullet-}}$ (Table 6-2), affecting the energy of the HOMO but not of the LUMO of the pyrene chromophore. This narrowing of the HOMO− LUMO gap, which is related to π-conjugation between the pyrene chromophore and the amide substituent, is characteristic of $Py_{N\text{-}C}$ as compared with the other three derivatives.

Discussion

The evidence suggests that π-conjugation of the amides with the pyrene rings is the underlying reason for observed trends. Amides have substantial permanent electric dipoles[15] that can readily affect not only the electrochemical behavior of these derivatives by stabilizing or destabilizing the formed radical ions but also may affect the optical properties of the polarizable pyrene via an intramolecular Stark effect.[83] The amide dipole, however, points from the oxygen to the nitrogen of the bond,[15] which is tangential to the pyrene rings for the four derivatives under investigation. The two methylene-linked derivatives, $Py_{mN\text{-}C}$ and $Py_{mC\text{-}N}$, provide the most important evidence that the amide dipoles do not play a significant role in the observed trends. When the amide substituent cannot participate in direct π-conjugation with the pyrene chromophore, the inversion of the orientation of the amide dipole does not alter the reduction or oxidation propensities of these pyrenes ($Py_{mC\text{-}N}$ vs $Py_{mN\text{-}C}$, Table 6-2). Furthermore, if the amide dipoles had exerted significant effects, a lowering of the solvent polarity should induce differences between the reduction potentials or the IE and EA of $Py_{mN\text{-}C}$ and $Py_{mC\text{-}N}$. Therefore, it is safe to assume that direct electronic interactions between the amides and the pyrene chromophore govern

the observed trends in this study. Thus, field effects, prevalent for $Py_{C\text{-}N}$, represent induction through σ bonds, rather than through-space interactions provoked by the orientation of the amide dipole-generated fields.

The Hammett substituent constants, σ_p and σ_m, suggest that amide groups should be preferentially electron-withdrawing, regardless of the orientation in which they are bound to an aromatic ring. When attached via carbon, e.g., $-CONHCH_3$, the Hammett sigma constants are $\sigma_p = 0.34$ and $\sigma_m = 0.35$,[43] characterizing the amide as a moderately good electron- withdrawing group in ground-state reactions. Likewise, when the amide is attached via its nitrogen, e.g., $-NHCOCH_3$,[43] the values are $\sigma_p = 0.00$ and $\sigma_m = 0.21$, which makes it electron- withdrawing in the meta and neither electron withdrawing nor electron donating in the para position on a benzene ring, contradicting our spectroscopic and electrochemical findings.

Amide bonds oxidize at about 1.3−1.8 V versus SCE, which is relatively close to the $E_{Py^{\bullet+}|Py}$ of pyrene, ensuring effective mixing between the HOMOs of the pyrene and the amide substituent. The large HOMO−LUMO gap of amides, however, indicate that the reduction of an amide group should occur at potentials more negative than about −4 V versus SCE. Hence, this precludes strong mixing between the high-energy LUMO of the amide and the much lower energy LUMO of pyrene.

Considering the HOMOs of pyrene and the amide reveals a drastic difference between the propensities for π-conjugation of the carbon-bonded and nitrogen-bonded

orientations of the substituent. Driven by protein science, semiclassical studies of the electronic structures of amides clearly reveal that the HOMO of the amide group is a nonbonding orbital on the oxygen and HOMO − 1 is a π-orbital, also with a nonbonding character, localized on nitrogen and oxygen with a node on the carbon.[11] Although HOMO − 2 of the amide is delocalized over the carbon, nitrogen, and oxygen, it is much lower in energy than the HOMO − 1.[11]

DFT calculations of the simplest carboxamide, i.e., formamide, illustrate these trends (Figure 6-3). Many of the frontier orbitals have nonbonding or σ-character distribution over the plane of the amide bond and cannot mix with the π- orbitals of coplanar aromatic rings. Even though the amide LUMO has a π character, its high energy level makes such π- conjugation

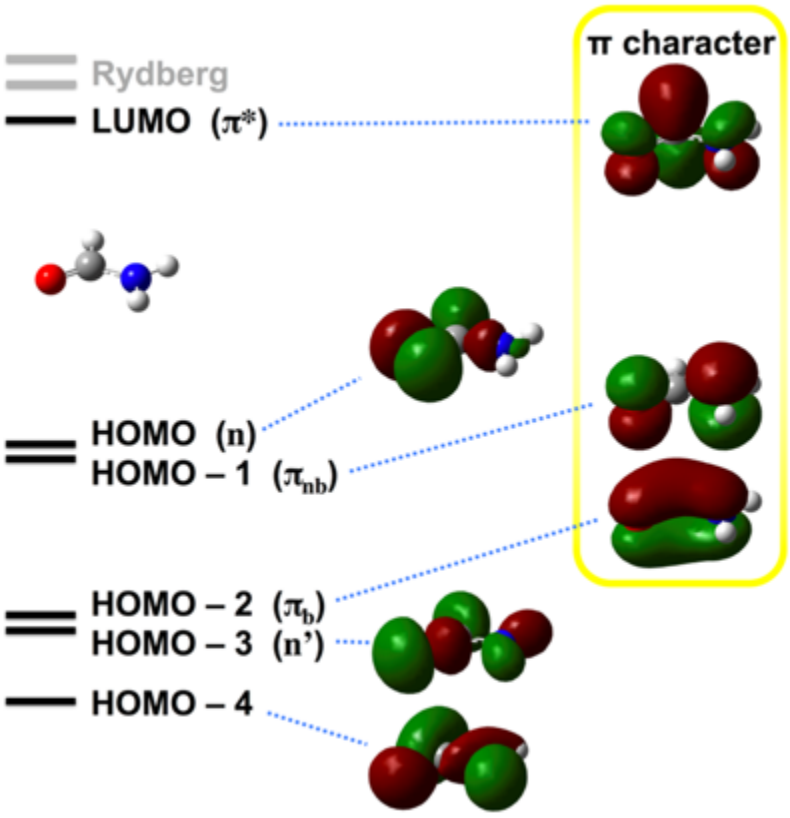

Figure 6-3. Molecular-orbital diagram of $CHONH_2$ showing the frontier orbitals obtained from DFT calculation at the B3LYP/6- 311G(3df,3dp) level of theory with implementation of MeCN as a solvation medium ($\varepsilon_{HOMO\text{-}LUMO}$ = 7.7 eV, IE – EA = 7.2 eV, $\varepsilon_{optical} \approx$ 5.6 eV, i.e., 222 nm, $E_A{}^{\bullet+}{}_{|A} \approx$ 1.8 V vs SCE[39]).

unfavorable, which is consistent with the observed trends in the reduction potentials and the EA (Table 6-2).

The HOMO – 1 of the amide reveals the underlying reason for the orientation dependence of the observed effects. The HOMO – 1 has a π-character with a node on the carbon (Figure 6-3) that would suppress π-conjugation with coplanar aromatic rings connected directly to the carbonyl carbon. The HOMOs of pyrene connected to the amide nitrogen, however, could interact with the HOMO – 1 of the amide. The HOMO – 2 of the amide is its only π-orbital with no orthogonal nodal planes but it's much lower energy (than the HOMO) makes mixing with the frontier orbitals of pyrene energetically unfavorable. Overall, attaching the amide group directly to the pyrene chromophore via the nitrogen favors mixing between the HOMO – 1 of the amide and the HOMOs of pyrene. Conversely, mixing with the HOMOs of pyrene is much less favorable when the amide is attached via its carbon.

Unlike conventional Hammett sigma constants, the Swain– Lupton field (F) and resonance (R) parameters for substituent effects[44] of an amide group capture this dependence on the bonding orientation and thus provide a much better rationalization of the experimentally observed trends than the Hammett sigma values. For $-CONHCH_3$, the Swain–Lupton parameters are F = 0.35 and R = −0.01 and for $-NHCOCH_3$, = 0.31 and = −0.31.[43] Hence, the inductive or field effects are indicative of electron withdrawal and would be expected to be similar for both bonding orientations. In contrast, the

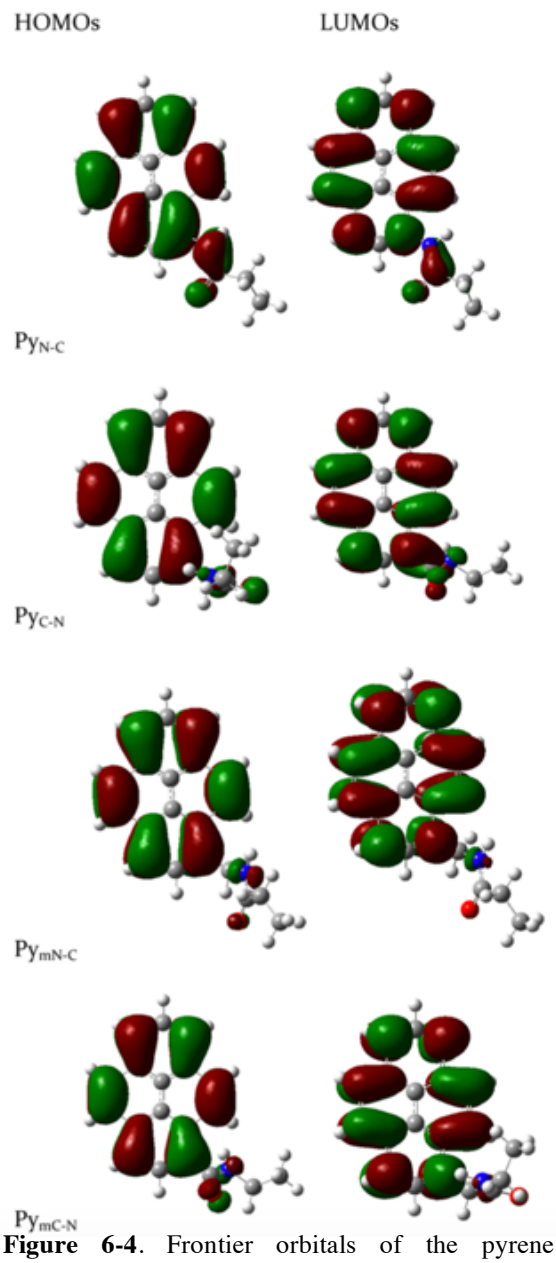

Figure 6-4. Frontier orbitals of the pyrene derivatives obtained from DFT calculations at the B3LYP/6-311+G(d,p) level of theory: HOMO and LUMO, showing the different extents of delocalization over the amide substituents, which is most pronounced for Py_{N-C} and least pronounced for Py_{mN-C} and Py_{mC-N}. In fact, the delocalization in the HOMO of Py_{C-N} is quite similar to that in the HOMOs of Py_{mN-C} and Py_{mC-N}.

electron-donating mesomeric effect of the electron pair on nitrogen should dominate in the latter orientation, consistent with the observed difference between the properties of Py_{N-C} and Py_{C-N}.

The Swain–Lupton empirical parameters can also rationalize the differences between the effects observed here for amides and those of other carbonyl substituents. As an example, for an acetyl group, $-COCH_3$, F = 0.33 and R = 0.17. These values indicate that the propensity of $-COCH_3$ for mesomeric electron withdrawal should be stronger than that of $-CONHCH_3$. Indeed, alkanoyl pyrene derivatives not only undergo reduction at potentials that are less negative than those of Py [53] but also exhibit a C-N bathochromic shift of the first $\pi \rightarrow \pi^*$ absorption band to 400 nm.[84]

This example emphasizes another important point. Bathochromic spectral shifts indicate that the substituent lowers the energies of the excited states more than that of the ground state. In our compounds, such shifts do not occur even when the amide is directly attached to the pyrene moiety. Such direct attachment, however, does affect the reduction potentials (Table 6-2), implying that the amide substituents have much stronger effects on the radical ions than on the singlet excited states. In classical terms, this trend is consistent with through- resonance, which is pronounced for electron-donating substituents bound to aromatic rings with positively charged groups and for electron-withdrawing substituents bound to aromatics with negatively charged groups. The pyrene derivatives under investigation have only one substituent. Nevertheless, upon electrochemical oxidation or reduction, the doublet states of the radical ions are considerably more susceptible to through-resonance interactions with the amides than is the case for the electroneutral singlet states.

Although the Swain–Lupton parameters for methylene- linked amides suggest the possibility of a hyperconjugation effect across the methylene group (i.e., for $-CH_2NHCOCH_3$ R = −0.17 and for $-CH_2CONHCH_3$ R = −0.01),[43] DFT calculations reveal that the frontier orbitals of $Py_{mN\text{-}C}$ and $Py_{mC\text{-}N}$ are practically the same: localized on the pyrene chromophore with a negligible delocalization over the amide group. The HOMO of $Py_{C\text{-}N}$ shows similar patterns. In contrast, the HOMO and the LUMO of $Py_{N\text{-}C}$ are heavily delocalized over the amide and pyrene rings (Figure 6-4). These DFT results agree with the spectroscopic and electrochemical trends and confirm that the amide effects arise from

differences in the propensity for π-conjugation between the different bonding orientations.

Conclusions

This study demonstrates that amides are not benign linking groups and manifest additional complexity in the interaction of their electronic structures with π-conjugated chromophores. Along with their enormous electric dipoles and ability to form ordered hydrogen-bonded networks, the judicious inclusion and orientation of amide substituents provides a powerful tool for molecular, supramolecular, and materials designs. Elucidation of the origins of the observed effects in the present set of duly chosen pyrene conjugates suggests that the present findings can be safely extrapolated to other amide-substituted polycyclic aromatic hydrocarbon derivatives, as well as to other π-conjugated chromophores in general.

Experimental Section

Synthetic Procedures

N-(Heptan-4-yl)-2-(pyren-1-yl)acetamide ($Py_{mC\text{-}N}$). 1-Pyreneacetic acid (200 mg, 0.77 mmol), chloro-N,N,N′,N′- tetramethylformamidinium hexafluorophosphate (TCFH, 384 mg, 1.15 mmol), and 4-dimethylamino pyridine (10 mg, 0.082 mmol) were placed in a 50 mL round bottom flask equipped with a magnetic stir bar. While purging with argon, 5 mL of dry DCM was added and the reaction vessel was immersed in a dry ice/acetone bath. 4-Heptylamine (92 μL, 0.615 mmol) was slowly added, followed by the slow addition of 4-methylmorpholine (0.5 mL, 4.5 mmol). The reaction mixture was allowed to warm up to

room temperature and was stirred overnight. The solution was diluted with 25 mL of DCM and washed with water (3 × 100 mL). The organic layer was collected, dried over Na_2SO_4, and concentrated in vacuo. Purification using flash chromatography (stationary phase: silica gel: eluent gradient: from 100% hexanes to 100% ethyl acetate) afforded 118 mg (0.330 mmol, 43% yield) of $Py_{mC\text{-}N}$ as a yellow powder; 55 mg (0.15 mmol) of the sample was recrystallized from ethanol to afford 37 mg (0.10 mmol, 67% recrystallization yield and 29% overall yield) of $Py_{mC\text{-}N}$. ^{1}H NMR (400 MHz, $CDCl_3$) δ/ppm: 8.07 (8H, m), 7.86 (1H, d, J = 7.6 Hz), 4.91 (1H, d, J = 8.8 Hz), 4.26 (2H, s), 3.91 (1H, td, J_1 = 8.3, J_2 = 4.2 Hz), 1.2 (2H, m), 1.02 (6H, m), 0.72 (6H, t, J = 7.1 Hz). ^{13}C NMR (100 MHz, $CDCl_3$) δ/ppm: 170.58, 131.41, 131.15, 130.98, 129.70, 128.79, 128.65, 128.35, 127.71, 127.47, 126.36, 125.62, 125.55, 125.25, 124.77, 123.19, 49.00, 42.43, 37.21, 19.03, 14.01. HRMS (m/z): $[M + H]^+$ calculated for $C_{25}H_{28}NO^+$, 358.2171; found 358.2174.

2-Propyl-N-(pyren-1-ylmethyl)pentanamide ($Py_{mN\text{-}C}$). 1-Pyrenemethylamine hydrochloride (200 mg, 0.75 mmol) was placed in a 50 mL round bottom flask equipped with a magnetic stir bar. While purging with argon, 5 mL of dry DCM was added and the reaction vessel was immersed in a dry ice/acetone bath. 2-Propylpentanoyl chloride (193 μL, 1.125 mmol) was slowly added, followed by the slow addition of 4- methylmorpholine (0.6 mL, 5.45 mmol). The reaction mixture was allowed to warm up to room temperature and was stirred overnight. The solution was diluted with 25 mL of DCM and washed with water (3 × 100 mL). The organic layer was collected, dried over Na_2SO_4, and concentrated in vacuo. The crude solid was dissolved in 5 mL of DCM, and the clear solution was slowly

diluted with 25 mL of hexane. The precipitate formed was collected and dried to produce 213 mg (0.6 mmol, 80%) of $Py_{mN\text{-}C}$; 45 mg (0.13 mmol) of the sample was recrystallized from ethanol to afford 25 mg (0.07 mmol, 57% recrystallization yield and 46% overall yield) of $Py_{mN\text{-}C}$. ^{1}H NMR (300 MHz, $CDCl_3$) δ/ppm: 8.15 (3H, m), 8.08 (1H, s), 8.05 (1H, d, J = 2.3 Hz), 7.97 (3H, m), 7.88 (1H, d, J = 7.9 Hz), 5.83 (1H, s), 5.07 (2H, d, J = 5.3 Hz), 2.00 (1H, dt, J_1 = 9.2 Hz, J_2 = 4.7 Hz), 1.65 (2H, m), 1.28 (6H, m), 0.85 (6H, m). ^{13}C NMR (75 MHz, $CDCl_3$) δ/ppm: 176.21, 131.84, 131.78, 131.34, 129.59, 128.60, 128.09, 127.89, 126.65, 125.92, 125.56, 125.26, 123.61, 48.37, 42.47, 35.89, 21.50, 14.76. HRMS (m/z): $[M + H]^+$ calculated for $C_{25}H_{28}NO^+$, 358.2171; found 358.2187.

N-(Heptan-4-yl)pyrene-1-carboxamide ($Py_{C\text{-}N}$). 1- Pyrenecarboxylic acid (205 mg, 0.83 mmol), chloro- N,N,N′,N′-tetramethylformamidinium hexafluorophosphate (TCFH, 404 mg, 1.22 mmol), and 4-dimethylamino pyridine (10 mg, 0.082 mmol) were placed in a 50 mL round bottom flask equipped with a magnetic stir bar. While purging with argon, 5 mL of dry DCM was added and the reaction vessel was immersed in a dry ice/acetone bath. 4-Heptylamine (101 μL, 0.675 mmol) was slowly added, followed by the slow addition of 4-methylmorpholine (0.5 mL, 4.5 mmol). The reaction mixture was allowed to warm up to room temperature and stirred overnight. The solution was diluted with 25 mL of DCM and washed with water (3 × 100 mL). The organic layer was collected, dried over Na_2SO_4, and concentrated in vacuo. Purification using flash chromatography (stationary phase: silica gel; eluent gradient: from 100% hexanes to 100% ethyl acetate) afforded 100 mg (0.29 mmol, 36% column yield) of $Py_{C\text{-}N}$ as a white powder; 49 mg (0.14 mmol) of the sample

were recrystallized from ethanol to afford 38 mg (0.11 mmol, 78% recrystallization yield and 28% overall yield) of $Py_{C\text{-}N}$. ^{1}H NMR (400 MHz, $CDCl_3$) δ/ppm: 8.51 (1H, d, J = 9.2 Hz), 8.18 (2H, d, J = 7.6 Hz), 8.08 (3H, m), 8 (3H, m), 5.84 (1H, d, J = 9.2 Hz), 4.34 (1H, m), 1.56 (9H, m), 1.01 (6H, m). ^{13}C NMR (100 MHz, $CDCl_3$) δ/ppm: 169.84, 132.49, 131.12, 131.39, 130.94, 128.79, 128.67, 128.62, 127.30, 126.48, 125.90, 125.83, 124.94, 124.66, 124.62, 124.46, 124.43, 49.85, 37.93, 19.58, 14.37. HRMS (m/z): $[M + H]^+$ calculated for $C_{24}H_{26}NO^+$, 344.2014; found 344.2001.

2-Propyl-N-(pyren-1-yl)pentanamide ($Py_{N\text{-}C}$). 1- Aminopyrene (104 mg, 0.48 mmol) was placed in a 50 mL round bottom flask equipped with a magnetic stir bar. While purging with argon, dry DCM (5 mL) was added and the reaction vessel was immersed in a dry ice/acetone bath. 2- Propylpentanoyl chloride (118 μL, 0.69 mmol) was slowly added, followed by the slow addition of pyridine (116 μL, 1.4 mmol). The reaction mixture was allowed to warm up to room temperature and was stirred overnight. The solution was diluted with 25 mL of DCM and washed with water (3 × 100 mL). The organic layer was collected, dried over Na_2SO_4, and concentrated in vacuo. Purification using flash chromatography (stationary phase: silica gel; eluent gradient: from 100% hexanes to 100% ethyl acetate) afforded 115 mg (0.336 mmol, 70% column yield) of $Py_{N\text{-}C}$ as a white powder; 55 mg (0.16 mmol) of the column-purified sample was recrystallized from ethanol to afford 49 mg (0.14 mmol, 88% recrystallization yield and 62% overall yield) of $Py_{N\text{-}C}$. ^{1}H NMR (400 MHz, $CDCl_3$) δ/ppm: 8.36 (1H, d, J = 7.8 Hz), 8.1 (4H, m), 7.97 (1H, m), 7.79 (1H, s), 2.47 (1H, m), 1.83 (2H, m), 1.54 (8H, m),

1.01 (6H, m). ^{13}C NMR (100 MHz, $CDCl_3$) δ/ppm: 175.33, 131.52, 130.97, 130.47, 129.28, 128.16, 127.54, 127.00, 126.31, 125.67, 125.34, 125.20, 124.94, 123.79, 122.84, 120.29, 48.98, 35.83, 21.32, 14.48. HRMS (m/z): $[M + H]^+$ calculated for $C_{24}H_{26}NO^+$, 344.2014; found 344.2140.

Optical Spectroscopy

Steady-state absorption spectra are recorded in the transmission mode using a JASCO V-670 spectrophotometer (Tokyo, Japan). The steady-state emission spectra and the time-correlated single- photon counting (TCSPC) fluorescence decays are measured using a FluoroLog-3 spectrofluorometer (Horiba Jobin Yvon, Edison, NJ), equipped with a pulsed diode laser (λ = 278 nm, 0.9 ns pulse width), as previously reported.[85–87]

The wavelengths of the maxima of the absorption and emission spectra were obtained from fitting the spectral peaks with Gaussian functions. For estimating zero-to-zero energy, ε_{00}, of a conjugate, we plot its absorption and fluorescence spectra on the same graph where the fluorescence maximum is adjusted to be equal to the maximum of the band at the red edge of the absorption spectrum. ε_{00} is estimated from the wavelength at which the thus normalized spectra cross (Table 1a). The fluorescence quantum yields, ϕ_f (Table 6-1), were determined by comparing the integrated emission intensities of the samples with those of the reference, an ethanol solution of Coumarin 151 ($\phi_{f0} = 0.49$)[88–92]

$$\varphi_f = \varphi_{f_0} \frac{\int F(\lambda)\, d\lambda}{\int F_0(\lambda)\, d\lambda} \times \frac{1 - 10^{-A_0(\lambda_{ex})}}{1 - 10^{-A(\lambda_{ex})}} \times \frac{n^2}{n_0^2} \qquad (1)$$

where $F(\lambda)$ is the fluorescence intensity at wavelength λ, $A(\lambda_{ex})$ is the absorbance at the excitation wavelength, n is the refractive index of the medium, and the subscript "0" indicates the quantities for the reference solution.

Electrochemistry

Cyclic voltammetry was conducted using a Reference 600TM potentiostat/galvanostat/ZRA (Gamry Instruments, PA), connected to a three-electrode cell, as previously described.[80,82] Glassy carbon electrode and platinum wire were used for the working and counter electrodes, respectively. A saturated calomel electrode (Gamry Instruments) was used for a reference electrode. To prevent contamination, the reference electrode was brought in contact with the sample solution via a salt bridge. When not in use, the reference electrode is stored submersed in saturated potassium chloride solution.

Anhydrous aprotic solvents with different polarity, dichloro- methane (DCM) and acetonitrile (MeCN), were employed with different concentrations of tetrabutylammonium hexa- fluorophosphate ($(n\text{-}C_4H_9)_4NPF_6$) as the supporting electrolyte. Prior to recording each voltammogram, the sample was extensively purged with argon while maintaining its volume constant by adding more anhydrous solvent. For each solvent, a set of voltammograms was recorded from 25 to 200 mM, increasing the electrolyte concentration in increments of 25 mM. The half-wave potentials, $E^{(1/2)}$, were determined from the

midpoints between the cathodic and anodic peak potentials for reversible or quasireversible voltammograms and from the inflection points of the waves for irreversible oxidation and reduction. The anodic and cathodic peak potentials, E_a and E_c, respectively, were determined from the zeros of the first derivatives of the voltammograms, i.e., as the potentials at which $\partial I/\partial E = 0$ when $\partial E/\partial t$ = constant. The inflection points were determined from the zeros of the second derivatives of the voltammograms, $\partial^2 I/\partial E^2 = 0$ at $\partial E/\partial t$ = constant.[81,93] The second derivatives of the reversible and quasireversible voltammograms indicated that the inflection-point potentials were quite close to the midpoints between E_a and E_c, ensuring the reliability for the estimates of $E^{(1/2)}$ from the inflection points of the irreversible voltammograms. The voltammograms were recorded at a scan rate of 100 mV s^{-1}. To correct for potential drifts in the reference electrode (SCE, connected to the cell via a salt bridge), ferrocene was used as a standard ($E^{(1/2)} = 0.45 \pm 0.01$ V vs SCE for MeCN, 100 mM NBu_4BF_4).[80] Voltammograms of the standard were recorded before and after each set of measurements. To correct for the dependence of $E^{(1/2)}$ on the electrolyte concentration, the potentials in neat electrolyte-free solvent were estimated from extrapolations to zero supporting electrolyte concentration (Figure 6-2b).[80,82]

Computational Analysis

The pyrene derivatives (Chart 1) were modeled using density functional theory (DFT). For simplicity, the aliphatic chains were truncated to two carbons, i.e., to ethyl groups (Figure 6-3). The DFT calculations were performed at the at the B3LYP/6-311G-(3df,3dp) level of theory for the formamide and at the B3LYP/ 6-311+G(d,p) level of

theory for the pyrene derivatives[94–96] for the gas phase using Gaussian 09.[97] Although the calculations for formamide are sensitive to the selection of basis set, the results for the pyrene derivatives were practically the same for the different levels of theory tested (see Supporting Information). On the basis of Koopman's theorem, we estimate IE and EA from the energies of the radical-ion doublet states and the ground states. Spin-unrestricted calculations are used for the calculations of the radical-cation and radical-anion doublet states. Solvent effects were estimated by comparing the results from gas-phase calculations to those in an integral equation formalism polarizable continuum model (PCM).[9]

References

(1) Brylinski, M.; Gao, M.; Skolnick, J. Why not consider a spherical protein? Implications of backbone hydrogen bonding for protein structure and function. Phys. Chem. Chem. Phys. 2011, 13, 17044– 17055.

(2) Taylor, W. R.; Thornton, J. M. Prediction of super-secondary structure in proteins. Nature 1983, 301, 540–542.

(3) Williams, R. W.; Dunker, A. K. Determination of the secondary structure of proteins from the amide I band of the laser Raman spectrum. J. Mol. Biol. 1981, 152, 783–813.

(4) Carothers, W. H. Linear Polyamides Suitable for Spinning into Strong Pliable Fibers. US2130523A1938.

(5) Jang, Y.; Champion, J. A. Self-assembled materials made from functional recombinant proteins. Acc. Chem. Res. 2016, 49, 2188– 2198.

(6) Song, Z.; Han, Z.; Lv, S.; Chen, C.; Chen, L.; Yin, L.; Cheng, J. Synthetic polypeptides: From polymer design to supramolecular assembly and biomedical application. Chem. Soc. Rev. 2017, 46, 6570–6599.

(7) Rueda, F.; Cespedes, M. V.; Conchillo-Sole, O.; Sanchez-Chardi, A.; Seras-Franzoso, J.; Cubarsi, R.; Gallardo, A.; Pesarrodona, M.; Ferrer-Miralles, N.; Daura, X.; Vazquez, E.; Garcia-Fruitos, E.; Mangues, R.; Unzueta, U.; Villaverde, A. Bottom-up instructive quality control in the biofabrication of smart protein materials. Adv. Mater. 2015, 27, 7816–7822.

(8) Deming, T. J. Polypeptide materials. New synthetic methods and applications. Adv. Mater. 1997, 9, 299–311.

(9) Crespo, L.; Sanclimens, G.; Pons, M.; Giralt, E.; Royo, M.; Albericio, F. Peptide and amide bond-containing dendrimers. Chem. Rev. 2005, 105, 1663–1681.

(10) Fischer, G. Chemical aspects of peptide bond isomerisation. Chem. Soc. Rev. 2000, 29, 119–127.

(11) Bulheller, B. M.; Rodger, A.; Hirst, J. D. Circular and linear dichroism of proteins. Phys. Chem. Chem. Phys. 2007, 9, 2020–2035. (12) Temussi, P. A.; Tancredi, T.; Quadrifoglio, F. Conformational rigidity of the amide bond. Variable-temperature nuclear magnetic resonance study of the system Ag^{+}-n,n-dimethylacetamide. J. Phys. Chem. 1969, 73, 4227–4232. (13) Tonelli, A. E. On the stability of cis and trans amide bond conformations in polypeptides. J. Am. Chem. Soc. 1971, 93, 7153– 7155.

(14) Vasudev, P. G.; Chatterjee, S.; Shamala, N.; Balaram, P. Structural chemistry of peptides containing backbone expanded amino acid residues: Conformational features of β, γ, and hybrid peptides. Chem. Rev. 2011, 111, 657–687.

(15) Upadhyayula, S.; Bao, D.; Millare, B.; Sylvia, S. S.; Habib, K. M. M.; Ashraf, K.; Ferreira, A.; Bishop, S.; Bonderer, R.; Baqai, S.; Jing, X.; Penchev, M.; Ozkan, M.; Ozkan, C. S.; Lake, R. K.; Vullev, V. I. Permanent electric dipole moments of carboxyamides in condensed media: What are the limitations of theory and experiment? J. Phys. Chem. B 2011, 115, 9473–9490.

(16) Suydam, I. T.; Snow, C. D.; Pande, V. S.; Boxer, S. G. Electric fields at the active site of an enzyme: Direct comparison of experiment with theory. Science 2006, 313, 200–204.

(17) Doyle, D. A.; Cabral, J. M.; Pfuetzner, R. A.; Kuo, A.; Gulbis, J. M.; Cohen, S. L.; Chait, B. T.; MacKinnon, R. The structure of the potassium channel: Molecular basis of k+ conduction and selectivity. Science 1998, 280, 69–77.

(18) Hol, W. G. J.; van Duijnen, P. T.; Berendsen, H. J. C. The α- helix dipole and the properties of proteins. Nature 1978, 273, 443– 446.

(19) Wada, A. Dielectric properties of polypeptide solutions. I. The electric dipole moment of the α helix in dioxane. J. Chem. Phys. 1958, 29, 674–675.

(20) Shin, Y.-g. K.; Newton, M. D.; Isied, S. S. Distance dependence of electron transfer across peptides with different secondary structures: The role of peptide energetics and electronic coupling. J. Am. Chem. Soc. 2003, 125, 3722–3732.

(21) Vullev, V. I. From biomimesis to bioinspiration: What's the benefit for solar energy conversion applications? J. Phys. Chem. Lett. 2011, 2, 503–508.

(22) Ferrand, Y.; Huc, I. Designing helical molecular capsules based on folded aromatic amide oligomers. Acc. Chem. Res. 2018, 51, 970– 977.

(23) Zhang, D.-W.; Zhao, X.; Hou, J.-L.; Li, Z.-T. Aromatic amide foldamers: Structures, properties, and functions. Chem. Rev. 2012, 112, 5271–5316.

(24) Ziach, K.; Chollet, C.; Parissi, V.; Prabhakaran, P.; Marchivie, M.; Corvaglia, V.; Bose, P. P.; Laxmi-Reddy, K.; Godde, F.; Schmitter, J.-M.; Chaignepain, S.; Pourquier, P.; Huc, I. Single helically folded aromatic oligoamides that mimic the charge surface of double- stranded B-DNA. Nat. Chem. 2018, 10, 511–518.

(25) Ashraf, M. K.; Pandey, R. R.; Lake, R. K.; Millare, B.; Gerasimenko, A. A.; Bao, D.; Vullev, V. I. Theoretical design of bioinspired macromolecular electrets based on anthranilamide derivatives. Biotechnol. Prog. 2009, 25, 915–922.

(26) Xia, B.; Bao, D.; Upadhyayula, S.; Jones, G.; Vullev, V. I. Anthranilamides as bioinspired molecular electrets: Experimental evidence for a permanent ground-state

electric dipole moment. J. Org. Chem. 2013, 78, 1994–2004.

(27) Hamuro, Y.; Geib, S. J.; Hamilton, A. D. Oligoanthranilamides. Non-peptide subunits that show formation of specific secondary structure. J. Am. Chem. Soc. 1996, 118, 7529–7541.

(28) Li, X.; Markandeya, N.; Jonusauskas, G.; McClenaghan, N. D.; Maurizot, V.; Denisov, S. A.; Huc, I. Photoinduced electron transfer and hole migration in nanosized helical aromatic oligoamide foldamers. J. Am. Chem. Soc. 2016, 138, 13568–13578.

(29) Meńdez-Ardoy,A.;Markandeya,N.;Li,X.;Tsai,Y.-T.; Pecastaings, G.; Buffeteau, T.; Maurizot, V.; Muccioli, L.; Castet, F.; Huc, I.; Bassani, D. M. Multi-dimensional charge transport in supramolecular helical foldamer assemblies. Chem. Sci. 2017, 8, 7251–7257.

(30) Wolffs, M.; Delsuc, N.; Veldman, D.; Vanˆ Anh, N.; Williams, R. M.; Meskers, S. C. J.; Janssen, R. A. J.; Huc, I.; Schenning, A. P. H. J. Helical aromatic oligoamide foldamers as organizational scaffolds for photoinduced charge transfer. J. Am. Chem. Soc. 2009, 131, 4819– 4829.

(31) Larsen-Clinton, J. M.; Espinoza, E. M.; Mayther, M. F.; Clark, J.; Tao, C.; Bao, D.; Larino, C. M.; Wurch, M.; Lara, S.; Vullev, V. I. Fluorinated aminoanthranilamides: Non-native amino acids for bringing proteomic approaches to charge-transfer systems. Phys. Chem. Chem. Phys. 2017, 19, 7871–7876.

(32) Dutzler, R.; Campbell, E. B.; Cadene, M.; Chait, B. T.; MacKinnon, R. X-ray structure of a clc chloride channel at 3.0 å reveals the molecular basis of anion selectivity. Nature 2002, 415, 287–294.

(33) Bao, D.; Upadhyayula, S.; Larsen, J. M.; Xia, B.; Georgieva, B.; Nunez, V.; Espinoza, E. M.; Hartman, J. D.; Wurch, M.; Chang, A.; Lin, C.-K.; Larkin, J.; Vasquez, K.; Beran, G. J. O.; Vullev, V. I. Dipole- mediated rectification of intramolecular photoinduced charge separation and charge recombination. J. Am. Chem. Soc. 2014, 136, 12966–12973.

(34) Galoppini, E.; Fox, M. A. Effect of the electric field generated by the helix dipole on photoinduced intramolecular electron transfer in dichromophoric α-helical peptides. J. Am. Chem. Soc. 1996, 118, 2299–2300.

(35) Yasutomi, S.; Morita, T.; Imanishi, Y.; Kimura, S. A molecular photodiode system that can switch photocurrent direction. Science 2004, 304, 1944–1947.

(36) Shlizerman, C.; Atanassov, A.; Berkovich, I.; Ashkenasy, G.; Ashkenasy, N. De novo designed coiled-coil proteins with variable conformations as components of molecular electronic devices. J. Am. Chem. Soc. 2010, 132, 5070–5076.

(37) Garbuio, L.; Antonello, S.; Guryanov, I.; Li, Y.; Ruzzi, M.; Turro, N. J.; Maran, F. Effect of orientation of the peptide-bridge dipole moment on the properties of fullerene-peptide-radical systems. J. Am. Chem. Soc. 2012, 134, 10628–10637.

(38) Krzeszewski, M.; Espinoza, E. M.; Červinka, C.; Derr, J. B.; Clark, J. A.; Borchardt, D.; Beran, G. J. O.; Gryko, D. T.; Vullev, V. I. Dipole effects on electron transfer are enormous. Angew. Chem., Int. Ed. 2018, 57, 12365–12369.

(39) Odonnell, J. F.; Mann, C. K. Controlled-potential oxidation of aliphatic amides. J. Electroanal. Chem. Interfacial Electrochem. 1967, 13, 157–162.

(40) Nichols, E. M.; Derrick, J. S.; Nistanaki, S. K.; Smith, P. T.; Chang, C. J. Positional effects of second-sphere amide pendants on electrochemical CO_2 reduction catalyzed by iron porphyrins. Chem. Sci. 2018, 9, 2952–2960.

(41) Srujan, M.; Chandrashekhar, V.; Reddy, R. C.; Prabhakar, R.; Sreedhar, B.; Chaudhuri, A. The influence of the structural orientation of amide linkers on the serum compatibility and lung transfection properties of cationic amphiphiles. Biomaterials 2011, 32, 5231–5240.

(42) Han, X.; Remsburg, J. W.; He, L.; Beesly, T. E.; Armstrong, D. W. Effect of the orientation of amide linkage groups on the enantioselectivity of two related synthetic polymeric chiral stationary phases. Chromatographia 2008, 67, 199–210.

(43) Hansch, C.; Leo, A.; Taft, R. W. A survey of Hammett substituent constants and resonance and field parameters. Chem. Rev. 1991, 91, 165–195.

(44) Swain, C. G.; Lupton, E. C., Jr. Field and resonance components of substituent effects. J. Am. Chem. Soc. 1968, 90, 4328–4337.

(45) Dobrowolski‚J.C.;Lipiński‚P.F.J.;Karpińska‚G.Substituent effect in the first excited singlet state of monosubstituted benzenes. J. Phys. Chem. A 2018, 122, 4609–4621.

(46) Østergaard, M. E.; Hrdlicka, P. J. Pyrene-functionalized oligonucleotides and locked nucleic acids (lnas): Tools for fundamental research, diagnostics, and nanotechnology. Chem. Soc. Rev. 2011, 40, 5771–5788.

(47) Vullev, V. I.; Jiang, H.; Jones, G., II Excimer Sensing. In Advanced Concepts in Fluorescence Sensing; Geddes, C. D., Lakowicz, J. R., Eds.; Topics in Fluorescence Spectroscopy; Springer: Boston, MA, 2005; vol. 10, pp 211–239.

(48) Winnik, F. M. Photophysics of preassociated pyrenes in aqueous polymer solutions and in other organized media. Chem. Rev. 1993, 93, 587–614.

(49) Karpovich, D. S.; Blanchard, G. J. Relating the polarity- dependent fluorescence response of pyrene to vibronic coupling. Achieving a fundamental understanding of the py polarity scale. J. Phys. Chem. 1995, 99, 3951–3958.

(50) Kathiravan, A.; Srinivasan, V.; Khamrang, T.; Velusamy, M.; Jaccob, M.; Pavithra, N.; Anandan, S.; Velappan, K. Pyrene based d-π- a architectures: Synthesis, density functional theory, photophysics and electron transfer dynamics. Phys. Chem. Chem. Phys. 2017, 19, 3125– 3135.

(51) Hofmann, O. T.; Glowatzki, H.; Buerker, C.; Rangger, G. M.; Broeker, B.; Niederhausen, J.; Hosokai, T.; Salzmann, I.; Blum, R. P.; Rieger, R.; Vollmer, A.; Rajput, P.; Gerlach, A.; Muellen, K.; Schreiber, F.; Zojer, E.; Koch, N.; Duhm, S. Orientation-dependent work-function modification using substituted pyrene-based acceptors. J. Phys. Chem. C 2017, 121, 24657–24668.

(52) Williams, R. M.; Vanˆ Anh, N.; van Stokkum, I. H. M. Triplet formation by charge recombination in thin film blends of perylene red and pyrene: Developing a target model for the photophysics of organic photovoltaic materials. J. Phys. Chem. B 2013, 117, 11239– 11248.

(53) Jones, G., II; Vullev, V. I. Photoinduced electron transfer between non-native donor-acceptor moieties incorporated in synthetic polypeptide aggregates. Org. Lett. 2002, 4, 4001–4004.

(54) Vullev, V. I.; Jones, G. Photoinduced electron transfer in alkanoylpyrene aggregates in conjugated polypeptides. Tetrahedron Lett. 2002, 43, 8611–8615.

(55) Jones, G., II; Vullev, V.; Braswell, E. H.; Zhu, D. Multistep photoinduced electron transfer in a de novo helix bundle: Multimer self-assembly of peptide chains including a chromophore special pair. J. Am. Chem. Soc. 2000, 122, 388–389.

(56) Jones, G., II; Lu, L. N.; Vullev, V.; Gosztola, D.; Greenfield, S.; Wasielewski, M. Photoactive peptides. 6. Photoinduced electron transfer for pyrenesulfonamide conjugates of tryptophan-containing peptides. Mitigation of fluoroprobe behavior in n-terminal labeling experiments. Bioorg. Med. Chem. Lett. 1995, 5, 2385–2390.

(57) Jones, G., II; Vullev, V. I. Ground- and excited-state aggregation properties of a pyrene derivative in aqueous media. J. Phys. Chem. A 2001, 105, 6402–6406.

(58) Daugherty, D. L.; Gellman, S. H. A fluorescence assay for leucine zipper dimerization: Avoiding unintended consequences of fluorophore attachment. J. Am. Chem. Soc. 1999, 121, 4325–4333.

(59) Jones, G., II; Vullev, V. I. Contribution of a pyrene fluorescence probe to the aggregation propensity of polypeptides. Org. Lett. 2001, 3, 2457–2460.

(60) Figueira-Duarte, T. M.; Muellen, K. Pyrene-based materials for organic electronics. Chem. Rev. 2011, 111, 7260–7314.

(61) Mateo-Alonso, A. Pyrene-fused pyrazaacenes: From small molecules to nanoribbons. Chem. Soc. Rev. 2014, 43, 6311–6324.

(62) Guo, L.; Wang, M.; Cao, D. A novel Zr-MOF as fluorescence turn-on probe for real-time detecting H_2S gas and fingerprint identification. Small 2018, 14, No. 1703822.

(63) Noh, H.; Kung, C.-W.; Islamoglu, T.; Peters, A. W.; Liao, Y.; Li, P.; Garibay, S. J.; Zhang, X.; DeStefano, M. R.; Hupp, J. T.; Farha, O. K. Room temperature synthesis of an 8-connected zr-based metal- organic framework for top-down nanoparticle encapsulation. Chem. Mater. 2018, 30, 2193–2197.

(64) Thomas, S. S.; Tang, H.; Gaudes, A.; Baggesen, S. B.; Gibb, C. L. D.; Gibb, B. C.; Bohne, C. Tuning the binding dynamics of a guest- octaacid capsule through noncovalent anchoring. J. Phys. Chem. Lett. 2017, 8, 2573–2578.

(65) Blakemore, J. D.; Gupta, A.; Warren, J. J.; Brunschwig, B. S.; Gray, H. B. Noncovalent immobilization of electrocatalysts on carbon electrodes for fuel production.

J. Am. Chem. Soc. 2013, 135, 18288– 18291.

(66) Tang, H.; de Oliveira, C. S.; Sonntag, G.; Gibb, C. L. D.; Gibb, B. C.; Bohne, C. Dynamics of a supramolecular capsule assembly with pyrene. J. Am. Chem. Soc. 2012, 134, 5544–5547.

(67) Malig, J.; Romero-Nieto, C.; Jux, N.; Guldi, D. M. Integrating water-soluble graphene into porphyrin nanohybrids. Adv. Mater. 2012, 24, 800–805.

(68) Bartelmess, J.; Ballesteros, B.; de la Torre, G.; Kiessling, D.; Campidelli, S.; Prato, M.; Torres, T.; Guldi, D. M. Phthalocyanine- pyrene conjugates: A powerful approach toward carbon nanotube solar cells. J. Am. Chem. Soc. 2010, 132, 16202–16211.

(69) Schulz-Drost, C.; Sgobba, V.; Gerhards, C.; Leubner, S.; Calderon, R. M. K.; Ruland, A.; Guldi, D. M. Innovative inorganic- organic nanohybrid materials: Coupling quantum dots to carbon nanotubes. Angew. Chem., Int. Ed. 2010, 49, 6425–6429.

(70) Udit, A. K.; Hill, M. G.; Bittner, V. G.; Arnold, F. H.; Gray, H. B. Reduction of dioxygen catalyzed by pyrene-wired heme domain cytochrome p450 bm3 electrodes. J. Am. Chem. Soc. 2004, 126, 10218–10219.

(71) Espinoza, E. M.; Xia, B.; Darabedian, N.; Larsen, J. M.; Nunez, V.; Bao, D.; Mac, J. T.; Botero, F.; Wurch, M.; Zhou, F.; Vullev, V. I. Nitropyrene photoprobes: Making them, and what are they good for? Eur. J. Org. Chem. 2016, 2016, 343–356.

(72) Casas-Solvas, J. M.; Howgego, J. D.; Davis, A. P. Synthesis of substituted pyrenes by indirect methods. Org. Biomol. Chem. 2014, 12, 212–232.

(73) Feng, X.; Hu, J.-Y.; Redshaw, C.; Yamato, T. Functionalization of pyrene to prepare luminescent materials-typical examples of synthetic methodology. Chem. – Eur. J. 2016, 22, 11898–11916.

(74) Zimerman, O. E.; Weiss, R. G. Static and dynamic fluorescence from α,ω-di(1-pyrenyl)alkanes in polyethylene films. Control of probe conformations and information about microstructure of the media. J. Phys. Chem. A 1998, 102, 5364–5374.

(75) Saliba,M.;Correa-Baena,J.-P.;Graïzel,M.;Hagfeldt,A.;Abate, A. Perovskite solar cells: From the atomic level to film quality and device performance. Angew. Chem., Int. Ed. 2018, 57, 2554–2569.

(76) Guo, S.; Bao, D.; Upadhyayula, S.; Wang, W.; Guvenc, A. B.; Kyle, J. R.; Hosseinibay, H.; Bozhilov, K. N.; Vullev, V. I.; Ozkan, C. S.; Ozkan, M. Photoinduced electron transfer between pyridine coated cadmium selenide quantum dots and single sheet graphene. Adv. Funct. Mater. 2013, 23, 5199–5211.

(77) Klimov, V. I. Optical nonlinearities and ultrafast carrier dynamics in semiconductor nanocrystals. J. Phys. Chem. B 2000, 104, 6112–6123.

(78) Namiki, A.; Nakashima, N.; Yoshihara, K. Fluorescence quenching due to the electron-transfer - indole-chloromethanes in rigid ethanol glass. J. Chem. Phys. 1979, 71, 925–930.

(79) Uno, B.; Okumura, N. Molecular Scientific Approach in Electroorganic Chemistry. Recent Research Developments in Pure & Applied Analytical Chemistry; Gifu Pharmaceutical University: Gifu, 1998; Vol. 2, pp 83–99.

(80) Bao, D.; Millare, B.; Xia, W.; Steyer, B. G.; Gerasimenko, A. A.; Ferreira, A.; Contreras, A.; Vullev, V. I. Electrochemical oxidation of ferrocene: A strong dependence on the concentration of the supporting electrolyte for nonpolar solvents. J. Phys. Chem. A 2009, 113, 1259–1267.

(81) Espinoza, E. M.; Larsen, J. M.; Vullev, V. I. What makes oxidized n-

acylanthranilamides stable? J. Phys. Chem. Lett. 2016, 7, 758–764.

(82) Bao, D.; Ramu, S.; Contreras, A.; Upadhyayula, S.; Vasquez, J. M.; Beran, G.; Vullev, V. I. Electrochemical reduction of quinones: Interfacing experiment and theory for defining effective radii of redox moieties. J. Phys. Chem. B 2010, 114, 14467–14479.

(83) Lockhart, D. J.; Kim, P. S. Internal stark-effect measurement of the electric-field at the amino terminus of an alpha-helix. Science 1992, 257, 947–951.

(84) Armbruster, C.; Knapp, M.; Rechthaler, K.; Schamschule, R.; Parusel, A. B. J.; Kohler, G.; Wehrmann, W. Fluorescence properties of 1-heptanoylpyrene: A probe for hydrogen bonding in micro- aggregates and biological membranes. J. Photochem. Photobiol., A 1999, 125, 29–38.

(85) Lu, H.; Bao, D.; Penchev, M.; Ghazinejad, M.; Vullev, V. I.; Ozkan, C. S.; Ozkan, M. Pyridine-coated lead sulfide quantum dots for polymer hybrid photovoltaic devices. Adv. Sci. Lett. 2010, 3, 101– 109.

(86) Ghazinejad, M.; Kyle, J. R.; Guo, S.; Pleskot, D.; Bao, D.; Vullev, V. I.; Ozkan, M.; Ozkan, C. S. Non-invasive high-throughput metrology of functionalized graphene sheets. Adv. Funct. Mater. 2012, 22, 4519–4525.

(87) Upadhyayula, S.; Nunez, V.; Espinoza, E. M.; Larsen, J. M.; Bao, D.; Shi, D.; Mac, J. T.; Anvari, B.; Vullev, V. I. Photoinduced dynamics of a cyanine dye: Parallel pathways of non-radiative deactivation involving multiple excited-state twisted transients. Chem. Sci. 2015, 6, 2237–2251.

(88) Crosby, G. A.; Demas, J. N. The measurement of photo- luminescence quantum yields. A review. J. Phys. Chem. 1971, 75, 991–1024.

(89) Jung, B.; Vullev, V. I.; Anvari, B. Revisiting indocyanine green: Effects of serum and physiological temperature on absorption and fluorescence characteristics. IEEE J. Sel. Top. Quantum Electron. 2014, 20, No. 7000409.

(90) Vasquez, J. M.; Vu, A.; Schultz, J. S.; Vullev, V. I. Fluorescence enhancement of warfarin induced by interaction with β-cyclodextrin. Biotechnol. Prog. 2009, 25, 906–914.

(91) Sjöback, R.; Nygren, J.; Kubista, M. Absorption and fluorescence properties of fluorescein. Spectrochim. Acta, Part A 1995, 51, L7–L21.

(92) Zhang, X. F.; Zhang, J. L.; Liu, L. M. Fluorescence properties of twenty fluorescein derivatives: Lifetime, quantum yield, absorption and emission spectra. J. Fluoresc. 2014, 24, 819–826.

(93) Roth, H. G.; Romero, N. A.; Nicewicz, D. A. Experimental and calculatedelectrochemicalpotentialsofcommonorganicmolecules for applications to single-electron redox chemistry. Synlett 2016, 27, 714–723.

(94) Becke, A. D. Density-functional thermochemistry. III. The role of exact exchange. J. Chem. Phys. 1993, 98, 5648–5652.

(95) Krishnan, R.; Binkley, J. S.; Seeger, R.; Pople, J. A. Self- consistent molecular orbital methods. XX. A basis set for correlated wave functions. J. Chem. Phys. 1980, 72, 650–654.

(96) Lee, C.; Yang, W.; Parr, R. Development of the colle-salvetti correlation-energy formula into a functional of the electron-density. Phys. Rev. B 1988, 37, 785–789.

(97) Frisch, M. J. et al. Gaussian 09, revision a.1; Gaussian Inc.: Wallingford, CT, 2009.

(98) Tomasi, J.; Mennucci, B.; Cammi, R. Quantum mechanical continuum solvation models. Chem. Rev. 2005, 105, 2999–3093.

Supplemental Figures

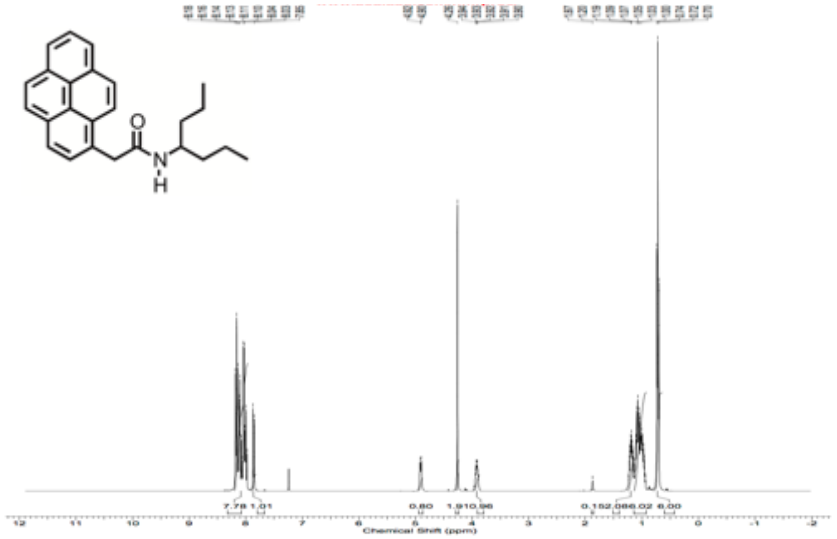

a

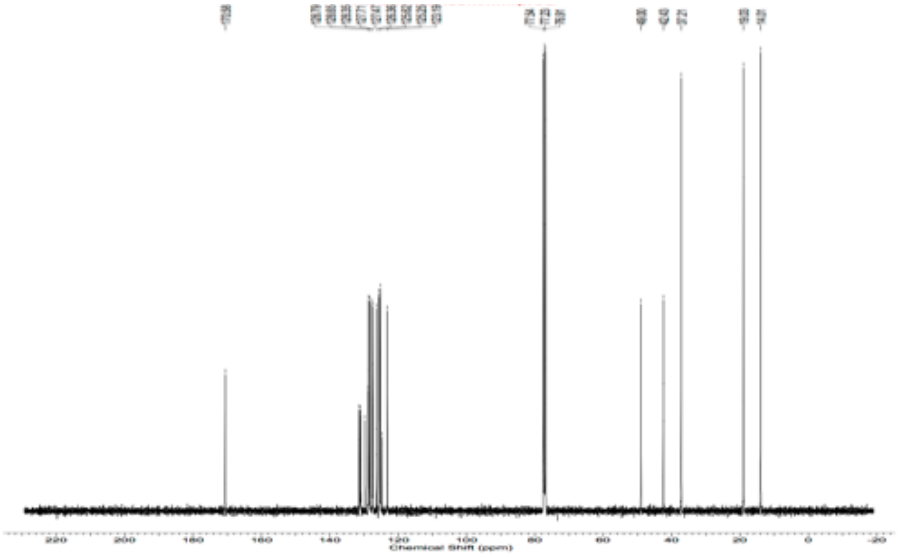

b

Figure 6S-1. (a) ^{1}HNMR of $Py_{mC\text{-}N}$ (300 MHz, $CDCl_3$); (b) ^{13}C NMR of $Py_{mC\text{-}N}$ (75 MHz, $CDCl_3$)

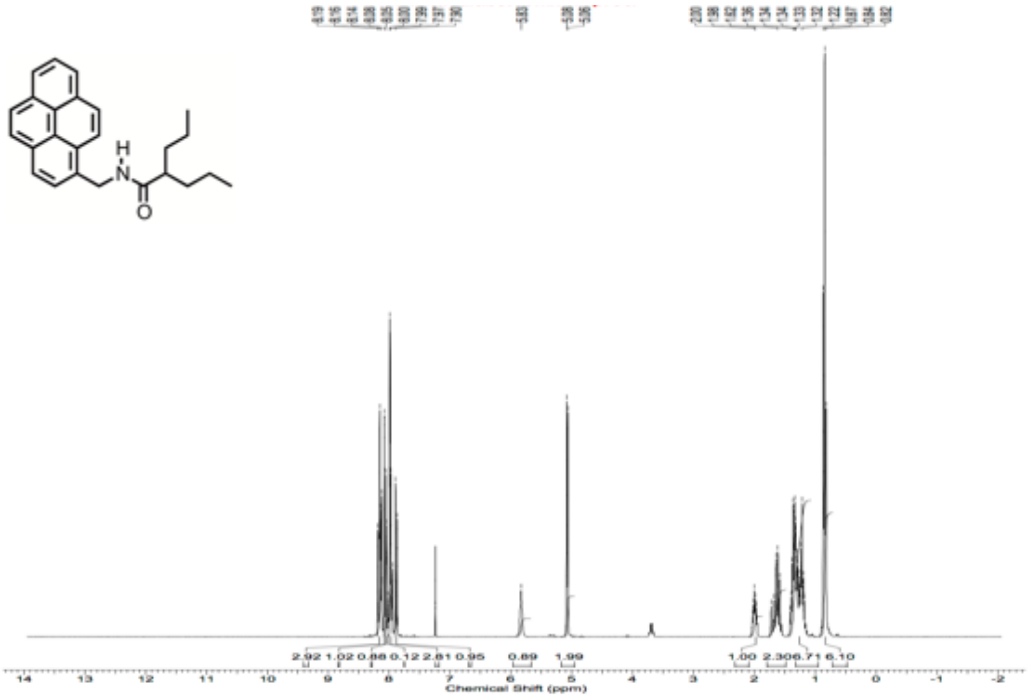

a

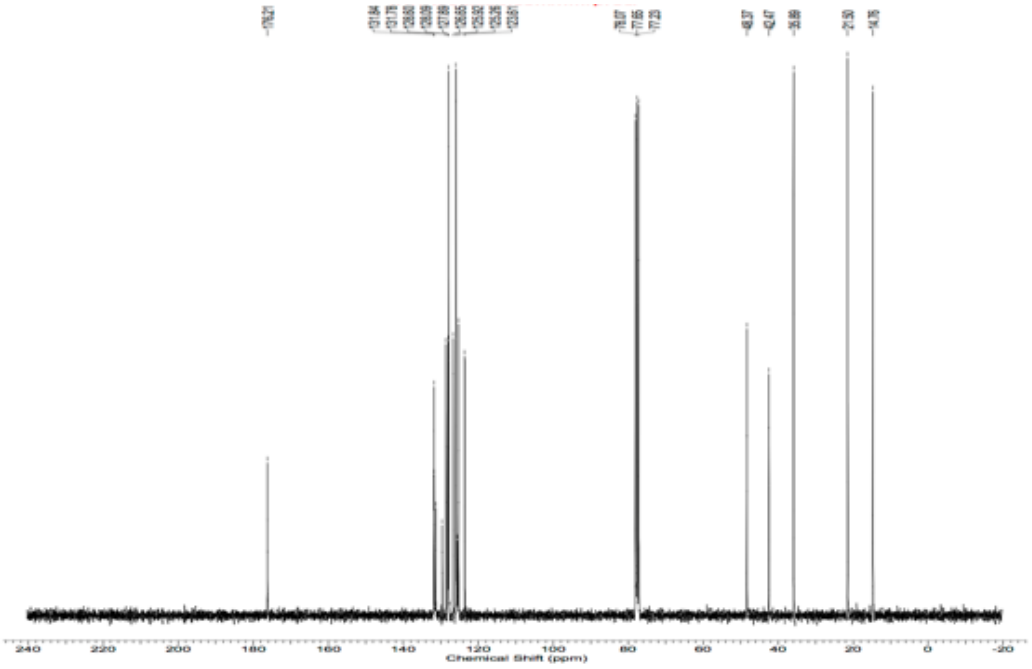

b

Figure 6S-2. (a) ^{1}HNMR of $Py_{mN\text{-}C}$ (300 MHz, $CDCl_3$); (b) ^{13}C NMR of $Py_{mN\text{-}C}$ (75 MHz, $CDCl_3$)

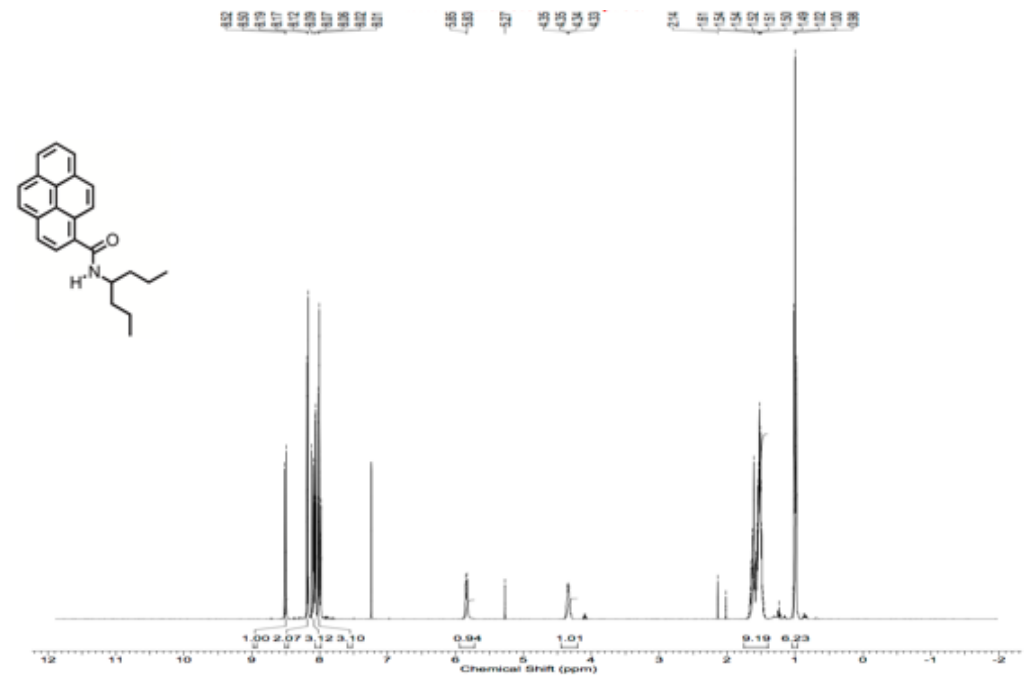

a

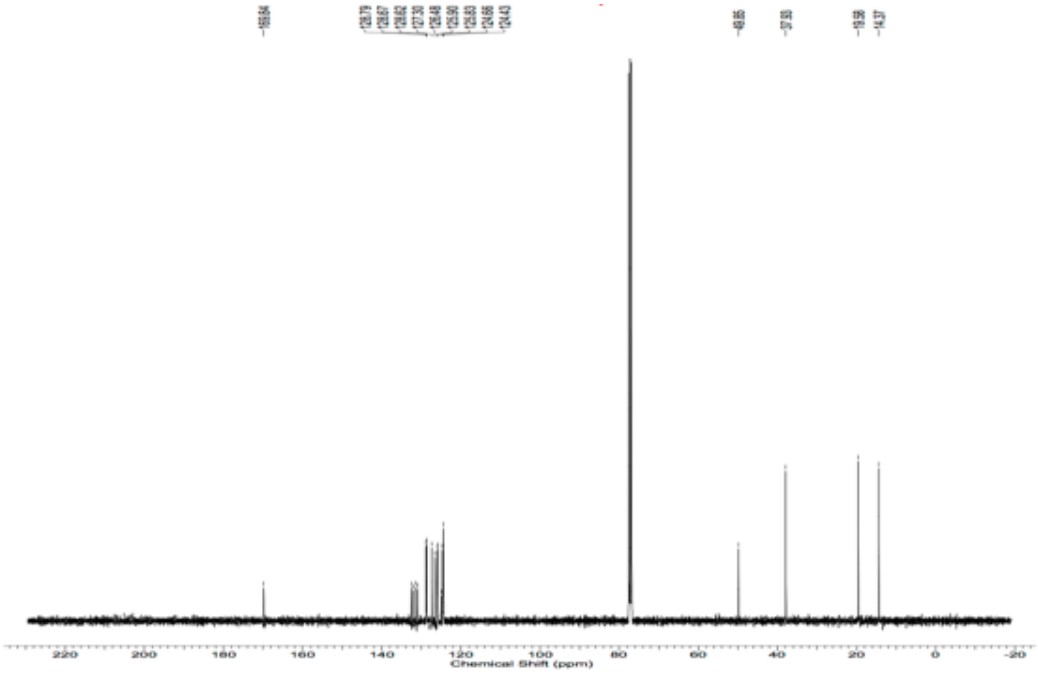

b

Figure 6S-3. (a) ^{1}HNMR of $Py_{C\text{-}N}$ (400 MHz, $CDCl_3$); (b) ^{13}C NMR of $Py_{C\text{-}N}$ (100 MHz, $CDCl_3$).

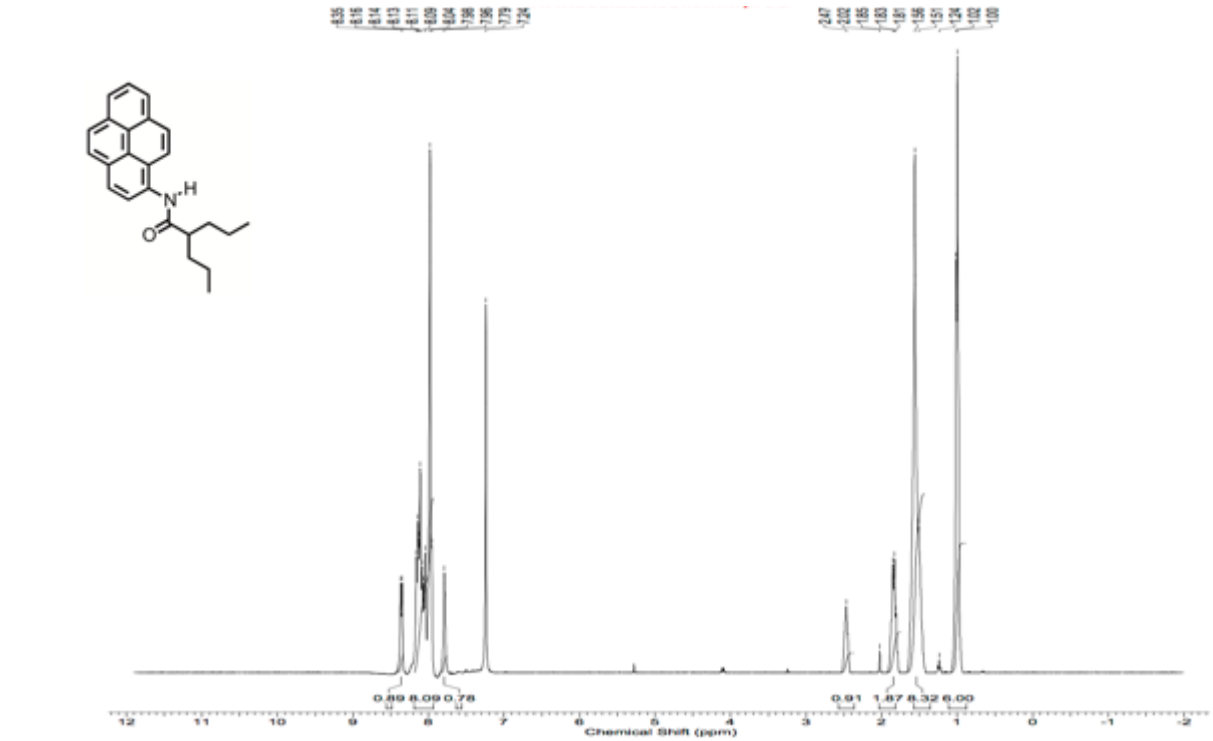

a

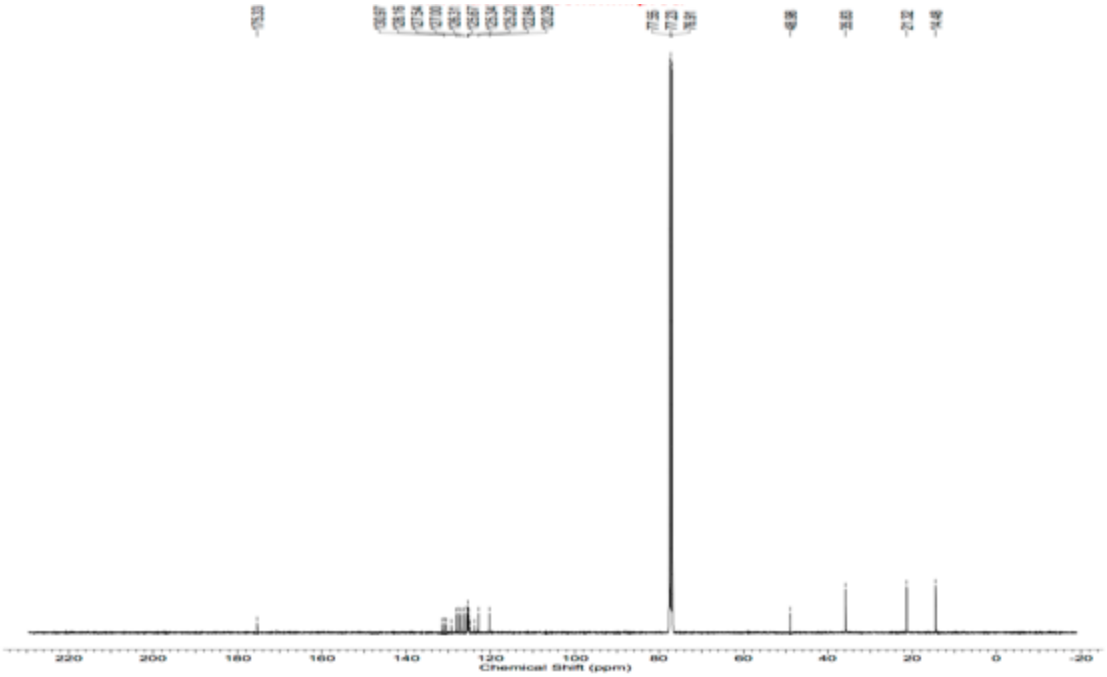

b

Figure 6S-4. (a)[1] HNMR of $Py_{N\text{-}C}$ (400 MHz, $CDCl_3$); (b) ^{13}C NMR of $Py_{N\text{-}C}$ (100 MHz, $CDCl_3$).

Chapter 7

Gating That Suppresses Charge Recombination- The Role of Mono-N-Arylated Diketopyrrolopyrrole

Abstract

Suppressing the charge recombination (CR) that follows an efficient charge separation (CS) is of key importance for energy, electronics, and photonics applications. We focus on the role of dynamic gating for impeding CR in a molecular rotor, comprising an electron donor and acceptor directly linked via a single bond. The media viscosity has an unusual dual effect on the dynamics of CS and CR in this dyad. For solvents with intermediate viscosity, CR is 1.5−3 times slower than CS. Lowering the viscosity below ~0.6 mPa s or increasing it above ~10 mPa s makes CR 10−30 times slower than CS. Ring rotation around the donor−acceptor bond can account only for the trends observed for nonviscous solvents. Media viscosity, however, affects not only torsional but also vibrational modes. Suppressing predominantly slow vibrational modes by viscous solvents can impact the rates of CS and CR to a different extent. That is, an increase in the viscosity can plausibly suppress modes that are involved in the transition from the charge-transfer (CT) to the ground state, i.e., CR, but at the same time are not important for the transition from the locally excited to the CT state, i.e., CS. These results provide a unique example of synergy between torsional and vibronic modes and their drastic effects on charge-transfer dynamics, thus setting paradigms for controlling CS and CR.

Introduction

Controlling electron transfer (ET) at a molecular and nanoscale level is paramount for improving the performance of energy- conversion materials and devices. Suppressing charge recombination (CR) that follows photoinduced charge separation (CS) renders solar energy conversion-efficient. Local fields originating from molecular electric dipoles, anisotropic covalency, and cascade ET events, bypassing localized charge-transfer (CT) states and changes in multiplicity, provide an invaluable means for suppressing undesired CR.[1-6]

Optimizing CS driving force, $-\Delta G_{CS}^{(0)}$, and reorganization energy, λ, to attain activationless CS ($-\Delta G_{CS}^{(0)} \approx \lambda$) can impede CR by placing it in the Marcus inverted region ($-\Delta G^{(0)}$ CS $> \lambda$).[7-9] This nonadiabatic semiclassical view focuses on the Franck–Condon aspects of ET.

Conformational gating, which is important for biology, presents another approach for controlling ET.[10] By impacting the electronic coupling along the ET pathways, non-Condon effects from torsional dynamics can define the CT properties of molecular systems.[11, 12] The utility of such effects for energy materials and organic electronics cannot be overstated.

With structural features resembling those of indigo and with superior thermal stability and light-fastness, diketopyrrolopyrrole (DPP) derivatives are organic dyes with promising properties for optoelectronics.[13] Due to their strong light absorption, high fluorescence quantum yields and reduction potentials making them relatively good electron

donors and acceptors, DPPs have undergone significant repositioning from high-quality pigments[14] to organic electronic materials[15, 16] toward dyes for fluorescence-based applications.[17-21]

To explore the effects of gating on single-step CS and CR processes, herein we focus on the ET properties of an electron- deficient diketopyrrolopyrrole (**DPP**, Figure 7-1a) that we derivatize with moderately good electron donors. While **DPP** is strongly fluorescent, the emission of **DPP-Ph** with the donor, 4-acylaminophenyl, directly linked to one of the lactam nitrogens (Figure 1a), is considerably quenched (Figure 1b). This is fluorescence loss due to highly efficient intramolecular CS that the photoexcited **DPP-Ph** undergoes to produce a non- fluorescent CT state. As expected, the rate constants of CS and CR, k_{CS} and k_{CR}, respectively, manifest correlations with the media polarity. An important characteristic for efficient conversion of the harvested light energy is k_{CS}/k_{CR}, representing how CS CR much slower CR is in comparison with CS. The polarity and proticity of the solvent do not

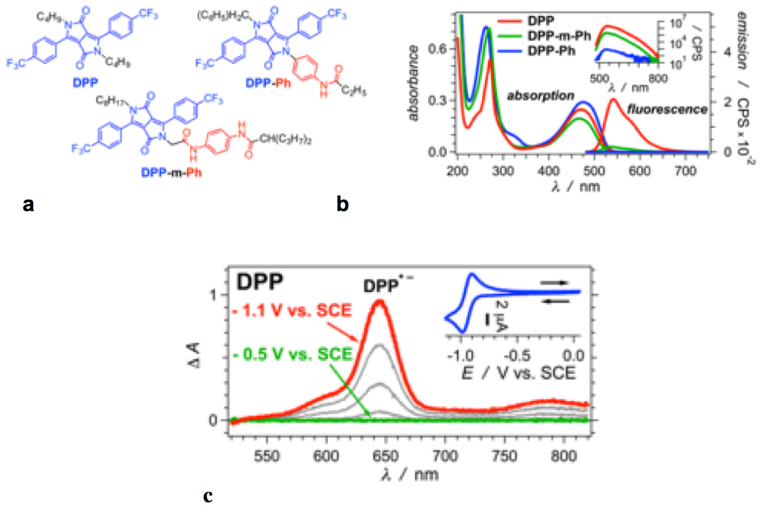

Figure 7-1. Basic characteristics of DPP, DPP-Ph and DPP-m-Ph. (a) Structures. (b) UV/visible absorption and fluorescence spectra (10 μM in acetonitrile, MeCN). Inset: fluorescence spectra plotted against logarithmic ordinate (λ_{ex} = 470 nm, fluorescence quantum yields: $\phi_f^{(DPP)}$ = 0.75, $\phi_f^{(DPP\text{-}m\text{-}Ph)}$ = 0.073, $\phi_f^{(DPP\text{-}Ph)}$ = 3.6 × 10^{-4}). (c) Differential absorption spectra recorded during electrochemical reduction of DPP (for MeCN with 100 mM NBu_4PF_6). Inset: cyclic voltammogram of DPP (scan rate = 50 mV s^{-1}).

appear to correlate with k_{CS}/k_{CR}. Conversely, k_{CS}/k_{CR} exhibits a defined bimodal correlation with the media viscosity. That is, k_{CS}/k_{CR} is largest for the most and the least viscous solvents, regardless their polarity or proticity.

Results and Discussion

Synthetic Strategies

The synthesis of the CT conjugates requires the preparation of asymmetrically substituted DPP derivatives. While the synthesis and double N-alkylation of these pigments is easy and well established,[13] the N-arylation is extremely challenging; currently, we know of only two reported cases that utilize strongly activated aryl fluorides.[22] Our design requires full control over the pattern of substituents. Therefore, we adopted a general strategy reported by Morton et al.[23-25]

The selected route is based on the synthesis of the targeted furo[3,4-c]pyrrole, **5**, followed by a sequence of alkylation and amidation steps (Scheme 1). Initial alkylation of β-keto ester, **1**, with ethyl bromoacetate in the presence of a strong base affords **2** in a good yield. Ammonia-induced ring closure results in the dihydropyrrolone, **3**, with one of the electron-deficient aryl substituents attached to it. A somewhat challenging alkenylation of the methylene carbon, followed by microwave-induced ring closure yields 5. Alkyl bromides, regardless the use of different bases (K_2CO_3, Cs_2CO_3, t-BuOK, and NaH), solvents (DMF, NMP, and THF), catalysts (TBAHS, KI, and crown ethers), and ultrasonication, manifest limited reactivity with 5. Therefore, we resort to benzyl bromide as a more active alkylation agent, affording N-benzylfuro[3,4-c]pyrrole **6** in 27% yield.

Asymmetrically N,N-disubstituted **DPP**, obtained via amidation from **6**, is readily acylated to the final compound, **DPP-Ph**, with excellent yield (Scheme 7-1).

Scheme 7-1. Synthesis of Asymmetrically Arylated Diketopyrrolopyrrole DPP-Ph[a]

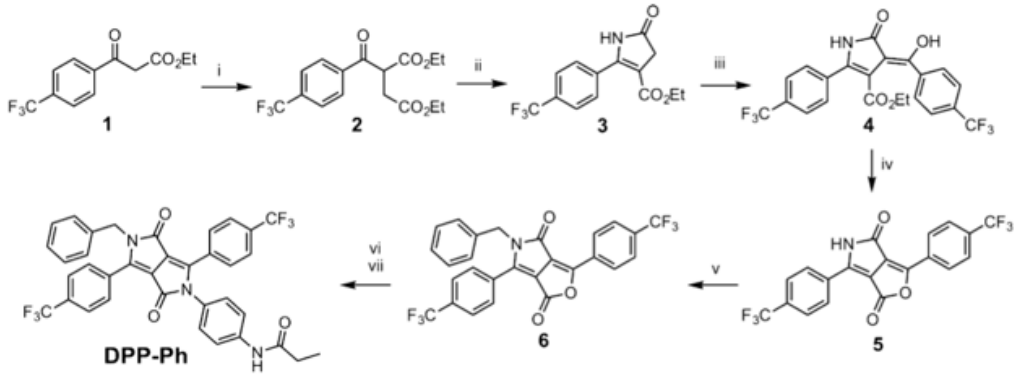

[a](i) $BrCH_2CO_2Et$, EtONa, EtOH, 0 °C → rt, 89%; (ii) NH_4OAc, AcOH, reflux, 63%; (iii) 1-CF_3-$C_6H_4CO_2Et$, t-AmONa, t-AmOH, 60 °C, 23%; (iv) microwave, 230 °C, 10 min, 74%; (v) $C_6H_5CH_2Br$, K_2CO_3, DMF, 40 °C, 29%; (vi) 1,4-$(NH_2)_2C_6H_4$, EDC, TFA, DCM, rt, 59%; and (vii) $(CH_3CH_2CO)_2O$, NEt_3, DCM, 0 °C → rt, 99%.

The other CT conjugate, **DPP-m-Ph**, possesses the same electron-deficient chromophore, but a methylene links it with the donor (Figure 1a). For the synthesis of this asymmetric conjugate, we use statistical N,N-dialkylation of a symmetric DPP derivative, **7** (Scheme 7-2).

Scheme 7-2. Synthesis of Asymmetrically Alkylated Diketopyrrolopyrrole DPP-m-Ph[a]

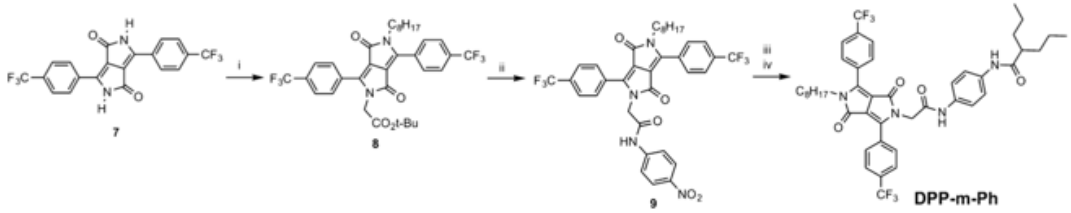

[a](i) $BrCH_2CO_2$-t-Bu, $C_8H_{17}I$, Cs_2CO_3, NMP, 120 °C, 25%; (ii) 1. TFA, DCM, 0 °C → rt; 2. $(COCl)_2$, DCM, rt, 1 h, 3. p-nitroaniline, pyridine, DCM, rt, 1 h, overall 84%; (iii) $Co_2(CO)_8$, H_2O, DME, reflux, 1 h, 67%; and (iv) $(H_7C_3)_2CHCOCl$, pyridine, rt, 1 h, 89%.

Basic Photophysical Properties.

DPP exhibits visible absorption and fluorescence, with zero-to-zero energy, ε_{00}, of about 2.4 eV. Addition of the electron donors does not cause substantial wavelength shifts in the absorption and emission spectra, but does considerably quench the fluorescence (Figure 7-1b). The absorption maxima for **DPP**, **DPP-Ph**, and **DPP-m-Ph** are at 470, 476, and 467 nm. Because $\Delta G_{CS}^{(0)}$ values for **DPP-Ph** and **DPP-m-Ph** are around –0.2 eV for acetonitrile media (Table 7-1), the 6 nm bathochromic shift in the absorption of DPP-Ph (corresponding to 33 meV) cannot be unequivocally ascribed to a CT band. These results suggest that while the DPP-donor dyads undergo highly efficient CS the donor–acceptor

Table 7-1. Estimates for CS Driving Forces, $-\Delta G_{CS}^{(0)}$

			$E^{(1/2)}$ (V vs SCE)[b]		
		$\mathcal{E}_{00}$ (eV)[a]	$D^{\bullet+}/D$	$A/A^{\bullet-}$	$\Delta G_{CS}^{(0)}$ (eV)[c]
DPP-Ph	MeCN	2.42	1.39	−0.89	−0.21
	DCM	2.39	1.54	−0.87	−0.29
DPP-m-Ph	MeCN	2.43	1.32	−0.90	−0.25
	DCM	2.42	1.55	−0.84	−0.23

[a]The values of the zero-to-zero energy, ε_{00}, were obtained from the wavelengths, λ_{00}, of the crossing points of the normalized absorption and fluorescence spectra: i.e., $\varepsilon_{00} = hc/\lambda_{00}$.[26, 27] [b] Values of half-wave potentials, $E^{(1/2)}$, extrapolated to zero electrolyte concentration, representing the reduction potentials for neat solvents.[28-32] $E^{(1/2)}$ for $D^{\cdot+}/D$ was obtained from the first oxidation waves of the cyclic voltammograms of the dyads, and for $A/A^{\cdot-}$, it was obtained from the first reduction waves. [C] Calculated from eq 1, where $\Delta G_S = 0$ and $W = e^2/4\pi\varepsilon_0\varepsilon R_{DA}$:[33] e, electron charge, ε, static dielectric constant of the solvent (Table 2), $\varepsilon_0 = 5.526 \times 10^{-3}$ e V^{-1} $Å^{-1}$, and R_{DA} the donor–acceptor center-to-center distances, was ~5.2 Å for **DPP-Ph** and 7.2 Å for **DPP-m-Ph**.

electronic coupling in these conjugates is not strong enough to considerably perturb the DPP absorption.

While this finding is not surprising for methylene-linked donor–acceptor systems[1, 34] such as **DPP-m-Ph**, it is unusual for **DPP-Ph**. CT conjugates, in which the donor and the acceptor are linked with a single bond, tend to exhibit defined bathochromic CT absorption.[35, 36] In **DPP-Ph**, however, the link is via a lactam nitrogen, which is spatially near some of the nodes of the frontier orbitals.[37, 38] Indeed, the C–C bonds anchoring the trifluoromethylphenyl moieties to the principal DPP ring system at positions 3 and 6 provide strong π-electronic coupling. Therefore, the trifluoromethyl groups affect the whole chromophore, making it electron-deficient. Conversely, groups attached to the lactam nitrogens do not truly perturb the DPP electronic properties as evident from the spectroscopic and electrochemical results.

Thermodynamics of Charge Separation.

The Rehm–Weller equation provides a means for estimating the driving force, $-\Delta G^{(0)}$, of photoinduced CS (Table 1):[28, 39]

$$\Delta G_{CS}^{(0)} = F\left(E_{D^{\bullet+}/D}^{(0)} - E_{A/A^{\bullet-}}^{(0)}\right) - \mathscr{E}_{00} + \Delta G_S + W \qquad (7\text{-}1)$$

Electrochemically estimated half-wave reduction potentials, $E^{(1/2)}$, provide a good approximation for $E^{(0)}$ of the oxidation of the donor, D, and the reduction of the acceptor, A.[28] For solvents in which $\mathscr{E}_{00}$ is estimated from spectral data, we extrapolate $E^{(1/2)}$ to zero electrolyte concentration.[30,31,40] Thus, we eliminate the Born solvation term, ΔG_S, which corrects for the interactions of the formed radical ions with the solvent environment.[1,28] The Coulomb work term, W, accounts for the interactions between the generated radical ions.

We obtain $E^{(1/2)}_{D^{+\bullet}/D}$, and $E^{(1/2)}_{A/A^{\bullet-}}$ from the first oxidation and the first reduction waves, respectfully, in the cyclic voltammograms of **DPP-Ph** and **DPP-m-Ph** (Figure 7-2a). Extrapolation of the half-wave potentials to zero salt concentration allows for eliminating the effect of the supporting electrolyte (Figure 2b).[30-32] The close similarity between the reduction potentials of **DPP-Ph** and **DPP-m-Ph** (Table 7-1) suggests that the electron donors in the two dyads have: (1) the same susceptibility to oxidation, and (2) no effect on the reduction of DPP.

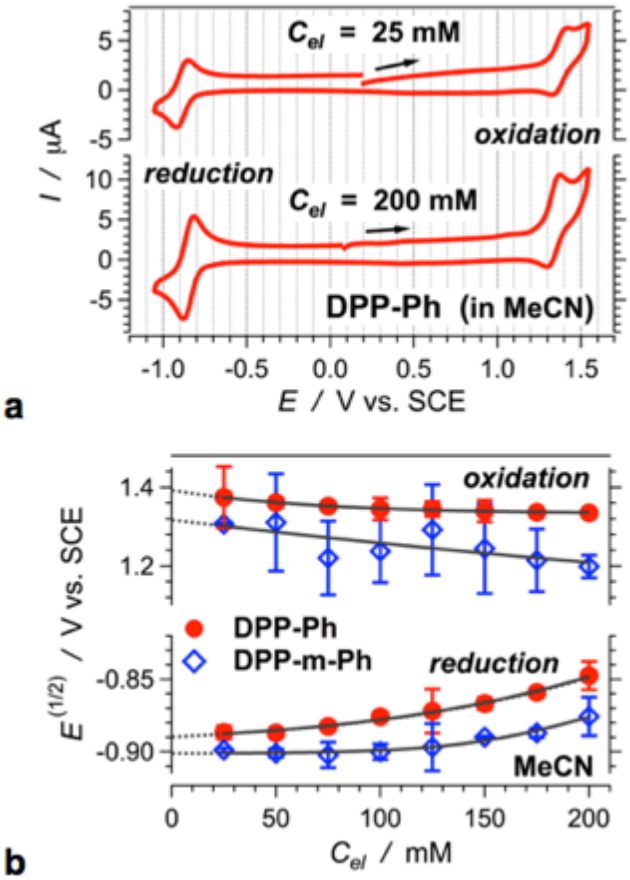

Figure 7-2. Electrochemical oxidation and reduction of DPP-Ph and DPP-m-Ph. (a) Cyclic voltammograms of DPP-Ph for MeCN at different concentrations, C_{el}, of supporting electrolyte, NBu_4PF_6. (b) Dependence of the half-wave reduction potentials on electrolyte concentration for MeCN. The solid lines are the data fits and the dotted lines show the extrapolations to zero electrolyte concentration.

Employing these estimates for $E^{(1/2)}$ in eq 1 and factoring W yields similar CS driving forces for the two dyads (Table 7-1). In addition, the CS driving forces for the relatively polar acetonitrile (MeCN) appear slightly less favorable (with 50 – 80 meV) than those for the relatively non-polar dichloromethane (DCM). Because the values of $-\Delta G_{CS}^{(0)}$ are relatively small, the Coulomb term, W (eq. 7-1), has a major contribution to the estimates. The values of W, however, could be underestimates, especially for polar solvents. Typically, the

calculations of W assume spherical radical ions of the oxidized donor and the reduced acceptor separated by a continuum media characterized with the dielectric constant, ε, of the bulk solvent. For linked donor-acceptor systems, the donor and the acceptor are in the same solvation cavity and the space between them cannot be necessarily characterized with ε of the bulk media.[41] Therefore, the small differences between the calculated values for the CS driving forces are within the uncertainty of the W estimates, and $-\Delta G_{CS}^{(0)}$ should be larger, especially for MeCN.

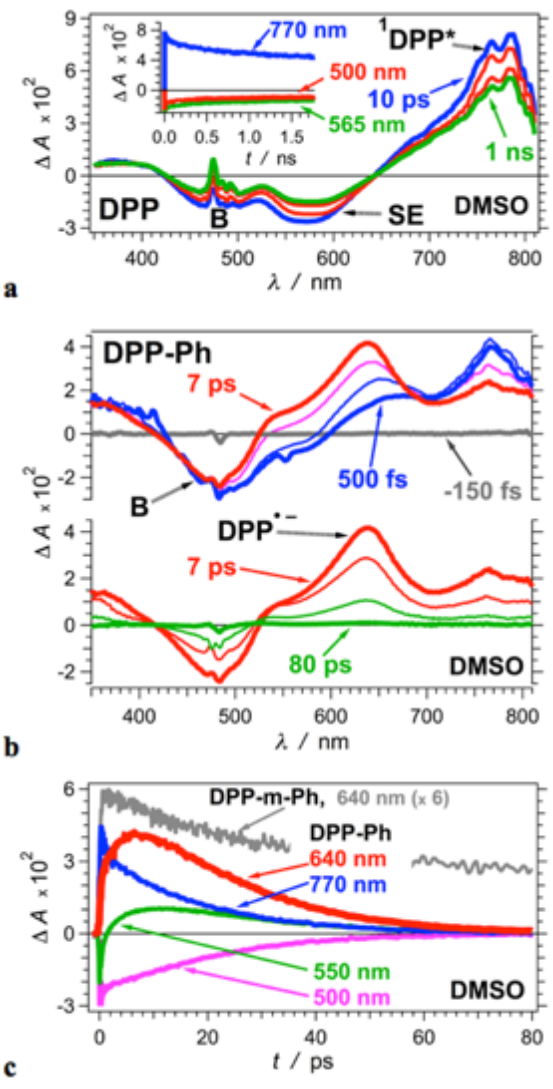

Figure 7-3. Transient absorption (TA) dynamics of **DPP** and **DPP-Ph** for DMSO (λ_{ex} = 480 nm, 6 μJ per pulse, $FWHM_{(for\ 800\ nm)}$ = 50 fs). (a,b) TA spectra (SE = stimulated emission, B = ground-state bleach). (c) TA dynamics monitored at different wavelengths: 770 nm for ^{1}DPP*, 640 nm for DPP$^{\bullet-}$, 550 nm for SE, and 500 nm for B. For comparison, the top gray line is for **DPP-m-Ph** monitored at 640 nm (Figure 7-5b). The rest of the kinetic curves are for **DPP-Ph**.

Kinetics of Electron Transfer

Upon illumination, **DPP-Ph** forms a locally excited state, ^{1}DPP*-Ph, manifesting a broad transient absorption (Figure 7-3a,b). The picosecond decay of ^{1}DPP* is concurrent with the rise of a band at 640 nm, which corresponds to the reduced chromophore, DPP$^{\bullet-}$ (Figure 7-1c, 7-3b). DPP$^{\bullet-}$ decays simultaneously with the recovery of the ground state, as monitored at the bleach (Figure 7-

3c). Therefore, we determine k_{CS} from the rise of the 640-nm band, and k_{CR} – from its decay, as quantified using global analysis.

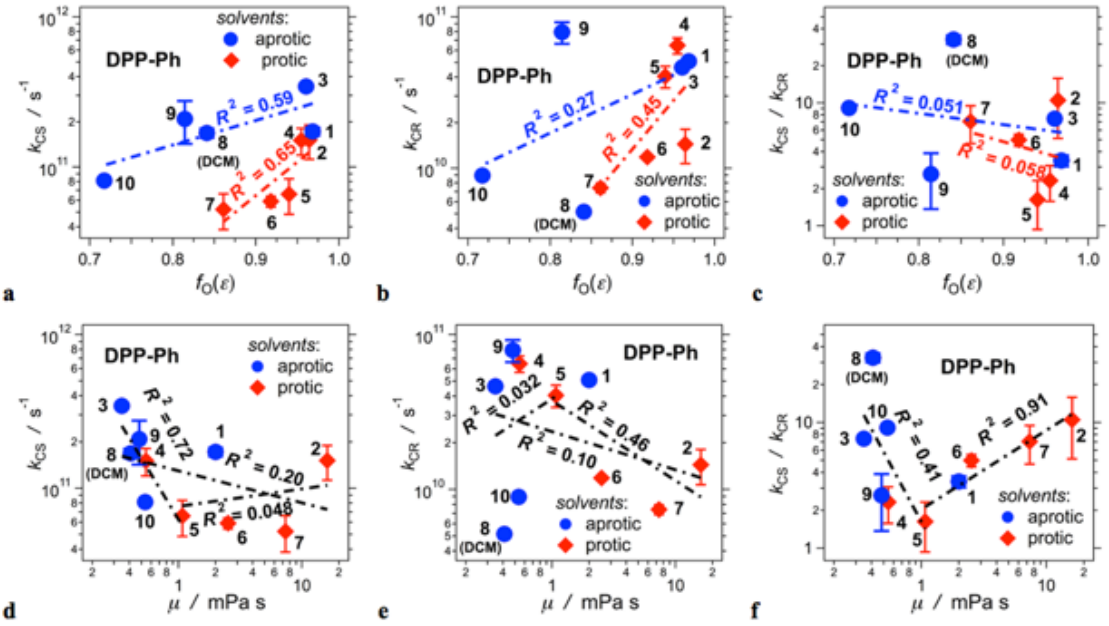

Figure 7-4. Solvent dependence of the rate constants of the photoinduced intramolecular charge separation, k_{CS}, and charge recombination, k_{CR}, of DPP-Ph (Table 2). (Solvents: 1 = DMSO, 2 = EG, 3 = MeCN, 4 = MeOH, 5 = EtOH, 6 = BuOH, 7 = OctOH, 8 = DCM, 9 = THF, and 10 = $CHCl_3$). The values of the rate constants are from global-fit analysis (see Supporting Information). (a-c) Dependence of k_{CS}, k_{CR} and the ratio, k_{CS}/k_{CR}, on the media polarity, represented by the Onsager function for solvent polarity, $f_O(\varepsilon)$ (Table 2), with results from correlation analyses for protic (2, 4, 5, 6, 7) and aprotic (1, 3, 8, 9, 10) solvents. (d-f) Dependence of k_{CS}, k_{CR} and the ratio, k_{CS}/k_{CR}, on the media viscosity, represented by the solvent dynamic viscosity, μ (Table 2), with results from correlation analyses: (d) for all solvents (R^2 = 0.20), for low-viscosity solvents with $\mu \leq 1$ mPa s (R^2 = 0.72), and for viscous solvents with $\mu \geq 1$ mPa s (R^2 = 0.048); (e) for all solvents (R^2 = 0.10), for low-viscosity solvents with $\mu \leq 1$ mPa s (R^2 = 0.032), and for viscous solvents with $\mu \geq 1$ mPa s (R^2 = 0. 46); and (f) for low-viscosity solvents with $\mu \leq 1$ mPa s (R^2 = 0.41), and for viscous solvents with $\mu \geq 1$ mPa s (R^2 = 0.91).

A decrease in the media polarity tends to slow down both, CS and CR, which can be expected (Table 7-2).[1,33] This polarity dependence of k_{CS} and k_{CR}, appears more pronounced for protic than for aprotic solvents; and the correlations are stronger for CS than for CR (Figure 7-4a,b). These observations underline the effects of discrete solvent-solute interactions, such as hydrogen bonding, on the ET properties of **DPP-Ph**, and especially on the initial photoinduced CS.

Conversely, the ratio, k_{CS}/k_{CR}, shows no apparent correlation with the solvent polarity. For protic and aprotic media, the correlations between k_{CS}/k_{CR} and the different representations of polarity are negligibly weak, i.e., $R^2 < 0.1$ (Figure 7-4c). A close examination of the k_{CS}/k_{CR}-vs.-f_O plots, however, reveals two separate trends (Figure 7-4c): (1) for solvents more polar than EtOH, k_{CS}/k_{CR} tends to increase with polarity (R^2 ($\lg(k_{CS}/k_{CR})$ vs. $f_O(\varepsilon)$) = 0.47); and (2) for solvent less polar than EtOH, k_{CS}/k_{CR} tends to slightly decrease with polarity (R^2 ($\lg(k_{CS}/k_{CR})$ vs. $f_O(\varepsilon)$) = 0.16). The media polarity, indeed, affects the Franck-Condon components of ET kinetics via the outer reorganization energy and via the driving force (eq. 7-1), i.e., via the polarity dependence of reduction potentials, of W, and sometime of $\mathscr{E}_{00}$ (for light sensitizers exhibiting solvatochromism). The scattered nature of the plots showing the polarity dependence of the CT kinetics and the moderate to weak correlations, however, indicate that other characteristics of the solvent media also govern the rates of CS and CR, and especially the ratio between them, k_{CS}/k_{CR}.

Considering the solvent viscosity, μ, reveals additional trends. Both, k_{CS} and k_{CR}, tend to decrease with an increase in media viscosity (Figure 7-4d,e, Table 7-2). For CS, the media viscosity causes a distinct decrease in the rates only for relatively non-viscous solvents, i.e., for $\mu \leq 1$ mPa s (Figure 7-4d). An increase in media viscosity beyond 1 mPa s does not have a strong effect on k_{CS}, i.e., $R^2 \approx 0.05$ (Figure 4d). In addition to this weak correlation for media with $\mu \geq 1$ mPa, predominantly the polarity, rather than the viscosity, appears to affect CS. For the relatively viscous solvents, the polar ones (EG and DMSO) manifest noticeably higher k_{CS} than those of the relatively non-polar ones (OctOH, BuOH, and EtOH) (Figure 7-4d).

Conversely, an increase in media viscosity impedes CR only for relatively viscous solvents, i.e., with $\mu \geq 1$ mPa s (Figure 4e). For non-vicious media, i.e., with $\mu \leq 1$ mPa s, the correlation between k_{CR} and μ is practically negligible (Figure 4e). This difference in the dependence of CS and CR on the media viscosity results in a bimodal effect of μ on k_{CS}/k_{CR} (Figure 7-4f). Indeed, the ratio k_{CS}/k_{CR} shows a well-defined dual dependence on the viscosity. The smallest k_{CS}/k_{CR} is for ethanol (μ = 1.1 mPa s). Both, a decrease and an increase in the solvent viscosity cause an increase in k_{CS}/k_{CR} (Figure 7-4f).

Rigidity of the environment, governed by the solvent viscosity, affects the frequency of molecular motions. Stretching, bending and rotation around the N-C bond, linking the donor with the acceptor, are modes that can influence the kinetics of ET in **DPP-Ph**. While an increase in solvent viscosity may damp mostly low-frequency molecular vibrations, it also slows down the rotations around the N-C bond

For systems such as **DPP-Ph**, in which a single covalent bond directly links a planar donor and acceptor, usually non-Condon (i.e., torsional) modes dominate the suppression of CR for non-viscous media. As observed for molecular rotors and particularly for those with propensity to form twisted intramolecular charge-transfer (TICT) states,[42] photoexcitation induces CS in states with a certain level of planarity and good electronic coupling between the π-conjugated systems of the donor and the acceptor. The formed CT sates exhibit a preference for conformers with orthogonality between the rings of the donor and the acceptor. Fast torsional modes produce these TICT states with decreased donor-

acceptor electronic coupling and suppressed CR. As expected for molecular rotors, an increase in solvent viscosity impedes the fast torsional modes[43] that can compete with CR.

The excites-state behavior of **DPP-Ph** deviates from what would be expected for donor-acceptor dyads with propensity to form TICT excited states. Similar to TICT-forming conjugates, k_{CS}/k_{CR} for **DPP-Ph** decreases with an increase in media viscosity (for $\mu \leq 1$ mPa s, Figure 7-4f). While for TICT-forming conjugates a decrease in media viscosity leads to suppression of CR due to fast torsional modes, we cannot quite claim the same for **DPP-Ph**. Indeed, for solvents with $\mu \leq 1$ mPa s, an increase in μ tends to cause an increase in k_{CR} (Figure 7-4e), which appears consistent with the formation of a TICT excited state. The weak correlation between k_{CR} and μ, i.e., $R^2 < 0.05$ (Figure 4e), however, places a question on the significance of this trend for **DPP-Ph**. Conversely, the strong correlation ($R^2 = 0.72$) between k_{CS} and μ for **DPP-Ph** in relatively non-viscous solvents (Figure 4d) suggests that it is CS, rather than CR, that the media viscosity predominantly affects for $\mu \leq 1$ mPa s. That is, the distinct decrease in k_{CS} with an increase in viscosity (for $\mu \leq 1$ mPa s, Figure 7-4d) is the dominating effect responsible for the observed k_{CS}/k_{CR} vs. μ trends (Figure 7-4f). This viscosity-induced suppression of CS suggests for solvent-coupled structural alterations of the locally excited state, ^{1}DPP*-Ph, that are essential for attaining fast ET rates. While faster than CR, the dynamics of non-viscous solvents is comparable with the picosecond time scales of CS (Table 7-2).

What appears quite unusual for DPP-Ph, however, is the suppression of CR and the increase in k_{CS}/k_{CR} by further increase in solvent viscosity, i.e., beyond 1 mPa s (Figure 7-

4e,f). This trend is contrary to the expected behavior of TICT-forming donor-acceptor conjugates. While non-Condon modes can be behind the low-viscosity trends, they cannot account for the correlations observed for viscous media (Figure 7-4e,f). Furthermore, for all solvents, except EG, the TA decays of the CT state, representing CR, are mono-exponential, indicating that the time constants of CR significantly exceed the time scales of the involved structural dynamic modes.

Table 7-2. Kinetics of CS and CR of DPP-Ph for Solvents with Different Polarities and Viscosities[a]

solvent[b]	ε^c	$f_O{}^d$	μ (mPa s)[e]	$k_{CS} \times 10^{-10}$ (s^{-1})	$k_{CR} \times 10^{-10}$ (s^{-1})	k_{CS}/k_{CR}
1. DMSO	47.0	0.968	1.996	17.2 ± 1.1	5.09 ± 0.21	3.38 ± 0.35
2. EG	41.4	0.965	16.1	15.1 ± 3.9	1.44 ± 0.37	10.5 ± 5.4
3. MeCN	37.5	0.961	0.347	34.4 ± 1.2	4.63 ± 0.04	7.42 ± 0.33
4. MeOH	32.7	0.955	0.544	15.1 ± 3.0	6.48 ± 0.78	2.33 ± 0.75
5. EtOH	24.5	0.940	1.074	6.60 ± 1.74	4.05 ± 0.66	1.63 ± 0.70
6. *n*-BuOH	17.8	0.918	1.399	5.91 ± 0.48	1.18 ± 0.03	4.99 ± 0.55
7. OctOH	10.3	0.861	7.36	5.23 ± 1.39	0.741 ± 0.054	7.06 ± 2.40
8. DCM	8.93	0.841	0.410	16.9 ± 1.2	0.515 ± 0.006	32.7 ± 2.7
9. THF	7.58	0.814	0.481	20.9 ± 6.6	7.93 ± 1.28	2.63 ± 1.26
10. $CHCl_3$	4.81	0.718	0.536	8.12 ± 0.22	0.894 ± 0.010	9.08 ± 0.35

[a]The CS and CR rate constants, k_{CS} and k_{CR}, are obtained from global fits of DPP-Ph TA kinetics (see Supporting Information). [b] Solvents: dimethyl sulfoxide (DMSO), ethylene glycol (EG), acetonitrile (MeCN), methanol (MeOH), ethanol (EtOH), 1-butanol (BuOH), 1-octanol (OctOH), dichloromethane (DCM), tetrahydrofuran (THF), and chloroform ($CHCl_3$). [C] Static dielectric constant, i.e., relative permittivity. [d] Onsager function for solvent polarity, $f_0(\varepsilon) = 2(\varepsilon - 1)/(2\varepsilon + 1)$. [e] Dynamic viscosity.

A potential reason for this viscosity-induced decrease in k_{CR} and increase in k_{CS}/k_{CR} (for $\mu > 1$ mPa s) can be a suppression of vibrational and bending modes that are more important for CR than for CS. For example, fast vibrational modes that are not significantly affected by the solvent viscosity could dominate the Franck-Condon contribution to the rate constant of the transition from the locally excited to the CT state, i.e., CS: ^{1}DPP*-Ph → $DPP^{\bullet-}$-$Ph^{\bullet+}$. Conversely, for the transition from the CT to the ground state, i.e., CR: $DPP^{\bullet-}$-$Ph^{\bullet+}$ → DPP-Ph, may involve relatively slow vibrational modes that are susceptible to suppression by increased media viscosity.[44,45] The driving forces for CS are much

smaller than those for CR. Hence, similar Frank-Codon effects on the ET kinetics most likely would affect CS more significantly than CR, which is opposite to the observed trends (Figure 7-4d,e). Therefore, the modes that govern CS should be quite different from those that are responsible for CR in order to attain the observed kinetic trends.

The dynamics of solvent reorganization may present another plausible contribution to the observed viscosity-dependence trends (Figure 7-4d-f).[46-48] Despite the favorable thermodynamics, an increase in the viscosity slows down the dynamics of solvent response that can make it rate limiting for ET. This behavior would be expected for viscous polar solvents, such as EG. It appears, however, that the viscosity affects CS only for media with $\mu \leq 1$ mPa (Figure 4d). In addition, the similar values of k_{CS} for the two most polar alcohols, EG and MeOH that have drastically different viscosities (Figure 7-4d, Table 7-2), place a question about the contribution of viscosity-limiting reorganization dynamics to the observed CS kinetics. Furthermore, the increase in k_{CS}/k_{CR} with the increase in solvent viscosity beyond 1 mPa s suggests that if such solvent reorganization dynamics plays a role in the observed kinetics, it should affect the CR more than the CS processes. Such a discriminative impact on the CR, rather than CS, kinetics requires a significant difference between the polarity of the ground and the locally excited states. The solvent reorganization dynamics, hence, cannot provide a solid rationale for the observed suppression of CR as the viscosity increases beyond 1 mPa s.

When two saturated covalent bonds link the donor and the acceptor, as in **DPP-m-Ph**, the singlet-excited state of DPP is still significantly quenched (Figure 7-1b, 7-5a,b).

The lifetime of ^{1}DPP*-m-Ph is between 0.2 to 1 ns for the different solvents, i.e., 10 to 40 times smaller than that of ^{1}DPP*. While the fluorescence lifetime of **DPP** shows no solvent dependence, the rates of decay of ^{1}DPP*-m-Ph increase with an increase in the media polarity for solvents with $\varepsilon > 15$ (Figure 7-5c), which is consistent with photoinduced CS.

A transient absorption band at 640 nm, corresponding to DPP$^{\bullet-}$, appears along with the band of ^{1}DPP* upon the excitation of **DPP-m-Ph**. We, however, do not observe growth of DPP$^{\bullet-}$ as ^{1}DPP* decays (Figure 7-3c, 7-5c). In addition, the 640-nm transient absorption is less pronounced for less polar solvents, appearing mostly as a shoulder.

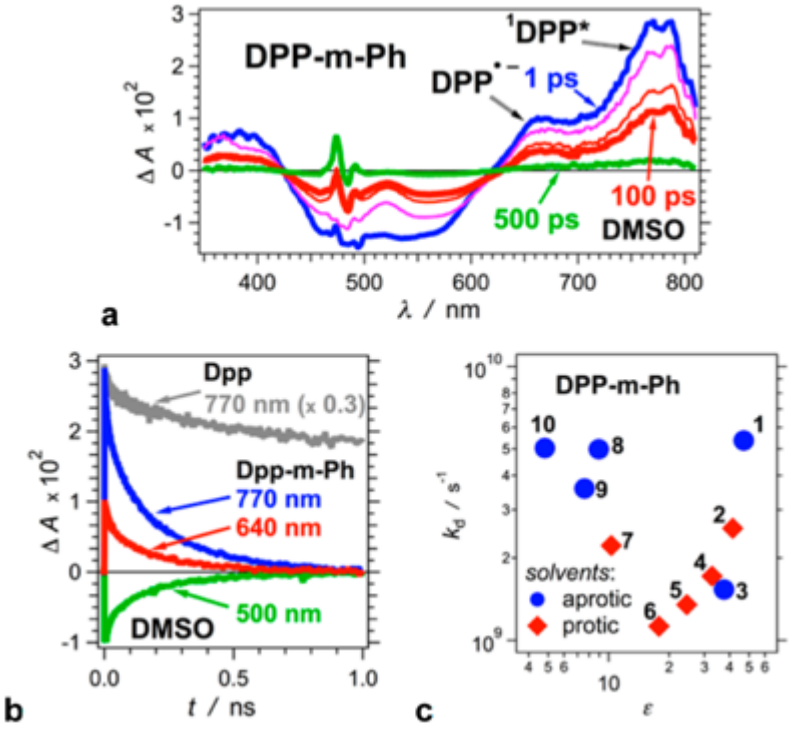

Figure 7-5. Transient absorption (TA) dynamics of **DPP-m-Ph**. (a) TA spectra for DMSO (λ_{ex} = 480 nm, 6 μJ per pulse, FWHM$_{(for\ 800\ nm)}$ = 50 fs). (b) TA dynamics monitored at different wavelengths: 770 nm for ^{1}DPP*, 640 nm for DPP$^{\bullet-}$, 500 nm for ground-state bleach recovery. For comparison, the top gray line is for **DPP** monitored at 770 nm (Figure 3a). The rest of the kinetic curves are for **DPP-m-Ph**. (c) Dependence of the decay rate constant, kd, recorded at 770 nm, on the solvent polarity represented by the solvent static relative dielectric constant, ε. The solvent numeration is the same as in Table 7-2 and Figure 7-4.

The flexibility of the methylene linker promotes heterogeneous CT kinetics representative of the multiple possible conformations of **DPP-m-Ph** with different donor-

acceptor coupling. As a result, we observe CS and formation of $DPP^{\bullet-}$ within the excitation of **DPP-m-Ph**, as well as bi-exponential decays for some of the solvent media.

These findings suggest that while ^{1}DPP*-m-Ph undergoes efficient CS, the consecutive CR occurs with comparable or faster rates. That is, CS is the rate-limiting step and the competing CR is fast enough to prevent accumulation of the CT state, except when CS occurs within the duration of the femtosecond excitation pulse. Indeed, the appearance of both $DPP^{\bullet-}$ and ^{1}DPP* transients within the femtosecond excitation pulse, while ^{1}DPP* lives 100s of ps, suggests for multiple CS pathways. The flexible methylene linker provides access to conformer where the donor contacts directly one of the trifluoromethylphenyl moieties, providing pathways for ultrafast CS. Folded conformers with improved donor-acceptor coupling dominating the locally excited states in non-polar media can explain the relatively large decay constants for solvents with $\varepsilon < 15$ (Figure 7-5c).

Along with the conformational heterogeneity, in comparison with **DPP-Ph**, an increase in the inner reorganizational energy for **DPP-m-Ph** can push the tips of the Marcus curves closer to the CR and away from the CS rates, making $k_{CS} < k_{CR}$. Overall the findings for the excited-state dynamics of **DPP-m-Ph** reveal a key advantage in the molecular-rotor design of **DPP-Ph** for suppressing the undesired CR.

Conclusion

While $\Delta G_{CS}^{(0)}$ and $\Delta G_{CR}^{(0)}$ are similar for both dyads, $k_{CS} > k_{CR}$ for **DPP-Ph**, whereas $k_{CS} \leq k_{CR}$ for **DPP-m-Ph**. This feature reiterates the importance of the molecular-rotor design of the **DPP-Ph** dyad for impeding CR while attaining efficient CS. Suppressing CR and boosting CS in non-viscous solvents can, indeed, be in accordance

with expected non-Condon effects. The viscosity-induced increase in the difference between the rates of CS and CR, however, suggests for dominating synergy with vibronic modes and perhaps, solvent reorganizational dynamics. Impeding CR, while conserving the efficiency of CS, is key for organic electronic materials and devices where molecular confinement can govern their properties. The findings for viscous media provide a potential platform for translation of molecular design to solid-state applications.

References

(1) Bao, D.; Upadhyayula, S.; Larsen, J. M.; Xia, B.; Georgieva, B.; Nunez, V.; Espinoza, E. M.; Hartman, J. D.; Wurch, M.; Chang, A.; Lin, C.-K.; Larkin, J.; Vasquez, K.; Beran, G. J. O.; Vullev, V. I. *J. Am. Chem. Soc.* **2014**, *136*, 12966-12973.

(2) Savoie, B. M.; Rao, A.; Bakulin, A. A.; Gelinas, S.; Movaghar, B.; Friend, R. H.; Marks, T. J.; Ratner, M. A. *J. Am. Chem. Soc.* **2014**, *136*, 2876-2884.

(3) Gust, D.; Moore, T. A.; Moore, A. L.; Lee, S. J.; Bittersmann, E.; Luttrull, D. K.; Rehms, A. A.; DeGraziano, J. M.; Ma, X. C.; Gao, F.; Belford, R. E.; Trierm, T. T. *Science* **1990**, *248*, 199-201.

(4) Jones, G., II; Vullev, V.; Braswell, E. H.; Zhu, D. *J. Am. Chem. Soc.* **2000**, *122*, 388-389.

(5) Whitesell, J. K.; Chang, H. K.; Fox, M. A.; Galoppini, E.; Watkins, D. M.; Fox, H.; Hong, B. *Pure Appl. Chem.* **1996**, *68*, 1469-1474.

(6) Jones, G., II; Vullev, V. I. *Org. Lett.* **2002**, *4*, 4001-4004.

(7) Marcus, R. A.; Sutin, N. *Biochim. Biophys. Acta* **1985**, *811*, 265-322.

(8) Thomas, K. G.; George, M. V.; Kamat, P. V. *Helv. Chim. Acta* **2005**, *88*, 1291-1308.

(9) Rosspeintner, A.; Angulo, G.; Vauthey, E. *J. Am. Chem. Soc.* **2014**, *136*, 2026-2032.

(10) Laine´, P. P.; Campagna, S.; Loiseau, F. *Coord. Chem. Rev.* **2008**, *252*, 2552-2571.

(11) Jang, S.; Newton, M. D. *J. Chem. Phys.* **2005**, *122*, 024501/024501-024501/024515.

(12) Berlin, Y. A.; Grozema, F. C.; Siebbeles, L. D. A.; Ratner, M. A. *J. Phys. Chem. C* **2008**, *112*, 10988-11000.

(13) Grzybowski, M.; Gryko, D. T. *Adv. Opt. Mater.* **2015**, *3*, 280-320.

(14) Iqbal, A.; Jost, M.; Kirchmayr, R.; Pfenninger, J.; Rochat, A.; Wallquist, O. *Bull. Soc. Chim. Belg.* **1988**, *97*, 615-643.

(15) Qu, S.; Tian, H. *Chem. Commun.* **2012**, *48*, 3039-3051.

(16) Nielsen, C. B.; Turbiez, M.; McCulloch, I. *Adv. Mater.* **2013**, *25*, 1859-1880.

(17) Grzybowski, M.; Glodkowska-Mrowka, E.; Stoklosa, T.; Gryko, D. T. *Org. Lett.* **2012**, *14*, 2670-2673.

(18) Kaur, M.; Choi, D. H. *Chem. Soc. Rev.* **2015**, *44*, 58-77.

(19) Ftouni, H.; Bolze, F.; de Rocquigny, H.; Nicoud, J. F. *Bioconjugate Chem.* **2013**, *24*, 942-950.

(20) Shimizu, S.; Iino, T.; Araki, Y.; Kobayashi, N. *Chem. Commun.* **2013**, *49*, 1621-1623.

(21) Fischer, G. M.; Ehlers, A. R.; Zumbusch, A.; Daltrozzo, E. *Angew. Chem. Int. Edit.* **2007**, *46*, 3750-3753.

(22) Yue, W.; Suraru, S.-L.; Bialas, D.; Mueller, M.; Wuerthner, F. *Angew. Chem. Int. Edit.* **2014**, *53*, 6159-6162.

(23) Morton, C. J. H.; Gilmour, R.; Smith, D. M.; Lightfoot, P.; Slawin, A. M. Z.; MacLean, E. J. *Tetrahedr.* **2002**, *58*, 5547-5565.

(24) Morton, C. J. H.; Riggs, R. L.; Smith, D. M.; Westwood, N. J.; Lightfoot, P.; Slawin, A. M. Z. *Tetrahedr.* **2005**, *61*, 727-738.

(25) Riggs, R. L.; Morton, C. J. H.; Slawin, A. M. Z.; Smith, D. M.; Westwood, N. J.; Austen, W. S. D.; Stuart, K. E. *Tetrahedr.* **2005**, *61*, 11230-11243.

(26) Guo, S.; Bao, D.; Upadhyayula, S.; Wang, W.; Guvenc, A. B.; Kyle, J. R.; Hosseinibay, H.; Bozhilov, K. N.; Vullev, V. I.; Ozkan, C. S.; Ozkan, M. *Adv. Funct. Mater.* **2013**, *23*, 5199-5211.

(27) Vullev, V. I.; Jones, G. *Tetrahedr. Lett.* **2002**, *43*, 8611-8615.

(28) Bao, D.; Millare, B.; Xia, W.; Steyer, B. G.; Gerasimenko, A. A.; Ferreira, A.; Contreras, A.; Vullev, V. I. *J. Phys. Chem. A* **2009**, *113*, 1259-1267.

(29) Bao, D.; Ramu, S.; Contreras, A.; Upadhyayula, S.; Vasquez, J. M.; Beran, G.; Vullev, V. I. *J. Phys. Chem. B* **2010**, *114*, 14467-14479.

(30) Larsen, J. M.; Espinoza, E. M.; Hartman, J. D.; Lin, C.-K.; Wurch, M.; Maheshwari, P.; Kaushal, R. K.; Marsella, M. J.; Beran, G. J. O.; Vullev, V. I. *Pure Appl. Chem.* **2015**, *87*, 779-792.

(31) Espinoza, E. M.; Larsen, J. M.; Vullev, V. I. *J. Phys. Chem. Lett.* **2016**, *7*, 758-764.

(32) Espinoza, E. M.; Xia, B.; Darabedian, N.; Larsen, J. M.; Nunez, V.; Bao, D.; Mac, J. T.; Botero, F.; Wurch, M.; Zhou, F.; Vullev, V. I. *Eur. J. Org. Chem.* **2016**, *2016*, 343-356.

(33) Wan, J.; Ferreira, A.; Xia, W.; Chow, C. H.; Takechi, K.; Kamat, P. V.; Jones, G.; Vullev, V. I. *J. Photochem. Photobiol. A* **2008**, *197*, 364-374.

(34) Flamigni, L.; Ventura, B.; Tasior, M.; Becherer, T.; Langhals, H.; Gryko, D. T. *Chem. Eur. J.* **2008**, *14*, 169-183.

(35) Jones, G., II; Yan, D.; Hu, J.; Wan, J.; Xia, B.; Vullev, V. I. *J. Phys. Chem. B* **2007**, *111*, 6921-6929.

(36) Hu, J.; Xia, B.; Bao, D.; Ferreira, A.; Wan, J.; Jones, G.; Vullev, V. I. *J. Phys. Chem. A* **2009**, *113*, 3096-3107.

(37) Jin, R. *Theor. Chem. Acc.* **2012**, *131*, 1-10.

(38) Shi, H.; Sun, W.; Wang, Q.; Gu, G.; Si, W.; Huang, W.; Zhang, Q.; Dong, X. *ChemPlusChem* **2016**, *81*, 515-520.

(39) Rehm, D.; Weller, A. *Israel. J. Chem.* **1970**, *8*, 259-&.

(40) Xia, B.; Bao, D.; Upadhyayula, S.; Jones, G.; Vullev, V. I. *J. Org. Chem.* **2013**, *78*, 1994-2004.

(41) Upadhyayula, S.; Bao, D.; Millare, B.; Sylvia, S. S.; Habib, K. M. M.; Ashraf, K.; Ferreira, A.; Bishop, S.; Bonderer, R.; Baqai, S.; Jing, X.; Penchev, M.; Ozkan, M.; Ozkan, C. S.; Lake, R. K.; Vullev, V. I. *J. Phys. Chem. B* **2011**, *115*, 9473-9490.

(42) Sasaki, S.; Drummen, G. P. C.; Konishi, G.-i. *J. Mater. Chem. C* **2016**, *4*, 2731-2743.

(43) Zhou, F.; Shao, J.; Yang, Y.; Zhao, J.; Guo, H.; Li, X.; Ji, S.; Zhang, Z. *Eur. J. Org. Chem.* **2011**, 4773-4787.

(44) Bagchi, B.; Biswas, R. *Adv. Chem. Phys.* **1999**, *109*, 207-433.

(45) Sokoloff, J. B. *J. Chem. Phys.* **1988**, *89*, 2330-2335.

(46) Clark, C. D.; Hoffman, M. Z. *Coord. Chem. Rev.* **1997**, *159*, 359-373.

(47) Canzi, G.; Kubiak, C. P. *J. Phys. Chem. C* **2012**, *116*, 6560-6566.

(48) Chakrabarti, S.; Liu, M.; Waldeck, D. H.; Oliver, A. M.; Paddon-Row, M. N. *J. Phys. Chem. A* **2009**, *113*, 1040-1048.

Experimental

General methods

All chemicals were used as received unless otherwise noted. All reported ^{1}H-NMR and ^{13}C-NMR spectra were recorded on 500 or 600 MHz spectrometer. Chemical shifts (δ ppm) were determined with TMS as the internal reference; *J* values are given in Hz. Mass spectra were obtained *via* EI or electrospray MS (ESI-MS). Chromatography was performed on silica (Kieselgel 60, 200-400 mesh). 2,5-Dibutyl-1,4-diketo-3,6-bis(4-trifuloromethylphenyl)-pyrrolo[3,4-*c*]pyrrole (**DPP**), 3,6-Bis(4-(trifluoromethyl)phenyl)-2,5-dihydropyrrolo[3,4-*c*]pyrrole-1,4-dione (**7**, starting material for **DPP-m-Ph**, Scheme 2) were prepared according to the literature procedures.[1,2]

Synthesis

For the synthesis of the asymmetrically arylated CT conjugate, **DPP-Ph**, we adopt a procedure reported by Morton *et al.* (Scheme 1).[3-5] For DPP-m-Ph, we employ Statistical *N,N*-dialkylation of **7** with octylhalide and *t*-butyl ester of chloroacetic acid, followed by acid-catalyzed hydrolysis of the ester and amide coupling with 4-nitroaniline (Scheme 2). We tested different strategies for selectively reducing the nitro group to amine, using for example H_2/Pd/C, $SnCl_2$, and $Na_2S_2O_4$. All these established procedures for relatively selective reduction of nitroaryls, unfortunately, also reduce the DPP chromophore. Therefore, we resorted to an approach reported by Lee and An,[6,7] which affords the amine with a good yield (step iii in Scheme 2). Acylation of this amine produces **DPP-m-Ph**.

1.3. Synthetic procedures

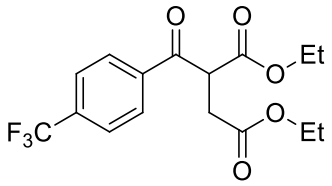

2-(4-Trifluoromethylbenzoyl)maleic acid diethyl ester (2). Sodium (1.84 g, 80 mmol) was dissolved in 77 mL of EtOH and the resulted solution was cooled down to 0 °C. Subsequently, 3-oxo-3-(4-trifluoromethylphenyl)propionic acid ethyl ester (**1**, 20.0 g, 77.0 mmol) and ethyl bromoacetate (18.0 mL, 162.0 mmol) were added dropwise and reaction mixture was stirred overnight at room temperature under an argon atmosphere. After the reaction was complete, water was added until complete dissolution of NaBr, followed by removal of ethanol under reduced pressure. The aqueous solution was extracted three times with diethyl ether. The combined organic phases were then washed with water, dried over anhydrous Na_2SO_4 and concentrated. The remaining oil was distilled under the reduced pressure (125-127 °C, 1.6 mbar) yielding 23.8 g (89%); ^{1}H NMR ($CDCl_3$, 500 MHz) δ 1.58 (3H, t, *J*=7.2 Hz), 1.23 (3H, t, *J*=7.0 Hz), 3.04 (1H, dd, J_1=17.6 Hz, J_2=5.8 Hz), 3.18 (3H, dd, J_1=17.6 Hz, J_2=8.7 Hz), 4.13 (2H, q, *J*=7.5 Hz), 4.15 (2H, q, *J*=7.2 Hz), 4.88 (1H, dd, J_1=8.7 Hz, J_2=5.8 Hz), 7.76 (2H, d, *J*=8.2 Hz), 8.17 (2H, d, *J*=8.2 Hz); ^{13}C NMR ($CDCl_3$, 125 MHz) δ 193.6, 171.1, 168.1 138.9 (d, *J*=1.1 Hz), 134.7 (q, *J*=33 Hz), 129.1, 125.6 (q, *J*=3.5 Hz), 123.5 (q, *J*=273 Hz), 61.9, 61.0, 49.7, 33.1, 13.9, 13.7; HRMS calcd for $C_{16}H_{17}F_3O_5$ (M^+): 346.1028; found: 346.1024; Elemental analysis calcd. (%) for $C_{16}H_{17}F_3O_5$: C 55.49, H 4.95, F 16.46; found: C 55.52, H 5.07, F 16.26.

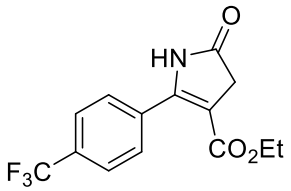

Ethyl 4,5-dihydro-5-oxo-2-(4-trifluoromethylbenzoyl)-1*H*-pyrrole-3-carboxylate (3). 2-(4-Trifluoromethylbenzoyl)maleic acid diethyl ester (**2**, 26.0 g, 75.0 mmol) and ammonium acetate (16.0 g, 77.1 mmol) were refluxed in glacial acetic acid (45 mL) overnight. Next, reaction mixture was cooled to 0 °C and poured into 500 mL of cold water. A crystalline precipitate was isolated by suction filtration and washed with water. The crude product was dissolved in a small amount of methanol and precipitated with water yielding 14.1 g (63%) of the expected compound; m.p.: decomposition > 170 °C; ^{1}H NMR ($CDCl_3$, 500 MHz) δ 1.20 (3H, t, *J*=7.1 Hz), 3.53 (2H, s), 4.14 (2H, q, *J*=7.1 Hz), 7.72 (2H, d, *J*=8.5 Hz), 7.76 (2H, d, *J*=8.5 Hz), 8.84 (1H, s); ^{13}C NMR ($CDCl_3$, 125 MHz) δ 177.4, 162.8, 149.6, 132.8, 132.3 (q, *J*= 33 Hz), 129.2, 125.3 (q, *J*=3.5 Hz), 123.6 (q, *J*=273 Hz), 105.9, 60.4, 38.7, 14.1; HRMS calcd for $C_{14}H_{12}F_3NO_3Na$ ($[M+Na]^+$): 322.0667; found: 322.0668; Elemental analysis calcd (%) for $C_{14}H_{12}F_3NO_3$: C 56.19, H 4.04, N 4.68, F 19.05; found: C 56.22, H 3.99, N 4.56, F 19.23.

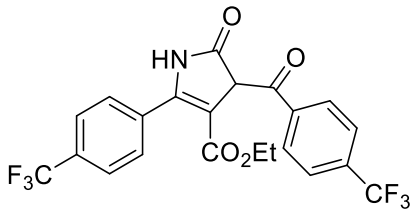

Ethyl 4-(4-trifluoromethylbenzoyl)-4,5-dihydro-5-oxo-2-(4-trifluoromethylphenyl)-pyrrole-3-carboxylate (**4**). Sodium (2.69 g, 117.0 mmol) was dissolved in *t*-amyl alcohol (270 mL) at 105 °C. Next, the solution was cooled down to room temperature and ethyl 4,5-dihydro-5-oxo-2-(4-trifluoromethylbenzoyl)-1*H*-pyrrole-3-carboxylate (**3**, 11.7 g, 39.0

mmol) and 4-trifluoro-methylbenzoic acid (8.50 g, 39.0 mmol) were added. The resulting mixture was slowly heated to 60 °C allowed to react for 8 h. The reaction mixture was then cooled down and poured into ice-cooled water (270 mL) followed by acidification with concentrated HCl and extraction with DCM. The organic fractions were combined, dried over anhydrous Na_2SO_4 and concentrated. The crude product was recrystallized from DCM yielding 4.35 g (23%) of expected product as a mixture of two tautomeric forms; m.p.: decomposition > 150 °C; ^{1}H NMR ($CDCl_3$, 500 MHz) δ 0.67 (major, 3H, t, *J*=7.1 Hz), 1.00 (minor, 3H, t, *J*=7.1 Hz), 3.05 (1H, s), 3.56 (major, 2H, q, *J*=7.1 Hz), 4.18 (minor, 2H, q, *J*=7.1 Hz), 7.55-7.78 (minor, 8H, m), 7.55-7.78 (major, 8H, m), 9.33 (major, 1H, bs), 9.63 (minor, 1H, bs), 14.73 (1H, s); ^{13}C NMR ($CDCl_3$, 125 MHz) δ 175.4, 169.2, 163.7, 138.71, 138.4, 135.3, 134.8, 133.3, 133.0, 131.6, 131.4, 129.6, 129.4, 129.3, 128.9, 128.8, 128.5, 125.5, 125.3, 125.2, 125.0, 124.8, 124.6, 122.6, 122.5, 107.6, 104.9, 62.4, 60.9, 13.4, 13.1; HRMS calcd for $C_{22}H_{16}F_6NO_4$ ($[M+H]^+$): 472.0984; found: 472.0984; Elemental analysis calcd (%) for $C_{22}H_{15}F_6NO_4$: C 56.06, H 3.21, N 2.97, F 24.18; found: C 56.04, H 3.31, N 2.97, F 24.04.

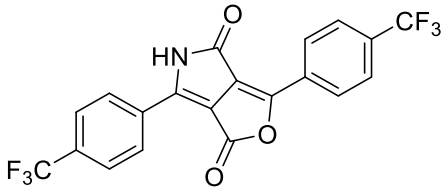

3,6-Bis-(4-trifluoromethylphenyl)-1*H*-furo[3,4-*c*]pyrrole-1,4(5*H*)-dione (5). Ethyl 4-(4-trifluoromethylbenzoyl)-4,5-dihydro-5-oxo-2-(4-trifluoromethylphenyl)-pyrrole-3-carboxylate (**4,** 400.0 mg, 8.24 mmol) was heated without solvent for 10 min at 230 °C in a microwave reactor. Next, methanol was added to the cooled reaction mixture and the

precipitate was filtered off yielding 262 mg (74%) of the expected orange pigment, which was used without further purification; m.p.: decomposition > 330 °C; HRMS calcd for $C_{20}H_9F_6NO_3$ ($[M+H]^+$): 425.0487 ; found: 425.0481.

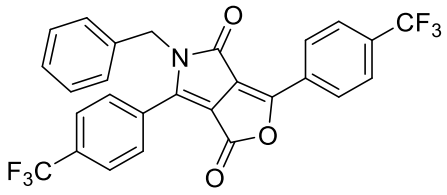

5-Benzyl-3,6-bis-(4-trifluoromethylphenyl)-1*H*-furo[3,4-*c*]pyrrole-1,4(5*H*)-dione (6). 3,6-Bis-(4-trifluoromethylphenyl)-1*H*-furo[3,4-*c*]pyrrole-1,4(5*H*)-dione (**5**, 670 mg, 1.58 mmol) and K_2CO_3 (437 mg, 3.16 mmol) were added to 22 mL of dry DMF. Subsequently, benzyl bromide (280.0 µL, 2.36 mmol) was introduced *via* syringe to the resulted solution and reaction mixture was stirred for 4 h at 40 °C. After reaction completion, 25 mL of water was added and the solution was extracted with DCM. Combined organic phases were dried over anhydrous $MgSO_4$ and concentrated. The crude product was purified by column chromatography (DCM : hexanes, 1:1), yielding 236 mg (29%) of **6**; m.p.: decomposition > 195 °C; ^{1}H NMR ($CDCl_3$, 500 MHz) δ 5.06 (2H, s), 7.15 (2H, d, *J*=6.8 Hz), 7.28-7.37 (3H, m), 7.75 (4H, d, *J*=1.7 Hz), 7.80 (2H, d, *J*=8.5 Hz), 8.52 (2H, d, *J*=8.2 Hz); ^{13}C NMR ($CDCl_3$, 125 MHz) δ 161.1, 158.8, 154.7, 149.3, 136.0, 134.2 (q, *J*=32 Hz), 133.5 (q, *J*=33 Hz), 130.1, 130.1, 129.5, 129.5, 129.3, 129.2, 128.6, 128.1, 126.5, 126.2 (q, *J*=3.4), 126.1 (q, *J*=4.0), 123.5 (q, *J*=273 Hz), 123.3 (q, *J*= 273 Hz), 115.0, 105.9, 46.2; HRMS calcd for $C_{27}H_{15}F_6NO_3Na$ ($[M+Na]^+$): 538.0854; found: 538.0852; Elemental analysis calcd (%) for $C_{27}H_{15}F_6NO_3$: C 62.92, H 2.93, N 2.72, F 22.12; found: C 62.70, H 2.75, N 2.63, F 22.18.

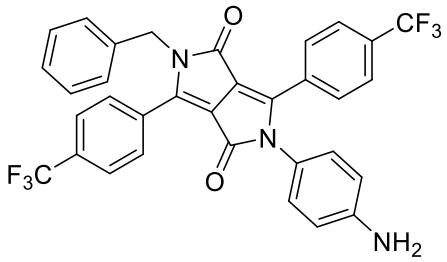

5-Benzyl-2-(4-aminophenyl)-3,6-(4-trifluoromethylphenyl)-2,5-dihydropyrrolo[3,4-*c*]pyrrole-1,4-dione (7). A mixture of **6** (202.0 mg, 0.39 mmol), 1,4-phenylenediamine (84.0 mg, 0.78 mmol), EDC (149 mg, 0.78 mmol), 0.1 M TFA in DCM (0.3 mL) and DCM (50 mL) were reacted at room temperature for 48 h. Next, the solvent was removed under reduced pressure. Crude product was washed with cold MeOH and filtered off. Analytically pure **7** was obtained by means of column chromatography (Al_2O_3, DCM) with 59% yield (179 mg); m.p.: decomposition > 125 °C; ^{1}H NMR ($CDCl_3$, 500 MHz) δ 4.44 (2H, bs), 5.02 (2H, s), 6.73 (2H, d, *J*=8.4 Hz), 6.96 (2H, d, *J*=8.6 Hz), 7.19 (2H, d, *J*=7.2 Hz), 7.25-7.29 (3H, m), 7.30-7.34 (2H, m), 7.59 (2H, d, *J*=8.4 Hz), 7.68 (2H, d, *J*=8.3 Hz), 7.85 (2H, d, *J*=7.3 Hz); ^{13}C NMR ($CDCl_3$, 125 MHz) δ 162.5, 161.9, 147.8, 146.7, 136.9, 132.7 (q, *J*=26 Hz), 130.9, 130.8, 130.0, 129.4, 129.0, 126.8, 127.7, 126.6, 125.8 (q, *J*=3.8 Hz), 125.3 (q, *J*=3.8 Hz), 124.6, 122.5, 122.4, 116.2, 110.9, 110.8, 45.8; HRMS calcd for $C_{33}H_{22}F_6N_3O_2$ ($[M+H]^+$): 606.1616; found: 606.1606.

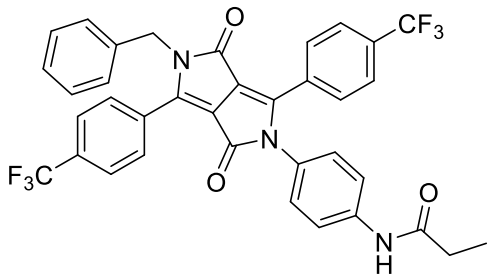

5-Benzyl-2-(4-propionylamidophenyl)-3,6-(4-trifluoromethylphenyl)-2,5-dihydropyrrolo[3,4-*c*]pyrrole-1,4-dione (DPP-Ph). A solution of propionic anhydride

(0.30 mL, 1.0 mmol) in DCM (1.0 mL) was added dropwise to a solution of 5-benzyl-2-(4-aminophenyl)-3,6-(4-trifluoromethylphenyl)-2,5-dihydropyrrolo[3,4-*c*]pyrrole-1,4-dione (**7,** 61 mg, 0.1 mmol) and triethylamine (0.30 ml, 2.0 mmol) in DCM (3 mL) at 0 °C. After 20 minutes the reaction was poured into ice-cold water and extracted with DCM. The combined organic phases were dried over anhydrous $MgSO_4$ and concentrated. The crude product was purified by column chromatography (DCM : hexanes, 1:1) yielding 65 mg (99%) of **8**; m.p.: 220-221 °C; ^{1}H NMR ($CDCl_3$, 500 MHz) δ 1.21 (3H, t, *J*=7.7 Hz), 2.35 (2H, q, *J*=7.7 Hz), 5.01 (2H, s), 7.10 (2H, d, *J*=8.9 Hz), 7.18 (2H, d, *J*=7.1 Hz), 7.26-7.35 (3H, m), 7.38 (1H, s), 7.53-7.60 (4H, m), 7.69 (2H, d, *J*=8.6 Hz), 7.79 (2H, d, *J*=8.3 Hz), 7.85 (2H, d, *J*=8.3 Hz); ^{13}C NMR ($CDCl_3$, 125 MHz): δC 172.0, 162.5, 161.6, 148.3, 146.2, 138.1, 136.8, 133.1 (q, *J*=33 Hz), 132.6 (q, *J*=33 Hz), 130.8, 130.5, 130.5, 129.9, 129.4, 129.0, 128.2, 127.8, 126.5, 125.9 (q, *J*=3.5 Hz), 125.5 (q, *J*=4.0 Hz), 123.5 (q, *J*=273 Hz), 120.1, 111.4, 110.5, 45.8, 30.7, 9.5; HRMS calcd for $C_{36}H_{25}F_6N_3O_3Na$ ($[M+Na]^+$): 684.1698; found: 684.1685; Elemental analysis calcd (%) for $C_{36}H_{25}F_6N_3O_3$: C 65.36, H 3.81, N 6.35, F 17.23; found: C 65.28, H 3.92, N 6.28, F 17.16.

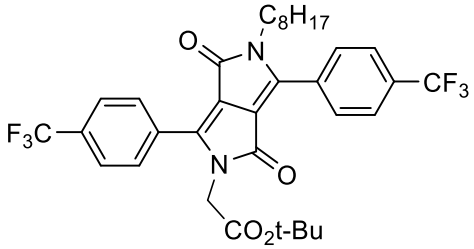

***Tert*-butyl-2-(5-octyl-1,4-dioxo-3,6-bis(4-(trifluoromethyl)phenyl)-4,5-dihydropyrrolo [3,4-*c*] pyr-rol-2(1*H*)-yl)acetate (8).** A mixture of pigment **7** (1.275 g, 3 mmol), cesium carbonate (2.95 g, 9.05 mmol) and 8 mL of NMP was heated to 120 °C under an argon atmosphere. Iodooctane (2.7 mL, 14.95 mmol) and *tert*-butyl bromoacetate

(2.2 mL, 14.9 mmol) were added dropwise using a syringe (30 min). The reaction mixture was stirred for 3 h, cooled and diluted with water and methylene chloride. The aqueous layer was extracted with methylene chloride and the combined organic layers were washed with water and brine and dried over sodium sulfate. The solvent was evaporated *in vacuo* and the product was purified using flash chromatography (SiO_2, EtOAc : Hexane, 1:25 - 1:9) to afford 505 mg of **8** as orange solid (25%); m.p.: decomposition > 125 °C; ^{1}H NMR (500 MHz, $CDCl_3$) δ 7.93 – 7.88 (m, 4H), 7.82 – 7.75 (m, 4H), 4.39 (s, 2H), 3.77 – 3.73 (m, 2H), 1.51 – 1.46 (m, 4H), 1.38 (s, 9H), 1.30 – 1.22 (m, 8H), 0.85 (t, J = 7.1 Hz, 3H); ^{13}C NMR ($CDCl_3$, 125 MHz) δ 167.3, 162.3, 161.7, 147.9, 146.5, 132.9 (m), 129.0, 128.9, 126.0 (m), 124.6 (m), 111.3, 109.8, 83.0, 43.9, 41.9, 31.6, 29.7. 29.6, 29.3, 29.0, 28.9, 27.8, 26.6, 22.5, 14.0; HRMS (ESI) calcd for $C_{34}H_{36}N_2O_4F_6Na$ ($[M+Na]^+$): 673.2477; found: 673.2469.

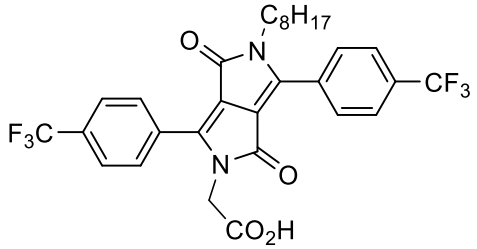

2-(5-Octyl-1,4-dioxo-3,6-bis(4-(trifluoromethyl)phenyl)-4,5-dihydropyrrolo[3,4-*c*]pyrrol-2(1*H*)-yl)acetic acid (DPP-m-CO_2H). Compound **8** (1.30 g, 2 mmol) was dissolved in DCM (30 mL), TFA (3.08 mL, 20 mmol) was added and the resulting reaction mixture was stirred for 4 h. The reaction was checked for completion by TLC and the mixture was evaporated under reduced pressure. The residual TFA was co-evaporated with toluene. The resulting solid residue was washed with cyclohexane (2 x 50 mL), dried under

vacuum to give expected compound as red oil, which was used without further purification; HRMS (ESI) calcd for $C_{30}H_{27}F_6N_2O_4$ ([M-H]$^-$): 593.1875; found: 593.1870.

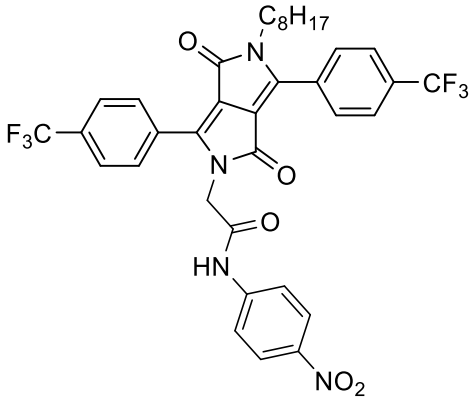

***N*-(4-Nitrophenyl)-2-(5-octyl-1,4-dioxo-3,6-bis(4-(trifluoromethyl)phenyl)-4,5-dihydropyrrolo [3,4-*c*]pyrrol-2(1*H*)-yl)acetamide (9).** In a dry argon-filled flask **DPP-m-CO_2H** (534 mg, 0.90 mmol) was dissolved in dry DCM (10 mL) and DMF (10 µL). The solution was cooled to -70 °C and oxalyl chloride (154.58 µL, 1.80 mmol), was added dropwise. Then, the dry ice bath was removed and the reaction mixture allowed to warm to room temperature and stirred for 1 hour. The reaction mixture was evaporated in vacuo in the presence of argon to obtain the acid chloride. The crude acid chloride was dissolved in DCM (10 mL) under argon and added slowly to a cooled to -70 °C solution of 4-nitroaniline (162 mg, 1.17 mmol) in anhydrous DCM (10 mL) and pyridine (145 µL, 1.80 mmol). The mixture was stirred at room temperature for an additional 1 h. The solution was poured into 1N HCl and the organic layer was separated. The organic phase was dried ($MgSO_4$) and concentrated in vacuo. The product was purified by column chromatography (SiO_2, EtOAc : Hexane, 1:4) afforded **9** as orange solid with 84% overall yield. $R_f \sim 0.65$ (hexanes: EtOAc = 2 : 1); m.p.: decomposition > 196 °C; ^{1}H NMR (500 MHz, $CDCl_3$) δ

9.44 (s, 1H), 8.18 (d, J = 8.9 Hz, 4H), 7.93 (d, J = 8.0 Hz, 2H), 7.86 (dd, J_1 = 8.2, J_2 = 4.0 Hz, 4H), 7.70 (d, J = 9.1 Hz, 2H), 4.46 (s, 2H), 3.80 – 3.75 (m, 2H), 1.58 (s, 4H), 1.29 – 1.22 (m, 8H), 0.85 (t, J = 7.1 Hz, 3H); ^{13}C NMR (125 MHz, $CDCl_3$) δ 166.2, 163.5, 162.1, 150.5, 146.1, 143.9, 143.1, 133.6 (m), 130.9, 129.9, 129.8, 129.2, 126.2 (m), 125.0, 119.5, 111.6, 108.9, 48.4, 42.2, 31.7, 30.3, 29.7, 29.4, 29.0, 28.9, 26.6, 22.5, 14.0; HRMS (ESI) calcd for $C_{36}H_{33}N_4O_5F_6$ ($[M+H]^+$): 715.2342; found: 715.2343.

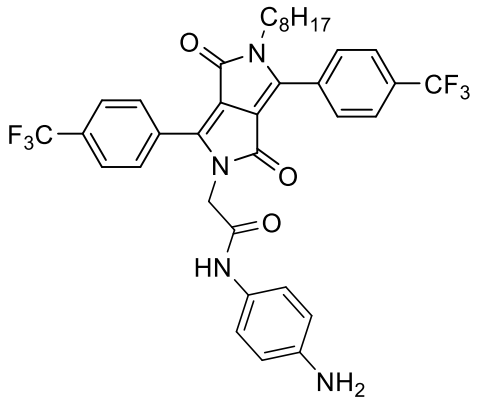

***N*-(4-Aminophenyl)-2-(5-octyl-1,4-dioxo-3,6-bis(4-(trifluoromethyl)phenyl)-4,5-dihydropyrrolo [3,4-*c*]pyrrol-2(1*H*)-yl)acetamide (DPP-m-Ph-NH$_2$).** In a dry argon-filled compound **9** (427 mg, 0.59 mmol), $Co_2(CO)_8$ (409 mg, 1.19 mmol), water (215.22 μL, 11.95 mmol) in DME (5 mL) were added and the reaction mixture was refluxed until TLC indicated complete conversion of the starting material (1 hour). The reaction mixture was cooled to room temperature, concentrated and purification by flash chromatography (SiO_2, EtOAc : Hexane = 1:2) afforded the amine, **DPP-m-Ph-NH$_2$**, as yellow crystals with 67% yield. R_f ~ 0.62 (hexanes: EtOAc = 1 : 1); ^{1}H NMR (500 MHz, $CDCl_3$) δ 8.37 (s, 1H), 8.22 (d, J = 8.1 Hz, 2H), 7.92 (d, J = 7.7 Hz, 2H), 7.86 – 7.80 (m, 4H), 7.29 – 7.26 (m, 2H), 6.63 (d, J = 8.1 Hz, 2H), 4.39 (s, 2H), 3.79 – 3.74 (m, 2H), 3.65 (bs, 2H, -NH_2), 1.58 (s, 4H), 1.30 – 1.20 (m, 8H), 0.85 (t, J = 7.0 Hz, 3H); ^{13}C NMR ($CDCl_3$, 125 MHz) δ

165.2, 163.0, 162.2, 149.2, 147.3, 146.7, 133.3 (m), 131.1, 130.2, 129.8, 129.1, 126.1 (m), 124.4, 123.9, 122.0, 119.1, 115.3, 111.2, 109.4,47.6, 42.1, 348, 31.6, 31.4, 30.2, 29.6,29.4, 28.9, 26.6, 22.5, 14.0; HRMS (ESI) calcd for $C_{36}H_{35}N_4O_3F_6$ ($[M+H]^+$): 685.2613; found: 685.2609.

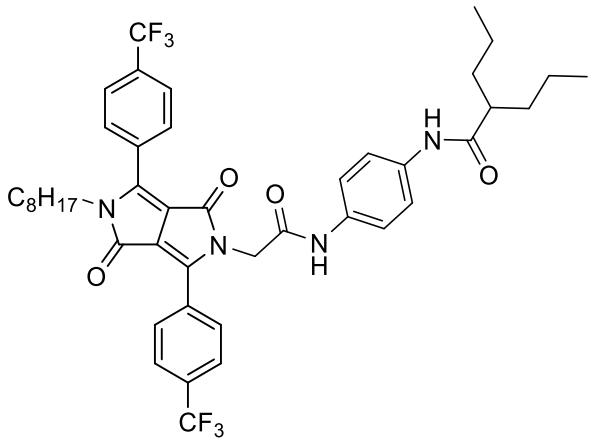

***N*-(4-(2-(5-Octyl-1,4-dioxo-3,6-bis(4-(trifluoromethyl)phenyl)-4,5-dihydropyrrolo[3,4-*c*]pyrrol-2(1*H*)-yl)acetamido)phenyl)-2-propylpentanamide (DPP-m-Ph).** 2,2-Di-*n*-propylacetyl chloride (49 mg, 0.30 mmol) was added to a solution of **DPP-m-Ph-NH$_2$** (102 mg, 0.15 mmol) in dry DCM (10 mL) containing dry pyridine (24 μL, 0.30 mmol) at -78 °C. The dry ice was removed and the reaction mixture was allowed to warm to room temperature. After stirring for a further 1 h, TLC indicated the reaction was complete. DCM (50 mL) was added to the mixture which was then washed with 1 N HCl (5 mL), saturated aqueous $NaHCO_3$ (100 mL), and brine (50 mL). The organic layer was dried over $MgSO_4$, concentrated under reduced pressure and purification by flash chromatography (SiO_2, EtOAc : Hexane = 1:10) afforded **S5** red solid with 89% yield. R_f ~ 0.60 (hexanes : EtOAc = 5 : 1); m.p.: decomposition > 265 °C; ^{1}H NMR (600 MHz, DMSO) δ 10.22 (s, 1H), 9.78 (s, 1H), 8.06 (d, *J* = 8.2 Hz, 4H), 8.00 – 7.94 (m, 4H), 7.51

(d, J = 9.0 Hz, 2H), 7.39 (d, J = 9.0 Hz, 2H), 4.52 (s, 2H), 3.74 (t, J = 7.3 Hz, 2H), 2.37 – 2.33 (m, 1H), 1.56 – 1.49 (m, 2H), 1.44 – 1.38 (m, 2H), 1.35 – 1.24 (m, 6H), 1.21 – 1.16 (m, 2H), 1.14 – 1.07 (m, 8H), 0.86 (t, J = 7.3 Hz, 6H), 0.81 (t, J = 7.3 Hz, 3H); ^{13}C NMR (125 MHz, $CDCl_3$ +TFA-d) δ 178.2, 167.1, 163.4, 163.2, 151.9, 148.3, 134.3 (m), 134.0 (m), 133.7, 133.2, 130.2, 129.5, 129.4, 129.0, 126.6 (m), 126.5 (m), 124.3, 122.6, 122.2, 122.0, 117.6, 115.4, 113.1, 111.4, 110.8, 109.0, 48.6, 46.4, 42.5, 35.0, 31.6, 29.2, 29.0, 28.8, 26.5, 22.5, 20.7, 13.9, 13.8; HRMS calcd for $C_{44}H_{49}F_6N_4O_4$ ($[M+H]^+$): 811.3653; found: 811.3647.

Methods

Steady-state UV/visible absorption and emission spectroscopy

Steady-state absorption spectra are recorded in a transmission mode using a JASCO V-670 spectrophotometer (Tokyo, Japan); and steady-state fluorescence spectra are measured, also in a transmission mode, with a FluoroLog-3 spectrofluorometer (Horiba-Jobin-Yvon, Edison, NJ, USA) equipped with double-grating excitation and emission monochromators. The experiments are conducted at room temperature using 1-cm quartz cuvette and all samples are purged with argon for 5 to 10 min per 1 mL of sample. The zero-to-zero energy for each sample is estimated from the wavelength where the normalized absorption and fluorescence spectra cross.

The fluorescence quantum yields, ϕ_f, are determined by comparing the integrated emission intensities of the samples with the integrated fluorescence of a reference sample with a known fluorescence quantum yield, $\phi_f^{(0)}$:

$$\phi_f = \phi_f^{(0)} \frac{\int F(\lambda) d\lambda}{\int F^{(0)}(\lambda) d\lambda} \frac{\left(1-10^{-A^{(0)}(\lambda_{ex})}\right)}{\left(1-10^{-A(\lambda_{ex})}\right)} \left(\frac{n}{n^{(0)}}\right)^2 \quad (7S\text{-}1)$$

where $F(\lambda)$ is the fluorescence intensity at wavelength λ; $A(\lambda_{ex})$ is the absorbance at the excitation wavelength; n is the refractive index of the media; and the superscript "(0)" indicates the quantities for the reference sample. For DPP samples we use aqueous solutions of fluorescein (pH = 12) for reference, $\phi_f^{(0)} = 0.93$.[8]

Electrochemistry

Cyclic voltammetry is conducted using Reference 600 Potentiostat/Galvanostat/ZRA (Gamry Instruments, PA, U.S.A.), connected to a three-electrode cell, at scan rates of 20 to 500 mV s^{-1}, as previously described.[7] Anhydrous solvents are employed for the sample preparation, with different concentrations of tetrabutylammonium hexafluorophosphate (NBu_4PF_6) as supporting electrolyte. Prior to recording the voltammograms, the samples are extensively purged with argon while maintaining constant volume by adding more of the anhydrous solvent. For each sample and each solvent, a set of voltammograms is recorded where the electrolyte concentration is increased from 25 mM to 200 mM in steps of 25 mM. The half-wave potentials, $E^{(1/2)}$, are determined from the midpoints between the anodic and cathodic peak potentials for reversible or quasireversible oxidation and from the inflection points of the anodic waves for irreversible oxidation or the cathodic waves for irreversible reduction. The anodic and cathodic peak potentials are determined from the zero points of the first derivatives of the voltammograms, that is, the potentials where $\partial I/\partial E = 0$ at $\partial E/\partial t$ = constant. The inflection points are determined from the zero point of the second derivatives of the voltammograms,

$\partial^2 I/\partial E^2 = 0$ at $\partial E/\partial t$ = constant. To correct for potential drifts in the reference electrode (which is SCE, connected with the cell via a salt bridge), ferrocene was used as a standard ($E^{(1/2)} = 0.45 \pm 0.01$ V vs. SCE for MeCN, 100 mM NBu_4BF_4).[9] Voltammograms of the standard are recorded before and after each set of measurements. From the dependence of $E^{(1/2)}$ on the electrolyte concentration, the potential for each neat solvents are estimated from extrapolation to zero electrolyte concentration (Figure 7-2b).[9-11]

Employing the Rehm-Weller equation (eq. 7-1), we estimate the driving force for the photoinduced charge separation, $\Delta G_{CS}^{(0)}$. For each donor-acceptor conjugate, we use the zero-to-zero energy as determined from the measured absorption and fluorescence spectra of the dyad when selectively exciting the acceptor, DPP. In the case of **DPP-Ph**, for the acceptor we use the reduction potential of reduction of **DPP-Ph**; and for the donor – the reduction potential of oxidation of **DPP-Ph**. Similarly, in the case of **DPP-m-Ph**, we use the potentials of reduction and oxidation of **DPP-m-Ph**, similar to the other dyad. For MeCN and DCM, both dyads show reversible reduction for all electrolyte concentrations, i.e., 25 – 200 mM. Only **DPP-Ph**, however, showed reversible oxidation for the same two solvents; the electrochemical oxidation of **DPP-m-Ph** for MeCN and DCM was chemically irreversible. Most data were recorded at scan rate of 50 mV s^{-1}.

Time-resolved emission spectroscopy

Time-correlated single photon counting (TCSPC) measurements are conducted with a FluoroLog-3 spectrofluorometer equipped with a NanoLED laser source (λ_{ex} = 406 nm; FWHM = 195 ps), and a TBX detector run in a single-photon-counting mode. Placing selected reflection neutral-density filters in front of the laser controls the intensity of the

excitation light. All samples are purged with argon for 5 to 10 min per 1 mL of sample. **DPP** manifests monoexponential decays with lifetimes of about 8 ns that is practically solvent independent (Figure 7S-1).

Transient absorption spectroscopy

The transient-absorption (TA) data, $\Delta A(\lambda, t)$, are recorded in transmission mode with 2-mm quartz cuvettes using a Helios pump-probe spectrometer (Ultrafast Systems, LLC, Florida, USA) equipped with a delay stage allowing maximum probe delays of 3.2 ns at 7 fs temporal step resolution. Following chirp correction, we extract the TA spectra and decays from $\Delta A(\lambda, t)$ (Figure S2 and S3). Immediately prior the measurements, all samples are purged with argon for 5 to 10 min per 1 mL of sample. The laser source for the Helios is a SpitFire Pro 35F regenerative amplifier yielding (Spectra Physics, Newport, CA, USA) generating 800-nm pulses (>35 fs, 4.0 mJ, at 1 kHz). The amplifier is pumped with an Empower 30 Q-switched laser ran at 20 W. A MaiTai SP oscillator provided the seed beam (55 nm bandwidth). The wavelength of the pump is tuned using an optical parametric amplifier, OPA-800CU (Newport Corporation, Newport, CA, USA), equipped with reflectors for removing the 800-nm fundamental and the signal; and the idler is subjected to a second and a forth harmonic generator. For optimal OPA performance, the pulse duration from the amplifier is tuned to 50 fs. The idler is tuned in the range between 1,840 and 1,940 nm for selective excitation of DPP chromophore after upconversion to fourth harmonic. The power of the signal and the idler removing the removal of the fundamental is stabilized at about 170 mW.

Kinetic analysis

For **DPP-Ph**, using multi-exponential global fits allows for quantifying the kinetics of the TA dynamics:

$$\Delta A(\lambda,t) = \sum_{i=1}^{n} \alpha_{\lambda,i} \exp(-k_i t) \quad \text{(7S-2)}$$

where the kinetic curve at each wavelength, λ, is fit to a sum of n exponential terms. The n rate constants, k_i. are identical for the curves recorded at the different wavelengths. For this study we employ five protic and five aprotic solvents with different viscosity and polarity: i.e., ethylene glycol (EG), methanol (MeOH), ethanol (EtOH), 1-butanol (BuOH), 1-octanol (OctOH), dimethyl sulfoxide (DMSO), acetonitrile (MeCN), dichloromethane (DCM), tetrahydrofuran (THF), and chloroform ($CHCl_3$). For each solvent, the global fits are performed on four wavelengths: 500 nm for the ground-state bleach (B), 550 nm for the stimulated emission (SE), 640 nm for the charge-transfer (CT) state, and 770 nm for the locally excited (LE) state, i.e., ^{1}DPP*-Ph (Figure 7S-4). Indeed, the absorbance of the different transients overlap: e.g., LE state has absorption at 640 nm, and the CT state absorbs weakly at 550 and 770 nm.

For all solvents, except EG, a biexponetnial rise and a monoexponential decay provide excellent fits for the CT transient absorption (Table 7S-1). A monoexponential rise and a biexponential decay fit the CT kinetics for EG (Table 7S-1). The biexponential fits of the CT rises produce principal components that are in the picosecond to tens-of-picosecond time domain. The minor rise components, which are in the subpicosecond and picosecond times, do not significantly affect the average rate constants, $\overline{k^{(r)}}$, of the growth of the CT

state, i.e., $\overline{k^{(r)}} \approx k_1^{(r)}$ (Table S1). We ascribe them to the rate constants of CS, i.e., $k_{CS} \approx \overline{k^{(r)}}$, and for EG, $k_{CS} \approx k^{(r)}$ (Table S1). Similarly, the CT decay kinetics provides a means for evaluating the CR rate constants, i.e., $k_{CS} \approx k^{(d)}$, and for EG, $k_{CR} \approx \overline{k^{(d)}}$ (Table 7S-1).

Increasing the number of wavelengths for the global-fit analysis does not affect significantly the resultant values for the CT rise and decay rate constants. In fact, kinetic analysis at a single-wavelength (at 640 nm) allows for good fits with functions comprising solely a mono-exponential rise and a mono-exponential decay term (Figure 7S-5). The values for the CS and CR rate constants, as well as for k_{CS}/k_{CR}, obtained from the single-wavelength analysis are quite similar to those obtained from the global fits (Figure S6). Furthermore, the dependence of k_{CS}, k_{CR}, and k_{CS}/k_{CR} on media polarity and viscosity follows exactly the same trends regardless if the rate constants are obtained from single-wavelength or global analysis of the TA kinetics (Figure 7S-7). The Onsager function, f_O, allows for quantifying solvent polarity from the static relative dielectric constant, $f_O(\varepsilon) = 2(\varepsilon - 1) / (2\varepsilon + 1)$. Using the logarithmic values of ε instead of $f_O(\varepsilon)$, however, provides similar trends about the dependence of the rate constants on the media polarity (Figure 7S-7). Indeed, while single-wavelength analysis of the TA kinetics offers incomparable simplicity, the global analysis provides completeness for the quantification of presented observations.

Figures
^{1}H and ^{13}C NMR spectra of the new compounds and the key intermediates

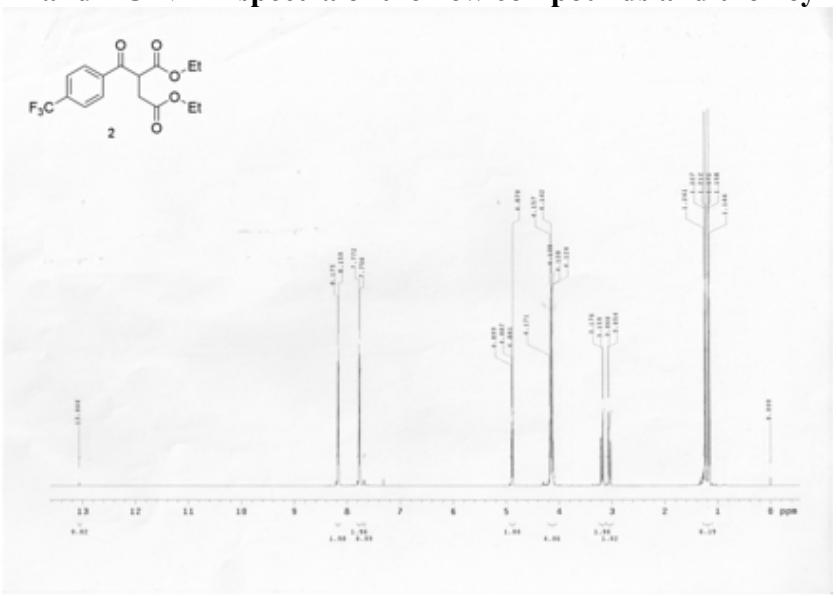

a

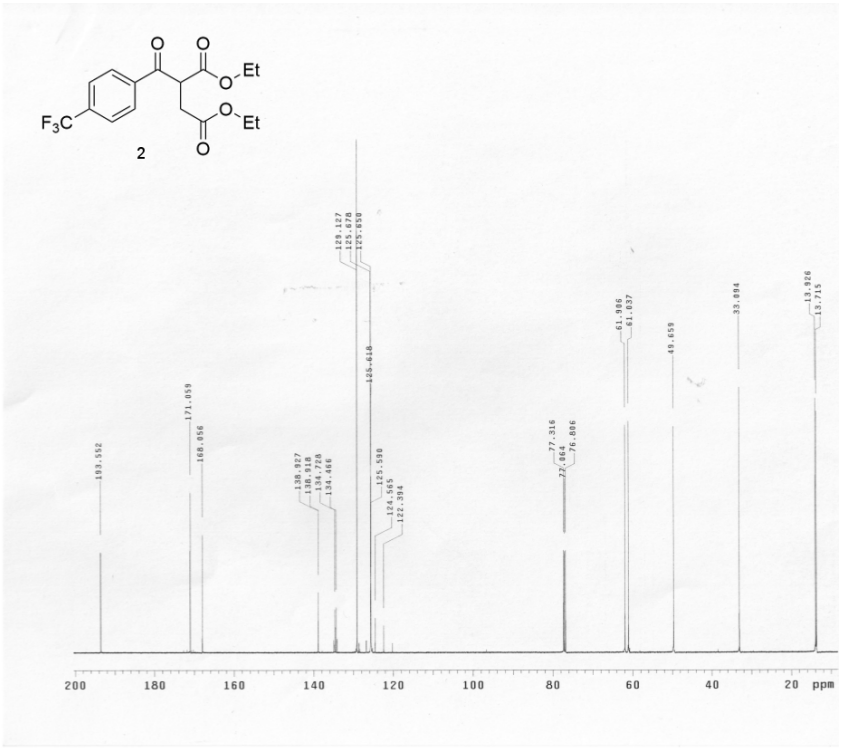

b

Figure 7S-1. (a)[1] HNMR of **2** (500 MHz, $CDCl_3$); (b) ^{13}C NMR of **2** (125 MHz, $CDCl_3$).

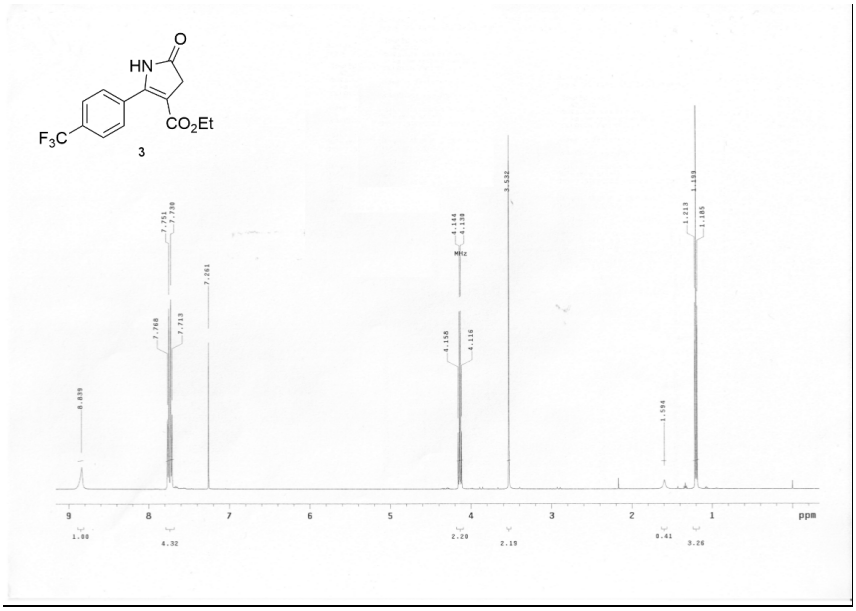

a

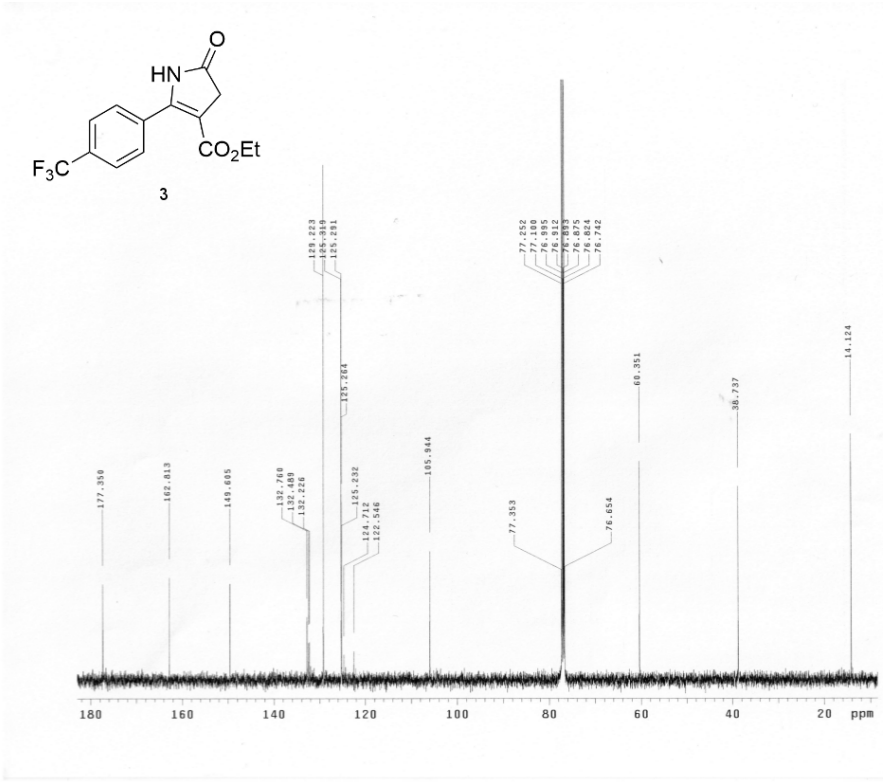

b

Figure 7S-2. (a)[1] HNMR of **3** (500 MHz, $CDCl_3$); (b) ^{13}C NMR of **3** (125 MHz, $CDCl_3$).

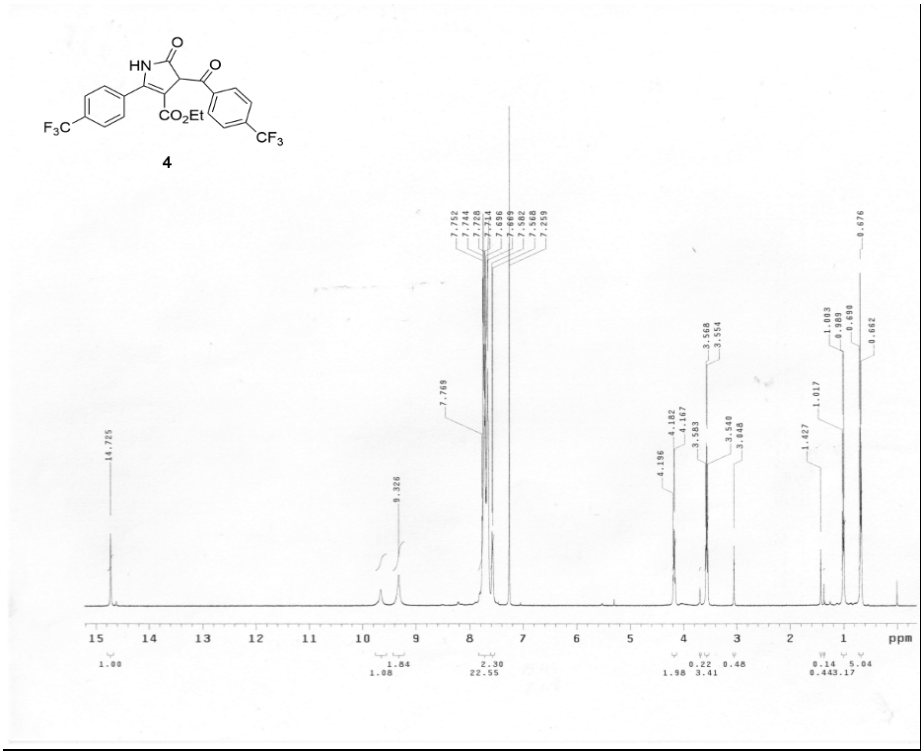

a

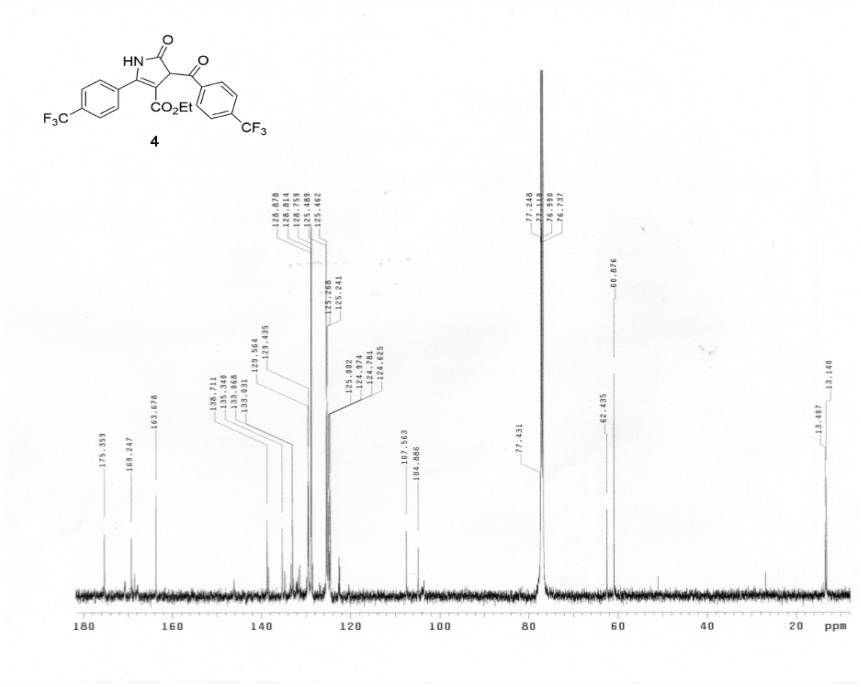

b

Figure 7S-3. (a)[1] HNMR of **4** (500 MHz, $CDCl_3$); (b) ^{13}C NMR of **4** (125 MHz, $CDCl_3$).

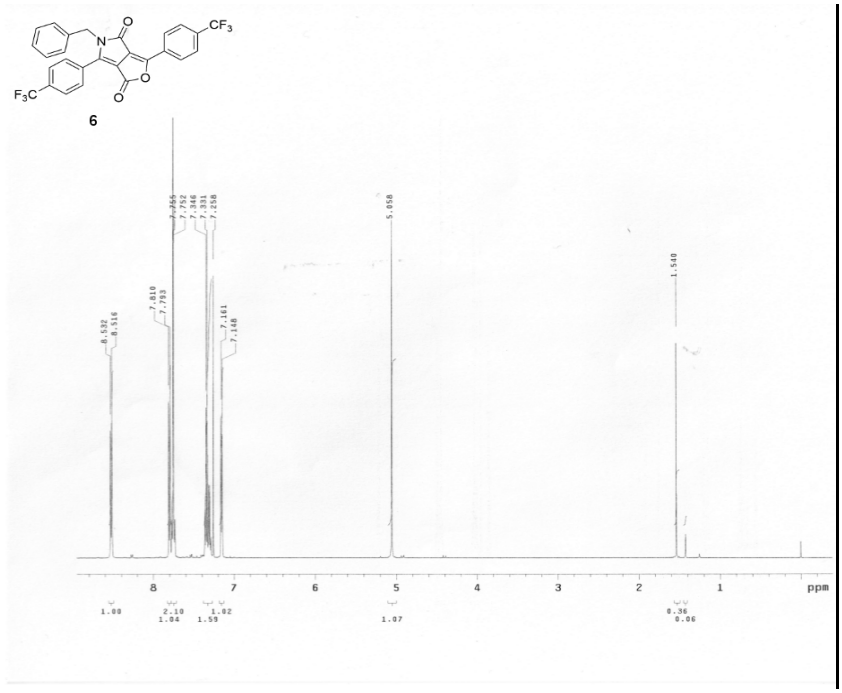

a

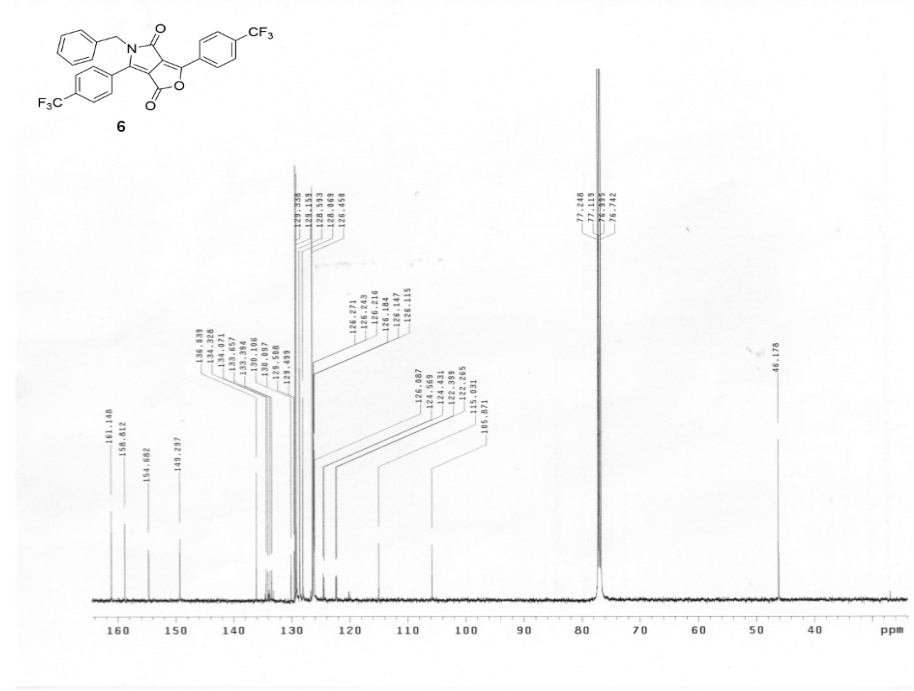

b

Figure 7S-4. (a)[1] HNMR of **6** (500 MHz, $CDCl_3$); (b) ^{13}C NMR of **6** (125 MHz, $CDCl_3$).

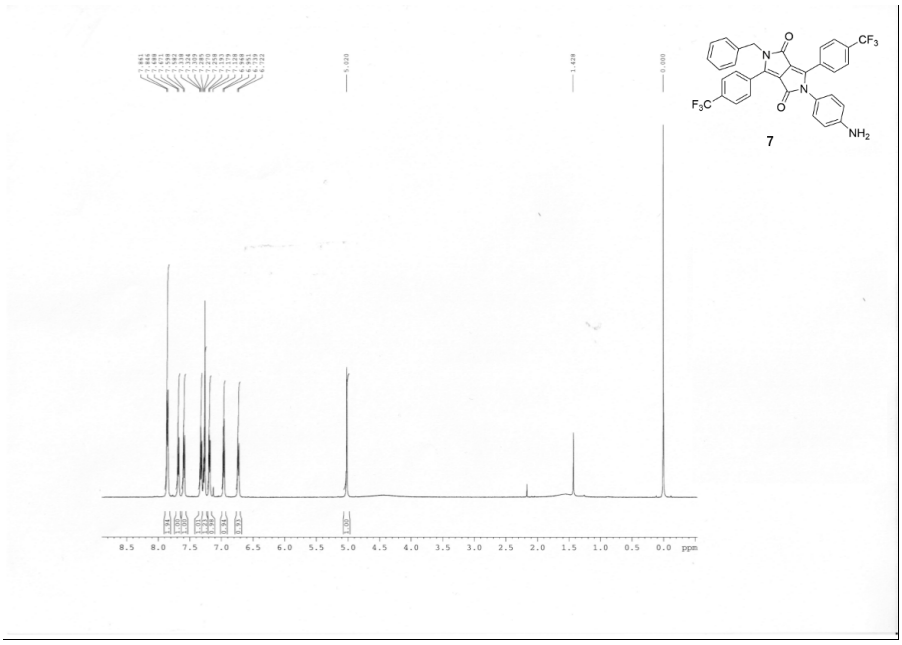

a

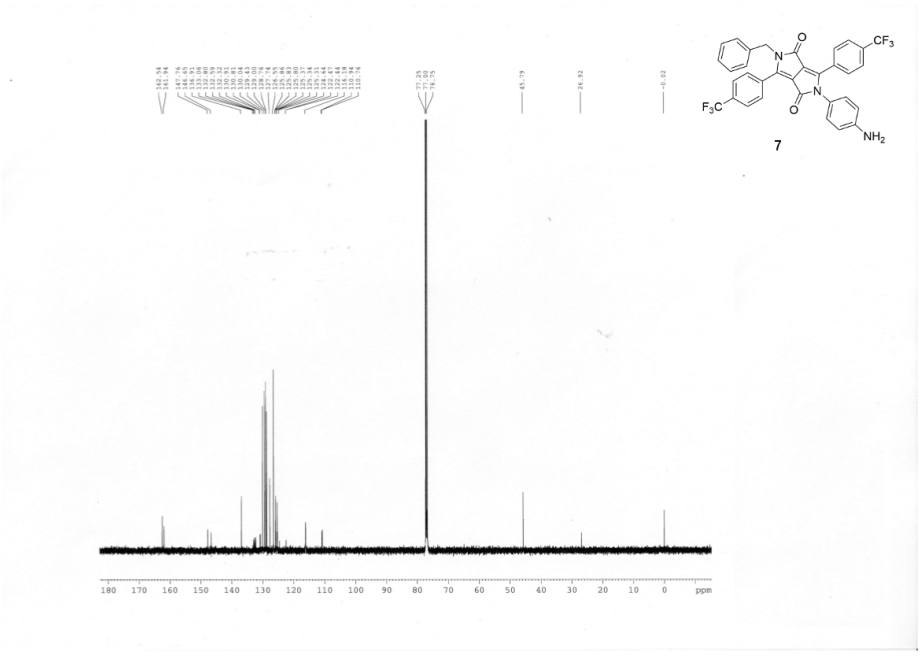

b

Figure 7S-5. (a)[1] HNMR of **7** (500 MHz, $CDCl_3$); (b) ^{13}C NMR of **7** (125 MHz, $CDCl_3$)

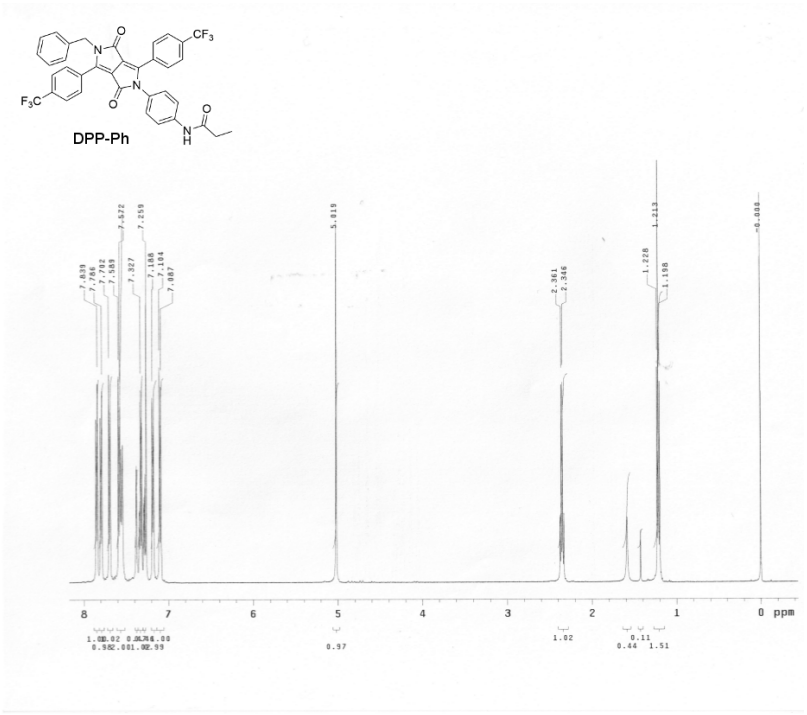

a

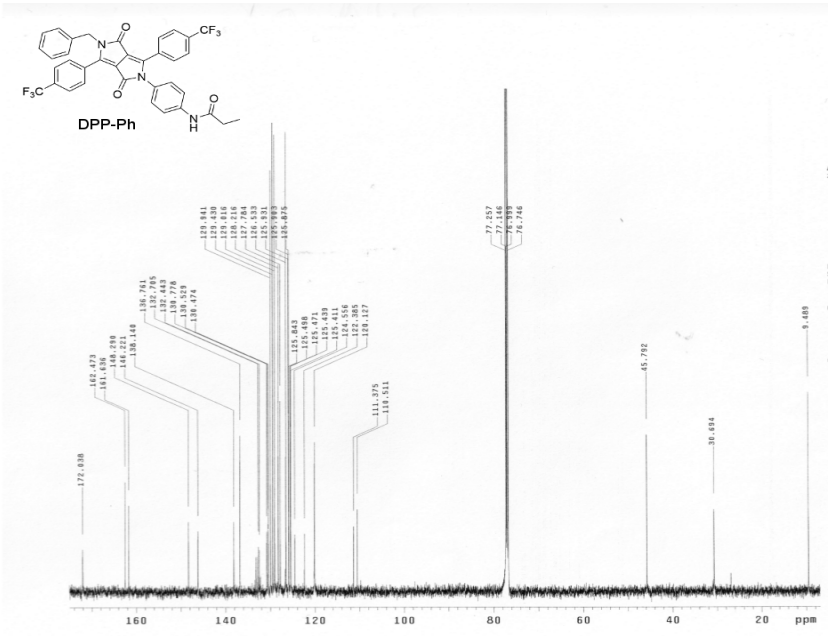

b

Figure 7S-6. (a)[1] HNMR of **Dpp-Ph** (500 MHz, $CDCl_3$); (b) ^{13}C NMR of **Dpp-Ph** (125 MHz, $CDCl_3$).

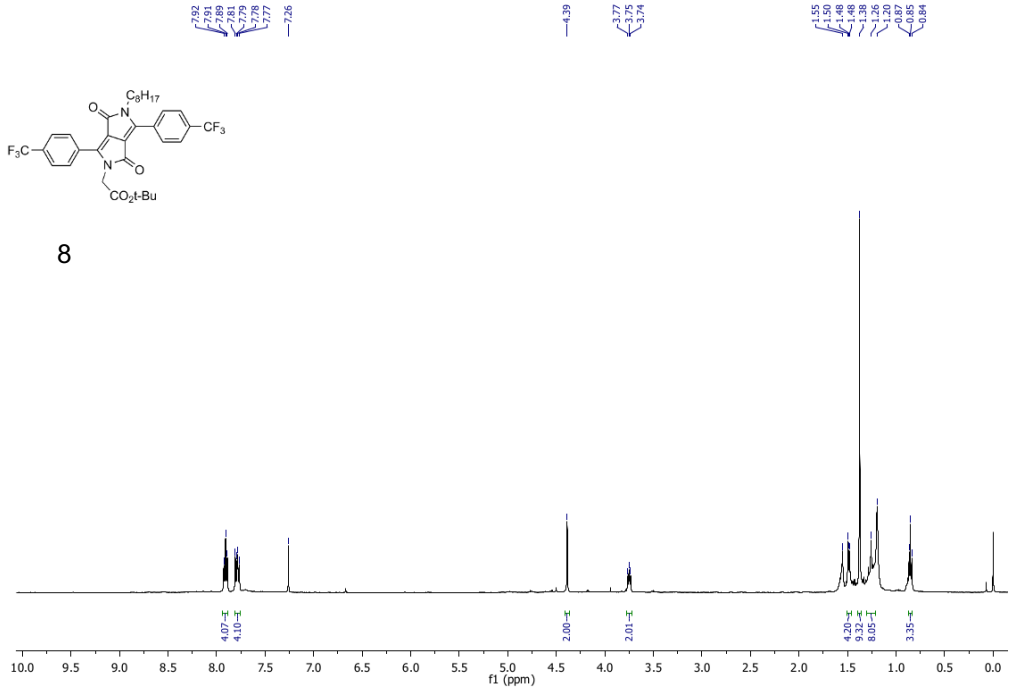

a

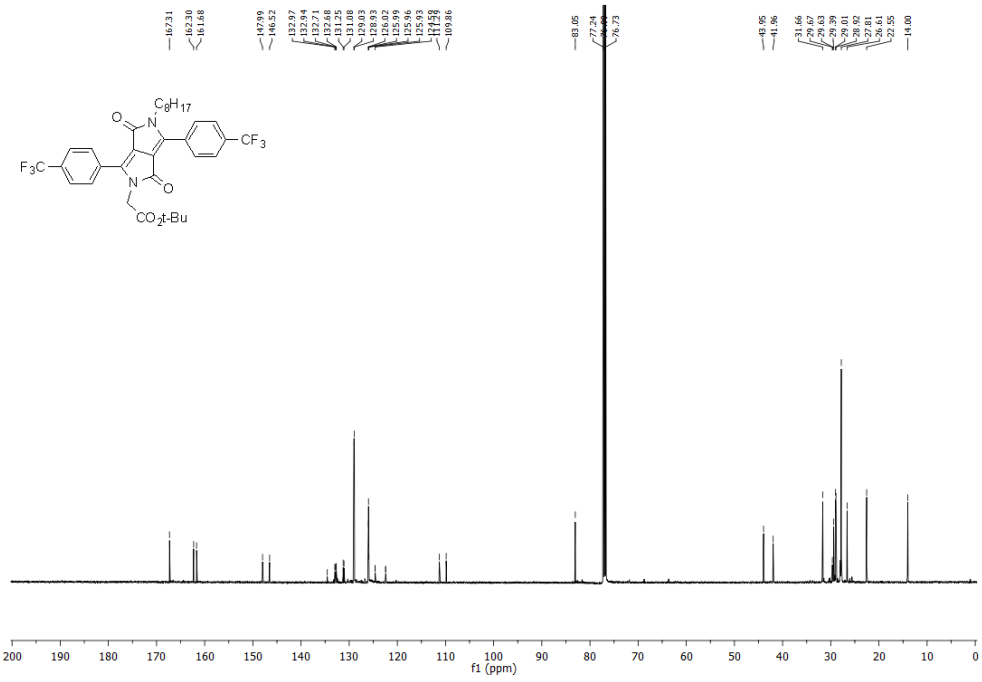

b

Figure 7S-7. (a)[1] HNMR of **8** (500 MHz, $CDCl_3$); (b) ^{13}C NMR of **8** (125 MHz, $CDCl_3$).

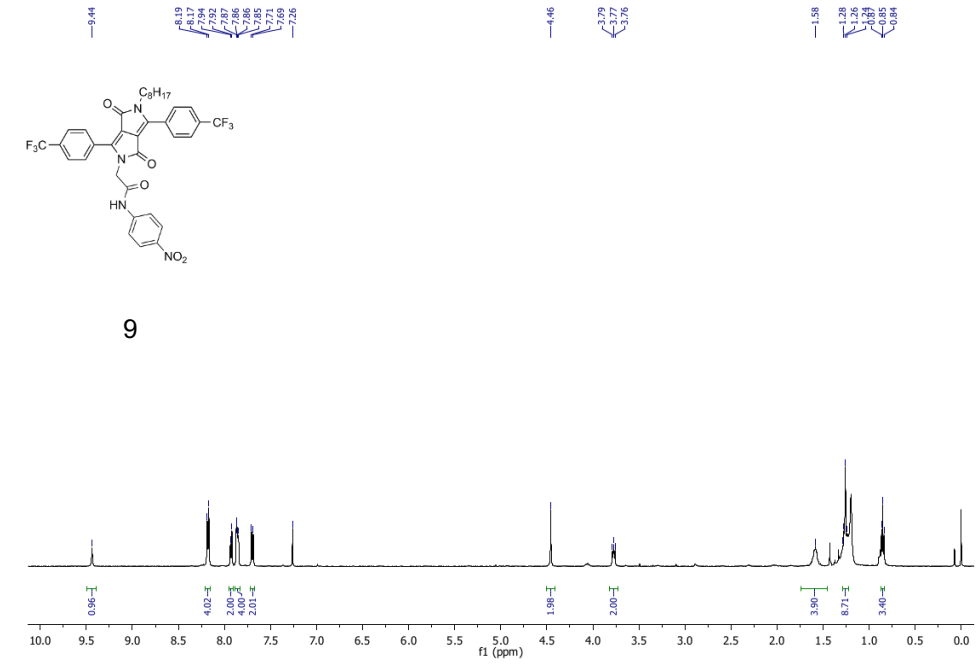

a

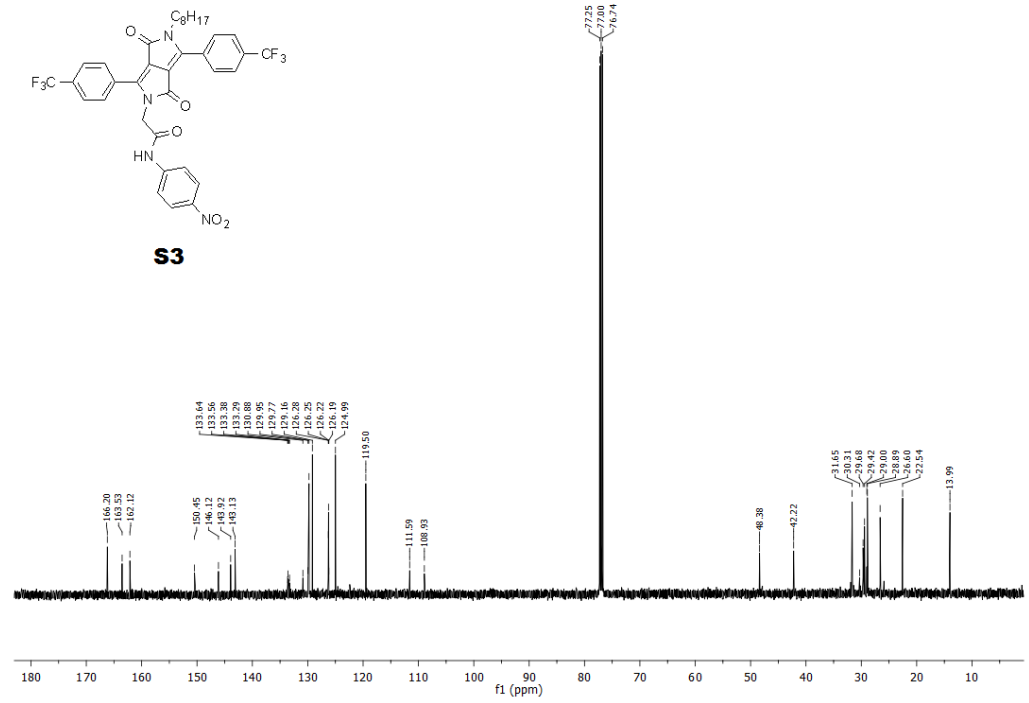

b

Figure 7S-8. (a)[1] HNMR of **9** (500 MHz, $CDCl_3$); (b) ^{13}C NMR of **9** (125 MHz, $CDCl_3$).

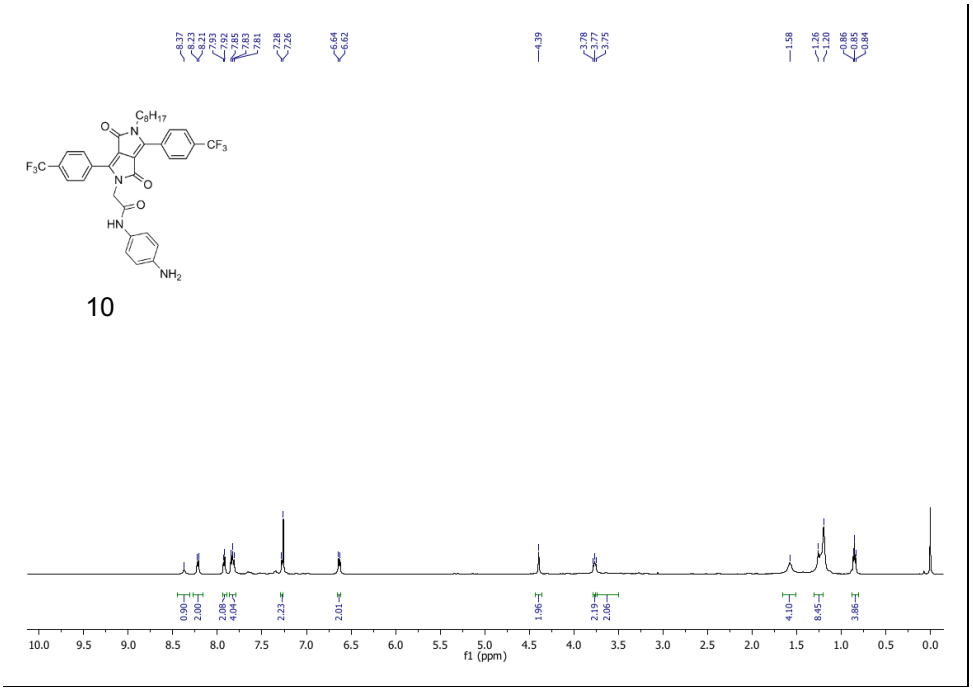

a

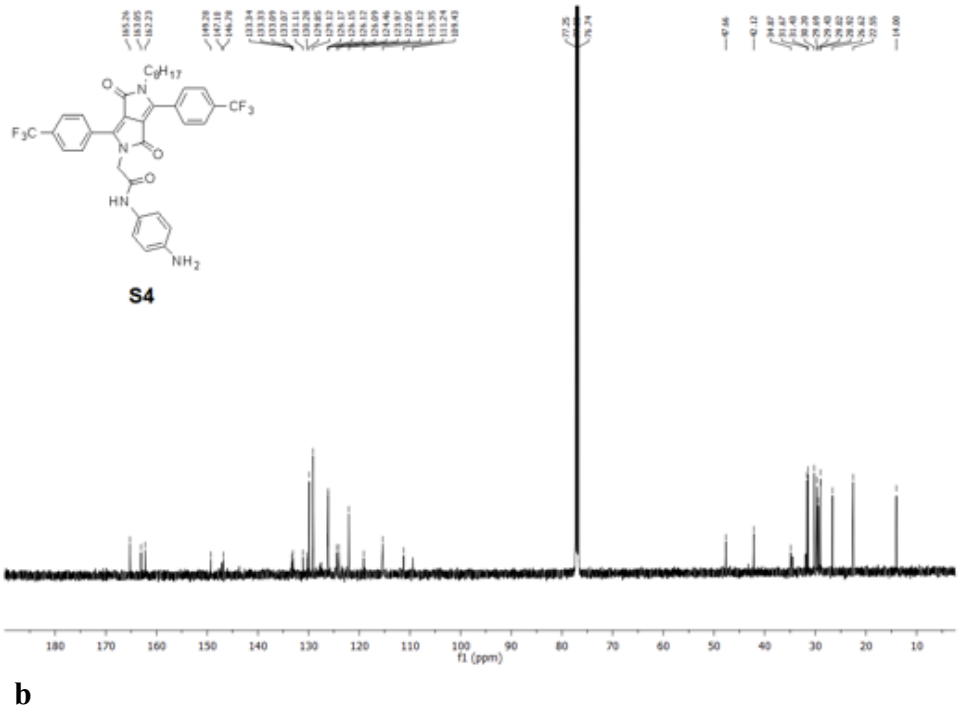

b

Figure 7S-9. (a)[1] HNMR of **10** (500 MHz, $CDCl_3$); (b) ^{13}C NMR of **10** (125 MHz, $CDCl_3$).

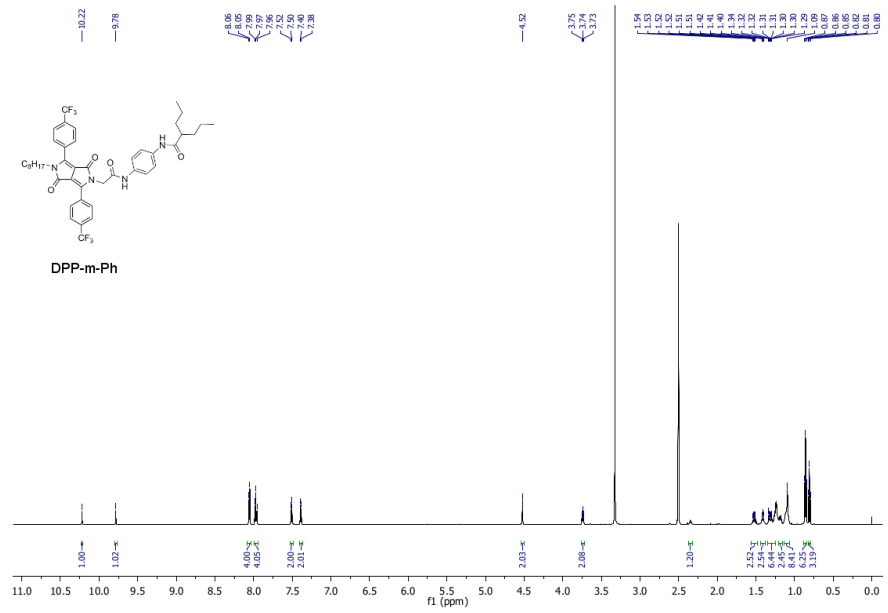

a

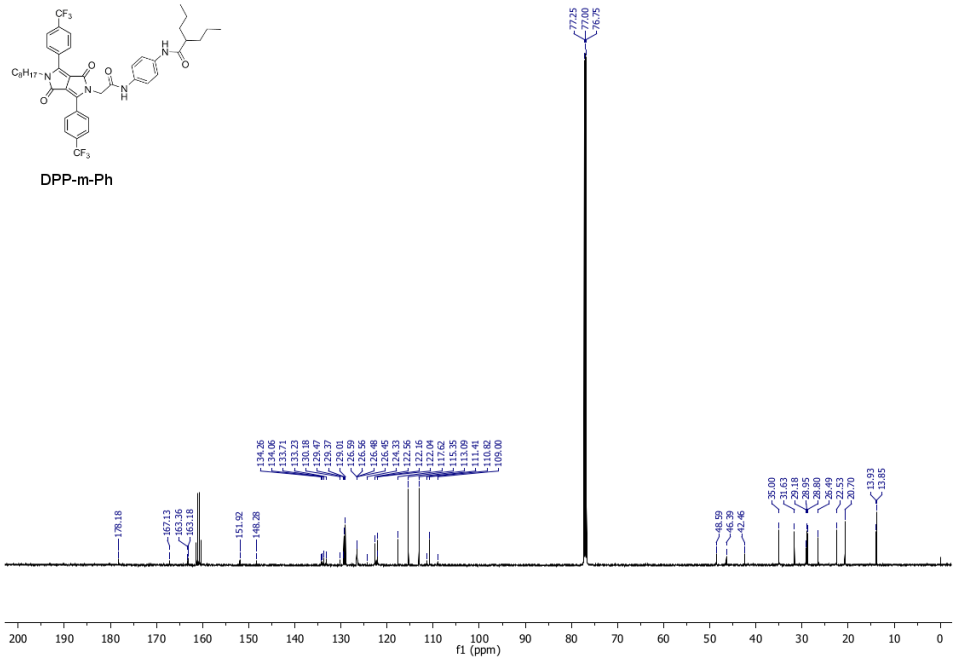

b

Figure 7S-10. (a)[1] HNMR of **Dpp-m-Ph** (500 MHz, $CDCl_3$); (b) ^{13}C NMR of **Dpp-m-Ph** (125 MHz, $CDCl_3$).

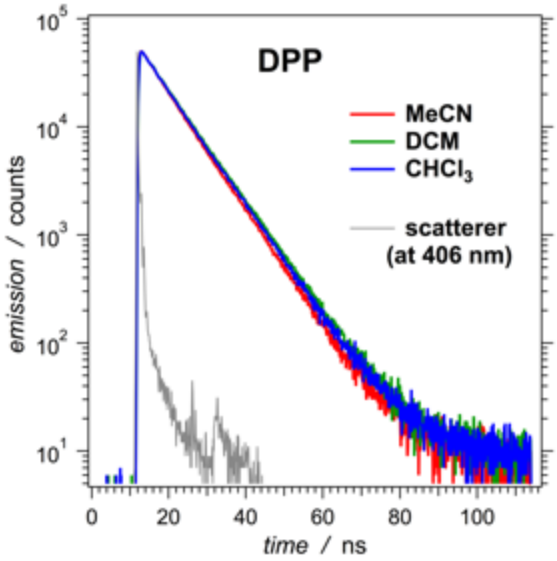

Figure 7S-11. Emission decays of DPP, recorded using TCSPC, for different solvents (λ_{ex} = 406 nm; λ_{em} = 540 nm).

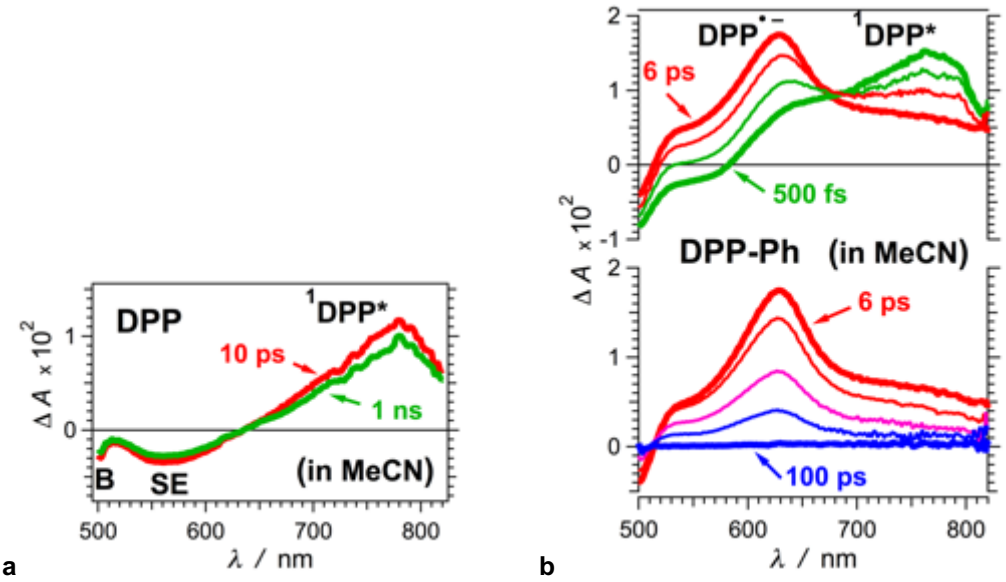

Figure 7S-12. Transient-absorption spectra of (a) **DPP** and, (b) **DPP-Ph** for MeCN (λ_{ex} = 480 nm, introduced by 4-μJ 50-fs pulses).

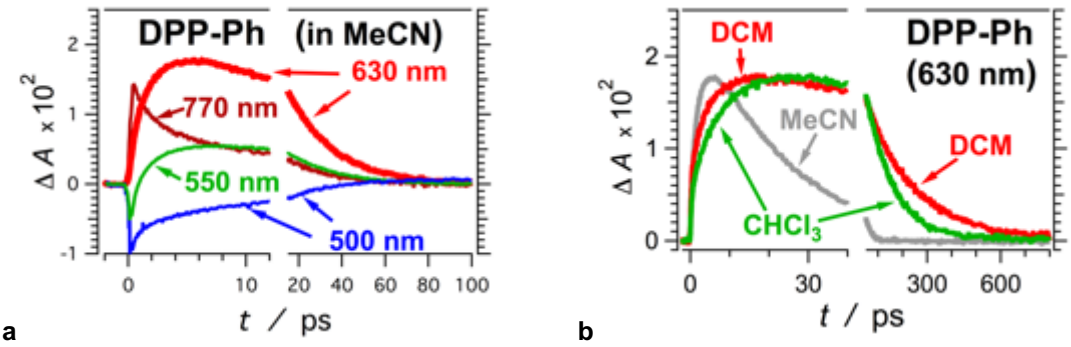

Figure 7S-13. Transient-absorption decays of **DPP-Ph** (a) for MeCN measured at different wavelengths; and (b) measured at 630 nm (monitoring $DPP^{\bullet-}$) for different solvents (λ_{ex} = 480 nm, introduced by 4-μJ 50-fs pulses).

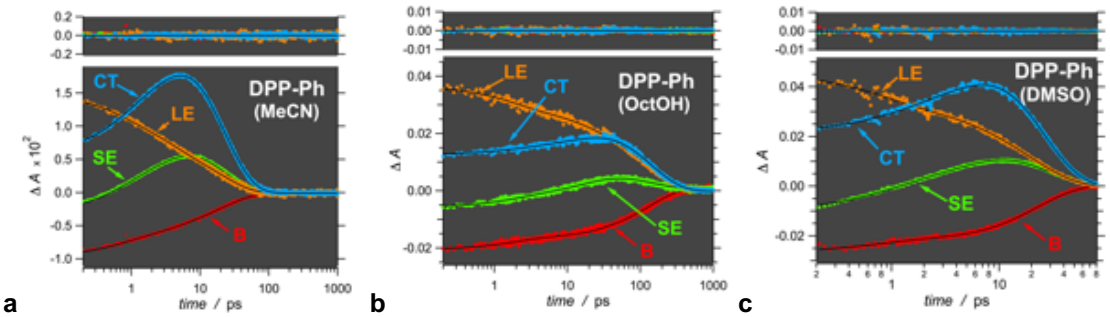

Figure 7S-14. Global fits (eq. S2) using three exponential terms for four wavelengths: 770 nm (LE), 640 nm (CT), 550 nm (SE) and 500 nm (B). The data points are colored differently for the different wavelengths as labeled. The solid black lines represent the fitting functions obtained from the least-squares regression analysis for each solvent. The upper section of each graph shows the residuals from the global fits.

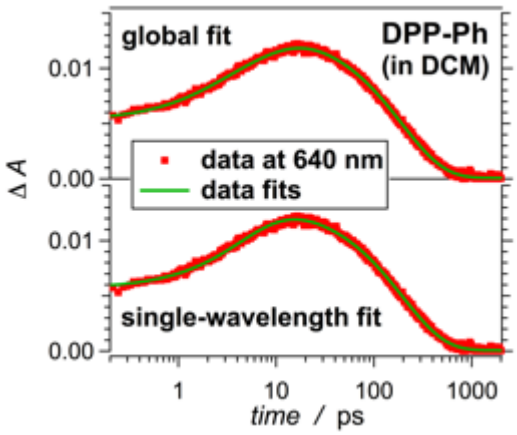

Figure 7S-15. Comparison between global fit and single-wavelength fit analysis at 640 nm for **DPP-Ph** in DCM.

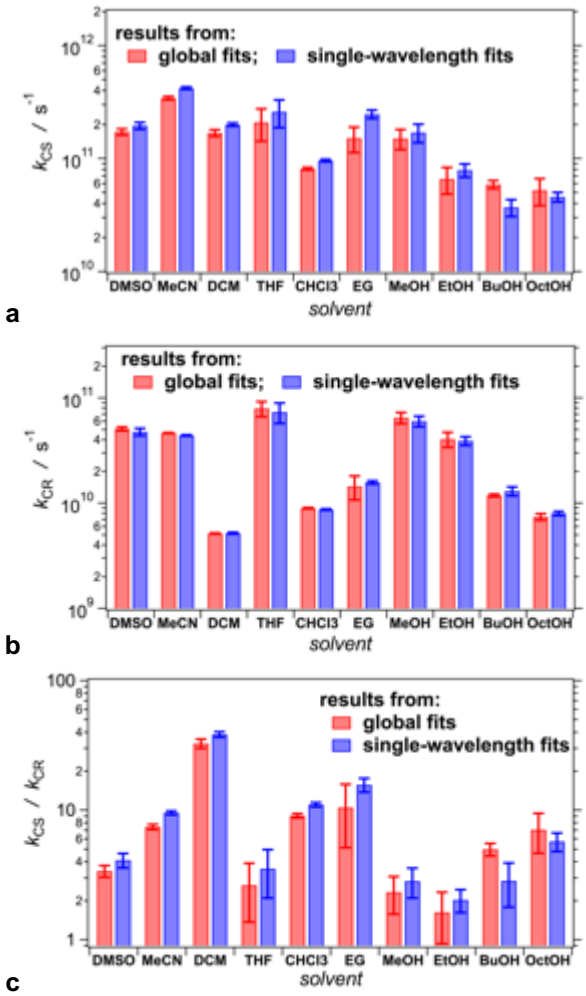

Figure 7S-16. Comparison between the values of the rate constants of CS and CR for **DPP-Ph** in different solvents, as well as of the ratio between the rate constants, obtained from global fits ($\overline{k^{(r)}}$ and $k^{(r)}$ for k_{CS}; and $\overline{k^{(d)}}$, and $k^{(d)}$ for k_{CR}), and from single-wavelength analysis (mono-exponential rise for k_{CS} and mono-exponential decay for k_{CR}).

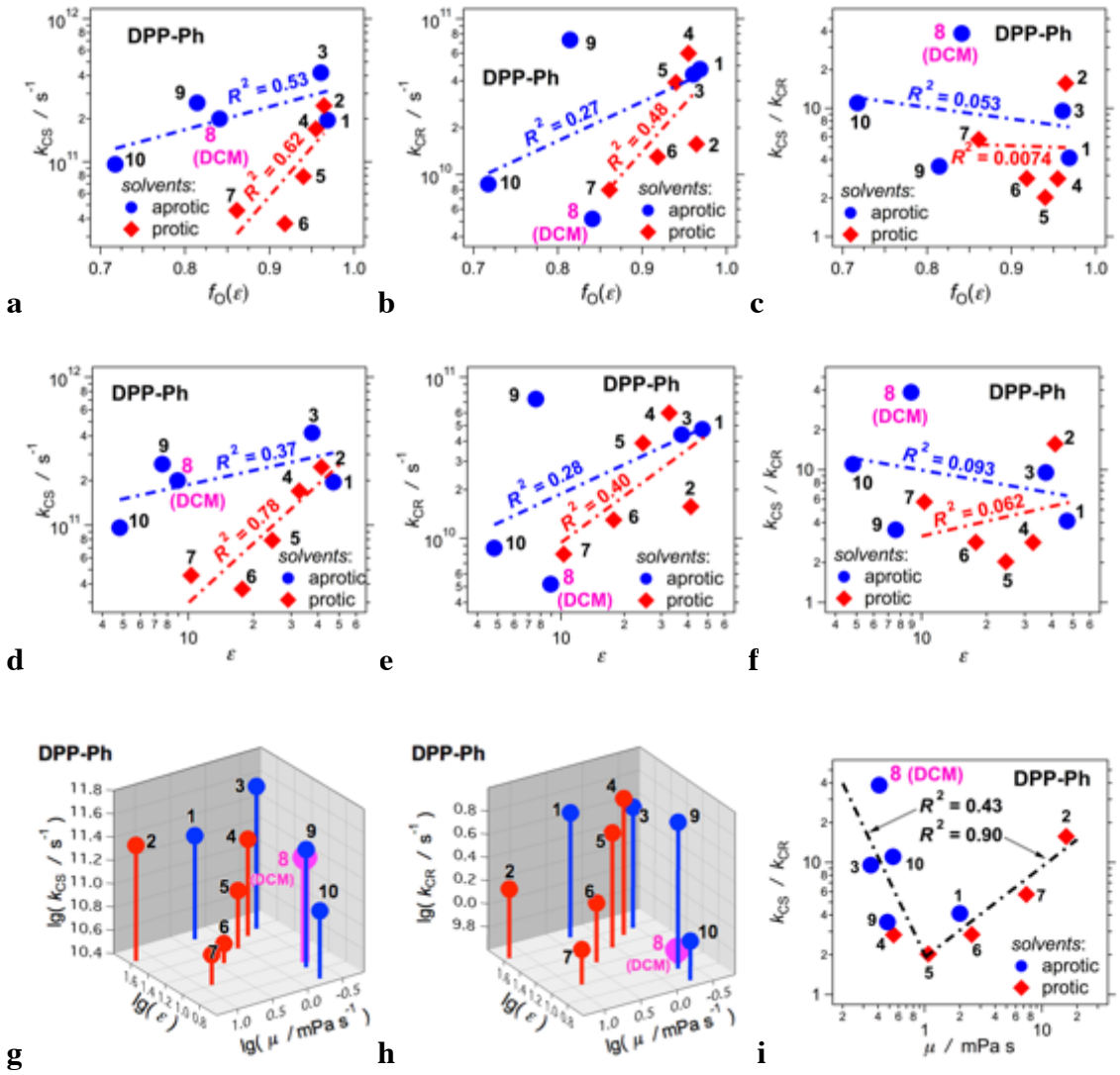

Figure 7S-17. Solvent dependence of the rate constants of the photoinduced intramolecular charge separation, k_{CS}, and charge recombination, k_{CR}, of **DPP-Ph**, obtained from single-wavelength data fits at 640 nm. (Solvents: 1 = DMSO, 2 = EG, 3 = MeCN, 4 = MeOH, 5 = EtOH, 6 = *n*-BuOH, 7 = OctOH, 8 = DCM, 9 = THF, and 10 = $CHCl_3$). (a-c) Dependence of k_{CS}, k_{CR} and the ratio, k_{CS}/k_{CR}, on the media polarity, represented by the Onsager function for solvent polarity, $f_O(\varepsilon)$, with separate correlation analyses for protic (2, 4, 5, 6, 7) and aprotic (1, 3, 8, 9, 10) solvents. (d-f) Dependence of k_{CS}, k_{CR} and the ratio, k_{CS}/k_{CR}, on the media polarity, represented by the solvent static relative dielectric constant, ε, with correlation analyses for protic (2, 4, 5, 6, 7) and aprotic (1, 3, 8, 9, 10) solvents. The correlation analyses using $f_O(\varepsilon)$ and lg(ε) as a representation of solvent polarity yield pretty much the same results. (g,h) Dependence of k_{CS} and k_{CR} on the solvent polarity and dynamic viscosity, μ. (i) Dependence of the ratio between the rate constants, k_{CS}/k_{CR}, on the solvent dynamic viscosity. The two sets of correlation analyses encompass the results for (1) EtOH and all solvents with $\mu < 1$ mPa s^{-1}, and (2) EtOH and the other solvents with $\mu > 1$ mPa s^{-1}.

Tables

Table 7S-1. Rate constants of rise and decay of the **DPP-Ph** transient absorbing at 640 nm, obtained from global fits.[a]

solvent	Rise at 640 nm		Decay at 640 nm	
	$k_i^{(r)} \times 10^{-10}/\mathrm{s}^{-1}$ ($\alpha_i^{(r)}$) [b]	$\overline{k^{(r)}} \times 10^{-10}/\mathrm{s}^{-1}$ [c]	$k_i^{(d)} \times 10^{-10}/\mathrm{s}^{-1}$ ($\alpha_i^{(d)}$) [b]	$\overline{k^{(d)}} \times 10^{-10}/\mathrm{s}^{-1}$ [c]
DMSO	$k_1^{(r)} = 17.1$; $k_2^{(r)} = 135$ ($\alpha_1^{(r)} = 0.93$; $\alpha_2^{(r)} = 0.07$)	17.2	$k^{(d)} = 5.09$	
EG	$k^{(r)} = 15.1$		$k_1^{(d)} = 9.56$; $k_2^{(d)} = 1.27$ ($\alpha_1^{(d)} = 0.54$; $\alpha_2^{(d)} = 0.46$)	1.44
MeCN	$k_1^{(r)} = 31.7$; $k_2^{(r)} = 164$ ($\alpha_1^{(r)} = 0.69$; $\alpha_2^{(r)} = 0.31$)	34.4	$k^{(d)} = 4.63$	
MeOH	$k_1^{(r)} = 14.9$; $k_2^{(r)} = 104$ ($\alpha_1^{(r)} = 0.92$; $\alpha_2^{(r)} = 0.08$)	15.1	$k^{(d)} = 6.48$	
EtOH	$k_1^{(r)} = 6.57$; $k_2^{(r)} = 84.9$ ($\alpha_1^{(r)} = 0.92$; $\alpha_2^{(r)} = 0.08$)	6.58	$k^{(d)} = 4.05$	
n-BuOH	$k_1^{(r)} = 5.84$; $k_2^{(r)} = 110$ ($\alpha_1^{(r)} = 0.81$; $\alpha_2^{(r)} = 0.19$)	5.91	$k^{(d)} = 1.18$	
OctOH	$k_1^{(r)} = 5.15$; $k_2^{(r)} = 56.3$ ($\alpha_1^{(r)} = 0.85$; $\alpha_2^{(r)} = 0.15$)	5.23	$k^{(d)} = 0.741$	
DCM	$k_1^{(r)} = 15.5$; $k_2^{(r)} = 60.9$ ($\alpha_1^{(r)} = 0.68$; $\alpha_2^{(r)} = 0.32$)	16.9	$k^{(d)} = 0.515$	
THF	$k_1^{(r)} = 20.4$; $k_2^{(r)} = 99.0$ ($\alpha_1^{(r)} = 0.88$; $\alpha_2^{(r)} = 0.12$)	20.9	$k^{(d)} = 7.93$	
$CHCl_3$	$k_1^{(r)} = 8.08$; $k_2^{(r)} = 58.5$ ($\alpha_1^{(r)} = 0.96$; $\alpha_2^{(r)} = 0.04$)	8.12	$k^{(d)} = 0.895$	

[a] The global fits (eq. S2) for 640 nm yield $-\Sigma_i A_i^{(r)} \exp(-k_i^{(r)} t) + \Sigma_i A_i^{(d)} \exp(-k_i^{(r)} t)$, where the negative terms (with $-A_i^{(r)}$ as pre-exponential coefficients) represent rise kinetic components of the fits, and the positive terms (with $A_i^{(d)}$ as pre-exponential coefficients) represent decay components. [b] Components, k_i, of the rate constants and the weighted pre-exponential coefficients, $\alpha_i = A_i / (\Sigma_j A_j)$. For mono-exponential rise or decay fits, a single value is listed for $k^{(r)}$ or $k^{(d)}$, respectively, with no pre-exponential coefficients. Although all rise pre-exponential coefficients, $A_i^{(r)}$, have negative values, the weighted coefficients, $\alpha_i^{(r)}$, are, indeed, positive. [c] Average rate constants, $\bar{k} = (\bar{\tau})^{-1}$ and $\bar{\tau} = (\Sigma_i \alpha_i \tau_i^2) / (\Sigma_i \alpha_i \tau_i)$, where $\tau_i = k_i^{-1}$.[12]

References

(1) Wang, L.; Bi, S.; Wu, S.; Zhang, G.; Wang, F.; Wang, G.; Tian, H.; Wang, Z.; Chen, L.; Huang, Z. (East China University of Science and Technology, Peop. Rep. China; Lily Group Co., Ltd.). "Preparation of pyrrolo[3,4-c]pyrrole-1,4-dione derivatives as fluorescent material" Application: CN, CN 2014-10844017, 104447764, **2015**.

(2) Kaul, B. L. (MCA Technologies GmbH, Switz.). "Solvent-free production and use of pyrrolo[3,4-c]pyrroledione pigments" Application: WO, WO 2003-IB758, 2004076457, **2004**.

(3) Morton, C. J. H.; Gilmour, R.; Smith, D. M.; Lightfoot, P.; Slawin, A. M. Z.; MacLean, E. J. *Tetrahedron* **2002**, *58*, 5547-5565.

(4) Morton, C. J. H.; Riggs, R. L.; Smith, D. M.; Westwood, N. J.; Lightfoot, P.; Slawin, A. M. Z. *Tetrahedron* **2005**, *61*, 727-738.

(5) Riggs, R. L.; Morton, C. J. H.; Slawin, A. M. Z.; Smith, D. M.; Westwood, N. J.; Austen, W. S. D.; Stuart, K. E. *Tetrahedron* **2005**, *61*, 11230-11243.

(6) Lee, H.-Y.; An, M. *Bull. Korean Chem. Soc.* **2004**, *25*, 1717-1719.

(7) Espinoza, E. M.; Larsen, J. M.; Vullev, V. I. *J. Phys. Chem. Lett.* **2016**, *7*, 758-764.

(8) Martin, M. M.; Lindqvist, L. *J. Lumin.* **1975**, *10*, 381-390.

(9) Bao, D.; Millare, B.; Xia, W.; Steyer, B. G.; Gerasimenko, A. A.; Ferreira, A.; Contreras, A.; Vullev, V. I. *J. Phys. Chem. A* **2009**, *113*, 1259-1267.

(10) Bao, D.; Ramu, S.; Contreras, A.; Upadhyayula, S.; Vasquez, J. M.; Beran, G.; Vullev, V. I. *J. Phys. Chem. B* **2010**, *114*, 14467-14479.

(11) Larsen, J. M.; Espinoza, E. M.; Hartman, J. D.; Lin, C.-K.; Wurch, M.; Maheshwari, P.; Kaushal, R. K.; Marsella, M. J.; Beran, G. J. O.; Vullev, V. I. *Pure Appl. Chem.* **2015**, *87*, 779-792.

(12) Lakowicz, J. R. *Principles of Fluorescence Spectroscopy*, 3rd ed.; Springer Science & Business Media, LLC, 2007; pp. 141-143.

Chapter 8

Dipole Effects on Electron Transfer are Enormous

Abstract

Electric dipoles are everywhere, and the importance of understanding how they affect chemical, physical and biological processes cannot be overstated. Electron transfer (ET) is essential for sustaining life and for making energy conversion possible. Molecular dipoles present important, but underutilized, paradigms for guiding ET processes. While dipoles generate fields of Gigavolts per meter in their vicinity, reported differences between rates of ET along vs. against dipoles are often small or undetectable. Here we show unprecedentedly large dipole effects on ET. Depending on their orientation, dipoles either ensure picosecond ET, or turn ET completely off. Furthermore, favourable dipole orientation makes ET possible even in lipophilic medium, which appears counterintuitive for non-charged donor-acceptor systems. Our analysis reveals that dipoles can substantially alter the ET driving force for low solvent polarity, which accounts for these unique trends. This discovery opens doors for guiding forward ET processes, while suppressing undesired backward electron transduction, which is one of the holy grails of photophysics and energy science.

Introduction

Employing molecular dipoles for guiding electron transfer **(ET)** is logical and of multifaceted importance. It still, however, remains underutilized. The concepts of how electric dipoles affect ET have evolved since the middle of the 20th century.[1] In the 1990s, Galoppini and Fox reported an unequivocal demonstration of dipole effects on long-range ET.[2] Using the macrodipole of a polypeptide helix, they showed that ET along the dipole is up to 27 faster than against it.[2] Since then, a broad range of studies have focused on unraveling how dipoles affect ET, encompassing (1) systems containing polypeptide helices,[3] (2) native proteins with dipolar asymmetry,[4] and (3) small dipolar molecules and their assemblies for optimizing the performance of nanomaterials and devics.[5]

Dipole-generated fields alter the reduction potentials of donors and acceptors, and modulate the ET driving force, $-\Delta G_{ET}^{(0)}$. This effect on $-\Delta G_{ET}^{(0)}$ illustrates the accepted notion of how dipoles affect ET.[2b, 6] The electric fields near molecular dipoles are enormous, with potentials varying by hundreds of millivolts and volts over nanometer distances. Such localized fields should strongly affect $-\Delta G_{ET}^{(0)}$ and ET rates, as theory predicts.[7] Experimentally measured dependence of ET and electric currents on dipole orientation, however, often falls short of showing dramatic trends.[4, 5e] The ET rates and the currents along vs. against the dipoles rarely differ by more than an order of magnitude,[3b, 4a] and occasionally, such differences are undetectable.[3d, 4b, 5e] This discrepancy suggests that the dipole effects on ET still remain not truly well understood, despite their importance.

Here we demonstrate how dipoles strongly affect ET in donor-acceptor dyads (Figure 8-1a,b) by considering the complex dependence of ET kinetics on medium polarity. While lowering medium polarity enormously enhances the dipole effects, it also decreases $-\Delta G_{ET}^{(0)}$ and the reorganization energy of ET between non-charged donors and acceptors. Our results reveal key paradigms for optimizing the dipole effects on ET.

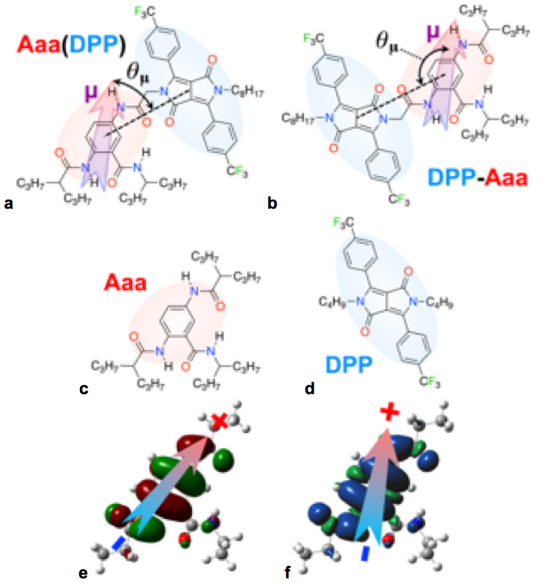

Figure 8-1. Electron donor-acceptor dyads (donor = **Aaa**, acceptor = **DPP**). (a,b) Structures of the dyads showing the electric dipole, **μ**, of the oxidized donor, **Aaa**$^{\bullet+}$. (Electric dipoles point from their negative to their positive poles.[8]) (c,d) Structures of **Aaa** and **DPP**. (e) HOMO and the dipole of **Aaa** (ground state). (f) Spin-density distribution and the dipole of **Aaa**$^{\bullet+}$ (dipole referenced to the center of mass). (e,f) From DFT calculations for DCM.

Electron donor

A 5-*N*-amido-anthranilamide **(Aaa)** electret residue serves as an electron donor and a source of a molecular dipole (Figure 8-1c).[5c, 9] Upon oxidation of **Aaa**, its dipole increases with 20% to 40% and shifts about 30° to 35° (Figure 8-1e,f). We focus on the dipole of the oxidized donor, **Aaa**$^{\bullet+}$, since it affects the energy of the charge-transfer **(CT)** state. In toluene the **Aaa**$^{\bullet+}$ dipole is 5.5 D and increases with the increase in medium polarity to 6.8 D for acetonitrile **(MeCN)**, due to the Onsager field in the solvated cavity.[10] Defining an electric dipole of charged species such as **Aaa**$^{\bullet+}$, however, is not straightforward. A dipole, **μ**, represents a positive and a negative charge, $+q$ and $-q$, displaced at a distance, **d**, from each other, i.e., $\boldsymbol{\mu} = q\mathbf{d}$. In general, for moieties with multiple charges, $\boldsymbol{\mu} = \Sigma_i q_i(\mathbf{r}_i - \mathbf{r}_0)$, where $\mathbf{r}_i$ is a vector representing the position of the i^{th} charge, q_i, and $\mathbf{r}_0$ represents the coordinates of the

reference for the multipole expansion, i.e., the origin of the coordinate system for $\mathbf{r}_i$. For electroneutral species, i.e., for $\Sigma_i q_i = 0$, the dipole is invariant to the reference $\mathbf{r}_0$. This invariance, however, is not true for charged moieties, i.e., for $\Sigma_i q_i \neq 0$. Following an accepted notion, the molecular center of mass serves as the reference, and the dipole of **Aaa**$^{\bullet+}$, therefore, is actually an "electroinertial dipole."

Electron acceptor

An electron-deficient diketopyrrolopyrrole **(DPP)** acts as a photosensitizer and an electron acceptor (Figure 8-1d).[11] In one of the dyads, **DPP-Aaa**, the acceptor is at the negative pole of the dipole, i.e., attached to the N-terminal amide; and in the other, **Aaa(DPP)** – at the positive pole, i.e., attached to the side-chain amide at position 5 (Figure 8-1a,b). Photoexcitation of the acceptor generates a vacancy on its highest occupied molecular orbital **(HOMO)** and improves its oxidizing propensity, allowing it to extract an electron from the HOMO of the donor.

The HOMO of **Aaa** stretches between its N-terminal amide and the side-chain amide (Figure 8-1e), which ensures the same electronic coupling with **DPP** when attached at the positive and the negative pole of the dipole. Hence, the differences between the ET properties of these two dyads should result from the dipole orientation and not from differences in donor-acceptor electronic coupling.

DPP has a structure with pseudo C_2 symmetry. Attaching an electron donor to one of the lactam nitrogens of **DPP** via a methylene linker warrants efficient photoinduced ET, resulting in charge separation **(CS)**.[11a] The charge recombination **(CR)** for such methylene-linked **DPP** dyads, however, tends to be faster than the CS, and prevents

accumulation of CT states, **Aaa$^{\bullet+}$(DPP$^{\bullet-}$)** and **DPP$^{\bullet-}$-Aaa$^{\bullet+}$**. Thus, the decay rates of the singlet-excited state of the acceptor, ^{1}DPP*, provide a means for quantifying the CS kinetics.[11a]

2D NMR

The methylene linker ensures that the donor does not perturb the electronic properties of the acceptor, and vice versa.[5c] Still, the two σ-bonds of the linker provide sufficient coupling to mediate sub-nanosecond ET, i.e., faster than the lifetime of **^{1}DPP*** without a donor.[11a] Nuclear magnetic resonance **(NMR)** analysis, including proton-proton nuclear Overhauser effect spectroscopy **(^{1}H-^{1}H NOESY)** and proton-fluorine heteronuclear Overhauser effect spectroscopy **(^{1}H-^{19}F HOESY)**, indicates no through-space correlations of the **Aaa** protons with the protons or the fluorines of **DPP** for either of the dyads, which is consistent with through-bond ET pathways. Computational studies confirm the NMR results, and also reveal that in the most stable conformers of the dyads the **DPP** acceptor is close to the poles of the **Aaa** dipole, i.e., θ_{μ} close to 0° for **Aaa(DPP)** and close to 180° for **DPP-Aaa** (Figure 8-1a,b).

Aaa is an UV absorber, allowing us to selectively excite **DPP** in the visible spectral region. The close resemblance between the absorption and emission spectra of **DPP** and the two dyads (Figure 8-2a,b) confirms that attaching **DPP** to either side of **Aaa** negligibly perturbs its electronic properties. Placing **DPP** near the positive pole of the **Aaa** dipole, however, quenches its fluorescence (Figure 8-2a,b), which we ascribe to ET as a decay pathway for **Aaa(^{1}DPP*)**.[11a] Conversely, **DPP-Aaa** exhibits such fluorescence quenching only for the polar solvent, MeCN (Figure 8-2b). Transient-absorption **(TA)** dynamics

shows the same trends for the decays of **Aaa(**^{1}**DPP*)** and ^{1}**DPP*-Aaa**, as well as for the depletion of the stimulated emission and the recovery of the ground-state bleach (Figure 8-2c-f).

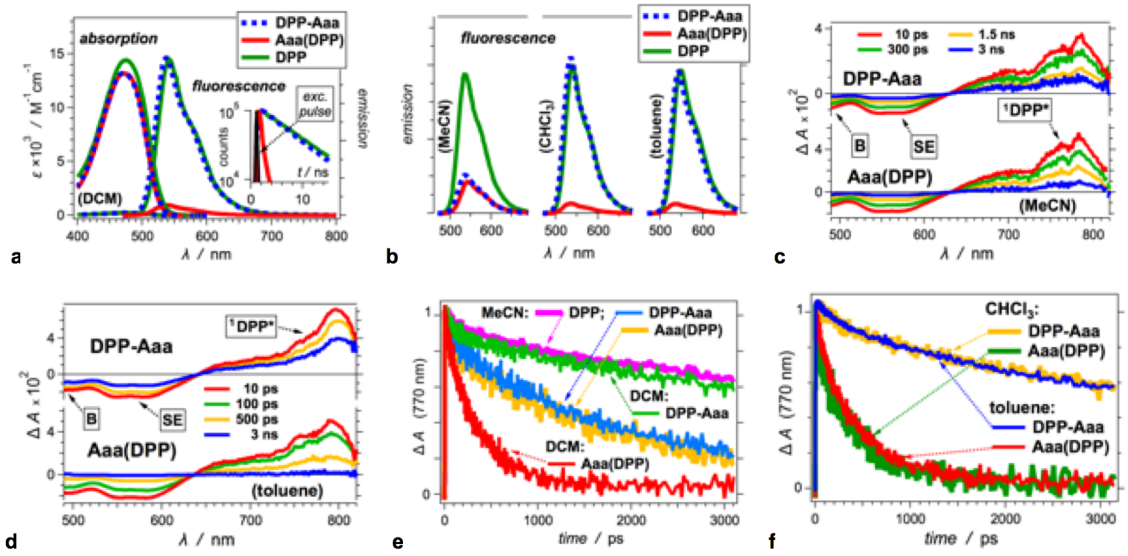

Figure 8-2. Optical properties of the dyads for different solvents. (a,b) Optical absorption and emission spectra of **Aaa(DPP)**, **DPP-Aaa** and **DPP** (10 μM for MeCN and toluene and 15 μM for DCM and $CHCl_3$, λ_{ex} = 460 nm, emission spectra are divided by $1\text{-}10^{-A(\lambda ex)}$). Inset in a: emission decays (λ_{ex} = 406 nm). (c,d) Transient-absorption (TA) spectra of **Aaa(DPP)** and **DPP-Aaa** (B = ground-state bleach, SE = stimulated emission). (e,f) Normalized TA decays of **Aaa(**^{1}**DPP*)**, ^{1}**DPP*-Aaa** and ^{1}**DPP***. (For TA, λ_{ex} = 465 nm, 50-fs pulses, 4 μJ per pulse, and measurements are carried out with 2-mm quartz cuvettes.) To ensure sufficiently large A(λ_{ex}) through a 2-mm cuvettes, $C_{Aaa(DPP)}$ = 180 μM for MeCN, 240 μM for DCM, 150 μM for $CHCl_3$, and 140 μM for toluene, and $C_{DPP\text{-}Aaa}$ = 120 μM for MeCN, 160 μM for DCM, 220 μM for $CHCl_3$, and 140 μM for toluene. These elevated sample concentrations of hundreds of μM do not cause

Dipole effects on charge transfer

The decay rates of **Aaa(**^{1}**DPP*)** and ^{1}**DPP*-Aaa** for solvents with different polarity (Figure 8-2e,f) reveal truly important aspects of the multifaceted complexity of how dipoles impact ET. For MeCN, the CS rate constants, k_{CS}, for both dyads are quite similar (Table 8-1), indicating that for solvents with such polarity, the dipole effects on ET are negligible. For **Aaa(DPP)**, decreasing the polarity to that of dichloromethane **(DCM)** leads to a sharp increase in k_{CS}, which remains almost the same as the medium polarity decreases further (Table 8-1). For **DPP-Aaa**, however, lowering the solvent polarity suppresses ET. These

results illustrate a dramatic dipole effect. Low medium polarity, indeed, decreases $-\Delta G_{CS}^{(0)}$. Conversely, low polarity also enhances electric-field permeation and depending on its orientation, the dipole accelerates or completely shuts off ET in non-polar solvents.

Table 8-1. Rates of charge separation estimated from the transient-absorption and the emission decays of the dyads and **DPP**.

Solvent	$k_{CS} \times 10^9 / s^{-1}$ [a]	
	DPP-Aaa	**Aaa(DPP)**
MeCN	0.357 ± 0.025	0.404 ± 0.051
DCM	— [b]	2.53 ± 0.33
$CHCl_3$	— [b]	3.09 ± 0.04
Toluene	— [b]	2.13 ± 0.29

[a] For each solvent, the charge-separation (CS) rate constants, k_{CS}, are estimated from the lifetimes of ^{1}DPP*, **^{1}DPP*-Aaa**, and **Aaa(^{1}DPP*)**, i.e., $k_{CS} = 1/\tau_{dyad} - 1/\tau_{DPP}$. The lifetimes are obtained from global fits of the transient-absorption (TA) data, $\Delta A(\lambda,t) = \Delta A_\infty(\lambda) + \Sigma_i\, \alpha_i(\lambda)\, \exp(-t/\tau_i)$. The large time constants, i.e., $\tau_i > 1$ ns, were obtained from time-correlated single photon counting (TCSPC) emission decays and introduced as held parameters in the TA global fits. [b] The difference between τ_{DPP} and $\tau_{DPP\text{-}Aaa}$ is smaller than 10%, and does not have statistical significance.

The Rehm-Weller **(RW)** equation[12] estimates that in the absence of the **Aaa** dipole, $\Delta G_{CS}^{(0)}$ assumes: (1) practically the same values for both dyads; and (2) positive values for non-polar solvents (Table 8-2). Both contradict the experimental findings. The positive values of $\Delta G_{CS}^{(0)}$ cannot account for the emission quenching of **Aaa(DPP)** and for the accelerated decay of **Aaa(^{1}DPP*)** when in this hydrocarbon solvent. It is essential, therefore, to consider how the donor dipole affects the energy of the CT states. We modify the RW equation to include the effect of the dipole-field potential, $\phi_{\boldsymbol{\mu}}(\theta_{\boldsymbol{\mu}},\alpha_{DA},R_{DA},\varepsilon)$, on the reduction potential of **DPP**:

$$\Delta G_{CS,\boldsymbol{\mu}}^{(0)} = F\left(E_{D^{\bullet+}|D} - \left(E_{A|A^{\bullet-}} + \phi_{\boldsymbol{\mu}}\right)\right) - \mathscr{E}_{00} + \Delta G_S + W \qquad (8\text{-}1)$$

Table 8-2. Driving forces of charge separation estimated using the modified Rehm-Weller equation (eq. 1).

Solvent	$\Delta G_{CS}^{(0)}$ / eV [a]		$\Delta G_{CS,\mu}^{(0)}$ / eV [b]	
	DPP-Aaa [c]	**Aaa(DPP)** [c]	**DPP-Aaa** [c]	**Aaa(DPP)** [c]
MeCN	-0.18 ± 0.02	-0.18 ± 0.02	-0.16 ± 0.02	-0.20 ± 0.02
DCM	-0.022 ±0.027	-0.023 ±0.024	0.068 ±0.038	-0.11 ± 0.04
$CHCl_3$	0.007 ± 0.042	0.010 ± 0.041	0.17 ± 0.04	-0.16 ± 0.05
Toluene	0.041 ± 0.036	0.051 ± 0.035	0.35 ± 0.04	-0.26 ± 0.05

[a] From eq. 1 with φ_{μ} set to zero (classical RW equation) to produce the driving force without accounting for the **Aaa**$^{\bullet+}$ dipole, i.e., $\Delta G_{CS}^{(0)} = \Delta G_{CS,\mu}^{(0)}(\varphi_{\mu} = 0)$. [b] From eq. 1. [c] For **DPP-Aaa**, $\theta_{\mu} = 180° \pm 20°$, and for **Aaa(DPP)**, $\theta_{\mu} = 0° \pm 20°$; α_{DA}, which is the angle between the plane of the pyrrolopyrrole rings and the plane defined by the dipole and the axis connecting it with **DPP**, is close to orthogonal. Altering θ_{μ} changes R_{DA}, hence, they are not independent variables.

Where $E_{D^{\bullet+}|D}$ and $E_{A|A^{\bullet-}}$ are the reduction potentials for oxidation of **Aaa** and reduction of **DPP**, respectively; F is the Faraday constant; E_{00} is the zero-to-zero energy of **DPP**; the solvation energy, ΔG_S, accounts for the polarity dependence of $E_{D^{\bullet+}|D}$ and $E_{A|A^{\bullet-}}$; and the Coulomb work, W, accounts for interaction between the formed charges.[12b] The dipole-field potential, ϕ_{μ}, depends on: (1) the angle θ_{μ} between the dipole and the axis connecting it with **DPP** (Figure 8-1a,b); (2) the **DPP** tilt angle, α_{DA}; (3) the center-to-center donor-acceptor distance, R_{DA}; and (4) the dielectric constant of the solvating media, ε.

For MeCN, $\Delta G_{CS,\mu}^{(0)} < 0$ for both dyads. Conversely, for non-polar solvents $\Delta G_{CS,\mu}^{(0)}$ assumes negative values only for **Aaa(DPP)** (Table 8-2). The difference in the CS driving force for the two dyads, which we ascribe to the dipole orientation, increases as the solvent polarity decreases, and for toluene, it reaches half an electronvolt (Table 8-2). As a result, $\Delta G_{CS,\mu}^{(0)}$ tends to become more negative with the decrease in polarity (Table 8-2), while the CS rates for DCM and toluene remain practically the same (Table 8-1).

Unlike the solvent dependence of the dipole effects on $\Delta G_{CS,\boldsymbol{\mu}}^{(0)}$, variations in medium polarity have opposing impacts on the CS kinetics. For example, lowering the solvent polarity decreases the reorganization energy, which slows down ET operating in the Marcus inverted region while accelerating ET in the normal region.

Marcus-Hush **(MH)** and Marcus-Levich-Jortner **(MLJ)** formalisms allow us to examine how the **Aaa**$^{\bullet+}$ dipole affects the CS kinetics by employing $\Delta G_{CS,\boldsymbol{\mu}}^{(0)}$ from the modified RW equation (eq. 8-1). In general, can the estimated driving forces (Table 8-2) account for the rates extracted from the experimental results (Table 8-1)? Conformational fluctuations of the dyads, especially around the flexible methylene linker, may cause variations in the donor-acceptor electronic coupling, H_{if}, the inner reorganization energy, λ_v, and the average high frequency, $\langle \nu_C \rangle$, involved in the ET steps. Nevertheless, these characteristics should be invariant to the solvent environment. Therefore, MH and MLJ analysis should produce the values of the experimentally obtained k_{CS} for the same (or similar) H_{if}, λ_v and $\langle \nu_C \rangle$. Varying H_{if} and λ_v in the MH equation, indeed, yields the experimental k_{CS} values for all four solvents when $H_{if} \approx 1$ meV and $\lambda_v \approx 0.1$ eV (Figure 8-3a-d). MLJ analysis produces similar results at relatively low ν_C, i.e., $h\langle \nu_C \rangle \approx 0.05$ eV.

While these results testify that **Aaa**$^{\bullet+}$ dipole induces the observed asymmetry in the CT kinetics, the analysis for toluene (Figure 8-3c) exhibits different patterns than the ones for the other solvents. To generalize the analysis further, we allow the driving force to vary as one of the parameters, which basically generates Marcus curves (Figure 8-3e,f). The trends reveal that for $\Delta G_{CS,\boldsymbol{\mu}}^{(0)} > -0.5$ eV the ET for all solvents, except toluene, occur in

the Marcus normal region. For toluene, however, the Marcus inverted region can also become plausibly accessible.

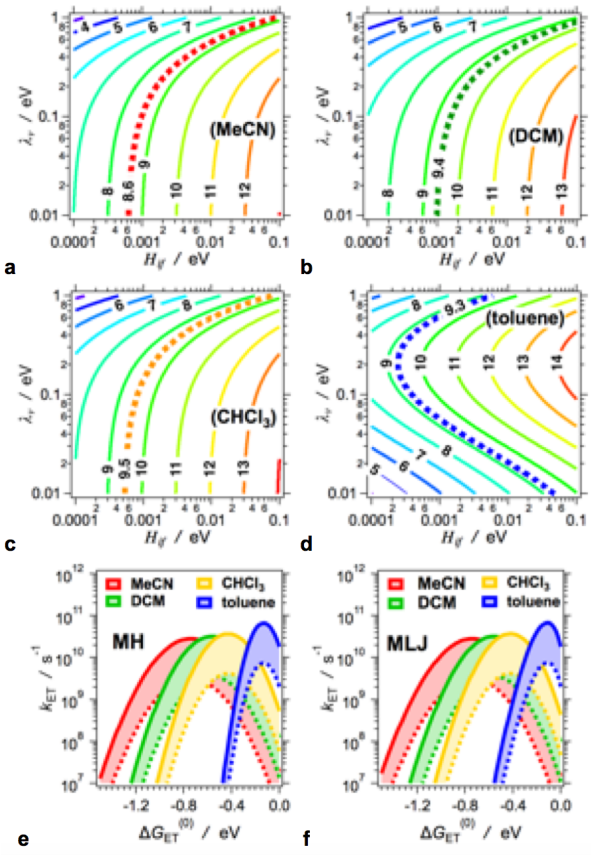

Figure 8-3. Kinetic analysis employing MH and MLJ formalisms. (a-d) Contour plots showing the dependence of the CS rates on the donor-acceptor electronic coupling, H_{if}, and the inner reorganization energy, λ_v, calculated for different solvents, using the MH equation with $\Delta G_{CS,\mu}^{(0)}$ (eq. 1) as an input. The contours represent the logarithmic values of the ET rate constants, $\lg(k_{CS} / s^{-1})$. The thick dashed contours represent the experimentally obtained k_{CS} values (Table 1). (e,f) Dependence of the ET rate constants on the ET driving force, which for these particular plots was allowed to vary as an independent parameter while inputting the other dyad and solvent features in the MH and the MLJ equations. H_{if} ranges between 0.4 meV (dashed lines) and 1.2 meV (solid lines), λ_v = 0.1 eV, and for (f), $h\langle\nu_C\rangle$ = 0.05 eV.

Dipole effects on ET are, indeed, enormous. This study demonstrates that for harnessing such effects it is essential to: (1) employ low-polarity media; and (2) place the dipole as close as possible to the CT moieties. Despite the inherent challenges with defining an electric dipole of a charged moiety, incorporating permanent dipoles in electron donors or acceptors is an invaluable strategy for the latter.[5c]

As simple as the presented electrostatic analysis may appear, it shows layers of complexity of the dipole effects on ET kinetics. The similarity between k_{CS} for the two dyads in MeCN illustrates the basis for previously reported small and undetectable dipole effects on ET when using polar media and electrolyte solutions. Conversely, the dramatic effects for non-polar solvents, i.e., picosecond CS for **Aaa(DPP)**

vs. no ET for **DPP-Aaa**, present a key example of making CS possible in lipophilic media that is pertinent to natural systems mediating ET within proteins and across lipid bilayers. Realization of CS in hydrocarbons is significant on its own. Revealing the role of molecular dipoles for making it possible is of key scientific importance. Balancing the complexity of dipole effects is crucial for exploring their benefits for materials engineering and energy science.

References

[1] a) R. A. Marcus, *Discuss. Faraday Soc.* **1960**, 21-31; b) S. Yomosa, *Sup. Prog. Theor. Phys.* **1967**, 249-263; c) M. A. Steffen, K. Q. Lao, S. G. Boxer, *Science* **1994**, *264*, 810-816.

[2] a) E. Galoppini, M. A. Fox, *J. Am. Chem. Soc.* **1996**, *118*, 2299-2300; b) M. A. Fox, E. Galoppini, *J. Am. Chem. Soc.* **1997**, *119*, 5277-5285.

[3] a) S. Yasutomi, T. Morita, Y. Imanishi, S. Kimura, *Science* **2004**, *304*, 1944-1947; b) C. Shlizerman, A. Atanassov, I. Berkovich, G. Ashkenasy, N. Ashkenasy, *J. Am. Chem. Soc.* **2010**, *132*, 5070-5076; c) L. Garbuio, S. Antonello, I. Guryanov, Y. Li, M. Ruzzi, N. J. Turro, F. Maran, *J. Am. Chem. Soc.* **2012**, *134*, 10628-10637; d) A. Fedorova, A. Chaudhari, M. Y. Ogawa, *J. Am. Chem. Soc.* **2003**, *125*, 357-362; e) M. Lauz, S. Eckhardt, K. M. Fromm, B. Giese, *Phys. Chem. Chem. Phys.* **2012**, *14*, 13785-13788.

[4] a) S. M. Kapetanaki, M. Ramsey, Y. M. Gindt, J. P. M. Schelvis, *J. Am. Chem. Soc.* **2004**, *126*, 6214-6215; b) F. Hannemann, A. Guyot, A. Zollner, J. J. Muller, U. Heinemann, R. Bernhardt, *J Inorg. Biochem.* **2009**, *103*, 997-1004.

[5] a) A. Vilan, A. Shanzer, D. Cahen, *Nature* **2000**, *404*, 166-168; b) J. Albero, E. Martinez-Ferrero, D. Iacopino, A. Vidal-Ferran, E. Palomares, *Phys. Chem. Chem. Phys.* **2010**, *12*, 13047-13051; c) D. Bao, S. Upadhyayula, J. M. Larsen, B. Xia, B. Georgieva, V. Nunez, E. M. Espinoza, J. D. Hartman, M. Wurch, A. Chang, C.-K. Lin, J. Larkin, K. Vasquez, G. J. O. Beran, V. I. Vullev, *J. Am. Chem. Soc.* **2014**, *136*, 12966-12973; d) P. K. Santra, A. F. Palmstrom, J. T. Tanskanen, N. Yang, S. F. Bent, *J. Phys. Chem. C* **2015**, *119*, 2996-3005; e) J. Nieto-Pescador, B. Abraham, J. J. Li, A. Batarseh, R. A. Bartynski, E. Galoppini, L. Gundlach, *J. Phys. Chem. C* **2016**, *120*, 48-55.

[6] a) Y.-G. K. Shin, M. D. Newton, S. S. Isied, *J. Am. Chem. Soc.* **2003**, *125*, 3722-3732; b) S. G. Boxer, *Annu. Rev. Biophys. Bio.* **1990**, *19*, 267-299; c) S. Franzen, K. Q. Lao, S. G. Boxer, *Chem. Phys. Lett.* **1992**, *197*, 380-388; d) G. R. Moore, G. W. Pettigrew, N. K. Rogers, *Proc. Natl. Acad. Sci. USA* **1986**, *83*, 4998-4999.

[7] S. H. Lin, C. Y. Yeh, G. Y. C. Wu, *Chem. Phys. Lett.* **1990**, *166*, 195-202.

[8] J. W. Hovick, J. C. Poler, *J. Chem. Educ.* **2005**, *82*, 889-889.

[9] a) E. M. Espinoza, J. M. Larsen, V. I. Vullev, *J. Phys. Chem. Lett.* **2016**, *7*, 758-764; b) J. M. Larsen-Clinton, E. M. Espinoza, M. F. Mayther, J. Clark, C. Tao, D. Bao, C. M. Larino, M. Wurch, S. Lara, V. I. Vullev, *Phys. Chem. Chem. Phys.* **2017**, *19*, 7871-7876; c) B. Xia, D. Bao, S. Upadhyayula, G. Jones, V. I. Vullev, *J. Org. Chem.* **2013**,

78, 1994-2004.

[10] a) L. Onsager, *J. Am. Chem. Soc.* **1936**, *58*, 1486-1493; b) S. Upadhyayula, D. Bao, B. Millare, S. S. Sylvia, K. M. M. Habib, K. Ashraf, A. Ferreira, S. Bishop, R. Bonderer, S. Baqai, X. Jing, M. Penchev, M. Ozkan, C. S. Ozkan, R. K. Lake, V. I. Vullev, *J. Phys. Chem. B* **2011**, *115*, 9473-9490.

[11] a) A. Purc, E. M. Espinoza, R. Nazir, J. J. Romero, K. Skonieczny, A. Jeżewski, J. M. Larsen, D. T. Gryko, V. I. Vullev, *J. Am. Chem. Soc.* **2016**, *138*, 12826-12832; b) M. Grzybowski, E. Głodkowska-Mrówka, T. Stokłosa, D. T. Gryko, *Org. Lett.* **2012**, *14*, 2670-2673.

[12] a) D. Rehm, A. Weller, *Israel J. Chem.* **1970**, *8*, 259-271; b) D. Bao, B. Millare, W. Xia, B. G. Steyer, A. A. Gerasimenko, A. Ferreira, A. Contreras, V. I. Vullev, *J. Phys. Chem. A* **2009**, *113*, 1259-1267.

Synthetic procedures

General information. All reagents and solvents were purchased from commercial sources and were used as received unless otherwise specified. Reagent grade solvents, such as dichloromethane (DCM) and hexanes, were distilled prior to use. *N*,*N*-dimethylformamide (DMF) was dried over magnesium sulfate, then distilled and stored under argon. Reactions with moisture and oxygen sensitive compounds were carried out under a stream of argon. The reaction progress was monitored by the means of thin layer chromatography (TLC), which was performed with aluminium foil plates, covered with silica gel 60 F_{254} (Merck) or aluminium oxide 60 F_{254} (neutral, Merck). Products purification was done by the means of column chromatography with Kieselgel 60 (Merck) or aluminium oxide (Fluka). Some of the obtained products were purified by dry column vacuum chromatography (DCVC**)** using silica gel Type D 5F. The identity and purity of prepared compounds were confirmed using ^{1}H NMR and ^{13}C NMR spectroscopy as well as by HRMS (*via* EI-MS or ESI-MS). NMR spectra were recorded on Bruker AM 500 MHz, Bruker AM 600 MHz, Varian 600 MHz, Varian 400 MHz and Varian 200 MHz instruments with TMS as internal standard. All chemical shifts are reported in ppm. All melting points for crystalline products were measured with automated melting point apparatus EZ-MELT and are reported without correction.

The synthesis of **Aaa**, **DPP**, **Feb-COOH**, and **DPP-CH$_2$-COOH** (Figure 8-1, Scheme 8S-1, 8S-2) are described elsewhere.[1] The synthesis of anthranilamide residues employs the corresponding 2-nitrobenzoic acid analogues as starting materials, and involves reduction of the 2-nitrogroup to amine.[2] In the synthesis of the two dyads,

therefore, we introduce the acceptor, **DPP**, in last step to prevent its damage during the reduction of the nitro group (Scheme S3, S4, S5).

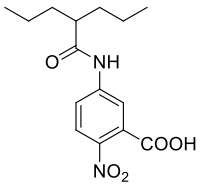

2-nitro-5-(2-propylpentanamido)benzoic acid (2).[1b] **1** (730 mg, 4 mmol) was placed in a baked round bottom flask with a stir bar, and blanked with argon. 10 mL of dry THF was added, and the mixture was cooled down in a dry ice/acetone bath. While stirring, 2,2-di-*n*-propylacetyl chloride (1 mL, 6 mmol) was added slowly, followed by a drop-wise addition of pyridine (400 μL, 5 mmol). The solution was allowed to warm up to room temperature for 30 min and stirred for 3 hours. After that time 10 mL of 5% HCl was added to the reaction mixture and stirred for 10 minutes. The solution was diluted with 10 mL of H_2O and extracted with ethyl acetate (3×25 mL). The organic layer was collected, dried over Na_2SO_4, concentrated in vacuo, and purified using flash chromatography (stationary phase: silica gel; eluent gradient: from 1:2 (v:v) with 1% acetic acid to 1:1 (v:v) with 1% acetic acid ratio of ethyl acetate and hexanes to afford 860 mg (70%) of **2**. ^{1}H NMR (300 MHz, DMSO-d_6) δ/ppm: 10.60 (s, 1H), 8.03 (m, 2H), 7.87 (d, J = 8.8 Hz, 1H), 2.43 (m, 1H), 1.53 (m, 2H), 1.37 (m, 2H), 1.23 (m, 4H), 8.03 (t, J = 6.7 Hz, 6H); ^{13}C NMR (75 MHz, DMSO-d_6) δ/ppm: 175.9, 166.9, 143.9, 141.5, 130.6, 125.9, 120.5, 118.6, 46.7, 34.9, 20.4, 14.2. HRMS (ESI) *m/z* calculated for $C_{15}H_{20}N_2NaO_5$: $[M+Na]^+$ 331.1264, found 331.1260.

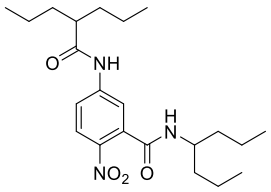

***N*-(heptan-4-yl)-2-nitro-5-(2-propylpentanamido)benzamide (3).**[1b] **2** (740 mg, 2.4 mmol) was placed in a baked round bottom flask with a stir bar, and blanked with argon. Anhydrous DCM (7 mL) and five drops of amine-free dry DMF were added, and the mixture was cooled down in a dry ice/acetone bath. While stirring, oxalyl chloride (310 μL, 3.6 mmol) was added drop-wise and allowed to react for 30 min. The progress of the reaction was monitored using TLC, i.e. a drop of the reaction was quenched with dry methanol to form methyl ester that shows distinctly different R_f values than the starting material. After the completion of the reaction, the mixture was concentrated *in vacuo*, and resuspended in dry DCM (5 mL) and dried *in vacuo*. This resuspending and drying was repeated three times. Under argon, the dried mixture was suspended in dry DCM (5 mL) and cooled down in a dry ice/acetone bath. While stirring, 4-heptylamine (600 μL, 4.0 mmol) was added drop-wise, followed by drop-wise addition of pyridine (300 μL, 3.6 mmol). The reaction was allowed to reach room temperature and stirred for 3 hours. The mixture was diluted with 5% HCl and stirred for additional 10 minutes. The mixture was diluted with water and DCM. The organic layer was collected, and the aqueous layer was extracted with additional amounts of DCM. The combined DCM extracts were washed with water and brine and dried over sodium sulfate. The solvent was evaporated *in vacuo* and the product was purified using flash chromatography (stationary phase: silica gel; eluent gradient: from 1:4 to 1:2 ratio of ethyl acetate and hexanes) to afford 650 mg (67%)

of **3**. Yellowish solid, R_f= 0.43 (SiO_2, AcOEt/hexanes, 1:2). ^{1}H NMR (500 MHz, $CDCl_3$) *δ*/ppm 9.04 (s, 1H), 7.97 (d, *J* = 9.1 Hz, 1H), 7.92 (dd, *J* = 9.1, 2.3 Hz, 1H), 7.41 (d, *J* = 2.2 Hz, 1H), 5.84 (d, *J* = 9.0 Hz, 1H), 4.15 – 4.05 (m, 1H), 2.38 – 2.32 (m, 1H), 1.66 – 1.38 (m, 12H), 1.34 – 1.25 (m, 4H), 0.96 (t, *J* = 7.2 Hz, 6H), 0.89 (t, *J* = 7.3 Hz, 6H). ^{13}C NMR (125 MHz, $CDCl_3$) *δ*/ppm 176.0, 166.7, 143.8, 140.1, 134.3, 126.2, 120.2, 118.8, 50.0, 48.2, 36.8, 35.0, 20.7, 19.0, 14.1, 14.0. HRMS (ESI) calculated for $C_{22}H_{36}N_3O_4$: 406.2706 $[M+H]^+$, found: 406.2714.

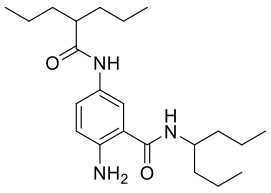

2-amino-*N*-(heptan-4-yl)-5-(2-propylpentanamido)benzamide (4). 3 (324 mg, 0.8 mmol) and $Co_2(CO)_8$ (550 mg, 1.6 mmol) were placed in a 25-mL pressure tube with a magnetic stir bar in it. While purging with argon, 10 mL of 1,2-dimethoxyethane (DME) and five drops of DI water were added and the tube was tightly closed. While mixing, the pressure tube was immersed in a temperature-controlled oil bath. The mixture was heated to 90 °C and stirred for an hour. It was taken out of the oil bath and allowed to cool to room temperature prior to opening it. The reaction mixture was filtered; the filtrate was collected, diluted with 25 mL DCM, and washed with water (100 mL). The organic layer was collected, dried over Na_2SO_4, and concentrated *in vacuo*. The product was purified using flash chromatography (stationary phase: silica gel; eluent gradient: from 1:4 to 1:2 ratio of ethyl acetate and hexanes) to afford 270 mg (90%) of **4**. Brownish solid. Yield 90%. R_f=

0.35 (SiO_2, AcOEt/hexanes, 1:2). ^{1}H NMR (500 MHz, $CDCl_3$) *δ*/ppm 7.76 (d, *J* = 2.3 Hz, 1H), 7.09 (dd, *J* = 8.7, 2.4 Hz, 1H), 7.06 (s, 1H), 6.62 (d, *J* = 8.6 Hz, 1H), 5.89 (d, *J* = 8.9 Hz, 1H), 5.36 (bs, 2H), 4.16 – 4.06 (m, 1H), 2.20 – 2.12 (m, 1H), 1.73 – 1.63 (m, 2H), 1.58 – 1.43 (m, 6H), 1.42 – 1.30 (m, 8H), 0.93 (t, *J* = 7.2 Hz, 6H), 0.92 (t, *J* = 7.2 Hz, 6H). ^{13}C NMR (125 MHz, $CDCl_3$) *δ*/ppm 174.4, 168.4, 145.5, 127.5, 124.7, 119.3, 117.5, 116.8, 49.0, 48.6, 37.5, 35.3, 26.9, 20.9, 19.3, 14.1, 14.0. HRMS (ESI-TOF) calcd for $C_{22}H_{38}N_3O_2$: 376.2964 $[M+H]^+$, found: 376.2964.

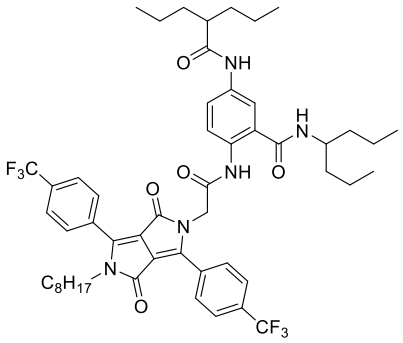

***N*-(heptan-4-yl)-2-(2-(5-octyl-1,4-dioxo-3,6-bis(4-(trifluoromethyl)phenyl)-4,5-dihydropyrrolo[3,4-*c*]pyrrol-2(1*H*)-yl)acetamido)-5-(2-propylpentanamido)benzamide (DPP-Aaa). DPP-CH_2-COOH** (100 mg, 0.17 mmol) was placed in a baked round bottom flask with a stir bar, and blanked with argon. Anhydrous DCM (3 mL) and three drops of amine-free dry DMF were added, and the mixture was cooled down in a dry ice/acetone bath. While stirring, oxalyl chloride (25 µL, 0.26 mmol) was added drop-wise and allowed to react for 30 min. The progress of the reaction was monitored using TLC, i.e. a drop of the reaction was quenched with dry methanol to form methyl ester that shows distinctly different R_f values than the starting

material. After the completion of the reaction, the mixture was concentrated *in vacuo*, and resuspended in dry DCM (5 mL) and dried *in vacuo*. This resuspending and drying was repeated three times. Under argon, the dried mixture was suspended in dry DCM (5 mL) and cooled down in a dry ice/acetone bath. While stirring, solution of **4** (95 mg, 0.26 mmol in 5 mL of DCM) was added drop-wise, followed by drop-wise addition of pyridine (25 μL, 0.26 mmol). The reaction was allowed to reach room temperature and stirred for 3h. The mixture was diluted with water and DCM. The organic layer was collected, and the aqueous layer was extracted with additional amounts of DCM. The combined DCM extracts were washed with water and brine and dried over sodium sulfate. The solvent was evaporated *in vacuo* and the product was purified using flash chromatography (stationary phase: silica gel; eluent gradient: from 1:4 to 1:2 ratio of ethyl acetate and hexanes) to afford 32 mg (20%) of **DPP-Aaa**. Orange solid, R_f= 0.55 (SiO_2, AcOEt/hexanes, 1:2). ^{1}H NMR (500 MHz, $CDCl_3$) *δ*/ppm 11.87 (s, 1H), 8.50 (d, *J* = 9.0 Hz, 1H), 8.25 (d, *J* = 2.4 Hz, 1H), 7.96 (dd, *J* = 11.5, 8.4 Hz, 4H), 7.77 (dd, *J* = 16.0, 8.4 Hz, 4H), 7.20 (s, 1H), 7.09 (dd, *J* = 9.0, 2.4 Hz, 1H), 6.08 (d, *J* = 9.1 Hz, 1H), 4.52 (s, 2H), 4.01 – 3.95 (m, 1H), 3.79 – 3.74 (m, 2H), 2.12 – 2.16 (m, 1H), 1.72 – 1.64 (m, 2H), 1.52 – 1.44 (m, 6H), 1.41 – 1.29 (m, 10H), 1.25 – 1.16 (m, 10H), 0.97 – 0.81 (m, 15H). ^{13}C NMR (125 MHz, $CDCl_3$) *δ*/ppm 174.8, 167.9, 165.6, 162.3, 162.0, 148.0, 146.7, 135.2, 133.5, 133.0, 132.9, 132.7, 131.3, 130.8, 129.2, 129.1, 126.10, 126.07, 125.95, 125.92, 124.6, 122.8, 121.8, 120.8, 117.2, 111.6, 110.0, 49.6, 48.9, 46.2, 42.0, 37.2, 35.2, 31.7, 29.7, 29.5, 29.0, 28.9, 26.6, 22.5, 20.9, 19.2, 14.10, 14.0, 13.9. HRMS (ESI-TOF) calculated for $C_{52}H_{62}F_6N_5O_5$: 950.4661 $[M-H]^-$, found: 950.4661.

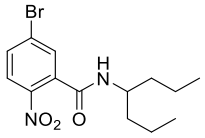

5-bromo-*N*-(heptan-4-yl)-2-nitrobenzamide (6). 5 (2.46 g, 10 mmol) was placed in a baked round bottom flask with a stir bar, and blanked with argon. Anhydrous DCM (30 mL) and fifteen drops of amine-free dry DMF were added, and the mixture was cooled down in a dry ice/acetone bath. While stirring, oxalyl chloride (1.3 mL, 15 mmol) was added drop-wise and allowed to react for 30 min. The progress of the reaction was monitored using TLC, i.e. a drop of the reaction was quenched with dry methanol to form methyl ester that shows distinctly different R_f values than the starting material. After the completion of the reaction, the mixture was concentrated *in vacuo*, and resuspended in dry DCM (25 mL) and dried *in vacuo*. This resuspending and drying was repeated three times. Under argon, the dried mixture was suspended in dry DCM (25 mL) and cooled down in a dry ice/acetone bath. While stirring, 4-heptylamine (2.69 mL, 18 mmol) was added drop-wise, followed by drop-wise addition of pyridine (1.21 mL, 15 mmol). The reaction was allowed to reach room temperature and stirred for 3 hours. The mixture was diluted with 5% HCl and stirred for additional 10 minutes. The resulting mixture was extracted with DCM (3×25 mL). The combined DCM extracts were washed with water and brine and dried over sodium sulfate. The solvent was evaporated *in vacuo* and the product was purified using flash chromatography (stationary phase: silica gel; eluent gradient: from 1:3 to 1:2 ratio of ethyl acetate and hexanes) to afford 2.61 g of **6** (76%). Yellowish solid, R_f= 0.53 (SiO_2, AcOEt/hexanes, 1:3). ^{1}H NMR (500 MHz, $CDCl_3$) δ/ppm 7.93 (d, J = 8.7 Hz,

1H), 7.68 (dd, J = 8.7, 2.1 Hz, 1H), 7.59 (d, J = 2.1 Hz, 1H), 5.57 (d, J = 8.7 Hz, 1H), 4.16 – 4.06 (m, 1H), 1.60 – 1.53 (m, 2H), 1.52 – 1.38 (m, 6H), 0.97 (t, J = 7.1 Hz, 6H). ^{13}C NMR (125 MHz, $CDCl_3$) δ/ppm 164.4, 145.1, 135.0, 133.3, 131.7, 128.6, 126.0, 50.0, 37.1, 19.1, 14.0. HRMS (ESI-TOF) calculated for $C_{14}H_{20}BrN_2O_3$: 343.0657 $[M+H]^+$, found: 343.0662.

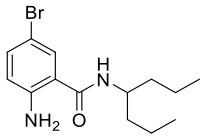

2-amino-5-bromo-*N*-(heptan-4-yl)-benzamide (7). 6 (1.71 g, 5 mmol) and $Co_2(CO)_8$ (3.42 g, 10 mmol) were placed in a 100-mL pressure tube with a magnetic stir bar in it. While purging with argon, 40 mL of 1,2-dimethoxyethane (DME) and fifteen drops of DI water were added and the tube was tightly closed. While mixing, the pressure tube was immersed in a temperature-controlled oil bath. The mixture was heated to 90 °C and stirred for an hour. It was taken out of the oil bath and allowed to cool to room temperature prior to opening it. The reaction mixture was filtered; the filtrate was collected, diluted with 50 mL DCM, and washed with water (100 mL). The organic layer was collected, dried over Na_2SO_4, and concentrated *in vacuo*. The product was purified using flash chromatography (stationary phase: silica gel; eluent gradient: from 1:4 to 1:2 ratio of ethyl acetate and hexanes) to afford 1.56 g (75%) of **7**. Off-white solid, R_f= 0.50 (SiO_2, AcOEt/hexanes, 1:3). ^{1}H NMR (500 MHz, $CDCl_3$) δ/ppm 7.36 (d, J = 2.2 Hz, 1H), 7.26 (dd, J = 9.0, 2.3 Hz, 1H), 6.57 (d, J = 8.7 Hz, 1H), 5.63 (d, J = 8.2 Hz, 1H), 5.47 (s, 2H), 4.14 – 4.06 (m, 1H), 1.59 – 1.50 (m, 2H), 1.48 – 1.35 (m, 6H), 0.94 (t, J = 7.2 Hz, 6H). ^{13}C NMR (125

MHz, $CDCl_3$) *δ*/ppm 167.6, 147.5, 134.6, 129.2, 118.8, 118.3, 107.6, 49.0, 37.5, 19.2, 14.0. HRMS (ESI-TOF) calculated for $C_{14}H_{21}BrN_2ONa$: 335.0735 $[M+Na]^+$, found: 335.0732.

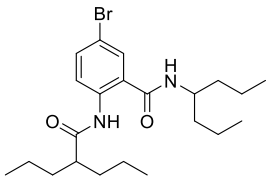

5-bromo-*N*-(heptan-4-yl)-2-(2-propylpentanamido)benzamide (8). 7 (312 mg, 1 mmol) was placed in a baked round bottom flask with a stir bar, and blanked with argon. 6 mL of dry THF was added, and the mixture was cooled down in a dry ice/acetone bath. While stirring 2,2-di-*n*-propylacetyl chloride (300 μL, 1.8 mmol) was added slowly, followed by a drop-wise addition of pyridine (120 μL, 1.5 mmol). The solution was allowed to warm up to room temperature for 30 min and stirred overnight at room temperature. After that time 6 mL of 5% HCl was added to the reaction mixture and stirred for 10 minutes. The solution was diluted with 10 mL of H_2O and extracted with ethyl acetate (3×20 mL). The organic layer was collected, dried over Na_2SO_4, concentrated in vacuo, and purified using flash chromatography (stationary phase: silica gel; eluent gradient: from 1:8 to 1:4 ratio of ethyl acetate and hexanes to afford 400 mg (91%) of **8**. White solid, R_f= 0.70 (SiO_2, AcOEt/hexanes, 1:4). ^{1}H NMR (500 MHz, $CDCl_3$) *δ*/ppm 10.79 (s, 1H), 8.51 (d, *J* = 8.9 Hz, 1H), 7.54 (dd, *J* = 8.9, 2.2 Hz, 1H), 7.50 (d, *J* = 2.3 Hz, 1H), 5.77 (d, *J* = 9.3 Hz, 1H), 4.15 – 4.12 (m, 1H), 2.32 – 2.24 (m, 1H), 1.70 – 1.54 (m, 4H), 1.50 – 1.30 (m, 12H), 0.94 (t, *J* = 7.2 Hz, 6H), 0.90 (t, *J* = 7.3 Hz, 6H). ^{13}C NMR (125 MHz, $CDCl_3$) *δ*/ppm 175.2,

167.3, 138.2, 134.9, 128.7, 123.4, 123.3, 114.9, 49.5, 49.2, 37.5, 35.3, 20.7, 19.2, 14.1, 14.0. HRMS (EI) calculated for $C_{22}H_{35}N_2O_2Br$: 438.1882 $[M]^+$, found: 438.1877.

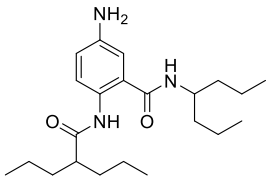

5-amino-*N*-(heptan-4-yl)-2-(2-propylpentanamido)benzamide (9). 8 (330 mg, 0.75 mmol), NaN_3 (290 mg, 4.5 mmol), CuI (85 mg, 0.45 mmol), sodium ascorbate 200 mg, 1.0 mmol), DMEDA (215 μL, 2.0 mmol) were placed in a 25-mL pressure tube with a magnetic stir bar in it. While purging with argon, 6 mL of dry DMF was added and the tube was tightly closed. While mixing, the pressure tube was immersed in a temperature-controlled oil bath. The mixture was heated to 100 °C and stirred for an hour. It was taken out of the oil bath and allowed to cool to room temperature prior to opening it. The reaction mixture was diluted with water and extracted with ethyl acetate (3×20 mL). The organic layer was collected, dried over Na_2SO_4, and concentrated *in vacuo*. The product was purified using flash chromatography (stationary phase: silica gel; eluent gradient: from 1:2 to 1:1 ratio of ethyl acetate and hexanes) to afford 170 mg (60%) of **9**. Yellowish oil, R_f= 0.50 (SiO_2, AcOEt/hexanes, 1:1). ^{1}H NMR (500 MHz, $CDCl_3$) *δ*/ppm 10.32 (s, 1H), 8.28 (d, *J* = 8.8 Hz, 1H), 6.78 (dd, *J* = 8.8, 2.6 Hz, 1H), 6.69 (d, *J* = 2.6 Hz, 1H), 5.74 (d, *J* = 9.2 Hz, 1H), 4.16 – 4.07 (m, 1H), 3.63 (bs, 2H), 2.27 – 2.19 (m, 1H), 1.72 – 1.61 (m, 2H), 1.59 – 1.51 (m, 2H), 1.48 – 1.28 (m, 12H), 0.93 (t, *J* = 7.2 Hz, 6H), 0.90 (t, *J* = 7.3 Hz, 6H).^{13}C NMR (125 MHz, $CDCl_3$) *δ*/ppm 174.6, 168.6, 141.7, 130.4, 123.6, 123.5, 118.8, 112.0, 49.2,

49.0, 37.6, 35.4, 20.8, 19.2, 14.1, 14.0. HRMS (EI) calculated for $C_{22}H_{37}N_3O_2$: 375.2886 $[M]^+$, found: 375.2876.

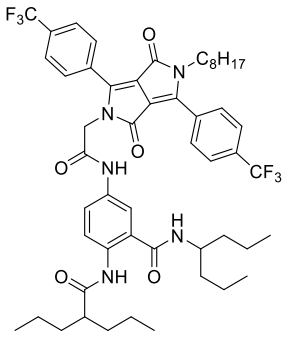

***N*-(heptan-4-yl)-5-(2-(5-octyl-1,4-dioxo-3,6-bis(4-(trifluoromethyl)phenyl)-4,5-dihydropyrrolo[3,4-*c*]pyrrol-2(1*H*)-yl)acetamido)-2-(2-propylpentanamido)benzamide (Aaa(DPP)). DPP-CH_2-COOH** (100 mg, 0.17 mmol) was placed in a baked round bottom flask with a stir bar, and blanked with argon. Anhydrous DCM (3 mL) and three drops of amine-free dry DMF were added, and the mixture was cooled down in a dry ice/acetone bath. While stirring, oxalyl chloride (30 µL, 0.35 mmol) was added drop-wise and allowed to react for 30 min. The progress of the reaction was monitored using TLC, i.e. a drop of the reaction was quenched with dry methanol to form methyl ester that shows distinctly different R_f values than the starting material. After the completion of the reaction, the mixture was concentrated *in vacuo*, and resuspended in dry DCM (5 mL) and dried *in vacuo*. This resuspending and drying was repeated three times. Under argon, the dried mixture was suspended in dry DCM (5 mL) and cooled down in a dry ice/acetone bath. While stirring, solution of **9** (85 mg, 0.23 mmol in 5 mL of DCM) was added drop-wise, followed by drop-wise addition of pyridine (25

μL, 0.26 mmol). The reaction was allowed to reach room temperature and stirred for 2 hours. The mixture was diluted with water and DCM. The organic layer was collected, and the aqueous layer was extracted with additional amounts of DCM. The combined DCM extracts were washed with water and brine and dried over sodium sulfate. The solvent was evaporated *in vacuo* and the product was purified using flash chromatography (stationary phase: silica gel; eluent gradient: from 1:4 to 1:2 ratio of ethyl acetate and hexanes) to afford 30 mg (20%) of **Aaa(DPP)**. Orange solid. R_f= 0.50 (SiO_2, AcOEt/hexanes, 1:2). ^{1}H NMR (500 MHz, $CDCl_3$) *δ*/ppm 10.76 (s, 1H), 9.10 (s, 1H), 8.44 (d, *J* = 9.0 Hz, 1H), 8.17 (d, *J* = 8.2 Hz, 2H), 7.85 (dd, *J* = 8.5, 3.0 Hz, 4H), 7.80 (d, *J* = 8.4 Hz, 2H), 7. 47 (s, 1H), 7.43 (d, *J* = 8.5 Hz, 1H), 6.54 (s, 1H), 4.48 (s, 2H), 4.16 – 4.08 (m, 1H), 3.73 (t, *J* = 7.5 Hz, 2H), 2.28 – 2.21 (m, 1H), 1.69 – 1.62 (m, 2H), 1.58 – 1.44 (m, 6H), 1.41 – 1.26 (m, 12H), 1.25 – 1.16 (m, 8H), 0.92 – 0.87 (m, 12H), 0.85 (t, *J* = 7.1 Hz, 3H). ^{13}C NMR (125 MHz, $CDCl_3$) *δ*/ppm 174.9, 168.1, 165.9, 163.0, 162.1, 150.1, 146.4, 136.0, 133.5, 133.3, 131.7, 130.8, 130.2, 129.6, 129.0, 126.3, 126.2, 126.2, 124.7, 124.5, 123.0, 121.8, 121.7, 117.7, 111.2, 108.9, 49.2, 49.1, 47.2, 42.2, 37.3, 35.3, 31.6, 30.3, 29.7, 29.4, 29.0, 28.9, 26.6, 22.5, 20.7, 19.2, 14.1, 14.00, 13.97. HRMS (ESI- TOF) calculated for $C_{52}H_{64}F_6N_5O_5$: 952.4812 $[M+H]^+$, found: 952.4819.

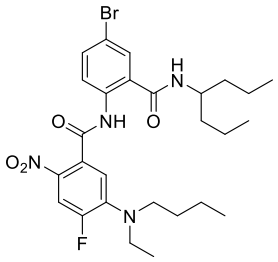

N-(4-bromo-2-(heptan-4-ylcarbamoyl)phenyl)-5-(butyl(ethyl)amino)-4-fluoro-2-nitrobenzamide (10).

Feb-COOH (625 mg, 2.2 mmol) was placed in a baked round bottom flask with a stir bar, and blanked with argon. Anhydrous DCM (15 mL) and six drops of amine-free dry DMF were added, and the mixture was cooled down in a dry ice/acetone bath. While stirring, oxalyl chloride (380 μL, 4.4 mmol) was added drop-wise and allowed to react for 30 min. The progress of the reaction was monitored using TLC, i.e. a drop of the reaction was quenched with dry methanol to form methyl ester that shows distinctly different R_f values than the starting material. After the completion of the reaction, the mixture was concentrated *in vacuo*, and resuspended in dry DCM (15 mL) and dried *in vacuo*. This resuspending and drying was repeated three times. Under argon, the dried mixture was suspended in dry DCM (15 mL) and cooled down in a dry ice/acetone bath. While stirring, solution of **7** (750 mg, 2.4 mmol in 15 mL of DCM) was added drop-wise, followed by drop-wise addition of pyridine (200 μL, 2.5 mmol). The reaction was allowed to reach room temperature and stirred for 3 hours. The mixture was diluted with 15 mL of 5% HCl and stirred for additional 10 minutes. The resulting mixture was extracted with DCM (3x25 mL). The organic layer was collected, and the aqueous layer was extracted with additional amounts of DCM. The combined DCM extracts were washed with water and brine and dried over sodium sulfate. The solvent was evaporated *in vacuo* and the product was purified using flash chromatography (stationary phase: silica gel; eluent gradient: from 1:4 to 1:2 ratio of ethyl acetate and hexanes) to afford 1.12 g (88%) of **10**. Yellow solid, R_f= 0.62 (SiO_2, AcOEt/hexanes, 1:4). ^{1}H NMR (500 MHz, $CDCl_3$) δ 11.18 (s, 1H), 8.61 (d, *J*

= 8.9 Hz, 1H), 7.84 (d, *J* = 14.8 Hz, 1H), 7.63 (dd, *J* = 8.9, 2.2 Hz, 1H), 7.55 (d, *J* = 2.2 Hz, 1H), 6.72 (d, *J* = 8.6 Hz, 1H), 5.87 (d, *J* = 9.1 Hz, 1H), 4.06 – 3.98 (m, 1H), 3.46 (q, *J* = 7.0 Hz, 2H), 3.37 (t, *J* = 8.0 Hz, 2H), 1.66 – 1.60 (m, 2H), 1.56 – 1.50 (m, 2H), 1.48 – 1.29 (m, 8H), 1.23 (t, *J* = 7.1 Hz, 3H), 0.95 (t, *J* = 7.4 Hz, 3H), 0.92 (t, *J* = 7.3 Hz, 6H). ^{13}C NMR (125 MHz, $CDCl_3$) δ 167.0, 165.2, 150.8, 148.9, 142.74, 142.68, 138.2, 135.2, 133.3, 133.2, 131.7, 128.8, 123.8, 123.1, 115.8, 114.8, 114.5, 113.8, 113.8, 52.05, 52.00, 49.7, 47.24, 47.19, 37.2, 30.2, 20.1, 19.1, 13.9, 13.8, 13.1. HRMS (ESI) calcd for $C_{27}H_{37}BrFN_4O_4$: 579.1982 $[M+H]^+$, found: 579.1977.

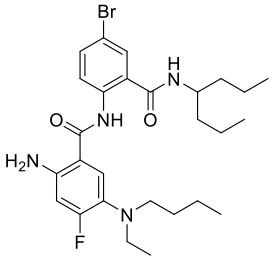

2-amino-N-(4-bromo-2-(heptan-4-ylcarbamoyl)phenyl)-5-(butyl(ethyl)amino)-4-fluorobenzamide (11). 10 (1.00 g, 1.73 mmol) and $Co_2(CO)_8$ (1.18 g, 3.46 mmol) were placed in a 25-mL pressure tube with a magnetic stir bar in it. While purging with argon, 15 mL of 1,2-dimethoxyethane (DME) and six drops of DI water were added and the tube was tightly closed. While mixing, the pressure tube was immersed in a temperature-controlled oil bath. The mixture was heated to 90 °C and stirred for an hour. It was taken out of the oil bath and allowed to cool to room temperature prior to opening it. The reaction mixture was filtered; the filtrate was collected, diluted with 30 mL DCM, and washed with water (100 mL). The organic layer was collected, dried over Na_2SO_4, and concentrated *in*

vacuo. The product was purified using flash chromatography (stationary phase: silica gel; eluent gradient: from 1:4 to 1:2 ratio of ethyl acetate and hexanes) to afford 0.9 g (95%) of **11**. Yellowish solid, R_f= 0.65 (SiO_2, AcOEt/hexanes, 1:4). ^{1}H NMR (500 MHz, $CDCl_3$) δ 11.86 (s, 1H), 8.64 (d, J = 9.0 Hz, 1H), 7.59 (dd, J = 9.0, 2.3 Hz, 1H), 7.55 (d, J = 2.2 Hz, 1H), 7.40 (d, J = 8.9 Hz, 1H), 6.38 (d, J = 13.0 Hz, 1H), 5.82 (d, J = 8.9 Hz, 1H), 5.67 (s, 2H), 4.20 – 4.09 (m, 1H), 3.10 (q, J = 7.1 Hz, 2H), 3.04 (t, J = 8.0 Hz, 2H), 1.59 – 1.53 (m, 2H), 1.51 – 1.30 (m, 10H), 1.04 (t, J = 7.1 Hz, 3H), 0.94 (t, J = 7.3 Hz, 6H), 0.89 (t, J = 7.3 Hz, 3H). ^{13}C NMR (125 MHz, $CDCl_3$) δ 167.4, 167.3, 162.4, 160.4, 147.2, 147.1, 139.1, 135.0, 128.8, 128.6, 128.5, 123.7, 123.6, 123.0, 122.6, 114.7, 111.4, 104.6, 104.4, 53.1, 49.5, 48.1, 37.4, 29.4, 20.4, 19.2, 14.0, 13.9, 12.2. HRMS (ESI-TOF) calcd for $C_{27}H_{39}BrFN_4O_2$: 549.2240 $[M+H]^+$, found: 549.2239.

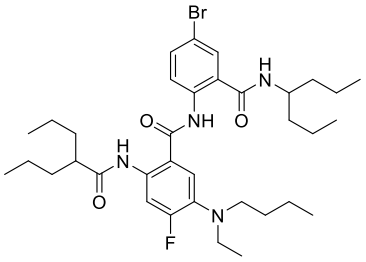

N-(4-bromo-2-(heptan-4-ylcarbamoyl)phenyl)-5-(butyl(ethyl)amino)-4-fluoro-2-(2-propylpentanamido)benzamide (12). 11 (440 mg, 0.8 mmol) was placed in a baked round bottom flask with a stir bar, and blanked with argon. 6 mL of dry THF was added, and the mixture was cooled down in a dry ice/acetone bath. While stirring 2,2-di-*n*-propylacetyl chloride (200 μL, 1.2 mmol) was added slowly, followed by a drop-wise addition of pyridine (100 μL, 1.2 mmol). The solution was allowed to warm up to room

temperature for 30 min and stirred for 4 hours. After that time 6 mL of 5% HCl was added to the reaction mixture and stirred for 10 minutes. The solution was diluted with 10 mL of H_2O and extracted with ethyl acetate (3x20 mL). The organic layer was collected, dried over Na_2SO_4, concentrated in vacuo, and purified using flash chromatography (stationary phase: silica gel; eluent gradient: from 1:8 to 1:6 ratio of ethyl acetate and hexanes to afford 510 mg (95%) of **12**. Yellowish solid, R_f= 0.57 (SiO_2, AcOEt/hexanes, 1:6). ^{1}H NMR (500 MHz, $CDCl_3$) δ 12.24 (s, 1H), 11.29 (s, 1H), 8.65 (d, J = 8.9 Hz, 1H), 8.51 (d, J = 15.2 Hz, 1H), 7.63 (dd, J = 8.9, 2.2 Hz, 1H), 7.58 (d, J = 2.2 Hz, 1H), 7.43 (d, J = 8.9 Hz, 1H), 5.91 (d, J = 9.0 Hz, 1H), 4.18 – 4.10 (m, 1H), 3.23 (q, J = 7.1 Hz, 2H), 3.17 (t, J = 7.5 Hz, 2H), 2.35 – 2.27 (m, 1H), 1.75 – 1.64 (m, 2H), 1.59 – 1.55 (m, 2H), 1.54 – 1.44 (m, 6H), 1.44 – 1.30 (m, 10H), 1.09 (s, 3H), 0.94 (t, J = 7.3 Hz, 6H), 0.91 (t, J = 7.0 Hz, 6H), 0.89 (t, J = 7.5 Hz 3H). ^{13}C NMR (125 MHz, $CDCl_3$) δ 175.0, 167.23, 167.19, 159.7, 157.7, 138.7, 135.8, 135.7, 135.3, 133.7, 133.6, 129.0, 123.1, 122.6, 120.2, 120.2, 115.7, 115.5, 109.9, 109.7, 51.8, 49.6, 49.3, 46.9, 46.2, 37.3, 35.3, 33.9, 29.4, 20.8, 20.4, 20.3, 19.2, 14.1, 13.98, 13.94, 13.90, 12.3. HRMS (ESI-TOF) calcd for $C_{35}H_{53}BrFN_4O_3$: 675.3285 $[M+H]^+$, found: 675.3314.

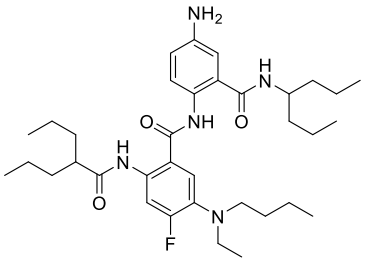

N-(4-amino-2-(heptan-4-ylcarbamoyl)phenyl)-5-(butyl(ethyl)amino)-4-fluoro-2-(2-propylpentanamido)benzamide (13). 12 (440 mg, 0.65 mmol), NaN_3 (260 mg, 4.0 mmol), CuI (75 mg, 0.4 mmol), sodium ascorbate 200 mg, 1.0 mmol), DMEDA (215 μL, 2.0 mmol) were placed in a 25-mL pressure tube with a magnetic stir bar in it. While purging with argon, 6 mL of dry DMF was added and the tube was tightly closed. While mixing, the pressure tube was immersed in a temperature-controlled oil bath. The mixture was heated to 100 °C and stirred for an hour. It was taken out of the oil bath and allowed to cool to room temperature prior to opening it. The reaction mixture was diluted with water and extracted with ethyl acetate (3x 20 mL). The organic layer was collected, dried over Na_2SO_4, and concentrated *in vacuo*. The product was purified using flash chromatography (stationary phase: silica gel; eluent gradient: from 1:2 to 1:1 ratio of ethyl acetate and hexanes) to afford 310 mg (78%) of **13**. Brownish solid, R_f= 0.37 (SiO_2, AcOEt/hexanes, 1:2). ^{1}H NMR (500 MHz, $CDCl_3$) δ 11.74 (s, 1H), 11.42 (s, 1H), 8.50 (d, J = 15.1 Hz, 1H), 8.44 (d, J = 8.8 Hz, 1H), 7.42 (d, J = 8.9 Hz, 1H), 6.87 (dd, J = 8.8, 2.4 Hz, 1H), 6.77 (d, J = 2.4 Hz, 1H), 5.82 (d, J = 9.1 Hz, 1H), 4.15 – 4.09 (m, 1H), 3.71 (bs, 2H), 3.23 (q, J = 7.0 Hz, 2H), 3.16 (t, J = 7.5 Hz, 2H), 2.35 – 2.27 (m, 1H), 1.75 – 1.65 (m, 2H), 1.59 – 1.53 (m, 2H), 1.52 – 1.43 (m, 6H), 1.42 – 1.32 (m, 10H), 1.09 (t, J = 7.0 Hz, 3H), 0.95 – 0.88 (m, 15H). ^{13}C NMR (125 MHz, $CDCl_3$) δ 175.0, 168.4, 166.6, 159.4, 157.4, 142.2, 135.5, 135.4, 133.5, 130.8, 123.2, 122.9, 120.3, 119.0, 116.3, 112.1, 109.8, 109.6, 51.9, 49.25, 49.22, 47.0, 37.4, 35.3, 29.4, 20.8, 20.3, 19.2, 14.1, 13.98, 13.94, 12.3. HRMS (ESI-TOF) calcd for $C_{35}H_{54}FN_5O_3$: 611.4211 $[M]^+$, found: 611.4216.

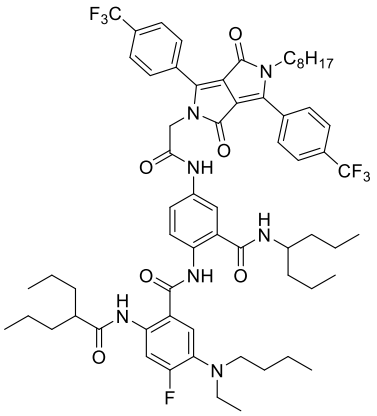

5-(butyl(ethyl)amino)-4-fluoro-N-(2-(heptan-4-ylcarbamoyl)-4-(2-(5-octyl-1,4-dioxo-3,6-bis(4-(trifluoromethyl)phenyl)-4,5-dihydropyrrolo[3,4-c]pyrrol-2(1H)-yl)acetamido)phenyl)-2-(2-propylpentanamido)benzamide (Feb-Aaa(DPP). DPP-CH_2-COOH (100 mg, 0.17 mmol) was placed in a baked round bottom flask with a stir bar, and blanked with argon. Anhydrous DCM (3 mL) and three drops of amine-free dry DMF were added, and the mixture was cooled down in a dry ice/acetone bath. While stirring, oxalyl chloride (30 μL, 0.35 mmol) was added drop-wise and allowed to react for 30 min. The progress of the reaction was monitored using TLC, i.e. a drop of the reaction was quenched with dry methanol to form methyl ester that shows distinctly different R_f values than the starting material. After the completion of the reaction, the mixture was concentrated *in vacuo*, and resuspended in dry DCM (5 mL) and dried *in vacuo*. This resuspending and drying was repeated three times. Under argon, the dried mixture was suspended in dry DCM (5 mL) and cooled down in a dry ice/acetone bath. While stirring, solution of **13** (110 mg, 0.18 mmol in 5 mL of DCM) was added drop-wise, followed by drop-wise addition of pyridine (20 μL, 0.25 mmol). The reaction was allowed to reach room temperature and stirred for 2 hours. The mixture was diluted with water and DCM.

The organic layer was collected, and the aqueous layer was extracted with additional amounts of DCM. The combined DCM extracts were washed with water and brine and dried over sodium sulfate. The solvent was evaporated *in vacuo* and the product was purified using flash chromatography (stationary phase: silica gel; eluent gradient: from 1:4 to 1:2 ratio of ethyl acetate and hexanes) to afford 50 mg (25%) of **Feb-Aaa(DPP)**. Orange solid, R_f= 0.46 (SiO_2, AcOEt/hexanes, 1:2). ^{1}H NMR (500 MHz, $CDCl_3$) δ 12.32 (s, 1H), 11.34 (s, 1H), 9.23 (s, 1H), 8.64 (d, J = 8.9 Hz, 1H), 8.48 (d, J = 15.3 Hz, 1H), 8.18 (d, J = 8.1 Hz, 2H), 7.86 (dd, J = 7.8, 5.3 Hz, 4H), 7.79 (d, J = 8.4 Hz, 2H), 7.53 (d, J = 8.6 Hz, 1H), 7.44 (d, J = 8.5 Hz, 1H), 7.37 – 7.35 (m, 1H), 7.12 (dd, J = 8.7, 2.5 Hz, 1H), 4.49 (s, 2H), 4.17 – 4.10 (m, 1H), 3.79 – 3.72 (m, 2H), 3.21 (q, J = 7.2 Hz, 2H), 3.16 (t, J = 7.5 Hz, 2H), 2.29 – 2.24 (m, 1H), 1.70 – 1.62 (m, 4H), 1.62 – 1.45 (m, 10H), 1.42 – 1.35 (m, 4H), 1.33 – 1.28 (m, 6H), 1.23 – 1.17 (m, 8H), 1.08 (t, J = 7.0 Hz, 3H), 0.94 – 0.82 (m, 18H). ^{13}C NMR (125 MHz, $CDCl_3$) δ 175.0, 168.0, 167.0, 166.1, 163.1, 162.1, 157.5, 150.3, 147.1, 146.3, 136.5, 133.6, 133.3, 132.2, 130.8, 130.1, 129.6, 129.0, 126.3, 126.21, 126.18, 124.5, 123.9, 123.7, 121.6, 121.1, 119.1, 117.9, 111.3, 109.9, 109.6, 108.9, 51.8, 49.3, 49.2, 47.4, 46.9, 42.2, 37.2, 35.3, 34.8, 34.5, 31.9, 31.6, 31.4, 30.3, 30.2, 29.7, 29.0, 28.9, 26.6, 22.7, 22.5, 20.7, 20.3, 19.3, 14.08, 14.00, 13.96, 13.91, 12.3. HRMS (ESI-TOF) calcd for $C_{65}H_{81}F_7N_7O_6$: 1188.6137 $[M+H]^+$, found: 1188.6136.

2D NMR analysis

Two-dimensional (2D) NMR analysis provides information about the structural features of the dyads, and especially for their preferred conformations. All 2D NMR studies were done on either a Bruker Avance or Bruker NEO 600 MHz NMR spectrometer,

equipped with either a 5mm SEF probe for one-dimensional ^{19}F and one-dimensional ^{1}H-^{19}F HOESY measurements, or a 5mm TXI probe for ^{1}H-^{1}H correlation measurements. ^{1}H-^{1}H correlation spectroscopy (COSY) reveals the protons covalently attached to neighboring carbons and provides information for assigning the chemical shift of the hydrogens in the two dyads (Chart 8S-1, Figure 8S-15, 8S-16).

2D nuclear Overhauser effect spectroscopy (NOESY) provides invaluable information about through-space correlations between magnetic nuclei, reveling atoms that are in proximity to one another. For both dyads, homonuclear ^{1}H-^{1}H NOESY does not reveal correlations between the **DPP** protons (d_1, d_2, d_3, and d_4, Chart S1), and the protons of **Aaa**, a_3, a_4 and a_6 (Figure 8S-17a,b and 8S-18a,b). The aromatic protons of **Aaa** show NOE correlations with each other, e.g., a_3-a_4 (Figure 8S-18b), and with the amides at position 1 and 5, e.g., a_6-a_1 and a_4-a_5 (Figure S18a). Conversely, the **DPP** protons, d_1, d_2, d_3 and d_4, correlate through space with the methylene-linker protons, i.e., d_4-m, and with the octyl protons closest to the lactam nitrogen, e.g., d_2-o_1 and d_2-o_2 (Figure 8S-17a, 8S-17b).

For both dyads, ^{1}H-^{19}F heteronuclear Overhauser effect spectroscopy (HOESY) reveals that the six fluorines in the trifluoromethyl groups show NOE correlations only with the **DPP** protons (Figure 8S-17c,d, and 8S-18c,d). It further confirms that direct van der Waals contacts between the donor and the acceptor in the two dyads is not detectable. The summary of the NOE correlations (Chart 8S-2) is consistent with conformations where the amides are in trans (i.e., *Z*) conformation, and the substituents attached to the amides are oriented away from the **Aaa** ring.

Computational analysis

Molecular structures of both neutral **Aaa** and its radical cation are optimized using the Gaussian 09 program package[3] within the density functional theory (DFT) framework. B3LYP functional[4] along with the Coulomb attenuated method (CAM)[5] and the 6-311+G(d,p) basis set are used for all DFT calculations. We use spin-unrestricted DFT for the radical-ion calculations. Solvation effects are studied using the integral equation formalism coupled with the polarizable continuum model (IEF-PCM).[6] The HOMO and the LUMO of both the neutral molecule and the radical cation are predominantly located on the aromatic core, and the orbital shape does not change appreciably upon solvation.

Molecular dipoles are recalculated using the CHELPG fitting procedure.[7] For this analysis, we choose an x axis pointing from the side-chain amide at position 5 to the N-terminal amide (Figure 8S-19), i.e., between the amides to which the acceptor is attached in **Aaa(DPP)** and **DPP-Aaa**, respectively. For **Aaa**, an increase in solvent polarity increases the magnitude of the molecular dipole as expected from the Onsager solvation model,[8] while its direction remains largely unchanged, pointing along the *x* axis (Table 8S-1). Upon oxidation, i.e., **Aaa** → $\mathbf{Aaa}^{\bullet+} + e^-$, the dipole shifts 30° – 35° toward the carbon 4 of the **Aaa** aromatic ring (Table 8S-1). Similar to **Aaa**, the medium polarity affects the magnitude but not the orientation of the dipole of the radical cation (Table 8S-1).

The **Aaa(DPP)** and **DPP-Aaa** dyads are treated with the CAM-B3LYP/6-31G(d) level of theory. Conformational analysis reveals two prevailing types of structures with different orientations of the **DPP** and **Aaa** moieties around the flexible methylene linker: (1) dyad conformers with θ_{μ} close to 0° and 180° for **Aaa(DPP)** and **DPP-Aaa**, respectively, and

(2) dyad conformers with θ_{μ} larger than about 60° for **Aaa(DPP)** and smaller than about 120° for **DPP-Aaa**. The former structures appear to be more stable than the latter by about 0.09 – 0.27 eV and 0.07 eV for **Aaa(DPP)** and **DPP-Aaa**, respectively. It suggests that more than 95% of the **Aaa(DPP)** molecules assume conformation with θ_{μ} close to 0° and more than 90% of the **DPP-Aaa** conformers have θ_{μ} close to 180°.

Electrochemistry

Cyclic voltammetry is conducted using Reference 600TM Potentiostat/Galvanostat/ZRA (Gamry Instruments, PA, U.S.A.), connected to a three-electrode cell, as previously described.[1a, 9] Anhydrous aprotic solvents with different polarity, dichloromethane (DCM), benzonitrile (PhCN), acetonitrile (MeCN), and propylene carbonate (PC) are employed with different concentrations of tetrabutylammonium hexafluorophosphate (NBu_4PF_6) as a supporting electrolyte. Prior to recording each voltammogram, each sample is extensively purged with argon while maintaining its volume constant by adding more of the anhydrous solvent. For each solvent, a set of voltammograms is recorded where the electrolyte concentration is increased from 25 mM to 200 mM in increments of 25 mM. The half-wave potentials, $E^{(1/2)}$, are determined form the midpoints between the cathodic and anodic peak potentials for reversible or quasi-reversible voltammograms; and from the inflection points of the waves for irreversible oxidation and reduction. The anodic and cathodic peak potentials, E_a and E_c, respectively, are determined from the zero points of the first derivatives of the voltammograms, i.e., the potentials where $\partial I/\partial E = 0$ at $\partial E/\partial t$ = constant. The inflection points are determined from the zero point of the second derivatives of the voltammograms, $\partial^2 I/\partial E^2 = 0$ at $\partial E/\partial t$ =

constant.[9] The second derivatives of reversible and quasi-reversible voltammograms show that the inflection-point potentials are quite close to the mid-points between E_a and E_c, ensuring the reliability for the estimates of $E^{(1/2)}$ from the inflection points of irreversible voltammograms. The voltammograms are recorded at a scan rate of 50 mV/s. To correct for potential drifts in the reference electrode (which is SCE, connected with the cell via a salt bridge), ferrocene is used as a standard ($E^{(1/2)}$ = 0.45 ± 0.01 V vs. SCE for MeCN, 100 mM NBu_4BF_4).[10] Voltammograms of the standard are recorded before and after each set of measurements. From the dependence of $E^{(1/2)}$ on the electrolyte concentration, the potentials for each neat solvents are estimated from extrapolations to zero.[11]

To estimate the reduction potentials of **Aaa** and **DPP** for non-polar, which is challenging for carrying out electrochemical measurements, we resort to the Born solvation model, which for *n*-electron reduction potential of an acceptor with a charge z_A is:[10]

$$E_i = E_j + \frac{n(2z_A - n)e^2}{8\pi\varepsilon_0 F R_{eff}}\left(\frac{1}{\varepsilon_i} - \frac{1}{\varepsilon_j}\right) \quad \text{(S1a)}$$

for *n*-electron oxidation of a donor with charge z_D is:

$$E_i = E_j + \frac{n(2z_D + n)e^2}{8\pi\varepsilon_0 F R_{eff}}\left(\frac{1}{\varepsilon_i} - \frac{1}{\varepsilon_j}\right) \quad \text{(S1b)}$$

and for single-electron oxidation or reduction of non-charged species can be simplified to:

$$E_i = E_j + \frac{ze^2}{8\pi\varepsilon_0 F R_{eff}}\left(\frac{1}{\varepsilon_i} - \frac{1}{\varepsilon_j}\right) \quad \text{(S1c)}$$

Where E_i and E_j are the reduction potentials of the sample for solvents with dielectric constants ε_i and ε_j, respectively; z is the charge of the formed radical ion; e is the elementary charge; ε_0 is the electric permittivity of vacuum; F is the Faraday constant; and R_{eff} is the

Born effective radius that we estimate from the charge distribution (from DFT calculations) of the corresponding neutral and charged components of the redox pairs.[11a] For **Aaa** and **DPP**, R_{eff} is 3.14 Å and 4.00 Å, respectively.

Optical spectroscopy and analysis

Steady-state absorption spectra are recorded in a transmission mode using a JASCO V-670 spectrophotometer (Tokyo, Japan).[12] The steady-state emission spectra and the time-correlated single-photon counting (TCSPC) fluorescence decays are measured, using a FluoroLog-3 spectrofluorometer (Horiba-Jobin-Yvon, Edison, NJ, USA), equipped with a pulsed diode laser (λ = 406 nm, 196 ps pulse width) as previously reported.[13]

The wavelengths of the maxima of the absorption and emission spectra are obtained from fitting the spectra peaks with Gaussian function. For estimating zero-to-zero energy, E_{00}, of a conjugate we plot its absorption and fluorescence spectra on the same graph where the fluorescence maximum is adjusted to be equal to the maximum of the band at the red edge of the absorption spectrum. E_{00} is estimated from the wavelength at which the thus normalized spectra cross (Table 8S-1).

The fluorescence quantum yields, Φ_f (Table 8S-2), are determined by comparing the integrated emission intensities of the samples with the integrated fluorescence of a reference sample with a known fluorescence quantum yield, Φ_{f0}:[14]

$$\Phi_f = \Phi_{f0} \frac{\int F(\lambda) d\lambda}{\int F(\lambda) d\lambda} \times \frac{1-10^{-A_0(\lambda_{ex})}}{1-10^{-A(\lambda_{ex})}} \times \frac{n^2}{n_0^2} \qquad \text{(8S-2)}$$

Where $F(\lambda)$ is the fluorescence intensity at wavelength λ; $A(\lambda_{ex})$ is the absorbance at the excitation wavelength; n is the refractive index of the media; and the suffix "0" indicates the quantities for the reference sample used. For a reference sample we used an aqueous solution of fluorescein buffered at pH 10 ($\Phi_{f0} = 0.93$).[15]

For concentration-dependence studies of the ground-state absorption, we employ 1-cm and 1-mm cuvettes. The 1-mm cuvette allows for reliable measurements of concentrated **DPP** samples with $A > 1.5$ for 1-cm cuvette. An increase in **DPP** concentration linearly increases the absorbance, and does not alter the spectral shape and maxima (Figure 8S-20). These findings rule out detectable aggregation within the investigated concentration ranges. While **DPP** is modified with butyls, the dyads are decorated with octyl and heptyl groups to ensure their solubility and suppress aggregation in organic solvents. Similar to **DPP**, elevating the concentrations of the dyads in organic media does not perturb their optical absorption spectra (Figure 8S-21).

Transient-absorption spectroscopy

The transient-absorption (TA) data, $\Delta A(\lambda, t)$, are recorded in transmission mode with 2-mm quartz cuvettes using a Helios pump-probe spectrometer (Ultrafast Systems, LLC, Florida, USA) equipped with a delay stage allowing maximum probe delays of 3.2 ns at 7 fs temporal step resolution.[16] Following chirp correction, we extract the TA spectra and decays from $\Delta A(\lambda, t)$ (Figure 8-2c-f, 8-S22). The absorbance of the samples at the excitation wavelength, $A(\lambda_{ex})$, is adjusted to about 0.4 to 0.6 in the 2-mm cuvettes (Figure S21). Immediately prior to the measurements, all samples are purged with argon for 5 to 10 min per 1 mL of sample. The photostability of the samples during the exposure to the

pump laser was confirmed by comparing the absorption spectra recorded before and after each set of TA measurements. The laser source for the Helios is a SpitFire Pro 35F regenerative amplifier yielding (Spectra Physics, Newport, CA, USA) generating 800-nm pulses (>35 fs, 4.0 mJ, at 1 kHz). The amplifier is pumped with of an Empower 30 Q-switched laser ran at 20 W at the 2nd harmonic. A MaiTai SP oscillator provided the seed beam (55 nm bandwidth). The wavelength of the pump is tuned using an optical parametric amplifier, OPA-800CU (Newport Corporation, Newport, CA, USA), equipped with reflectors for removing the 800-nm fundamental and the signal; and the idler is subjected to second and forth harmonic generators. For optimal OPA performance, the pulse duration from the amplifier is tuned to 50 fs. The idler is tuned in the range between 1,840 and 1,940 nm for selective excitation of **DPP** chromophore after upconversion to fourth harmonic. The power of the signal and the idler removing the removal of the fundamental is stabilized at about 170 mW.

Evidence for charge transfer

Favorable driving forces, calculated using eq. 8-1, indicate that electron transfer from **Aaa** to **^{1}DPP*** can plausibly be responsible for the decrease in the lifetimes of **Aaa(^{1}DPP*)** for all solvents, and of **^{1}DPP*-Aaa** for MeCN. Conversely, charge recombination that is faster than the initial charge separation can account for the lack of accumulation of CT transients, i.e., of **DPP$^{\bullet-}$** and **Aaa$^{\bullet+}$**, as examined using TA spectroscopy. That is, the photoinduced charge separation is the rate-limiting step of the CT pathway of deactivation of the locally excited states of the dyads.

This type of behavior is not unprecedented for electron donor-acceptor dyads. In fact, a dyads of a **DPP** acceptor, connected with a donor via a methylene linker, manifests similar excited-state dynamics for most solvents.[1a] For some polar solvents, the presence of certain conformers of such a **DPP**-donor dyad leads to formation of CT transients within subpicosecond timescales and presents evidence for photoinduced electron transfer.[1a] In the case of **Aaa(DPP)** and **DPP-Aaa**, however, we do not detect any folded conformers, as evident from the 2D MNR studies (most likely because of the bulky heptyl chains capping the amides of **Aaa**), and we do not observe the formation of CT transients.

What other processes, in addition to CT, can plausibly lead to the deactivation of **Aaa(^{1}DPP*)** and **^{1}DPP*-Aaa** that is significantly faster than the decay of **^{1}DPP***? The presence of **Aaa** drastically increases the rates of non-radiative decay of **Aaa(^{1}DPP*)**, as well as of **^{1}DPP*-Aaa** when in polar media (Table 8S-2), which leads to the shortening of the excited-state lifetimes observed in the time-resolved spectroscopy studies. Such non-radiative processes can include energy transfer, intersystem crossing (i.e., triplet formation), internal conversion, and indeed, charge transfer. The possibility for **Aaa** to increase the rates of internal conversion from **^{1}DPP*** to **^{1}DPP** is quite improbable. That is, **Aaa**-induced changes in the vibrational (and torsional) coupling between the electronic ground and excited states[17] are highly unlikely because of the lack of detectable direct contact between the **Aaa** and **DPP** moieties in the dyads. Considering energy transfer as an alternative pathway of deactivation is also unacceptable. **Aaa** is a UV absorber,[1b] while **DPP** absorbs in the visible spectral region.[1a] Thus, energy transfer from **^{1}DPP*** to **Aaa** (via resonance or electron-exchange mechanisms) is impossible. While intersystem-

crossing pathways of deactivation may present an alternative, the lack of growth of long-lived transients (while the pheotoexcited dyads decay)[11b] precludes the possibility for triplet formation. Therefore, it appears that charge transfer is the most plausible pathway for the observed trends of shortening the lifetimes of the locally excited states of the dyads.

What other evidence support the occurrence of CT as a pathway for deactivation of **Aaa(**^{1}**DPP*)** and ^{1}**DPP*-Aaa**, especially for non-polar solvents? Non-polar solvents, such as toluene, destabilize charged charge-transfer (CT) states, and can completely suppress photoinduced electron transfer. Nevertheless, DFT studies reveal trends in the frontier oribtals of the dyads that are consistent with favorable photoinduced electron transfer from **Aaa** to ^{1}**DPP***. For non-polar media, the HOMO and the LUMO of **DPP-Aaa** are localized on the **DPP** moiety, while the HOMO-1 is located on the **Aaa** residue. Also, there is no spatial overlap between the HOMO-1 and the LUMO (Figure S24a). These findings are consistent with absorption and emission localized on the **DPP** chromophore, and no electron transfer from **Aaa** to ^{1}**DPP***. In **Aaa(DPP)**, however, the energy levels of the HOMO and the HOMO-1 switch. That is, while the HOMO-1 and the LUMO are on the **DPP** moiety and spatially overlap, the HOMO is on **Aaa** (Figure S24b). This orbital configuration is consistent with optical transition between HOMO-1 and the LUMO, located on **DPP**, and energetically favorable electron transfer from the HOMO of **Aaa** to the singly occupied "HOMO-1" of ^{1}**DPP***.

The principal difference between the two dyads is switching the position of the **DPP** acceptor in relevance to the **Aaa** dipole (Figure 8-1, 8S-24). Indeed, the switch

between the energy levels and the localization of the HOMOs and the HOMOs-1 for the two dyads correlates with the orientation of the **Aaa** dipole.

Observing the formation of the CT state in the dyads is experimentally impossible because of the fast charge recombination. As an alternative, an auxiliary donor that is electronically coupled only to **Aaa** but not to **DPP** can extract the hole (i.e., the positive charge) formed on **Aaa** upon electron transfer to ^{1}**DPP***, and "trap" the CT state for long enough time to observe it using TA spectroscopy. For this test, we resort to another anthranilamide residue, **Feb**, which is a better electron donor than **Aaa**.[1b, 1c] Attaching **Feb** to the N-terminus of **Aaa** yields a triad, **Feb-Aaa(DPP)** (Scheme 8S-6a). 2D NMR analysis of **Feb-Aaa(DPP)** reveals that it assumes extended conformation and there are no through-space interactions between **Feb** and **DPP**, and the presence of **Feb** does not perturb the structure of **Aaa(DPP)** component of the triad.

Similar to **Aaa**, **Feb** is also a UV absorber.[1c] Hence, we selectively excite the **DPP** acceptor in the visible spectral region to form **Feb-Aaa(^{1}DPP*)**. While it can lead to electron transfer from **Aaa** to ^{1}**DPP***, it can also result in a long-range electron transfer directly from **Feb** to ^{1}**DPP***. For the latter, in addition to the favorable the driving forces, it is essential for the electronic coupling between the **Feb** and **DPP** moieties in the triad be sufficiently strong to produce rates of electron transfer from **Feb** to ^{1}**DPP*** that are comparable or faster than those from **Aaa** to ^{1}**DPP***. Theoretical and experimental evidence, however, exclude the possibility for direct formation of **Feb$^{\bullet+}$-Aaa(DPP$^{\bullet-}$)** from **Feb-Aaa(^{1}DPP*)**. DFT studies reveal that the frontier orbitals of the **Feb** residue do not extend over to **Aaa** and to the linker with **DPP**, indicating that the electronic coupling

between **DPP** and **Aaa** is considerably stronger than the coupling between **DPP** and **Feb**. Most importantly, the locally excited states of the dyad and the triad, i.e., **Aaa(^{1}DPP*)** and **Feb-Aaa(^{1}DPP*)**, decay with practically the same rates (Figure 8S-25a). A direct formation of **Feb$^{\bullet+}$-Aaa(DPP$^{\bullet-}$)** from **Feb-Aaa(^{1}DPP*)** results in additional pathways for deactivation of ^{1}**DPP*** in the triad, making **Feb-Aaa(^{1}DPP*)** decay faster than **Aaa(^{1}DPP*)**, which is not what we observe (Figure 8S-25a). Therefore, the addition of **Feb** to **Aaa(DPP)** does not perturb the initial photoinduced processes of deactivation of ^{1}**DPP***.

While the experimental findings precludes the possibility for a long-range electron transfer from **Feb** to ^{1}**DPP***, the TA spectra of the triad clearly show the formation of a CT state, **Feb$^{\bullet+}$-Aaa(DPP$^{\bullet-}$)** (Figure 8S-25b). Because the observed CT state cannot originate from direct electron transfer from **Feb to** ^{1}**DPP***, its formation requires a multi-step transition through an intermediate. The observed formation of the **DPP$^{\bullet-}$** transient accompanies the decay of ^{1}**DPP** (Figure 8S-25b), indicating that the photoexcited **DPP** extracts an electron from another moiety, which is neither **Feb** nor a solvent molecule. Neither of the solvents we employ has the reduction potential to participate in CT with ^{1}**DPP***, and as expected, the lifetimes of ^{1}**DPP***, τ_{DPP}, are practically the same for the different solvents (Table 8S-2). Therefore, **Aaa** is the only moiety in the triad that can be the source of an electron to reduce ^{1}**DPP***, leading to the formation of **Feb-Aaa$^{\bullet+}$ (DPP$^{\bullet-}$)**. On the other hand, the formation of **Feb$^{\bullet+}$** is consistent with **Feb** transferring an electron to **Aaa$^{\bullet+}$**, because **Feb** cannot directly transfer an electron to ^{1}**DPP*** in the triad. When the rate of electron transfer from **Feb** to **Aaa$^{\bullet+}$** in

Feb-Aaa$^{\bullet+}$ (DPP$^{\bullet-}$) is faster than the charge recombination between **DPP$^{\bullet-}$** and **Aaa$^{\bullet+}$** (and between **DPP**$^{\blacksquare-}$ and **Feb$^{\bullet+}$**) the CT state, **Feb$^{\bullet+}$-Aaa(DPP$^{\bullet-}$)**, will readily accumulate, which is what the TA results show (Figure 8S-25b). These findings suggest that the decay of **^{1}DPP*** involves an electron transfer from **Aaa** leading to **Feb-Aaa$^{\bullet+}$ (DPP$^{\bullet-}$)**. Because **Aaa(^{1}DPP*)** and **Feb-Aaa(^{1}DPP*)** appear to have the same dynamics of deactivation, the decay of **^{1}DPP** in the dyad should leads to a similar CT sate with oxidized **Aaa** and reduced **DPP**, i.e., to **Aaa$^{\bullet+}$ (DPP$^{\bullet-}$)** (Scheme 8S-6).

In summary, all evidence point out that charge transfer is responsible for the observed decrease in the lifetime of the **DPP** singlet excited state when in the dyad, i.e., linked with **Aaa**.

Charge-transfer analysis

Experimentally obtained rates of charge transfer. The difference between the decay rates of the dyads and of **DPP** provides estimates for the rates of the photoinduced CS (Table 8-1, 8S-3):

$$k_{CS} = \frac{1}{\tau_{dyad}} - \frac{1}{\tau_{DPP}} \qquad (8S\text{-}3)$$

Where τ_{dyad} is either $\tau_{Aaa(DPP)}$, or $\tau_{DPP\text{-}Aaa}$. The difference between the non-radiative rate constants, k_{nr} (Table 8S-2), of the dyads and **DPP** gives similar estimates for k_{CS}.

The values of $1/\tau_{DPP\text{-}Aaa}$ and $1/\tau_{DPP}$ for DCM, $CHCl_3$ and toluene, however, differ by less than 10%, and these differences do not have statistical significance. Even if we ascribe the values from $1/\tau_{DPP\text{-}Aaa} - 1/\tau_{DPP}$ to k_{CS}(**DPP-Aaa**) for DCM, $CHCl_3$ and toluene,

they hardly exceed 10^7 s^{-1} (Table 8S-3), while k_{CS}(**Aaa(DPP)**) for the same non-polar solvents are larger than 2×10^9 s^{-1}. That is, k_{CS}(**Aaa(DPP)**) (i.e., the ET along the dipole) would be 200 to 400 times greater than k_{CS}(**DPP-Aaa**) (i.e., the ET against the dipole) for the three non-polar solvents; and it still would be a record-large difference between the rates of ET along vs. against the dipole. Indeed, the differences between k_{nr} for **DPP-Aaa** and **DPP**, i.e., $k_{nr,\text{DPP-Aaa}} - k_{nr,\text{DPP}}$, for these non-polar solvents amount to about 10^{-7} s^{-1} or less (Table 8S-2), which could be assigned to rate constants of slow CS. These values (of 10^{-7} s^{-1} or less), however, are comparable and even smaller than the uncertainties for their estimates. Therefore, it is unfeasible to claim photoinduced CS for **DPP-Aaa** in toluene, chloroform and dichloromethane (Table 8-1).

While for MeCN, the values of k_{CS} are indiscernible within statistical uncertainty (Table 8S-3), decreasing the solvent polarity, increases k_{CS} for **Aaa(DPP)** and suppresses CS for **DPP-Aaa**. Can the dipole of **Aaa** account for the trends in the observed CS rates? To quantify the answer to this question, we focus on the effect on the reduction potential of **DPP** induced by the local electric field from the **Aaa** dipole, and modify the Rehm-Weller (RW) equation to account for it (eq. 8-1). RW formalism allows for estimating the driving force for the transition from the locally-excites states of the dyads, **Aaa(**^{1}**DPP*)** and ^{1}**DPP*-Aaa**, to their CT states, **Aaa**$^{\bullet+}$ **(DPP**$^{\bullet-}$**)** and **DPP**$^{\bullet-}$**Aaa**$^{\bullet+}$.

In the CT state, the reduced acceptor, **DPP**$^{\bullet-}$, experiences the local field from the dipole of the oxidized charged donor, **Aaa**$^{\bullet+}$. The localized field from **Aaa**$^{\bullet+}$ originates from its dipole and from its positive charge. The RW equation accounts for the charge-charge interaction between **Aaa**$^{\bullet+}$ and **DPP**$^{\bullet-}$ via the Coulomb-work term, W (eq. 8-1).[10, 18] RW

equation, however, does not account for the dipole-charge interaction between the oxidized donor and the reduced acceptor. Conversely, the locally excited states of the dyads involve the effect of the dipole from the ground state of **Aaa** on ^{1}**DPP***. Field effects on non-charged species, such as ^{1}**DPP***, however, are considerably smaller than field effects on charged ones, such as **DPP**$^{\bullet-}$. Therefore, we focus on the electrostatic interactions between **Aaa**$^{\bullet+}$ and **DPP**$^{\bullet-}$ in the CT states of the dyads. While the charge-charge interaction between the two radical ions proves favorable by making $\Delta G_{CS}^{(0)}$ more negative (i.e., the term W in the RE equation, eq. 8-1), it is the **Aaa**$^{\bullet+}$ dipole that causes asymmetry in the field around the oxidized donor and produces the observed differences between the CT kinetics of the two dyads.

Dipole potentials and their effect on charge-transfer driving force. As an important characteristic of the electron-transfer kinetics, the driving force, $-\Delta G_{CS}^{(0)}$, represents the energy differences between the CT states (i.e., **Aaa**$^{\bullet+}$ **(DPP**$^{\bullet-}$**)** and **DPP**$^{\bullet-}$**-Aaa**$^{\bullet+}$) and the locally excited states (i.e., **Aaa(**^{1}**DPP*)** and ^{1}**DPP*-Aaa**). Ideally, *ab initio* computed energies of the CT and the locally excited sates of the dyads can serve as a reference for estimating $\Delta G_{CS}^{(0)}$. In addition to the substantial demands on the TD DFT computations presented by the flexibility of the methylene linker, however, relatively high levels of theory, e.g., EOM-CCSD, is essential for predicting dark (i.e., non-fluorescent) CT states that are physical and non-spurious.[19] Therefore, the RW equation provides a feasible and attractive alternative for estimating the CT driving forces from experimental electrochemical and spectroscopic data:[10, 18]

$$\Delta G_{CS}^{(0)} = F\left(E_{D^{\bullet+}|D} - E_{A|A^{\bullet-}}\right) - \mathscr{E}_{00} + \Delta G_S + W \tag{8S-4}$$

Where $E_{D^{\bullet+}|D}$ and $E_{A|A^{\bullet-}}$ are the reduction potentials for oxidation of **Aaa** and reduction of **DPP**, respectively; F is the Faraday constant; E_{00} is the zero-to-zero energy, i.e., optical HOMO-LUMO gap, of the photosensitizer; ΔG_S is the Born solvation energy that accounts for the polarity dependence of $E_{D^{\bullet+}|D}$ and $E_{A|A^{\bullet-}}$;[10] and W is the Coulomb work representing the electrostatic interactions between the formed charged radical ions. Such electrostatic interactions, which the W term can implement, can account for the observed asymmetric CT behavior of the two dyads for non-polar media.

Classic Coulomb expression allows for calculating the distribution of the electric potential around **Aaa**$^{\bullet+}$:

$$\phi(x,y,z) = \frac{1}{4\pi\varepsilon_0\varepsilon}\iiint_{x'y'z'}\frac{\rho_{Aaa^{\bullet+}}(x',y',x')}{\left|\mathbf{r}(x,y,x) - \mathbf{r}'(x',y',x')\right|}dx'dy'dz' \approx \frac{1}{4\pi\varepsilon_0\varepsilon}\sum_{i=1}^{n}\frac{q_i}{\left|\mathbf{r}(x,y,z) - \mathbf{r}_i(x_i,y_i,z_i)\right|} \tag{8S-5}$$

Where the integrated potential from the charge density, ρ, can be approximated to the cumulative effect of the multiple discreet charges, q, that **Aaa**$^{\bullet+}$ contains, such the charges of its n atoms (Figure 8S-26).

The cationic nature of **Aaa**$^{\bullet+}$ dominates the electric potential around it, and outside the van der Waals boundaries of **Aaa**, $\varphi_{Aaa^{\bullet+}}(x,y,z)$ appears to assume almost spherical symmetry (Figure 8S-26b,c). Conversely, while the center of mass of **Aaa** sets origin of the coordinate system, i.e., $\varphi(0,0,0)$, inside its aromatic ring, the isopotential surfaces are

shifted by about 5 Å in the positive direction of the *x* axis which is set along the dipole (Figure 8S-26a-c).

A superposition of the electric potential, $\varphi_{\boldsymbol{\mu}}$, around the **Aaa**$^{\bullet+}$ dipole (from DFT calculations, Table S1) and the potential, φ_Q, around the point charge, Q, of the radical cation reproduces the asymmetry of $\varphi_{\mathrm{Aaa}_\bullet}{}^{+}(x,y,z)$ obtained from eq. 8S-5 (Figure 8S-26d):

$$\phi(x,y,z) = \phi_Q(x,y,z) + \phi_{\boldsymbol{\mu}}(x,y,z) \tag{8S-6a}$$

$$\phi_Q(x,y,z) = \frac{Q}{4\pi\varepsilon_0\varepsilon R(x,y,z)} \tag{8S-6b}$$

$$\phi_{\boldsymbol{\mu}}(x,y,z) = \frac{q}{4\pi\varepsilon_0\varepsilon}\left(\frac{1}{R_+(x,y,z)} - \frac{1}{R_-(x,y,z)}\right) \tag{8S-6c}$$

Where R is the distance between a point with coordinates (*x*,*y*,*z*) and the point charge or the center of the dipole; and R_+ and R_- are the distances between a point with coordinates (*x*,*y*,*z*) and the positive and negative poles of the dipole, respectively (Figure 8S-26e,g):

$$R_\pm(x,y,z) = \sqrt{R^2(x,y,z) + (d/2)^2 \mp d\ R_\pm(x,y,z)\cos(\theta)} \tag{8S-6d}$$

Except the slight underestimation of $\varphi_{\mathrm{Aaa}_\bullet}{}^{+}(x,y,z)$ along the *x* axis by the charge-dipole-superposition treatment (Figure 8S-26b,c vs. Figure 8S-26d), this approximation presents a reasonable and straightforward approach for estimating the distribution of the electric potential around the oxidized donor.

In this type of analysis, the multipole expansion for the potential originating from distribution of charges within ionic species should be approached with caution. Generalizing eq. 8S-6 yields:

$$\phi(x,y,z) \approx \frac{1}{4\pi\varepsilon_0\varepsilon}\sum_{i=1}^{n}\frac{Q^{(i-1)}}{R^i(x,y,z)} \qquad \text{(8S-7a)}$$

Where $Q^{(i)}$ is magnitude of i^{th}-order multipole (from an i^{th}-order tensor, $\mathbf{Q}^{(i)}$, that represents it), e.g., $Q^{(0)}$ is the total charge, and $Q^{(1)}$ is the dipole magnitude projected on $R(x,y,z)$, i.e., $Q^{(1)} = |\boldsymbol{\mu}| \cos(\theta)$. The electric potentials from quadrupoles, $\mathbf{Q}^{(2)}$, and higher order multipoles, become important only for truly short distances, R, around symmetric structures. The total charge, Q, and the dipole, $\boldsymbol{\mu}$, can be readily estimated from the n charges and their distribution within a system:

$$Q^{(0)} = Q = \sum_{i=1}^{n} q_i \qquad \text{(8S-7b)}$$

$$\mathbf{Q}^{(1)} = \boldsymbol{\mu} = \sum_{i=1}^{n} q_i(\mathbf{r}_i - \mathbf{r}_0) \qquad \text{(8S-7c)}$$

Where $\mathbf{r}_i$ is the vector determining the position of charge q_i, and $\mathbf{r}_0$ is a vector representing the coordinates of a reference for the multipole expansion.

While the generalization of eq. S6a readily produces eq. 8S-7a, the definition of dipoles and higher order multipoles is not as straightforward for charged species. When $Q^{(0)} \neq 0$, the dipole depends on the position of the reference, $\mathbf{r}_0$ (eq. 8S-7c). That is, dipole

moments, obtained from the multipole expansion for charged moieties, depend on the reference $\mathbf{r}_0$. The use of center of mass as a reference, $\mathbf{r}_0$, provides a common means for a reliable multipole expansion for charged species. Therefore, for all our analysis, the origins of each coordinate system is placed at the molecular center of mass, $\mathbf{r}_{CM}$, and the dipoles of the charge radicals, e.g., **Aaa**$^{\bullet+}$, estimated for $\mathbf{r}_0 = \mathbf{r}_{CM}$ could be referred as "electroinertial."

The distribution of the electric potential, $\varphi_{\mathrm{Aaa}^{\bullet+}}$, around the oxidized donor, obtained from eq. 8S-5, 8S-6 and 8S-7, proves key for estimating the Coulomb term, W, of the RW equation (eq. 8S-4):

$$W = \iiint_{x\,y\,z} \rho_{\mathrm{DPP}^{\bullet-}}(x,y,x)\,\phi_{\mathrm{Aaa}^{\bullet+}}(x,y,x)\,dx\,dy\,dz \approx \sum_{i=1}^{n} q_{\mathrm{DPP}^{\bullet-},\,i}(x,y,x)\,\phi_{\mathrm{Aaa}^{\bullet+}}(x,y,x) \approx Q_{\mathrm{DPP}^{\bullet-}}(x,y,z)\,\phi_{\mathrm{Aaa}^{\bullet+}}(x,y,z)$$

(8S-8a)

Where $\rho_{\mathrm{DPP}^{\bullet-}}$ and $q_{\mathrm{DPP}^{\bullet-}}$ are the charge density and the charges, respectively, of the reduced acceptor. The use of the total charge of **DPP**$^{\bullet-}$, $Q_{\mathrm{DPP}^{\bullet-}}$, represents a point-charge approximation:

$$\Delta G_{\mathrm{CS}}^{(0)} = F\left(E_{\mathrm{D}^{\bullet+}\mathrm{lD}} - E_{\mathrm{AlA}^{\bullet-}}\right) - \mathscr{C}_{00} + \Delta G_S + Q_{\mathrm{DPP}^{\bullet-}}(x,y,z)\,\phi_{\mathrm{Aaa}^{\bullet+}}(x,y,z) \qquad \text{(8S-8b)}$$

Separating the electric potential around **Aaa**$^{\bullet+}$ into the contributions from its charge and its dipole (eq. S6) provides a reasonable approximation (i.e., Figure 8S-26b,c vs. Figure 8S-

26d). Therefore, we can rearrange eq. S8b to represent the dipole contribution to the driving force as a separate term:

$$\Delta G_{\mathrm{CS},\boldsymbol{\mu}}^{(0)} = F\left(E_{\mathrm{D}^{\bullet+}|\mathrm{D}} - \left(E_{\mathrm{A}|\mathrm{A}^{\bullet-}} + \phi_{\boldsymbol{\mu}}\left(\theta_{\boldsymbol{\mu}}, \alpha_{\mathrm{DA}}, R_{\mathrm{DA}}, \varepsilon\right)\right)\right) - \mathscr{E}_{00} + \Delta G_S + \frac{Q_{\mathrm{DPP}^{\bullet-}} Q_{\mathrm{Aaa}^{\bullet+}}}{4\pi\varepsilon_0 \varepsilon R_{\mathrm{DA}}} \tag{8S-8c}$$

The last rearrangement produces eq. S8c, which is eq. 1, and setting $\varphi_{\boldsymbol{\mu}} = 0$ results in the RW equation broadly used for CT analysis. Indeed, eq. 8S-8b and 8S-8c are quite flexible for implementing explicitly the electric potential terms as outelined in eq. S8a, as well as eq. 8S-5 and 8S-6.

While eq. 8S-8b and eq. 8S-8c produce identical results, separating $\varphi_{\boldsymbol{\mu}}$ from the W term provides an important illustration about the contribution of molecular dipoles to the CT driving force. Grouping $\varphi_{\boldsymbol{\mu}}$ with the reduction-potential terms emphasizes that the effects from the dipole-generated fields can be viewed as intramolecular Stark effects. Indeed, Stark effects on CT involve modulation of the reduction potentials of the donor and acceptor.

Indeed, to account for the dipole effect on $\Delta G_{\mathrm{CS}}^{(0)}$, we consider the shift in the reduction potential of **DPP** in the presence of externally applied field. Indeed, the "external field" originates from the dipole of the donor, which underlines the reason for adding the potential $\phi_{\boldsymbol{\mu}}$ to the reduction potential of **DPP** (eq. 8-1, 8S-8c).

A point-charge approximation of **DPP**$^{\bullet-}$ involves $\theta \approx \theta_{\boldsymbol{\mu}}$ and $R \approx R_{\mathrm{DA}}$ (Figure 8-1a,b and 8S-26g). Varying $\theta_{\boldsymbol{\mu}}$ requires structural changes of the dyads and changes R_{DA}.

Presenting R_{DA} as a function of θ_{μ} reduces the number of variables. Because of the preference for conformers with θ_{μ} close to 0° (for **Aaa(DPP)**) and 180° (for **DPP-Aaa**) as revealed by the computational studies, we focus on **Aaa(DPP)** structures with θ_{μ} varying between 0° and 20°, and on **DPP-Aaa** structures with θ_{μ} between 160° and 180°.

Point-charge approximation is attractive due to its simplicity for implementing it in kinetic analysis. The dimensions of **DPP**, however, are comparable with R_{DA}. Therefore, we also integrate ϕ_{μ} over the span of **DPP** and estimate the average dipole potential that the acceptor experiences for each value of θ_{μ}. Such averaged potentials are slightly smaller than the potentials that the point-charge approximation yields, but overall result in the same trends, validating the relatively simple straightforward analysis as implemented by the modified RW equation.

For each dyad and each solvent, the modified RW equation (eq. 8S-8c, eq. 8-1) allows for estimating the driving force $\Delta G_{CS,\mu}^{(0)}$ in the presence of the **Aaa**$^{\bullet+}$ dipole, as well as the driving force $\Delta G_{CS}^{(0)}$ in the absence of any dipole by setting φ_{μ} to zero, i.e., $\Delta G_{CS}^{(0)} = \Delta G_{CS,\mu}^{(0)}$ ($\varphi_{\mu} = 0$). Comparison between $\Delta G_{CS,\mu}^{(0)}$ and $\Delta G_{CS}^{(0)}$ reveals how the dipole affects the CS in the dyads. For MeCN, CS occurs in both dyads and should occur even in the absence of the **Aaa**$^{\bullet+}$ dipole. For DCM, both dyads should mediate CS if a dipole were not present. The introduction of the **Aaa**$^{\bullet+}$ dipole induces ET rectification by enhancing the rate for **Aaa(DPP)** and completely suppresses the CS mediated by **DPP-Aaa** (Table 8-2). For toluene, the dipole not only causes CS rectification, but also makes the photoinduced ET possible (Table 8-2).

Kinetic analysis. These trends revealed by the dipole effect on $\Delta G_{CS}^{(0)}$ are consistent with the observed solvent-dependence of the CS kinetics (Table 8-1, 8S-3). (1) The CS rates for MeCN are practically the same for both dyads. (2) For **Aaa(DPP)**, the CS rates for DCM, $CHCl_3$ and toluene are about six times faster than for MeCN. (3) For **Aaa-DPP**, DCM, $CHCl_3$ and toluene suppress CS. While (3) is consistent with $\Delta G_{CS,\boldsymbol{\mu}}^{(0)} > 0$, to examine if the dipole effect can account for (1) and (2), we implement Marcus-Hush (MH), eq. S9a, and Marcus-Levich-Jortner (MLJ) , eq. 8S-9b, formalisms to test if the driving forces $\Delta G_{CS,\boldsymbol{\mu}}^{(0)}(\theta_{\boldsymbol{\mu}})$, obtained from eq. 8-1 can relate to the rate constants extracted from the time-resolved spectroscopy results:

$$k_{CS} = \frac{4\pi^2}{h}\left|H_{if}\right|^2 \frac{1}{\sqrt{4\pi\lambda k_B T}} \exp\left(-\frac{\left(\Delta G_{CS,\boldsymbol{\mu}}^{(0)} + \lambda\right)^2}{4\lambda k_B T}\right) \tag{8S-9a}$$

$$k_{CS} = \frac{4\pi^2}{h}\left|H_{if}\right|^2 \frac{\exp\left(-S_C\right)}{\sqrt{4\pi\lambda_S k_B T}} \sum_{j=0}^{\infty} \frac{S_C^i}{j!} \exp\left(-\frac{\left(\Delta G_{CS,\boldsymbol{\mu}}^{(0)} + \lambda_S + jh\langle\nu_C\rangle\right)^2}{4\lambda_S k_B T}\right) \tag{8S-9b}$$

Where H_{if} is the coupling between the initial locally excited state and the final CT state, which represents the donor-acceptor electronic coupling; S_C is the Huang-Rhys parameter, $S_C = \lambda_v / h\langle\nu_C\rangle$; $\langle\nu_C\rangle$ is an average high-frequency mode contributing to the CS kinetics; T is the temperatire; and h and k_B are the Planck and Boltzmann's constants, respectively. The reorganization energy, λ, is separated into solvent reorganization energy, λ_S, and inner

vibrational reorganization energy, λ_v, i.e., $\lambda = \lambda_S + \lambda_v$. For estimating λ_S, we use the classical Marcus expression:

$$\lambda_S = \frac{\gamma e^2}{4\pi\varepsilon_0}\left(\frac{1}{2r_{\mathrm{Aaa}}} + \frac{1}{2r_{\mathrm{DPP}}} - \frac{1}{R_{\mathrm{DA}}}\right) \tag{8S-9c}$$

Where γ is a polarity function (for a solvent with a refractive index n and a relative dielectric constant ε), which is based on the contributions from the orientational and nuclear polarization to the Born solvation energy, $\gamma = n^{-2} - \varepsilon^{-1}$; r_{Aaa} and r_{DPP} are the Born effective radii of the donor and the acceptor; ε_0 is the electric permittivity of vacuum; and e is the transferred charge.

In the MH equation (eq. 8S-9a), varying the values of λ_v varied between 0.01 and 1 eV, and of H_{if} – between 10^{-4} and 0.1 eV, allows for finding combination of H_{if} and λ_v that yields k_{CS} close to the experimentally obtained ones (Figure 3a-d). The same procedure, using the MLJ equation (eq. S9b), allows for testing if any high-frequency modes may be involved in the CS kinetics, where $h\langle\nu_C\rangle$ is varied between 0.05 and 0.4 eV. Decreasing $\langle\nu_C\rangle$ improves the match between the paramteres that can yield k_{CS} matching the experiemtnal ones for the different solvents, suggesting that high frequencies do not noticeably contribute to the CS kinetics of the dyads.

To generalize this analysis, we allow the driving force to vary indpendently, while keeping all other parameters inhernet for the dyads and the solvents parameters. The thus

gneeretaed Marcus curves show that decreasing $\theta_{\boldsymbol{\mu}}$ improves the match between the estimated $\Delta G_{CS,\boldsymbol{\mu}}^{(0)}$ and the experiemtnally obtained k_{CS} (Figure 8S-27).

The experimental results for non-polar solvents suggest for ET for **Aaa(DPP)** vs. no ET for **DPP-Aaa**. Changing the donor-acceptor electronic coupling can accelerate or slow down the ET, but cannot completely shut it off, i.e., it cannot be that small over the two σ-bonds of the linker. Therefore, the observed differences between the photopohysics of the two dyads are most likely corollary of differences in the driving force, i.e., $\Delta G_{CS,\boldsymbol{\mu}}^{(0)} < 0$ for **Aaa(DPP)** vs. $\Delta G_{CS,\boldsymbol{\mu}}^{(0)} > 0$ for **DPP-Aaa**. The kinetic analysis shows that the $\Delta G_{CS,\boldsymbol{\mu}}^{(0)}$ estimates can feasibly yield the observed k_{CS}.

Figures

NMR spectra of new compounds and key intermediates

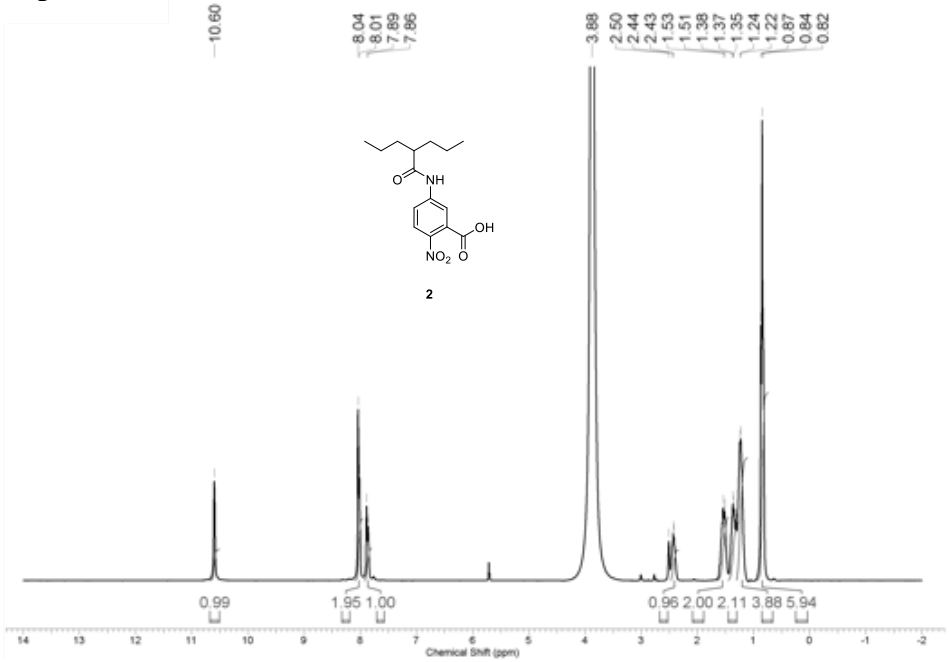

a

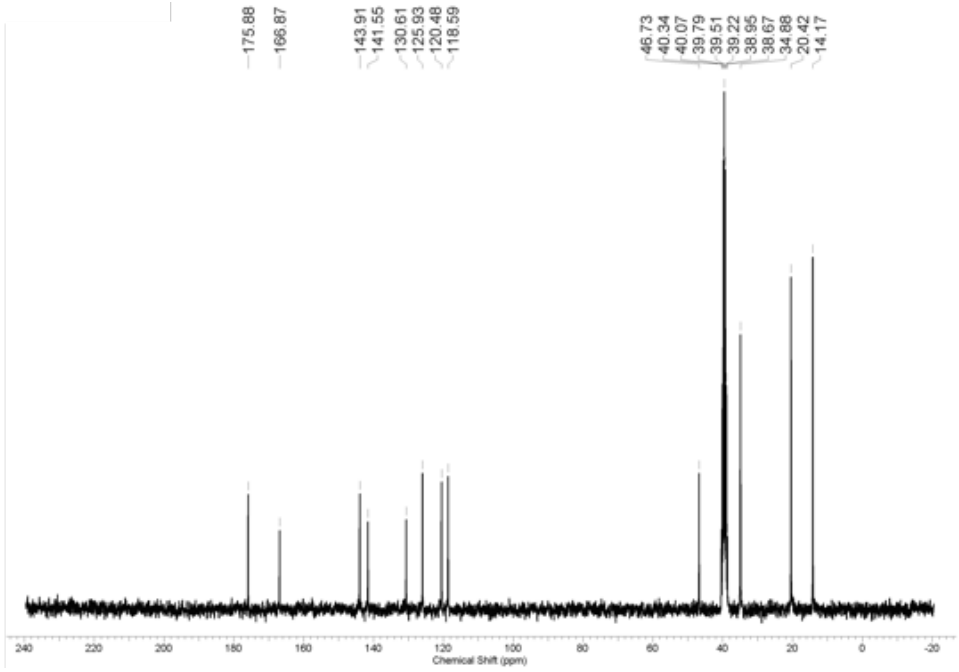

b

Figure 8S-1. (a) ^{1}H NMR of **2** (300 MHz, DMSO-d_6); (b) ^{13}C NMR of **2** (75 MHz, DMSO-d_6)

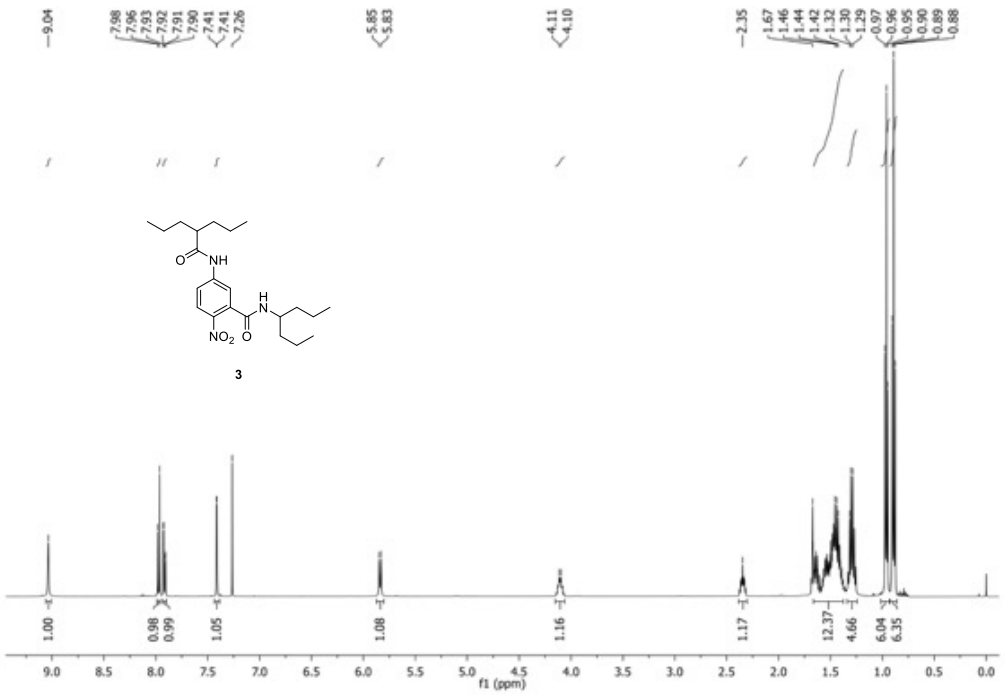

a

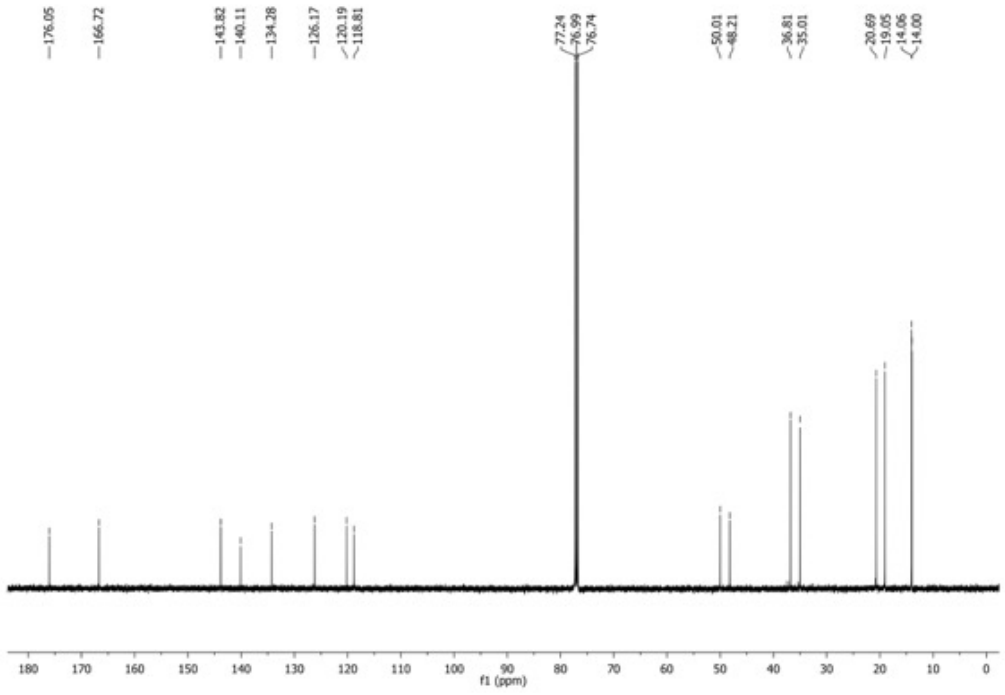

b

Figure 8S-2. (a) ^{1}H NMR of **3** (500 MHz, $CDCl_3$); (b) ^{13}C NMR of **3** (125 MHz, $CDCl_3$)

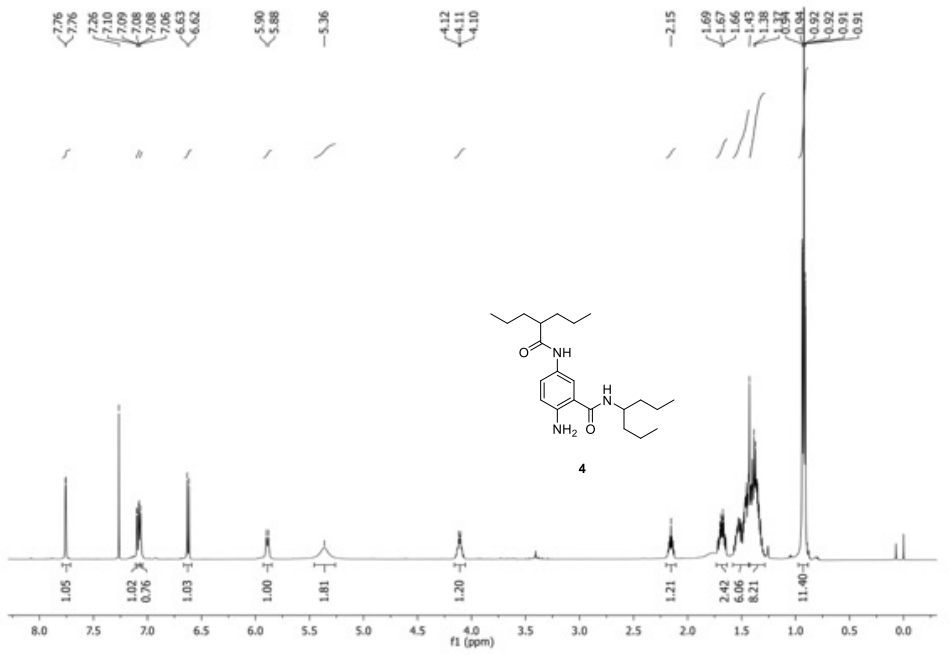

a

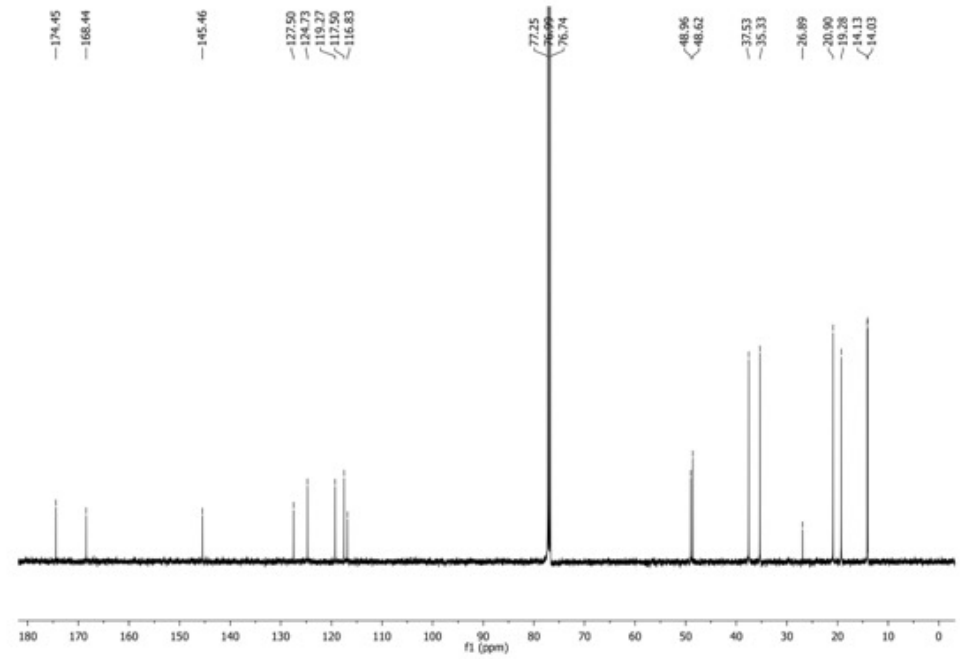

b

Figure 8S-3. (a) ^{1}H NMR of **4** (500 MHz, $CDCl_3$); (b) ^{13}C NMR of **4** (125 MHz, $CDCl_3$)

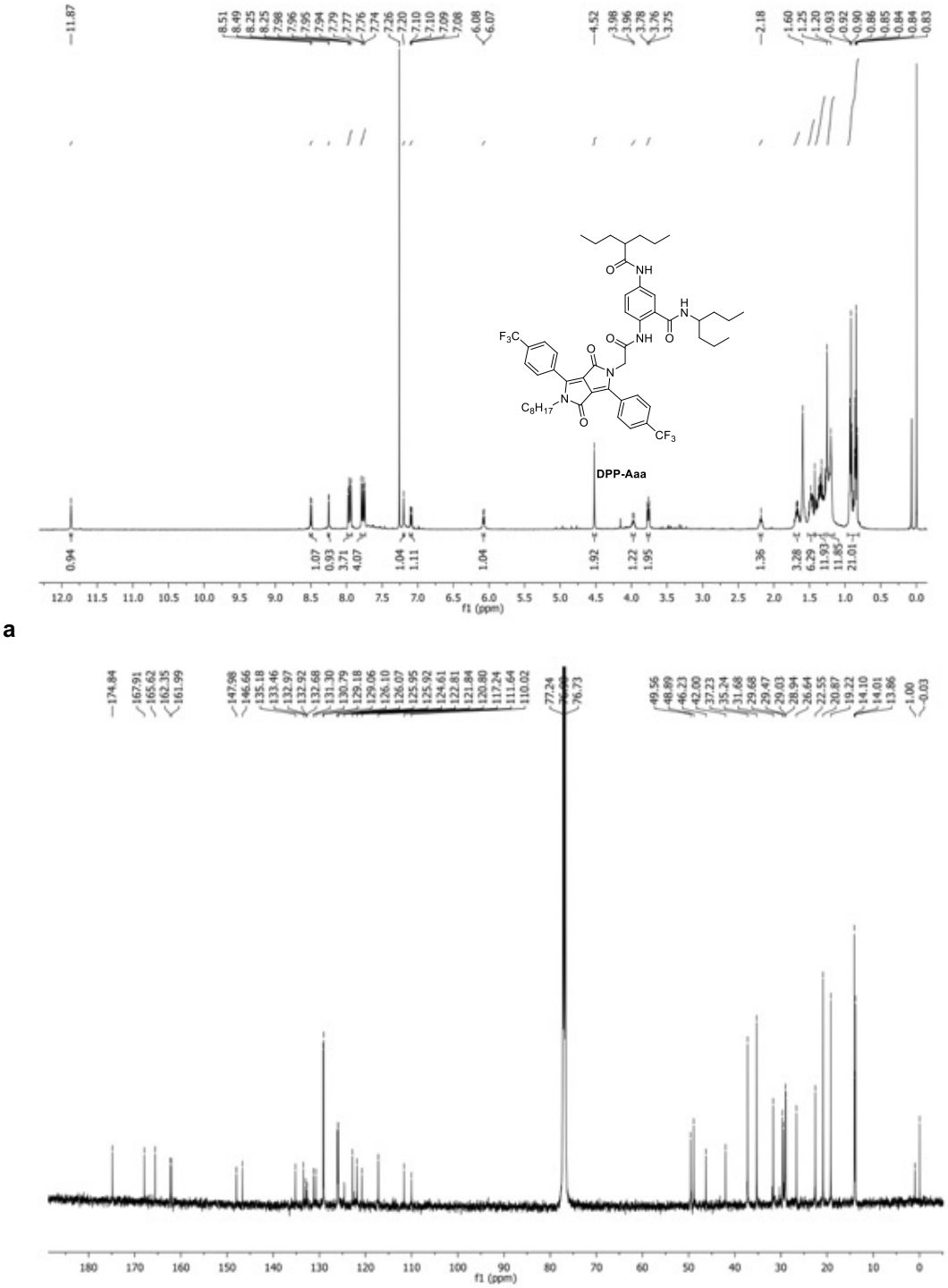

Figure 8S-4. (a) ^{1}H NMR of **DPP-Aaa** (500 MHz, $CDCl_3$); (b) ^{13}C NMR of **DPP-Aaa** (125 MHz, $CDCl_3$)

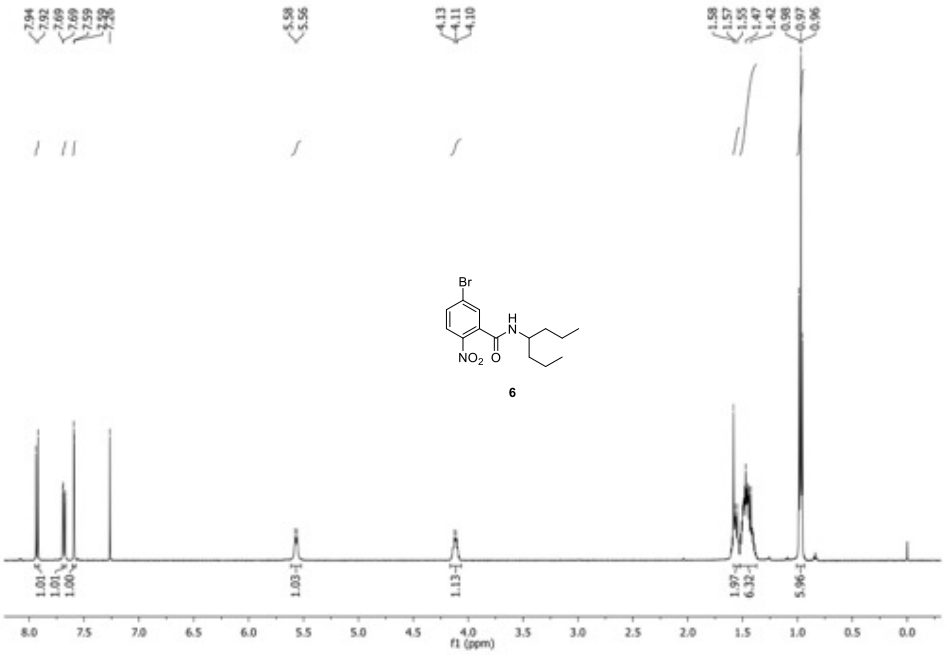

a

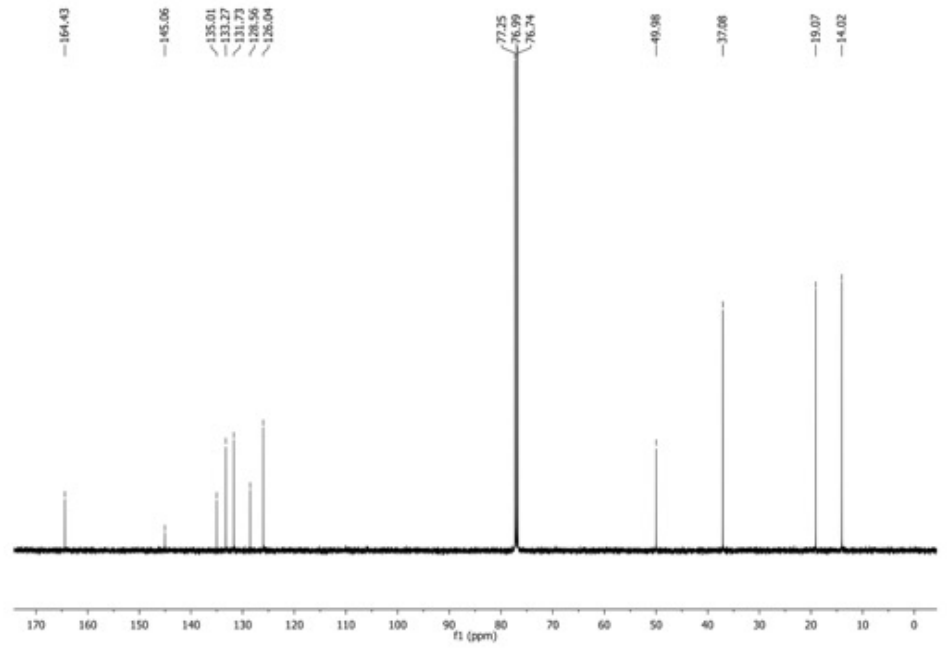

b

Figure 8S-5. (a) ^{1}H NMR of **6** (500 MHz, $CDCl_3$); (b) ^{13}C NMR of **6** (125 MHz, $CDCl_3$)

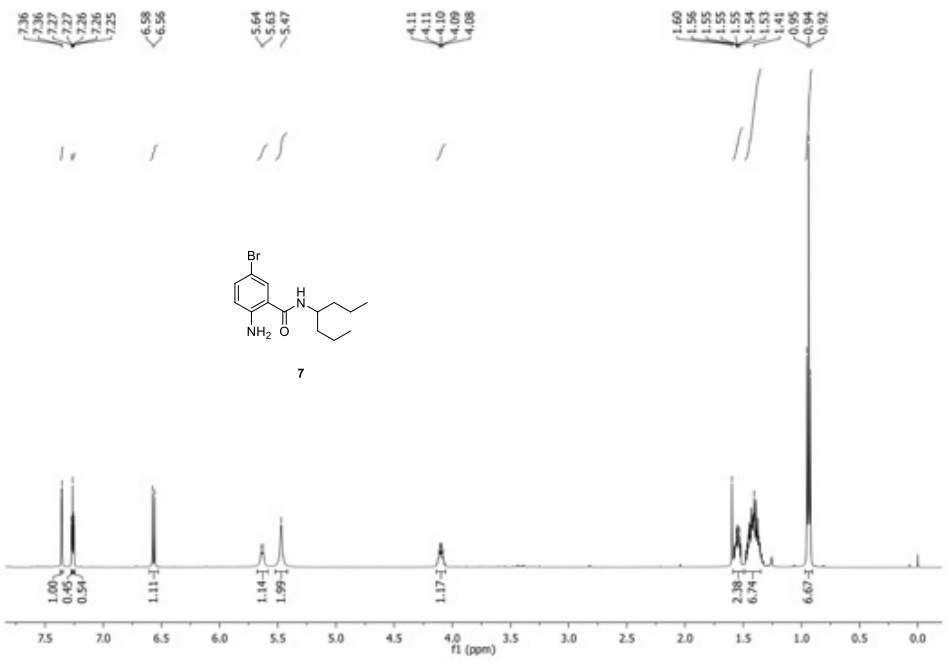

a

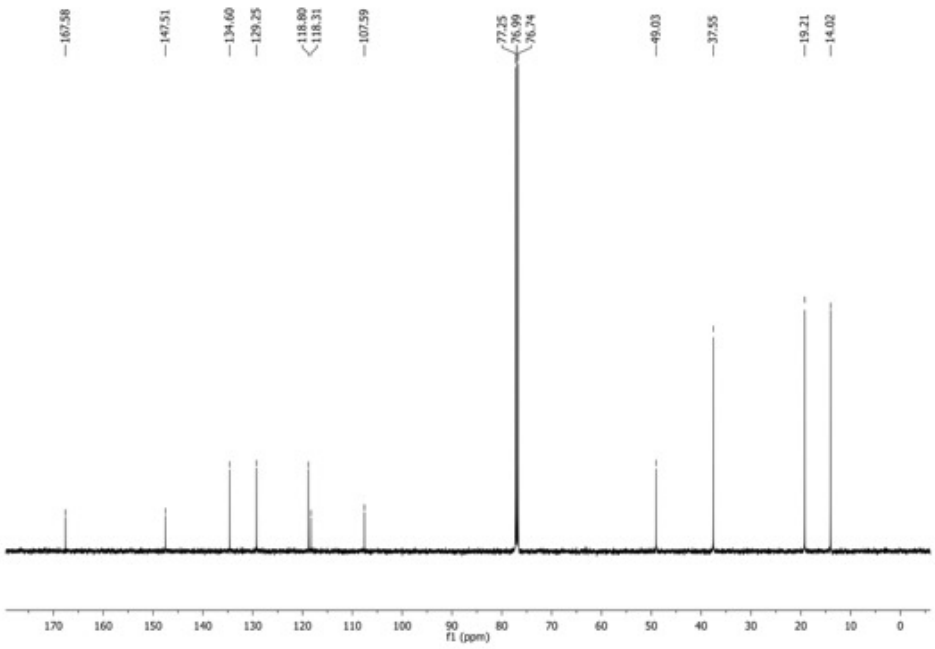

b

Figure 8S-6. (a) ^{1}H NMR of **7** (500 MHz, $CDCl_3$); (b) ^{13}C NMR of **7** (125 MHz, $CDCl_3$)

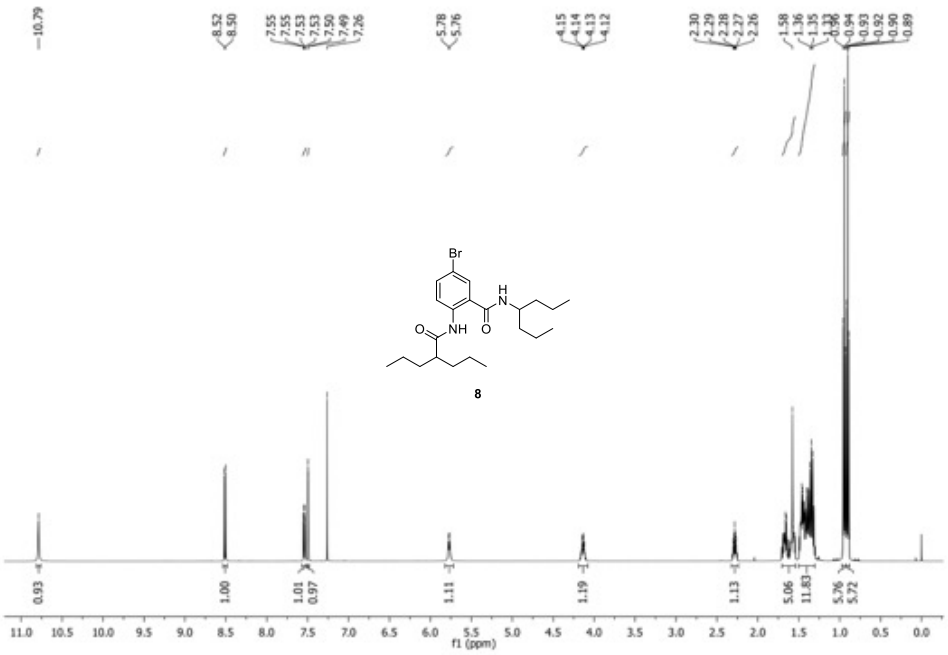

a

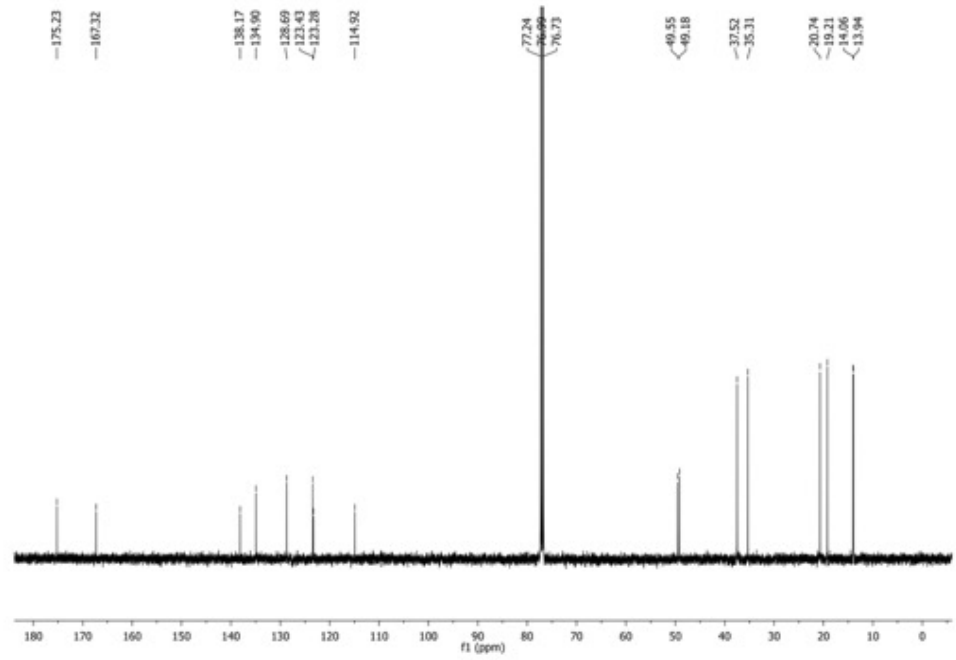

b

Figure 8S-7. (a) ^{1}H NMR of **8** (500 MHz, $CDCl_3$); (b) ^{13}C NMR of **8** (125 MHz, $CDCl_3$)

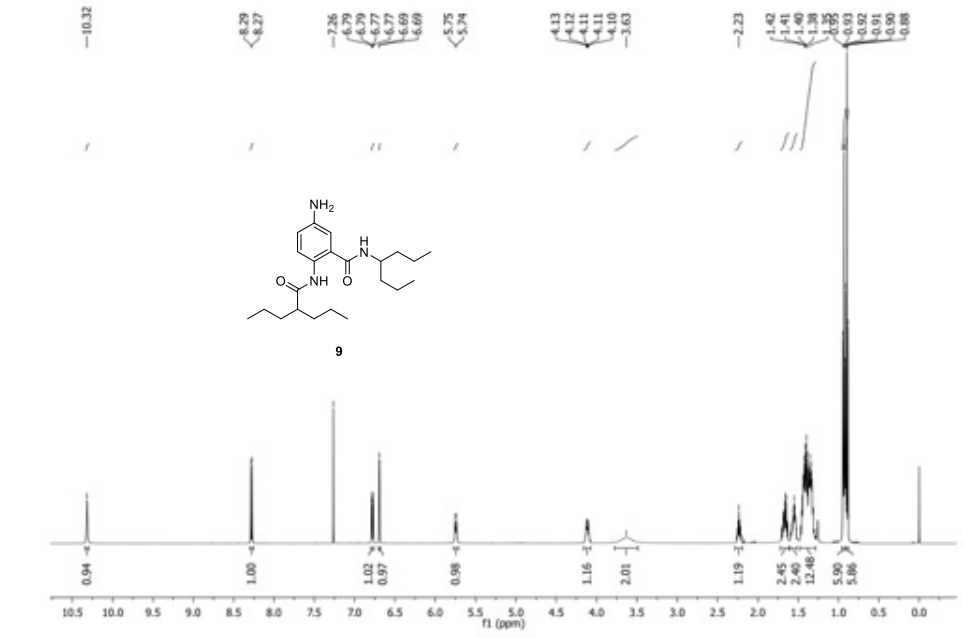

a

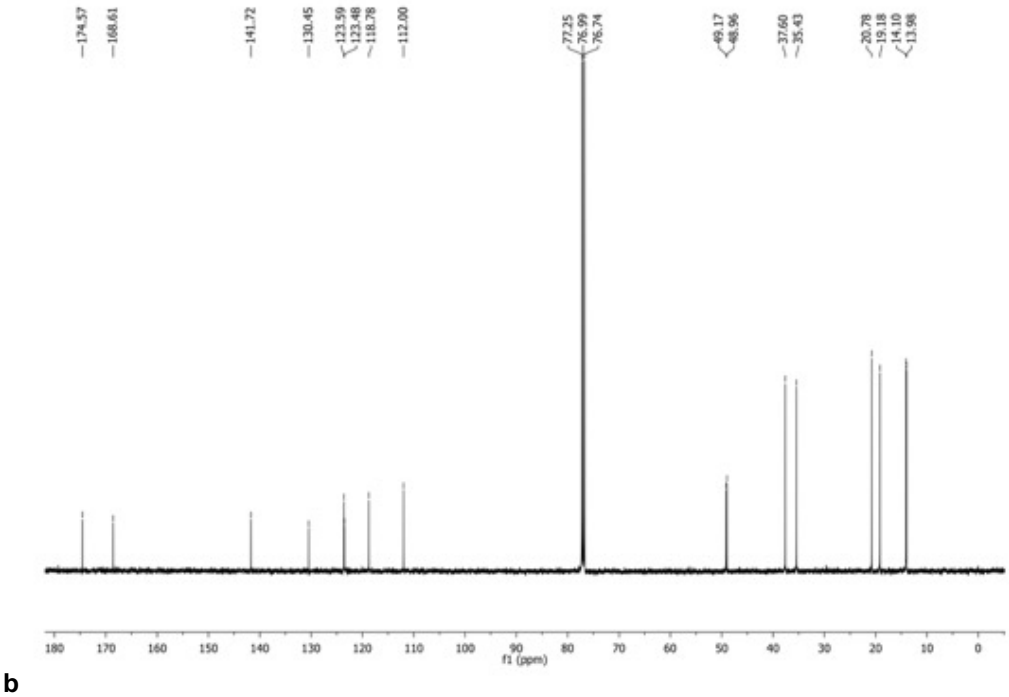

b

Figure 8S-8. (a) ^{1}H NMR of **9** (500 MHz, $CDCl_3$); (b) ^{13}C NMR of **9** (125 MHz, $CDCl_3$)

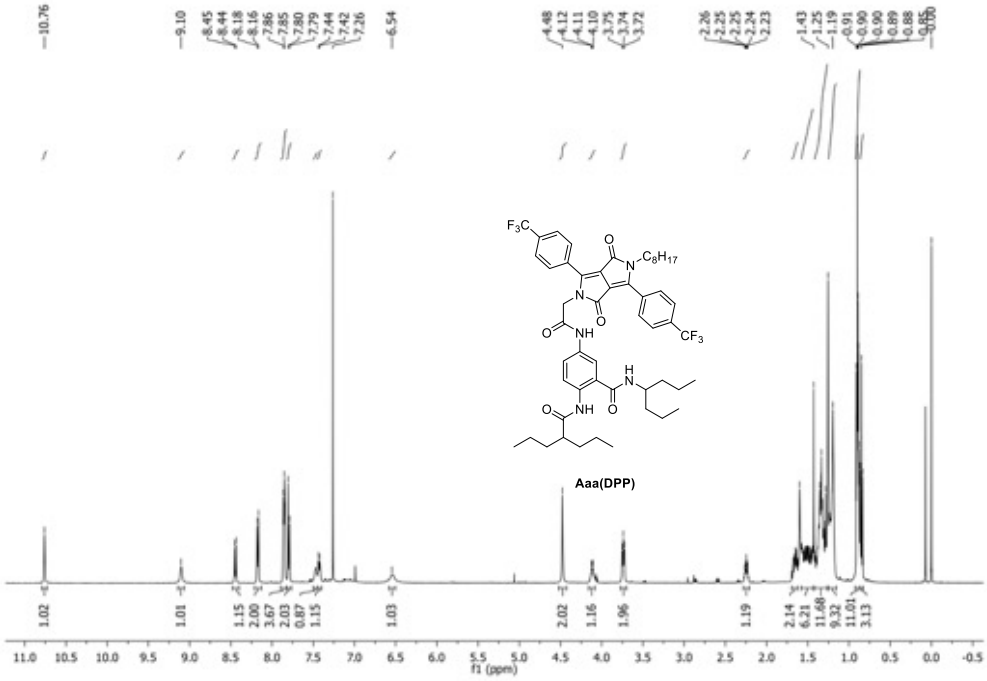

a

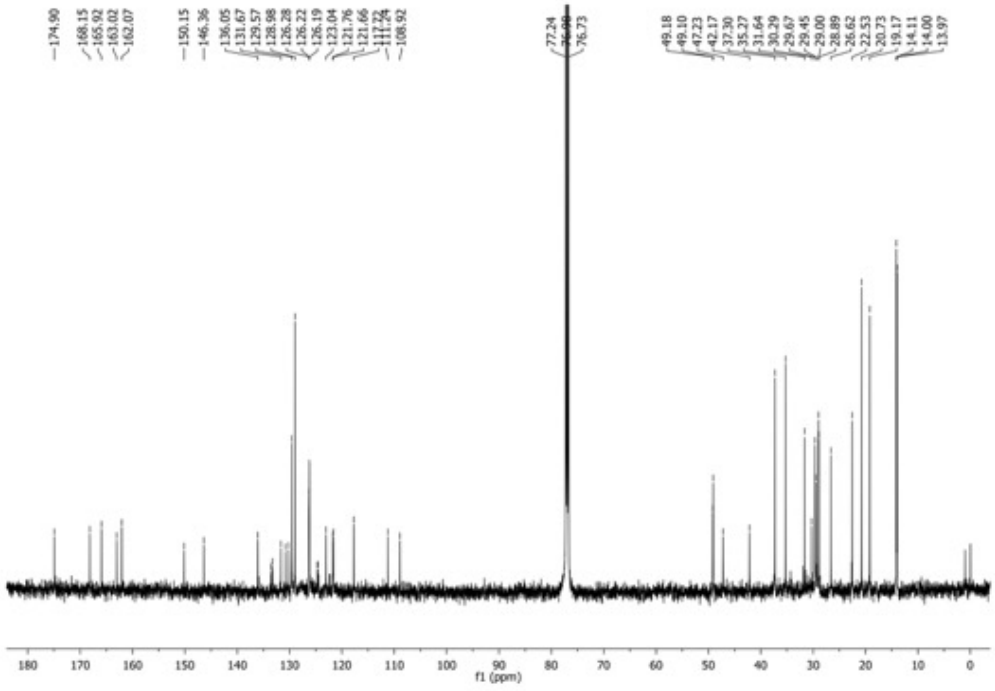

b

Figure 8S-9. (a) ^{1}H NMR of **Aaa(DPP)** (500 MHz, $CDCl_3$); (b) ^{13}C NMR of **Aaa(DPP)** (125 MHz, $CDCl_3$)

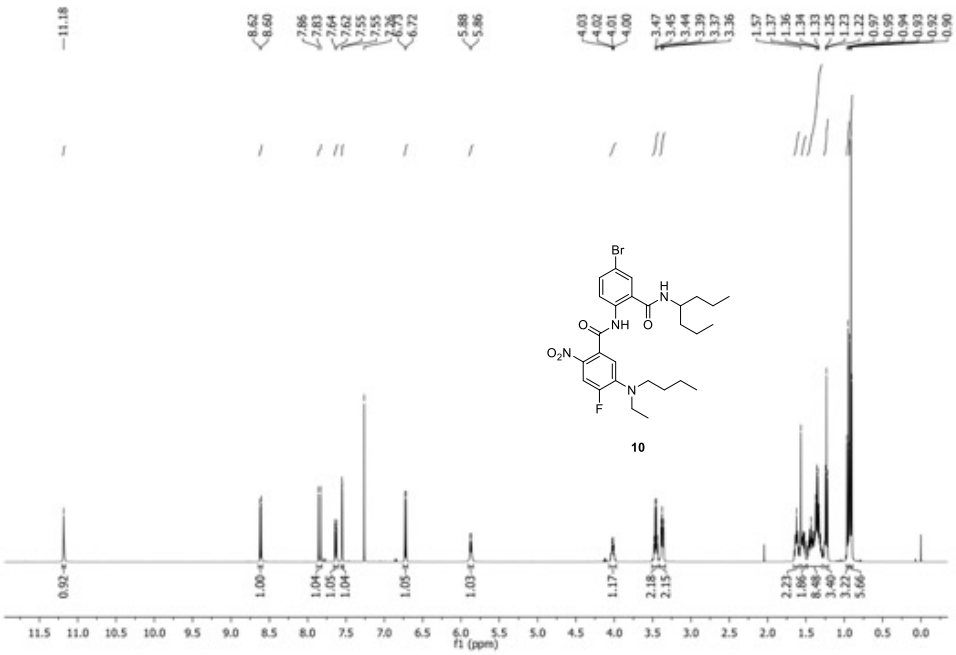

a

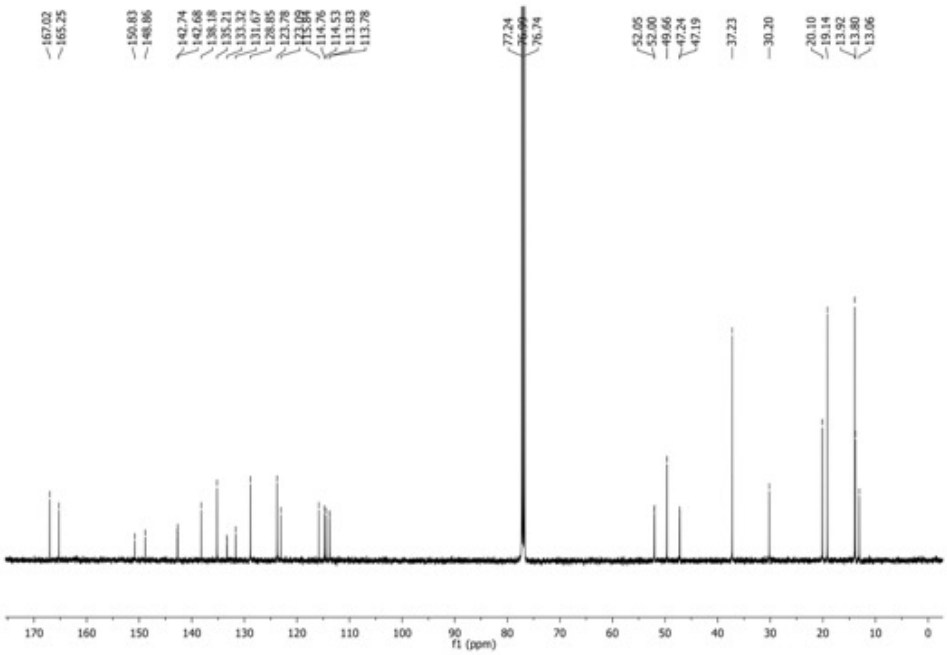

b

Figure 8S-10. (a) ^{1}H NMR of **10** (500 MHz, $CDCl_3$); (b) ^{13}C NMR of **10** (125 MHz, $CDCl_3$)

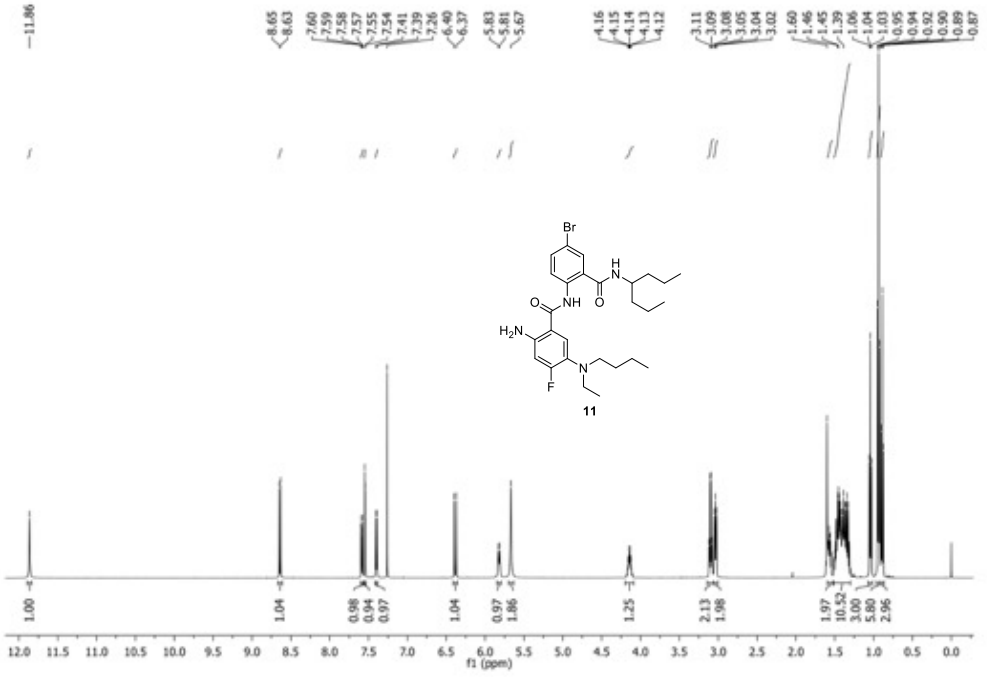

a

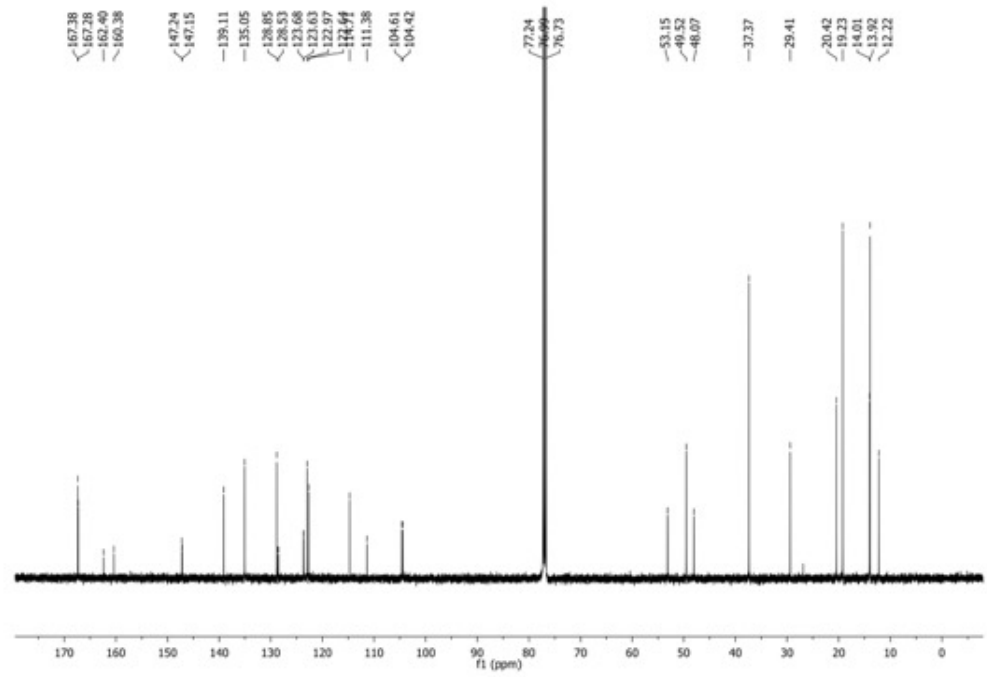

b

Figure 8S-11. (a) ^{1}H NMR of **11** (500 MHz, $CDCl_3$); (b) ^{13}C NMR of **11** (125 MHz, $CDCl_3$)

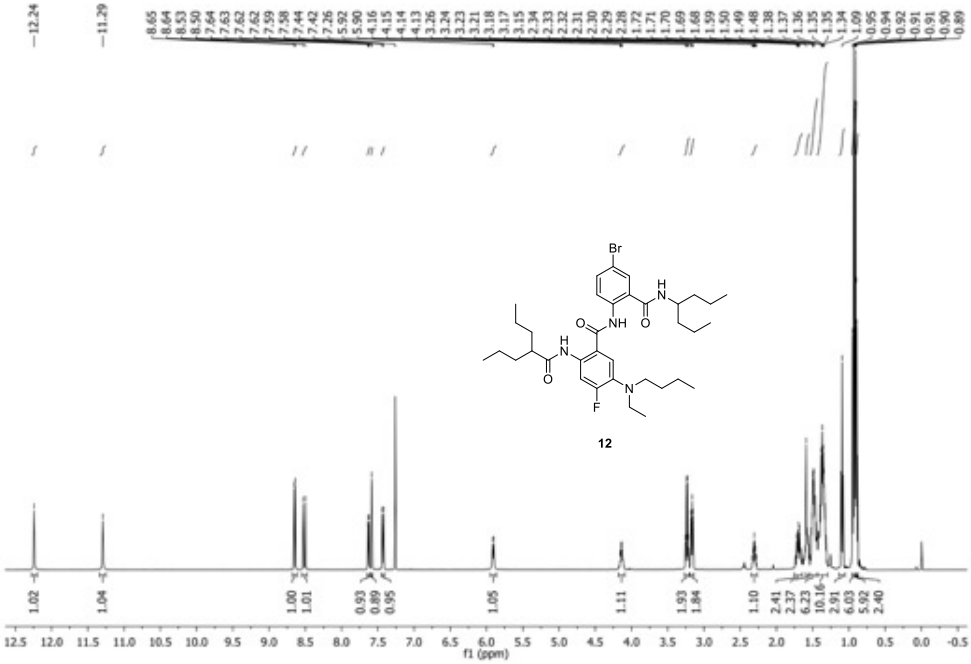

a

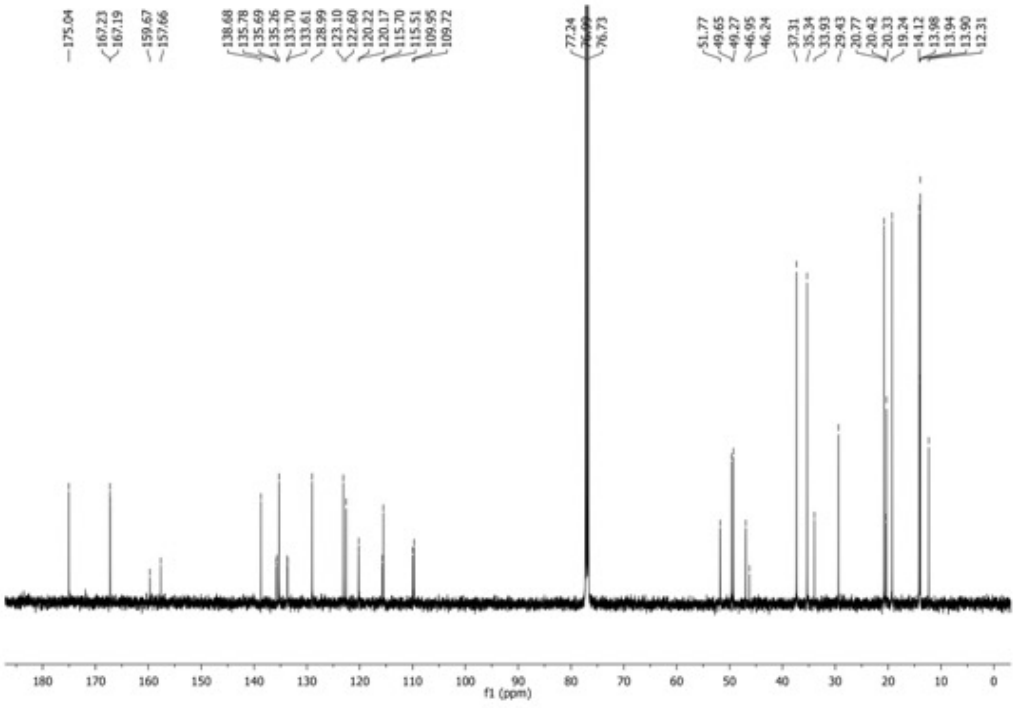

b

Figure 8S-12. (a) ^{1}H NMR of **12** (500 MHz, $CDCl_3$); (b) ^{13}C NMR of **12** (125 MHz, $CDCl_3$)

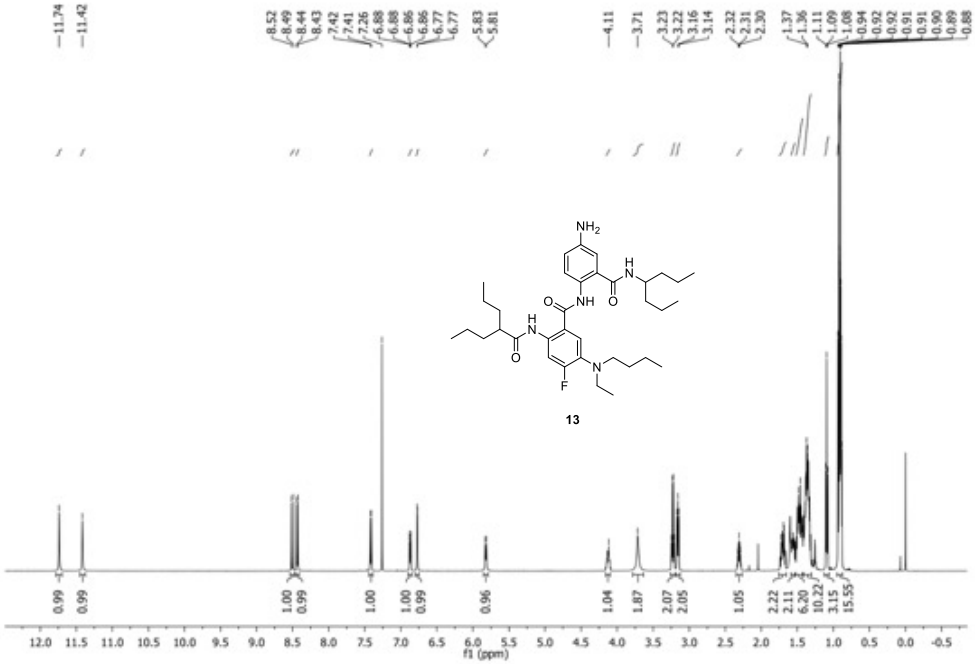

a

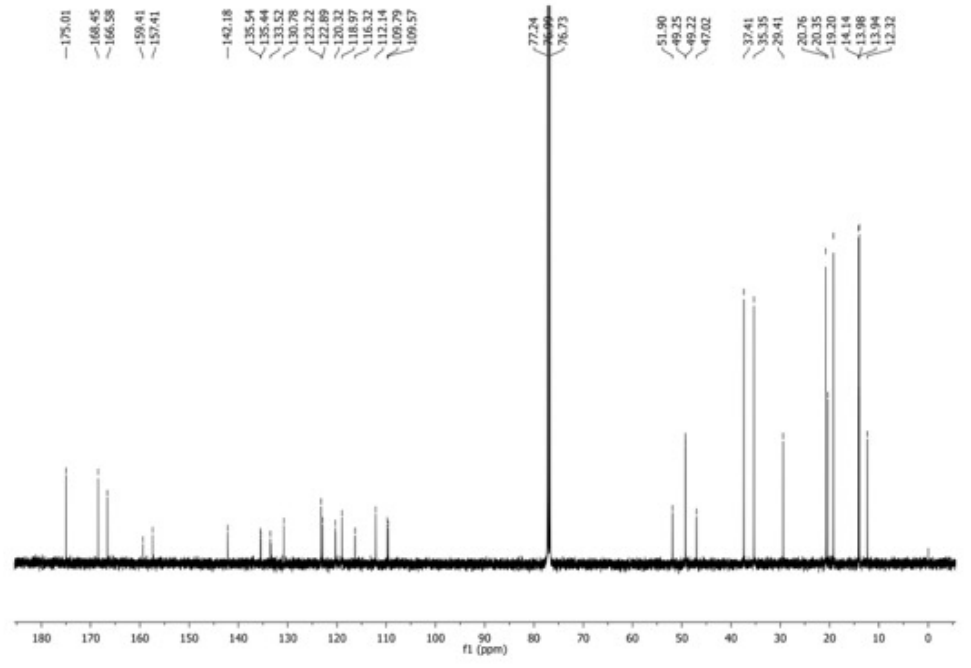

b

Figure 8S-13. (a) ^{1}H NMR of **13** (500 MHz, $CDCl_3$); (b) ^{13}C NMR of **13** (125 MHz, $CDCl_3$)

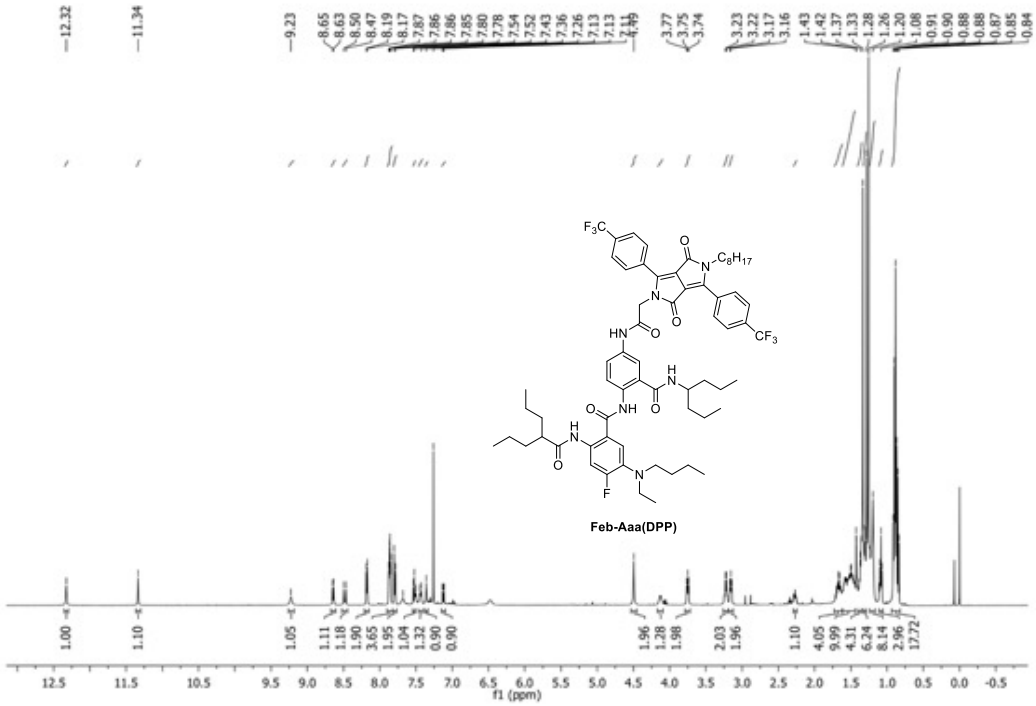

a

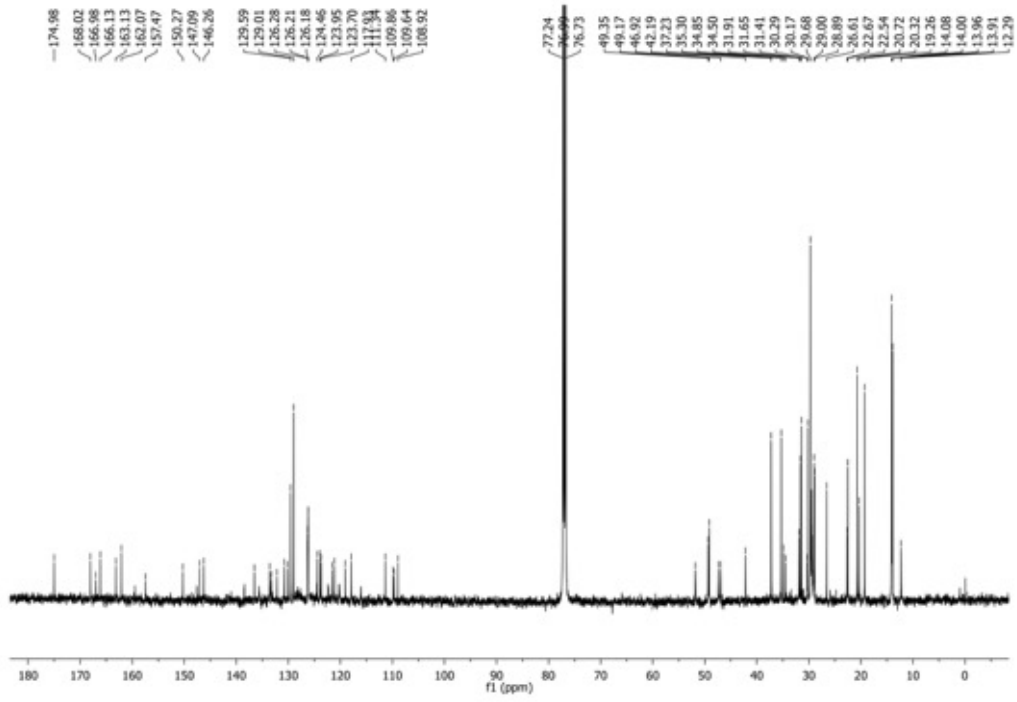

b

Figure 8S-14. (a) ^{1}H NMR of **Feb-Aaa(DPP)** (500 MHz, $CDCl_3$); (b) ^{13}C NMR of **Feb-Aaa(DPP)** (125 MHz, $CDCl_3$)

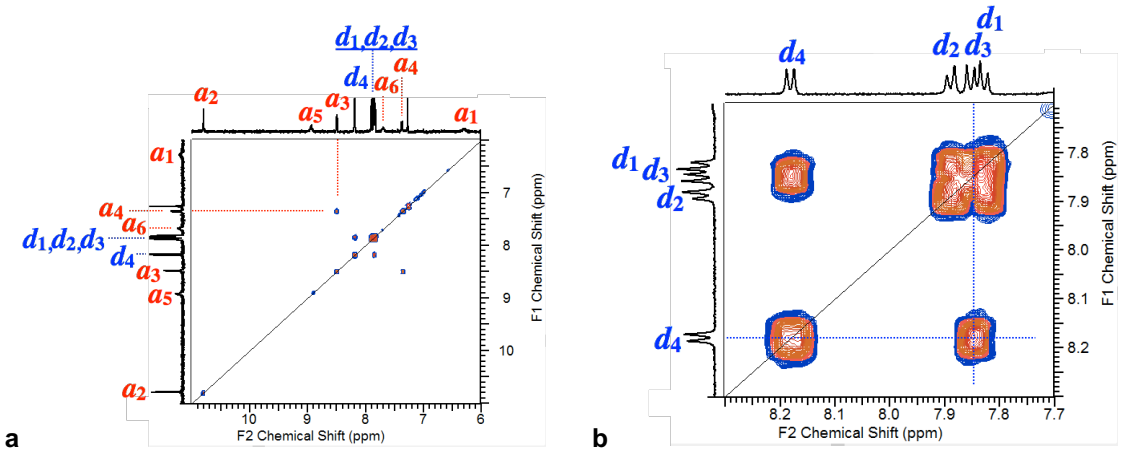

Figure 8S-15. ^{1}H-^{1}H correlation spectroscopy (COSY) NMR of **Aaa(DPP)**, focusing on (a) the aromatic region, and (b) the DPP protons. (600 MHz, $CDCl_3$).

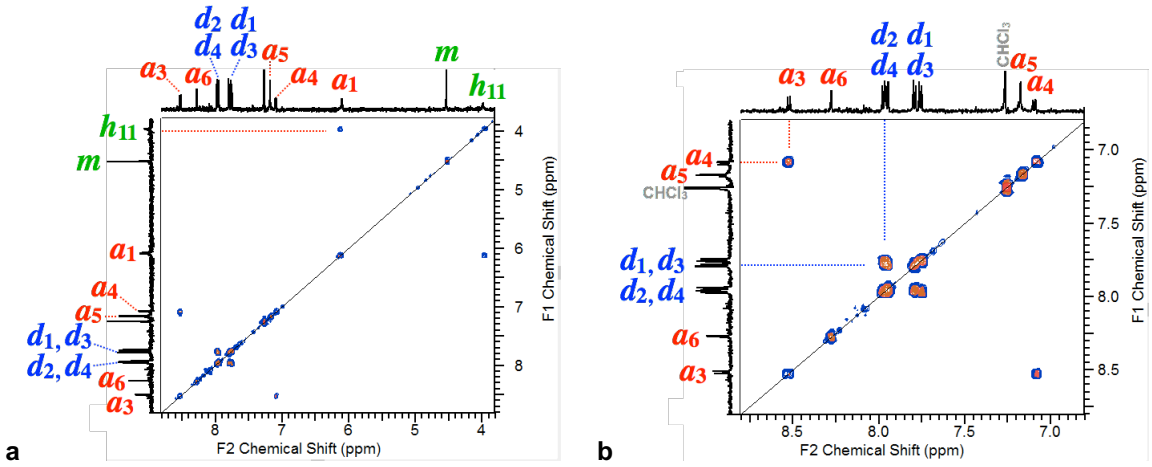

Figure 8S-16. COSY of **DPP-Aaa**, focusing on (a) the aromatic and a part of the aliphatic regions; and (b) the aromatic region. (600 MHz, $CDCl_3$).

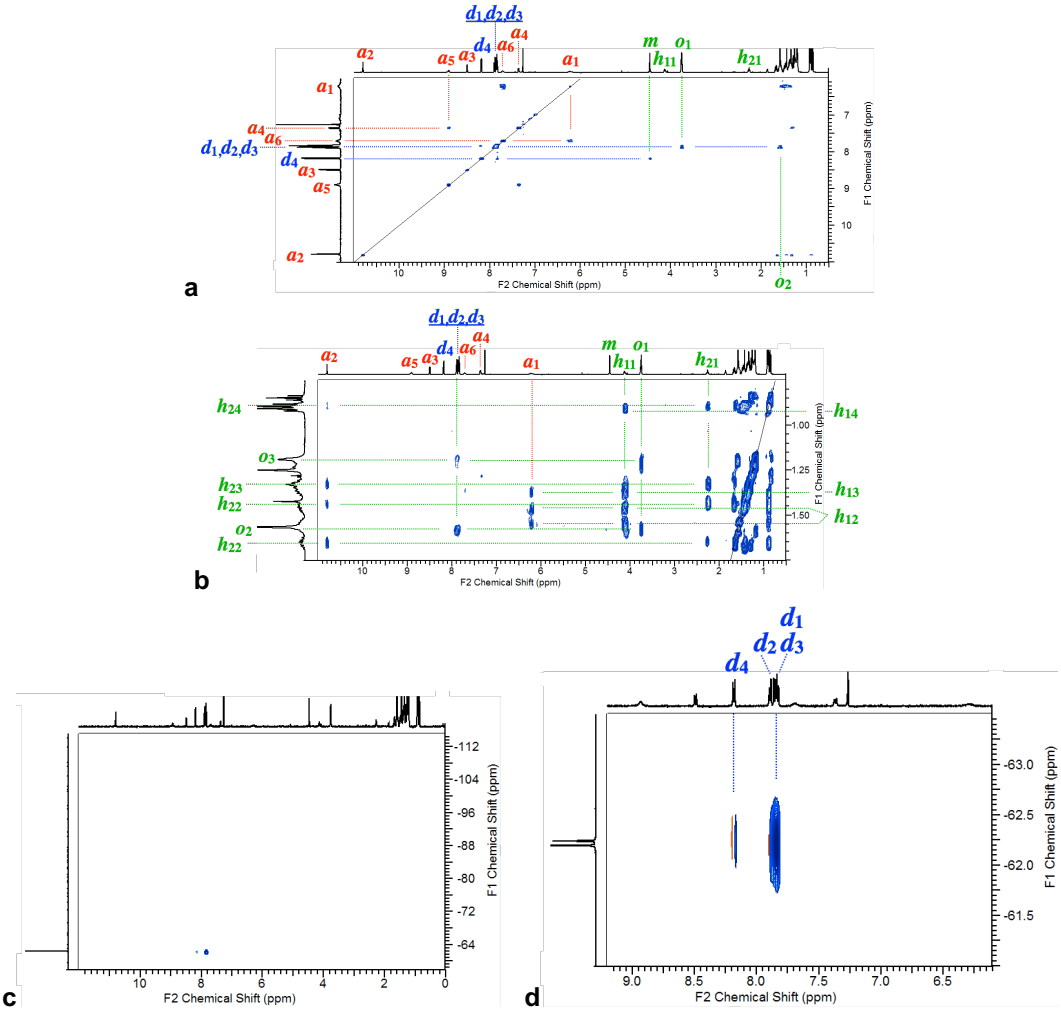

Figure 8S-17. Nuclear Overhauser effect spectroscopy (NOESY) of **Aaa(DPP)**. (a,b) ^{1}H-^{1}H NOESY with expanded (a) aromatic and (b) aliphatic regions along F1. (c,d) ^{1}H-^{19}F heteronuclear Overhauser effect spectroscopy (HOESY). (600 MHz, $CDCl_3$).

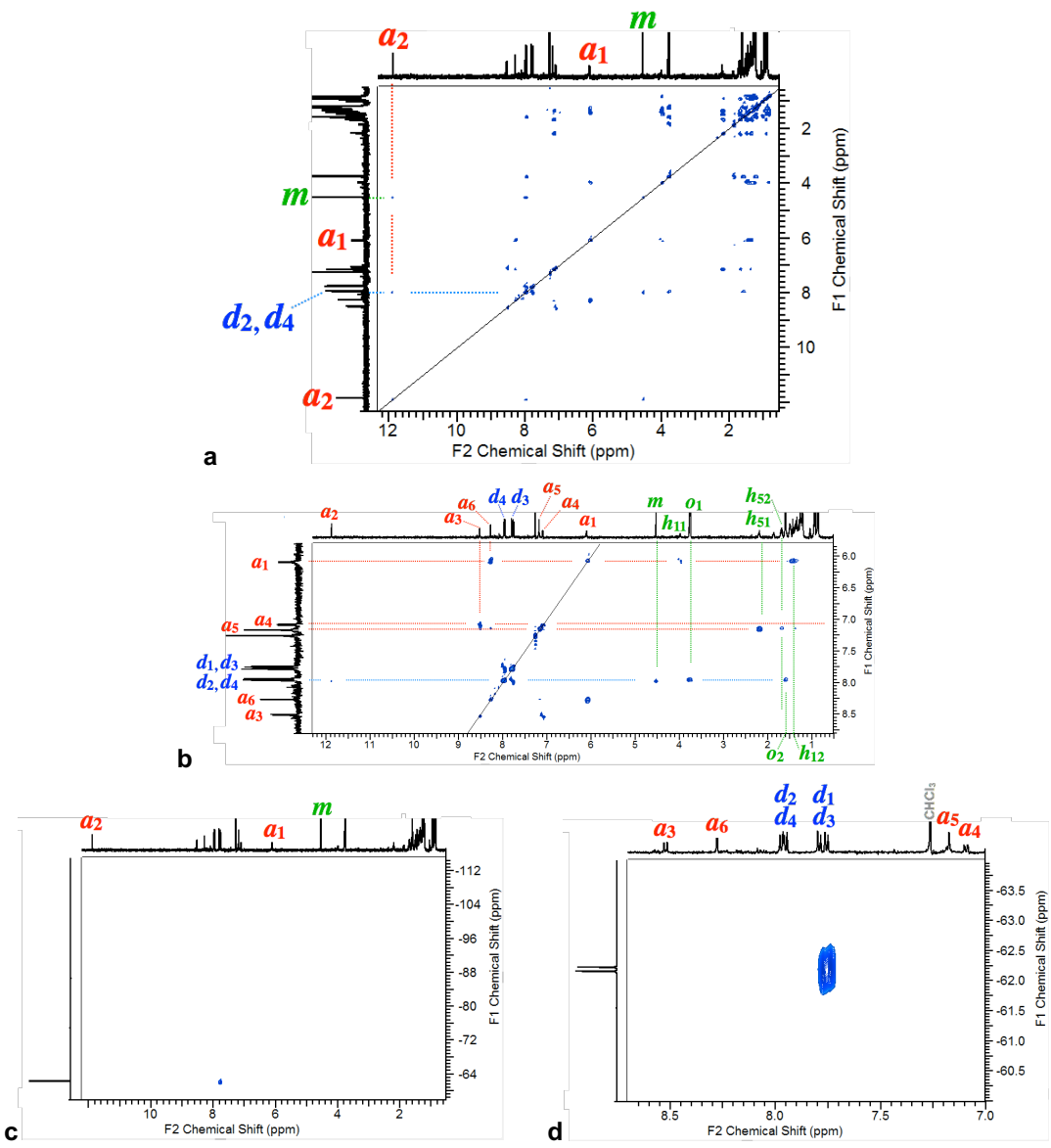

Figure 8S-18. Nuclear Overhauser effect spectroscopy (NOESY) of **DPP-Aaa**. (a) ^{1}H-^{1}H NOESY. (b) ^{1}H-^{1}H NOESY with expanded aromatic region along F1. (c,d) ^{1}H-^{19}F HOESY. (600 MHz, $CDCl_3$).

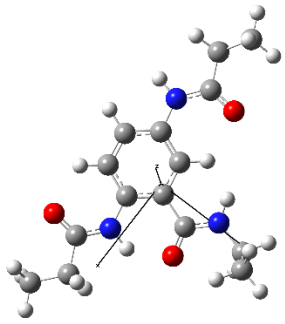

Figure 8S-19. Molecular structure of **Aaa** (with truncated alkyls) along with the coordinate system, used for the computational studies.

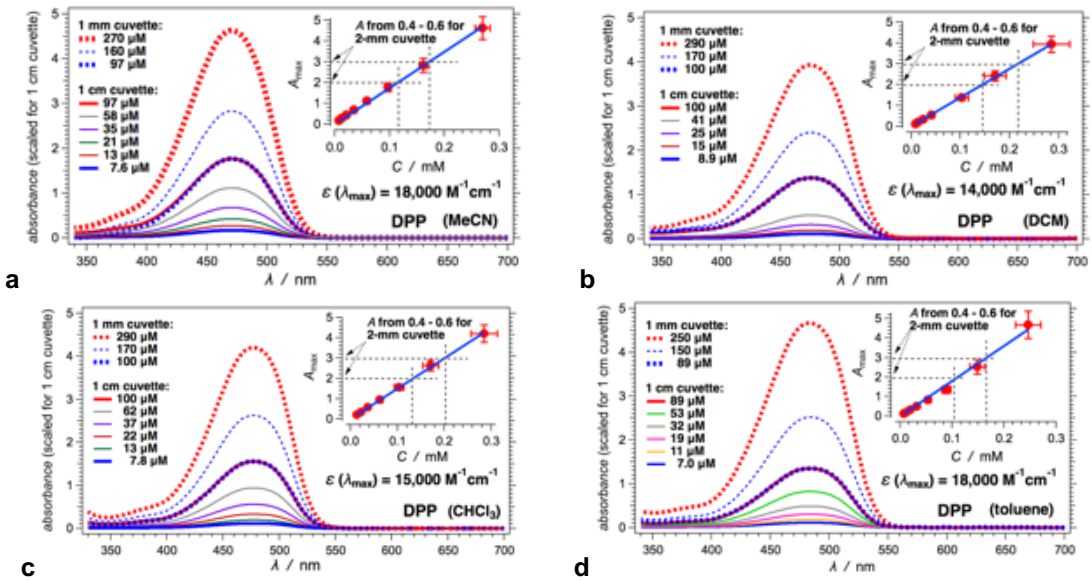

Figure 8S-20. Concentration dependence of the optical absorption of **DPP** for various solvents, recorded with 1-cm and 1-mm cuvettes. The spectra measured with 1-mm cuvettes are multiplied by 10 to scale them up to the spectra recorded with 1-cm optical path length. Insets: the slopes of the linear fits of the absorbance at the maxima vs. the concentration yield the molar extinction coefficients. The dashed gray lines show the absorbance and concentration ranges that we use for transient-absorption measurements, requiring $A(\lambda_{ex})$ between about 0.4 and 0.6 for 2-mm cuvette.

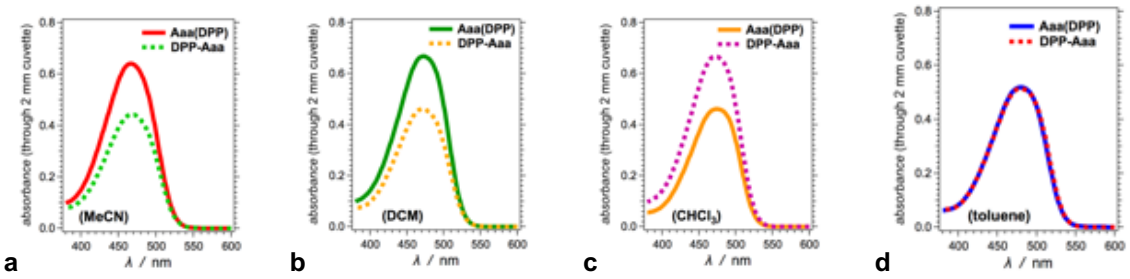

Figure 8S-21. Optical absorption spectra (recorded with 2-mm cuvettes) of dyad samples for TA measurements. $C_{\text{Aaa(DPP)}}$ = 180 μM for MeCN, 240 μM for DCM, 150 μM for CHCl3, and 140 μM for toluene; and $C_{\text{DPP-Aaa}}$ = 120 μM for MeCN, 160 μM for DCM, 220 μM for CHCl3, and 140 μM for toluene.

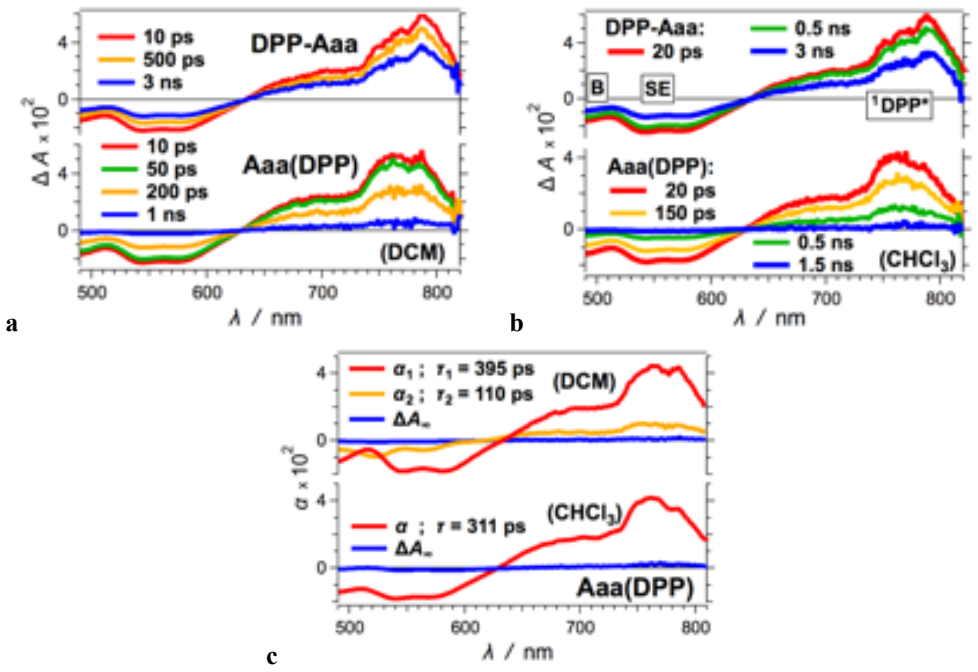

Figure 8S-22. (a,b) TA spectra of **DPP-Aaa** and **Aaa(DPP)** for DCM and $CHCl_3$ (λ_{ex} = 465 nm, 50-fs pulses, 4 μJ per pulse). For the spectra for MeCN and toluene, see Figure 2b. (c) Wavelength dependence of the amplitudes, α_i, from (multi)exponential global fits to $\Delta A(\lambda,t)$ of **Aaa(DPP)** for DCM and $CHCl_3$, i.e., $\Delta A(\lambda,t) = \Delta A_\infty(\lambda) + \Sigma_i\, \alpha_i(\lambda)\, \exp(-\, t / \tau_i)$.

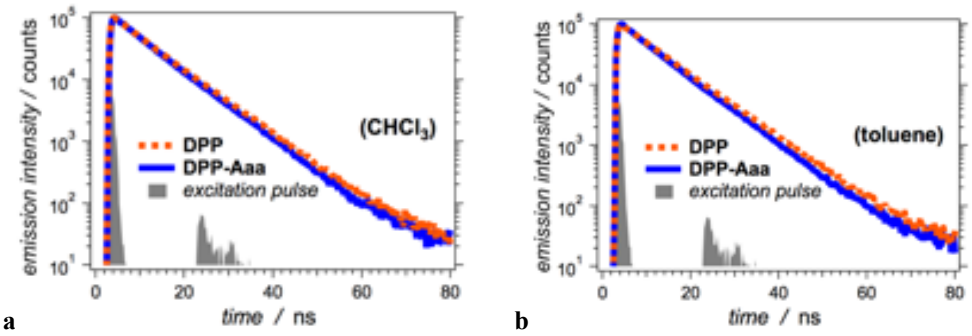

Figure 8S-23. Time-correlated single-photon counting (TCSPC) emission decays of **DPP-Aaa** and **DPP** for chloroform and toluene (λ_{ex} = 406 nm, 196-ps pulse, λ_{em} = 540 nm,).

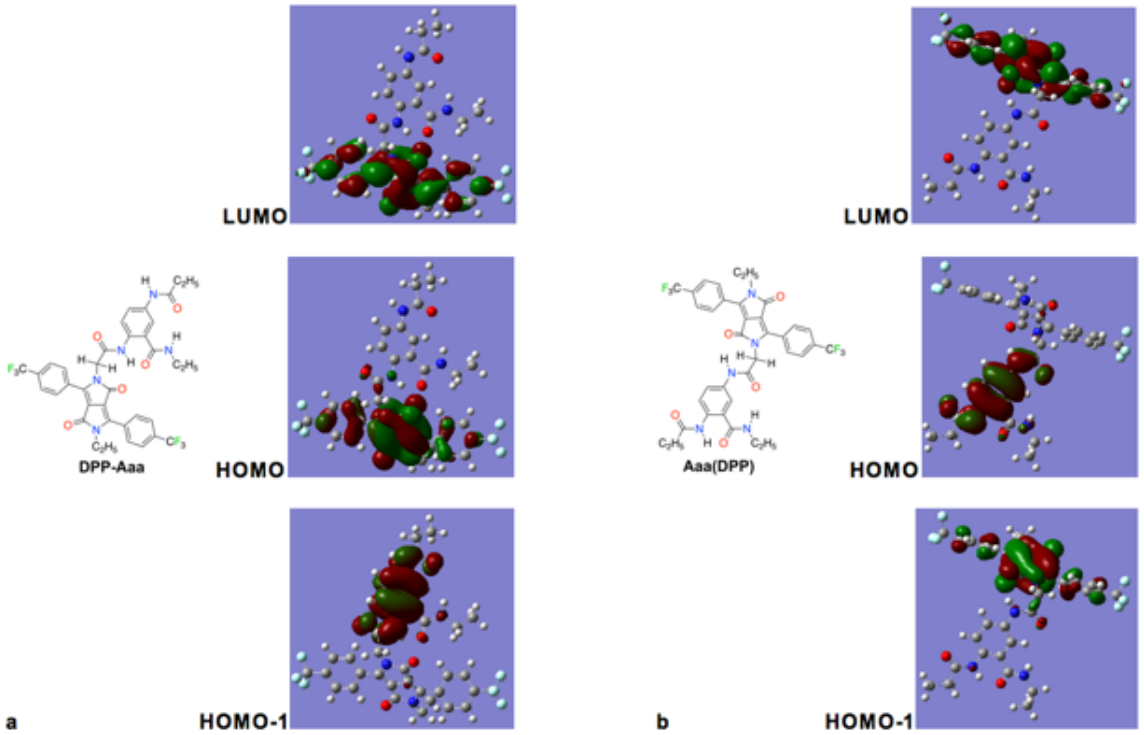

Figure 8S-24. Frontier orbitals of the two dyads placed on minimized structures, obtained from DFT calculations for the ground states with implementation of toluene as a solvent medium. For reducing the computational times, the alkyl chains are truncated to ethyls.

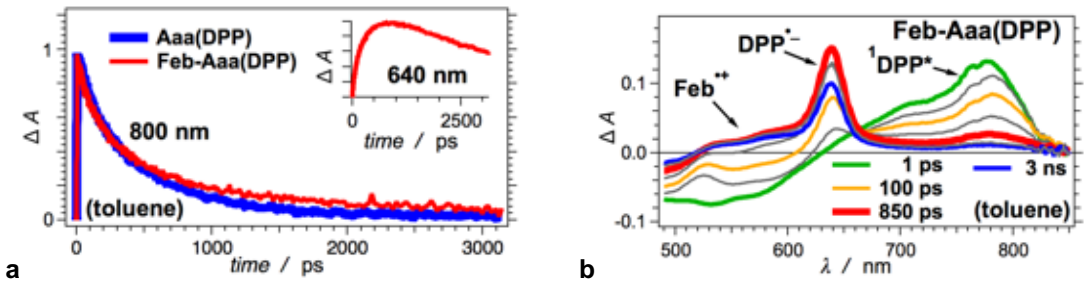

Figure 8S-25. TA kinetic curves and spectra depicting the excited-state dynamics of **Feb-Aaa(DPP)** for toluene (λ_{ex} = 465 nm, 50-fs pulses, 4 μJ per pulse). (a) Comparison between normalized ^{1}**DPP*** decays, monitored at 800 nm, of **Feb-Aaa(DPP)** and **Aaa(DPP)**. Beyond 1,000 ps, it appears that the decay of **Feb-Aaa(**^{1}**DPP*)** has a small-amplitude long-lived component that **Aaa(**^{1}**DPP*)** does not have. The absorption of the **DPP** radical anion, however, tails to 800 nm,[1a] resulting in the slight difference between the decays for the dyad and the triad in the nanosecond time scale. Inset: the kinetic curve showing the rise and decay of **DPP**$^{\bullet-}$ in **Feb-Aaa(DPP)**, monitored at 640 nm. (b) TA spectra of **Feb-Aaa(DPP)** for toluene, showing the decay of the **DPP** singlet excited state and the rise and decay of the CT state, i.e., of the radical ions of **DPP** and **Feb**.

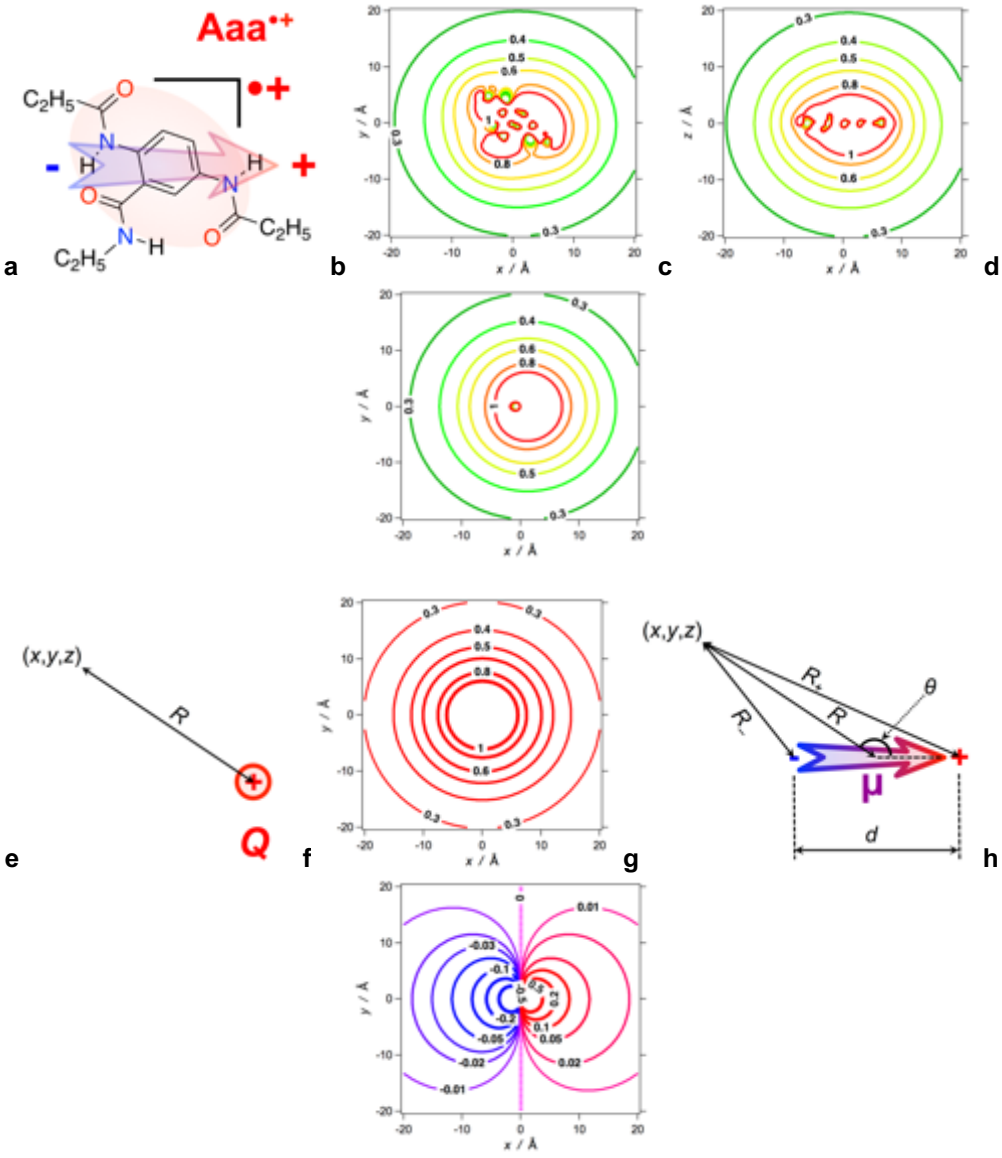

Figure 8S-26. Spatial distribution of the electric potential around the oxidized electron donor, Aaa$^{\bullet+}$, for toluene. (The values of the isopotential curves on the contour plots are in V) (a) Structure of **Aaa**$^{\bullet+}$ with dipole moment as estimated from DFT calculations (Table S1). (b,c) Distribution of the potential obtained from the charges and coordinates of the **Aaa**$^{\bullet+}$ atoms, calculated using eq. S5. (d) Distribution of superposed potentials originating from the **Aaa**$^{\bullet+}$ total charge, Q, and the **Aaa**$^{\bullet+}$ dipole, **μ** (eq. S6). (e,f) Spherically symmetric distribution of the electric potential, φ_Q, around a point charge +1, corresponding to the total charge of **Aaa**$^{\bullet+}$ (eq. S6b). (g,h) Cylindrically symmetric distribution of the potential, φ_{μ}, around the **Aaa**$^{\bullet+}$ dipole, **μ** (Table 8S-1), corresponding to charges $+q$ and $-q$ at distance d from each other (eq. 8S-6c,d).

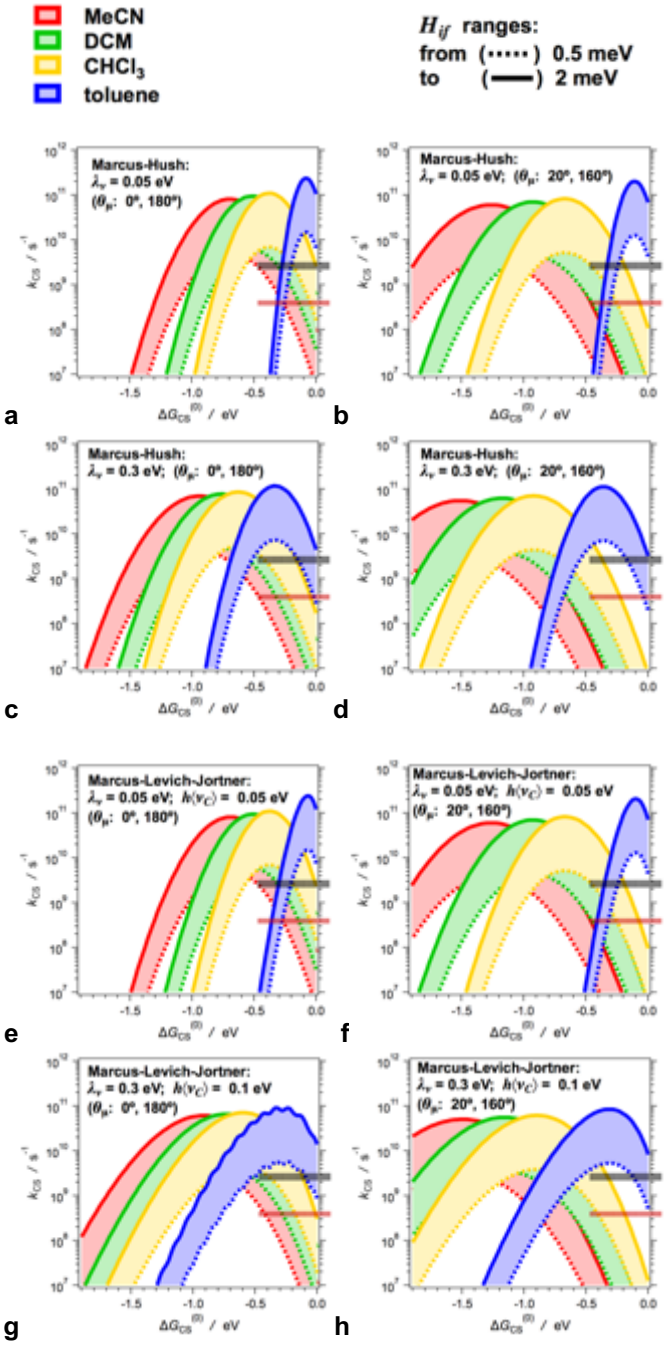

Figure 8S-27. Dependence of the ET rate constants on the ET driving force produced by the MH and MLJ formalisms for different conditions and input parameters. The striped red lines represent the CS rate constants for MeCN, and the black striped lies represent the CS rate constants for **Aaa(DPP)** in DCM, $CHCl_3$, and toluene.

Charts

Chart 8S-1. Labels of the protons of (a) **Aaa(DPP)** and (b) **DPP-Aaa**.

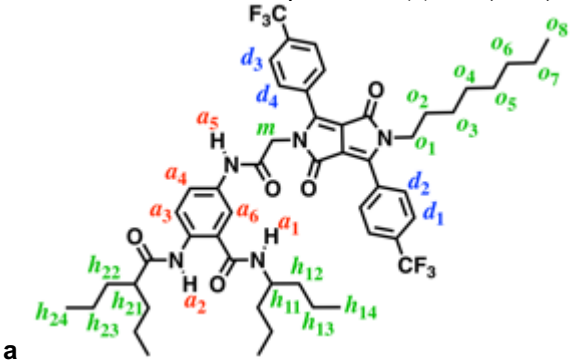

a

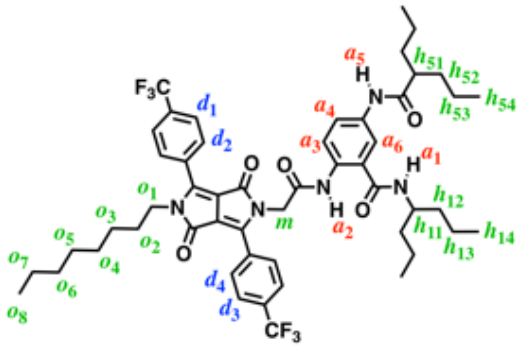

b

Tables

Table 8S-1. Dipole moments of the neutral ground-state **Aaa** and its radical cation, **Aaa**$^{\bullet+}$, for various solvation media.[a]

solvent	**Aaa**				**Aaa**$^{\bullet+}$				$\Delta\alpha_{\mu}$ / deg [c]
	μ / D [b]	dipole-vector components			μ / D [b]	dipole-vector components			
		μ_x / D	μ_y / D	μ_z / D		μ_x / D	μ_y / D	μ_z / D	
gas phase	3.6961	-3.6920	0.1018	0.1412	4.5362	-3.7353	-2.445	0.8039	35.47
toluene	4.2367	-4.2254	0.1406	0.2753	5.4719	-4.5069	-2.904	1.0942	35.23
$CHCl_3$	4.4953	-4.4794	0.1147	0.3595	6.0546	-4.9879	-3.1389	1.3879	34.31
DCM	4.6532	-4.6190	0.0966	0.5551	6.1828	-5.1338	-3.2969	1.0007	33.65
MeCN	4.7906	-4.7132	0.0365	0.8570	6.8031	-5.6102	-3.3604	1.8749	31.03

[a] For **Aaa**, dipoles are calculated using the CHELPG procedure at the CAM-B3LYP/6-311+G(d,p) level of theory; and for **Aaa**$^{\bullet+}$ – using the CHELPG procedure at the unrestricted CAM-B3LYP/6-311+G(d,p) level of theory. [b] Magnitude of the dipoles. [c] The angle between the dipoles of **Aaa** and **Aaa**$^{\bullet+}$, representing the shift of the dipole orientation upon single-electron oxidation of **Aaa**.

Table 8S-2. Photophysical properties of **DPP**, **DPP-Aaa** and **Aaa(DPP)** for various solvents.

sample	λ_{abs} / nm [a]	λ_{fl} / nm [a]	$\mathscr{E}_{00}$ / eV [b]	Φ_f [c]	τ / ns [d]	k_f / ns^{-1} [e]	k_{nr} / ns^{-1} [e]
DPP							
MeCN	470	536	2.42	0.75 ± 0.15	8.39 ± 0.12	0.090 ± 0.018	0.029 ± 0.006
DCM	475	542	2.39	0.84 ± 0.18	8.33 ± 0.10	0.10 ± 0.02	0.019 ± 0.004
$CHCl_3$	477	540	2.40	0.80 ± 0.11	8.12 ± 0.11	0.098 ± 0.013	0.025 ± 0.003
toluene	481	549	2.37	0.77 ± 0.09	7.95 ± 0.46	0.097 ± 0.012	0.029 ± 0.004
DPP-Aaa							
MeCN	468	536	2.42	0.21 ± 0.04	2.10 ± 0.11	0.098 ± 0.019	0.38 ± 0.08
DCM	472	537	2.41	0.85 ± 0.09	7.59 ± 0.28	0.11 ± 0.01	0.020 ± 0.002
$CHCl_3$	472	536	2.42	0.86 ± 0.10	7.62 ± 0.31	0.11 ± 0.01	0.018 ± 0.002
toluene	480	543	2.38	0.76 ± 0.13	7.57 ± 0.21	0.10 ± 0.02	0.031 ± 0.005
Aaa(DPP)							
MeCN	480	544	2.38	0.17 ± 0.06	1.91 ± 0.19	0.088 ± 0.031	0.44 ± 0.16
DCM	473	539	2.42	0.054 ± 0.006	0.369 ± 0.020	0.14 ± 0.02	2.6 ± 0.3
$CHCl_3$	474	536	2.43	0.051 ± 0.006	0.398 ± 0.023	0.13 ± 0.02	2.4 ± 0.3
toluene	461	536	2.42	0.051 ± 0.002	0.437 ± 0.010	0.12 ± 0.01	2.2 ± 0.1

[a] Wavelengths of the absorption and fluorescence spectral maxima. [b] Zero-to-zero energy obtained from the crossing point of the normalized absorption and emission spectra. [c] Fluorescence quantum yields. [d] Intensity-averaged lifetimes (Table S3). [e] Radiateive and non-radiative decay rate constants, i.e., $k_f = \Phi_f / \tau$, and $k_{vp} = (1 - \Phi_f) / \tau$,

Table 8S-3. Lifetimes of the singlet-excited state of **DPP** and its dyads for various solvents.

sample	τ_1 / ns (α_1) [a]	τ_2 / ns (α_2) [a]	$\bar{\tau}$ / ns [b]	$(\bar{\tau}_{dyad}^{-1} - \bar{\tau}_{DPP}^{-1})$ / ns^{-1}
DPP				
MeCN	8.39 ± 0.12		8.39 ± 0.12	
DCM	8.33 ± 0.10		8.33 ± 0.10	
$CHCl_3$	8.12 ± 0.11		8.12 ± 0.11	
toluene	2.46 ± 0.06	8.15 ± 0.21	7.95 ± 0.46	
	(0.110 ± 0.017)	(0.890 ± 0.019)		
DPP-Aaa				
MeCN	0.208 ± 0.018	2.12 ± 0.06	2.10 ± 0.11	0.357 ± 0.025
	(0.108 ± 0.007)	(0.892 ± 0.009)		
DCM	0.186 ± 0.018	7.61 ± 0.13	7.59 ± 0.28	0.0117 ± 0.0050
	(0.102 ± 0.005)	(0.898 ± 0.014)		
$CHCl_3$	0.332 ± 0.019	7.66 ± 0.15	7.62 ± 0.31	0.00809 ± 0.00557
	(0.113 ± 0.003)	(0.887 ± 0.014)		
toluene	0.292 ± 0.005	7.61 ± 0.11	7.57 ± 0.21	0.00623 ± 0.00812
	(0.124 ± 0.001)	(0.876 ± 0.006)		
Aaa(DPP)				
MeCN	0.145 ± 0.010	1.937 ± 0.106	1.91 ± 0.19	0.404 ± 0.051
	(0.166 ± 0.009)	(0.834 ± 0.014)		
DCM	0.110 ± 0.018	0.395 ± 0.022	0.378 ± 0.047	2.53 ± 0.33
	(0.191 ± 0.010)	(0.809 ± 0.040)		
$CHCl_3$	0.311 ± 0.004		0.311 ± 0.004	3.09 ± 0.04
toluene	0.0850 ± 0.0093	0.463 ± 0.028	0.444 ± 0.057	2.13 ± 0.29
	(0.226 ± 0.011)	(0.773 ± 0.039)		

[a] Obtained from global fits of TA data, i.e., $\Delta A(\lambda,t) = \Delta A_\infty(\lambda) + \Sigma_i\, \alpha_i(\lambda) \exp(-t / \tau_i)$. The amplitudes, α_i, are selected for the decay region of ^{1}**DPP***, i.e., 700 – 800 nm, where potential interference from the TA of other species, such as **DPP**$^{\bullet-}$ and **Aaa**$^{\bullet+}$ is minimal. The large time constants, i.e., $\tau_i > 1$ ns, were obtained from TCSPC data fits and introduced as held parameters in the TA global fits (Figure 8-2, 8S-22, 8S-23).
[b] Intensity-averaged lifetimes, $\bar{\tau} = (\Sigma_i\, \alpha_i \tau_i^2) / (\Sigma_i\, \alpha_i \tau_i)$.

Schemes

Scheme 8S-1. Activation of DPP carboxyl derivative.

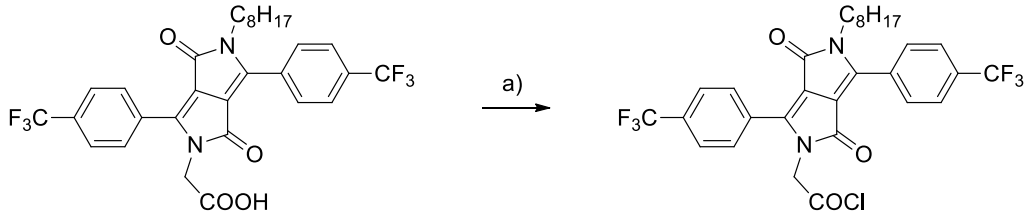

DPP-CH_2-COOH **DPP-CH_2-COCl**

a) $(COCl)_2$, DCM, pyridine, -78 °C to r.t., 30 min, quant.

Scheme 8S-2. Activation of Feb carboxyl derivative.

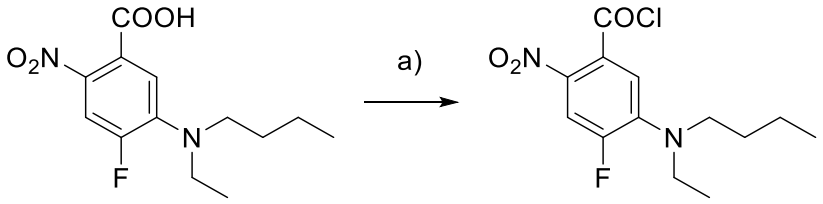

Feb-COOH **Feb-COCl**

a) $(COCl)_2$, DCM, pyridine, -78 °C to r.t., 30 min, quant.

Scheme 8S-3. Synthesis of DPP-Aaa.

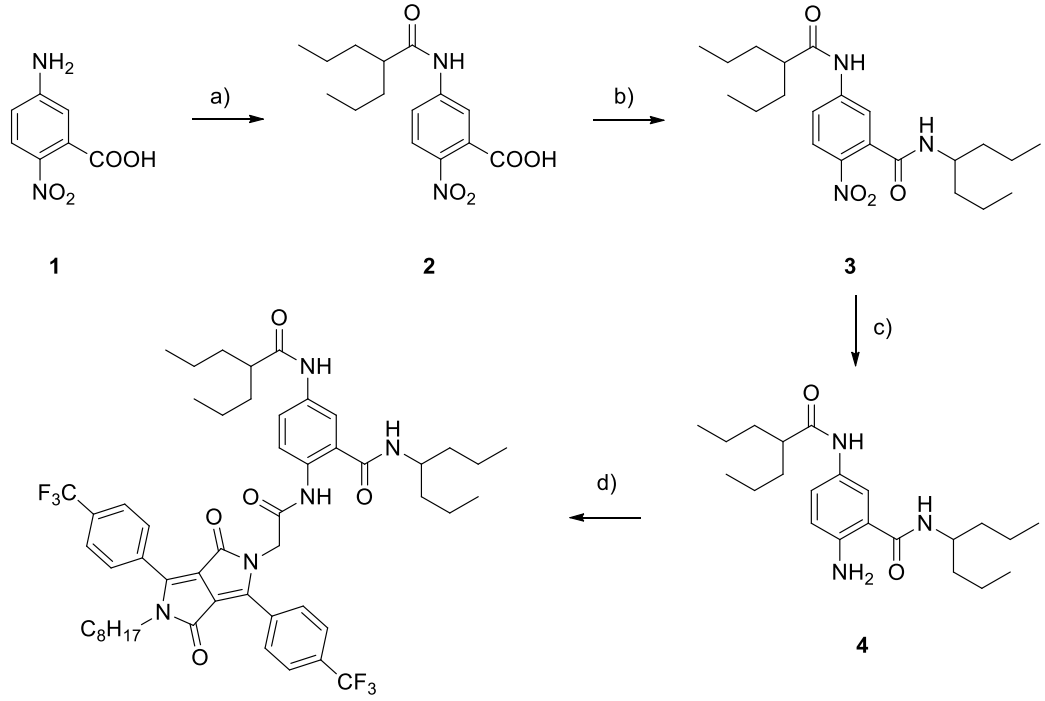

a) 2,2-Di-*n*-propylacetyl chloride, pyridine, THF, -78 °C to r.t., 3h, 70%; b) (1) $(COCl)_2$, DCM, DMF, -78 °C to r.t., 30 min, quant.; (2) 4-heptylamine, DCM, pyridine, -78 °C to r.t., 3h, 67%; c) $Co_2(CO)_8$, DME, H_2O, 90 °C, 1h, 90%; d) **DPP-CH_2-COCl**, DCM, pyridine, -78 °C to r.t., 3h, 20%.

Scheme 8S-4. Synthesis of Aaa(DPP).

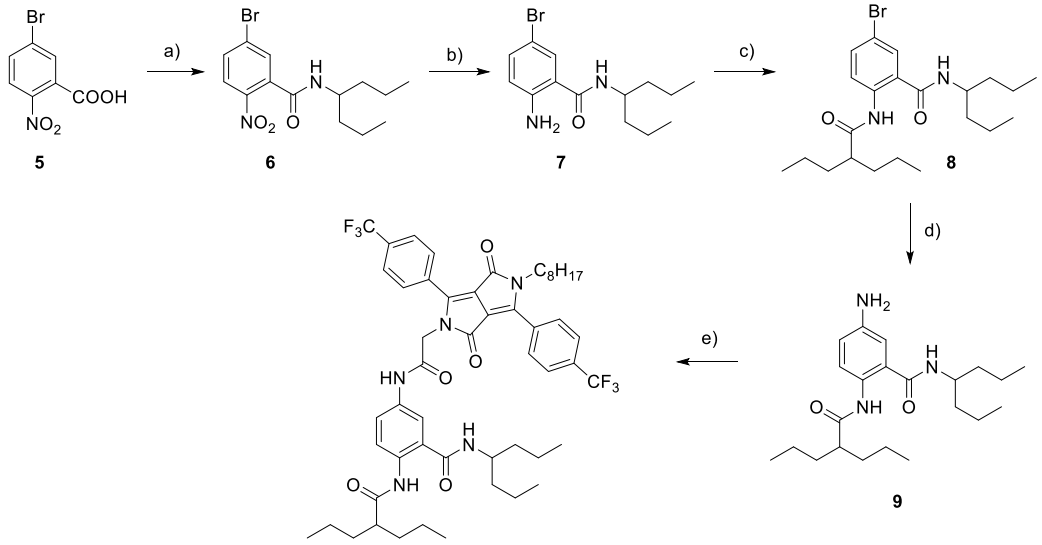

a) (1) $(COCl)_2$, DCM, DMF, -78 °C to r.t., 30 min, quant.; (2) 4-heptylamine, DCM, pyridine, -78 °C to r.t., 3h, 76%; b) $Co_2(CO)_8$, DME, H_2O, 90 °C, 1h, 75%; c) 2,2-Di-*n*-propylacetyl chloride, pyridine, THF, -78 °C to r.t., overnight, 91%; d) NaN_3, CuI, DMEDA, sodium ascorbate, DMF, 100 °C, 1h, 60% e) **DPP-CH_2-COCl**, DCM, pyridine, -78 °C to r.t., 3h, 20%.

Scheme 8S-5. Synthesis of Feb-Aaa(DPP).

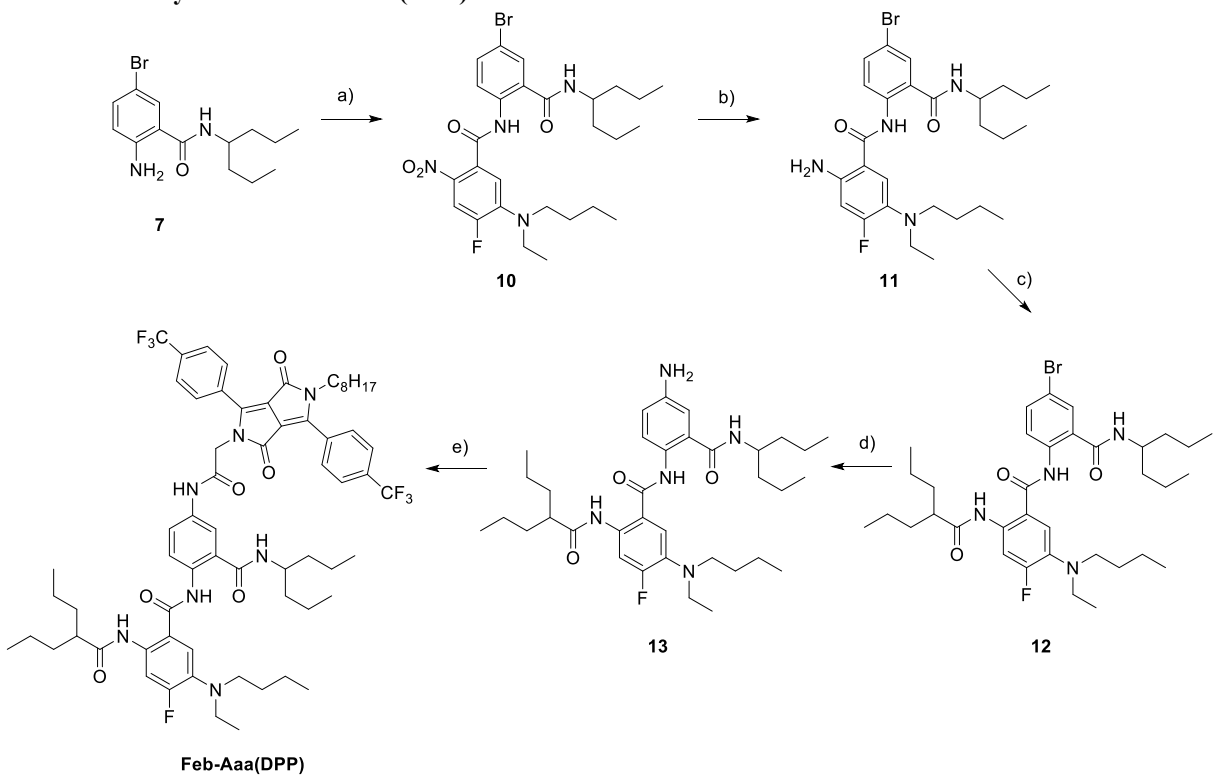

a) **Feb-COCl**, DCM, pyridine, -78 °C to r.t., 3h, 88%; b) $Co_2(CO)_8$, DME, H_2O, 90 °C, 1h, 95%; c) 2,2-Di-*n*-propylacetyl chloride, pyridine, THF, -78 °C to r.t., 4h, 95%; d) NaN_3, CuI, DMEDA, sodium ascorbate, DMF, 100 °C, 1h, 78%; e) **DPP-CH_2-COCl**, DCM, pyridine, -78 °C to r.t., 2h, 25%.

Scheme 8S-6. Structure of the Feb-Aaa(DPP) triad and its charge-transfer properties.

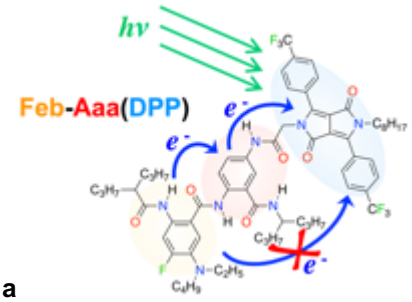

a

b

References

[1] a) A. Purc, E. M. Espinoza, R. Nazir, J. J. Romero, K. Skonieczny, A. Jeżewski, J. M. Larsen, D. T. Gryko, V. I. Vullev, *J. Am. Chem. Soc.* **2016**, *138*, 12826-12832; b) E. M. Espinoza, J. M. Larsen-Clinton, M. Krzeszewski, N. Darabedian, G. D. T., V. I. Vullev, *Pure Appl. Chem.* **2017**, *89*, 1777-1797; c) J. M. Larsen-Clinton, E. M. Espinoza, M. F. Mayther, J. Clark, C. Tao, D. Bao, C. M. Larino, M. Wurch, S. Lara, V. I. Vullev, *Phys. Chem. Chem. Phys.* **2017**, *19*, 7871-7876.

[2] H. Y. Lee, M. An, *B. Kor. Chem. Soc.* **2004**, *25*, 1717-1719.

[3] M. J. Frisch, G. W. Trucks, H. B. Schlegel, G. E. Scuseria, M. A. Robb, J. R. Cheeseman, G. Scalmani, V. Barone, B. Mennucci, G. A. Petersson, H. Nakatsuji, e. al., in *Gaussian 09, Revision D.01, Vol. Gaussian 09, Revision D.01*, Gaussian 09, Revision D.01 ed., Gaussian, Inc., Wallingford, **2013**.

[4] a) A. D. Becke, *J. Chem. Phys.* **1993**, *98*, 5648-5652; b) C. T. Lee, W. T. Yang, R. G. Parr, *Phys. Rev. B* **1988**, *37*, 785-789.

[5] T. Yanai, D. P. Tew, N. C. Handy, *Chem. Phys. Lett.* **2004**, *393*, 51-57.

[6] M. Cossi, V. Barone, R. Cammi, J. Tomasi, *Chem. Phys. Lett.* **1996**, *255*, 327-335.

[7] C. M. Breneman, K. B. Wiberg, *Journal of Comput. Chem.* **1990**, *11*, 361-373.

[8] a) L. Onsager, *J. Am. Chem. Soc.* **1936**, *58*, 1486-1493; b) S. Upadhyayula, D. Bao, B. Millare, S. S. Sylvia, K. M. M. Habib, K. Ashraf, A. Ferreira, S. Bishop, R. Bonderer, S. Baqai, X. Jing, M. Penchev, M. Ozkan, C. S. Ozkan, R. K. Lake, V. I. Vullev, *J. Phys. Chem. B* **2011**, *115*, 9473-9490.

[9] E. M. Espinoza, J. M. Larsen, V. I. Vullev, *J. Phys. Chem. Lett.* **2016**, *7*, 758-764.

[10] D. Bao, B. Millare, W. Xia, B. G. Steyer, A. A. Gerasimenko, A. Ferreira, A. Contreras, V. I. Vullev, *J. Phys. Chem. A* **2009**, *113*, 1259-1267.

[11] a) D. Bao, S. Ramu, A. Contreras, S. Upadhyayula, J. M. Vasquez, G. Beran, V. I. Vullev, *J. Phys. Chem. B* **2010**, *114*, 14467-14479; b) E. M. Espinoza, B. Xia, N. Darabedian, J. M. Larsen, V. Nunez, D. Bao, J. T. Mac, F. Botero, M. Wurch, F. Zhou, V. I. Vullev, *Eur. J. Org. Chem.* **2016**, *2016*, 343-356.

[12] a) B. Bahmani, S. Gupta, S. Upadhyayula, V. I. Vullev, B. Anvari, *J. Biomed. Opt.* **2011**, *16*, 051303/051301-051303/051310; b) B. Bahmani, C. Y. Lytle, A. M. Walker, S. Gupta, V. I. Vullev, B. Anvari, *Int. J. Nanomedicine* **2013**, *8*, 1609-1620; c) V. Nuñez, S. Upadhyayula, B. Millare, J. M. Larsen, A. Hadian, S. Shin, P.

Vandrangi, S. Gupta, H. Xu, A. P. Lin, G. Y. Georgiev, V. I. Vullev, *Anal. Chem.* **2013**, *85*, 4567-4577; d) B. Bahmani, Y. Guerrero, D. Bacon, V. Kundra, V. I. Vullev, B. Anvari, *Laser Surg. Med.* **2014**, *46*, 582-592; e) K. Chau, B. Millare, A. Lin, S. Upadhyayula, V. Nuñez, H. Xu, V. I. Vullev, *Microfluid. Nanofluid.* **2011**, *10*, 907-917; f) S. Gupta, M. R. Chatni, A. L. N. Rao, V. I. Vullev, L. V. Wang, B. Anvari, *Nanoscale* **2013**, *5*, 1772-1776.

[13] a) J. Wan, A. Ferreira, W. Xia, C. H. Chow, K. Takechi, P. V. Kamat, G. Jones, V. I. Vullev, *J. Photochem. Photobiol. A* **2008**, *197*, 364-374; b) H. Lu, D. Bao, M. Penchev, M. Ghazinejad, V. I. Vullev, C. S. Ozkan, M. Ozkan, *Advanced Science Letters* **2010**, *3*, 101-109; c) B. Jung, V. I. Vullev, B. Anvari, *IEEE J. Select. Top. Quantum Electron.* **2014**, *20*, 7000409/7000401-7000409/7000409.

[14] J. N. Demasa, G. A. Crosby, *J. Phys. Chem.* **1971**, *75*, 991-1024.

[15] a) R. Sjöback, J. Nygren, M. Kubista, *Spectrochim. Acta A* **1995**, *51*, L7-L21; b) X. F. Zhang, J. L. Zhang, L. M. Liu, *J. Fluoresc.* **2014**, *24*, 819-826.

[16] a) S. Guo, D. Bao, S. Upadhyayula, W. Wang, A. B. Guvenc, J. R. Kyle, H. Hosseinibay, K. N. Bozhilov, V. I. Vullev, C. S. Ozkan, M. Ozkan, *Adv. Funct. Mater.* **2013**, *23*, 5199-5211; b) G. Jones, II, L. N. Lu, V. Vullev, D. Gosztola, S. Greenfield, M. Wasielewski, *Bioorg. Med. Chem. Lett.* **1995**, *5*, 2385-2390; c) M. Krzeszewski, T. Kodama, E. M. Espinoza, V. I. Vullev, T. Kubo, D. T. Gryko, *Chem. - Eur. J.* **2016**, Ahead of Print; d) K. Skonieczny, J. Yoo, J. M. Larsen, E. M. Espinoza, M. Barbasiewicz, V. I. Vullev, C.-H. Lee, D. T. Gryko, *Chem. - Eur. J.* **2016**, *22*, 7485-7496; e) V. Gray, P. Xia, Z. Huang, E. Moses, A. Fast, D. A. Fishman, V. I. Vullev, M. Abrahamsson, K. Moth-Poulsen, M. Lee Tang, *Chem. Sci.* **2017**, *8*, 5488-5496.

[17] S. Upadhyayula, V. Nunez, E. M. Espinoza, J. M. Larsen, D. Bao, D. Shi, J. T. Mac, B. Anvari, V. I. Vullev, *Chem. Sci.* **2015**, *6*, 2237-2251.

[18] D. Rehm, A. Weller, *Israel J. Chem.* **1970**, *8*, 259-271.

[19] a) R. J. Magyar, S. Tretiak, *J. Chem. Theory Comput.* **2007**, *3*, 976-987; b) H. G. Ryu, M. F. Mayther, J. Tamayo, C. Azarias, E. M. Espinoza, M. Banasiewicz, L. G. Lukasiewicz, Y. M. Poronik, A. Jezewski, J. Clark, J. B. Derr, K. H. Ahn, D. T. Gryko, D. Jacquemin, V. I. Vullev, *J. Phys. Chem. C* **2018**, ASAP. DOI: 10.1021/acs.jpcc.7b11194